

APRIL 2021

AJNR

VOLUME 42 • PP 617-806

AJNR

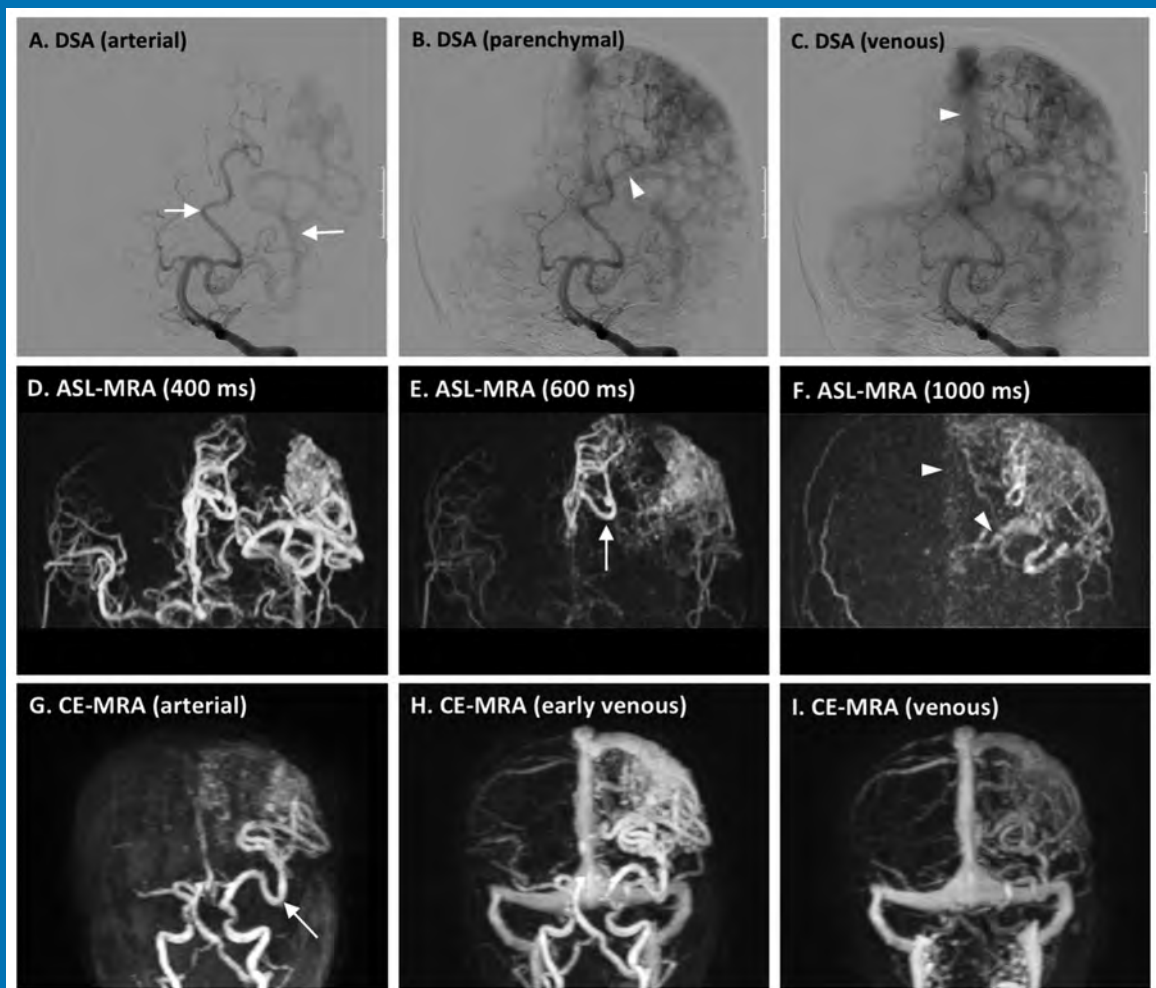
AMERICAN JOURNAL OF NEURORADIOLOGY

APRIL 2021
VOLUME 42
NUMBER 4
WWW.AJNR.ORG

THE JOURNAL OF DIAGNOSTIC AND
INTERVENTIONAL NEURORADIOLOGY

Imaging treated AVMs with ASL and CE-MRA
Vessel architectural imaging in glioblastoma
Deep learning model for metastatic disease
Clinical, imaging, and lab correlates of severe COVID-19

Official Journal ASNR • ASFNR • ASHNR • ASPNR • ASSR



FRED™

Flow Re-Direction
Endoluminal Device

FLOW DIVERSION.



SIMPLIFIED.



MicroVention Worldwide
Innovation Center
35 Enterprise
Aliso Viejo, CA 92656 USA
MicroVention UK Limited
MicroVention Europe S.A.R.L.
MicroVention Deutschland GmbH
Web

PH +1 714.247.8000

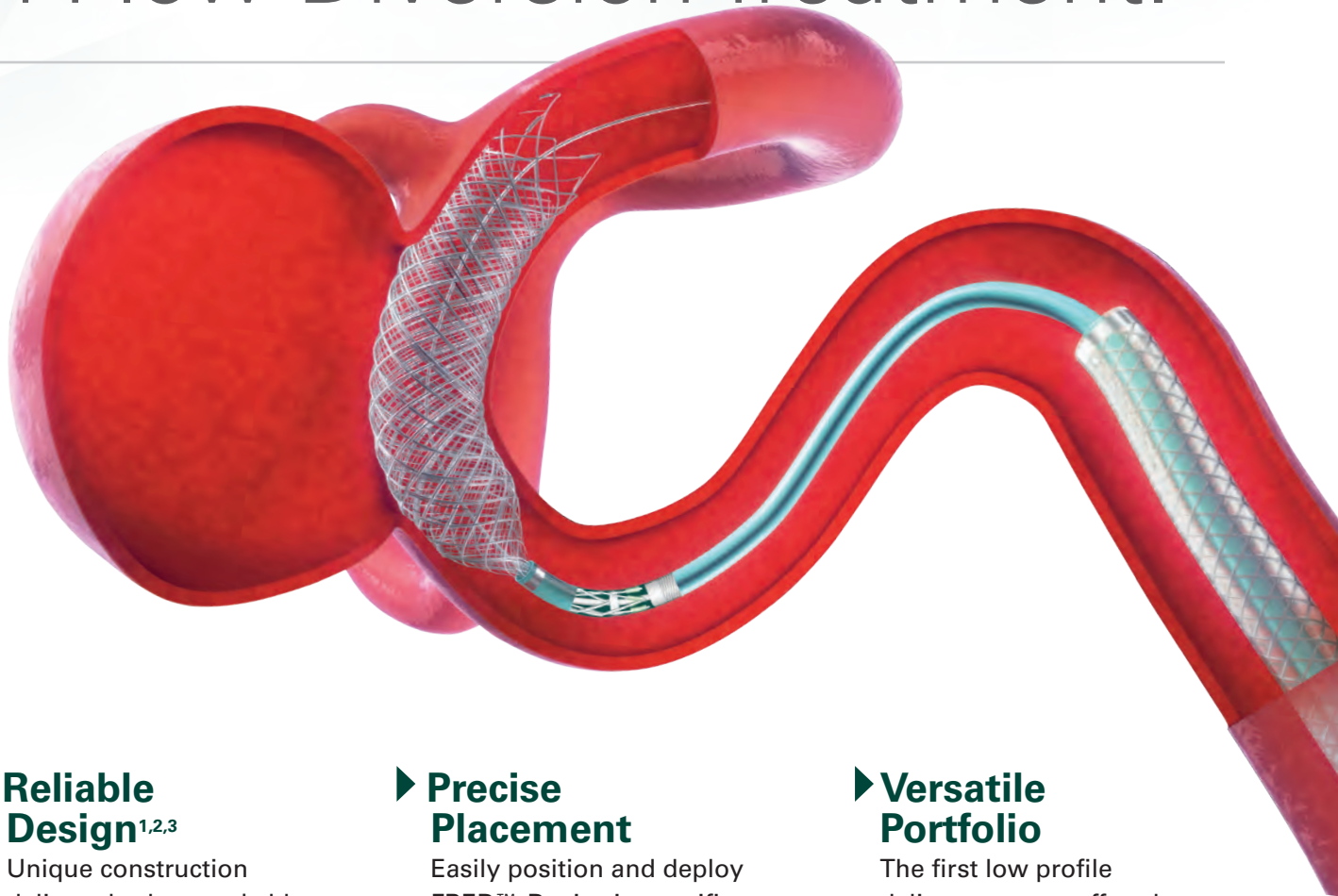
PH +1 44 (0) 191 258 6777

PH +33 (1) 39 21 77 46

PH +49 211 210 798-0

microvention.com

The New Standard of **Ease and Simplicity** in Flow Diversion Treatment.



► **Reliable Design**^{1,2,3}

Unique construction delivers both remarkable ease of use and excellent flow diversion^{1,2,3}

► **Precise Placement**

Easily position and deploy FRED™ Device in specific, targeted locations^{4,5,6}

► **Versatile Portfolio**

The first low profile delivery system offered in combination with large diameter and long length options

References:

1. TR11-211 2. TR13-171 3. TR15-055 4. TR13-192 5. TR15-072 6. TR19-145

The Flow Re-Direction Endoluminal Device (FRED™) System is indicated for use in the internal carotid artery from the petrous segment to the terminus for the endovascular treatment of adult patients (22 years of age or older) with wide-necked (neck width ≥ 4 mm or dome-to-neck ratio < 2) saccular or fusiform intracranial aneurysms arising from a parent vessel with a diameter ≥ 2.0 mm and ≤ 5.0 mm.

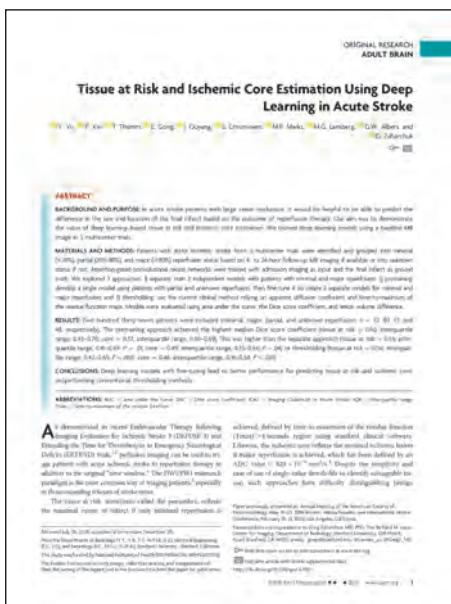
Use of the FRED™ System is contraindicated under these circumstances: Patients in whom anticoagulant, anti-platelet therapy, or thrombolytic drugs are contraindicated. Patients with known hypersensitivity to metal such as nickel-titanium and metal jewelry. Patients with anatomy that does not permit passage or deployment of the FRED™ System. Patients with an active bacterial infection. Patients with a pre-existing stent in place at the target aneurysm. Patients in whom the parent vessel size does not fall within the indicated range. Patients who have not received dual anti-platelet agents prior to the procedure. For complete indications, contraindications, potential complications, warnings, precautions, and instructions, see instructions for use (IFU provided in the device).

RX Only: Federal (United States) law restricts this device to sale by or on the order of a physician.

MICROVENTION™ and FRED™ are registered trademarks of MicroVention, Inc. in the United States and other jurisdictions. © 2020 MicroVention, Inc. 04/2020.

LUCIEN LEVY BEST RESEARCH ARTICLE AWARD WINNER AND NOMINEES NAMED

This award is named for the late *AJNR* Senior Editor who championed its establishment and recognizes the best original research paper accepted in 2020. The winning paper was published electronically on March 25, 2021. It was selected by a vote of the *Journal's* Editor-in-Chief and Senior Editors.



The Editors of *AJNR* are pleased to announce the annual Lucien Levy Best Research Article Award has been presented to

“Tissue at Risk and Ischemic Core Estimation Using Deep Learning in Acute Stroke”

by Y. Yu, Y. Xie, T. Thamm, E. Gong, J. Ouyang, S. Christensen, M.P. Marks, M.G. Lansberg, G.W. Albers, and G. Zaharchuk

Other nominated papers were:

“Characterizing White Matter Tract Organization in Polymicrogyria and Lissencephaly: A Multifiber Diffusion MRI Modeling and Tractography Study” by F. Arrigoni, D. Peruzzo, S. Mandelstam, G. Amoroso, D. Redaelli, R. Romaniello, R. Leventer, R. Borgatti, M. Seal, and J.Y.-M. Yang

“COVID-19 Is an Independent Risk Factor for Acute Ischemic Stroke” by P. Belani, J. Schefflein, S. Kihira, B. Rigney, B.N. Delman, K. Mahmoudi, J. Mocco, S. Majidi, J. Yeckley, A. Aggarwal, D. Lefton, and A.H. Doshi

“Posttreatment Imaging in Patients with Head and Neck Cancer without Clinical Evidence of Recurrence: Should Surveillance Imaging Extend Beyond 6 Months?” by A. Gore, K. Baugnon, J. Beitler, N.F. Saba, M.R. Patel, X. Wu, B.J. Boyce, and A.H. Aiken

“Analysis of Stroke Detection during the COVID-19 Pandemic Using Natural Language Processing of Radiology Reports” by M.D. Li, M. Lang, F. Deng, K. Chang, K. Buch, S. Rincon, W.A. Mehan, T.M. Leslie-Mazwi, and J. Kalpathy-Cramer

“MRI Vessel Wall Imaging after Intra-Arterial Treatment for Acute Ischemic Stroke” by A. Lindenholz, I.C. van der Schaaf, A.G. van der Kolk, H.B. van der Worp, A.A. Harteveld, L.J. Kappelle, and J. Hendrikse

“Contrast-Induced Acute Kidney Injury in Radiologic Management of Acute Ischemic Stroke in the Emergency Setting” by J.W. Myung, J.H. Kim, J. Cho, I. Park, H.Y. Kim, and J.H. Beom

“Tailored Vessel-Catheter Diameter Ratio in a Direct Aspiration First-Pass Technique: Is It a Matter of Caliber?” by E. Pampana, S. Fabiano, G. De Rubeis, L. Bertaccini, A. Stasolla, A. Vallone, A. Pingi, M. Mangiardi, S. Anticoli, C. Gasperini, and E. Cotroneo

AJNR

AMERICAN JOURNAL OF NEURORADIOLOGY

APRIL 2021
VOLUME 42
NUMBER 4
WWW.AJNR.ORG

Publication Preview at www.ajnr.org features articles released in advance of print. Visit www.ajnrblog.org to comment on AJNR content and chat with colleagues and AJNR's News Digest at <http://ajnrdigest.org> to read the stories behind the latest research in neuroimaging.

617 **PERSPECTIVES** *M. Hauben*

REVIEW ARTICLE

 618 **Retinoblastoma: What the Neuroradiologist Needs to Know** *V.M. Silvera, et al.*

HEAD & NECK

PRACTICE PERSPECTIVES

 627 **Time to Reconsider Routine Percutaneous Biopsy in Spondylodiscitis?** *Ö. Kasalak, et al.*

SPINE

GENERAL CONTENTS

   632 **Clinical, Imaging, and Lab Correlates of Severe COVID-19 Leukoencephalopathy** *O. Rapalino, et al.*

ADULT BRAIN

  639 **A Stacked Generalization of 3D Orthogonal Deep Learning Convolutional Neural Networks for Improved Detection of White Matter Hyperintensities in 3D FLAIR Images** *L. Umapathy, et al.*

**ADULT BRAIN
FUNCTIONAL**

  648 **Machine Learning–Based Prediction of Small Intracranial Aneurysm Rupture Status Using CTA-Derived Hemodynamics: A Multicenter Study** *Z. Shi, et al.*

**ADULT BRAIN
FUNCTIONAL**

  655 **Automated Detection and Segmentation of Brain Metastases in Malignant Melanoma: Evaluation of a Dedicated Deep Learning Model** *L. Pennig, et al.*

**ADULT BRAIN
FUNCTIONAL**

  663 **Vessel Type Determined by Vessel Architectural Imaging Improves Differentiation between Early Tumor Progression and Pseudoprogression in Glioblastoma** *M. Kim, et al.*

**ADULT BRAIN
FUNCTIONAL**

  671 **Are Dynamic Arterial Spin-Labeling MRA and Time-Resolved Contrast-Enhanced MRA Suited for Confirmation of Obliteration following Gamma Knife Radiosurgery of Brain Arteriovenous Malformations?** *A. Rojas-Villabona, et al.*

**ADULT BRAIN
FUNCTIONAL**

679 **Commentary**
Is Catheter Angiography Still Necessary to Evaluate Obliteration of Brain Arteriovenous Malformations Treated with Stereotactic Radiosurgery? *C.-J. Chen, et al.*

ADULT BRAIN

AJNR (Am J Neuroradiol ISSN 0195–6108) is a journal published monthly, owned and published by the American Society of Neuroradiology (ASNR), 800 Enterprise Drive, Suite 205, Oak Brook, IL 60523. Annual dues for the ASNR include approximately 21% for a journal subscription. The journal is printed by Intellicor Communications, 330 Eden Road, Lancaster, PA 17601; Periodicals postage paid at Oak Brook, IL and additional mailing offices. Printed in the U.S.A. POSTMASTER: Please send address changes to American Journal of Neuroradiology, P.O. Box 3000, Denville, NJ 07834, U.S.A. Subscription rates: nonmember \$410 (\$480 foreign) print and online, \$320 online only; institutions \$470 (\$540 foreign) print and basic online, \$935 (\$1000 foreign) print and extended online, \$380 online only (basic), \$825 online only (extended); single copies are \$35 each (\$40 foreign). Indexed by PubMed/MEDLINE, BIOSIS Previews, Current Contents (Clinical Medicine and Life Sciences), EMBASE, Google Scholar, HighWire Press, Q-Sensei, RefSeek, Science Citation Index, SCI Expanded, Meta/CZI, ReadCube, and Semantic Scholar. Copyright © American Society of Neuroradiology.



MIDRC

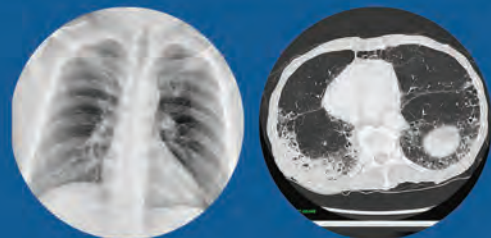
MEDICAL IMAGING AND DATA RESOURCE CENTER.

Medical Imaging in the Fight against COVID-19 Call for Contributions

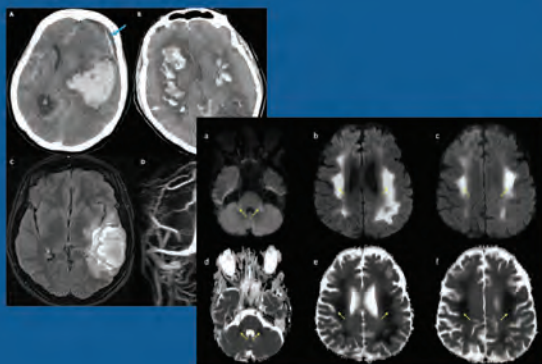
The Medical Imaging and Data Resource Center (MIDRC) is a multi-organizational initiative in the fight against the ongoing worldwide pandemic co-led by the ACR®, the RSNA, and the AAPM and is hosted at the University of Chicago.



The primary goal is to accelerate machine learning research by creating a high quality COVID-19 image commons linked to relevant clinical data made available as a public resource.



ASNR has teamed up with MIDRC to advance the understanding of the neuroimaging manifestations of COVID-19 and to enhance the MIDRC image commons.



- To ensure success, MIDRC encourages all institutions and hospitals, both small and large, to donate their COVID-19 medical images and data to the cause.
- MIDRC provides a HIPAA-compliant mechanism to securely submit medical images and clinical metadata, and is committed to helping institutions throughout the submission process.

Visit midrc.org for more information



THE UNIVERSITY OF
CHICAGO



National Institute of Biomedical Imaging and Bioengineering
Creating Biomedical Technologies to Improve Health

	681	Determining the Degree of Dopaminergic Denervation Based on the Loss of Nigral Hyperintensity on SMWI in Parkinsonism <i>Y.J. Bae, et al.</i>	ADULT BRAIN	
	688	Microstructural Tissue Changes in Alzheimer Disease Brains: Insights from Magnetization Transfer Imaging <i>I. Colonna, et al.</i>	ADULT BRAIN	
	694	Ivy Sign in Moyamoya Disease: A Comparative Study of the FLAIR Vascular Hyperintensity Sign Against Contrast-Enhanced MRI <i>L.-X. Wang, et al.</i>	ADULT BRAIN	
	701	CTA Evaluation of Basilar Septations: An Entity Better Characterized as Aberrant Basilar Fenestrations <i>J.E. Small, et al.</i>	ADULT BRAIN	
	708	Intra-Arterial Thrombolysis after Unsuccessful Mechanical Thrombectomy in the STRATIS Registry <i>S.F. Zaidi, et al.</i>	INTERVENTIONAL	
	713	The Prophylactic Use of Tirofiban versus Oral Antiplatelet Medications in Stent-Assisted Coiling of Intracranial Aneurysms: A Meta-analysis <i>Y. Xiang, et al.</i>	INTERVENTIONAL	
	720	Ruptured Intracranial Aneurysms Treated with the Pipeline Embolization Device: A Systematic Review and Pooled Analysis of Individual Patient Data <i>P.M. Foreman, et al.</i>	INTERVENTIONAL	
		726	Fast Stent Retrieval during Mechanical Thrombectomy Improves Recanalization in Patients with the Negative Susceptibility Vessel Sign <i>S. Soize, et al.</i>	INTERVENTIONAL
	732	Clot Meniscus Sign: An Angiographic Clue for Choosing between Stent Retriever and Contact Aspiration in Acute Basilar Artery Occlusion <i>S.H. Baik, et al.</i>	INTERVENTIONAL	
	738	Low-Dose Eptifibatid for Tandem Occlusion in Stroke: Safety and Carotid Artery Patency <i>A. Jost, et al.</i>	INTERVENTIONAL EXTRACRANIAL VASCULAR	
	743	Value of Emergent Neurovascular Imaging for “Seat Belt Injury”: A Multi-institutional Study <i>F.G. Sherbaf, et al.</i>	EXTRACRANIAL VASCULAR	
	749	Variations in the Course of the Carotid Arteries in Patients with Retropharyngeal Parathyroid Adenomas <i>G.K. Steinl, et al.</i>	HEAD & NECK EXTRACRANIAL VASCULAR	
	753	Postoperative Imaging Appearance of Iliac Crest Free Flaps Used for Palatomaxillary Reconstructions <i>M.L. Sandler, et al.</i>	HEAD & NECK	
		759	Radiomics of Pediatric Low-Grade Gliomas: Toward a Pretherapeutic Differentiation of <i>BRAF</i> -Mutated and <i>BRAF</i> -Fused Tumors <i>M.W. Wagner, et al.</i>	PEDIATRICS FUNCTIONAL
	766	Longitudinal Assessment of Enhancing Foci of Abnormal Signal Intensity in Neurofibromatosis Type 1 <i>N. Hainc, et al.</i>	PEDIATRICS	
	774	Evaluation of DISORDER: Retrospective Image Motion Correction for Volumetric Brain MRI in a Pediatric Setting <i>K. Vecchiato, et al.</i>	PEDIATRICS	
		782	Beyond Isolated and Associated: A Novel Fetal MR Imaging–Based Scoring System Helps in the Prenatal Prognostication of Callosal Agenesis <i>S. Glatter, et al.</i>	PEDIATRICS
	787	Validation of the National Institute of Neurological Disorders and Stroke Spinal Cord Injury MRI Common Data Elements Instrument <i>J. Fisher, et al.</i>	SPINE	
	794	Cervical Cordotomy for Intractable Pain: Do Postoperative Imaging Features Correlate with Pain Outcomes and Mirror Pain? <i>A. Berger, et al.</i>	SPINE	
	801	MRI Hyperintense Signal Structures in the Cervical Spinal Cord: Anterior Median Fissure versus Central Canal in Chiari and Control—An Exploratory Pilot Analysis <i>T.A. Tomsick, et al.</i>	SPINE	

AJNR *go green*

***AJNR* urges American Society of Neuroradiology members to reduce their environmental footprint by voluntarily suspending their print subscription.**

The savings in paper, printing, transportation, and postage directly fund new electronic enhancements and expanded content.

The digital edition of *AJNR* presents the print version in its entirety, along with extra features including:

- Publication Preview
- Case Collection
- Podcasts
- The *AJNR* News Digest
- The *AJNR* Blog

It also reaches subscribers much faster than print. An electronic table of contents will be sent directly to your mailbox to notify you as soon as it publishes.

Readers can search, reference, and bookmark current and archived content 24 hours a day on www.ajnr.org.

ASNR members who wish to opt out of print can do so by using the *AJNR* Go Green link on the *AJNR* Website (<http://www.ajnr.org/content/subscriber-help-and-services>). Just type your name in the email form to stop print and spare our ecosystem.

ONLINE FEATURES

MEMORIAL

E18 **D. Gordon Potts, MD** *K. ter Brugge*

LETTERS

E19 **Evolution of Radial Access in Neurointerventional Surgery** *D. Dornbos III*

 E21 **COVID-19-Associated Acute Disseminated Encephalomyelitis–Like Disease** *F.B. Assunção, et al.*

E24 **Primary Angiitis of the CNS with Unremarkable Vessel Wall MR Imaging: How the “T1 Shinethrough” Effect on SWI Adds to the Detection of Gadolinium Enhancement of Small Intraparenchymal Brain Vessels** *A.P.A. Fonseca, et al.*

E27 **Inconsistencies between Radiologic and Cadaveric Studies of the Occipital Sinus** *N. Balak*

E28 **Reply** *A.S. Larson, et al.*

E29 **The So-Called Cranial Dural Channels and Their Relationship with the Bridging Veins** *G. Baltasvias, et al.*

E31 **Reply** *M. Shapiro, et al.*

BOOK REVIEWS

R.M. Quencer, Section Editor

Please visit www.ajnrblog.org to read and comment on Book Reviews.



Rojas-Villabona, et al.
in this issue:
Characterization of a
residual AVM (case
19) using ASL (D–F)
and CE-MRA (G–I)
compared with DSA
(A–C).



Indicates Editor's
Choices selection



Indicates Fellows'
Journal Club selection



Indicates open access to non-
subscribers at www.ajnr.org



Indicates article with
supplemental online data



Indicates article with
supplemental online video



Evidence-Based
Medicine Level 1



Evidence-Based
Medicine Level 2



Simplify the MOC Process



Manage your CME Credits Online

CMEgateway.org

Available to Members of Participating Societies

American Board of Radiology (ABR)
American College of Radiology (ACR)
American Roentgen Ray Society (ARRS)
American Society of Neuroradiology (ASNR)
Commission on Accreditation of Medical
Physics Educational Programs, Inc. (CAMPEP)
Radiological Society of North America (RSNA)
Society of Interventional Radiology (SIR)
SNM
The Society for Pediatric Radiology (SPR)

It's Easy and Free!

Log on to CME Gateway to:

- View or print reports of your CME credits from multiple societies from a single access point.
- Print an aggregated report or certificate from each participating organization.
- Link to SAMs and other tools to help with maintenance of certification.

American Board of Radiology (ABR) participation!

By activating ABR in your organizational profile, your MOC-fulfilling CME and SAM credits can be transferred to your own personalized database on the ABR Web site.

Sign Up Today!

go to CMEgateway.org

EDITOR-IN-CHIEF

Jeffrey S. Ross, MD

Professor of Radiology, Department of Radiology,
Mayo Clinic College of Medicine, Phoenix, AZ

SENIOR EDITORS

Harry J. Cloft, MD, PhD

Professor of Radiology and Neurosurgery,
Department of Radiology, Mayo Clinic College of
Medicine, Rochester, MN

Christopher G. Filippi, MD

Professor and Alice Ettinger-Jack R. Dreyfuss
Chair of Radiology,
Tufts University School of Medicine,
Radiologist-in-Chief
Tufts University Medical Center, Boston, MA

Thierry A.G.M. Huisman, MD

Radiologist-in-Chief, Texas Children's Hospital,
Houston, TX

Yvonne W. Lui, MD

Associate Professor of Radiology,
Chief of Neuroradiology,
New York University School of Medicine,
New York, NY

C.D. Phillips, MD, FACR

Professor of Radiology, Weill Cornell Medical
College, Director of Head and Neck Imaging,
New York-Presbyterian Hospital, New York, NY

Lubdhra M. Shah, MD, MS

Professor of Radiology and Director of Spine
Imaging, University of Utah Department of
Radiology and Imaging Sciences, Salt Lake City, UT

STATISTICAL SENIOR EDITOR

Bryan A. Comstock, MS

Senior Biostatistician,
Department of Biostatistics,
University of Washington, Seattle, WA

ARTIFICIAL INTELLIGENCE DEPUTY EDITOR

Peter D. Chang, MD

Assistant Professor-in-Residence,
Departments of Radiological Sciences,
Computer Sciences, and Pathology,
Director, Center for Artificial Intelligence in
Diagnostic Medicine (CAIDM),
University of California, Irvine, Irvine, CA

EDITORIAL BOARD

Ashley H. Aiken, Atlanta, GA

Lea M. Alhilali, Phoenix, AZ

Mohammed A. Almekhlafi, Calgary, Alberta,
Canada

Joachim Berkefeld, Frankfurt, Germany

Aashim Bhatia, Pittsburgh, PA

Waleed Brinjikji, Rochester, MN

Judah Burns, New York, NY

Danielle Byrne, Dublin, Ireland

Federico Cagnazzo, Montpellier, France

J. Levi Chazen, New York, NY

James Y. Chen, San Diego, CA

Gloria C. Chiang, New York, NY

Daniel Chow, Irvine, CA

Kars C.J. Compagne, Rotterdam, The Netherlands

Arturo Consoli, Suresnes, France

Seena Dehkharghani, New York, NY

Nilesh K. Desai, Houston, TX

Yonghong Ding, Rochester, MN

Birgit Ertl-Wagner, Toronto, Ontario, Canada

Clifford J. Eskey, Hanover, NH

Massimo Filippi, Milan, Italy

Nils D. Forkert, Calgary, Alberta, Canada

Ana M. Franceschi, New York, NY

Frank Gaillard, Melbourne, Australia

Joseph J. Gemmete, Ann Arbor, Michigan

Wende N. Gibbs, Phoenix, AZ

Philipp Gölitz, Erlangen, Germany

Brent Griffith, Detroit, MI

Joseph M. Hoxworth, Phoenix, Arizona

Raymond Y. Huang, Boston, MA

Gábor Janiga, Magdeburg, Germany

Christof Karmonik, Houston, TX

Timothy J. Kaufmann, Rochester, MN

Hillary R. Kelly, Boston, MA

Toshibumi Kinoshita, Akita, Japan

Alexander W. Korutz, Chicago, IL

Stephen F. Kralik, Houston, TX

Alexander Lerner, Los Angeles, CA

Yinsheng Li, Madison, WI

Franklin A. Marden, Chicago, IL

Markus A. Möhlenbruch, Heidelberg, Germany

Kambiz Nael, Los Angeles, CA

Renato Hoffmann Nunes, Sao Paulo, Brazil

Sasan Partovi, Cleveland, OH

Johannes A.R. Pfaff, Salzburg, Austria

Laurent Pierot, Reims, France

Alireza Radmanesh, New York, NY

Prashant Raghavan, Baltimore, MD

Eytan Raz, New York, NY

Paul M. Ruggieri, Cleveland, OH

Sebastian Schafer, Madison, WI

Maksim Shapiro, New York, NY

Timothy Shepherd, New York, NY

James Shin, New York, NY

Mark S. Shiroishi, Los Angeles, CA

Bruno P. Soares, Baltimore, MD

Jason F. Talbott, San Francisco, CA

Ruth Thiex, Everett, Washington

Vincent Thijs, Melbourne, Victoria, Australia

Anderanik Tomasian, Los Angeles, CA

Fabio Triulzi, Milan, Italy

Anja G. van der Kolk, Utrecht, the Netherlands

Arastoo Vossough, Philadelphia, PA

Elysa Widjaja, Toronto, Ontario, Canada

Leonard Yeo, Singapore

Woong Yoon, Gwangju, South Korea

David M. Yousem, Evergreen, CO

Carlos Zamora, Chapel Hill, NC

Chengcheng Zhu, Seattle, WA

EDITORIAL FELLOW

Matthew D. Alvin, Baltimore, MD

SPECIAL CONSULTANTS TO THE EDITOR

AJNR Blog Editor

Neil Lall, Denver, CO

Case of the Month Editor

Nicholas Stence, Aurora, CO

Case of the Week Editors

Matylda Machnowska, Toronto, Ontario, Canada

Anvita Pauranik, Calgary, Alberta, Canada

Sapna Rawal, Toronto, Ontario, Canada

Classic Case Editor

Sandy Cheng-Yu Chen, Taipei, Taiwan

Health Care and Socioeconomics Editor

Pina C. Sanelli, New York, NY

Physics Editor

Greg Zaharchuk, Stanford, CA

Podcast Editor

Courtney Tomblinson, Nashville, TN

Twitter Editor

Roger Jordan, Houston, TX

Official Journal:

American Society of Neuroradiology

American Society of Functional Neuroradiology

American Society of Head and Neck Radiology

American Society of Pediatric Neuroradiology

American Society of Spine Radiology

Founding Editor

Juan M. Taveras

Editors Emeriti

Mauricio Castillo, Robert I. Grossman,

Michael S. Huckman, Robert M. Quencer

Managing Editor

Karen Halm

Assistant Managing Editor

Laura Wilhelm

Editorial Assistant

Margaret B. Sabato

Executive Director, ASNR

Mary Beth Hepp

We're Inside Every Great Neuroradiologist!

ASNR MEMBERS RECEIVE

American Journal of Neuroradiology (AJNR)

The leading neuroradiology research journal, published monthly

Neurographics

Bimonthly educational journal with CME for members

ASNR Annual Meeting

Discounts for members on the field's premier conference

eCME

Online collection of lectures and articles with SA-CME and Category 1 credit

Advocacy

Coding/reimbursement, quality standards and practice guidelines; demonstrating neuroradiology's value!

Networking

Access to 5,000 peers

... And More!

Join the leaders in neuroradiology today!

Learn more at www.asnr.org/join

ASNR

American Society of Neuroradiology

800 Enterprise Dr., Suite 205, Oak Brook, IL 60523 • (630)574-0220 • membership@asnr.org • www.asnr.org

Explore the New ASNR Career Center



Your Premier Resource for Professional Development

- Access to jobs in the National Healthcare Career Network
- Confidential resume posting
- One-time free resume review
- Professional online profile
- Saved jobs capability

Start here: careers.asnr.org

ASNR
American Society of Neuroradiology

ASNR 59TH ANNUAL MEETING

ASNR21

MAY 22–26

BRIDGING NEW HORIZONS
OF INNOVATION & PRACTICE

Join us for the All-Virtual and On-Demand ASNR21!

More than 800 speakers and thought leaders to present the latest updates in general neuroradiology, including:

- Dedicated specialty programming from the ASFNR, ASHNR, ASPNR, ASSR and SNIS
- The latest information about COVID-19
- Health policy, legislative and regulatory updates
- Artificial intelligence neuroimaging applications
- Global outreach in neuroradiology
- More than 700 ePosters and Educational Exhibits, available 24/7

Earn up to 75.5 AMA PRA Category 1 Credits™, 27.5 SA-CME/SAM credits

EARLY BIRD REGISTRATION IS NOW OPEN!

Act now to take advantage of this discounted price.

Register at <https://www.asnr.org/annualmeeting/register/>



Title: Chrysler Trylons. In The heart of New York City, adjacent to Chrysler Building (*left*) we have one of many visual reminders that the epicenter of the COVID-19 pandemic in the United States is still a bejeweled city. Here for you are the Chrysler Trylons. The famed architect Philip Johnson designed them " . . . as a monument for 42nd street . . . to give you the top of the Chrysler building at street level" by visual analogy with the chevron spire of its namesake.

Manfred Hauben, MD, MPH, Pfizer Inc and NYU Langone Health, New York City

Retinoblastoma: What the Neuroradiologist Needs to Know

V.M. Silvera, J.B. Guerin, W. Brinjikji, and L.A. Dalvin



ABSTRACT

SUMMARY: Retinoblastoma is the most common primary intraocular tumor of childhood. Accurate diagnosis at an early stage is important to maximize patient survival, globe salvage, and visual acuity. Management of retinoblastoma is individualized based on the presenting clinical and imaging features of the tumor, and a multidisciplinary team is required to optimize patient outcomes. The neuroradiologist is a key member of the retinoblastoma care team and should be familiar with characteristic diagnostic and prognostic imaging features of this disease. Furthermore, with the adoption of intra-arterial chemotherapy as a standard of care option for globe salvage therapy in many centers, the interventional neuroradiologist may play an active role in retinoblastoma treatment. In this review, we discuss the clinical presentation of retinoblastoma, ophthalmic imaging modalities, neuroradiology imaging features, and current treatment options.

ABBREVIATIONS: IAC = intra-arterial chemotherapy; IVC = IV chemotherapy; IvtC = intravitreal chemotherapy; EBRT = external-beam radiation therapy; OA = ophthalmic artery

Retinoblastoma is the most common primary intraocular malignancy in children. Prompt diagnosis is essential to preserving life, eye, and sight. Neuroradiologists play an important role in diagnosis, staging, and treatment of patients with retinoblastoma. In this review, we aim to educate neuroradiologists regarding retinoblastoma imaging features and basic principles of treatment.

EPIDEMIOLOGY

Retinoblastoma affects 1 in 16,000 births,¹ with 8000–10,000 children diagnosed annually. There are no known geographic, racial, or sex predilections. Heritable retinoblastoma is diagnosed at a median age of 12 months and nonheritable disease at 24 months, with 80% diagnosed before 4 years of age.

CLINICAL PRESENTATION AND DIAGNOSIS

Retinoblastoma is diagnosed by physical examination and classified as International Classification of Retinoblastoma groups A through E according to increasing severity. The most common

presenting feature is a white pupillary reflex called leukocoria, often recognized first by parents. Strabismus and decreased vision are also common. Patients with advanced disease can present with iris color changes, an enlarged cornea and globe, orbital inflammation, and exophthalmos. Biopsy is avoided because of a risk of tumor seeding, though aqueous biopsy is under investigation.

PATHOPHYSIOLOGY

Retinoblastoma results from a biallelic mutation of the retinoblastoma gene (*RB-1*) in developing retinal cells, following the 2-hit model of tumor suppressor gene inactivation.² In the heritable form, seen in up to 50% of patients, a germline mutation is followed by a second acquired somatic mutation. In the nonheritable form, 2 somatic mutations must occur in the same gene in a single cell.

Retinoblastoma originates in the retina and can display endophytic growth into the vitreous chamber; exophytic growth into the subretinal space; or diffuse, infiltrative growth along the retina. Most tumors demonstrate both endophytic and exophytic growth and can cause retinal detachment as well as vitreous and subretinal tumor seeding.

OPHTHALMIC IMAGING

Color Fundus Photography

The first step in diagnosing retinoblastoma is a complete dilated eye examination, often performed under anesthesia. Widefield

Received June 9, 2020; accepted after revision October 14.

From the Departments of Neuroradiology (V.M.S., J.B.G., W.B.), Neurosurgery (W.B.), and Ophthalmology (L.A.D.), Mayo Clinic, Rochester, Minnesota.

Please send correspondence to Lauren A. Dalvin, MD, Department of Ophthalmology, Mayo Clinic, 200 1st St SW, Rochester, MN 55905; e-mail: dalvin.lauren@mayo.edu; @VMSilvera; @WBrinjikji; @LADalvinMD

Indicates open access to non-subscribers at www.ajnr.org

<http://dx.doi.org/10.3174/ajnr.A6949>

color fundus, anterior segment, and external photography facilitate serial monitoring.

Ultrasonography

Ocular ultrasonography is a critical diagnostic test with resolution approaching 150 microns using 10-MHz frequency. On B-scan ultrasonography, retinoblastoma is an attenuated, round tumor with focal areas of high internal reflectivity, corresponding to calcification, which create shadowing that persists with low sonography gain.³ Sonography biomicroscopy uses higher frequencies (50–100 MHz) to obtain anterior segment images and detect anterior segment, iris, ciliary body, and anterior chamber angle invasion.⁴

Fluorescein Angiography

Fluorescein angiography uses IV sodium fluorescein dye to allow direct visualization of blood flow through retinal vasculature. The dye emits green fluorescent light (520–530 nm) after excitation by blue light (465–490 nm). Key imaging features that this technique may highlight include iris neovascularization, dilated tumor-associated retinal vessels, intrinsic tumor vasculature, venous leakage, and microvasculature changes.⁵ Compared with completely perfused tumors, partially perfused tumors may require fewer cycles of intra-arterial chemotherapy (IAC) to achieve regression.⁶ Fluorescein angiography can also detect treatment-related ischemic side effects.⁷

Optical Coherence Tomography

Optical coherence tomography uses low-coherence light to provide a high-resolution cross-sectional image of the retina, showing details as small as 10 microns and permitting detection of clinically invisible tumors.^{8,9} Newer optical coherence tomography angiography can image retinal vasculature without injection of IV dye and may prove useful for future diagnosis and monitoring.¹⁰

Neuroradiology Imaging

High-resolution contrast-enhanced MR imaging is important for optimal assessment of key features that impact treatment decisions in children with retinoblastoma, such as optic nerve invasion, extraocular tumor extension, and intracranial disease. Imaging approaches differ per institution and individual preferences with variations regarding the use of small surface coils or multichannel head coils and imaging at 1.5T or 3T magnet strength. In this regard, the European Retinoblastoma Imaging Collaboration has published imaging guidelines for diagnostic evaluation of retinoblastoma that specify hardware considerations, optimal pulse sequences, and acceptable minimum spatial resolution.¹¹ Carefully performed MR imaging can help confirm retinoblastoma diagnosis, exclude alternative diagnoses, assess tumor extent and stage, and provide long-term monitoring. Poor prognostic features of choroidal invasion and optic nerve extension cannot be reliably detected on clinical examination, so MR imaging detection of extraocular disease and intracranial tumor is crucial. MR imaging can also provide intraocular tumor detail in patients with tumor-related media opacity and can detect congenital brain anomalies in patients with retinoblastoma and 13q-deletion syndrome.¹²

On imaging, retinoblastoma is typically irregular in contour. On CT, retinoblastoma has intermediate attenuation with variable calcification and mild to moderate enhancement. On MR imaging, tumor is slightly hyperintense relative to vitreous on T1-weighted images, is dark on T2-weighted images, shows reduced diffusivity on diffusion-weighted images, and demonstrates heterogeneous enhancement with gadolinium. Tumor calcification may be evident as signal voids on susceptibility-weighted sequences.

Calcification is a key diagnostic feature present in approximately 95% of cases. Although CT has been used historically to detect tumor calcification, ultrasonography has good sensitivity, and because of potential increased risk for second cancers with ionizing radiation exposure, especially in germline retinoblastoma, sonography for detection of calcification has replaced CT, and the role of CT in the evaluation of retinoblastoma is now considered obsolete.^{13–16}

IMAGING APPROACH TO DISEASE

Intraocular Tumor

The smallest intraocular retinoblastomas are well-circumscribed and confined to the retina. These are typically best visualized on heavily T2-weighted 3D images, such as 3D CISS/FIESTA (Fig 1A). Larger endophytic tumors are associated with vitreous seeding and exophytic tumors with subretinal seeding. Diffusely infiltrating retinoblastoma is uncommon, accounts for approximately 2% of cases, presents at an older mean age of 6 years with inflammatory features, and demonstrates linear growth without a discrete mass or calcification.^{17,18}

Anterior Chamber Involvement

Tumor extension into the anterior chamber is uncommon, may be evident by enhancement on MR imaging, and is associated with iris neovascularization, hyperemia, and inflammation.^{19,20} Anterior chamber, ciliary body, or iris invasion may necessitate enucleation.^{21,22}

Vitreous Seeding

Vitreous involvement can range from small conglomerates of tumor cells to scattered, discrete tumor foci to diffuse involvement. High-resolution MR imaging can identify vitreous seeding as small foci of T2 signal shortening within the vitreous chamber, but clinical examination is more sensitive with a potential role for optical coherence tomography monitoring.^{23,24}

Vitreous Hemorrhage

Vitreous hemorrhage complicates tumor assessment in children with retinoblastoma, obscuring tumor margins on clinical and MR imaging examination, and is present in fewer than 3% of cases.

Subretinal Tumor Invasion

Retinoblastoma that proliferates within the subretinal space between the retina and the choroid is termed subretinal tumor seeding. Subretinal tumor can be complicated by secondary serous retinal detachment and less frequently retinal hemorrhage (Figs 2 and 3).²⁵

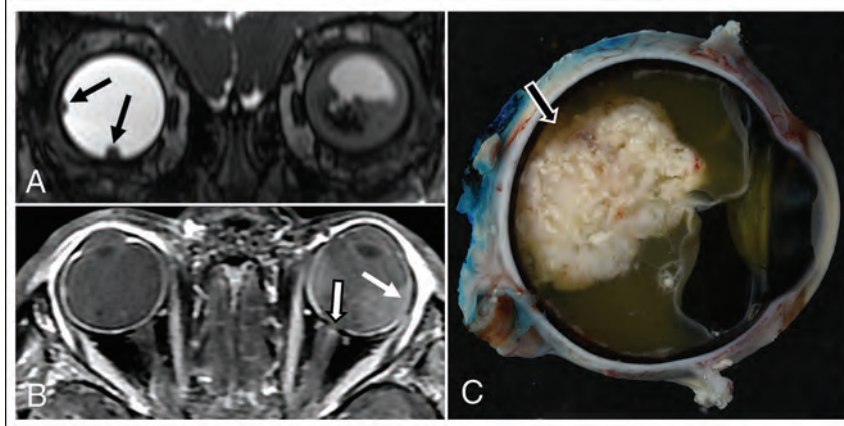


FIG 1. A 21-month-old boy with right group B and left group E retinoblastoma. Coronal reformat of 3D FIESTA (A) shows a hypointense calcified mass in the left globe with serous retinal detachment. Two of 3 small retinoblastoma tumors in the right globe are shown (black solid arrows). Axial post-gadolinium T1-weighted image with fat saturation (B) shows enhancing tumor abutting the normally enhancing choroid (white arrow) making focal tumor invasion challenging to assess. Tiny foci of enhancement surrounding the left optic nerve cuff represent normal small vessels (black and white arrow). The left globe was larger than the right consistent with buphthalmos. Gross pathology specimen of the enucleated left eye (C) shows the posteriorly located intraocular neoplasm (arrow). Histopathologic examination showed moderately differentiated retinoblastoma without choroidal invasion and with tumor involving the optic nerve head and lamina cribrosa, but without postlaminar tumor.

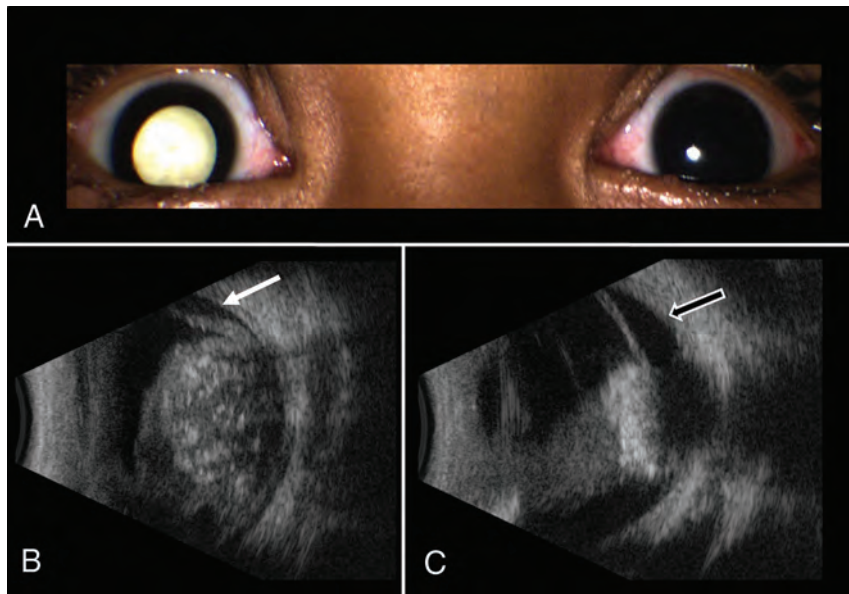


FIG 2. Group E retinoblastoma managed with IAC and IvitC. A 2-year-old boy presented with leukocoria in the right eye (A). Ultrasonography (B) revealed a large, round, hyperechoic retinal mass with intrinsic calcifications seen as foci of high reflectivity and serous retinal detachment (white arrow). After 3 cycles of IAC and IvitC using melphalan and topotecan, a follow-up sonography image (C) shows regression of tumor to a calcified hyperechoic scar with persistent serous retinal detachment (black arrow).

Choroidal Invasion

Exophytic growth, breaching the Bruch membrane, can result in tumor invasion of the choroid between the retina and sclera. On MR imaging, the choroid normally appears as a linear, uniformly

enhancing layer deep to the hypointense sclera. Choroidal invasion is suggested by a focal region of choroidal thickening, either enhancing or nonenhancing, or a focal region of choroidal thinning with decreased enhancement (Fig 1B).²⁵⁻²⁸ Subtle choroidal invasion remains challenging to discern when enhancing tumor abuts the normally enhancing choroid with accuracies estimated at 57%–72%.^{25,29} Massive choroidal invasion ≥ 3 mm is associated with increased metastatic risk, warranting enucleation and adjuvant systemic chemotherapy.^{30,31}

Additional Intraocular Complications

Additional tumor-related complications include a subluxed or dislocated lens, an enlarged globe from secondary glaucoma (Fig 1B), a shallow anterior chamber with increased intraocular pressure, intraocular hemorrhage, and rarely phthisis bulbi.³² Advanced retinoblastoma can cause exophthalmos and periorbital soft tissue swelling from tumor necrosis that can mimic periorbital cellulitis.³³

Extraocular Retinoblastoma

Extraocular tumor can manifest by extension of tumor through the sclera into the retrobulbar fat and by growth along the optic nerve and meningeal sheath (Figs 1, 3, and 4).³⁴

Scleral and Extrascleral Involvement

Tumor infiltration of the sclera may be apparent on MR imaging by interruption of its normally thin, linear hypointense appearance on both T1-weighted and T2-weighted images and by extrascleral extension of tumor into the retro-ocular fat. The normal discontinuity of the sclera where the optic nerve inserts into the globe should not be mistaken for pathology, though tumor can extend into the optic nerve through the lamina cribrosa at this site. Scleral invasion and extraocular tumor extension are rare in developed countries

and signify a poor prognosis and increased likelihood of metastasis.³⁵ Occasionally, enhancement of retrobulbar fat without a tumor mass is observed, which can represent peritumoral inflammation rather than extraocular tumor extension.

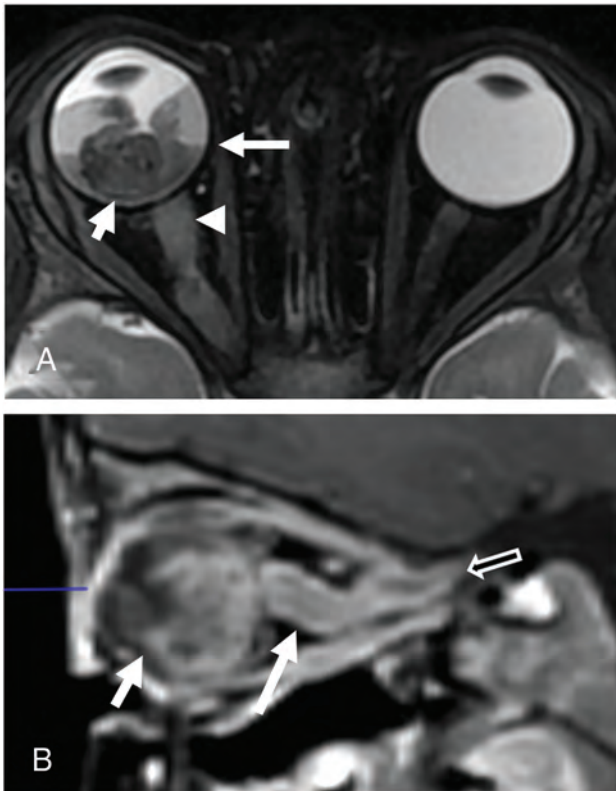


FIG 3. A 21-month-old boy with group E retinoblastoma of the right eye. Axial fat-saturated T2-weighted image (A) shows a large hypointense intraocular tumor (*short white arrow*) in the right globe with retinal detachment and hemorrhage with a fluid–fluid level (*long white arrow*). Abnormal thickening of the right optic nerve (*arrow-head*) is consistent with optic nerve invasion. Sagittal postgadolinium T1-weighted image with fat saturation (B) demonstrates enhancing tumor contacting the lens (*short arrow*) and tumor invading the optic nerve and extending posteriorly along the optic nerve sheath (*long arrow*) to the level of the optic canal (*open arrow*). Histopathologic examination showed poorly differentiated retinoblastoma with choroidal and extensive postlaminar optic nerve invasion.

Optic Nerve Involvement

Assessment of the optic nerve is essential for accurate staging. Prelaminar and intralaminar invasion of the optic nerve are not considered high-risk features.³⁴ Postlaminar optic nerve invasion occurs in approximately 8% of patients³⁶ and typically requires enucleation followed by systemic chemotherapy because of increased risk for metastatic disease and mortality.^{28,34,37,38} On MR imaging, the location of the lamina can be estimated at the junction between the optic disc and the midpoint between the enhancing choroid and the low intensity sclera. A definitive diagnosis of postlaminar optic nerve invasion is based on histopathology, which may not be available if eye-preserving treatment is considered. Thickening and enhancement of the postlaminar optic nerve on MR imaging usually indicates tumor extension (Fig 4). However, more subtle abnormalities at the globe–nerve junction can be challenging to accurately classify. Enhancement of the optic nerve at the globe–nerve junction can represent postlaminar tumor, pre- or intralaminar tumor with a posteriorly displaced lamina cribrosa, central retinal vessels, or inflammation (Fig 1).^{20,36,39–43} Postlaminar optic nerve invasion can be diagnosed based on visual assessment of optic nerve enhancement and tumor size with sensitivity estimated at 59% and specificity estimated at 94%.^{39,44,45} Lower accuracy may be related to differences in the level of suspicion, imaging technique, and the experience of the interpreting radiologist.^{46–48} The most reliable direct MR imaging criteria to rule out advanced optic nerve invasion are normal optic nerve size, normal optic nerve signal on T2-weighted images, and optic nerve enhancement of ≤ 3 mm on postcontrast imaging.^{36,39} Normal enhancement of the central retinal vessels in the optic nerve and “double-dot” enhancement, seen as punctate foci of enhancement straddling the central retinal vessels at the globe–nerve junction, should not be mistaken for tumor.³⁹ In addition, increased intraocular pressure can cause posterior bulging of the lamina cribrosa that can simulate optic nerve invasion and result in a false-positive interpretation.^{36,41} MR imaging remains limited in its ability to detect early stage optic nerve invasion with pathology remaining the criterion standard for assessing high-risk features.^{28,39}

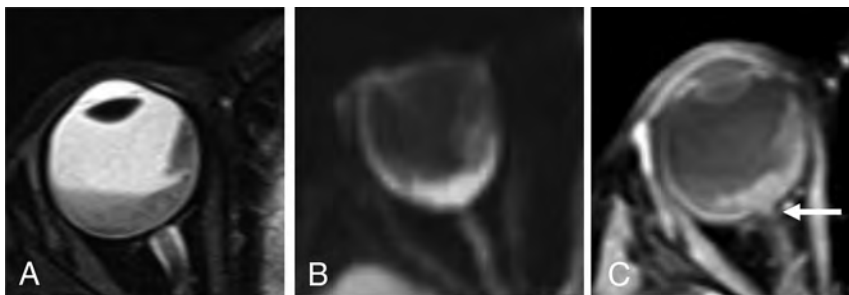


FIG 4. A 2-year-old girl with group E retinoblastoma. Axial fat-saturated T2-weighted image (A) shows a hypointense intraocular tumor centered within the posterior right globe with retinal detachment. Axial trace DWI shows reduced diffusivity of the tumor (B). Axial postgadolinium T1-weighted image with fat saturation (C) shows enhancement of the distal optic nerve in continuity with tumor over 1.2 mm (*arrow*) and enhancing tumor abutting the enhancing choroid, limiting the assessment for focal choroidal invasion. Histopathologic examination showed poorly differentiated retinoblastoma (grade IV of IV) largely confined to the posterior eye with postlaminar optic nerve invasion and no choroidal invasion.

TREATMENT MODALITIES

Retinoblastoma treatment is individualized depending on International Classification of Retinoblastoma group staging, laterality of involvement, germline testing results, institutional resources, and psychosocial factors.⁴⁹ Current treatment modalities include IV chemotherapy (IVC), IAC, intravitreal chemotherapy (IvitC), intracameral chemotherapy, consolidation therapies (cryotherapy and transpupillary thermotherapy), radiation-based therapies (external-beam radiation therapy [EBRT] and plaque radiation therapy), and enucleation.

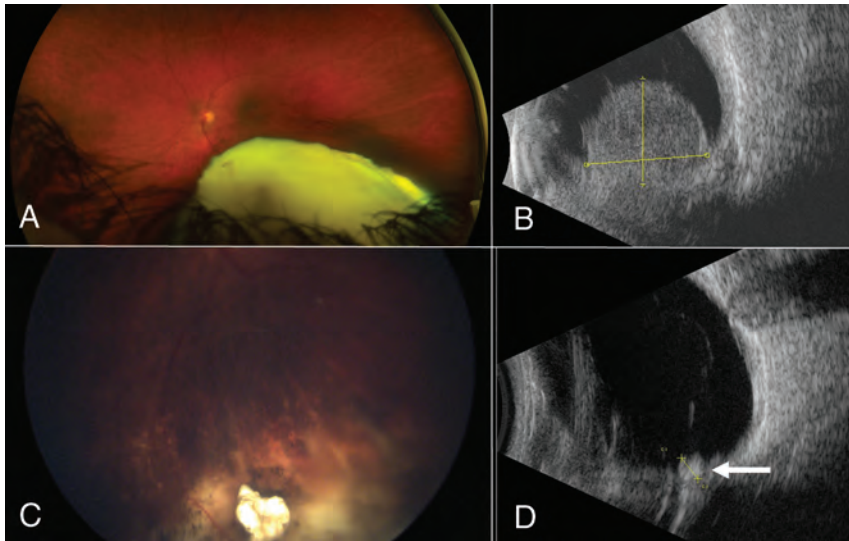


FIG 5. Group D retinoblastoma managed with IAC and IvtC. A 7-year-old boy presented with a large, white inferiorly located orbital tumor shown in the color fundus photograph (A). Ultrasonography revealed a round, hyperechoic retinal mass (B). After 4 cycles of IAC and IvtC using melphalan and topotecan, the tumor regressed to a small, calcified scar seen on fundoscopy (C) and confirmed by ultrasonography (D) (white arrow).

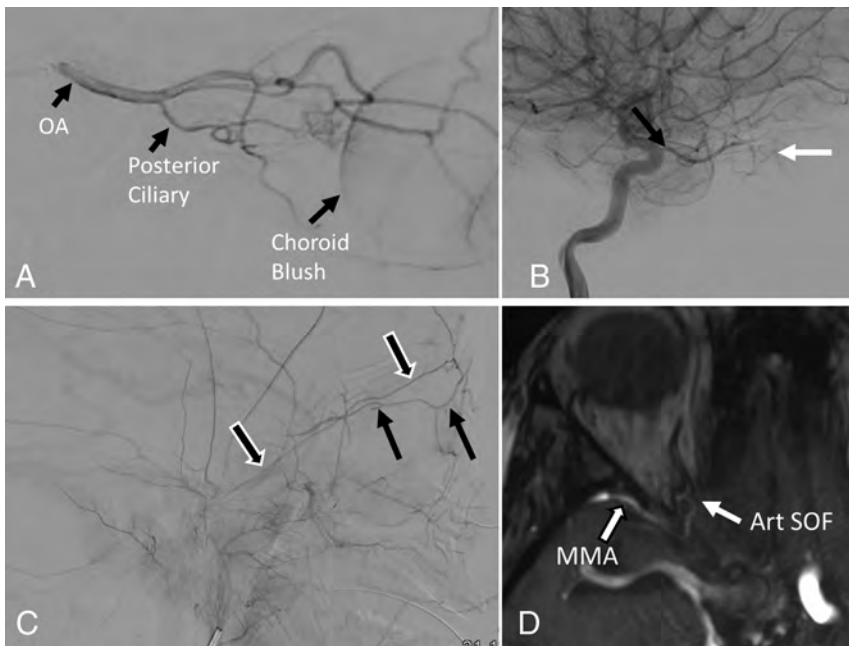


FIG 6. Competitive flow to the choroid from the OA and middle meningeal artery (MMA). A lateral angiographic image provides reference for OA supply to the globe (A); the posterior ciliary artery is the vascular supply to the choroid and produces the choroid blush. This is the imaging surrogate for the origin of the central retinal artery. Right ICA injection (B) shows the normal OA origin (black arrow) and expected choroid blush (white arrow). Right ECA injection (C) shows the artery of the superior orbital fissure (Art SOF; black and white arrows), which anastomoses with distal branches of the OA and then fills the OA in a retrograde fashion (black arrows) indicating competitive flow between the MMA and OA for supply to the retina. MR angiogram (D) shows supply to the orbit through the artery of the superior orbital fissure (white arrow), a branch of the MMA (white and black arrow).

Intravenous Chemotherapy

Systemic IVC, introduced in the 1990s, remains a key treatment tool, especially for bilateral and germline disease. The most

frequently used regimen consists of vincristine, etoposide, and carboplatin (VEC), administered through a central or peripheral catheter monthly for 6 cycles.⁵⁰ Tumor control is best for less advanced disease.⁵¹ Systemic chemotherapy may provide protection against second cancers, metastasis, and pineal embryonal tumor in patients with germline disease.^{52,53} Intensified chemotherapy regimens are used to treat high-risk disease after enucleation. Neoadjuvant chemotherapy can be used in advanced disease with choroidal or postlaminar optic nerve invasion before enucleation and may prevent exenteration in orbital retinoblastoma.^{54,55}

Intra-arterial Chemotherapy

Introduced in 2004, IAC is now a standard of care first-line therapy, especially for advanced, unilateral tumors, and carries a lower risk of side effects such as ototoxicity and neurotoxicity associated with systemic chemotherapy.⁵⁶⁻⁵⁹ Melphalan, topotecan, and carboplatin are the most commonly used drugs, administered as combinations of 1, 2, or 3 agents depending on tumor severity.⁵⁰ Treatment is usually administered monthly for 3 or 4 cycles. IAC can be used as a primary or secondary treatment and has higher success rates for globe salvage in advanced tumors compared with IVC (Fig 5).^{49,60}

An experienced interventional neurosurgeon or neuroradiologist is required to perform this procedure and this approach achieves superselective delivery of 10 times the chemotherapy dose to the eye compared with IVC.⁶¹ The target artery into which the chemotherapy is administered is the central retinal artery, a branch of the ophthalmic artery (OA). The central retinal artery is too small to visualize on conventional angiography, so the posterior ciliary arteries, which cause the choroid blush, are often used as the surrogate (Fig 6). The OA is the first intradural branch of the internal carotid artery and it is the dominant arterial supply to the retina in more than 98% of adults. However, during fetal life, there are robust connections between the OA and branches of the middle meningeal artery. These connections persist into early childhood, and compared with adults, there

may be a higher prevalence of dual supply to the retina from both the middle meningeal artery (ie, the artery of the superior orbital fissure) and the OA (Fig 6).⁶² Preoperative MRA can detect anatomic variations.

Regarding technical aspects, IAC delivery is a relatively straightforward procedure. At our center, we typically place a 4F Berenstein catheter (Boston Scientific) in the femoral artery and advance it to the carotid artery on the side of the lesion. Internal and external carotid artery injections are performed to identify the source of the choroid blush. After this, a microcatheter (Headway Duo, MicroVenting; or Magic, Balt; 1.2F) is advanced in a flow-directed technique (ie, wireless) to the ostium of the OA, and after confirmation of positioning, the chemotherapeutic agents are administered over the course of 1 hour.

Complications can occur. Catheterization and contrast injection into the OA can trigger an oculocardiac reflex and severe bradycardia. Ocular side effects can include transient periorbital edema, cutaneous hyperemia, madarosis, blepharoptosis, scalp hair loss, and extraocular motility abnormalities.^{63–65} More lasting vision-threatening ophthalmic vascular events include vitreous hemorrhage, retinal and choroidal ischemia with resulting atrophy, branch or central retinal artery occlusion, and OA spasm or occlusion.^{7,60,63,66–68} Retinal detachment occurs in up to 25% of treated eyes presumably because of rapid tumor regression. The rate of serious ophthalmic vascular events that result in chorioretinal atrophy and vision loss has decreased over time and correlates with increased experience of the treating physician.⁶⁸ Risks are similar when IAC is used as primary or secondary therapy.⁶⁹ Complications related to chemotherapy administration include neutropenia, fever, and intraoperative bronchospasm.

Intraocular Chemotherapy

IvitC is used in combination with IAC to treat vitreous seeding. The most common drugs are melphalan and topotecan, used alone or in combination. Treatment is administered every 2–4 weeks and tailored to tumor response. Globe salvage for group E eyes has improved to >50% by combining IAC and IvitC (Fig 5).^{70,71} Small chemotherapy doses can be delivered to the anterior chamber (intracameral chemotherapy) for aqueous seeding.⁷²

Focal Therapies

Focal therapies may be the primary treatment for small retinoblastomas but are typically used for consolidation in combination with IVC.⁷³ Whereas cryotherapy with a triple-freeze–thaw technique is used for peripheral tumors, transpupillary thermotherapy with a diode laser is typically used for posteriorly located tumors that cannot be reached with the cryotherapy probe.

External-Beam Radiation Therapy

EBRT is generally avoided because of associated side effects, the most serious of which is increased risk for second primary malignancies, especially in patients with germline retinoblastoma.^{16,74,75} EBRT maintains a role in treating extraocular tumor extension, orbital recurrence, and a positive optic nerve margin following enucleation.⁷⁶

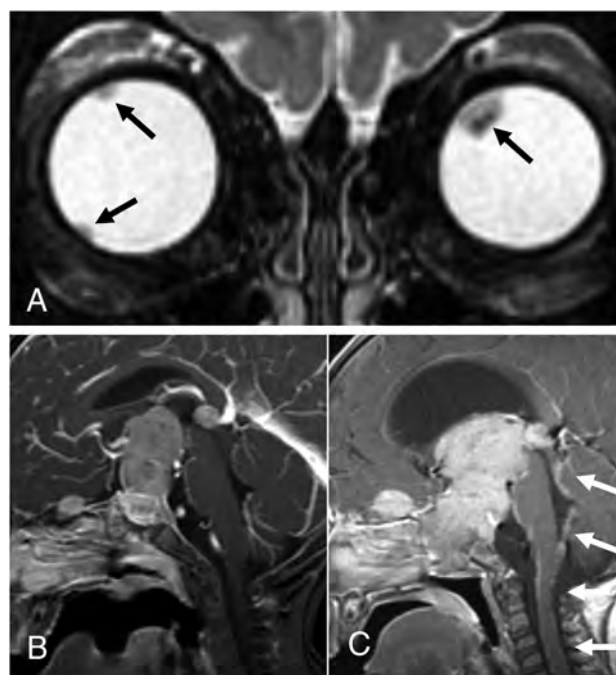


FIG 7. A 16-month-old boy presented with extensive metastatic disseminated quadrilateral retinoblastoma. Coronal T2-weighted image from the initial MR imaging (A) showed hypointense retinal tumors in both globes (black arrows). Sagittal postgadolinium T1-weighted image from the initial MR imaging (B) showed a large enhancing mass occupying the sella, suprasellar cistern, and third ventricle, with separate tumors involving the pineal gland and extending along the planum sphenoidale. Sagittal postgadolinium T1-weighted image from an MR imaging 5 weeks later (C) shows tumor growth, obstructive hydrocephalus, and leptomeningeal dissemination of tumor within the fourth ventricle and along the brain stem and upper cervical cord (white arrows).

Plaque Radiation Therapy

Plaque radiation therapy, also known as brachytherapy, delivers localized, low-dose radiation, often as secondary treatment for small- to medium-sized tumors that are chemoresistant or for localized recurrence.⁷⁷ Unlike EBRT, plaque radiation therapy is not associated with increased risk for second cancers.^{78,79}

Enucleation

Enucleation is sometimes necessary to protect the life of patients with advanced disease. Enucleation is typically reserved for advanced group E tumors, especially if there is poor visualization of the fundus or concern for optic nerve or extraocular extension.^{21,80–83} Tumors that have failed other therapies may also require enucleation. If there are high-risk features on histopathology of the enucleated globe, additional systemic chemotherapy is required for prevention of metastatic disease.⁸⁴

Advanced Disease

Trilateral Retinoblastoma. Trilateral retinoblastoma refers to the presence of intracranial tumor histologically similar to retinoblastoma in the pineal gland or suprasellar cistern (supratentorial CNS embryonal tumor) in addition to bilateral ocular involvement.⁸⁵ This occurs in 10%–15% of patients with heritable retinoblastoma.⁸⁶ The presence of CNS tumor in both midline

locations is sometimes referred to as quadrilateral retinoblastoma (Fig 7). The incidence of trilateral retinoblastoma is 3.2%. These intracranial tumors can be synchronous with intraocular retinoblastoma at diagnosis but are more frequently found on surveillance MR imaging. The lead time from asymptomatic to symptomatic pineal trilateral tumor is approximately 1 year. The prognosis for trilateral retinoblastoma is poor.⁸⁷⁻⁸⁹

Scrutiny of the pineal gland at presentation and on surveillance MR imaging is important for detecting developing pineal region tumor. It is important to not mistake pineal cysts for tumor; pineal cysts are a common incidental finding in the general pediatric population, particularly at 3T. Incidental pineal cysts may grow, have proteinaceous content, and may show enhancement of the cyst wall with mild central enhancement.^{90,91} Embryonal tumors of the pineal gland, on the other hand, have imaging characteristics similar to retinoblastoma and are predominantly solid and dark on T2-weighted images, enhance, and show reduced diffusivity (Fig 7).

CNS Dissemination and Metastatic Disease. Tumor spread into the intracranial space is uncommon and carries a poor prognosis. Retinoblastoma can spread through direct extension via the optic nerve and its meningeal sheath into the intracranial compartment and can metastasize systemically via hematogenous or lymphatic routes (Fig 7).^{28,34} The most commonly affected lymph nodes are in the preauricular and cervical regions. Systemic metastases are most frequently observed in the lung, liver, bone, and brain.

Tumor Surveillance and Treatment-Related Findings

Posttreatment imaging includes tumor surveillance to identify local or intracranial recurrence, new intracranial or spinal CSF seeding, and development of trilateral or quadrilateral retinoblastoma. The contralateral globe must be monitored to identify metachronous tumor. Treatment-related complications include cataract, vitreous hemorrhage from radiation retinopathy, enophthalmos, phthisis bulbi, myositis, nonspecific inflammatory changes, enhancement of orbital fat and optic nerve, and orbital and midface hypoplasia from EBRT.⁹²⁻⁹⁴ Secondary tumors are seen in heritable forms of retinoblastoma, especially after radiation. Patients with germline disease are at increased risk for osteosarcoma and soft tissue sarcoma, melanoma, and malignancies of the brain and nasal cavities. The cumulative incidence for new cancer at 50 years after retinoblastoma diagnosis is 36% for those with hereditary retinoblastoma and 5.7% for those with nonhereditary retinoblastoma.⁷⁵

CONCLUSIONS

Retinoblastoma is a complex disease that requires careful work-up for accurate diagnosis and an expert, multidisciplinary team for appropriate treatment, optimized vision-sparing survival, and long-term surveillance. The neuroradiologist is a critical part of the retinoblastoma care team and should be familiar with key diagnostic and prognostic features of this disease.

REFERENCES

1. Dimaras H, Kimani K, Dimba EA, et al. **Retinoblastoma.** *Lancet* 2012;379:1436-46 CrossRef Medline
2. Dimaras H, Corson TW, Cobrinik D, et al. **Retinoblastoma.** *Nat Rev Dis Primers* 2015;1:15021 CrossRef Medline
3. Shields JA, Leonard BC, Michelson JB, et al. **B-scan ultrasonography in the diagnosis of atypical retinoblastomas.** *Can J Ophthalmol* 1976;11:42-51 Medline
4. Chawla B, Bhaskaran K, Dada T, et al. **Evaluation of the role of ultrasound biomicroscopy in advanced retinoblastoma: a prospective study on Asian Indian children.** *Ophthalmic Genet* 2020;1-6 CrossRef Medline
5. Kim JW, Ngai LK, Sadda S, et al. **Retcam fluorescein angiography findings in eyes with advanced retinoblastoma.** *Br J Ophthalmol* 2014;98:1666-71 CrossRef Medline
6. Lim LS, Dalvin LA, Ancona-Lezama D, et al. **Retinoblastoma vascular perfusion and intra-arterial chemotherapy cycle requirements.** *Clin Exp Ophthalmol* 2019;47:1164-72 CrossRef Medline
7. Bianciotto C, Shields CL, Iturralde JC, et al. **Fluorescein angiographic findings after intra-arterial chemotherapy for retinoblastoma.** *Ophthalmology* 2012;119:843-49 CrossRef Medline
8. Seider MI, Grewal DS, Mruthyunjaya P. **Portable optical coherence tomography detection or confirmation of ophthalmoscopically invisible or indeterminate active retinoblastoma.** *Ophthalmic Surg Lasers Imaging Retina* 2016;47:965-68 CrossRef Medline
9. Gonzalez-Montpetit ME, Samara WA, Magrath GN, et al. **Detection of minimally visible recurrent retinoblastoma by hand-held spectral-domain optical coherence tomography.** *J Pediatr Ophthalmol Strabismus* 2017;54:e6-e8 CrossRef Medline
10. Nadiarnykh O, Davidoiu V, Grafe MGO, et al. **Phase-based OCT angiography in diagnostic imaging of pediatric retinoblastoma patients: abnormal blood vessels in post-treatment regression patterns.** *Biomed Opt Express* 2019;10:2213-26 CrossRef Medline
11. de Graaf P, Göricke S, Rodjan F, et al. **Guidelines for imaging retinoblastoma: imaging principles and MRI standardization.** *Pediatr Radiol* 2012;42:2-14 CrossRef Medline
12. Rodjan F, de Graaf P, Moll AC, et al. **Brain abnormalities on MR imaging in patients with retinoblastoma.** *AJNR Am J Neuroradiol* 2010;31:1385-89 CrossRef Medline
13. Galluzzi P, Hadjistilianou T, Cerase A, et al. **Is CT still useful in the study protocol of retinoblastoma?** *AJNR Am J Neuroradiol* 2009;30:1760-65 CrossRef Medline
14. Marees T, Moll AC, Imhof SM, et al. **Risk of second malignancies in survivors of retinoblastoma: more than 40 years of follow-up.** *J Natl Cancer Inst* 2008;100:1771-79 CrossRef Medline
15. Murray T. **Cancer incidence after retinoblastoma: radiation dose and sarcoma risk.** *Surv Ophthalmol* 1998;43:288-89 CrossRef Medline
16. Wong FL, Boice JD Jr, Abramson DH, et al. **Cancer incidence after retinoblastoma. Radiation dose and sarcoma risk.** *JAMA* 1997;278:1262-67 CrossRef Medline
17. Brisse HJ, Lumbroso L, Freneaux PC, et al. **Sonographic, CT, and MR imaging findings in diffuse infiltrative retinoblastoma: report of two cases with histologic comparison.** *AJNR Am J Neuroradiol* 2001;22:499-504 Medline
18. Shields CL, Ghassemi F, Tuncer S, et al. **Clinical spectrum of diffuse infiltrating retinoblastoma in 34 consecutive eyes.** *Ophthalmology* 2008;115:2253-58 CrossRef Medline
19. de Graaf P, van der Valk P, Moll AC, et al. **Contrast-enhancement of the anterior eye segment in patients with retinoblastoma: correlation between clinical, MR imaging, and histopathologic findings.** *AJNR Am J Neuroradiol* 2010;31:237-45 CrossRef Medline
20. Galluzzi P, Cerase A, Hadjistilianou T, et al. **Retinoblastoma: abnormal gadolinium enhancement of anterior segment of eyes at MR imaging with clinical and histopathologic correlation.** *Radiology* 2003;228:683-90 CrossRef Medline
21. Chintagumpala M, Chevez-Barrios P, Paysse EA, et al. **Retinoblastoma: review of current management.** *Oncologist* 2007;12:1237-46 CrossRef Medline

22. Kopelman JE, McLean IW, Rosenberg SH. **Multivariate analysis of risk factors for metastasis in retinoblastoma treated by enucleation.** *Ophthalmology* 1987;94:371–77 CrossRef Medline
23. Barkhof F, Smeets M, van der Valk P, et al. **MR imaging in retinoblastoma.** *Eur Radiology* 1997;7:726–31 CrossRef Medline
24. Schueler AO, Hosten N, Bechrakis NE, et al. **High resolution magnetic resonance imaging of retinoblastoma.** *Br J Ophthalmol* 2003;87:330–35 CrossRef Medline
25. de Graaf P, Barkhof F, Moll AC, et al. **Retinoblastoma: MR imaging parameters in detection of tumor extent.** *Radiology* 2005;235:197–207 CrossRef Medline
26. Rauschecker AM, Patel CV, Yeom KW, et al. **High-resolution MR imaging of the orbit in patients with retinoblastoma.** *Radiographics* 2012;32:1307–26 CrossRef Medline
27. Sirin S, Schlamann M, Metz KA, et al. **High-resolution MRI using orbit surface coils for the evaluation of metastatic risk factors in 143 children with retinoblastoma: part 1: MRI vs. histopathology.** *Neuroradiology* 2015;57:805–14 CrossRef Medline
28. Khelifaoui F, Validire P, Auperin A, et al. **Histopathologic risk factors in retinoblastoma: a retrospective study of 172 patients treated in a single institution.** *Cancer* 1996;77:1206–13 CrossRef Medline
29. Chawla B, Sharma S, Sen S, et al. **Correlation between clinical features, magnetic resonance imaging, and histopathologic findings in retinoblastoma: a prospective study.** *Ophthalmology* 2012;119:850–56 CrossRef Medline
30. Novetsky DE, Abramson DH, Kim JW, et al. **Published International Classification of Retinoblastoma (ICRB) definitions contain inconsistencies—an analysis of impact.** *Ophthalmic Genet* 2009;30:40–44 CrossRef Medline
31. Chévez-Barríos P, Eagle RC Jr, Krailo M, et al. **Study of unilateral retinoblastoma with and without histopathologic high-risk features and the role of adjuvant chemotherapy: a Children's Oncology Group study.** *J Clin Oncol* 2019;37:2883–91 CrossRef Medline
32. Kashyap S, Meel R, Pushker N, et al. **Phthisis bulbi in retinoblastoma.** *Clin Exp Ophthalmol* 2011;39:105–10 CrossRef Medline
33. Shields JA, Shields CL, Suvaramani C, et al. **Retinoblastoma manifesting as orbital cellulitis.** *Am J Ophthalmol* 1991;112:442–49 CrossRef Medline
34. Shields CL, Shields JA, Baez K, et al. **Optic nerve invasion of retinoblastoma. Metastatic potential and clinical risk factors.** *Cancer* 1994;73:692–98 CrossRef Medline
35. Cuenca A, Giron F, Castro D, et al. **Microscopic scleral invasion in retinoblastoma: clinicopathological features and outcome.** *Arch Ophthalmol* 2009;127:1006–10 CrossRef Medline
36. Brisse HJ, Guesmi M, Aerts I, et al. **Relevance of CT and MRI in retinoblastoma for the diagnosis of postlaminar invasion with normal-size optic nerve: a retrospective study of 150 patients with histological comparison.** *Pediatr Radiol* 2007;37:649–56 CrossRef Medline
37. Li Z, Guo J, Xu X, et al. **Diagnosis of postlaminar optic nerve invasion in retinoblastoma with MRI features.** *J Magn Reson Imaging* 2020;51:1045–52 CrossRef Medline
38. Magrann I, Abramson DH, Ellsworth RM. **Optic nerve involvement in retinoblastoma.** *Ophthalmology* 1989;96:217–22 CrossRef Medline
39. Brisse HJ, de Graaf P, Galluzzi P, et al. **Assessment of early-stage optic nerve invasion in retinoblastoma using high-resolution 1.5 Tesla MRI with surface coils: a multicentre, prospective accuracy study with histopathological correlation.** *Eur Radio* 2015;25:1443–52 CrossRef Medline
40. Cui Y, Luo R, Wang R, et al. **Correlation between conventional MR imaging combined with diffusion-weighted imaging and histopathologic findings in eyes primarily enucleated for advanced retinoblastoma: a retrospective study.** *Eur Radiol* 2018;28:620–29 CrossRef Medline
41. Lee BJ, Kim JH, Kim DH, et al. **The validity of routine brain MRI in detecting post-laminar optic nerve involvement in retinoblastoma.** *Br J Ophthalmol* 2012;96:1237–41 CrossRef
42. Khurana A, Eisenhut CA, Wan W, et al. **Comparison of the diagnostic value of MR imaging and ophthalmoscopy for the staging of retinoblastoma.** *Eur Radiol* 2013;23:1271–80 CrossRef Medline
43. de Graaf P, Moll AC, Imhof SM, et al. **Retinoblastoma and optic nerve enhancement on MRI: not always extraocular tumour extension.** *Br J Ophthalmol* 2006;90:800–01 CrossRef Medline
44. Lemke AJ, Kazi I, Mergner U, et al. **Retinoblastoma—MR appearance using a surface coil in comparison with histopathological results.** *Eur Radiol* 2007;17:49–60 CrossRef Medline
45. Song KD, Eo H, Kim JH, et al. **Can preoperative MR imaging predict optic nerve invasion of retinoblastoma?** *Eur J Radiol* 2012;81:4041–45 CrossRef Medline
46. Wilson MW, Rodriguez-Galindo C, Billups C, et al. **Lack of correlation between the histologic and magnetic resonance imaging results of optic nerve involvement in eyes primarily enucleated for retinoblastoma.** *Ophthalmology* 2009;116:1558–63 CrossRef Medline
47. Hiasat JG, Saleh A, Al-Hussaini M, et al. **The predictive value of magnetic resonance imaging of retinoblastoma for the likelihood of high-risk pathologic features.** *Eur J Ophthalmol* 2019;29:262–68 CrossRef Medline
48. de Jong MC, de Graaf P, Noij DP, et al. **Diagnostic performance of magnetic resonance imaging and computed tomography for advanced retinoblastoma: a systematic review and meta-analysis.** *Ophthalmology* 2014;121:1109–18 CrossRef Medline
49. Shields CL, Mashayekhi A, Au AK, et al. **The International Classification of Retinoblastoma predicts chemoreduction success.** *Ophthalmology* 2006;113:2276–80 CrossRef Medline
50. Shields CL, Lally SE, Leahey AM, et al. **Targeted retinoblastoma management: when to use intravenous, intra-arterial, periocular, and intravitreal chemotherapy.** *Curr Opin Ophthalmol* 2014;25:374–85 CrossRef Medline
51. Shields CL, Bas Z, Tadepalli S, et al. **Long-term (20-year) real-world outcomes of intravenous chemotherapy (chemoreduction) for retinoblastoma in 964 eyes of 554 patients at a single centre.** *Br J Ophthalmol* 2020;104:1548–55 CrossRef Medline
52. Shields CL, Meadows AT, Shields JA, et al. **Chemoreduction for retinoblastoma may prevent intracranial neuroblastic malignancy (trilateral retinoblastoma).** *Arch Ophthalmol* 2001;119:1269–72 CrossRef Medline
53. Turaka K, Shields CL, Meadows AT, et al. **Second malignant neoplasms following chemoreduction with carboplatin, etoposide, and vincristine in 245 patients with intraocular retinoblastoma.** *Pediatr Blood Cancer* 2012;59:121–25 CrossRef Medline
54. Luna-Fineman S, Chantada G, Alejos A, et al. **Delayed enucleation with neoadjuvant chemotherapy in advanced intraocular unilateral retinoblastoma: AHOPCA II, a prospective, multi-institutional protocol in Central America.** *J Clin Oncol* 2019;37:2875–82 CrossRef Medline
55. Radhakrishnan V, Kashyap S, Pushker N, et al. **Outcome, pathologic findings, and compliance in orbital retinoblastoma (International Retinoblastoma Staging System stage III) treated with neoadjuvant chemotherapy: a prospective study.** *Ophthalmology* 2012;119:1470–77 CrossRef Medline
56. Yamane T, Kaneko A, Mohri M. **The technique of ophthalmic arterial infusion therapy for patients with intraocular retinoblastoma.** *Int J Clin Oncol* 2004;9:69–73 CrossRef Medline
57. Abramson DH, Dunkel IJ, Brodie SE, et al. **A phase I/II study of direct intraarterial (ophthalmic artery) chemotherapy with melphalan for intraocular retinoblastoma initial results.** *Ophthalmology* 2008;115:1398–404, 404.e1 CrossRef Medline
58. Gobin YP, Dunkel IJ, Marr BP, et al. **Intra-arterial chemotherapy for the management of retinoblastoma: four-year experience.** *Arch Ophthalmol* 2011;129:732–37 CrossRef Medline

59. Shields CL, Bianciotto CG, Jabbour P, et al. **Intra-arterial chemotherapy for retinoblastoma: report No. 1, control of retinal tumors, subretinal seeds, and vitreous seeds.** *Arch Ophthalmol* 2011;129:1399–406 CrossRef Medline
60. Shields CL, Manjandavida FP, Lally SE, et al. **Intra-arterial chemotherapy for retinoblastoma in 70 eyes: outcomes based on the International Classification of Retinoblastoma.** *Ophthalmology* 2014;121:1453–60 CrossRef Medline
61. Jabbour P, Chalouhi N, Tjoumakaris S, et al. **Pearls and pitfalls of intraarterial chemotherapy for retinoblastoma.** *J Neurosurg Pediatr* 2012;10:175–81 CrossRef Medline
62. Bonasia S, Bojanowski M, Robert T. **Embryology and anatomical variations of the ophthalmic artery.** *Neuroradiology* 2020;62:139–52 CrossRef Medline
63. Shields CL, Bianciotto CG, Jabbour P, et al. **Intra-arterial chemotherapy for retinoblastoma: report No. 2, treatment complications.** *Arch Ophthalmol* 2011;129:1407–15 CrossRef Medline
64. Marr B, Gobin PY, Dunkel IJ, et al. **Spontaneously resolving periocular erythema and ciliary madarosis following intra-arterial chemotherapy for retinoblastoma.** *Middle East Afr J Ophthalmol* 2010;17:207–09 CrossRef Medline
65. Vajzovic LM, Murray TG, Aziz-Sultan MA, et al. **Supraselective intra-arterial chemotherapy: evaluation of treatment-related complications in advanced retinoblastoma.** *Clin Ophthalmol* 2011;5:171–76 CrossRef Medline
66. Zanaty M, Barros G, Chalouhi N, et al. **Update on intra-arterial chemotherapy for retinoblastoma.** *ScientificWorldJournal* 2014;2014:869604 CrossRef Medline
67. Monroy JE, Orbach DB, VanderVeen D. **Complications of intra-arterial chemotherapy for retinoblastoma.** *Semin Ophthalmol* 2014;29:429–33 CrossRef Medline
68. Dalvin LA, Ancona-Lezama D, Lucio-Alvarez JA, et al. **Ophthalmic vascular events after primary unilateral intra-arterial chemotherapy for retinoblastoma in early and recent eras.** *Ophthalmology* 2018;125:1803–11 CrossRef Medline
69. Ancona-Lezama D, Dalvin LA, Lucio-Alvarez JA, et al. **Ophthalmic vascular events following intra-arterial chemotherapy for retinoblastoma. Real-world comparison between primary and secondary treatments.** *Retina* 2019;39:2264–72 CrossRef Medline
70. Shields CL, Alset AE, Say EA, et al. **Retinoblastoma control with primary intra-arterial chemotherapy: outcomes before and during the intravitreal chemotherapy era.** *J Pediatr Ophthalmol Strabismus* 2016;53:275–84 CrossRef Medline
71. Dalvin LA, Kumari M, Essuman VA, et al. **Primary intra-arterial chemotherapy for retinoblastoma in the intravitreal chemotherapy era: five years of experience.** *Ocul Oncol Pathol* 2019;5:139–46 CrossRef Medline
72. Munier FL, Gaillard MC, Decembrini S, et al. **Intracameral chemotherapy (melphalan) for aqueous seeding in retinoblastoma: bicameral injection technique and related toxicity in a pilot case study.** *Ocul Oncol Pathol* 2017;3:149–55 CrossRef Medline
73. Lumbroso-Le Rouic L, Levy-Gabriel C, Desjardins L. **Local adjuvant therapy.** In: Ramasubramanian A, Shields CL, eds. *Retinoblastoma*. New Delhi: Jaypee Brothers Medical Publishers Ltd; 2012
74. Abramson DH, Frank CM. **Second nonocular tumors in survivors of bilateral retinoblastoma: a possible age effect on radiation-related risk.** *Ophthalmology* 1998;105:573–79; discussion 579–80 CrossRef Medline
75. Kleinerman RA, Tucker MA, Tarone RE, et al. **Risk of new cancers after radiotherapy in long-term survivors of retinoblastoma: an extended follow-up.** *J Clin Oncol* 2005;23:2272–79 CrossRef Medline
76. Kim JY, Park Y. **Treatment of retinoblastoma: the role of external beam radiotherapy.** *Yonsei Med J* 2015;56:1478–91 CrossRef Medline
77. Shields CL, Mashayekhi A, Sun H, et al. **Iodine 125 plaque radiotherapy as salvage treatment for retinoblastoma recurrence after chemoreduction in 84 tumors.** *Ophthalmology* 2006;113:2087–92 CrossRef Medline
78. Shields CL, Shields JA, Minelli S, et al. **Regression of retinoblastoma after plaque radiotherapy.** *Am J Ophthalmol* 1993;115:181–87 CrossRef Medline
79. Paramo DM, Firestone B, Mahajan A, et al. **External beam radiation therapy.** In: Ramasubramanian A, Shields CL, eds. *Retinoblastoma*. New Delhi: Jaypee Brothers Medical Publishers Ltd; 2012
80. Tsimpida M, Reddy MA, Sagoo M. **Enucleation.** In: Ramasubramanian A, Shields CL, eds. *Retinoblastoma*. New Delhi: Jaypee Brothers Medical Publishers Ltd; 2012
81. de Potter P. **Current treatment of retinoblastoma.** *Curr Opin Ophthalmol* 2002;13:331–36 CrossRef Medline
82. Shields JA, Shields CL, Sivalingam V. **Decreasing frequency of enucleation in patients with retinoblastoma.** *Am J Ophthalmol* 1989;108:185–88 CrossRef Medline
83. Shields CL, Uysal Y, Marr BP, et al. **Experience with the polymer-coated hydroxyapatite implant after enucleation in 126 patients.** *Ophthalmology* 2007;114:367–73 CrossRef Medline
84. Kaliki S, Shields CL, Shah SU, et al. **Postenucleation adjuvant chemotherapy with vincristine, etoposide, and carboplatin for the treatment of high-risk retinoblastoma.** *Arch Ophthalmol* 2011;129:1422–27 CrossRef Medline
85. Li MH, Bouffet E, Hawkins CE, et al. **Molecular genetics of supratentorial primitive neuroectodermal tumors and pineoblastoma.** *Neurosurg Focus* 2005;19:E3 CrossRef Medline
86. de Jong MC, Kors WA, Moll AC, et al. **Screening for pineal trilateral retinoblastoma revisited: a meta-analysis.** *Ophthalmology* 2020;127:601–07 CrossRef Medline
87. Rodjan F, de Graaf P, Brisse HJ, et al. **Trilateral retinoblastoma: neuroimaging characteristics and value of routine brain screening on admission.** *J Neurooncol* 2012;109:535–44 CrossRef Medline
88. de Jong MC, Kors WA, de Graaf P, et al. **The incidence of trilateral retinoblastoma: a systematic review and meta-analysis.** *Am J Ophthalmol* 2015;160:1116–26.e5 CrossRef Medline
89. Sirin S, de Jong MC, Galluzzi P, et al. **MRI-based assessment of the pineal gland in a large population of children aged 0–5 years and comparison with pineoblastoma: part II, the cystic gland.** *Neuroradiology* 2016;58:713–21 CrossRef Medline
90. Ramasubramanian A, Kytasty C, Meadows AT, et al. **Incidence of pineal gland cyst and pineoblastoma in children with retinoblastoma during the chemoreduction era.** *Am J Ophthalmol* 2013;156:825–29 CrossRef Medline
91. Gaillard F, Jones J. **Masses of the pineal region: clinical presentation and radiographic features.** *Postgrad Med J* 2010;86:597–607 CrossRef Medline
92. Imhof SM, Mourits MP, Hofman P, et al. **Quantification of orbital and mid-facial growth retardation after megavoltage external beam irradiation in children with retinoblastoma.** *Ophthalmology* 1996;103:263–68 CrossRef Medline
93. Tawansy KA, Samuel MA, Shamma M, et al. **Vitreoretinal complications of retinoblastoma treatment.** *Retina* 2006;26:S47–52 CrossRef Medline
94. Abramson DH, Beaverson KL, Chang ST, et al. **Outcome following initial external beam radiotherapy in patients with Reese-Ellsworth group Vb retinoblastoma.** *Arch Ophthalmol* 2004;122:1316–23 CrossRef Medline

Time to Reconsider Routine Percutaneous Biopsy in Spondylodiscitis?

Ö. Kasalak, M. Wouthuyzen-Bakker, R.A.J.O. Dierckx, P.C. Jutte, and T.C. Kwee



ABSTRACT

SUMMARY: Percutaneous image-guided biopsy currently has a central role in the diagnostic work-up of patients with suspected spondylodiscitis. However, on the basis of recent evidence, the value of routine image-guided biopsy in this disease can be challenged. In this article, we discuss this recent evidence and also share a new diagnostic algorithm for spondylodiscitis that was recently introduced at our institution. Thus, we may move from a rather dogmatic approach in which routine image-guided biopsy is performed in any case to a more individualized use of this procedure.

The incidence of spondylodiscitis is rising in the developed world due to aging of the population with inherent comorbidities that increase the risk of infection and improved diagnosis because of widespread use of MR imaging.¹ The diagnosis of spondylodiscitis and the microbiologic culprit can be confirmed by a combination of MR imaging findings with blood cultures or cultures of spinal or paraspinal tissue samples. The guidelines of the Infectious Diseases Society of America recommend performing MR imaging and obtaining blood cultures in all patients with suspected spondylodiscitis. They also recommend image-guided biopsy when the microbiologic diagnosis has not been established by blood cultures or serologic tests.^{2,3} The same guidelines advise repeat image-guided percutaneous biopsy or proceeding to open biopsy if the initial biopsy result remains negative.^{2,3} Thus, percutaneous image-guided biopsy currently has a central role in the diagnostic work-up of patients with suspected spondylodiscitis.

Arguments for Routinely Performing Percutaneous Image-Guided Biopsy

Proponents of routinely performing percutaneous image-guided biopsy argue that a microbiologic diagnosis should be established to target antimicrobial treatment and ultimately improve clinical outcome. In addition, antibiotic resistance may potentially be

reduced with such an approach because it allows exact targeting of the specific microbe. Furthermore, establishing a microbiologic diagnosis may prevent the need for an open or surgical intervention when infection progresses.^{2,3} It is also argued that pathologic examination of biopsy specimens may help differentiate an infectious from a malignant or degenerative process.^{2,3} Finally, the Infectious Diseases Society of America guidelines mention that the sensitivity of image-guided biopsy varies between 30% and 74%, which seems fairly high, though these numbers are based on only 3 studies that were cited in these guidelines.^{2,3}

Practical Issues of Percutaneous Image-Guided Biopsy

Percutaneous image-guided biopsy can be performed using conventional x-ray fluoroscopic or CT guidance, with most previously published studies using CT for this purpose in spondylodiscitis.⁴ The advantages of CT-guided biopsy over x-ray fluoroscopically guided biopsy are more accurate localization, multiplanar views, the ability to differentiate necrotic bone and solid lesions, and not exposing the operator to ionizing radiation.¹ Although CT-guided biopsy is relatively safe, it is still an invasive procedure with a non-negligible risk of complications. Minor complications such as transient paresis, hematoma, postbiopsy fever, pain, bruising, and swelling occur in around 2%.^{5,6} Major complications such as spinal cord injury are rare but have also been reported.⁷ Furthermore, lying still during the procedure may be burdensome to some patients who are ill and have severe back pain due to spondylodiscitis, in our experience. The use of potentially harmful ionizing radiation should also be taken into account.⁸

Culture Yield of Percutaneous Image-Guided Biopsy: The Actual Numbers

A crucial topic is the culture yield of the spinal or paraspinal biopsy samples that have been obtained. According to a meta-

Received October 14, 2020; accepted after revision November 9.

From the Departments of Radiology, Nuclear Medicine and Molecular Imaging (Ö.K., R.A.J.O.D., T.C.K.), Medical Microbiology and Infection Prevention (M.W.-B.), and Orthopedics (P.C.J.), University Medical Center Groningen, University of Groningen, Groningen, the Netherlands.

Please address correspondence to Ömer Kasalak, MD, PhD, University Medical Center Groningen, Department of Radiology, Nuclear Medicine and Molecular Imaging, Hanzeplein 1, PO Box 30.001, 9700 RB Groningen, the Netherlands; e-mail: o.kasalak@umcg.nl

<http://dx.doi.org/10.3174/ajnr.A6994>

Key findings of main studies discussed in this article

Study and Year	Key Findings
McNamara et al, 2017 ⁴	Meta-analysis that reported image-guided biopsy to have a positive culture yield of approximately 48% in patients with suspected spondylodiscitis
Sertic et al, 2019 ⁹	Meta-analysis that reported that CT-guided biopsy had a positive culture yield of 33% in patients with suspected spondylodiscitis
Kasalak et al, 2018 ¹⁰	Initial CT-guided biopsy was culture-positive in 31.3% of patients with suspected spondylodiscitis Repeat CT-guided biopsy (after initial negative biopsy findings) was culture-positive in 33.3% of patients with suspected spondylodiscitis 96.9% of 64 patients with suspected spondylodiscitis would have been adequately treated if a strategy was followed that would subject all patients without clinical findings suspicious for “atypical” micro-organisms and negative blood cultures to empiric antibiotics (ie, clindamycin for coverage of Gram-positive bacteria) without using biopsy results to determine the optimal antibiotic regimen Outcome within 6 months (development of neurologic or orthopedic complications, an operation, and/or death) was not significantly different between positive and negative findings on biopsy cultures in patients with suspected spondylodiscitis
Özmen et al, 2019 ¹¹	CT-guided biopsy was culture-positive in 33.8% with suspected spondylodiscitis
Kasalak et al, 2018 ¹²	Systematic review of 8 studies that reported that repeat percutaneous image-guided biopsy (after an initial biopsy with negative findings on cultures) had a positive culture yield ranging between 0% and 60.0% in patients with suspected spondylodiscitis, based on poor-quality evidence
Bae et al, 2018 ¹³	The species of blood and biopsy isolates in patients with pyogenic spondylodiscitis were identical in 95.7% Excluding 4 anaerobic isolates, antibiotic susceptibility patterns were identical between blood and biopsy isolates in 97.7%
Kim et al, 2014 ¹⁶	There were no significant differences in treatment success (defined as survival and absence of signs of infection at the end of the therapy) between 75 patients with microbiologically confirmed pyogenic spondylodiscitis (whether by means of blood or biopsy cultures) and 76 patients with clinically diagnosed pyogenic spondylodiscitis without microbiologic confirmation

analysis that included 33 studies, image-guided biopsy has a positive culture yield of approximately 48%.⁴ In another more recent meta-analysis that included 10 studies, the positive culture yield of CT-guided biopsy in suspected spinal infection was 33%.⁹ The latter percentage of 33% corroborates both the results of some more recent original studies investigating the microbiological yield of the first biopsy in suspected spondylodiscitis^{10,11} and a meta-analysis that included 8 studies on the culture yield of repeat biopsy after an initial biopsy with negative findings.¹² This percentage is also considerably lower than the 30%–74% range that was described in the Infectious Diseases Society of America guidelines.^{2,3} Furthermore, cultures may be positive for possible skin contaminants such as coagulase-negative *Staphylococcus* species (except *Staphylococcus lugdunensis*) and *Cutibacterium* species; thus, the spinal or paraspinal biopsy culture may be inconclusive.^{2,3}

Recent Evidence

The practical disadvantages of percutaneous image-guided biopsy⁵⁻⁸ and the relatively low positive culture yield of 33%⁹⁻¹² raise the question of whether this procedure should be routinely performed in all patients with suspected spondylodiscitis. Some recent evidence can also be considered supportive of this potential paradigm shift.

First, a recent study from Korea that included 141 patients with pyogenic spondylitis in whom micro-organisms were isolated from both blood and tissue cultures reported that the species of blood and tissue isolates were identical in 135 patients (95.7%, 135/141).¹³ If one excluded the 4 anaerobic isolates, antibiotic susceptibility patterns were identical in 128 patients (97.7%, 128/131).¹³ These results suggest that a positive blood culture from patients with pyogenic spondylitis could preclude the need for additional tissue cultures.¹³ This suggestion is also in

line with the Infectious Diseases Society of America guidelines that recommend against obtaining a tissue sample in the setting of positive blood cultures, particularly in patients with *Staphylococcus aureus*, *S lugdunensis*, or *Brucella* species bloodstream infection.^{2,3} Therefore, an argument can be made to delay any decision about the need for percutaneous image-guided biopsy until blood culture results are available. Broad spectrum antibiotics should be administered until blood cultures are known, covering the most common causative micro-organisms. This approach will save patients with blood cultures with positive findings an unnecessary biopsy.

Second, even when the microbiologic culprit remains unknown, it may still be possible to start an effective empiric treatment in patients with chronic spondylodiscitis without neurologic deficits. A recent study from the Netherlands included 64 patients with MR imaging findings compatible with spondylodiscitis who underwent CT-guided biopsy.¹⁰ Sixty-two patients (96.9%, 62/64) would have been adequately treated if a strategy were followed that would subject all patients with negative blood cultures to empiric antibiotics (i.e., clindamycin for coverage of Gram-positive bacteria) without using biopsy results to determine the optimal antibiotic regimen, provided that there are no clinical findings suspicious for “atypical” microorganisms.¹⁰ Refraining from routine biopsy and initiating empiric treatment when blood cultures have negative findings may be considered in patients with a nonacute chronic presentation and typical MR imaging findings of spondylodiscitis¹⁰ (ie, T2 hyperintensity and/or contrast enhancement of 2 consecutive vertebrae and the intervening disc after administration of a gadolinium-based contrast agent¹⁴). Patients who are immunocompromised and in whom atypical micro-organisms can be expected such as *Candida* species and patients with clinical and/or MR imaging



FIG 1. Proposed diagnostic algorithm for (suspected) acute spondylodiscitis. Acute spondylodiscitis is defined as acute pain in back or neck, fever and/or increased C-reactive protein levels, and characteristic imaging findings of spondylodiscitis on MR imaging or FDG-PET/CT (FDG-PET/CT should be considered when MR imaging cannot be performed). Explanation of annotations in this figure: 1) Addition of tobramycin 7 mg/kg once daily in case of sepsis, adjustment according to cultures; 2) Empiric antibiotics should be aimed at both Gram-positive and Gram-negative bacteria, and the most common pathogens of spondylodiscitis, with the final choice based on local antibiotics resistance data (in countries with a high prevalence of methicillin-resistant *S. aureus*, cefuroxime is not sufficient); 3) If sufficient material can be obtained, then biopsy samples should be sent in for both microbiological and pathological examination; 4) Additional diagnostics for atypical pathogens should be performed when clinically indicated, in consultation with an infectious disease specialist or medical microbiologist.

findings that may suggest tuberculous spondylodiscitis (including relative sparing of the intervertebral disc early in the stage of infection, involvement of the anterior vertebral body corner, subligamentous spread, multiple vertebral body involvement, extensive paraspinal abscess formation, abscess calcification, and vertebral destruction¹⁵) should be exempt from this strategy.¹⁰

Third, the final aim of a percutaneous image-guided biopsy is to improve patient outcome in terms of quality-adjusted life years

gained. A study in 64 patients with suspected spondylodiscitis did not show any significant difference in outcome (defined as either development of severe vertebral height loss, hyperkyphosis, neurologic deficits, or the need for an operation within 6 months after CT-guided biopsy, and/or death during hospitalization) between patients with CT-guided biopsy cultures with positive findings (6/25 patients with poor outcome) and CT-guided biopsy cultures with negative findings (7/39 patients with poor outcome) ($P = .751$).¹⁰ In another study, there were no significant

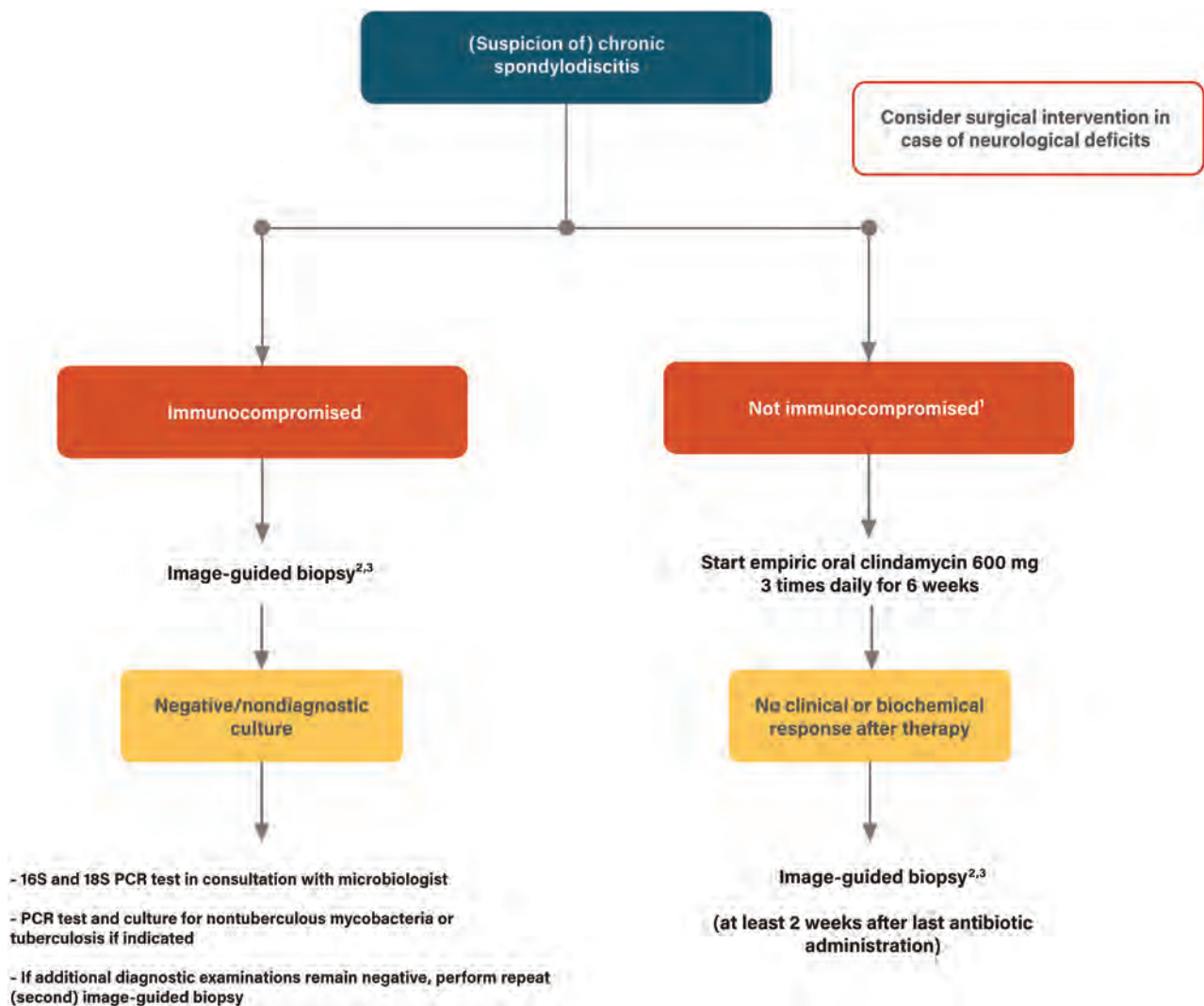


FIG 2. Proposed diagnostic algorithm for (suspected) chronic spondylodiscitis. Chronic spondylodiscitis is defined as chronic pain (weeks to months) in back or neck, and characteristic imaging findings of spondylodiscitis on MR imaging or FDG-PET/CT (FDG-PET/CT should be considered when MR imaging cannot be performed). Explanation of annotations in this figure: 1) If there is a suspicion of tuberculous spondylodiscitis or doubt about the diagnosis of spondylodiscitis, image-guided biopsy is recommended; 2) If sufficient material can be obtained, then biopsy samples should be sent in for both microbiological and pathological examination; 3) Additional diagnostics for atypical pathogens should be performed when clinically indicated, in consultation with an infectious disease specialist or medical microbiologist.

differences in treatment success (defined as survival and absence of signs of infection at the end of the therapy) either between 75 patients with microbiologically confirmed spondylodiscitis (whether by means of blood or biopsy cultures) and 76 patients without microbiologically confirmed spondylodiscitis ($P = .157$).¹⁶ Randomized studies in which the outcome of patients who underwent percutaneous image-guided biopsy were compared with those who did not undergo this procedure are lacking. Therefore, there is currently no evidence that routine percutaneous image-guided biopsy improves outcomes in patients with suspected spondylodiscitis and blood cultures with negative findings.

Proposal of a New Diagnostic Algorithm

On the basis of the previously mentioned underpinnings (key findings of the main studies discussed in this review article are shown in the Table) and our own 9-year single-center

experience,¹⁰ we have reconsidered the role of percutaneous image-guided biopsy in the diagnostic work-up of patients with suspected spondylodiscitis at our institution. First, we classify patients as either those with (suspicion of) acute spondylodiscitis or chronic spondylodiscitis. Patients with acute spondylodiscitis present with a sudden onset of pain, most often associated with fever and high serum inflammatory markers. Patients with chronic spondylodiscitis have long-standing pain for which the exact time of onset often cannot be determined, fever is frequently absent, and serum inflammatory markers are often only mildly increased. Rather than subjecting all patients with (suspicion of) acute spondylodiscitis to this procedure, only those with blood cultures with negative findings are now eligible for CT-guided biopsy. Biopsy is not performed in patients in whom the results of blood cultures are positive or still unknown within 48 hours. In the group of patients with (suspicion of) chronic

spondylodiscitis, biopsy is withheld and empiric treatment with clindamycin is started, provided that the patient is not immunocompromised, no clinical suspicion of a Gram-negative infection is present, and there is no suspicion of tuberculosis or doubt about the diagnosis of spondylodiscitis based on clinical and imaging grounds. If there is no improvement at the end of therapy (ie, 6 weeks after completion of antibiotic therapy), CT-guided biopsy will be performed. We also advise performing percutaneous image-guided biopsy at least 2 weeks after stopping antibiotics to reduce the chance of false-negative cultures.

The proposed diagnostic algorithm is shown in Fig 1 (acute spondylodiscitis) and Fig 2 (chronic spondylodiscitis). With this new approach, the number of unnecessary percutaneous image-guided biopsies can potentially be reduced. Our institution is located in a region where the prevalence of both tuberculosis and antibiotic resistance is low. Whether the shift from a routine to a more conditional role of percutaneous image-guided biopsy in spondylodiscitis can be implemented in other institutions is probably dependent on these 2 important conditions. Although the proposed diagnostic algorithm requires clinical validation, it can be considered as an important first step to open the debate on this topic and to initiate research to further refine the role of percutaneous image-guided biopsy in spondylodiscitis.

CONCLUSIONS

Percutaneous image-guided biopsy is a valuable tool in the diagnostic arsenal for spondylodiscitis. However, it is an invasive procedure, and recent evidence has shown rather disappointing positive microbiologic culture yields of around 33%. Recent evidence also has shown that percutaneous image-guided biopsy rarely adds any new information when blood cultures have positive findings and that an effective empiric treatment can be started in the far most of cases even when the microbiologic culprit remains unknown. Finally, there is currently no evidence that percutaneous image-guided biopsy improves patient outcome. On the basis of these underpinnings, it may be time to consider a shift from a routine to a more conditional role of percutaneous image-guided biopsy in spondylodiscitis.

REFERENCES

- Nickerson EK, Sinha R. **Vertebral osteomyelitis in adults: an update.** *Br Med Bull* 2016;117:121–38 CrossRef Medline
- Berbari EF, Kanj SS, Kowalski TJ, et al. **Executive summary: 2015 Infectious Diseases Society of America (IDSA) clinical practice guidelines for the diagnosis and treatment of native vertebral osteomyelitis in adults.** *Clin Infect Dis* 2015;61:859–63 CrossRef Medline
- Berbari EF, Kanj SS, Kowalski TJ, et al. **Infectious Diseases Society of America (IDSA) clinical practice guidelines for the diagnosis and treatment of native vertebral osteomyelitis in adults.** *Clin Infect Dis* 2015;61:e26–46 CrossRef Medline
- McNamara AL, Dickerson EC, Gomez-Hassan DM, et al. **Yield of image-guided needle biopsy for infectious discitis: a systematic review and meta-analysis.** *AJNR Am J Neuroradiol* 2017;38:2021–27 CrossRef Medline
- Huang AJ, Halpern EF, Rosenthal DI. **Incidence of delayed complications following percutaneous CT-guided biopsy of bone and soft tissue lesions of the spine and extremities: a 2-year prospective study and analysis of risk factors.** *Skeletal Radiol* 2013;42:61–68 CrossRef Medline
- Rimondi E, Rossi G, Bartalena T, et al. **Percutaneous CT-guided biopsy of the musculoskeletal system: results of 2027 cases.** *Eur J Radiol* 2011;77:34–42 CrossRef Medline
- Kesler K, Shamrock A, Hendrickson N, et al. **Complete spinal cord injury following computed tomography-guided biopsy of the thoracic spine: a case report.** *SAGE Open Med Case Rep* 2020;8:2050313X20927580 CrossRef Medline
- Shpilberg KA, Delman BN, Tanenbaum LN, et al. **Radiation dose reduction in CT-guided spine biopsies does not reduce diagnostic yield.** *AJNR Am J Neuroradiol* 2014;35:2243–47 CrossRef Medline
- Sertic M, Parkes L, Mattiassi S, et al. **The efficacy of computed tomography-guided percutaneous spine biopsies in determining a causative organism in cases of suspected infection: a systematic review.** *Can Assoc Radiol J* 2019;70:96–103 CrossRef Medline
- Kasalak Ö, Wouthuyzen-Bakker M, Adams HJ, et al. **CT-guided biopsy in suspected spondylodiscitis: microbiological yield, impact on antimicrobial treatment, and relationship with outcome.** *Skeletal Radiol* 2018;47:1383–91 CrossRef Medline
- Özmen D, Özkan N, Guberina N, et al. **Computed-tomography-guided biopsy in suspected spondylodiscitis: single-center experience including 201 biopsy procedures.** *Orthop Rev (Pavia)* 2019;11:7793 CrossRef Medline
- Kasalak Ö, Adams HJ, Jutte PC, et al. **Culture yield of repeat percutaneous image-guided biopsy after a negative initial biopsy in suspected spondylodiscitis: a systematic review.** *Skeletal Radiol* 2018;47:1327–35 CrossRef Medline
- Bae JY, Kim CJ, Kim UJ, et al. **Concordance of results of blood and tissue cultures from patients with pyogenic spondylitis: a retrospective cohort study.** *Clin Microbiol Infect* 2018;24:279–82 CrossRef Medline
- Hong SH, Choi JY, Lee JW, et al. **MR imaging assessment of the spine: infection or an imitation?** *Radiographics* 2009;29:599–612 CrossRef Medline
- Kumar Y, Gupta N, Chhabra A, et al. **Magnetic resonance imaging of bacterial and tuberculous spondylodiscitis with associated complications and non-infectious spinal pathology mimicking infections: a pictorial review.** *BMC Musculoskelet Disord* 2017;18:244 CrossRef Medline
- Kim J, Kim YS, Peck KR, et al. **Outcome of culture-negative pyogenic vertebral osteomyelitis: comparison with microbiologically confirmed pyogenic vertebral osteomyelitis.** *Semin Arthritis Rheum* 2014;44:246–52 CrossRef Medline

Clinical, Imaging, and Lab Correlates of Severe COVID-19 Leukoencephalopathy

O. Rapalino, A. Pourvaziri, M. Maher, A. Jaramillo-Cardoso, B.L. Edlow, J. Conklin, S. Huang, B. Westover, J.M. Romero, E. Halpern, R. Gupta, S. Pomerantz, P. Schaefer, R.G. Gonzalez, S.S. Mukerji, and M.H. Lev



ABSTRACT

BACKGROUND AND PURPOSE: Patients infected with the Severe Acute Respiratory Syndrome coronavirus 2 (SARS-CoV-2) can develop a spectrum of neurological disorders, including a leukoencephalopathy of variable severity. Our aim was to characterize imaging, lab, and clinical correlates of severe coronavirus disease 2019 (COVID-19) leukoencephalopathy, which may provide insight into the SARS-CoV-2 pathophysiology.

MATERIALS AND METHODS: Twenty-seven consecutive patients positive for SARS-CoV-2 who had brain MR imaging following intensive care unit admission were included. Seven (7/27, 26%) developed an unusual pattern of “leukoencephalopathy with reduced diffusivity” on diffusion-weighted MR imaging. The remaining patients did not exhibit this pattern. Clinical and laboratory indices, as well as neuroimaging findings, were compared between groups.

RESULTS: The reduced-diffusivity group had a significantly higher body mass index (36 versus 28 kg/m², $P < .01$). Patients with reduced diffusivity trended toward more frequent acute renal failure (7/7, 100% versus 9/20, 45%; $P = .06$) and lower estimated glomerular filtration rate values (49 versus 85 mL/min; $P = .06$) at the time of MRI. Patients with reduced diffusivity also showed lesser mean values of the lowest hemoglobin levels (8.1 versus 10.2 g/dL, $P < .05$) and higher serum sodium levels (147 versus 139 mmol/L, $P = .04$) within 24 hours before MR imaging. The reduced-diffusivity group showed a striking and highly reproducible distribution of confluent, predominantly symmetric, supratentorial, and middle cerebellar peduncular white matter lesions ($P < .001$).

CONCLUSIONS: Our findings highlight notable correlations between severe COVID-19 leukoencephalopathy with reduced diffusivity and obesity, acute renal failure, mild hypernatremia, anemia, and an unusual brain MR imaging white matter lesion distribution pattern. Together, these observations may shed light on possible SARS-CoV-2 pathophysiologic mechanisms associated with leukoencephalopathy, including borderzone ischemic changes, electrolyte transport disturbances, and silent hypoxia in the setting of the known cytokine storm syndrome that accompanies severe COVID-19.

ABBREVIATIONS: BMI = body mass index; COVID-19 = coronavirus disease 2019; ICU = intensive care unit; RT-PCR = reverse transcription polymerase chain reaction; SARS-CoV-2 = Severe Acute Respiratory Syndrome coronavirus 2; SOFA = Sequential Organ Failure Assessment

Among the neurologic disorders associated with Severe Acute Respiratory Syndrome coronavirus-2 (SARS-CoV-2)¹⁻³ infection, there have been several reports of diffuse white matter abnormalities, including a “leukoencephalopathy with

reduced diffusivity” on diffusion-weighted MR imaging.⁴ This pattern of severe, bilateral white matter involvement appears to develop late in the course of coronavirus disease 2019 (COVID-19) in critically ill patients and may be related to the prolonged hypoxemia that these patients experience, often even while asymptomatic.⁵

Indeed, although leukoencephalopathy can result from a diverse group of genetic, toxic/metabolic, inflammatory, and infectious conditions, several well-described leukoencephalopathy syndromes may have direct relevance to COVID-19 pathophysiology. These disorders, which are associated with distinct clinical features, imaging patterns, and laboratory findings, include but are not limited to both delayed posthypoxic leukoencephalopathy (which often develops days or

Received August 25, 2020; accepted after revision October 28.

From the Departments of Radiology (O.R., A.P., M.M., A.J.-C., J.C., S.H., J.M.R., R.G., S.P., P.S., R.G.G., M.H.L.) and Neurology (B.L.E., B.W., S.S.M.), and Institute for Technology Assessment (E.H.), Massachusetts General Hospital, Boston, Massachusetts.

Please address correspondence to Otto Rapalino, MD, Department of Radiology, Massachusetts General Hospital, 55 Fruit St, Boston, MA 02114; e-mail: orapalino@mg.harvard.edu

Indicates open access to non-subscribers at www.ajnr.org

Indicates article with online supplemental data.

<http://dx.doi.org/10.3174/ajnr.A6966>

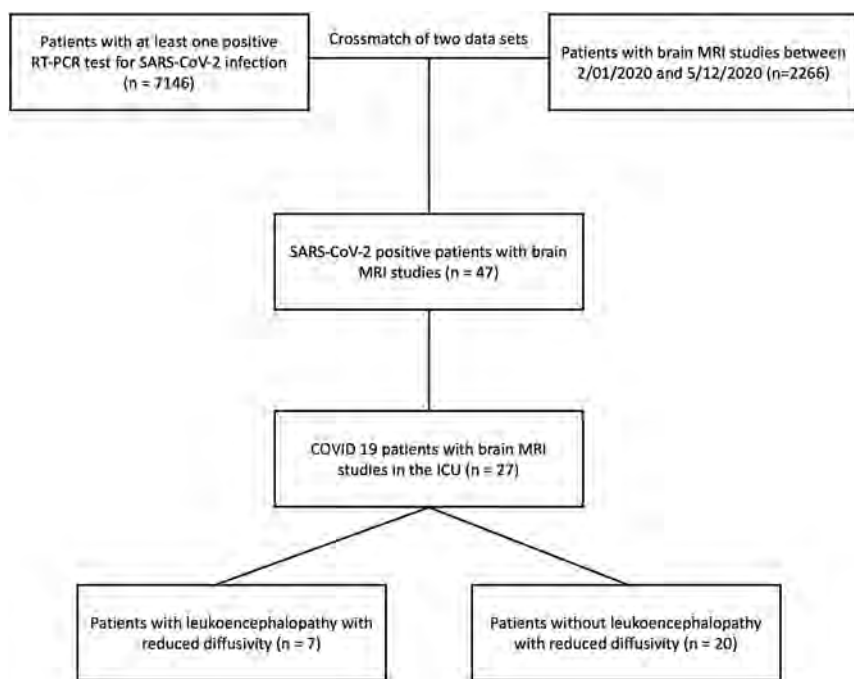


FIG 1. Flow chart of the patient-selection process.

weeks following an initial, typically catastrophic, global hypoxic event, such as carbon monoxide poisoning, drowning, opioid overdose, or other causes of cardiac arrest)⁶⁻⁹ and sepsis-related leukoencephalopathy (which occurs in critically ill patients and is likely due to deranged blood-brain barrier permeability caused by inflammatory mediators, allowing passage of cytokines and other neurotoxins into the cerebral white matter).¹⁰⁻¹³

Review of the current literature suggests possible roles for “silent hypoxia” and/or “cytokine storm” in the development of severe COVID-19-related leukoencephalopathy;^{5,14,15} the paucity of postmortem studies to date contributes to this uncertainty.¹⁶ Our purpose, therefore, has been to characterize the clinical, imaging, and laboratory correlates of COVID-19 leukoencephalopathy, which may provide insight into the SARS-CoV-2 pathophysiologic mechanisms of severe white matter cellular injury.

MATERIALS AND METHODS

Study Design

We performed an observational, retrospective study of consecutive patients admitted to Massachusetts General Hospital between February 1, 2020, and May 12, 2020. Data collection was approved by the institutional review board and followed Health Insurance Portability and Accountability Act guidelines. The institutional review board approved a waiver of informed consent for this retrospective analysis.

Patient Cohorts

Forty-seven consecutive adult patients positive for SARS-CoV-2 who had brain MR imaging were identified by overlapping an institutional database of adult patients with COVID-19

($n = 7146$) and a radiology database of brain MR imaging studies ($n = 2266$) acquired between February 1, 2020, and May 12, 2020. SARS-CoV-2 infection was confirmed by at least 1 positive real-time reverse transcription polymerase chain reaction (RT-PCR) test. Inclusion criteria were the following: 1) an assay positive for SARS-CoV-2; 2) age 18 years or older; 3) admission to the intensive care unit (ICU); and 4) brain MR imaging performed >24 hours following ICU admission (Fig 1). Patients not admitted to the ICU, younger than 18 years of age, or having undergone brain MR imaging before their ICU admission were excluded. One patient who had a brain MR imaging at the time of the ICU admission was excluded due to the presence of a pre-existent neurologic condition (suspected central pontine myelinolysis). During data collection, 308 patients (202 men, 66%) with COVID-19 were admitted to the ICU.

Of 47 patients positive for SARS-CoV-2 who had brain MR imaging, 28 (28/47, 60%) were admitted to the ICU (Fig 1).

Definition of Baseline and Clinical Variables

Demographic and baseline clinical characteristics were recorded, including the duration of symptoms before admission and the number of days from ICU admission to MR imaging acquisition, as well as documentation of organ involvement and standard laboratory data both at the time of ICU admission and within 24 hours before MR imaging acquisition. The Sequential Organ Failure Assessment (SOFA) score was calculated for every patient at ICU admission. All data were collected using predetermined guidelines from the patients’ electronic medical records. Baseline and ICU data collection was performed blinded to the imaging findings, including the diffusion abnormalities.

Imaging Protocol

The brain MR imaging studies were performed on 1.5T (Excite HDx; GE Healthcare) and 3T (Magnetom Skyra or Prisma; Siemens) scanners. The sequences and acquisition parameters of the typical MR imaging protocol included the following: axial diffusion (voxel size = $1.4 \times 1.4 \times 5.0$ mm, TR = 5000 ms, TE = 96.0 ms, b-values = 0 and 1000 s/mm²), axial SWI (voxel size = $0.8 \times 0.8 \times 1.8$ mm), axial FLAIR (voxel size = $0.4 \times 0.4 \times 4.0$ mm, TR = 9000 ms, TE = 85.0 ms, TI = 2500 ms), axial T1 (voxel size = $0.8 \times 0.8 \times 4.0$ mm, TR = 220 ms, TE = 2.46 ms), sagittal MPRAGE (voxel size = $1.0 \times 1.0 \times 1.0$ mm, TR = 2530 ms, multiple TE values), and axial T2 BLADE (Siemens) (voxel size = $0.7 \times 0.7 \times 7.0$ mm, TR = 5500 ms, TE = 17 ms). Patients without gadolinium contraindications were administered 0.1 mmol/kg of gadoterate meglumine (Dotarem; Guerbet). The following sequences were acquired following contrast

administration: axial T1-2D (voxel size = $0.8 \times 0.8 \times 4.0$ mm, TR = 220 ms, TE = 2.46 ms) and sagittal MPRAGE (voxel size = $1.0 \times 1.0 \times 1.0$ mm, TR = 2530 ms, multiple TE values).

Imaging Evaluation

Imaging was reviewed using the PACS by 2 neuroradiologists (O.R., M.M.), blinded to the clinical and laboratory findings. Discrepancies were resolved by consensus. Patients were dichotomized into 2 discrete groups: those with-versus-without “leukoencephalopathy with reduced diffusivity,” based on the presence or absence of white matter lesions with reduced diffusivity not consistent with an established pattern of ischemic infarction. The extent of supra- and infratentorial WM involvement was qualitatively graded for each patient on the basis of a 4-point Likert score (0 = normal, 1 = mild, 2 = moderate, and 3 = severe). The anatomic distribution of white matter signal abnormalities was recorded. The presence and number of microhemorrhages were assessed on SWI sequences when available ($n = 24$) or on gradient recalled-echo sequences ($n = 3$). Additional neuroimaging findings such as abnormal gray matter signal or intracranial enhancement were collected.

Statistical Analysis

Descriptive statistics were performed to summarize categorical variables as percentages and continuous variables using means and proportions, range, and 95% confidence intervals. Q-Q plots and Shapiro-Wilk tests were implemented for testing normality. Nonparametric data were described using median and interquartile range. For comparison of means of continuous variables with normal distribution, the Student *t* test was used. The Mann-Whitney *U* test was chosen for comparison of nonparametric variables. The Fisher exact test was used to analyze the association of clinical and laboratory findings between the groups with-versus-without reduced diffusivity. Differences and 95% confidence intervals were estimated using the *t* test for all variables reported. *P* values $< .05$ were considered significant. Analyses were conducted using SPSS, Version 24 (IBM).

RESULTS

Patient Cohort Characteristics

Twenty-seven patients (20/27 men, 74%; mean age, 63 years; 95% CI, 57–69 years) were included in the analysis. Seven (7/27, 26%) were identified as having leukoencephalopathy with reduced diffusivity (5/7 men, 71%; mean age, 63 years; 95% CI, 55–71 years); the remaining 20 in the control group did not exhibit this pattern (15/20 men, 75%; mean age, 63 years; 95% CI, 58–69 years) (Table 1 in the Online Supplemental Data). There were no significant differences in the percentage of Asian (0% vs. 5%), Black/African American (14% vs. 30%), White (29% vs. 30%), or Hispanic (57% vs. 35%) between the reduced diffusivity and control groups. The patients with reduced diffusivity compared with the control group had a significantly higher BMI (36 versus 28 kg/m^2 , $P < .01$). Other baseline characteristics, including prior tobacco use, concurrent illnesses, symptoms before admission, previous cardiac arrest, and number of days symptomatic (including dyspnea), were similar per the Online Supplemental Data. Except for a single patient in the control group, all patients

were intubated at ICU admission. One patient in the control group (1/20, 5%) received extracorporeal membrane oxygenation. Four patients in the reduced-diffusivity group and 5 in the control group were treated with nitric oxide (4/7, 57%, versus 5/20, 25%; $P = .17$). The most common comorbidities were obstructive sleep apnea (5/7, 71.4%, versus 14/20, 70%; $P = .26$), diabetes (4/7, 57%, versus 8/20, 40%; $P = .66$), and hypertension (3/7, 43%, versus 13/20, 65%; $P = .39$) (Table 1 in the Online Supplemental Data).

ICU Clinical Data

Patients in the reduced-diffusivity group trended toward more frequent acute renal failure documented in the ICU clinical notes (7/7, 100%, versus 9/20, 45%; $P = .06$) and lower estimated glomerular filtration rate values (49 versus 85 mL/min, $P = .06$) at MR imaging (Table 2 in the Online Supplemental Data). There were no significant differences between the 2 groups in the frequency of septic shock (6/7, 85.7%, versus 18/20, 90.0%), acute liver failure (1/7, 14.3%, versus 2/20, 10.0%), cardiac involvement (2/7, 28.6%, versus 2/20, 10.0%), ischemic bowel (1/7, 14.3%, versus 2/20, 10.0%), or other clinical and lab indices, including overt Disseminated Intravascular Coagulation, as listed in table 2 of the Online Supplemental Data. The reduced-diffusivity group showed significantly depressed mean values of the lowest hemoglobin levels (8.1 versus 10.2 g/dL, $P < .05$), elevated serum sodium levels (147 versus 139 mmol/L, $P = .04$), and a trend toward elevated highest D-dimers (4080 versus 2386 ng/L, $P = .09$), all obtained within 24 hours before MR imaging. Other clinical variables, including SOFA scores at admission, sedatives, nitric oxide treatment, and ICU length of stay (up through the time of data collection), were not significantly different between the 2 groups (Table 1 in the Online Supplemental Data).

One patient in the reduced-diffusivity group and one in the control group underwent lumbar puncture for CSF analysis. The patient in the control group was diagnosed with CNS cryptococcosis in the setting of HIV and SARS-CoV-2 co-infection; the CSF sample from this patient showed 108 white blood cells and protein levels at 141 mg/dL. CSF samples from the patient in the reduced-diffusivity group were without pleocytosis (≤ 4 cells) and had mean protein levels of 152 mg/dL.

Imaging Findings

The extent of bilateral, supra- and infratentorial white matter abnormalities was significantly greater in the reduced-diffusivity group than in the control group (median Likert scores, 3, 2 versus 1, 0, respectively; $P < .002$). White matter lesions in the reduced-diffusivity group were also more likely than in controls to show an unusual, confluent pattern of supratentorial ($P < .001$) and middle cerebellar peduncular (6/7, 86%, versus 1/20, 5%; $P < .001$) involvement (Online Supplemental Data, Figs 2–4). Cerebellar white matter ($P = .002$) and brain stem ($P = .04$) lesions were significantly more common in the reduced-diffusivity group than in the control group, whereas white matter lesions trended toward a predominantly symmetric pattern in the reduced-diffusivity group (7/7, 100%, versus 11/19, 58%; $P = .06$). There was no significant difference between groups regarding U-fiber or corpus callosum involvement, percentage of patients with

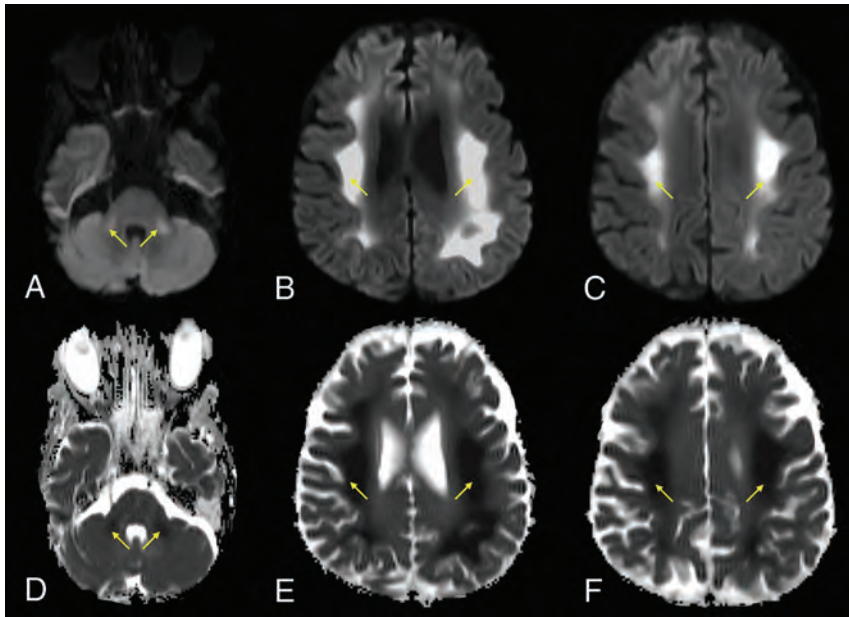


FIG 2. A 64-year-old man with a history of diabetes and hyperlipidemia, admitted with COVID-19-related hypoxemic respiratory failure and worsening septic shock. Axial DWI (A–C) and ADC images (D–F) show extensive, bilateral, predominantly symmetric, DWI-hyperintense signal in the white matter of the bilateral middle cerebellar peduncles, corona radiata, and centrum semiovale, with corresponding dark signal intensity on the ADC images (yellow arrows), reflecting leukoencephalopathic changes with marked, confluent reduced diffusivity.

>10 microbleeds, cortical laminar necrosis, or abnormal deep gray matter signal changes (all $P > .25$), per Online Supplemental Data.

Contrast was administered to 4/7 (57%) patients in the reduced-diffusivity group and 7/20 (35%) in the control group. One patient in each group had abnormal intraparenchymal enhancement (focal cortical enhancement in a region of laminar necrosis for a patient in the reduced-diffusivity group, and a small enhancing focus for a patient with cerebral cryptococcosis associated with HIV/SARS-CoV-2 co-infection in the control group). No definite abnormal leptomeningeal enhancement was present in any of our patients.

DISCUSSION

Our results show that in a consecutive cohort of adult patients positive for SARS-CoV-2 in the ICU requiring post-admission brain MR imaging, severe COVID-19 leukoencephalopathy with reduced diffusivity was associated with obesity, acute renal failure, mild hyponatremia, anemia, and an unusual, striking, and abnormal brain white matter lesion distribution pattern on MR imaging, featuring diffuse, confluent, predominantly symmetric supratentorial and middle cerebellar peduncular lesions. Although there were no significant differences in age, gender, race, or ethnicity between the reduced diffusivity and control groups, in both groups, older age (mean 63 years) and male sex (71–75%) were predominant.

Several articles to date have reported the occurrence of white matter signal abnormalities in patients with severe COVID-19.^{4,17–19} Kandemirli et al¹⁷ observed 3 (of 12) critically ill patients with subcortical or deep white matter lesions but without reduced diffusivity. More recently, Radmanesh et al⁴ described a series of patients with

leukoencephalopathy, reduced diffusivity, and microhemorrhages. A systematic analysis of the risk factors and laboratory and clinical variables associated with this unusual leukoencephalopathy, however, has not previously been emphasized in the literature.³

We saw no significant differences between groups regarding the duration of subjective dyspnea before ICU admission, the lowest reported pulse oximetry before admission, PaO₂/FiO₂ ratios on admission, the need for extracorporeal membrane oxygenation, or worst arterial partial pressure of oxygen (PO₂) and lowest oxygen saturation during the first 24 hours in the ICU (Online Supplemental Data). These similarities in baseline oxygenation parameters were surprising, given that hypoxia has been hypothesized to be a major culprit in the pathophysiology of these white matter changes. Indeed, oxygenation indices (worst arterial PO₂ and lowest O₂ saturation oxygenation) on the day of MR imaging were lower in the control group, likely reflecting that

45% of those patients had been extubated by that time (versus 14% extubated in the reduced-diffusivity group, Online Supplemental Data).

Except for body mass index (BMI), our reduced-diffusivity and control groups were well-matched (Online Supplemental Data). The reduced-diffusivity group had a significantly higher mean BMI of 36 versus 28 in the control group (corresponding to “moderately obese” versus “overweight,” respectively). Although there is no established direct link between obesity and leukoencephalopathy, obesity is a known risk factor for insulin resistance, lacunar infarcts, and chronic small-vessel disease.^{20–22} The effect of obesity on arteriosclerosis might be a contributing factor to the increasingly recognized thrombotic microangiopathy and endotheliitis associated with SARS-CoV-2 infection.²³ Lampe et al²⁴ described visceral obesity being associated with a predominance of deep white matter (rather than periventricular) MR imaging abnormalities and suggested a potential role for interleukin 6 and other proinflammatory cytokines in the development of white matter pathology. The microangiopathic effect of obesity (with potential superimposed effects mediated by cytokines) might further compromise borderzone regions located in the deep cerebral white matter and middle cerebellar peduncles.²⁵

Several clinical variables were different between our 2 cohorts, including a lower mean value for the lowest hemoglobin level within 24 hours before MR imaging (8.1 versus 10.2, $P < .05$), mildly higher mean values of the most elevated serum sodium at the same time point (147 versus 139, $P < .04$), and a trend toward more acute renal dysfunction (glomerular filtration rate = 49 versus 85 mL/min; $P < .06$) in the reduced-diffusivity group. Other organ system

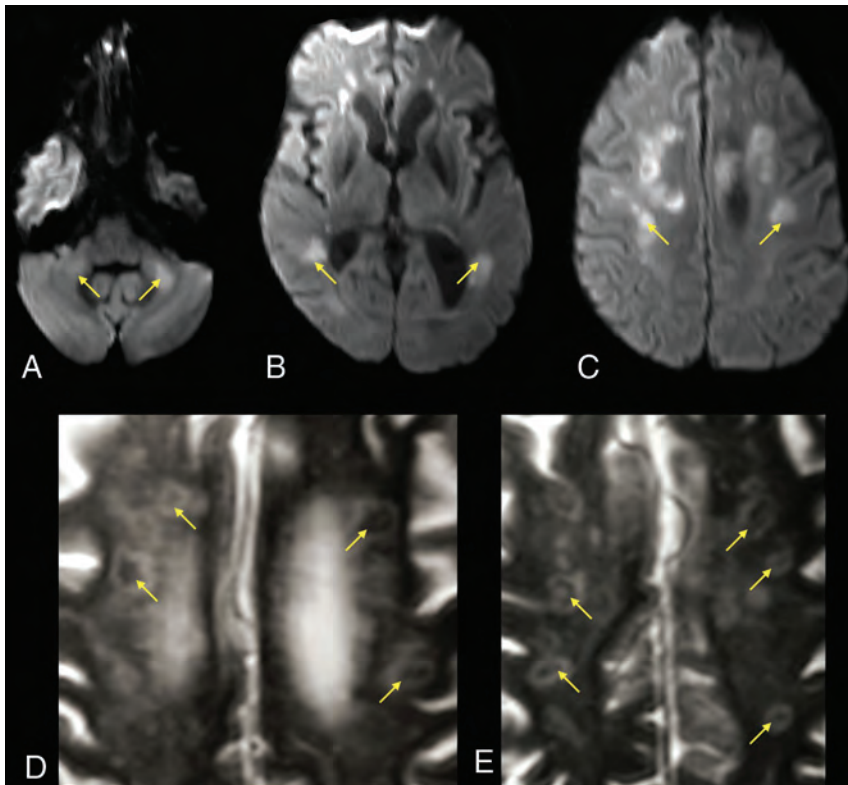


FIG 3. A 63-year-old male patient with a history of diabetes, hypertension, chronic kidney disease, and obstructive sleep apnea admitted with COVID-19–related hypoxic respiratory failure due to acute respiratory distress syndrome. DWI (A–C) shows bilateral areas of reduced diffusivity, involving the body of the corpus callosum, middle cerebellar peduncles, and periventricular white matter (arrows, ADC not shown). Magnified axial T2-weighted MR images (D and E) show a peculiar cavitory appearance of some of the lesions, with decreased signal centrally and a peripheral T2-hyperintense rim (yellow arrows). These lesions were interpreted as areas of early cavitation within the white matter abnormalities. A follow-up MR imaging (not shown) showed resolution of the restricted diffusion within these lesions but with progression of the cavitory/necrotic changes.

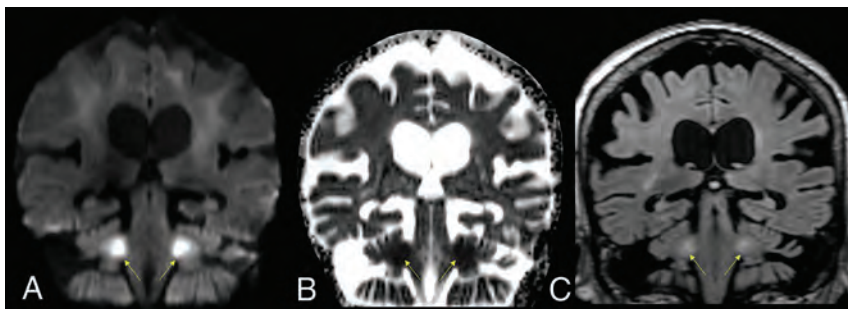


FIG 4. A 76-year-old female patient with a history of schizoaffective disorder and Grave's disease, admitted with COVID-19. Coronal DWI (A), ADC (B), and FLAIR (C) images. The brain MR images showed a leukoencephalopathy with restricted diffusion, predominantly affecting the middle cerebellar peduncles (yellow arrows) and adjacent cerebellar white matter.

damage was not significantly different between groups, including cardiac events, acute liver failure, overt Disseminated Intravascular Coagulation, ischemic bowel, and mean number of systems affected (Online Supplemental Data).

Although these differences may simply reflect an epiphenomenon, it is intriguing to speculate whether cytokine effects, which

could also be related to obesity, might contribute to some of these abnormal lab indices. For example, interleukin 6 and other proinflammatory cytokines (eg, interleukin 1 and tumor necrosis factor- α) are known to have a central role in the anemia seen during systemic inflammatory processes, impacting iron homeostasis and the reticuloendothelial system as well as impairing regulatory feedback of iron absorption in the gastrointestinal tract.^{26,27} Interleukin 6 has been shown to mediate low iron levels during inflammatory states via the production of hepcidin.²⁸ These cytokines might also modulate the transcription of the *erythropoietin (EPO)* gene and inhibit erythroid progenitor cells in the bone marrow.²⁶

The modest hypernatremia at the time of MR imaging is more challenging to explain. Both groups had similar critical illness severity (reflected by SOFA scores of 9.3 and 7, respectively; $P = .09$) and had no reported differences in water intake or extrarenal water losses (gastrointestinal- or skin-mediated). Although this finding might reflect hypothalamic involvement with impaired water homeostasis, renal dysfunction in COVID-19 has more often been reported to result in hyponatremia.^{29,30}

The pattern of MR imaging signal abnormalities we observed is striking. This pattern of diffuse, confluent, predominantly symmetric supra- and infratentorial involvement with middle cerebellar peduncle lesions (seen in 6/7 cases, 86%) is unusual and noteworthy. The neuroanatomic distribution of these abnormalities appears more selective than those reported in cases of delayed posthypoxic leukoencephalopathy at our institution and in the literature. Delayed posthypoxic encephalopathy is often more extensive, with subcortical white matter involvement and less frequent infratentorial involvement.^{7,31} None of the patients in our reduced-diffusivity group had a history of recent cardiac arrest, though 1 patient in the control group had an episode of cardiac arrest

without developing these findings.

There have been multiple reports of white matter abnormalities associated with sepsis and critical illness. Sharshar et al¹² described white matter lesions in 5/9 (55%) patients with septic shock and clinical brain dysfunction (mean SOFA, 8). Polito et al¹¹ published a similar study of 71 patients with septic shock and

noted 15 patients (21%) with leukoencephalopathy (median highest SOFA score, 9). These authors suggested that the leukoencephalopathy seen with septic shock may be related to an altered blood-brain barrier, allowing passage of proinflammatory molecules and neurotoxins.¹¹

Another possibility in the imaging-based differential diagnosis of the unusual pattern of leukoencephalopathy in these patients is a metabolic or toxic etiology.^{32,33} There were no differences between the reduced-diffusivity and control groups regarding sedatives, the use of opioid medications, nitric oxide, or extracorporeal membrane oxygenation treatment. The possibility of a metabolic etiology is intriguing because the anatomic distribution of white matter lesions in our patients overlaps the pattern seen with a genetic chloride channelopathy (*chloride voltage-gated channel 2 [CLCN2]-related leukoencephalopathy*).^{34,35} It has been established, however, that the angiotensin-converting enzyme 2 receptor used by the SARS-CoV-2 virus has a chloride-binding site and is regulated by this electrolyte.³⁶ There is also some degree of overlap between the angiotensin II and chloride channel pathways physiologically, with angiotensin II producing activation of chloride currents in cerebral vessels.^{37,38} A direct connection between COVID-19 and specific ion-transport abnormalities, however, has not been reported to date.

One of our patients showed cavitory, necrotic-appearing lesions in regions with reduced diffusivity, suggestive of the MR imaging findings that accompany multifocal necrotizing leukoencephalopathy (Fig 3).³⁹ The anatomic distribution of these lesions resembled that of our other patients with leukoencephalopathy with reduced diffusivity; hence, this appearance may reflect a more advanced stage of white matter cellular injury, as was described in some early case reports of COVID-19-associated acute necrotizing encephalopathy.^{39,40}

This observational study has several limitations, including a small sample size, which could be affecting the potential effect of some clinical variables. The patients included in the study may reflect a proportion of those with severe COVID-19 in the ICU who were stable enough to have a brain MR imaging, potentially biasing this analysis. The development of cavitory changes in only one of the patients in the group with restricted diffusion could be related to a more advanced stage of white matter injury, but this is difficult to confirm with the small number of cases included in the study. Nevertheless, we observed several significant correlations among the imaging, clinical, and laboratory findings, providing a basis for future hypothesis testing in larger cohorts. Different field strengths and susceptibility sequences in different MR imaging scanners limit comparison of the prevalence of microhemorrhages between cohorts. Lack of prior imaging in several patients limits assessment of pre-existing or other pathologies. Finally, the retrospective design also limits the availability of oxygenation data during ICU admission, which may have provided a more precise measure of the cumulative burden of hypoxia experienced by each patient.

CONCLUSIONS

The unusual pattern of white matter injury we observed, together with the clinical and laboratory correlates, overlaps that of several conditions that may help elucidate the pathophysiology of severe

COVID-19 encephalopathy. These include but are not limited to delayed posthypoxic leukoencephalopathy, sepsis-related leukoencephalopathy, and metabolic encephalopathies related to electrolyte disturbances. The anatomic distribution and presence of reduced diffusivity within these white matter lesions suggest a combination of several potential factors, including thrombotic microangiopathy, underlying microvascular changes related to electrolyte transport derangements that result in borderzone oligemia, potentially direct viral injury,⁴¹ and silent hypoxia^{5,16} in the context of the well-known cytokine storm seen in many critical patients with COVID-19.^{14,15}

Disclosures: Otto Rapalino—UNRELATED: *Travel/Accommodations/Meeting Expenses Unrelated to Activities Listed*: GE Healthcare, *Comments*: travel expenses to GE Healthcare-sponsored meeting August 2019. Brian L. Edlow—RELATED: *Grants*: James S. McDonnell Foundation COVID-19 Recovery of Consciousness Consortium. Susie Huang—UNRELATED: *Grants/Grants Pending*: Siemens, *Comments*: research grant for clinical translation of fast neuroimaging sequences*; *Payment for Lectures Including Service on Speakers Bureaus*: Siemens, *Comments*: speaker engagement at Organization for Human Brain Mapping Annual Meeting. Brandon Westover—RELATED: *Grant*: National Institutes of Health*; UNRELATED: *Employment*: Massachusetts General Hospital/Harvard Medical School; *Grants/Grants Pending*: National Institutes of Health.* Rajiv Gupta—UNRELATED: *Consultancy*: Idorsia, Facebook, Medtronic, Siemens; *Expert Testimony*: Dartmouth-Hitchcock Medical Center, Penn State; *Grants/Grants Pending*: National Institutes of Health, Department of Defense; *Payment for Lectures Including Service on Speakers Bureaus*: Siemens. Shibani Mukerji—RELATED: *Grant*: National Institute of Mental Health, *Comments*: K23MH115812.* Michael H. Lev—UNRELATED: *Consultancy*: Takeda Pharmaceutical Company, GE Healthcare; *Grants/Grants Pending*: GE Healthcare, National Institutes of Health.* *Money paid to the institution.

REFERENCES

1. Helms J, Kremer S, Merdji H, et al. **Neurologic features in severe SARS-CoV-2 infection.** *N Engl J Med* 2020;382:2268–70 CrossRef Medline
2. Pleasure SJ, Green AJ, Josephson SA. **The spectrum of neurologic disease in the severe acute respiratory syndrome coronavirus 2 pandemic infection: neurologists move to the frontlines.** *JAMA Neurol* 2020;77:679 CrossRef Medline
3. Yuki K, Fujiogi M, Koutsogiannaki S. **COVID-19 pathophysiology: a review.** *Clin Immunol* 2020;215:108427 CrossRef Medline
4. Radmanesh A, Derman A, Lui YW, et al. **COVID-19-associated diffuse leukoencephalopathy and microhemorrhages.** *Radiology* 2020;297:E223–27 CrossRef Medline
5. Couzin-Frankel J. **The mystery of the pandemic's "happy hypoxia."** *Science* 2020;368:455–56 CrossRef Medline
6. Balan S, Gupta K, Balasundaram P, et al. **Reversible hypoxic brain injury: the penumbra conundrum of Grinker.** *BMJ Case Rep* 2019;12:e228670 CrossRef Medline
7. Beeskov AB, Oberstadt M, Saur D, et al. **Delayed post-hypoxic leukoencephalopathy (DPHL): an uncommon variant of hypoxic brain damage in adults.** *Front Neurol* 2018;9:708 CrossRef Medline
8. Breit H, Jhaveri M, John S. **Concomitant delayed posthypoxic leukoencephalopathy and critical illness microbleeds.** *Neurol Clin Pract* 2018;8:e31–33 CrossRef Medline
9. Zamora CA, Nauen D, Hynecsek R, et al. **Delayed posthypoxic leukoencephalopathy: a case series and review of the literature.** *Brain Behav* 2015;5:e00364 CrossRef Medline
10. Garofalo AM, Lorente-Ros M, Goncalvez G, et al. **Histopathological changes of organ dysfunction in sepsis.** *Intensive Care Med Exp* 2019;7:45 CrossRef Medline
11. Polito A, Eischwald F, Maho AL, et al. **Pattern of brain injury in the acute setting of human septic shock.** *Crit Care* 2013;17:R204 CrossRef Medline

12. Sharshar T, Carlier R, Bernard F, et al. **Brain lesions in septic shock: a magnetic resonance imaging study.** *Intensive Care Med* 2007;33:798–806 CrossRef Medline
13. Shindo A, Suzuki K, Iwashita Y, et al. **Sepsis-associated encephalopathy with multiple microbleeds in cerebral white matter.** *Am J Med* 2018;131:e297–98 CrossRef Medline
14. Mehta P, McAuley DF, Brown M, et al; HLH Across Speciality Collaboration, UK. **COVID-19: consider cytokine storm syndromes and immunosuppression.** *Lancet* 2020;395:1033–34 CrossRef Medline
15. Moore BJ, June CH. **Cytokine release syndrome in severe COVID-19.** *Science* 2020;368:473–74 CrossRef Medline
16. Solomon IH, Normandin E, Bhattacharyya S, et al. **Neuropathological features of Covid-19.** *N Engl J Med* 2020;383:989–92 CrossRef Medline
17. Kandemirli SG, Dogan L, Sarikaya ZT, et al. **Brain MRI findings in patients in the intensive care unit with COVID-19 infection.** *Radiology* 2020;297:E232–35 CrossRef Medline
18. Sachs JR, Gibbs KW, Swor DE, et al. **COVID-19-associated leukoencephalopathy.** *Radiology* 2020;296:E184–85 CrossRef Medline
19. Lang M, Buch K, Li MD, et al. **Leukoencephalopathy associated with severe COVID-19 infection: sequela of hypoxemia?** *AJNR Am J Neuroradiol* 2020;41:1641–45 CrossRef Medline
20. Dearborn JL, Schneider AL, Sharrett AR, et al. **Obesity, insulin resistance, and incident small vessel disease on magnetic resonance imaging: Atherosclerosis Risk in Communities Study.** *Stroke* 2015;46:3131–36 CrossRef Medline
21. Hakim AM. **Small vessel disease.** *Front Neurol* 2019;10:1020 CrossRef Medline
22. Ter Telgte A, Wiegertjes K, Gesierich B, et al. **Contribution of acute infarcts to cerebral small vessel disease progression.** *Ann Neurol* 2019;86:582–92 CrossRef Medline
23. Varga Z, Flammer AJ, Steiger P, et al. **Endothelial cell infection and endotheliitis in COVID-19.** *Lancet* 2020;395:1417–18 CrossRef Medline
24. Lampe L, Zhang R, Beyer F, et al. **Visceral obesity relates to deep white matter hyperintensities via inflammation.** *Ann Neurol* 2019;85:194–203 CrossRef Medline
25. Kataoka H, Izumi T, Kinoshita S, et al. **Infarction limited to both middle cerebellar peduncles.** *J Neuroimaging* 2011;21:e171–72 CrossRef Medline
26. Hayden SJ, Albert TJ, Watkins TR, et al. **Anemia in critical illness: insights into etiology, consequences, and management.** *Am J Respir Crit Care Med* 2012;185:1049–57 CrossRef Medline
27. Houston DS. **Hepcidin and the anemia of critical illness.** *Crit Care Med* 2018;46:1030–31 CrossRef Medline
28. Nemeth E, Rivera S, Gabayan V, et al. **IL-6 mediates hypoferrremia of inflammation by inducing the synthesis of the iron regulatory hormone hepcidin.** *J Clin Invest* 2004;113:1271–76 CrossRef Medline
29. Lippi G, South AM, Henry BM. **Electrolyte imbalances in patients with severe coronavirus disease 2019 (COVID-19).** *Ann Clin Biochem* 2020;57:262–65 CrossRef Medline
30. Puelles VG, Lutgehetmann M, Lindenmeyer MT, et al. **Multiorgan and renal tropism of SARS-CoV-2.** *N Engl J Med* 2020;383:590–92 CrossRef Medline
31. Meyer MA. **Delayed post-hypoxic leukoencephalopathy: case report with a review of disease pathophysiology.** *Neurol Int* 2013;5:e13 CrossRef Medline
32. de Oliveira AM, Paulino MV, Vieira AP, et al. **Imaging patterns of toxic and metabolic brain disorders.** *Radiographics* 2019;39:1672–95 CrossRef Medline
33. Sener RN. **Diffusion magnetic resonance imaging patterns in metabolic and toxic brain disorders.** *Acta Radiol* 2004;45:561–70 CrossRef Medline
34. Gaitan-Penas H, Apaja PM, Arnedo T, et al. **Leukoencephalopathy-causing CLCN2 mutations are associated with impaired Cl(-) channel function and trafficking.** *J Physiol* 2017;595:6993–7008 CrossRef Medline
35. Guo Z, Lu T, Peng L, et al. **CLCN2-related leukoencephalopathy: a case report and review of the literature.** *BMC Neurol* 2019;19:156 CrossRef Medline
36. Rushworth CA, Guy JL, Turner AJ. **Residues affecting the chloride regulation and substrate selectivity of the angiotensin-converting enzymes (ACE and ACE2) identified by site-directed mutagenesis.** *FEBS J* 2008;275:6033–42 CrossRef Medline
37. Li RS, Wang Y, Chen HS, et al. **TMEM16A contributes to angiotensin II-induced cerebral vasoconstriction via the RhoA/ROCK signaling pathway.** *Mol Med Rep* 2016;13:3691–99 CrossRef Medline
38. Nelson MT, Conway MA, Knot HJ, et al. **Chloride channel blockers inhibit myogenic tone in rat cerebral arteries.** *J Physiol* 1997;502:259–64 CrossRef Medline
39. Premji S, Kang L, Rojiani MV, et al. **Multifocal necrotizing leukoencephalopathy: expanding the clinicopathologic spectrum.** *J Neuropathol Exp Neurol* 2019;78:340–47 CrossRef Medline
40. Poyiadji N, Shahin G, Noujaim D, et al. **COVID-19-associated acute hemorrhagic necrotizing encephalopathy: imaging features.** *Radiology* 2020;296:E119–20 CrossRef Medline
41. Paniz-Mondolfi A, Bryce C, Grimes Z, et al. **Central nervous system involvement by severe acute respiratory syndrome coronavirus-2 (SARS-CoV-2).** *J Med Virol* 2020;92:699–702 CrossRef Medline

A Stacked Generalization of 3D Orthogonal Deep Learning Convolutional Neural Networks for Improved Detection of White Matter Hyperintensities in 3D FLAIR Images

L. Umapathy,¹ G.G. Perez-Carrillo,² M.B. Keerthivasan,³ J.A. Rosado-Toro,⁴ M.I. Altbach,⁵ B. Winegar,⁶ C. Weinkauff,⁷ and A. Bilgin,⁸ for the Alzheimer's Disease Neuroimaging Initiative



ABSTRACT

BACKGROUND AND PURPOSE: Accurate and reliable detection of white matter hyperintensities and their volume quantification can provide valuable clinical information to assess neurologic disease progression. In this work, a stacked generalization ensemble of orthogonal 3D convolutional neural networks, StackGen-Net, is explored for improving automated detection of white matter hyperintensities in 3D T2-FLAIR images.

MATERIALS AND METHODS: Individual convolutional neural networks in StackGen-Net were trained on 2.5D patches from orthogonal reformatting of 3D-FLAIR ($n = 21$) to yield white matter hyperintensity posteriors. A meta convolutional neural network was trained to learn the functional mapping from orthogonal white matter hyperintensity posteriors to the final white matter hyperintensity prediction. The impact of training data and architecture choices on white matter hyperintensity segmentation performance was systematically evaluated on a test cohort ($n = 9$). The segmentation performance of StackGen-Net was compared with state-of-the-art convolutional neural network techniques on an independent test cohort from the Alzheimer's Disease Neuroimaging Initiative-3 ($n = 20$).

RESULTS: StackGen-Net outperformed individual convolutional neural networks in the ensemble and their combination using averaging or majority voting. In a comparison with state-of-the-art white matter hyperintensity segmentation techniques, StackGen-Net achieved a significantly higher Dice score (0.76 [SD, 0.08], FI-lesion (0.74 [SD, 0.13]), and area under precision-recall curve (0.84 [SD, 0.09]), and the lowest absolute volume difference (13.3% [SD, 9.1%]). StackGen-Net performance in Dice scores (median = 0.74) did not significantly differ ($P = .22$) from interobserver (median = 0.73) variability between 2 experienced neuroradiologists. We found no significant difference ($P = .15$) in white matter hyperintensity lesion volumes from StackGen-Net predictions and ground truth annotations.

CONCLUSIONS: A stacked generalization of convolutional neural networks, utilizing multiplanar lesion information using 2.5D spatial context, greatly improved the segmentation performance of StackGen-Net compared with traditional ensemble techniques and some state-of-the-art deep learning models for 3D-FLAIR.

ABBREVIATIONS: ADNI = Alzheimer's Disease Neuroimaging Initiative; AUC = area under curve; Ax = axial; CNN = convolutional neural network; E-A = ensemble average; E-MV = ensemble majority vote; FI-L = FI lesion; HD = Hausdorff distance; VD = volume difference; WMH = white matter hyperintensity

Received May 13, 2020; accepted after revision October 26.

From the Departments of Electrical and Computer Engineering (L.U., A.B.), Medical Imaging (L.U., G.G.P.-C., M.B.K., J.A.R.-T., M.I.A., B.W., A.B.), Surgery (C.W.), and Biomedical Engineering (A.B.), University of Arizona, Tucson, Arizona.

Data used in preparation of this article were obtained from the Alzheimer's Disease Neuroimaging Initiative (ADNI) database (adni.loni.usc.edu). Thus, the investigators within the ADNI contributed to the design and implementation of ADNI and/or provided data but did not participate in the analysis or writing of this report. A complete listing of ADNI investigators can be found at: http://adni.loni.usc.edu/wp-content/uploads/how_to_apply/ADNI_Acknowledgement_List.pdf.

Paper previously was presented in part at: Annual Meeting and Exhibition of International Society for Magnetic Resonance in Medicine, Virtual Conference and Exhibition, October 8–14, 2020.

This work was supported, in part, by the Arizona Health Sciences Center Translational Imaging Program Stimulus Fund, BIOS Team Scholar's Program, Technology and Research Initiative Fund Improving Health Initiative, and Arizona Alzheimer's Consortium. Data collection and sharing for this project were funded by the Alzheimer's Disease Neuroimaging Initiative (ADNI) (National Institutes of Health grant U01 AG024904) and Department of Defense ADNI (Department of Defense award number W81XWH-12-2-0012). ADNI is funded by the National Institute on Aging, the National Institute of Biomedical Imaging and Bioengineering, and through generous contributions from the following: AbbVie;

Alzheimer's Association; Alzheimer's Drug Discovery Foundation; Araclon Biotech; BioClinica; Biogen; Bristol-Myers Squibb; CereSpir; Cogstate; Eisai; Elan Pharmaceuticals; Eli Lilly; EuroImmun; F. Hoffmann-La Roche and its affiliated company Genentech; Fujirebio; GE Healthcare; IXICO; Janssen Alzheimer Immunotherapy Research and Development; Johnson & Johnson Pharmaceutical Research and Development; Lumosity; Lundbeck; Merck; Meso Scale Diagnostics; NeuroRx Research; Neurotrack; Novartis Pharmaceuticals; Pfizer; Piramal Imaging; Servier; Takeda Pharmaceutical Company; and Transition Therapeutics. The Canadian Institutes of Health Research is providing funds to support ADNI clinical sites in Canada. Private sector contributions are facilitated by the Foundation for the National Institutes of Health (www.fnih.org). The grantee organization is the Northern California Institute for Research and Education, and the study was coordinated by the Alzheimer's Therapeutic Research Institute at the University of Southern California. ADNI data are disseminated by the Laboratory for Neuro Imaging at the University of Southern California.

Please address correspondence to Ali Bilgin, PhD, Department of Biomedical Engineering, Thomas R. Keating Building, University of Arizona, 1657 E. Helen Street, Tucson, AZ, 85721; e-mail: bilgin@email.arizona.edu

Indicates open access to non-subscribers at www.ajnr.org

Indicates article with online supplemental data.

<http://dx.doi.org/10.3174/ajnr.A6970>

White matter hyperintensities (WMHs) correspond to pathologic features of axonal degeneration, demyelination, and gliosis observed within cerebral white matter.¹ Clinically, the extent of WMHs in the brain has been associated with cognitive impairment, Alzheimer's disease and vascular dementia, and increased risk of stroke.^{2,3} The detection and quantification of WMH volumes to monitor lesion burden evolution and its correlation with clinical outcomes have been of interest in clinical research.^{4,5} Although the extent of WMHs can be visually scored,⁶ the categoric nature of such scoring systems makes quantitative evaluation of disease progression difficult. Manually segmenting WMHs is tedious, prone to inter- and intraobserver variability, and is, in most cases, impractical. Thus, there is an increased interest in developing fast, accurate, and reliable computer-aided automated techniques for WMH segmentation.

Convolutional neural network (CNN)-based approaches have been successful in several semantic segmentation tasks in medical imaging.⁷ Recent works have proposed using deep learning-based methods for segmenting WMHs using 2D-FLAIR images.⁸⁻¹¹ More recently, a WMH segmentation challenge¹² was also organized (<http://wmh.isi.uu.nl/>) to facilitate comparison of automated segmentation of WMHs of presumed vascular origin in 2D multislice T2-FLAIR images. Architectures that used an ensemble of separately trained CNNs showed promising results in this challenge, with 3 of the top 5 winners using ensemble-based techniques.¹²

Conventional 2D-FLAIR images are typically acquired with thick slices (3–4 mm) and possible slice gaps. Partial volume effects from a thick slice are likely to affect the detection of smaller lesions, both in-plane and out-of-plane. 3D-FLAIR images, with isotropic resolution, have been shown to achieve higher resolution and contrast-to-noise ratio¹³ and have shown promising results in MS lesion detection using 3D CNNs.¹⁴ Additionally, the isotropic resolution enables viewing and evaluation of the images in multiple planes. This multiplanar reformatting of 3D-FLAIR without the use of interpolating kernels is only possible due to the isotropic nature of the acquisition. Network architectures that use information from the 3 orthogonal views have been explored in recent works for CNN-based segmentation of 3D MR imaging data.¹⁵ The use of data from multiple planes allows more spatial context during training without the computational burden associated with full 3D training.¹⁶ The use of 3 orthogonal views simultaneously mirrors how humans approach this segmentation task.

Ensembles of CNNs have been shown to average away the variances in the solution and the choice of model- and configuration-specific behaviors of CNNs.¹⁷ Traditionally, the solutions from these separately trained CNNs are combined by averaging or using a majority consensus. In this work, we propose the use of a stacked generalization framework (StackGen-Net) for combining multiplanar lesion information from 3D CNN ensembles to improve the detection of WMH lesions in 3D-FLAIR. A stacked generalization¹⁸ framework learns to combine solutions from individual CNNs in the ensemble. We systematically evaluated the performance of this framework and compared it with traditional ensemble techniques, such as averaging or majority voting, and state-of-the-art deep learning techniques.

MATERIALS AND METHODS

StackGen-Net CNN Architecture

Figure 1A shows an overview of the proposed StackGen-Net architecture. Our ensemble consists of 3 orthogonal 3D CNNs (DeepUNET3D), each trained on axial, sagittal, and coronal reformatting of 3D-FLAIR. This is followed by a stacked generalization¹⁸ of the orthogonal CNNs using a Meta CNN. The proposed multiscale, fully-connected DeepUNET3D architecture is shown in Fig 1B. Compared with a UNET,¹⁹ DeepUNET3D uses *convolutional blocks* instead of convolutional layers. These convolutional blocks consist of a sequence of convolutions with 3D kernels ($3 \times 3 \times 3$), batch normalization, and rectified linear activation layers separated by a dropout layer. A final convolution layer combines the feature maps in the native resolution space to generate posterior probabilities for WMHs.

The stacked generalization scheme attempts to maximize the overall accuracy of the ensemble by deducing the bias rate of the individual DeepUNET3D CNNs. If we consider p_a , p_s , p_c , and p_f to be the axial, sagittal, coronal, and final WMH posterior probabilities for a voxel, then the Meta CNN learns a new functional mapping $f(\cdot)$ from $[0,1]^3$ to $[0,1]$ where $p_f = f(p_a, p_s, p_c)$ and $p_f, p_a, p_s, p_c \in [0, 1]$. In this work, we consider the following mapping:

$$p_f = f(p_a, p_s, p_c) = \sigma(w_a p_a + w_s p_s + w_c p_c + b),$$

where w_a , w_s , w_c are the weights for axial, sagittal, and coronal posteriors, respectively; b is the bias term, and $\sigma(\cdot)$ represents a softmax operation. These weights are learned during training of the Meta CNN, which consists of a single convolution layer with a $1 \times 1 \times 1$ 3D kernel.

Study Population and Image Acquisition

A cohort of 35 subjects was prospectively recruited (2016–2017) for a study on extracranial carotid artery disease with approval of the local institutional review board. Adults 50–85 years of age with extracranial carotid artery disease (50%–90% stenosis) based on duplex sonography criteria were recruited from outpatient clinics/inpatient hospitals. Exclusion criteria included depression, dementia, MS, and contraindications to MR imaging.

Sagittal 3D-FLAIR images were acquired using the 3D spatial and chemical-shift-encoded excitation inversion recovery sequence on a 3T MR imaging scanner (Magnetom Skyra). Five of the 35 subjects were excluded due to poor FLAIR image quality (motion artifacts). The remaining study cohort (67.7 [SD, 8.7] years of age; 22 men, 8 women) was randomly split into groups for training ($n = 20$), validation ($n = 1$), and testing ($n = 9$). These test subjects formed test cohort 1.

To test the generalizability of the framework, we also evaluated its performance on a multi-institutional and multi-scanner external cohort (test cohort 2) from the Alzheimer's Disease Neuroimaging Initiative (ADNI) data base (adni.loni.usc.edu). The primary goal of ADNI, a public-private partnership led by Principal Investigator Michael W. Weiner, is to test whether imaging and biologic markers, along with clinical and neuropsychological assessments, can be combined to measure progression of mild cognitive impairment and early Alzheimer's Disease.

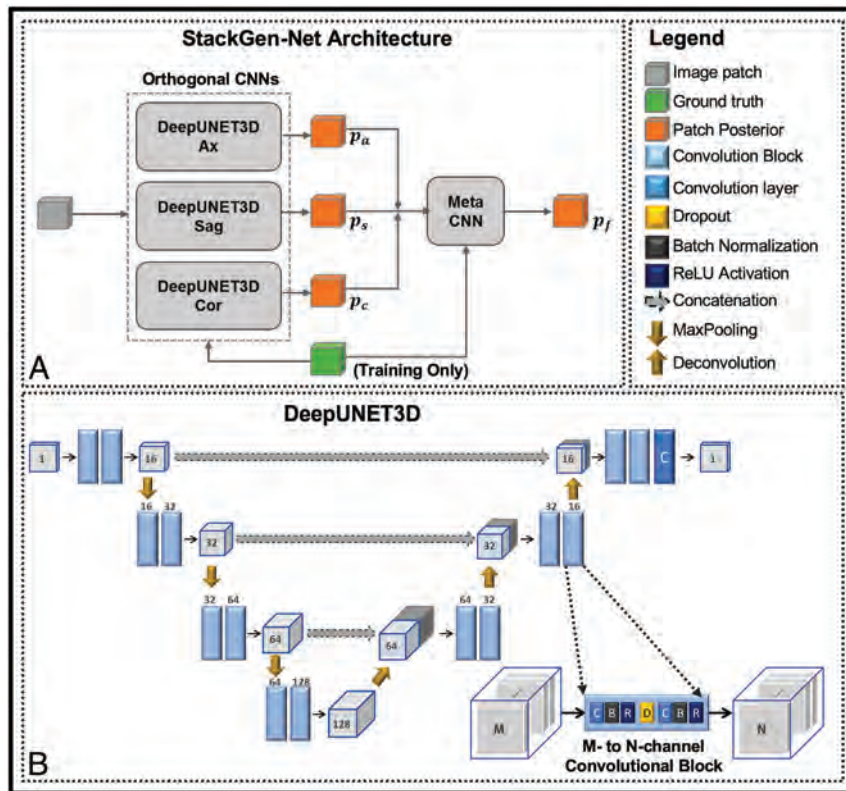


FIG 1. A, Overview of the proposed StackGen-Net. B, This consists of 3 DeepUNET3D CNNs, which are made up of convolutional blocks. The number of output feature maps is presented next to each convolutional block. Each DeepUNET3D predicts posterior probabilities for WMHs on orthogonal (axial, sagittal, and coronal) orientations of the 3D-FLAIR volumes. The Meta CNN combines axial, sagittal, and coronal posterior probabilities for a voxel to yield a final prediction for WMH. Sag indicates sagittal; Cor, coronal; ReLU, rectified linear unit.

Sagittal 3D-FLAIR volumes from 20 subjects (76.8 [SD, 9.3] years of age; 11 men, 9 women) were selected randomly from the cognitively normal and mild cognitive impairment groups. Additional information regarding the acquisition protocol and subject-selection criteria for ADNI3 is available in the Online Supplemental Data.

WMH Annotations

Two neuroradiologists, with certificate of added qualification, (observers 1 and 2) agreed on the following protocol to annotate WMH: 1) Deep WMHs should at least be 2 mm wide, spanning more than 1 imaging section; 2) periventricular WMHs should be >3 mm wide; 3) hyperintense regions due to partial volume effects near the ventricles or sulci or CSF flow artifacts should not be included; and 4) no deep gray matter lesions or cortical hyperintense lesions should be included.

Observer 1 manually annotated WMHs on 3D-FLAIR images for all the subjects. As part of an interobserver variability study to establish baseline human performance, observers 1 and 2 independently annotated 60 FLAIR images (12 imaging volumes, each with 5 consecutive images) from 3 subjects in test cohort 1. Observer 1 re-annotated these images after 5 months from the first annotations to avoid recall bias; these images were used to evaluate intraobserver variability. Observers 1 and 2 also

annotated 10 additional subjects (1600 images) from the test cohort 2 to establish human performance on the external set. Both observers used an in-house Matlab (MathWorks)-based graphical user interface. The observers manually traced the WMH pixels on axial cross-sections of the 3D-FLAIR images. The observers were allowed to adjust the window width and level to improve WMH contrast and use 3D spatial context to annotate/edit/delete individual WMH masks.

Training Data

Image preprocessing consisted of skull stripping,²⁰ N4 bias correction,²¹ total variation-based denoising, and contrast stretching. The image intensities were normalized, per subject, using a zero mean unit SD intensity normalization. Here, the mean signal was calculated from regions within the brain.

3D-FLAIR volumes in the training set were reformatted to axial, sagittal, and coronal orientations. From each orientation, overlapping 2.5D patches ($64 \times 64 \times 7$) were extracted using a sliding window over the entire brain to train the corresponding orthogonal CNNs. Patches with <30% brain voxels were discarded.

Training data were generated by sampling the remaining patches to ensure an equal representation of patches with and without WMHs. Data augmentation was performed using the following schemes: in-plane flipping of patches, through-plane flipping of patches, and image filtering using Gaussian kernels.

Training data for the Meta CNN were generated by first predicting WMH posteriors for each subject in the training set using the trained orthogonal CNNs. After being reformatted to the axial orientation, 3D patches ($16 \times 16 \times 16$) were extracted from each of the posteriors and concatenated along the channel dimension.

During the test phase, 3D-FLAIR images were passed through the StackGen-Net framework to predict WMHs on the images in 1 pass through the network.

Experiments

Several ablation studies were conducted to systematically evaluate the choice of training data and architecture made in this study. A version of the DeepUNET3D architecture with 2D convolution kernels (DeepUNET2D) was trained on axially oriented 2D patches (64×64) to study the impact of additional spatial context in 2.5D patches on WMH segmentation performance.

We also trained an ensemble of 3 DeepUNET3D CNNs on axially oriented 2.5D training patches. The final prediction for

WMHs for this ensemble (DeepUNET3D-Ax E-A) was obtained by averaging posteriors from individual CNNs. For comparisons, the WMH posteriors from the orthogonal CNNs used in StackGen-Net were averaged (orthogonal E-A) or combined using a majority-voting scheme (orthogonal E-MV). Together, these experiments allowed us to determine whether a stacked generalization of orthogonal CNNs improves WMH segmentation performance.

We also explored the impact of the in-plane and through-plane spatial extent of the 2.5D training patches on WMH segmentation performance by training a series of DeepUNET3D CNNs with varying patch sizes.

All experiments were implemented in Python using Keras (<https://keras.io>) with TensorFlow (<https://www.tensorflow.org/>)²² backend on a Linux system, with Titan P100 (NVIDIA) GPUs. The CNN implementation details, training parameters, and loss function definitions are available in the Online Supplemental Data. The StackGen-Net CNN used in this work will be available at <https://github.com/spacl-ua/wmh-segmentation>.

Comparisons with State-of-the-Art Techniques

We compared the performance of StackGen-Net with several state-of-the-art segmentation techniques. The UNET architecture¹⁹ (UNET2D) was modified with zero-padded convolutions to yield input image-sized predictions. The multiclass cross-entropy loss used in the original article was modified to a weighted binary cross-entropy function. This CNN was trained using the same axial 2D patches as the DeepUNET2D.

DeepMedic¹⁶ was trained with 3D-FLAIR images with the code and default training settings available at <https://github.com/deepmedic/deepmedic>. We also compared our performance with the ensemble technique¹⁰ that achieved the highest Dice score, modified Hausdorff distance (95th percentile; HD95), and lesion-recall values in the recent WMH segmentation challenge.¹² This winning submission (UNET2D-WS-E), an averaging ensemble of three 2D UNETs, was trained using 2D-FLAIR images with the author's provided code and training settings (https://github.com/hongweilibran/wmh_ibbmTum). In contrast to the proposed DeepUNET3D, these reference architectures did not use dropout.

Additionally, we also used the lesion-prediction algorithm from the Lesion Segmentation Toolbox²³ (FMRIB Automated Segmentation Tool; <https://www.applied-statistics.de/lst.html>). Although some of the techniques compared here^{10,16,23} can also use T1-weighted images, we made use of only FLAIR images to train and/or evaluate these techniques for a comparable assessment.

Evaluation Metrics

The WMH detection performance was evaluated using the metrics defined in the Online Supplemental Data: Dice score, precision, recall, F1, HD95, and absolute volume difference (VD). The precision, recall, and F1 metrics were evaluated at the pixel-level (Precision-P, Recall-P, F1-P) as well as lesion-level (Precision-L, Recall-L, F1-L). A connected component analysis was used to identify individual lesions in the predicted segmentations. We also generated precision-recall receiver operating curves to

compare the areas under the curve (AUCs) for this heavily imbalanced class-detection problem.

Statistical Analysis

Two-sided paired *t* tests were used to determine whether StackGen-Net performance significantly differed from other state-of-the-art comparisons. When applicable, *P* values were Bonferroni-corrected for multiple comparisons. The total lesion volume was calculated on the ground truth annotations as well as WMH predictions from StackGen-Net. A Bland-Altman analysis was performed to assess the agreement in the number of detected lesions and lesion volume between ground truth and StackGen-Net predictions. The reproducibility coefficient, coefficient of variation, and correlation statistics were computed. A 2-sided paired *t* test was used to assess whether the WMH volumes significantly differed between the ground truth and StackGen-Net predictions.

Pair-wise Dice scores were calculated on the interobserver variability set from test cohorts 1 and 2 between human observers and StackGen-Net predictions. Repeated measures ANOVA was used to test whether the pair-wise Dice scores were significantly different between StackGen-Net and human observers. The value of α was set to .05 for all statistical comparisons.

RESULTS

The training of each DeepUNET3D CNN in StackGen-Net took approximately 40 hours, whereas the Meta CNN took approximately 1 hour. The end-to-end prediction time for a preprocessed 3D-FLAIR test image (240 × 270 × 176) was approximately 45 seconds on a GPU. The training and validation loss curves for a subset of DeepUNET3D architectures are presented in the Online Supplemental Data.

Figure 2 shows WMH predictions from StackGen-Net for representative multiplanar 3D-FLAIR images from a test subject, along with reference manual annotations. We see that StackGen-Net is able to identify smaller lesions, even when individual orthogonal CNNs miss them (Fig 2B and Online Supplemental Data). A comparison of StackGen-Net segmentation performance with variants of the DeepUNET3D CNN on test cohort 1 is presented in Table 1 and the Online Supplemental Data. StackGen-Net achieved a higher Dice score (0.76) compared with the individual orthogonal CNNs in the stacked generalization ensemble or their ensemble using averaging and majority voting (range, 0.72–0.75) (Table 1). StackGen-Net also yielded an absolute VD (12.36%) lower than the other CNNs. We also observed differences among performances of the orthogonal CNNs. On average, DeepUNET3D-Ax achieved the highest Dice score (0.74), whereas DeepUNET3D-Sagittal achieved the lowest absolute VD (16.9%), though these differences were not significant.

The introduction of convolutional blocks (DeepUNET2D-Ax versus UNET2D) significantly improved Dice scores ($P = .002$), F1-L ($P < .001$), and absolute VD ($P = .02$). Additional spatial information in the form of 2.5D patches (DeepUNET3D-Ax versus DeepUNET2D-Ax) significantly improved the performance in Dice scores, F1-L ($P < .005$), and absolute VD ($P = .03$). WMH segmentation performance of DeepUNET3D-

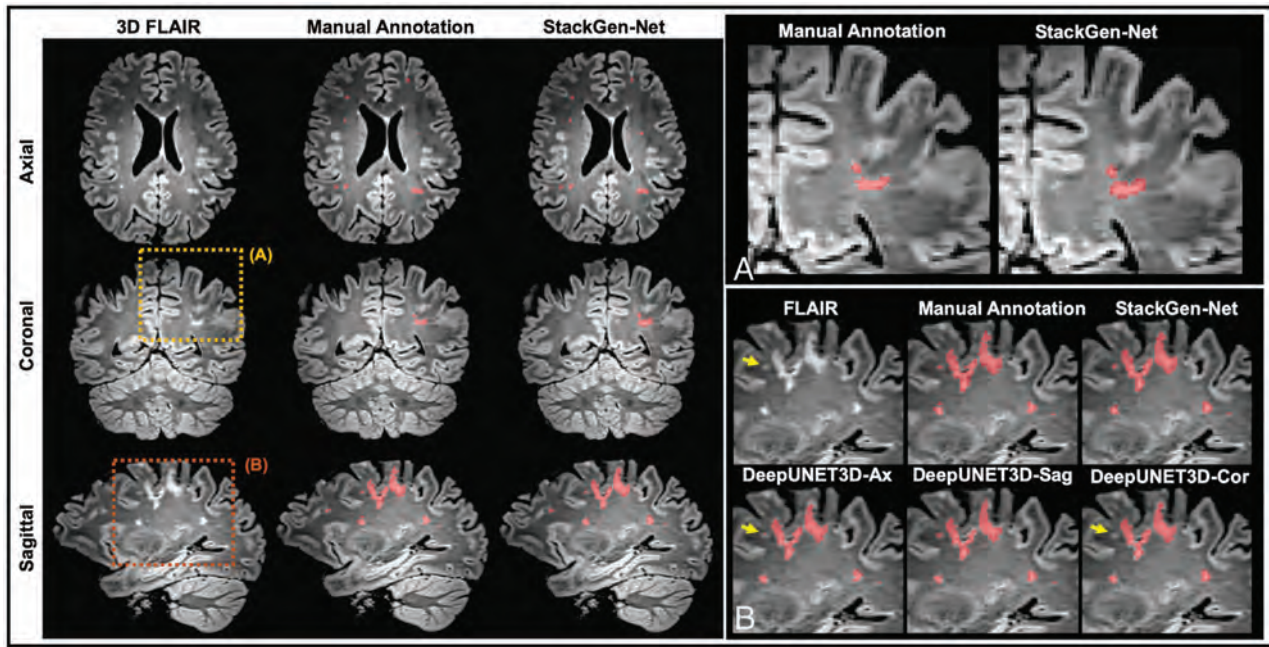


FIG 2. Qualitative evaluation of WMH detection performance by StackGen-Net. Representative axial, coronal, and sagittal slices from a test subject are shown in the left panel. Manual annotations and predictions from StackGen-Net are overlaid in red. *A*, The insets from coronal images are zoomed in for better comparison of the prediction with the ground truth. Compared with manual annotation, StackGen-Net slightly overestimates the lesion contour. *B*, A comparison of WMH predictions from the orthogonal CNNs (axial, sagittal, and coronal) is shown. The yellow arrows show WMHs that were missed by a majority of the CNNs in the ensemble. These lesions would have been missed by a simple averaging or majority voting of the orthogonal CNN predictions but are identified correctly by StackGen-Net. Sag indicates sagittal; Cor, coronal.

Table 1: Comparison^a of StackGen-Net with variants of DeepUNET3D architecture

	DeepUNET3D			Orthogonal		StackGen-Net	
	Axial	Sagittal	Coronal	Axial (E-A)	(E-A) (E-MV)		
Dice (F1-P)	0.74 [SD, 0.06]	0.73 [SD, 0.08]	0.72 [SD, 0.02]	0.73 [SD, 0.07]	0.75 [SD, 0.08]	0.75 [SD, 0.08]	0.76 [SD, 0.07]
Precision-P	0.84 [SD, 0.08]	0.81 [SD, 0.07]	0.83 [SD, 0.08]	0.84 [SD, 0.08]	0.87 [SD, 0.06]	0.87 [SD, 0.06]	0.73 [SD, 0.11]
Recall-P	0.66 [SD, 0.08]	0.67 [SD, 0.10]	0.64 [SD, 0.12]	0.78 [SD, 0.09]	0.66 [SD, 0.10]	0.67 [SD, 0.10]	0.79 [SD, 0.1]
Precision-L	0.81 [SD, 0.10]	0.79 [SD, 0.09]	0.85 [SD, 0.11]	0.84 [SD, 0.09]	0.88 [SD, 0.09]	0.87 [SD, 0.09]	0.75 [SD, 0.11]
Recall-L	0.80 [SD, 0.15]	0.80 [SD, 0.10]	0.78 [SD, 0.11]	0.77 [SD, 0.14]	0.80 [SD, 0.13]	0.81 [SD, 0.13]	0.87 [SD, 0.08]
F1-L	0.80 [SD, 0.11]	0.79 [SD, 0.07]	0.80 [SD, 0.08]	0.80 [SD, 0.09]	0.83 [SD, 0.08]	0.83 [SD, 0.08]	0.80 [SD, 0.09]
VD (%)	21.2 [SD, 10.5]	16.9 [SD, 10.8]	23.5 [SD, 13.0]	22.7 [SD, 11.2]	24.3 [SD, 11.3]	22.3 [SD, 10.9]	12.3 [SD, 12.7]

Note:—|VD| indicates absolute volume difference; P, pixel; L, lesion.

^a Mean [SD] on test cohort 1.

Ax with changes to the in-plane and through-plane spatial context of the training patch is shown in the Online Supplemental Data.

The predictions from StackGen-Net on test cohorts 1 and 2 are compared with state-of-the-art WMH segmentation techniques in Table 2 and the Online Supplemental Data. As expected, all deep learning CNNs outperformed the Lesion Segmentation Toolbox in all evaluation metrics. On average, StackGen-Net achieved significantly higher Dice scores (0.76 versus 0.33–0.66) ($P < .001$), F1-L (0.74 versus 0.40–0.65) ($P < .001$), and AUC

(0.84 versus 0.53–0.62) ($P < .001$) in the test cohorts ($n = 29$). The absolute VD was significantly lower (13.3% versus 32.7%–64.1%) than UNET2D-WS-E ($P = .03$), DeepMedic ($P < .001$), and UNET2D ($P < .001$). The UNET2D-WS-E architecture had the next best performance across most of the evaluation metrics. The boxplots (Fig 3) show the median scores and interquartile ranges for these techniques over the test cohorts ($n = 29$). The correlation and Bland-Altman plots to assess agreement between ground truth and StackGen-Net WMH predictions in terms of the total

Table 2: Comparison of StackGen-Net with other WMH detection techniques

	Test Cohort 1				Test Cohort 2			
	UNET2D	DeepMedic	UNET2D WS-E	StackGen-Net	UNET2D	DeepMedic	UNET2D WS-E	StackGen-Net
Dice (FI-P)	0.43 [SD, 0.17]	0.62 [SD, 0.09]	0.67 [SD, 0.09]	0.76 [SD, 0.07]	0.27 [SD, 0.20]	0.58 [SD, 0.15]	0.66 [SD, 0.17]	0.76 [SD, 0.09]
Precision-P	0.72 [SD, 0.19]	0.63 [SD, 0.13]	0.72 [SD, 0.15]	0.73 [SD, 0.11]	0.73 [SD, 0.32]	0.66 [SD, 0.22]	0.69 [SD, 0.23]	0.77 [SD, 0.11]
Recall-P	0.32 [SD, 0.19]	0.63 [SD, 0.18]	0.64 [SD, 0.07]	0.79 [SD, 0.1]	0.18 [SD, 0.16]	0.53 [SD, 0.13]	0.67 [SD, 0.12]	0.75 [SD, 0.09]
Precision-L	0.60 [SD, 0.20]	0.47 [SD, 0.23]	0.69 [SD, 0.18]	0.75 [SD, 0.11]	0.72 [SD, 0.24]	0.43 [SD, 0.23]	0.60 [SD, 0.23]	0.84 [SD, 0.14]
Recall-L	0.37 [SD, 0.09]	0.86 [SD, 0.09]	0.79 [SD, 0.15]	0.87 [SD, 0.08]	0.26 [SD, 0.14]	0.71 [SD, 0.10]	0.74 [SD, 0.13]	0.67 [SD, 0.13]
FI-L	0.44 [SD, 0.10]	0.54 [SD, 0.11]	0.71 [SD, 0.09]	0.80 [SD, 0.09]	0.37 [SD, 0.16]	0.50 [SD, 0.20]	0.63 [SD, 0.15]	0.73 [SD, 0.11]
VD (%)	54.4 [SD, 22.1]	26.9 [SD, 20.0]	17.6 [SD, 11.2]	12.3 [SD, 12.7]	77.4 [SD, 16.5]	30.6 [SD, 18.6]	37.6 [SD, 51.5]	13.7 [SD, 9.7]
HD95	19.5 [SD, 8.6]	15.9 [SD, 16.1]	10.8 [SD, 6.7]	5.27 [SD, 3.15]	30.6 [SD, 20.9]	21.8 [SD, 22.9]	19.5 [SD, 18.8]	17.1 [SD, 21.0]
AUC	0.53 [SD, 0.21]	0.66 [SD, 0.12]	0.61 [SD, 0.11]	0.84 [SD, 0.07]	0.54 [SD, 0.28]	0.60 [SD, 0.20]	0.60 [SD, 0.20]	0.84 [SD, 0.10]

Note:—HD95 indicates modified Hausdorff distance (mm); P, pixel; L, lesion; |VD| = absolute volume difference.

number of lesions (Online Supplemental Data) and their volumes (Fig 4) are also shown. The predicted WMH lesion volumes from StackGen-Net were highly correlated ($r = 0.99$) and were not significantly different from WMH volumes in ground truth ($P = .15$).

Table 3 compares human interobserver variability on the 2 test cohorts. The average intraobserver variability in Dice scores in observer 1 annotations on test cohort 1 was 0.70 (median = 0.71). The average pair-wise agreement in Dice scores between humans, calculated as an average of observer 1 versus observer 2, was 0.67 (median = 0.73) and 0.66 (median = 0.72) for test cohorts 1 and 2, respectively. The average agreement between human observers and StackGen-Net was 0.70 (median = 0.74) and 0.70 (median = 0.73) in these cohorts. Although the average pair-wise Dice scores for StackGen-Net were higher compared with human observers, we did not find this difference to be significant ($P = .22$).

DISCUSSION

Data and Architecture

In this work, we present the use of a stacked generalization of CNNs trained on 2.5D patches from orthogonal 3D-FLAIR orientations to improve WMH segmentation performance. The substantial improvement in performance as we move from UNET2D to DeepUNET2D illustrates the benefits of the convolutional blocks in the proposed architecture. The impact of additional spatial context provided by 2.5D training patches is evident in the superior performance of DeepUNET3D over its 2D counterpart.

The use of 2.5D training patches can be beneficial when working with a limited collection of annotated data or computational burden in optimally training a 3D network with 3D training patches.²⁴ Furthermore, in addition to random initialization in an ensemble framework, training each orthogonal CNN with 2.5D patches from a different orientation can provide training data diversity, a feature crucial to any ensemble-based training model.

The choice of CNN architecture, weights initialization, and hyperparameters has been shown to affect the task-specific performance of a CNN.^{10,17} An ensemble of CNNs has been shown to average away the variances in the solution and model- and configuration-specific behaviors.¹⁷ We also observed a similar trend (Table 1), in which the ensemble combination of CNNs performed better compared with individual CNNs in the ensemble.

The stacked generalization of orthogonal CNNs, with a higher Dice score and a lower absolute VD, outperformed individual DeepUNET3D CNNs or their ensemble combination using averaging or majority voting. An averaging ensemble assigns equal weights to WMH posteriors from individual CNNs, whereas majority voting prefers a majority consensus. Stacked generalization, on the other hand, learns a new functional mapping from individual CNN predictions in the ensemble to the target labels. This allows the Meta CNN to deduce the bias rate of individual DeepUNET3D CNNs in the ensemble and compensate for their flaws. In our experiments, we observed a difference in segmentation performance between the orthogonal CNNs, possibly due to learning different lesion characteristics that may depend on orientation. A stacked generalization framework is well-suited to learn and combine performance gains from the orthogonal CNNs. StackGen-Net is able to accurately detect WMHs, even when a majority in the ensemble predict a false-negative (Fig 2).

Human Observer Variability

The inter- and intraobserver variability in Dice scores between 2 experienced neuroradiologists reinforces the subjective nature of manual WMH annotations, even in the presence of pre-established annotation guidelines. The use of a trained CNN, with its deterministic framework, already eliminates intraobserver variability in predictions for a given FLAIR volume. Because we did not find the improvements in Dice scores between StackGen-Net and observers to be significant, we can say that StackGen-Net performance is comparable with human interobserver variability.

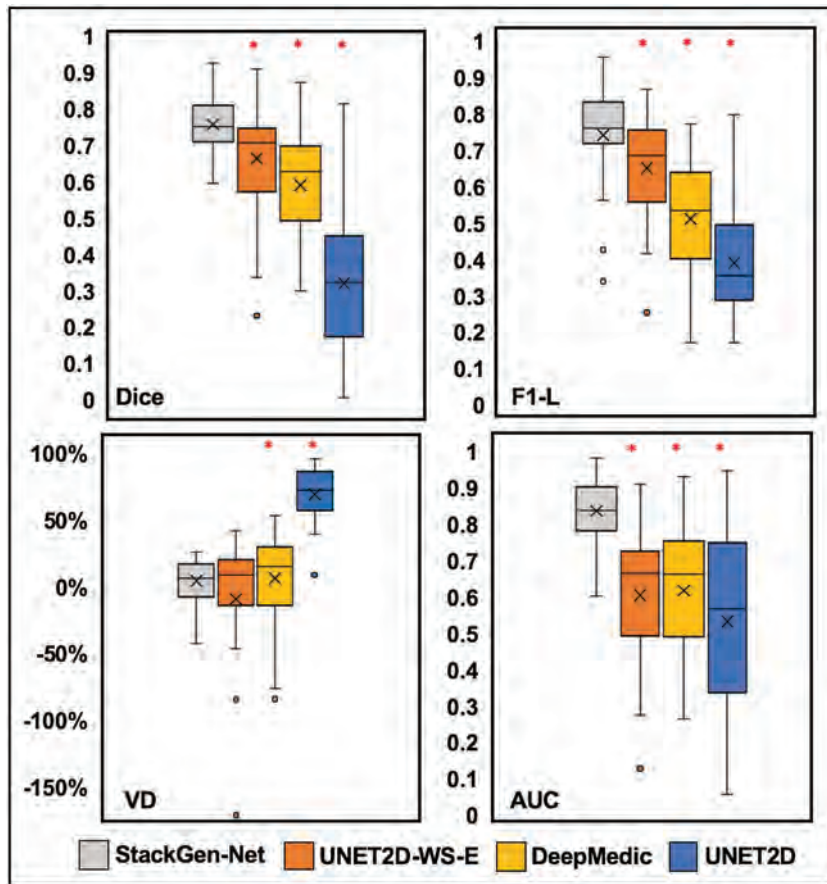


FIG 3. Boxplot comparison of Dice scores, lesion-based F1 (F1-L), volume difference (VD), and area under precision-recall curve (AUC) scores on the test set. We found a significant improvement in Dice scores, AUC, and F1-L in StackGen-Net compared with other WMH segmentation techniques compared here. The asterisk denotes $P < .001$ (2-sided paired t test, $n = 29$).

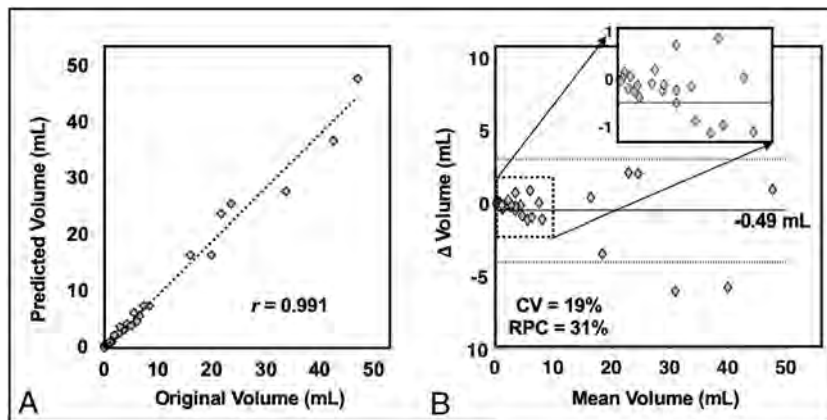


FIG 4. Correlation between WMH volumes (milliliters) in ground truth annotations and StackGen-Net predictions. *A*, We observed a strong correlation between the predictions and ground truth. *B*, Bland-Altman plot shows a good agreement in WMH volumes between the ground truth annotations and StackGen-Net predictions. We found no significant differences between the 2 volumes ($P = .15$, $n = 29$). The coefficient of variation (CV) and the repeatability coefficient (RPC) are also shown.

Comparison with Literature and Limitations

A wide range of Dice scores (0.51–0.80) have been reported in the literature for CNN-based WMH segmentation using 2D-FLAIR images.^{8–10,25,26} In comparison with some state-of-the-art techniques evaluated on the 2 test cohorts in this study, we observed higher average Dice scores of 0.76 and 0.75, respectively. Although the Dice scores reported in this work are slightly lower than those in some of these earlier studies, the human inter-observer variability baseline (0.67 compared with 0.77–0.79 reported in the literature) is also low in our study cohort.

The extent of WMH burden has been reported to affect evaluation metrics such as the Dice score.⁸ The Online Supplemental Data show the histogram of WMH volumes in our study cohort ($n = 50$) and scatterplots of total WMH volumes and average WMH volumes versus Dice scores on the test cohorts ($n = 29$). We observed that most subjects in our study cohort had low WMH volumes (8.04 [SD, 11.3] mL), which are associated with lower Dice scores. For a comparable assessment, we trained and evaluated some of these state-of-the-art techniques on our 3D-FLAIR dataset.

The orthogonal CNNs in StackGen-Net exploit the 3D nature of FLAIR acquisition and combine WMH information from the 3 orthogonal planes for segmentation. The use of 3D convolutions may result in suboptimal performance when training on anisotropic 2D-FLAIR images with thick slices.^{9,11} Interpolation to 3D space may affect the performance of 3D CNNs as a result of the blurring introduced along the slice direction. A similar observation was also made in Kuijff et al¹² regarding the results of the WMH segmentation challenge on 2D-FLAIR, in which most methods that used 3D convolutions appeared to perform poorly, ranking near the bottom.

Although 3D-FLAIR images are being widely used in research protocols such as ADNI, their clinical usage is not widespread. The clinical applicability of the proposed technique

Table 3: Interobserver variability in Dice scores^a

	Test Cohort 1		Test Cohort 2	
	Observer 2	StackGen-Net	Observer 2	StackGen-Net
Observer 1	0.68 (0.72)	0.76 (0.74)	0.66 (0.72)	0.74 (0.75)
Observer 2		0.65 (0.66)		0.65 (0.72)

^a Mean (median) pair-wise Dice scores.

needs to be further investigated on clinical 2D-FLAIR images to understand the impact of blurring on the detection of smaller lesions. Additionally, the CNNs in this study were all trained/evaluated on cohorts that excluded other pathologies that may produce hyperintensities on FLAIR images; the applicability of these CNNs requires further investigation on such images.

Although our study cohort is small compared with other published deep learning-based studies, the use of a 2.5D patch-based training framework, combined with data augmentation, has been useful to avoid the problem of limited annotated training data and overfitting. StackGen-Net, trained on images from a single scanner type, showed consistently improved performance on an independent cohort, demonstrating generalizability on images spanning multiple institutions and scanner manufacturers.

Clinical Outcomes

Results in the test cohorts show that StackGen-Net detects WMHs on 3D-FLAIR images with high Dice scores and lesion-wise F1. Fast and efficient 3D CNN architectures for WMH segmentation, such as StackGen-Net, can be used for the automatic, quantitative, and fast evaluation of WMH extent. With the demonstrated generalizability on a subset of ADNI data, the multiplanar StackGen-Net framework can be easily applied to larger 3D-FLAIR based longitudinal data repositories, including ADNI, to study the relationship between WMH burden and cognition. In conjunction with clinical visual rating scores, accurate WMH volume estimation can provide a better understanding of the relationship between lesion burden and clinical outcomes.

CONCLUSIONS

In this work, a stacked generalization of 3D orthogonal CNNs (StackGen-Net) was proposed to detect WMHs using multiplanar information from 3D-FLAIR images. We demonstrated that a stacked generalization ensemble outperforms traditional ensemble combinations as well as some state-of-the-art WMH detection frameworks. We also showed that we can reliably detect and quantify WMH in a time-efficient manner with performance comparable to human interobserver variability.

Disclosures: Gloria Guzman Perez-Carrillo—UNRELATED: Patents (Planned, Pending or Issued): Quantitative Differentiation of Tumor Heterogeneity using Diffusion MR Imaging Data, Patent No. 016652-PROI; Stock/Stock Options: Vanguard Mutual Funds. Mahesh Bharath Keerthivasan—OTHER RELATIONSHIPS: I am currently a paid employee of Siemens Healthineers.

REFERENCES

- Fazekas F, Kleinert R, Offenbacher H, et al. **Pathologic correlates of incidental MRI white matter signal hyperintensities.** *Neurology* 1993;43:1683–83 CrossRef Medline
- Brickman AM, Meier IB, Korgaonkar MS, et al. **Testing the white matter retrogenesis hypothesis of cognitive aging.** *Neurobiol Aging* 2012;33:1699–1715 CrossRef Medline
- Chutinet A, Rost NS. **White matter disease as a biomarker for long-term cerebrovascular disease and dementia.** *Curr Treat Options Cardiovasc Med* 2014;16:392 CrossRef Medline
- Carmichael O, Schwarz C, Drucker D, et al. **Longitudinal changes in white matter disease and cognition in the first year of the Alzheimer Disease Neuroimaging Initiative.** *Arch Neurol* 2010;67:1370–78 CrossRef Medline
- Bendfeldt K, Blumhagen JO, Egger H, et al. **Spatiotemporal distribution pattern of white matter lesion volumes and their association with regional grey matter volume reductions in relapsing-remitting multiple sclerosis.** *Hum Brain Mapp* 2010;31:1542–55 CrossRef Medline
- Fazekas F, Chawluk JB, Alavi A, et al. **MR signal abnormalities at 1.5 T in Alzheimer's dementia and normal aging.** *AJR Am J Roentgenol* 1987;149:351–56 CrossRef Medline
- Litjens G, Kooi T, Bejnordi BE, et al. **A survey on deep learning in medical image analysis.** *Med Image Anal* 2017;42:60–88 CrossRef Medline
- Rachmadi MF, Valdés-Hernández MD, Agan ML, et al; Alzheimer's Disease Neuroimaging Initiative. **Segmentation of white matter hyperintensities using convolutional neural networks with global spatial information in routine clinical brain MRI with none or mild vascular pathology.** *Comput Med Imaging Graph* 2018;66:28–43 CrossRef Medline
- Guerrero R, Qin C, Oktay O, et al. **White matter hyperintensity and stroke lesion segmentation and differentiation using convolutional neural networks.** *Neuroimage Clin* 2018;17:918–34 CrossRef Medline
- Li H, Jiang G, Zhang J, et al. **Fully convolutional network ensembles for white matter hyperintensities segmentation in MR images.** *Neuroimage* 2018;183:650–65 CrossRef Medline
- Ghafoorian M, Karssemeijer N, Heskes T, et al. **Location sensitive deep convolutional neural networks for segmentation of white matter hyperintensities.** *Sci Rep* 2017;7:1–12 CrossRef Medline
- Kuijff HJ, Casamitjana A, Collins DL, et al. **Standardized assessment of automatic segmentation of white matter hyperintensities and results of the WMH segmentation challenge.** *IEEE Trans Med Imaging* 2019;38:2556–68 CrossRef Medline
- Bink A, Schmitt M, Gaa J, et al. **Detection of lesions in multiple sclerosis by 2D FLAIR and single-slab 3D FLAIR sequences at 3.0 T: initial results.** *Eur Radiol* 2006;16:1104–10 CrossRef Medline
- Valverde S, Cabezas M, Roura E, et al. **Improving automated multiple sclerosis lesion segmentation with a cascaded 3D convolutional neural network approach.** *Neuroimage* 2017;155:159–68 CrossRef Medline
- Kushibar K, Valverde S, González-Villà S, et al. **Automated subcortical brain structure segmentation combining spatial and deep convolutional features.** *Med Image Anal* 2018;48:177–86 CrossRef Medline
- Kamnitsas K, Ledig C, Newcombe VFJ, et al. **Efficient multi-scale 3D CNN with fully connected CRF for accurate brain lesion segmentation.** *Med Image Anal* 2017;36:61–78 CrossRef Medline
- Kamnitsas K, Bai W, Ferrante E, et al. **Ensembles of multiple models and architectures for robust brain tumour segmentation.** In: *International MICCAI Brainlesion Workshop*: Springer; 2017: 450–62 Accessed September 14, 2017

18. Wolpert DH. **Stacked generalization.** *Neural Networks* 1992;5:241–59 CrossRef
19. Ronneberger O, Fischer P, Brox T. **U-Net: convolutional networks for biomedical image segmentation.** May 2015. <http://arxiv.org/abs/1505.04597>. Accessed July 19, 2019
20. Smith SM. **Fast robust automated brain extraction.** *Hum Brain Mapp* 2002;17:143–55 CrossRef Medline
21. Tustison NJ, Avants BB, Cook PA, et al. **N4ITK: improved N3 bias correction.** *IEEE Trans Med Imaging* 2010;29:1310–20 CrossRef Medline
22. Abadi M, Agarwal A, Barham P, et al. **Tensorflow: large-scale machine learning on heterogeneous distributed systems.** February 28, 2016. <https://arxiv.org/abs/1603.04467v2>. Accessed April 25, 2020
23. Schmidt P, Gaser C, Arsic M, et al. **An automated tool for detection of FLAIR-hyperintense white-matter lesions in multiple sclerosis.** *Neuroimage* 2012;59:3774–83 CrossRef Medline
24. Xing Y, Wang J, Chen X, et al. **2.5D convolution for RGB-D semantic segmentation.** *In: Proceedings of the International Conference on Image Processing (ICIP), Taipei, Taiwan, September 22–25, 2019* CrossRef
25. Ghafoorian M, Karssemeijer N, Heskes T, et al. **Deep multi-scale location-aware 3D convolutional neural networks for automated detection of lacunes of presumed vascular origin.** *Neuroimage Clin* 2017;14:391–99 CrossRef Medline
26. Duong MT, Rudie JD, Wang J, et al. **Convolutional neural network for automated flair lesion segmentation on clinical brain MR imaging.** *AJNR Am J Neuroradiol* 2019;40:1282–90 CrossRef Medline

Machine Learning–Based Prediction of Small Intracranial Aneurysm Rupture Status Using CTA-Derived Hemodynamics: A Multicenter Study

Z. Shi, G.Z. Chen, L. Mao, X.L. Li, C.S. Zhou, S. Xia, Y.X. Zhang, B. Zhang, B. Hu, G.M. Lu, and L.J. Zhang



ABSTRACT

BACKGROUND AND PURPOSE: Small intracranial aneurysms are being increasingly detected while the rupture risk is not well-understood. We aimed to develop rupture-risk models of small aneurysms by combining clinical, morphologic, and hemodynamic information based on machine learning techniques and to test the models in external validation datasets.

MATERIALS AND METHODS: From January 2010 to December 2016, five hundred four consecutive patients with only small aneurysms (<5 mm) detected by CTA and invasive cerebral angiography (or surgery) were retrospectively enrolled and randomly split into training (81%) and internal validation (19%) sets to derive and validate the proposed machine learning models (support vector machine, random forest, logistic regression, and multilayer perceptron). Hemodynamic parameters were obtained using computational fluid dynamics simulation. External validation was performed in other hospitals to test the models.

RESULTS: The support vector machine performed the best with areas under the curve of 0.88 (95% CI, 0.85–0.92) and 0.91 (95% CI, 0.74–0.98) in the training and internal validation datasets, respectively. Feature ranks suggested hemodynamic parameters, including stable flow pattern, concentrated inflow streams, and a small (<50%) flow-impingement zone, and the oscillatory shear index coefficient of variation, were the best predictors of aneurysm rupture. The support vector machine showed an area under the curve of 0.82 (95% CI, 0.69–0.94) in the external validation dataset, and no significant difference was found for the areas under the curve between internal and external validation datasets ($P = .21$).

CONCLUSIONS: This study revealed that machine learning had a good performance in predicting the rupture status of small aneurysms in both internal and external datasets. Aneurysm hemodynamic parameters were regarded as the most important predictors.

ABBREVIATIONS: AUC = area under the curve; AWSS = averaged WSS; CFD = computational fluid dynamics; CV = coefficient of variation; LR = logistic regression; ML = machine learning; MLP = multilayer perceptron; OSI = oscillatory shear index; ROC = receiver operating characteristic; SVM = support vector machine; WSS = wall shear stress

Unruptured intracranial aneurysms are common, with an overall prevalence of 3.2% in adults worldwide.¹ In the past decades, increasing unruptured aneurysms have been detected because of wide application of CTA and MRA. Notably, large numbers of incidentally detected aneurysms ($\leq 87.6\%$) have small sizes (<3–4 mm) and are usually

asymptomatic.² To date, small aneurysms account for 35%–47% of ruptured aneurysms and may impose a great burden on intracranial vessel diseases.^{3,4}

Treatment of patients with unruptured small aneurysms remains controversial. Some researchers recommend no preventive treatment or imaging follow-up for patients with aneurysms of <3 mm based on the evidence of low annual growth and rupture rates of small aneurysms.^{5,6} Current guidelines from the American Heart Association and American Stroke Association have no consensus opinion regarding the management of unruptured aneurysms with small (3–5 mm) and extra-small (≤ 3 mm) sizes.⁷ Thus,

Received March 20, 2020; accepted after revision November 9.

From the Department of Diagnostic Radiology (Z.S., C.S.Z., B.H., G.M.L., L.J.Z.), Jinling Hospital, Medical School of Nanjing University, Nanjing, Jiangsu, China; Department of Medical Imaging (G.Z.C.), Nanjing First Hospital, Nanjing, Jiangsu, China; Deepwise AI Lab (L.M., X.L.L.), Beijing, China; Department of Radiology (S.X.), Tianjin First Central Hospital, Tianjin, China; Laboratory of Image Science and Technology (Y.X.Z.), School of Computer Science and Engineering, Southeast University, Nanjing, China; and Department of Radiology (B.Z.), Taizhou People's Hospital, Taizhou, Jiangsu, China.

Paper previously presented as a preliminary report at: European Congress of Radiology, February 27 to March 3, 2019; Vienna, Austria.

This work was supported by the National Key Research and Development Program of China (2017YFC0113400 for L.J.Z.) and Key Projects of the National Natural Science Foundation of China (81830057 for L.J.Z.).

Please address correspondence to Long Jiang Zhang, MD, PhD, Department of Diagnostic Radiology, Jinling Hospital, Medical School of Nanjing University, 305 Zhongshan East Road, Nanjing, Jiangsu, 210002, China; e-mail: kevinzhj@163.com

Indicates open access to non-subscribers at www.ajnr.org

Indicates article with online supplemental data.

<http://dx.doi.org/10.3174/ajnr.A7034>

it is imperative to evaluate the rupture risk of small aneurysms to derive optimal clinical decision-making for further treatment and follow-up.

Various rupture risk factors and constructed scoring systems have been advocated by researchers.^{8,9} The correlation of risk factors (such as clinical, morphologic, and hemodynamic parameters) makes the prediction of aneurysm rupture complicated, leading to the unreliability of conventional methods such as logistic regression. Current scoring systems are not robust, especially for small aneurysms, which have to be modelled specifically due to their unique histologic characteristics.¹⁰⁻¹² Therefore, novel methodologies are required to construct rupture-risk models for small aneurysms to facilitate clinical decisions.^{13,14} Aneurysms were often treated only if any change in size or morphology of the aneurysm was detected during follow-up, which would result in a serious bias in the longitudinal study.¹³ It is feasible to perform a cross-sectional study to discriminate the ruptured aneurysms and, further, to apply the model in predicting rupture risk of unruptured aneurysms.

Machine learning (ML) techniques have attracted attention for their ability to identify patterns from a large sample dataset with multiple variables, using a highly effective method that facilitates the model construction for data-driven prediction or classification.¹⁵⁻¹⁷ Evidence has suggested that ML algorithms are superior to traditional counterparts in contexts in which data input is abundant and have potential for complex interactions.^{17,18} ML has also been used in the classification of aneurysm rupture status with relatively high accuracy.^{19,20} However, to the best of our knowledge, no report to date has developed ML methods for small aneurysm rupture prediction with routine clinical and morphologic features combined with hemodynamic variables.

The aim of this study was to characterize patients who have a higher risk of aneurysm rupture through developing and validating ML models using routinely collected clinical, morphologic, and hemodynamic variables in an internal cohort and to further test the indicated models in external datasets from other hospitals.

MATERIALS AND METHODS

Study Population

Between January 2010 and December 2016, one thousand five hundred seventy consecutive patients with suspected aneurysms or other cerebral vascular diseases who underwent cerebral CTA in Jinling Hospital verified by DSA or surgery were collected with the interval of no more than 3 months. The inclusion criterion was patients with small aneurysms (<5 mm).¹⁴ Exclusion criteria were as follows: 1) no aneurysms ($n=395$); 2) patients with fusiform, dissecting, and thrombotic aneurysms ($n=51$); 3) incomplete image/clinical data ($n=50$); 4) inadequate CTA image quality or failed computational fluid dynamics (CFD) simulation ($n=67$); and 5) patients with aneurysms of ≥ 5 mm ($n=503$). Finally, 504 small aneurysms (395 ruptured aneurysms and 109 unruptured aneurysms) were included and were randomly separated into training (410, 81%) and internal validation cohorts (94, 19%).

External validation cohorts enrolled patients who underwent cerebral CTA examinations from the other 2 medical centers (Tianjin First Central Hospital, Tianjin; and Taizhou People's Hospital, Taizhou, Jiangsu). Two neuroradiologists (G.Z.C. and

Z.S. with 7 and 3 years' experiences in neuroradiology) identified the location of aneurysms. In the case of disagreement between the 2 observers, consensus was reached after a joint reading with a senior neuroradiologist (C.S.Z. with 17 years of neuroimaging experience). The study flow chart is shown in Fig 1. Cerebral CTA protocols in the 3 medical centers are shown in the Online Supplemental Data. Ethics approval was obtained by the institutional review board of Jinling Hospital, Medical School of Nanjing University, Nanjing, China.

Patient and Aneurysm Characteristics

Clinical characteristics included age, sex, family history of aneurysmal SAH; comorbidities such as hypertension, diabetes mellitus, ischemic stroke, and coronary artery diseases; alcohol intake; and smoking status collected in the in-hospital medical record. Aneurysm characteristics included the multiplicity, size, shape, daughter sac, and location. Locations were divided into anterior communicating artery, ICA, MCA, posterior communicating artery, and others. Size was defined as the largest diameter measured on CTA with a volume-rendering algorithm. Specifically, the assessment of rupture status of an aneurysm was established as follows: For patients with SAH, when only 1 aneurysm adjacent to the cisternal clots was identified with CTA, the aneurysm was judged to be ruptured; when 1 aneurysm not adjacent to the cisternal clots was identified, its rupture status was judged intraoperatively; and when ≥ 2 aneurysms were identified, the rupture status of aneurysm was confirmed intraoperatively.¹⁹ Aneurysms with neither SAH nor symptoms were judged to be unruptured. We analyzed rupture risk on a per-patient basis for the analysis. When a patient had multiple aneurysms, the largest one served to categorize the patient.

Computational Fluid Dynamics–Derived Parameters

The computational model was constructed from CTA. CFD analysis was performed under pulsatile-flow conditions, and the procedure has been described in a previous study.²¹ The Online Supplemental Data shows the procedure of the development of the patient-specific CFD model reconstruction. Eleven quantitative hemodynamic parameters were used to describe and analyze the sophisticated blood flow conditions,^{21,22} including pressure, wall shear stress (WSS), averaged WSS-absolute (AWSS-ABSOLUTE), averaged WSS-mean (AWSS-MEAN), WSS gradient, AWSS gradient, oscillatory shear index (OSI), relative residence time, aneurysm formation index, gradient oscillatory number, and spatial WSS gradient (Online Supplemental Data). The coefficient of variation (CV) was used to describe the dispersion degree of data to demonstrate the hemodynamics of the aneurysm sac. Qualitative hemodynamic parameters included flow complexity, impingement zone, stability, and inflow concentration (Online Supplemental Data).²³ Two hundred aneurysms were randomly selected and evaluated independently by 2 observers trained for this task (G.Z.C. and Z.S.), who were blinded to the clinical history and rupture status. After validating good inter-reader agreement, 1 observer (G.Z.C.) performed the qualitative hemodynamic assessment of the remaining aneurysms.

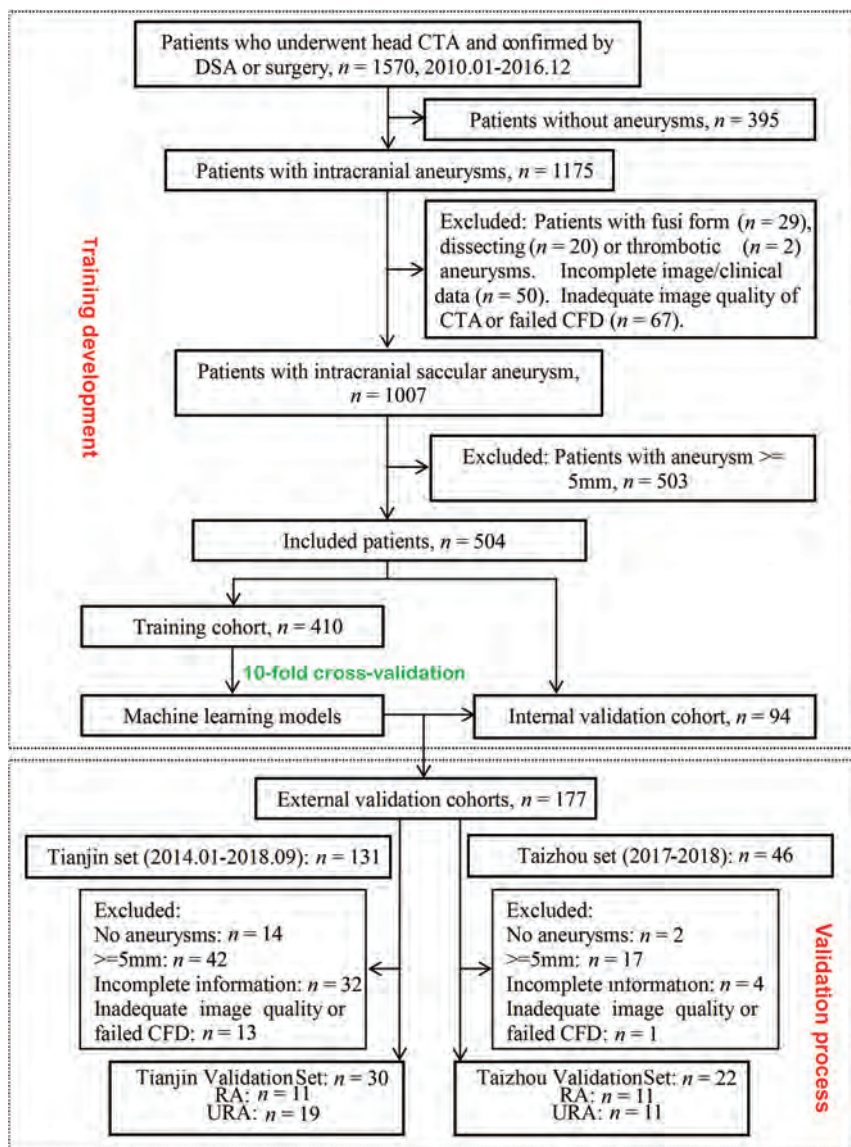


FIG 1. Flow chart of this study. RA indicates ruptured aneurysm; URA, Unruptured aneurysms; CFD, computational fluid dynamics.

Construction of Machine Learning Models

All features were preprocessed before model building. The quantitative features were normalized by z scores, while the qualitative features were encoded by one-hot encoder. ML methods were applied in the DeepWise Medical Research platform (<https://keyan.deepwise.com>). Supervised ML algorithms with binary classification (ruptured and unruptured aneurysm) were used to build predictive models, including logistic regression (LR), random forest, support vector machine with linear kernel (SVM), and multilayer perceptron (MLP). For implementing the procedure, the feature-selection method was used to reduce the overfitting problem. The best hyperparameters of the feature-selection method and models and regularization parameters of each model would be searched automatically on the basis of 10-fold cross-validation. After the optimal

hyperparameters and regularization parameters were chosen, the entire training cohort was used to train the model and the performance was evaluated on the internal and external validation cohorts. A brief overview of the models and the description of the feature-selection method are shown in the Online Supplemental Data.

Assessment of Model Performances

For the LR and MLP models, the predicted probability of rupture was estimated by the models directly. For the SVM model, the predicted probability was the normalized distance of the test sample to the separating hyperplane. For the random forest model, the predicted probability was computed as the mean predicted probabilities of the trees in the forest. The performances of the models were represented as the receiver operating characteristic (ROC) curve, the area under curve (AUC), and 95% confidence interval (CI). The sensitivity and specificity were determined by the Youden index. The calibration of the 4 ML models was assessed using the calibration curves in the internal validation dataset with Locally Weighted Scatterplot Smoothing.²⁴ The DeLong test and Bonferroni correction were applied to compare the AUCs of these models. Feature importance was ranked according to the coefficient of each parameter provided by the corresponding ML algorithms. Specifically, the feature importance of the random forest model refers to the Gini importance.

Statistical Analysis

Quantitative variables were expressed as mean \pm [SD] if normally distributed, while median and interquartile range were used for non-normally distributed data. Categorical variables (such as sex, the presence of hypertension, qualitative hemodynamic parameters) were expressed as frequencies or percentages; the difference in categorical variables was analyzed using the Pearson χ^2 test or Fisher exact test when appropriate. For normally distributed data (such as age, OSI_{CV}), an independent-samples t test was used; otherwise, a Mann-Whitney U test was applied. The independent-samples nonparametric test was used to analyze non-normally distributed data. The interreader agreement of the qualitative hemodynamic assessment was evaluated by the Cohen κ . The CI of the AUC was calculated by the method of Hanley and McNeil.²⁵ Statistical analyses were performed using SPSS statistical and computing software (Version 22.0.0; IBM), Medcalc for Windows

Performance of SVM to predict rupture status of small aneurysms in the training, internal validation, and external validation datasets

	Training Set (n = 410)	Internal Validation Set (n = 94)	External Validation Set (n = 52)	Tianjin Set (n = 30)	Taizhou Set (n = 22)
AUC	0.88	0.91	0.82	0.71	0.90
95% CI	0.85–0.92	0.74–0.98	0.69–0.94	0.52–0.86	0.70–0.99
Sensitivity	73.4%	77.3%	68.2%	54.5%	81.8%
Specificity	91.1%	84.2%	76.7%	73.7%	81.8%
Delong test	–	–	.21 ^a	–	.15 ^b

Note:—CI indicates confidence interval; LR, logistic regression; SVM, support vector machine; RF, random forest; ROC, receiver operation characteristic; RF, random forest; –, NA.

^a $P < .05$ means a significant difference exists in AUCs of SVM in the internal and external validation datasets.

^b $P < .05$ means a significant difference exists in AUCs of SVM in Taizhou and Tianjin sets.

(Version 18.2; MedCalc Software), R (Version 3.5.2; <http://www.r-project.org/>), and the Scikit-learn package²⁶ in Python (<https://scikit-learn.org/stable/>). A 2-sided P value $< .05$ was used to represent statistical significance.

RESULTS

Patient and Aneurysm Characteristics

In this retrospective study, most patients with ruptured small aneurysms were women. These patients were younger and had a higher proportion of hypertension and a lower proportion of ischemic stroke and coronary artery disease compared with those with unruptured aneurysms (all, $P < .05$). In addition, more small aneurysms with irregular shapes were found in the ruptured group. The anterior communicating artery and MCA tended to have more ruptured aneurysms (all, $P < .05$), while the ICA and other intracranial arteries had fewer ruptured aneurysms (all, $P < .05$). For hemodynamic parameters, the ruptured group was more likely to have complex flow patterns (52.9% versus 33.0%, $P < .001$), concentrated inflow streams (61.5% versus 18.3%, $P < .001$), a small flow-impingement zone (73.4% versus 28.4%, $P < .001$), and unstable flow patterns (57.0% versus 29.4%, $P < .001$), as well as a smaller PressureCV gradient oscillatory number, and OSI_{CV} and higher AWSS-MEAN_{CV}, WSS_{CV}, AWSS-ABSOLUTE_{CV}, WSS gradient, and aneurysm formation index (all, $P < .05$) (Online Supplemental Data). The interobserver agreement for the qualitative hemodynamic assessment of aneurysms ranged from good to excellent, with κ values from 0.646 to 0.827.

The internal training cohort had 410 cases (320 ruptured aneurysms), and the internal validation cohort had 94 cases (75 ruptured aneurysms). There were no significant differences for the clinical, morphologic, and hemodynamic parameters between the 2 cohorts (all, $P > .10$) (Online Supplemental Data). In the external cohorts, 177 patients with cerebral CTA (131 patients from the Tianjin center and 46 patients from the Taizhou center) were screened, and 52 patients with small aneurysms (19 unruptured and 11 ruptured aneurysms in the Tianjin center, 11 unruptured and 11 ruptured aneurysms in the Taizhou center) were included (Fig 1). There was a lower incidence of ruptured aneurysms in the Taizhou and Tianjin datasets ($P = .002$ and $< .001$, respectively). Because of the small sample size of both external datasets, we merged all the cases into 1 external dataset to validate the performance of ML models (Online Supplemental Data).

Performances of ML Models

The 4 ML models derived from the training dataset performed equally in all datasets (all, $P > .05$, DeLong test). The calibration curves are shown in the Online Supplemental Data. Among them, the SVM was well-calibrated with the highest AUC in the internal validation dataset (Table and Fig 2A). The performances of the other 3 models are shown in the Online Supplemental Data. The AUCs of the SVM model were 0.88 (95% CI, 0.85–0.92), 0.91 (95% CI, 0.74–0.98), and 0.82 (95% CI, 0.69–0.94) in the training, internal, and external validation datasets, respectively. The Delong test showed that the AUC had no significant difference between internal validation dataset and the external validation dataset ($P = .21$).

We further investigated the application of models in the Tianjin and Taizhou sets (Table and Online Supplemental Data). The SVM had a slightly higher AUC in the Taizhou set (AUC = 0.90; 95% CI, 0.70–0.99) than that in the Tianjin set (AUC = 0.71; 95% CI, 0.52–0.86), without a significant difference ($P = .15$).

Feature Ranks

Selected features used for model fitting are seen in the Online Supplemental Data.

The feature rank of the corresponding top 10 variants derived by the SVM algorithm is shown in Fig 2B. Hemodynamics-related parameters were the leading predictors contributing to the risk model. Stable flow stream, higher OSI_{CV}, male sex, and older age were protective variables, while concentrated inflow streams, a small (<50%) flow-impingement zone, MCA, hypertension, larger size, and irregular shape increased the risk of aneurysm rupture.

We also developed models based on sole clinical, morphologic, or hemodynamic features, respectively, and validated the models in the internal validation dataset for further evaluation. Figure 2C demonstrates that the hemodynamic feature-dependent model had a higher AUC (AUC = 0.90; 95% CI, 0.84–0.96) than morphologic features (AUC = 0.69; 95% CI, 0.5–0.83; $P = .01$) and clinical features (AUC = 0.55; 95% CI, 0.4–0.70; $P < .001$).

DISCUSSION

In this study, we derived and validated ML-based prediction models for rupture status of small aneurysms, depending on clinical, morphologic, and hemodynamic characteristics in the internal and external datasets. Our study highlighted the role of

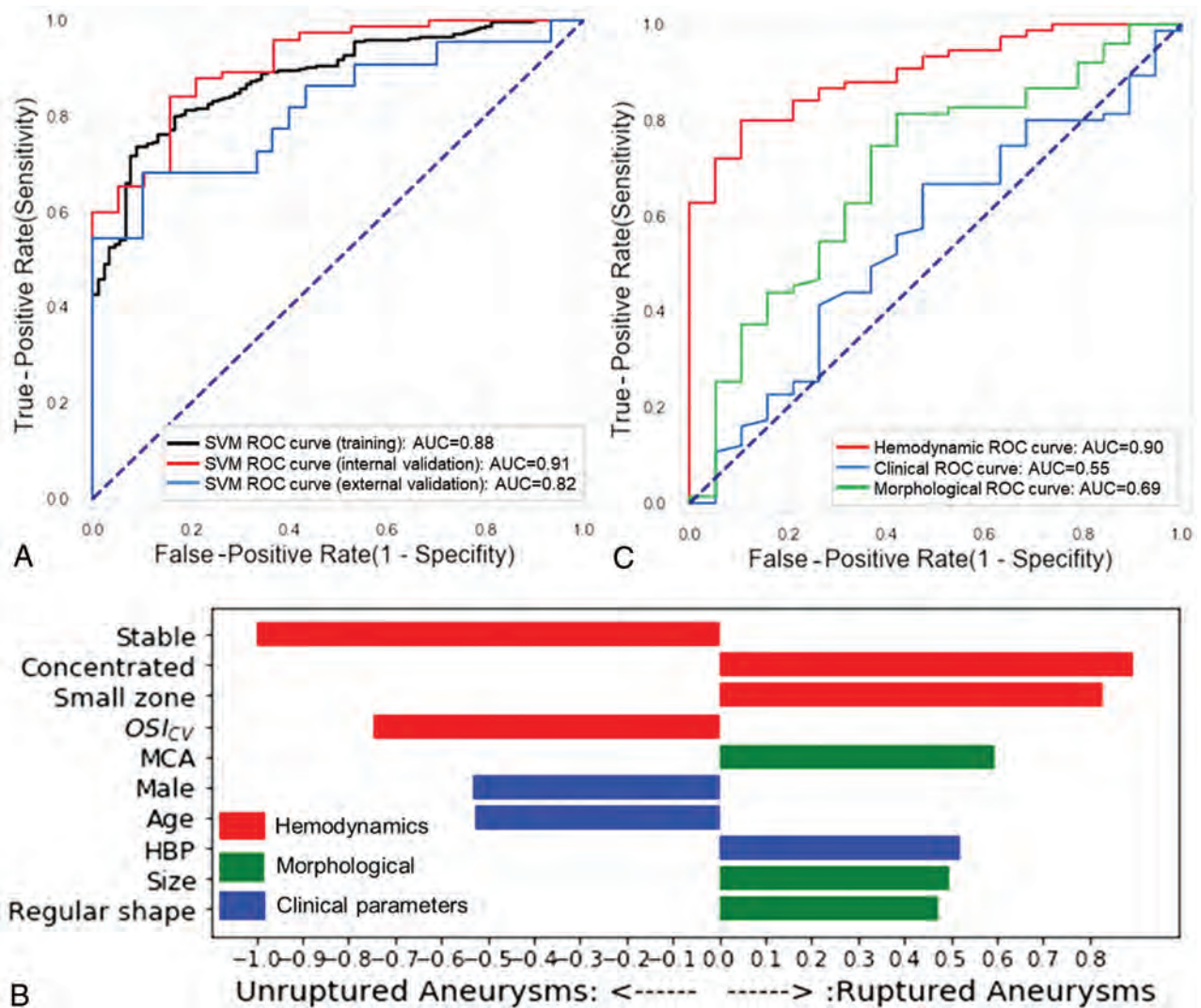


FIG 2. Performance of the SVM algorithm, the derived top 10 variables, and the performances of feature—dependent models in the internal validation dataset. **A**, ROC curves and AUCs for training and internal and external validation sets. **B**, The top 10 features of the variables derived from the SVM algorithm. **C**, ROCs of the SVM based on the features belonging to the 3 categories separately in the internal validation dataset.

hemodynamic parameters in predicting small aneurysm rupture status. We found that the ML models, especially the SVM, had good performance in the internal and external datasets, indicating the robustness and generalizability of ML models. Thus, the ML models provided in this study can be regarded as decision-support tools of unruptured small aneurysms, while further validation is required.

Traditional statistical methods, such as multivariable LR, have explored the association between specific features and the ruptured/unruptured end point. However, determination of rupture risk of aneurysms remains challenging, particularly when the exact underlying etiology is unclear.²⁷ In addition, multivariable LR has several limitations, primarily resting on assumptions of the existence of the linear relationship between the log-odd of the predicted probability and the variables. ML has shown the potential to improve diagnostic accuracy and prognostic outcomes compared with conventional statistical methods.^{17,20} Our study used 4

representative branches of ML, including the subtypes of logistic regression, ensemble model, SVM, and neural network. The 4 models had good performance in the internal and external cohorts. A previous study had compared the logistic regression probability model with ML classifiers and found that the performance of the logistic regression probability model was comparable, but the study did not specifically focus on small aneurysms.²⁸

A convolutional neural network based on images of 3D-DSA for detecting the rupture status of aneurysms of <7 mm had also been explored.²⁰ And in the presented study, we compared 4 ML methods combined with CTA-derived hemodynamics and found that the SVM and MLP had slightly higher AUCs in predicting small-aneurysm rupture status. The SVM performed better when applied in the 2 external datasets in terms of generalizability. Another interesting finding was that SVM, random forest, and MLP seemed to have less overfitting than LR when applied to the external validation dataset; among these, SVM had the lowest

overfitting. Considering the higher AUC and the lowest overfitting of the SVM, it is reasonable for us to regard SVM as the most valuable ML method in this context. The models did not seem well-calibrated, probably due to the small size of the dataset.

Most important, our findings highlighted the role of hemodynamics in the prediction of rupture status of small aneurysms, which had not been quantitatively identified. The process of rupture of an aneurysm is complex because of the intertwining relationship between the blood flow and pathologic responses in the endothelial cells and remodeling of vessel wall.^{29,30} Blood flow hemodynamics emerged as an important role that can uncover the underlying mechanism through hemodynamic-biologic pathways.¹¹ Higher WSS_{CV} and lower OSI_{CV} were further identified in our study as the paramount rupture risk factors by the ML algorithms. CV is a standardized measure of dispersion of a probability distribution or frequency distribution, and the smaller CV was, the smaller the extent of variation was. That feature means that the ruptured small aneurysms had higher WSS variation in the sac, while OSI had less variation. A similar result had been previously reported in a case-control study that showed a narrow cumulative WSS distribution characterizing a hemodynamic prone-to-rupture range for small-sized aneurysms.³¹ The spatial minimum, maximum, average WSS, normalized WSS, spatial WSS gradient, and OSI had been studied before, and low WSS and high OSI were known to upregulate endothelial surface adhesion molecules, causing dysfunction of flow-induced nitrous oxide, increasing endothelial permeability, thus, promoting inflammatory cell infiltration.³¹⁻³⁵ Our study offered a novel insight into the role of hemodynamics in rupture-risk prediction of unruptured small aneurysms and can be used as a supplement to the existing research. For example, the WSS in ruptured small aneurysms could be lower in minimum/maximum/mean value and more varied than in unruptured aneurysms, and OSI could be higher with less variation.

Our study also found that qualitative hemodynamic parameters had an important role in predicting the rupture status of small aneurysms. The study showed that complex flow patterns, concentrated inflow concentration, unstable flow, and a smaller flow impingement zone played a critical role in the prediction of rupture risk of aneurysms. These findings have been supported by previous studies that showed ruptured aneurysms were more likely to be associated with flow types with changing direction of the blood inflow jet, which will create a single vortex.³⁶ It appears very instructive to add the qualitative hemodynamic parameters in predicting rupture status of small aneurysms.

Specifically, we analyzed the distinctive performances of the 4 models in the 2 external datasets separately, among which random forest and MLP exhibited significant differences (both $P = .03$). The reasons can be attributed to the baseline characteristic differences, in which 9 variables in the Taizhou set and 12 in the Tianjin set were significantly different, and most of the variables are hemodynamics. Given the different scanner manufacturers in the Tianjin and Jinling sets (Revolution CT, GE Healthcare, versus Somatom Definition, Siemens), the hemodynamic differences may arise from them; this issue requires further investigation. Although the proportion of ruptured aneurysms was lower in the Taizhou

set (50% versus 78.4% for the Taizhou and Jinling datasets), the performance of the models was encouraging. These results highlight the influence of manufacturers on CFD simulation.

We acknowledged that our study had some limitations. First, this retrospective study aimed to identify the characteristics of ruptured aneurysms, and the model predicted only the current rupture status rather than future aneurysm risk. Whether the model can be used in the rupture-risk prediction of small aneurysms requires further longitudinal studies. Our model is reliable due to being derived from a large-scale internal cohort of small aneurysms demonstrated by DSA/surgery and validated in independent external validation datasets. Second, the morphologic changes of aneurysms after rupture were not considered in this study. Third, the external validation datasets from the other 2 medical centers had small sample sizes and were not verified by DSA or an operation. Fourth, features of the wall of the vessel and aneurysm have been investigated for precise evaluations using high-resolution MR imaging and optical coherence tomography, while the elements are not included in the study. Fifth, CFD itself has some limitations, such as a huge number of different parameters, the lack of consistency, and being time-consuming, resulting in difficulties in clinical use with CFD.³⁷ Sixth, the assessment of the qualitative hemodynamic parameters was based on the 2 observers, which was subjective and caused intra- and interobserver variations. Other metrics for automated flow-complexity assessment like the “inflow concentration index” and “vortex core line length” may help in this context. Thus, a large, prospective, multicenter study is needed to further demonstrate our findings.

CONCLUSIONS

Our study provided impressive ML models for predicting rupture status of small aneurysms by combining clinical, morphologic, and hemodynamic features. ML methods, especially SVM, had a good performance in internal and external validation datasets and highlighted the role of hemodynamics. Our model has the potential for identifying high-risk aneurysms and facilitating proper clinical management of incidentally found small aneurysms.

Disclosures: Zhao Shi—RELATED: Grant: Key Projects of the National Natural Science Foundation of China (81830057).* Xiuli Li—RELATED: Grant: Key Projects of the National Natural Science Foundation of China (81830057).* Long Jiang Zhang—RELATED: Grant: National Key Research and Development Program of China (2017YFC0113400) and Key Projects of the National Natural Science Foundation of China (81830057).* *Money paid to the institution.

REFERENCES

1. Vlak MH, Algra A, Brandenburg R, et al. **Prevalence of unruptured intracranial aneurysms, with emphasis on sex, age, comorbidity, country, and time period: a systematic review and meta-analysis.** *Lancet Neurol* 2011;10:626–36 CrossRef Medline
2. Murayama Y, Takao H, Ishibashi T, et al. **Risk analysis of unruptured intracranial aneurysms: prospective 10-year cohort study.** *Stroke* 2016;47:365–71 CrossRef Medline
3. Lee GJ, Eom KS, Lee C, et al. **Rupture of very small intracranial aneurysms: incidence and clinical characteristics.** *J Cerebrovasc Endovasc Neurosurg* 2015;17:217–22 CrossRef Medline
4. Bender MT, Wendt H, Monarch T, et al. **Small aneurysms account for the majority and increasing percentage of aneurysmal**

- subarachnoid hemorrhage: a 25-year, single-institution study. *Neurosurgery* 2018;83:692–99 CrossRef Medline
5. Malhotra A, Wu X, Forman HP, et al. **Management of tiny unruptured intracranial aneurysms: a comparative effectiveness analysis.** *JAMA Neurol* 2018;75:27–34 CrossRef Medline
 6. Malhotra A, Wu X, Forman HP, et al. **Growth and rupture risk of small unruptured intracranial aneurysms.** *Ann Intern Med* 2017;167:26–33 CrossRef Medline
 7. Thompson BG, Brown RD Jr, Amin-Hanjani S, et al. American Stroke Association, American Heart Association Stroke Council, Council on Cardiovascular and Stroke Nursing, and Council on Epidemiology and Prevention. **Guidelines for the management of patients with unruptured intracranial aneurysms: a guideline for healthcare professionals from the American Heart Association/American Stroke Association.** *Stroke* 2015;46:2368–400 CrossRef Medline
 8. Greving JP, Wermer MJ, Brown RD Jr, et al. **Development of the PHASES score for prediction of risk of rupture of intracranial aneurysms: a pooled analysis of six prospective cohort studies.** *Lancet Neurol* 2014;13:59–66 CrossRef Medline
 9. UCAS Japan Investigators, Morita A, Kirino T, et al. UCAS Japan Investigators. **The natural course of unruptured cerebral aneurysms in a Japanese cohort.** *N Engl J Med* 2012;366:2474–82 CrossRef Medline
 10. Kataoka K, Taneda M, Asai T, et al. **Difference in nature of ruptured and unruptured cerebral aneurysms.** *Lancet* 2000;355:203 CrossRef Medline
 11. Meng H, Tutino VM, Xiang J, et al. **High WSS or low WSS? Complex interactions of hemodynamics with intracranial aneurysm initiation, growth, and rupture: toward a unifying hypothesis.** *AJNR Am J Neuroradiol* 2014;35:1254–62 CrossRef Medline
 12. Suzuki T, Takao H, Rapaka S, et al. **Rupture risk of small unruptured intracranial aneurysms in Japanese adults.** *Stroke* 2020;51:641–43 CrossRef Medline
 13. Güresir E, Vatter H, Schuss P, et al. **Natural history of small unruptured anterior circulation aneurysms: a prospective cohort study.** *Stroke* 2013;44:3027–31 CrossRef Medline
 14. Varble N, Tutino VM, Yu J, et al. **Shared and distinct rupture discriminants of small and large intracranial aneurysms.** *Stroke* 2018;49:856–64 CrossRef Medline
 15. Krittanawong C, Zhang H, Wang Z, et al. **Artificial intelligence in precision cardiovascular medicine.** *J Am Coll Cardiol* 2017;69:2657–64 CrossRef Medline
 16. Darcy AM, Louie AK, Roberts LW. **Machine learning and the profession of medicine.** *JAMA* 2016;315:551–52 CrossRef Medline
 17. Beam AL, Kohane IS. **Big data and machine learning in health care.** *JAMA* 2018;319:1317–18 CrossRef Medline
 18. Zack CJ, Senecal C, Kinar Y, et al. **Leveraging machine learning techniques to forecast patient prognosis after percutaneous coronary intervention.** *JACC Cardiovasc Interv* 2019;12:1304–11 CrossRef Medline
 19. Tanioka S, Ishida F, Yamamoto A, et al. **Machine learning classification of cerebral aneurysm rupture status with morphologic variables and hemodynamic parameters.** *Radiology: Artificial Intelligence* 2020;2:e190077 CrossRef
 20. Kim HC, Rhim JK, Ahn JH, et al. **Machine learning application for rupture risk assessment in small-sized intracranial aneurysm.** *J Clin Med* 2019;8:683 CrossRef Medline
 21. Ren Y, Chen GZ, Liu Z, et al. **Reproducibility of image-based computational models of intracranial aneurysm: a comparison between 3D rotational angiography, CT angiography and MR angiography.** *Biomed Eng Online* 2016;15:50 CrossRef Medline
 22. Can A, Du R. **Association of hemodynamic factors with intracranial aneurysm formation and rupture: systematic review and meta-analysis.** *Neurosurgery* 2016;78:510–20 CrossRef Medline
 23. Cebral JR, Mut F, Weir J, et al. **Association of hemodynamic characteristics and cerebral aneurysm rupture.** *AJNR Am J Neuroradiol* 2011;32:264–70 CrossRef Medline
 24. Detmer FJ, Chung BJ, Mut F, et al. **Development and internal validation of an aneurysm rupture probability model based on patient characteristics and aneurysm location, morphology, and hemodynamics.** *Int J Comput Assist Radiology Surg* 2018;13:1767–79 CrossRef Medline
 25. Hanley JA, McNeil BJ. **The meaning and use of the area under a receiver operating characteristic (ROC) curve.** *Radiology* 1982;143:29–36 CrossRef Medline
 26. Pedregosa F, Varoquaux G, Gramfort A, et al. **Scikit-learn: machine learning in Python.** *Journal of Machine Learning Research* 2011;12:2825–30
 27. Hae H, Kang SJ, Kim WJ, et al. **Machine learning assessment of myocardial ischemia using angiography: development and retrospective validation.** *PLoS Med* 2018;15:e1002693 CrossRef Medline
 28. Detmer FJ, Lücke D, Mut F, et al. **Comparison of statistical learning approaches for cerebral aneurysm rupture assessment.** *Int J Comput Assist Radiology Surg* 2019;15:1401–50 CrossRef Medline
 29. Chiu JJ, Chien S. **Effects of disturbed flow on vascular endothelium: pathophysiological basis and clinical perspectives.** *Physiol Rev* 2011;91:327–87 CrossRef Medline
 30. Chatziprodromou I, Tricoli A, Poulikakos D, et al. **Haemodynamics and wall remodelling of a growing cerebral aneurysm: a computational model.** *J Biomech* 2007;40:412–26 CrossRef Medline
 31. Pereira VM, Brina O, Bijlenga P, et al. **Wall shear stress distribution of small aneurysms prone to rupture: a case-control study.** *Stroke* 2014;45:261–64 CrossRef Medline
 32. Lauric A, Hippelheuser J, Cohen AD, et al. **Wall shear stress association with rupture status in volume matched sidewall aneurysms.** *J Neurointerv Surg* 2014;6:466–73 CrossRef Medline
 33. Miura Y, Ishida F, Umeda Y, et al. **Low wall shear stress is independently associated with the rupture status of middle cerebral artery aneurysms.** *Stroke* 2013;44:519–21 CrossRef Medline
 34. Goubergrits L, Schaller J, Kertzscher U, et al. **Statistical wall shear stress maps of ruptured and unruptured middle cerebral artery aneurysms.** *J R Soc Interface* 2012;9:677–88 CrossRef Medline
 35. Chalouhi N, Hoh BL, Hasan D. **Review of cerebral aneurysm formation, growth, and rupture.** *Stroke* 2013;44:3613–22 CrossRef Medline
 36. Xiang J, Natarajan SK, Tremmel M, et al. **Hemodynamic-morphologic discriminants for intracranial aneurysm rupture.** *Stroke* 2011;42:144–52 CrossRef Medline
 37. Liang L, Steinman DA, Brina O, et al. **Towards the clinical utility of CFD for assessment of intracranial aneurysm rupture: a systematic review and novel parameter-ranking tool.** *J Neurointerv Surg* 2019;11:153–58 CrossRef Medline

Automated Detection and Segmentation of Brain Metastases in Malignant Melanoma: Evaluation of a Dedicated Deep Learning Model

L. Pennig, R. Shahzad, L. Caldeira, S. Lennartz, F. Thiele, L. Goertz, D. Zopfs, A.-K. Meißner, G. Fürtjes, M. Perkuhn, C. Kabbasch, S. Grau, J. Borggreffe, and K.R. Laukamp



ABSTRACT

BACKGROUND AND PURPOSE: Malignant melanoma is an aggressive skin cancer in which brain metastases are common. Our aim was to establish and evaluate a deep learning model for fully automated detection and segmentation of brain metastases in patients with malignant melanoma using clinical routine MR imaging.

MATERIALS AND METHODS: Sixty-nine patients with melanoma with a total of 135 brain metastases at initial diagnosis and available multi-parametric MR imaging datasets (T1-/T2-weighted, T1-weighted gadolinium contrast-enhanced, FLAIR) were included. A previously established deep learning model architecture (3D convolutional neural network; DeepMedic) simultaneously operating on the aforementioned MR images was trained on a cohort of 55 patients with 103 metastases using 5-fold cross-validation. The efficacy of the deep learning model was evaluated using an independent test set consisting of 14 patients with 32 metastases. Manual segmentations of metastases in a voxel-wise manner (T1-weighted gadolinium contrast-enhanced imaging) performed by 2 radiologists in consensus served as the ground truth.

RESULTS: After training, the deep learning model detected 28 of 32 brain metastases (mean volume, 1.0 [SD, 2.4] cm³) in the test cohort correctly (sensitivity of 88%), while false-positive findings of 0.71 per scan were observed. Compared with the ground truth, automated segmentations achieved a median Dice similarity coefficient of 0.75.

CONCLUSIONS: Deep learning-based automated detection and segmentation of brain metastases in malignant melanoma yields high detection and segmentation accuracy with false-positive findings of <1 per scan.

ABBREVIATIONS: CNN = convolutional neural network; DLM = deep learning model; GT = ground truth

Malignant melanoma is an aggressive skin cancer associated with high mortality and morbidity rates.^{1,2} Brain metastases are common in malignant melanoma,^{3,4} subsequently causing potential severe neurologic impairment and worsened outcome. Therefore, it is recommended that melanoma patients with an advanced stage undergo MR imaging of the head for screening purposes to detect metastases.⁵⁻⁸

Owing to an increased workload of radiologists, repetitive evaluation of MR imaging scans can be tiresome, hence bearing

an inherent risk of missed diagnosis for subtle lesions, with satisfaction of search effects leading to decreased sensitivity for additional lesions.^{9,10} Automatization of detection could serve as an adjunct tool for lesion preselection that can support image evaluation by radiologists and clinicians.^{11,12} Furthermore, automated segmentations may be used as a parameter to evaluate therapy response in oncologic follow-up imaging.^{13,14} Additionally, exact lesion determination and delineation of size are required for stereotactic radiosurgery.^{15,16} In clinical routine, brain lesions have to be segmented manually by the radiosurgeon. This task proves to be time-consuming, in particular if multiple metastases are present. Furthermore, manual segmentation is potentially hampered by interreader variabilities with reduced reproducibility, hence resulting in inaccuracies of lesion delineation.^{17,18} In this

Received March 17, 2020; accepted after revision October 21.

From the Institute for Diagnostic and Interventional Radiology (L.P., R.S., L.C., S.L., F.T., D.Z., M.P., C.K., J.B., K.R.L.) and Center for Neurosurgery (L.G., G.F., S.G.), Faculty of Medicine and University Hospital Cologne, University of Cologne, Cologne, Germany; Philips Innovative Technologies (R.S., F.T., M.P.), Aachen, Germany; Department of Stereotaxy and Functional Neurosurgery (A.-K.M., G.F.), Center for Neurosurgery, University Hospital Cologne, Cologne, Germany; Department of Radiology (K.R.L.), University Hospitals Cleveland Medical Center, Cleveland, Ohio, and Department of Radiology (K.R.L.), Case Western Reserve University, Cleveland, Ohio.

L. Pennig and R. Shahzad contributed equally to this work.

Paper previously presented and/or published as an abstract at: German Neuroradiology Congress, May 29 to June 1, 2019, Frankfurt, Germany; European Congress of Radiology, July 15-19, 2020, Virtual; German Neurosurgery Congress 2020; Virtual and German Radiology Congress 2020; Virtual.

Please address correspondence to Kai Roman Laukamp, MD, Institute for Diagnostic and Interventional Radiology, Faculty of Medicine and University Hospital Cologne, Kerpener Str 62, 50937 Cologne, Germany; e-mail: kai.laukamp@uk-koeln.de

Indicates article with online supplemental data.

<http://dx.doi.org/10.3174/ajnr.A6982>

context, accurate objective and automated segmentations of brain metastases would be highly beneficial.¹⁷⁻¹⁹

Recently, deep learning models (DLMs) have shown great potential in detection, segmentation and classification tasks in medical image analysis while having the potential to improve clinical workflow.²⁰⁻²⁵ The models apply multiple processing layers that result in deep convolutional neural networks (CNNs). Training data are used to create complex feature hierarchies.²⁶⁻²⁸ In general, a DLM includes different layers for convolution, pooling, and classification.²⁸ The required training data are supplied by manual segmentations, which usually serve as the segmentation criterion standard.^{18,28,29}

Previous studies on brain metastases from different tumor entities have demonstrated promising results, reporting a sensitivity for automated deep learning-based detection of lesions of around 80% or higher.^{17,30-32} However, the often reported relatively high number of false-positive findings questions their applicability in clinical routine.^{17,30}

The purpose of this study was to develop and evaluate a DLM for automated detection and segmentation of brain metastases in patients with malignant melanoma using heterogeneous MR imaging data from multiple vendors and study centers.

MATERIALS AND METHODS

The local institutional review board (Ethikkommission, Medizinische Fakultät der Universität zu Köln) approved this retrospective, single-center study (reference No: 19-1208) and waived the requirement for written informed patient consent.

Patient Population

MR imaging of patients treated for malignant melanoma at our tertiary care university hospital between May 2013 and October 2019 was reviewed using our institutional image archiving system. Ninety-two patients could be identified by applying the following inclusion criteria: 1) MR imaging scans at primary diagnosis of brain metastases; 2) distinct therapy following diagnosis of brain metastases, eg, stereotactic radiosurgery, resection, extended biopsy, targeted chemotherapy; and 3) a complete MR image set, being defined as T1-/T2-weighted, T1-weighted gadolinium contrast-enhanced imaging, and T2-weighted FLAIR. Patients with unclear lesions in which follow-up imaging could not confirm metastatic spread to the brain were not included ($n = 11$).

We applied the following exclusion criteria: 1) the presence of a second malignant tumor ($n = 3$); 2) large intracranial extraleSIONAL bleeding (the definition of extraleSIONAL bleeding was based on reviewing prior/follow-up imaging, $n = 3$); 3) acute ischemic stroke ($n = 1$) impeding delineation of brain metastases; 4) severe MR imaging artifacts impairing image quality ($n = 3$); and 5) insufficient contrast media application ($n = 2$).

The 69 enrolled patients were randomly split into a training cohort consisting of 55 patients and a test cohort with 14 patients, ensuring that there was no overlap of data between the 2 cohorts. The training cohort was used for training and performing 5-fold cross-validation of the DLM. On the contrary, the test cohort was used for independent testing of the DLM. MR images were anonymized and exported to IntelliSpace Discovery (ISD, Version 3.0; Philips Healthcare).

Image Acquisition

MR images were acquired on different scanners from our ($n = 48$) and referring institutions ($n = 21$), ranging between 1T and 3T. Detailed MR imaging parameters are given in the Online Supplemental Data. The imaging protocol of our institution included intravenous administration of gadolinium (gadoterate meglumine, Dotarem; Guerbet; 0.5 mmol/mL, 1 mL = 279.3 mg of gadoteric acid = 78.6 mg of gadolinium) with a concentration of 0.1 mmol/kg of body weight. Contrast medium application at referring institutions was not standardized.

Ground Truth

To establish the reference standard and lesion count, 2 radiologists (each with at least 3 years of experience in neuro-oncologic imaging) confirmed all metastases. A board-certified neuroradiologist with 13 years of experience in neuro-oncologic imaging was consulted when uncertainties occurred. They conducted a review of the original radiology report and double-reviewed the included MR imaging scans as well as prior/follow-up imaging.

By assessing nonenhanced T1- and T2-weighted, T1-weighted gadolinium contrast-enhanced imaging, and FLAIR images on ISD, the 2 radiologists performed manual segmentations of lesions on T1-weighted gadolinium contrast-enhanced imaging in a voxelwise manner in consensus, which served as the ground truth (GT). First, initial segmentations of the metastases were performed by 1 radiologist and then presented to/discussed with the second radiologist to define the final segmentations of the lesions in consensus.

Deep Learning Model

Before passing the sequences (T1/T2-weighted, T1-weighted gadolinium contrast-enhanced imaging, and FLAIR) to the DLM, we performed preprocessing of data, which included the following: bias field correction of all 4 sequences, coregistration of T1/T2-weighted and FLAIR to T1-weighted gadolinium contrast-enhanced imaging, skull-stripping, resampling to an isotropic resolution of $1 \times 1 \times 1 \text{ mm}^3$, and z score normalization.²⁴

In this study, a 3D CNN based on DeepMedic (Biomedical Image Analysis Group, Department of Computing, Imperial College London) was used. In recent studies, the DeepMedic architecture has demonstrated encouraging results for detection and segmentation of different brain tumors.^{24,33}

The network consists of a deep 3D CNN architecture with 2 identical pathways. 3D image patches provide input to the 2 pathways. For the first pathway, original isotropic patches are used. For the second pathway, the patches are down-sampled to a third of their original size. This approach helps to capture higher contextual information. The deep CNN model comprises 11 layers with size 3^3 kernels. The model consists of residual connections for layers 4, 6, and 8. Each layer is followed by batch normalization and a parametric rectified linear unit as the activation function. Layers 9 and 10 are fully connected. The last prediction layer has a kernel size of 1^3 and uses sigmoid as the activation function.³⁴

For training of the DLM, multichannel GT 3D image patches with a size of 25^3 were fed to the 3D CNN. These image patches

Detection and segmentation accuracy on the independent test cohort

	Majority Voting Scheme	First Fold	Second Fold	Third Fold	Fourth Fold	Fifth Fold
Detection						
Sensitivity	88%	88%	88%	81%	91%	91%
Precision	74%	49%	35%	40%	41%	51%
F1 score	0.80	0.63	0.50	0.53	0.57	0.65
Missed	4	4	4	6	3	3
FPs/scan	0.71	2.1	3.8	2.9	2.9	2.0
Segmentation						
Dice coefficient	0.75	0.78	0.73	0.73	0.76	0.78

Note:—Missed indicates missed brain metastases in the test cohort; FPs/scan, false-positive lesion findings per patient; Dice coefficient, similarity score reported as median; Majority Voting Scheme, fusion of the 5 deep learning models from the 5-fold cross-validation; First Fold, first deep learning model from the 5-fold cross-validation.

were extracted with a distribution of 50% between background and metastases, ensuring class balance. To increase the number of training samples, image augmentation was used by randomly flipping the image patches along their axes. The Dice similarity coefficient was used as the loss function, and root mean square propagation, as the optimizer. An adaptive learning rate schedule was used, in which the initial learning rate was halved every time the accuracy did not improve for >3 epochs. The training batch size was set to 10, and the number of training epochs was set to 35.

Training was performed on the training set ($n = 55$) using a 5-fold cross-validation approach using an 80%–20% training-validation split without overlapping data, which resulted in 5 trained models.

During inference on the independent test set ($n = 14$), 3D image patches of 45^3 in size are extracted. Larger patch sizes reduced the time spent during inference. The 5 individual models from the 5-fold cross-validation training were applied to the independent test data. The segmentation results from each of the 5 DLMs were fused using a majority voting scheme to reduce false lesion detections.³⁵ By default, automatically detected lesions of $<0.003 \text{ cm}^3$ (2 voxels on average) during inference of both the training and test sets were regarded as image noise and discarded. This threshold was based on the resolution of T1-weighted gadolinium contrast-enhanced sequences (in which a volume of 0.003 cm^3 is approximately 2 voxels) and is determined by referring to the smallest annotated metastases on training (0.0035 cm^3) and test (0.0041 cm^3) sets. Due to limitation of scan resolution, lesions smaller than this volume cannot be accurately detected or segmented by image readers.

Including image preprocessing, the average time needed to run a complete pipeline on a dataset is about 8 minutes: <1 second for bias field correction, 7 minutes for coregistration and skull-stripping, <1 minute for image standardization, and around 10 seconds to run the inference (using a Tesla-P100 GPU card (NVIDIA)).

Statistical Analysis

Statistical analysis was performed using JMP Software (Release 12; SAS Institute). Tumor volumes are displayed as mean [SD], and Dice similarity coefficients are reported as median with a 10–90 percentile range. The Wilcoxon rank sum test was applied for determination of a statistical difference with statistical significance being set to $P < .05$. To determine the detection accuracy of the metastases, we computed sensitivity (recall), precision (positive predictive value), and F1 score. Because no scans

without metastases were included, a true specificity could not be determined; hence, precision was calculated.

To evaluate the segmentation accuracy of the DLM on a voxelwise basis, we compared automatically obtained segmentations with the GT annotations with overlap measures between the segmentations being computed using the Dice similarity coefficient.^{23,24,35} For quantitative volumetric measurements, the Pearson correlation coefficient (r) was calculated.

RESULTS

Patient Characteristics

The 69 enrolled patients (mean age, 61.5 [SD, 13.4] years; 30 women) had a total of 135 brain metastases on MR imaging, of which 45 patients presented a single brain metastasis. Most ($n = 48$) patients received stereotactic radiosurgery using the CyberKnife System (Accuray). The Online Supplemental Data provide detailed patient information, including distribution of brain metastases and treatment received.

Evaluation of the DLM on the Training Cohort

In the training cohort, 103 metastases with a mean volume of 2.6 [SD, 8.1] cm^3 were identified as the GT.

Using 5-fold cross-validation, the DLM achieved a sensitivity of 87% with a median corresponding Dice similarity coefficient of 0.75 (range, 0.19–0.93). The DLM missed 13 metastases, yielding a mean volume of 0.06 [SD, 0.1] cm^3 . On average, the DLM produced 4 false-positive lesions per scan with a mean volume of 0.05 [SD, 0.17] cm^3 .

Evaluation of the DLM on the Independent Test Cohort

In the test cohort, 32 metastases with a mean volume of 1.0 [SD, 2.4] cm^3 were identified as the GT, being smaller than in the training cohort, though without a significant difference ($P > .05$). The 5 DLMs from the 5-fold cross-validation as well as their fusion using the majority voting scheme were tested on the independent test cohort. Detailed results of the DLM on the test set are given in the Table.

After we applied the majority voting scheme, the fused DLM detected 28 of 32 brain metastases correctly and missed 4, corresponding to a sensitivity of 88% and an F1 score of 0.80 (Figs 1 and 2 and Online Supplemental Data depict examples of true-positive findings of the DLM). Missed brain metastases were small and yielded a volume between 0.004 and 0.16 cm^3 (Fig 3 provides the metastases, which were missed by the DLM). Compared with manual segmentations, the fused DLM provided a median Dice

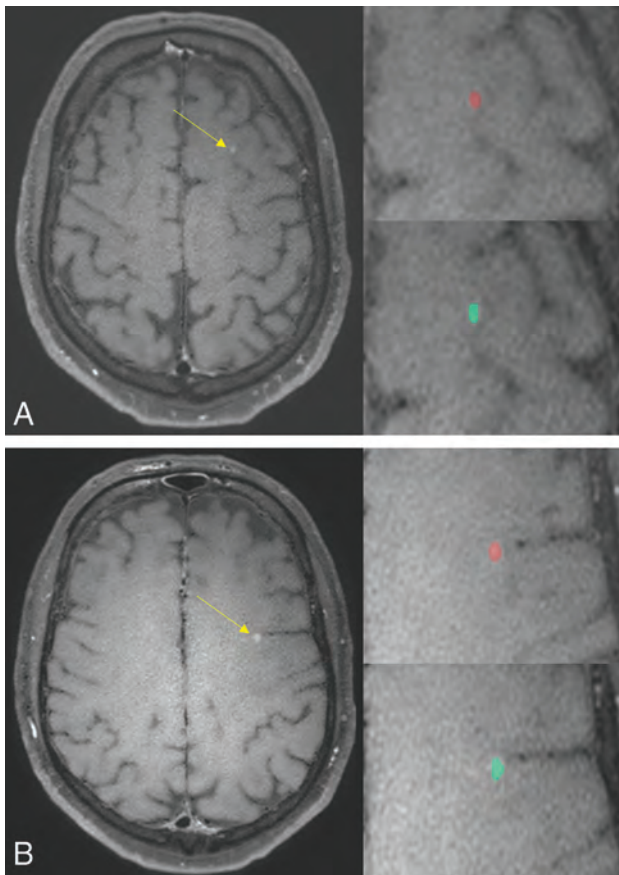


FIG 1. A 55-year-old male patient with malignant melanoma. The DLM (turquoise) detects and segments the metastases of the left frontal lobe (yellow arrows, A and B) comparable to the manual segmentations (red).

similarity coefficient of 0.75 (range, 0.09–0.93) and a volumetric correlation of $r = 0.97$. The Online Supplemental Data display the relationship between obtained Dice similarity coefficients and the volume of the metastases.

Figure 4A depicts a histogram demonstrating the volume of metastases in the training and test groups as well as the size of missed metastases and false-positive lesions. Figure 4B shows a boxplot comparing Dice similarity coefficients, false-positives, and false-negatives for the 5 different DLMs using the 5-fold cross-validation and the combined DLMs, applying the majority voting scheme. Figure 4C provides the volumetric correlation between automated detection of metastases using the fused DLM and the GT.

In addition, the fusion of all 5 DLMs reduced the number of false-positive lesions to 0.71 per scan (compared with 3.8 of the second fold, as seen in the Table) and increased the precision (74%). Examples of false-positive detections by the DLM are provided in Figs 3 and 4D, which show a free-response receiver operating characteristic curve displaying the relationship between the lesion-detection sensitivity and the average number of false-positive lesions per scan.

DISCUSSION

In this study, we developed and trained a dedicated DLM for automated detection and segmentation of brain metastases in

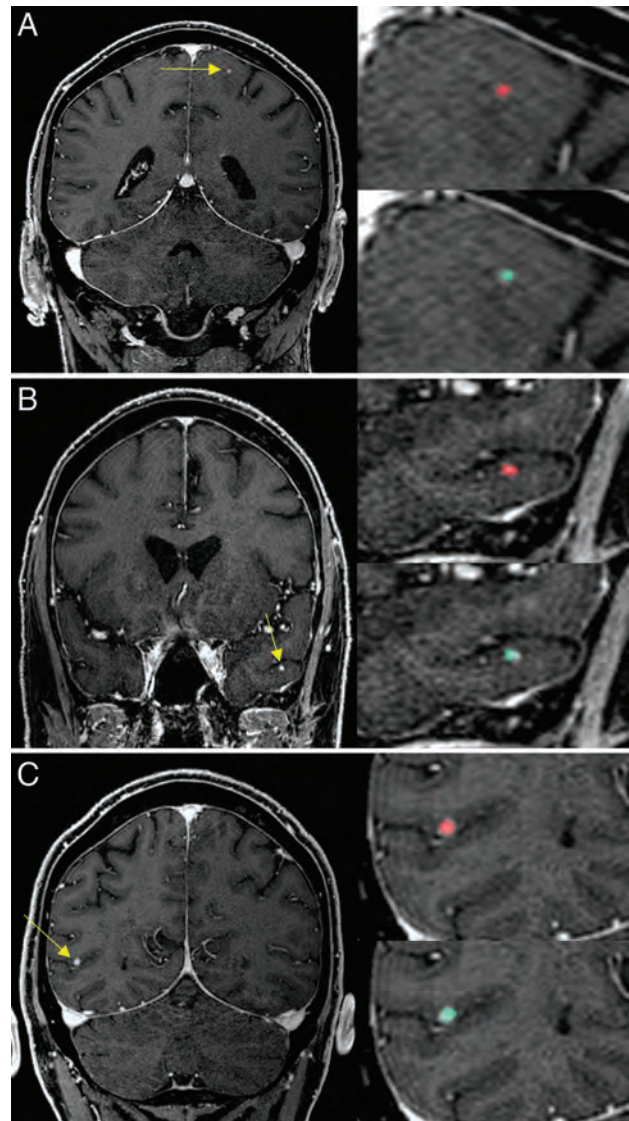


FIG 2. A 67-year-old male patient with malignant melanoma. The DLM (turquoise) detects the metastases (yellow arrows) of the left frontal lobe (A), the left temporal lobe (B), and the right parietal lobe (C) accurately and provides manual segmentations (red) comparable to segmentation performance.

malignant melanoma and evaluated its performance on an independent test set. On heterogeneous scanner data, the proposed DLM provided a detection rate of 88%, while producing an error of <1 false-positive lesion per scan. Furthermore, a high overlap between automated and manual segmentations was observed (Dice similarity coefficient = 0.75).

Recent studies investigating automated detection of brain metastases have not focused on a certain underlying pathology and reported lesion sizes between 1.3 and 1.9 cm^3 (Bousabarah et al³²) and 2.4 cm^3 (Charron et al¹⁷) for various primary tumors, which are comparable with the average tumor sizes in our training (2.6 [SD, 8.1] cm^3) and test cohorts (1.0 [SD, 2.4] cm^3). Despite the small lesion size, the DLM provided a high detection sensitivity (88%), similar to that in the aforementioned studies.^{16,17,30-32} Compared with the GT, the DLM obtained a median Dice similarity coefficient of 0.75, which is in line with recent studies,

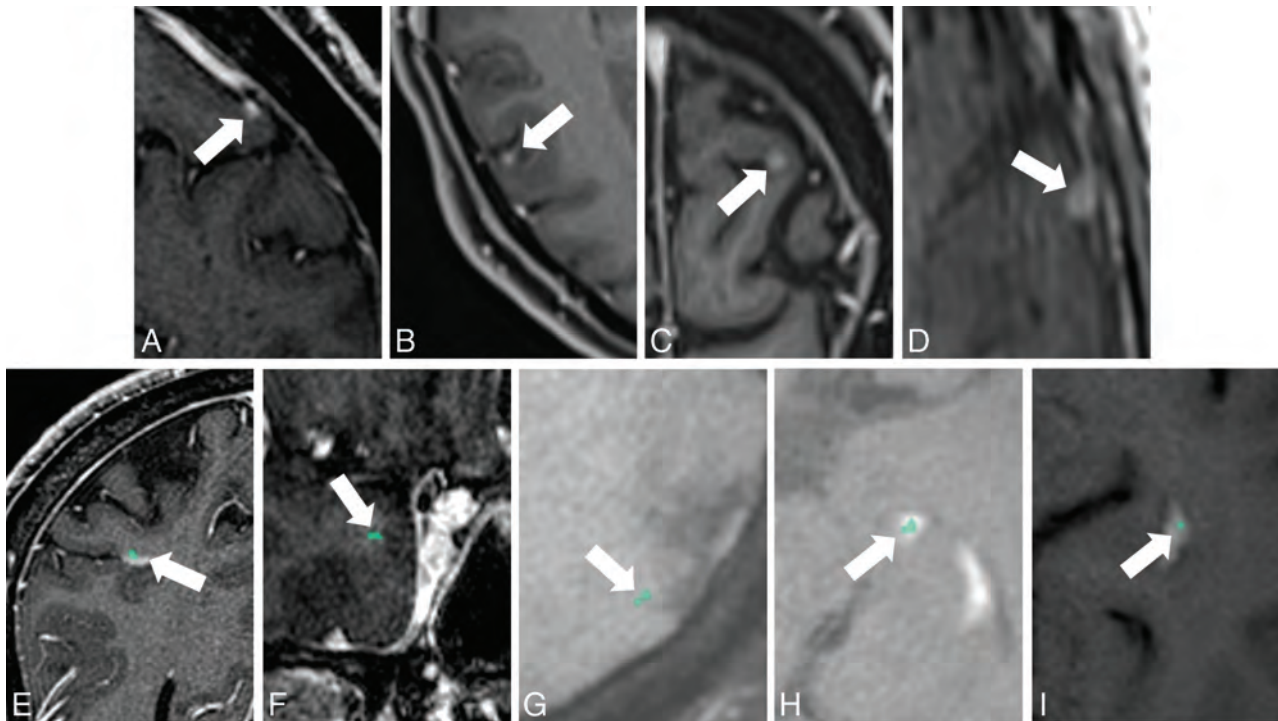


FIG 3. False-negative findings of the DLM (A–D, white arrows) as shown in a 67-year-old male patient (A, same patient as in Fig 2; metastasis volume: 0.004 cm³), a 56-year-old male patient (B and C, metastases volume: 0.008 and 0.01 cm³), and a 62-year-old male patient (E, metastasis volume: 0.016 cm³) with malignant melanoma. As demonstrated, the DLM missed small metastases. Examples of false-positive findings of the DLM (E–I, white arrows) as shown in a 50-year-old female patient (E), a 67-year-old male patient (F, same patient as in Fig 2), a 55-year-old male patient (G and H, same patient as in Fig 1), and a 62-year-old female patient (I) with malignant melanoma. False-positive findings (turquoise) were related to blood vessels (E, developmental venous anomaly), variations in brain tissue contrast (F and G), and the choroid plexus (H and I).

which reported Dice similarity coefficients between 0.67 and 0.79.^{16,30} The high number of false-positive lesions poses a common drawback in automated detection of brain metastases, which have been reported to be around 7–8 per scan.^{17,30} By combining 5 DLMs using a majority voting scheme, false-positive findings of <1 per patient were obtained in the present study, as could also recently be achieved by Bousabarah et al.³²

Given the high risk of metastatic spread, screening examinations are warranted in patients with malignant melanoma and are suggested according to current guidelines.^{5,7,8} For lung cancer, regular screening has also been proposed recently.³⁶ However, when diagnosed at an early stage in an asymptomatic patient, metastases are often small and more difficult to detect, even by experienced radiologists.^{1,2,5,6} Despite the small size of the metastases in the test set, the trained DLM yielded a sensitivity of 88%. Of note, the metastases in the test set were smaller compared with those in the training cohort without reaching a statistical significance. In part, this difference could be explained by the higher number of patients treated by surgery in the training cohort (18.2% versus 14.0%), who usually present with larger metastases.³⁷

Brain metastases screening examinations are increasing in number, making evaluation tiresome while bearing an inherent risk of missed diagnoses, in particular for subtle lesions.^{9,38} In this context, our DLM can provide assistance for detection of brain metastases in malignant melanoma. Compared with a human reader, the DLM is not impaired by “satisfaction of search,” which means that the physician may miss a second

metastasis when a first one has been found.^{9,10,38} Additionally, automation of brain metastasis segmentation by a DLM could serve as an accurate mechanism of lesion preselection, in particular when the number of false-positive lesions is <1 per scan, as obtained by the DLM of the present study.^{16,17,30,31} Automated segmentation may also provide assistance in evaluating treatment response during oncologic follow-up and may support radiologists in coping with an increased number of image readings, while maintaining high diagnostic accuracy.

Compared with manual segmentations, the proposed DLM achieved a high volumetric correlation despite the small size of the metastases. Automated segmentation of brain tumors such as metastases, being possible with the DLM of the current study, has several applications that potentially improve patient care. For instance, volumetric assessment proves to be a promising tool for quantification of tumor burden.^{14,39,40} Furthermore, volumetric assessment has advantages over user-dependent conventional linear measurements because metastatic lesions are not entirely spherical.¹⁸

Stereotactic radiosurgery requires reliable and objective lesion segmentation.^{15,16} Manual segmentation of multiple lesions proves to be time-consuming and is impeded by inter- and intra-reader variabilities. Next to increased efficiency, higher reproducibility of lesion delineation potentially boosts reliability of radiation therapy while improving patient outcome.¹⁷

Regarding automatic detection and segmentation of brain metastases, one must consider the following challenges: 1) multifocal lesion occurrence; 2) very small and subtle lesions; 3) more complex tumor structures when lesions enlarge

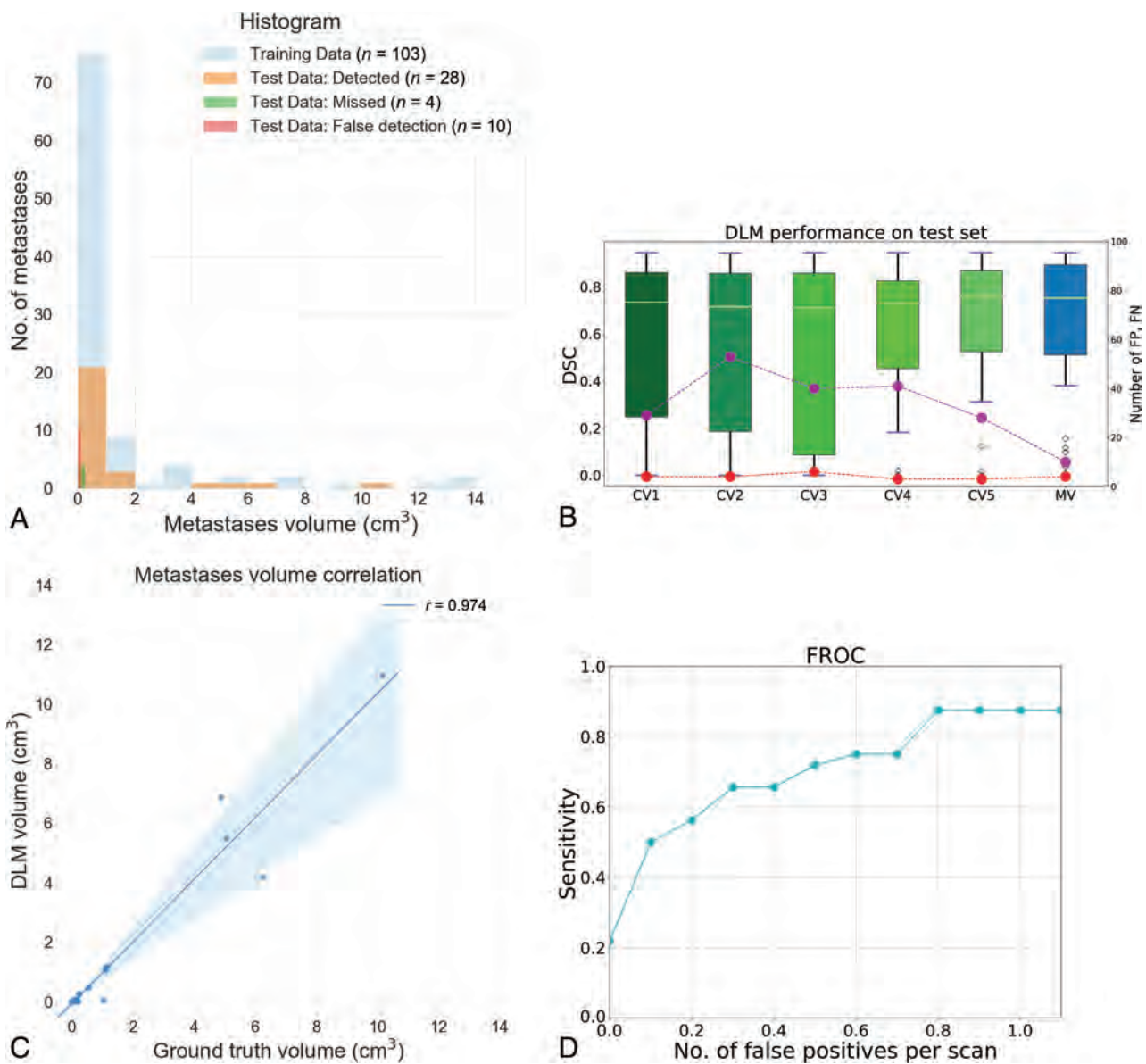


FIG 4. A, Histogram depicting the distribution of metastases volumes in the training and test cohorts. Furthermore, the volumes of missed metastases and false-positive findings in the test group are also depicted, all of which were small (mean missed metastases volume of 0.01 [SD, 0.005] cm³; mean volume of false-positive lesions of 0.02 [SD, 0.02] cm³). To better visualize the small volumes of false-positive and false-negative findings in the independent test set, we limited the x-axis to 15 cm². Hence, 5 metastases of the training data larger than this volume are not shown. B, Performance of the 5 different DLMs obtained using the 5-fold cross-validation training and the combined DLM using the majority voting scheme on the independent test cohort. *Magenta circles* represent the number of false-positives (FP) and *red circles* indicate the number of false-negatives (FN). DSC indicates the Dice similarity coefficient; CV1–5, the cross-validation folds; and MV, majority voting. C, Volume correlation of the metastases between the automatically segmented lesions and the ground truth on the independent test set on a lesion level. D, Free-response receiver operating characteristic (FROC) curve of the DLM on the independent test cohort.

(contrast-enhancing tumor, necrosis, bleeding, and edema); 4) variations in patient anatomy; and 5) heterogeneous imaging data due to varying vendors, MR imaging manufacturers, scanner generations, scan parameters, and unstandardized contrast media application.^{16,17,25,28,30,34,41,42} In the present study, our DLM provides high detection accuracy on heterogeneous scanner data as reflected by a large number of scans from referring institutions and examinations performed over a wide range of field strengths.

The results of this study indicate that training of an already established deep-learning architecture initially used for other

tumor entities, ie, glioma and glioblastoma,^{24,34} can be successfully applied to other brain tumors^{16,43,44} but dedicated retraining is usually warranted.^{16,32,33} Still, previous studies have also suggested that dedicated training might be omitted if tumor appearance is similar, although accuracy will/might be negatively impacted by the missing dedicated training.^{23,44} Therefore, our DLM, though dedicated to patients with melanoma, might also be applied, for example, to metastases of different origins, which may nurture further investigations.

The following limitations need to be discussed. The study has typical drawbacks of a retrospective setting, not allowing

evaluation if detection and segmentation accuracies are sufficient for clinical needs. This drawback may be addressed in future studies with a focus on specified clinical necessities and tasks. Although almost one-third of included scans were acquired at referring institutions, the application of the DLM should be investigated in a true multicenter setting. Our relatively small number of patients, which resulted from focusing exclusively on malignant melanoma, needs to be considered. This is especially important regarding our test cohort, which consisted of 14 patients only. Future studies, preferably including more cases from differing institutions, are warranted to further validate our DLM. Only patients with melanoma were included, which potentially limits the transferability of our DLM to brain metastases of other primary tumors. In this context, future studies are needed. Because no posttreatment MR images were included, the performance of the DLM in this setting is unknown and requires future research.

The applied DLM operates on 4 MR images, ie, FLAIR, T1-/T2-weighted, and T1-weighted gadolinium contrast-enhanced images. Consequently, this feature limits the application of the DLM if one of these sequences is unavailable. Our study included a relevant amount of imaging data from referring institutions where contrast media application was different and not standardized with our application protocol, potentially reflecting more inhomogeneous imaging data. Because we did not include MR images without any findings, our study did not capture the proper target population of interest. This bias might underestimate the false-positive rate in a true population. For our evaluation, we excluded 10% of initially identified patients due to, for example, a second cerebral tumor, strong artifacts, or insufficient contrast media application. Hence, images of these patients might not be suited to the proposed DLM.

CONCLUSIONS

Despite small lesion size and heterogeneous scanner data, our DLM detects brain metastases in malignant melanoma on multiparametric MR imaging with high detection and segmentation accuracy, while yielding a low false-positive rate.

ACKNOWLEDGMENT

Clinician Scientist position supported by the Deans Office, Faculty of Medicine, University of Cologne.

Disclosures: Lenhard Pennig—UNRELATED: Grants/Grants Pending: Philips Healthcare, Comments: He has received research support unrelated to this specific project.* Rahil Shahzad—OTHER RELATIONSHIPS: employee of Philips Healthcare. Simon Lennartz—UNRELATED: Grants/Grants Pending: Philips Healthcare, Comments: He has received research support unrelated to this specific project.* Frank Thiele—UNRELATED: Employment: Philips Healthcare. Jan Borggreffe—UNRELATED: Payment for Lectures Including Service on Speakers Bureaus: He received speaker honoraria from Philips Healthcare in 2018 and 2019, not associated with the current scientific study. Michael Perkuhn—UNRELATED: Employment: employee of Philips Healthcare, Germany, Comments: Besides my affiliation as an MD at the Radiology Department at the University Hospital Cologne, I am also employee of Philips Healthcare, in Germany. *Money paid to the institution.

REFERENCES

- Davies MA, Liu P, McIntyre S, et al. **Prognostic factors for survival in patients with melanoma with brain metastases.** *Cancer* 2011; 117:1687–96 CrossRef Medline
- Jakob JA, Bassett RL, Ng CS, et al. **NRAS mutation status is an independent prognostic factor in metastatic melanoma.** *Cancer* 2012; 118:4014–23 CrossRef Medline
- Goyal S, Silk AW, Tian S, et al. **Clinical management of multiple melanoma brain metastases a systematic review.** *JAMA Oncol* 2015; 1:668–76 CrossRef Medline
- Sperduto PW, Kased N, Roberge D, et al. **Summary report on the graded prognostic assessment: an accurate and facile diagnosis-specific tool to estimate survival for patients with brain metastases.** *J Clin Oncol* 2012;30:419–25 CrossRef Medline
- Michielin O, van Akkooi A, Ascierto P, et al; ESMO Guidelines Committee. **Cutaneous melanoma: ESMO Clinical Practice Guidelines for diagnosis, treatment and follow-up.** *Ann Oncol* 2019;30:1884–1901 CrossRef Medline
- Schlamann M, Loquai C, Goerick S, et al. **Cerebral MRI in neurological asymptomatic patients with malignant melanoma [in German].** *Rofo* 2008;180:143–47 CrossRef Medline
- Garbe C, Amaral T, Peris K, et al. **European consensus-based interdisciplinary guideline for melanoma. Part 1: Diagnostics - Update 2019.** *Eur J Cancer* 2020;126:141–158 CrossRef Medline
- Trotter SC, Sroa N, Winkelmann RR, et al. **A global review of melanoma follow-up guidelines.** *J Clin Aesthet Dermatol* 2013;6(9):18–26 Medline
- Berbaum KS, Franken EA, Dorfman DD, et al. **Satisfaction of search in diagnostic radiology.** *Invest Radiol* 1990;25:133–40 CrossRef Medline
- Brady AP. **Error and discrepancy in radiology: inevitable or avoidable?** *Insights Imaging* 2017;8:171–82 CrossRef Medline
- Conson M, Cella L, Pacelli R, et al. **Automated delineation of brain structures in patients undergoing radiotherapy for primary brain tumors: from atlas to dose-volume histograms.** *Radiother Oncol* 2014;112:326–31 CrossRef Medline
- Xue Y, Chen S, Qin J, et al. **Application of deep learning in automated analysis of molecular images in cancer: a survey.** *Contrast Media Mol Imaging* 2017;2017:9512370 CrossRef Medline
- Fountain DM, Soon WC, Matys T, et al. **Volumetric growth rates of meningioma and its correlation with histological diagnosis and clinical outcome: a systematic review.** *Acta Neurochir (Wien)* 2017; 159:435–45 CrossRef Medline
- Chang V, Narang J, Schultz L, et al. **Computer-aided volumetric analysis as a sensitive tool for the management of incidental meningiomas.** *Acta Neurochir* 2012;154:589–97 CrossRef Medline
- Suh JH. **Stereotactic radiosurgery for the management of brain metastases.** *N Engl J Med* 2010;362:1119–27 CrossRef Medline
- Liu Y, Stojadinovic S, Hryckushko B, et al. **A deep convolutional neural network-based automatic delineation strategy for multiple brain metastases stereotactic radiosurgery.** *PLoS One* 2017;12: e0185844 CrossRef Medline
- Charron O, Lallemand A, Jarnet D, et al. **Automatic detection and segmentation of brain metastases on multimodal MR images with a deep convolutional neural network.** *Comput Biol Med* 2018;95:43–54 CrossRef Medline
- Bauknecht HC, Romano VC, Rogalla P, et al. **Intra- and interobserver variability of linear and volumetric measurements of brain metastases using contrast-enhanced magnetic resonance imaging.** *Invest Radiol* 2010;45:49–56 CrossRef Medline
- Zhou Z, Sanders JW, Johnson JM, et al. **Computer-aided detection of brain metastases in T1-weighted MRI for stereotactic radiosurgery using deep learning single-shot detectors.** *Radiology* 2020;295:407–15 CrossRef Medline
- Larson DB, Chen MC, Lungren MP, et al. **Performance of a deep-learning neural network model in assessing skeletal maturity on pediatric hand radiographs.** *Radiology* 2018;287:313–22 CrossRef Medline
- Lakhani P, Sundaram B. **Deep learning at chest radiography: automated classification of pulmonary tuberculosis by using convolutional neural networks.** *Radiology* 2017;284:574–82 CrossRef Medline

22. Park A, Chute C, Rajpurkar P, et al. **Deep learning-assisted diagnosis of cerebral aneurysms using the HeadXNet model.** *JAMA Netw open* 2019;2:e195600 CrossRef Medline
23. Laukamp KR, Thiele F, Shakirin G, et al. **Fully automated detection and segmentation of meningiomas using deep learning on routine multiparametric MRI.** *Eur Radiol* 2019;29:124–32 CrossRef Medline
24. Perkuhn M, Stavrinou P, Thiele F, et al. **Clinical evaluation of a multiparametric deep learning model for glioblastoma segmentation using heterogeneous magnetic resonance imaging data from clinical routine.** *Invest Radiol* 2018;53:647–54 CrossRef Medline
25. Kickingereder P, Isensee F, Tursunova I, et al. **Automated quantitative tumour response assessment of MRI in neuro-oncology with artificial neural networks: a multicentre, retrospective study.** *Lancet Oncol* 2019;20:728–40 CrossRef Medline
26. Kooi T, Litjens G, van Ginneken B, et al. **Large-scale deep learning for computer aided detection of mammographic lesions.** *Med Image Anal* 2017;35:303–12 CrossRef Medline
27. LeCun Y, Bengio Y, Hinton G. **Deep learning.** *Nature* 2015;521:436–44 CrossRef Medline
28. Akkus Z, Galimzianova A, Hoogi A, et al. **Deep learning for brain MRI segmentation: state of the art and future directions.** *J Digit Imaging* 2017;30:449–59 CrossRef Medline
29. Mazzara GP, Velthuisen RP, Pearlman JL, et al. **Brain tumor target volume determination for radiation treatment planning through automated MRI segmentation.** *Int J Radiat Oncol Biol Phys* 2004;59:300–12 CrossRef Medline
30. Grovik E, Yi D, Iv M, et al. **Deep learning enables automatic detection and segmentation of brain metastases on multisequence MRI.** *J Magn Reson Imaging* 2020;51:175–82 CrossRef Medline
31. Noguchi T, Uchiyama F, Kawata Y, et al. **A fundamental study assessing the diagnostic performance of deep learning for a brain metastasis detection task.** *Magn Reson Med Sci* 2020;19:184–94 CrossRef Medline
32. Bousabarah K, Ruge M, Brand JS, et al. **Deep convolutional neural networks for automated segmentation of brain metastases trained on clinical data.** *Radiat Oncol* 2020;15:87 CrossRef Medline
33. Laukamp KR, Pennig L, Thiele F, et al. **Automated meningioma segmentation in multiparametric MRI: comparable effectiveness of a deep learning model and manual segmentation.** *Clin Neuroradiol* 2020 Feb 14. [Epub ahead of print] CrossRef Medline
34. Kamnitsas K, Ledig C, Newcombe VFJ, et al. **Efficient multi-scale 3D CNN with fully connected CRF for accurate brain lesion segmentation.** *Med Image Anal* 2017;36:61–78 CrossRef Medline
35. Crum WR, Camara O, Hill DL. **Generalized overlap measures for evaluation and validation in medical image analysis.** *IEEE Trans Med Imaging* 2006;25:1451–61 CrossRef Medline
36. Schoenmaekers J, Hofman P, Bootsma G, et al. **Screening for brain metastases in patients with stage III non-small-cell lung cancer, magnetic resonance imaging or computed tomography? A prospective study.** *Eur J Cancer* 2019;115:88–96 CrossRef Medline
37. Narita Y, Shibui S. **Strategy of surgery and radiation therapy for brain metastases.** *Int J Clin Oncol* 2009;14:275–80 CrossRef Medline
38. Bruno MA, Walker EA, Abujudeh HH. **Understanding and confronting our mistakes: the epidemiology of error in radiology and strategies for error reduction.** *Radiographics* 2015;35:1668–76 CrossRef Medline
39. Henson JW, Ulmer S, Harris GJ. **Brain tumor imaging in clinical trials.** *AJNR Am J Neuroradiol* 2008;29:419–24 CrossRef Medline
40. Lin NU, Lee EQ, Aoyama H, et al; Response Assessment in Neuro-Oncology (RANO) group. **Response assessment criteria for brain metastases: proposal from the RANO group.** *Lancet Oncol* 2015;16:e270–78 CrossRef Medline
41. Laukamp KR, Lindemann F, Weckesser M, et al. **Multimodal imaging of patients with gliomas confirms ¹¹C-MET PET as a complementary marker to MRI for noninvasive tumor grading and intraindividual follow-up after therapy.** *Mol Imaging* 2017;16 CrossRef Medline
42. Menze BH, Jakab A, Bauer S, et al. **The multimodal Brain Tumor Image Segmentation Benchmark (BRATS).** *IEEE Trans Med Imaging* 2015;34:1993–2024 CrossRef Medline
43. Laukamp KR, Pennig L, Thiele F, et al. **Automated meningioma segmentation in multiparametric MRI.** *Clin Neuroradiol* 2020 Feb 4. [Epub ahead of print] CrossRef Medline
44. Pennig L, Hoyer UC, Goertz L, et al. **Primary central nervous system lymphoma: clinical evaluation of automated segmentation on multiparametric MRI using deep learning.** *J Magn Reson Imaging* 2021;53:259–68 CrossRef Medline

Vessel Type Determined by Vessel Architectural Imaging Improves Differentiation between Early Tumor Progression and Pseudoprogression in Glioblastoma

M. Kim, J.E. Park, K. Emblem, A Bjørnerud, and H.S. Kim



ABSTRACT

BACKGROUND AND PURPOSE: Currently available perfusion parameters are limited in differentiating early tumor progression and pseudoprogression with no insight about vessel size and type. We aimed to investigate differences in vessel size and type between early tumor progression and pseudoprogression in posttreatment glioblastoma and to demonstrate diagnostic performance using vessel architectural imaging.

MATERIALS AND METHODS: Fifty-eight patients with enlarging contrast-enhancing masses in posttreatment glioblastomas underwent simultaneous gradient recalled-echo and spin-echo dynamic susceptibility contrast imaging. Relative CBV and vessel architectural imaging parameters, including the relative vessel size index, peak shift between gradient recalled echo and spin-echo bolus signal peaks, and arterial dominance scores using spatial dominance of arterial/venous vessel type, were calculated and compared between the 2 conditions. The area under the curve and cross-validation were performed to compare the diagnostic performance of the relative CBV, vessel architectural imaging parameters, and their combinations.

RESULTS: There were 41 patients with early tumor progression and 17 patients with pseudoprogression. Relative to pseudoprogression, early tumor progression showed a lower peak shift (-0.02 versus 0.33 , $P = .02$) and a lower arterial dominance score (1.46 versus 2.11 , $P = .001$), indicating venous dominance. Patients with early tumor progression had higher relative CBV (1.88 versus 1.38 , $P = .02$) and a tendency toward a larger relative vessel size index (99.67 versus 83.17 , $P = .15$) than those with pseudoprogression. Combining arterial dominance scores and relative CBV showed significantly higher diagnostic performance (area under the curve = 0.82 ; 95% CI, 0.70 – 0.94 ; $P = .02$) than relative CBV alone (area under the curve = 0.64 ; 95% CI, 0.49 – 0.79) in distinguishing early tumor progression from pseudoprogression.

CONCLUSIONS: Vessel architectural imaging significantly improved the diagnostic performance of relative CBV by demonstrating venous dominance and a tendency toward larger vessel size in early tumor progression.

ABBREVIATIONS: AUC = area under the curve; ETP = early tumor progression; CCRT = concurrent chemoradiotherapy; GRE = gradient recalled-echo; PP = pseudoprogression; rCBV = relative CBV; rVSI = relative vessel size index; SE = spin-echo; VAI = vessel architectural imaging

Pseudoprogression (PP) remains a diagnostic challenge in neuro-oncology, occurring in about 20% of patients with high-grade gliomas within 12 weeks of the completion of concurrent chemoradiotherapy (CCRT).¹ An accurate and timely diagnosis of PP is critical to avoid erroneous termination of successful treatment, which could negatively influence survival. However, a confirmatory scan may be required before PP can be

confidently distinguished from early tumor progression (ETP), which might delay a prompt therapeutic intervention. Both PP and ETP manifest as new or enlarging contrast-enhancing lesions on follow-up imaging after the completion of CCRT. Abnormal enhancement in PP likely results from increased permeability caused by direct damage to the blood-brain barrier and treatment-related cellular hypoxia, which results in increased expression of hypoxia-regulated molecules in surrounding cells.^{2,3} This

Received June 22, 2020; accepted after revision November 1.

From the Department of Radiology and Research Institute of Radiology (M.K., J.E.P., H.S.K.), University of Ulsan College of Medicine, Asan Medical Center, Seoul, Korea; Department of Diagnostic Physics, (K.E.) and Unit for Computational Radiology and Artificial Intelligence (A.B.), Division of Radiology and Nuclear Medicine, Oslo University Hospital, Oslo, Norway; and Department of Physics (A.B.), University of Oslo, Oslo, Norway.

This research was supported by a National Research Foundation of Korea grant funded by the Korean government (Ministry of Science, ICT and Future Planning) (grant Nos: NRF-2020RIA2B5B01001707 and NRF-2020RIA2C4001748).

Please address correspondence to Ji Eun Park, MD, PhD, Department of Radiology and Research Institute of Radiology, University of Ulsan College of Medicine, Asan Medical Center, 88 Olympic-ro 43-gil, Songpa-Gu, Seoul 05505, South Korea; e-mail: jjeunp@gmail.com

Indicates open access to non-subscribers at www.ajnr.org

Indicates article with online supplemental data.

<http://dx.doi.org/10.3174/ajnr.A6984>

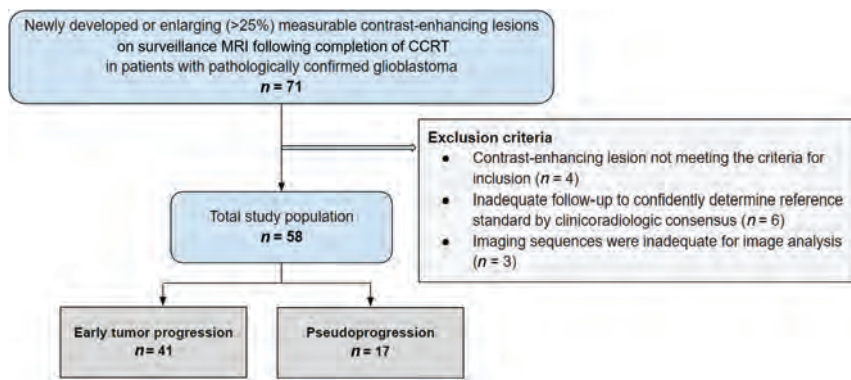


FIG 1. Flow diagram showing the patient-selection protocol and the inclusion and exclusion criteria.

appears indistinguishable from increased enhancement associated with early tumor progression, which represents tumoral neoangiogenesis. Such differences in tumoral vasculature and microenvironment cannot be shown by conventional MR imaging.

So far, perfusion parameters have shown promise in differentiating PP from ETP. CBV from DSC imaging has been found to be particularly useful for diagnosing PP.⁴⁻⁷ Although high CBV on DSC imaging may result from overall increased vascular density, it does not specify whether high CBV comes from vessel recruitment or dilation of vessels.⁸ In addition, CBV is unable to differentiate the dominant vessel type within the ROI. Vessel architectural imaging (VAI) is a recent MR imaging technique with the potential of providing further insight into vessel size and type. Emblem et al⁹ demonstrated the use of VAI to characterize the vessel architecture of recurrent glioblastoma and its changes in response to antiangiogenic agents to successfully identify responders to antiangiogenic treatment. It exploits the differences in observed proton relaxation from simultaneously acquired contrast agent-enhanced gradient recalled-echo (GRE) and spin-echo (SE) MR imaging for vessel-size estimation.¹⁰⁻¹² The temporal shift between the 2 relaxation rate curves from GRE and SE may be visualized in a hysteresis plot, and its slope and direction provide estimates of vessel size and type, respectively. It has been shown that vessel size measures on MR imaging accurately reflected histologic measures of vessel caliber while CBV correlated with vessel density in high-grade gliomas.⁸ Because VAI can estimate vessel size and type, it may be able to provide further insight into the mechanism of PP and to differentiate tumoral neoangiogenesis seen in ETP and treatment-induced change seen in PP.

We hypothesized that VAI could improve the diagnostic performance for identifying PP over DSC perfusion parameters by reflecting vessel size and type in the early posttreatment stage of glioblastoma. Thus, the purpose of this study was to investigate differences in vessel type and size between ETP and PP in post-treatment glioblastomas and to demonstrate the diagnostic performance in the enlarging contrast-enhancing mass using VAI.

MATERIALS AND METHODS

Study Patients and Inclusion Criteria

Asan Medical Center institutional review board approved this retrospective study, and the requirement for informed consent

was waived. We searched the electronic data base of the Department of Radiology at our tertiary center and retrospectively reviewed the records of patients between August 2018 and July 2019. Figure 1 shows the patient inclusion process. We identified 71 consecutive patients who met the following inclusion criteria: 1) histopathologic diagnosis of a newly diagnosed glioblastoma according to the 2016 World Health Organization criteria;¹³ 2) CCRT with temozolomide from Stupp et al¹⁴ and 6 cycles of adjuvant trimetazidine performed after surgical resection or biopsy; 3) newly developed or enlarging

(>25%) and measurable contrast-enhancing lesions on surveillance MR imaging following completion of CCRT;¹⁵ and 4) DSC perfusion and VAI sequences available at the time of newly developed or enlarging and measurable contrast-enhancing lesions, and 5) pathologic diagnosis or clinikoradiologic consensus of ETP or PP. Measurable contrast-enhancing lesions were defined as bidimensionally enhancing lesions with 2 perpendicular diameters of at least 10 mm being visible on ≥ 2 axial slices on conventional MR imaging.

A final diagnosis of PP and ETP was confirmed pathologically in second-look operations when clinically indicated. When second-look operations could not be performed, clinikoradiologic diagnoses were made by consensus between a neuro-oncologist (J.H.K. with 26 years of experience in neuro-oncology practice) and a neuroradiologist (H.S.K. with 18 years of experience in neuro-oncology imaging) according to the Response Assessment in Neuro-Oncology criteria.¹⁵ A final diagnosis of PP was made when there was an increase in contrast-enhancing lesions that subsequently regressed or became stable without any changes in the treatment for at least 6 months after an operation and completion of CCRT. Alternatively, a final diagnosis of ETP was made if enhancing lesions gradually increased on >2 subsequent follow-up MR imaging studies performed at 2- to 3-month intervals and required a prompt change in treatment. Patients were excluded if contrast-enhancing lesions did not meet the criteria for ETP or PP ($n = 4$), there was inadequate follow-up to confidently determine ETP or PP on clinikoradiologic consensus ($n = 6$), and VAI sequences were inadequate for image analysis ($n = 3$). Finally, 58 consecutive patients were enrolled in the study.

MR Imaging Protocol and Image Processing

The brain tumor imaging protocol after completion of CCRT at our institution included T2-weighted imaging, FLAIR imaging, T1-weighted imaging, diffusion-weighted imaging, simultaneous GRE-SE DSC perfusion, contrast-enhanced T1-weighted imaging, and conventional DSC perfusion MR imaging. Simultaneous GRE-SE DSC MR imaging was acquired using axial gradient-echo, spin-echo echo-planar images with TR = 1.33 seconds, TE = 34 and 103 ms (respectively), section thickness = 5 mm, intersection gap = 2.5 mm, in-plane resolution = 1.70×1.70 mm, matrix size = 128×128 , ten slices, and 120 volumes with a

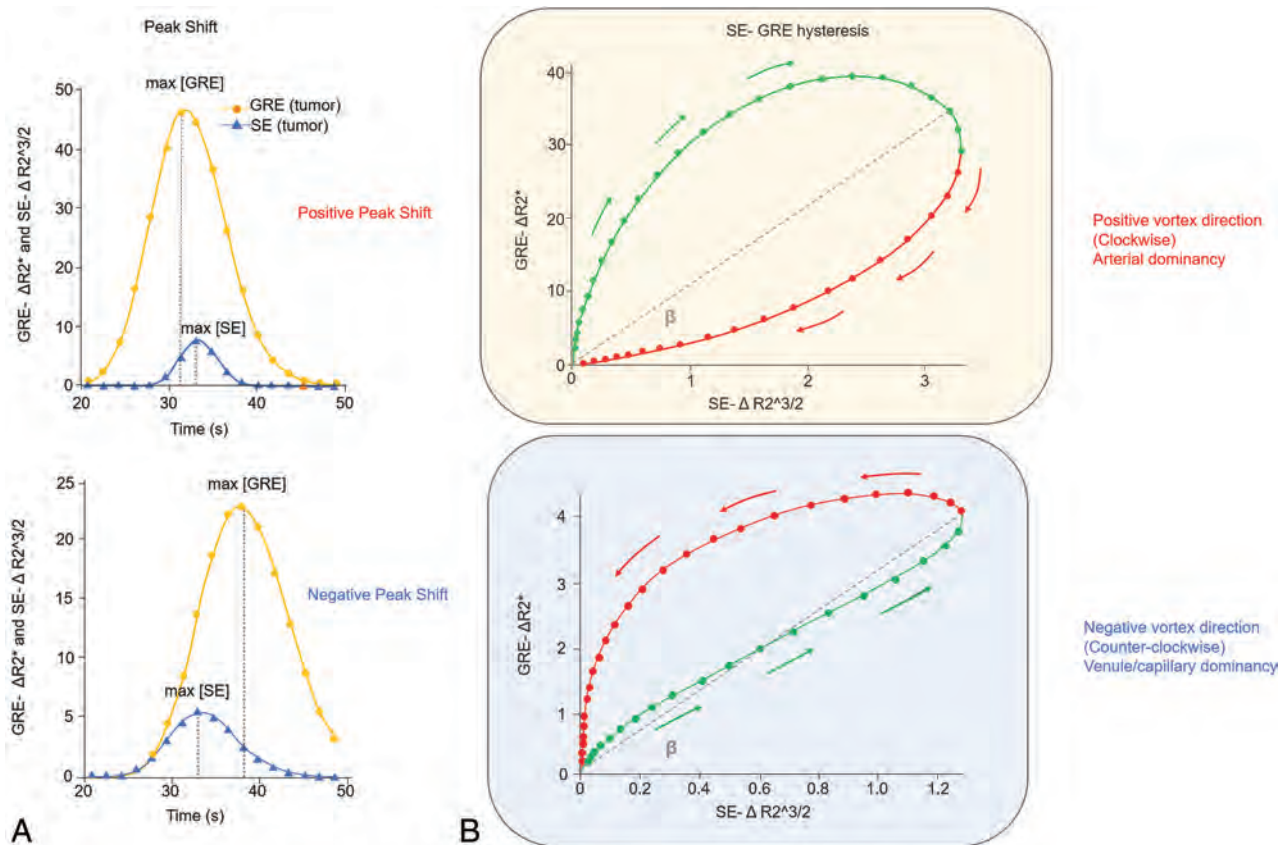


FIG 2. Peak shift and hysteresis plot. A, Peak shift: the time curves of GRE-based $\Delta R2^*$ and SE-based $\Delta R2^{3/2}$ were fitted to a γ -variate function. A positive peak shift indicates a GRE peak preceding the SE peak, while a negative peak shift indicates the SE peak preceding the GRE peak. B, Hysteresis plot: the fitted curves are plotted with $\Delta R2^{3/2}$ (SE-based) along the x-axis and $\Delta R2^*$ (GRE-based) along the y-axis. The clockwise rotation indicates that GRE-based changes precede SE-based changes, corresponding to the positive peak shift with arterial dominance. The counter-clockwise rotation indicates that SE-based change precedes GRE-based changes, corresponding to the negative peak shift with venous dominance. Max indicates maximum.

total acquisition time of 6 minutes 30 seconds. For simultaneous GRE-SE DSC perfusion, a dynamic bolus was administered as a standard dose of 0.1 mmol/kg of gadoterate meglumine (Dotarem; Guerbet) delivered at a rate of 4 mL/s by a MR imaging-compatible power injector (Spectris MR injector; Medrad). The bolus of contrast material was followed by a 20-mL bolus of saline, injected at the same rate. For conventional DSC perfusion, a second, standard dose of 0.1 mmol/kg of gadoterate meglumine was administered. Conventional DSC perfusion MR imaging was acquired using TR = 1.72 seconds, TE = 40 ms, flip angle = 35°, FOV = 240 mm, section thickness = 5 mm, intersection gap = 2 mm, matrix size = 128 × 128, and number of slices = 20 with a total acquisition time of 1 minute 50 seconds. The dynamic acquisition was performed with a temporal resolution of 1.5 seconds, and 60 dynamics were acquired.

Definition of CBV and VAI Parameters

The simultaneous GRE-SE DSC perfusion data obtained during the first injection were used for VAI analysis, while the conventional DSC perfusion data obtained during the second injection were used for whole-brain relative CBV (rCBV). The whole-brain rCBV, normalized to contralateral normal-appearing white matter, was calculated using numeric integration of the

time concentration curve after correcting for contrast agent leakage. Leakage correction was performed using the method of Weisskoff et al¹⁶ with further adaptations from Boxerman et al¹⁷ for both VAI perfusion analysis and conventional DSC perfusion analysis with leakage being estimated from the deviation in each voxel according to a nonleakage reference tissue response curve.

The VAI perfusion-related maps were generated according to previously published definitions and notations.^{9,18,19} In short, the pixel-wise GRE and SE dynamic signals were converted to changes in $R2^*$ and $R2$, respectively, for the GRE and SE signals. The resulting $\Delta R2$ values were then raised to the power of 3/2, and a Gaussian function was fitted to the resulting time curves. The fitted curves were then plotted with $\Delta R2^{3/2}$ along the x-axis and $\Delta R2^*$ along the y-axis, forming hysteresis loops. The hysteresis loops were characterized by the loop direction, long axis, and slope of long axis that are shown to be affected by changes in microvascular function and structure.²⁰ The voxelwise loop direction was visualized by the arrows representing the temporal vortex propagation (Fig 2). We estimated the following VAI metrics:

1) Relative vessel size index (rVSI):⁹ defined by $rVSI = \sqrt{rCBV \times ADC} \times \beta$, where β is the slope of the long axis of the resulting hysteresis curve, as shown in Fig 2, ADC is the apparent diffusion coefficient, and rCBV is relative cerebral blood

Table 1: Clinical characteristics of the patients^a

	ETP (n = 41)	PP (n = 17)	P
Age (yr)	57.2 [SD, 12.5]	55.1 [SD, 16.0]	.64
No. of female patients	17 (41.5%)	11 (64.7%)	.11
KPS \geq 70	35 (85.4%)	14 (82.4%)	.77
IDH wild-type	38 (92.7%)	15 (88.2%)	.36
MGMT promoter status (methylated/unmethylated/NA)	15/22/4	7/6/4	.28
Surgical extent ^b			.97
Biopsy	4 (9.8%)	2 (11.8%)	
Partial resection	13 (31.7%)	5 (29.4%)	
Gross total resection	24 (58.5%)	10 (58.8%)	
Mean time interval between completion of CCRT and imaging (days)	204.4 [SD, 523.0]	112.4 [SD, 123.9]	.48

Note:—KPS indicates Karnofsky Performance Status; IDH, *isocitrate dehydrogenase*; NA, not available.

^aData are expressed as the mean [SD]. Numbers in parentheses are percentages.

^bSurgical extent refers to the extent of surgical resection at the initial cytoreduction surgery.

volume obtained from the GRE signal normalized to contralateral normal-appearing white matter.

2) Peak shift: the shift in the peak (γ -fitted) GRE versus SE signals. Peak shift showed positive value when the GRE peak signal preceded the SE peak signal (Fig 2). Here, we applied a 2-stage fitting procedure for optimal stability. First, we approximated the γ variate model parameters from linear regression after pixel-wise transforming of the nonlinear γ variate expression to a linear form, as described by Madsen.²¹ The estimated parameters from the linear fit were then used as initial values in a nonlinear least-squares model using a standard implementation of the iterative Levenberg-Marquardt algorithm.²² In addition, Gaussian smoothing was applied to the raw data before analysis to reduce noise.

3) Arterial dominance score: dominant vessel type (artery versus venule/capillary) was assigned for each voxel depending on the direction of the vortex. Here, arterial dominance was assigned to the voxels with a positive (clockwise) vortex direction, while venule/capillary dominance was assigned to the voxels with a negative (counterclockwise) vortex direction. Because the average value of vortex direction for a given VOI representing the contrast-enhancing mass did not account for spatial dominance of arterial-versus-venous vessel type, 2 expert radiologists (J.E.P. with 7 years of experience in neuro-oncologic imaging, and H.S.K.) determined the dominant vessel type by observation of the spatial dominance of negative (venule/capillary dominance) or positive vortex directions (arterial dominance) based on the colorized VAI vessel-type map. The arterial dominance score was assigned on the following scale: 1, capillary/venule-dominant; 2, mixed; and 3, arterial-dominant. The readers were blinded to the clinical information and reference standard when assigning the score.

Lesion segmentation of the contrast-enhancing mass was performed using a 3D region-growing based on the multiplanar reconstruction view of 3D contrast-enhanced T1-weighted images by a neuroradiologist (M.K., with 2 years of experience in neuro-oncologic imaging) using segmentation threshold and region-growing segmentation algorithms provided by Medical Imaging Interaction Toolkit (MITK) software (www.mitk.org). All segmented images were re-evaluated and validated by an experienced neuroradiologist (H.S.K.). Finally, the lesion mask

and 3D contrast-enhanced T1-weighted images were coregistered to the rCBV and VAI maps. All image analyses were performed using the commercial software package (nordicICE, Version 4.0.6; NordicNeuroLab).

Statistical Analysis

The Student *t* test and χ^2 test were used to assess differences between PP and ETP groups regarding the demographic data. The Student *t* test was used to assess differences in the rCBV and VAI parameters between the PP and ETP groups. A receiver operating characteristic curve analysis was per-

formed to determine the diagnostic performance of each perfusion parameter for differentiating ETP and PP and was further validated using leave-one-out cross-validation with 100-fold bootstrapping. The diagnostic performance of each individual VAI parameter combined with the rCBV was also evaluated.²³ Subgroup analysis with patients diagnosed as ETP and PP within 9 months of completing CCRT was performed. *P* values of areas under the curve (AUCs) from each parameter were compared using the Wald test. For the comparison of the AUCs and cross-validation with bootstrap resampling, the pROC and cvTools packages in R, Version 3.4.3 (R Project for Statistical Computing, <http://www.r-project.org>) were used. A *P* value < .05 was considered statistically significant.

RESULTS

Patient Demographics

The clinical characteristics of the patients are summarized in Table 1. Of the 58 study patients, 41 (70.7%) were classified as ETP, and 17 (29.3%), as PP. Among 41 patients with ETP, 7 patients (17%) were pathologically confirmed and 34 cases (83%) were diagnosed as having ETP by clinic-radiologic consensus. There were no significant differences between the patients with PP and ETP in terms of age, sex, baseline Karnofsky Performance Status score, *isocitrate dehydrogenase* (IDH) mutation status, MGMT methylation status, extent of surgery, and mean time interval between the operation and imaging study. Subsequent to study imaging, patients were treated by reoperations or second-line agents including antiangiogenic treatment. There were no patients on experimental therapies such as vaccines or checkpoint inhibitors.

Comparison of rCBV and VAI Parameters in ETP and PP

DSC and VAI parameters are summarized in Table 2. Patients with PP showed significantly lower rCBV (mean PP = 1.38 [SD, 0.53] versus mean ETP = 1.88 [SD, 0.78], *P* = .02) and a tendency toward a smaller rVSI (PP = 83.17 [SD, 40.60] versus ETP = 99.67 [SD, 38.78], *P* = .15) compared with patients with ETP. Patients with PP showed a significantly higher positive peak shift compared with those with ETP (PP = 0.33 [SD, 0.77] versus ETP = -0.02 [SD, 0.36], *P* = .02). The arterial dominance score was significantly higher in the PP group compared with the ETP

Table 2: Mean perfusion and VAI parameters in ETP and PP

Imaging Parameters	ETP (n = 41)	PP (n = 17)	P Value ^a
rCBV	1.88 [SD, 0.78]	1.38 [SD, 0.53]	.02
rVSI	99.67 [SD, 38.78]	83.17 [SD, 40.60]	.15
Peak shift	-0.02 [SD, 0.36]	0.33 [SD, 0.77]	.02
Arterial dominance score	1.46 [SD, 0.7]	2.11 [SD, 0.6]	.001

^a P values from an independent-samples t test.

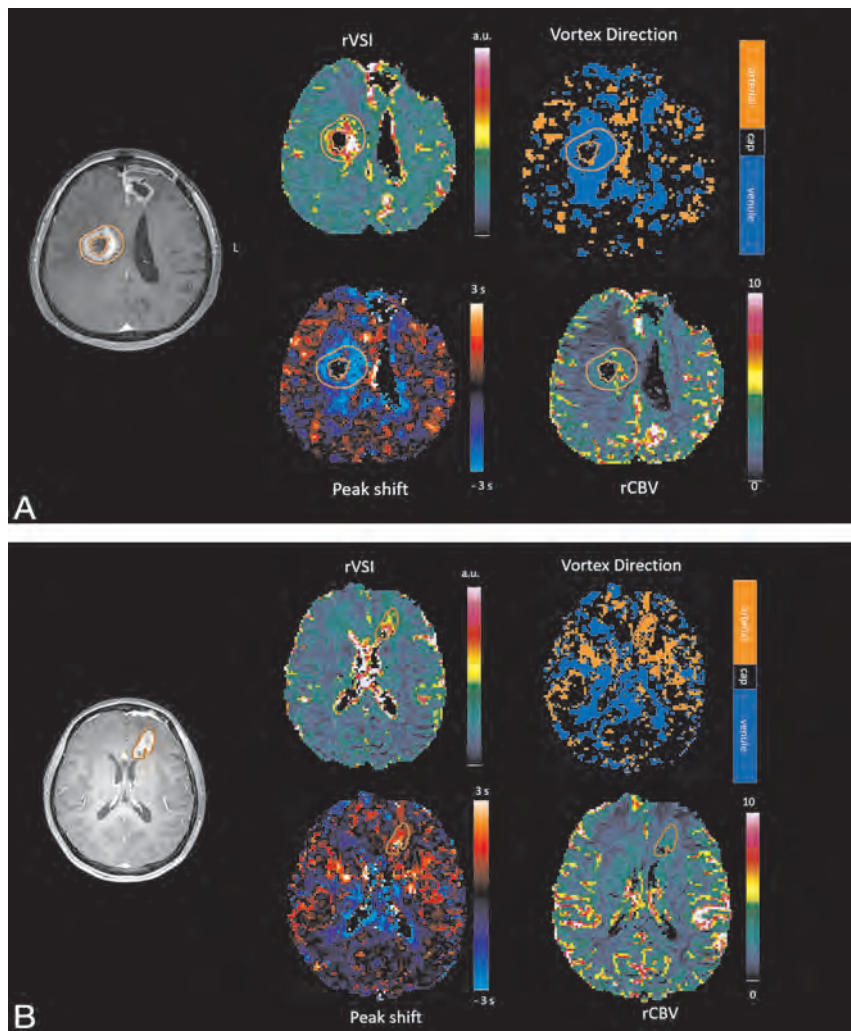


FIG 3. A, Early tumor progression. A 53-year-old woman who completed concurrent chemoradiotherapy 8 weeks ago developed a necrotic enhancing mass in the right frontal lobe surrounding the surgical cavity. On the rCBV map and rVSI map, rCBV is increased with a high rVSI in the corresponding area. A negative peak shift on the peak shift map with venous dominance on the vortex direction map is noted, and an arterial dominance score of 1 was assigned. B, Pseudoprogession. A 67-year-old woman who completed CCRT 10 weeks ago developed a necrotic enhancing mass in the left frontal lobe. On the rCBV and rVSI maps, rCBV is mildly increased with a lower rVSI than in the patient with ETP. A positive peak shift on the peak shift map and arterial dominance on the vortex direction map are shown, and an arterial dominance score of 3 was assigned.

group (PP = 2.11 [SD, 0.6] versus ETP = 1.46 [SD, 0.7], $P = .001$). Figure 3 shows representative cases of PP and ETP, and corresponding signal intensity curves with hysteresis plots are provided in the Online Supplemental Data.

Diagnostic Performance of Individual and Combined Parameters

Table 3 summarizes the diagnostic performance of VAI parameters when used individually and combined with rCBV. The diagnostic performance of rCBV was 0.64 (95% CI, 0.49–0.79) with a sensitivity of 88.2% and specificity of 48.8%. Among VAI parameters, the arterial dominance score showed the highest performance with an AUC of 0.76 (95% CI, 0.64–0.88; Wald test, $P = .005$), followed by peak shift (AUC = 0.60; 95% CI, 0.43–0.76; Wald test, $P = .20$) and rVSI (AUC = 0.60; 95% CI, 0.43–0.77; Wald test, $P = .58$).

The highest diagnostic performance was achieved when the rCBV was combined with the arterial dominance score with an AUC of 0.82 (95% CI, 0.70–0.94) with a sensitivity of 82.3%, specificity of 78.0%, and accuracy of 79.3%, which was significantly higher than rCBV alone ($P = .02$). The diagnostic performance also improved when the rCBV was combined with the rVSI (AUC = 0.67; 95% CI, 0.53–0.82) or peak shift (AUC = 0.70; 95% CI, 0.56–0.86), but these did not reach statistical significance.

Subgroup Analysis with Patients Diagnosed as ETP or PP within 9 Months of Completing CCRT

There were 28 patients with ETP (68%, 28/41) and 14 patients with PP (82%) diagnosed within 9 months of completing CCRT. DSC and VAI parameters in patients diagnosed with ETP or PP within 9 months of completing CCRT are summarized in the Online Supplemental Data. Patients with PP showed significantly lower rCBV (mean PP = 1.30 [SD, 0.54] versus ETP = 1.99 [SD, 0.82], $P = .003$) and a higher arterial dominance score (PP = 2.07 [SD, 0.46] versus ETP = 1.43 [SD, 0.68], $P = .001$). Patients with PP showed a tendency toward a higher peak shift and a smaller rVSI compared with patients with ETP.

The diagnostic performance of VAI parameters when used individually and combined with rCBV is shown in the Online Supplemental Data. Among VAI parameters, the arterial dominance score showed the highest performance with an AUC of

Table 3: Diagnostic performance of individual and combined imaging parameters from perfusion and VAI in differentiating PP from ETP

Individual Parameters	AUC	Criterion	95% CI	Sensitivity	Specificity	Accuracy
rCBV	0.64	≤1.74	0.49–0.79	88.2	48.8	60.3
rVSI	0.60	≤70.8	0.43–0.77	47.5	75.6	67.2
Peak shift	0.60	>0.345	0.43–0.76	29.4	92.6	74.1
Arterial dominance score	0.76	>1	0.64–0.88	88.2	65.8	72.4
rCBV + rVSI	0.67	NA	0.53–0.82	94.1	39.05	55.2
rCBV + peak shift	0.70	NA	0.56–0.86	100	39.0	56.9
rCBV + arterial dominance score	0.82	NA	0.70–0.94	82.3	78.0	79.3

Note:—NA indicates not available.

0.78 (95% CI, 0.64–0.91). The highest diagnostic performance was achieved when the rCBV was combined with the arterial dominance score with an AUC of 0.86 (95% CI, 0.75–0.98).

DISCUSSION

In this study, we demonstrated that vessel architectural imaging parameters derived from simultaneously acquired contrast agent-enhanced gradient-echo and spin-echo MR imaging improved the diagnostic performance of rCBV by determining vessel size and type in differentiating early tumor progression from pseudoprogression. Early tumor progression showed venous dominance and a tendency toward larger vessel size, while pseudoprogression showed arterial dominance and a tendency toward smaller vessel size. The spatial dominance of vessel type was analyzed using the arterial dominance score, which was lower in early tumor progression. VAI parameters were able to provide insight into tumor vasculature and mechanism of pseudoprogression by providing information about vessel size and type and may be used to improve the diagnostic performance of rCBV in diagnosing tumor progression in posttreatment glioblastoma.

The GRE and SE readouts have different sensitivities to contrast agent-induced susceptibility effects, with the GRE data reflecting vessels of all sizes and SE data predominantly reflecting capillaries.²⁰ Peak shift is mainly affected by the relationship between arterial and venous volumes,¹⁹ and negative peak shift indicates SE preceding the GRE peak with venous dominance. In our study, a negative peak shift was obtained in the ETP group, implying an SE peak preceding the GRE peak with venous dominance, which corresponds to a counterclockwise direction in the hysteresis plot. The venous dominance of the tumor vasculature may be attributed to arteriovenous connections within the tumor that lead to increased vessel size and venous flow and reduced flow in the feeding arterioles.²⁴ Tissue with treatment-related change, on the other hand, showed a positive peak shift (GRE peak preceding the SE peak) with arterial dominance. We speculate this as relatively less venous dominance in tissue with treatment-related change with low rCBV values. In recurrent tumor, proliferation of microvessels at early neovascularization²⁵ may be reflected in the SE peak by its high sensitivity to microvessels, while treatment-related change showed a less prominent SE peak resulting in a positive peak shift with the GRE peak preceding the SE peak.

In our study, the rVSI was not shown to be significantly different between ETP and PP, though there was a tendency toward larger vessel size in ETP. A previous study²⁶ showed that mean vessel size was higher in tumor progression (89 [SD, 45] μm) compared with contralateral normal white matter (40 [SD,

11] μm) with borderline significance in a subgroup analysis with patients suspected of tumor progression within 9 months after completing CCRT. In addition, vessel size measures on MR imaging were reported to demonstrate higher specificity and sensitivity in differentiating high-grade from low-grade gliomas compared with rCBV.⁸ VAI was able to provide information regarding vessel size and type better, reflecting underlying tumor vasculature, and hence showed improved diagnostic performance in detecting tumor progression.

The vasculature of viable tumor and damaged tissue is spatially complex and heterogeneous, and conventional perfusion parameters such as CBV cannot currently reflect such spatial complexity and heterogeneity.²⁶ The arterial dominance score in this study successfully accounted for the spatial dominance of arteries in PP over capillaries or venules. Previous studies reported vessel type using the hysteresis plot^{18,26} or binarized value²⁶ of arterial or venous dominance, but these reports were limited to selected voxels and did not account for dominance of a particular vessel type or spatial heterogeneity. The arterial dominance score was reported on a 3-number scale, and fraction of dominance was considered, which may suggest that vessel type as well as its spatial dominance can be helpful in differentiating PP from ETP in posttreatment glioblastoma. In the current study, the arterial dominance score was established by 2 experienced neuroradiologists. In future studies, reproducibility and interobserver agreement of the arterial dominance score among readers with different levels of experience may need to be evaluated to validate this parameter. Moreover, the possibility of deriving this score directly from the VAI images may be investigated to eliminate the need for manual expert analysis.

In the meta-analyses based on DSC perfusion MR imaging, pooled sensitivities and specificities for the best-performing parameters ranged from 82% to 90% and from 86% to 95%, respectively.^{6,7,27} However, these analyses did not strictly differentiate between late radiation necrosis and early treatment effects of pseudoprogression. Our results showed that rCBV was a sensitive parameter (88.2%) with low specificity (48.8%), while rVSI, peak shift, and the arterial dominance score had higher specificity (67.2%–74.1%). Angiogenesis and vascular recruitment may consist of a large number of small-caliber vessels or a small number of large-caliber vessels.²⁸ While rCBV may detect increased vascularity, it is unable to discriminate the composition of vessels from these potential circumstances.⁸ Because peak shift and arterial dominance scores were able to provide insight into the vascular composition and its spatial distribution, VAI parameters exhibited higher specificity in detecting PP compared with rCBV.

Alternative approaches of vascular analysis exist, including phase-sensitive and susceptibility-weighted imaging techniques with improved detection of microvasculature and iron-containing hemorrhagic foci. In patients with posttreatment glioblastoma, a previous study showed that the increase in the percentage of hypointensity on susceptibility imaging was higher in responders than in nonresponders, and nonresponders showed a sparse amount of hypointense signal in the area of contrast enhancement.²⁹ This finding revealed that radiation-induced damage to microvasculature resulted in the formation of microbleeds on susceptibility imaging.^{29,30} However, chronic hemorrhage also appears as hypointensity, and differentiation of arterial- or venous-type vasculature may not be feasible with susceptibility imaging.

This study has several limitations. First, the diagnostic performance of rCBV in our study was lower than previously reported in differentiating tumor progression from treatment-related change. This finding may be due to low rCBV values extracted from the conventional DSC MR imaging protocol with a flip angle of 35°, which is lower than that proposed by American Society of Functional Neuroradiology recommendations.³¹ The use of a lower flip angle may result in relatively small CBV from a low signal-to-noise ratio and low baseline signal³² and may undermine its discriminatory power between the 2 conditions. Previous studies^{33,34} quantified perfusion imaging metrics with histopathologic tumor fraction and yielded a higher diagnostic performance from active tumor portion. Because posttreatment glioblastoma exhibits spatial heterogeneity from admixed treatment effect and tumor cells, voxelwise quantification to measure distributions and parametric maps will be a preferred approach in imaging-based analysis.

In this study, we evaluated spatial heterogeneity using the arterial dominance score, but the measurement was qualitative, and future study with quantitative longitudinal assessment is deemed necessary. Second, the VAI sequence provides a limited scan range compared with conventional DSC MR imaging due to the need for an SE readout with long TEs and requires a double-dose injection of contrast material. However, the recent development of using the combined spin- and gradient-echo-based MR imaging³⁵ allows whole-brain coverage and acquisition of robust CBV without a pre-load in addition to VAI. Technical updates are necessary in our protocol, though double-dose perfusion studies have been performed for >20 years and were acknowledged by the consensus recommendations of the American Society of Functional Neuroradiology³¹ and Jumpstarting Brain Tumor Drug Development Coalition Imaging Standardization Steering Committee.³⁶

CONCLUSIONS

Vessel architectural imaging significantly improved the diagnostic performance of rCBV by demonstrating venous dominance and a tendency toward larger vessel size in early tumor progression and may serve as an early identifier of disease progression in posttreatment glioblastoma.

ACKNOWLEDGMENT

The authors thank Jeong Hoon Kim (J.H.K.) for the contribution in establishing final diagnoses of pseudoprogression and early tumor progression by clinicrodiologic consensus.

Disclosures: Kyrre Emblem—*RELATED: Grant:* the European Research Council; South-Eastern Norway Regional Health Authority; the Research Council of Norway, *Comments:* This work received funding from grant 261984, the South-Eastern Norway Regional Health Authority grants 2017073 and 2013069, and the European Research Council under the European Union's Horizon 2020 Program (European Research Council Grant agreement No. 758657-ImPRESS)*; *UNRELATED: Patents (Planned, Pending or Issued):* NordicNeuroLab AS, *Comments:* intellectual property rights.* Ho Sung Kim—*UNRELATED: Employment:* Asan Medical Center. Atle Bjørnerud—*UNRELATED: Grant:* This work received funding from the Research Council of Norway grant 191088/F20.* *Consultancy:* NordicNeuroLab AS; *Stock/Stock Options:* NordicNeuroLab AS. *Money paid to the institution.

REFERENCES

1. Kruser TJ, Mehta MP, Robins HI. **Pseudoprogression after glioma therapy: a comprehensive review.** *Expert Rev Neurother* 2013;13:389–403 CrossRef Medline
2. Jensen RL. **Brain tumor hypoxia: tumorigenesis, angiogenesis, imaging, pseudoprogression, and as a therapeutic target.** *J Neurooncol* 2009;92:317–35 CrossRef Medline
3. New P. **Radiation injury to the nervous system.** *Curr Opin Neurol* 2001;14:725–34 CrossRef Medline
4. Barajas RF Jr, Chang JS, Segal MR, et al. **Differentiation of recurrent glioblastoma multiforme from radiation necrosis after external beam radiation therapy with dynamic susceptibility-weighted contrast-enhanced perfusion MR imaging.** *Radiology* 2009;253:486–96 CrossRef Medline
5. Kong DS, Kim ST, Kim EH, et al. **Diagnostic dilemma of pseudoprogression in the treatment of newly diagnosed glioblastomas: the role of assessing relative cerebral blood flow volume and oxygen-6-methylguanine-DNA methyltransferase promoter methylation status.** *AJNR Am J Neuroradiol* 2011;32:382–87 CrossRef Medline
6. Suh CH, Kim HS, Jung SC, et al. **Multiparametric MRI as a potential surrogate endpoint for decision-making in early treatment response following concurrent chemoradiotherapy in patients with newly diagnosed glioblastoma: a systematic review and meta-analysis.** *Eur Radiol* 2018;28:2628–38 CrossRef Medline
7. Patel P, Baradaran H, Delgado D, et al. **MR perfusion-weighted imaging in the evaluation of high-grade gliomas after treatment: a systematic review and meta-analysis.** *Neuro Oncol* 2017;19:118–27 CrossRef Medline
8. Chakhoyan A, Yao J, Leu K, et al. **Validation of vessel size imaging (VSI) in high-grade human gliomas using magnetic resonance imaging, image-guided biopsies, and quantitative immunohistochemistry.** *Sci Rep* 2019;9:2846 CrossRef Medline
9. Emblem KE, Mouridsen K, Bjørnerud A, et al. **Vessel architectural imaging identifies cancer patient responders to anti-angiogenic therapy.** *Nat Med* 2013;19:1178–83 CrossRef Medline
10. Dennie J, Mandeville JB, Boxerman JL, et al. **NMR imaging of changes in vascular morphology due to tumor angiogenesis.** *Magn Reson Med* 1998;40:793–99 CrossRef Medline
11. Boxerman JL, Hamberg LM, Rosen BR, et al. **MR contrast due to intravascular magnetic susceptibility perturbations.** *Magn Reson Med* 1995;34:555–66 CrossRef Medline
12. Kiselev VG, Strecker R, Ziyeh S, et al. **Vessel size imaging in humans.** *Magn Reson Med* 2005;53:553–63 CrossRef Medline
13. Louis DN, Perry A, Reifenberger G, et al. **The 2016 World Health Organization Classification of Tumors of the Central Nervous System: a summary.** *Acta Neuropathol* 2016;131:803–20 CrossRef Medline
14. Stupp R, Mason WP, van den Bent MJ, et al; European Organisation for Research and Treatment of Cancer Brain Tumor and Radiotherapy Groups; National Cancer Institute of Canada Clinical Trials Group. **Radiotherapy plus concomitant and adjuvant temozolomide for glioblastoma.** *N Engl J Med* 2005;352:987–96 CrossRef Medline
15. Wen PY, Macdonald DR, Reardon DA, et al. **Updated Response Assessment Criteria for High-Grade Gliomas: Response Assessment**

- in Neuro-Oncology Working Group. *J Clin Oncol* 2010;28:1963–72 CrossRef Medline
16. Weisskoff RM, Boxerman JL, Sorensen AG, et al. **Simultaneous blood volume and permeability mapping using a single Gd-based contrast injection.** In: *Proceedings of the Society of Magnetic Resonance, second annual meeting*, San Francisco, CA, USA. August 6–12, 1994
 17. Boxerman JL, Schmainda KM, Weisskoff RM. **Relative cerebral blood volume maps corrected for contrast agent extravasation significantly correlate with glioma tumor grade, whereas uncorrected maps do not.** *AJNR Am J Neuroradiol* 2006;27:859–67 Medline
 18. Stadlbauer A, Zimmermann M, Oberndorfer S, et al. **Vascular hysteresis loops and vascular architecture mapping in patients with glioblastoma treated with antiangiogenic therapy.** *Sci Rep* 2017;7:8508 CrossRef Medline
 19. Xu C, Kiselev VG, Moller HE, et al. **Dynamic hysteresis between gradient echo and spin echo attenuations in dynamic susceptibility contrast imaging.** *Magn Reson Med* 2013;69:981–91 CrossRef Medline
 20. Digernes I, Bjornerud A, Vatnehol SA, et al. **A theoretical framework for determining cerebral vascular function and heterogeneity from dynamic susceptibility contrast MRI.** *J Cereb Blood Flow Metab* 2017;37:2237–48 CrossRef Medline
 21. Madsen MT. **A simplified formulation of the gamma variate function.** *Phys Med Biol* 1992;37:1597–1600 CrossRef
 22. Press WH, Flannery BP, Teukolsky SA, et al. *Numerical Recipes in C: The Art of Scientific Computing.* Cambridge University Press; 1988
 23. Han K, Song K, Choi BW. **How to develop, validate, and compare clinical prediction models involving radiological parameters: study design and statistical methods.** *Korean J Radiol* 2016;17:339–50 CrossRef Medline
 24. Pries AR, Hopfner M, Le Noble F, et al. **The shunt problem: control of functional shunting in normal and tumour vasculature.** *Nat Rev Cancer* 2010;10:587–93 CrossRef Medline
 25. Mathivet T, Bouleti C, Van Woensel M, et al. **Dynamic stroma reorganization drives blood vessel dysmorphia during glioma growth.** *Embo Mol Med* 2017;9:1629–45 CrossRef Medline
 26. Stadlbauer A, Eyupoglu I, Buchfelder M, et al. **Vascular architecture mapping for early detection of glioblastoma recurrence.** *Neurosurg Focus* 2019;47:E14 CrossRef Medline
 27. van Dijken BR, van Laar PJ, Holtman GA, et al. **Diagnostic accuracy of magnetic resonance imaging techniques for treatment response evaluation in patients with high-grade glioma: a systematic review and meta-analysis.** *Eur Radiol* 2017;27:4129–44 CrossRef Medline
 28. Nakada M, Kita D, Watanabe T, et al. **Aberrant signaling pathways in glioma.** *Cancers (Basel)* 2011;3:3242–78 CrossRef Medline
 29. Lupo JM, Essock-Burns E, Molinaro AM, et al. **Using susceptibility-weighted imaging to determine response to combined anti-angiogenic, cytotoxic, and radiation therapy in patients with glioblastoma multiforme.** *Neuro Oncol* 2013;15:480–89 CrossRef Medline
 30. Lupo JM, Chuang CF, Chang SM, et al. **7-Tesla susceptibility-weighted imaging to assess the effects of radiotherapy on normal-appearing brain in patients with glioma.** *Int J Radiat Oncol Biol Phys* 2012;82:e493–500 CrossRef Medline
 31. Welker K, Boxerman J, Kalnin A, et al; American Society of Functional Neuroradiology MR Perfusion Standards and Practice Subcommittee of the ASFN Clinical Practice Committee. **ASFN recommendations for clinical performance of MR dynamic susceptibility contrast perfusion imaging of the brain.** *AJNR Am J Neuroradiol* 2015;36:E41–51 CrossRef Medline
 32. Cha S, Knopp EA, Johnson G, et al. **Intracranial mass lesions: dynamic contrast-enhanced susceptibility-weighted echo-planar perfusion MR imaging.** *Radiology* 2002;223:11–29 CrossRef Medline
 33. Hu LS, Eschbacher JM, Heiserman JE, et al. **Reevaluating the imaging definition of tumor progression: perfusion MRI quantifies recurrent glioblastoma tumor fraction, pseudoprogression, and radiation necrosis to predict survival.** *Neuro Oncol* 2012;14:919–30 CrossRef Medline
 34. Prah MA, Al-Gizawiy MM, Mueller WM, et al. **Spatial discrimination of glioblastoma and treatment effect with histologically-validated perfusion and diffusion magnetic resonance imaging metrics.** *J Neurooncol* 2018;136:13–21 CrossRef
 35. Zhang K, Yun SD, Triphan SM, et al. **Vessel architecture imaging using multiband gradient-echo/spin-echo EPI.** *PLoS One* 2019;14:e0220939 CrossRef Medline
 36. Boxerman JL, Quarles CC, Hu LS, et al; Jumpstarting Brain Tumor Drug Development Coalition Imaging Standardization Steering Committee. **Consensus recommendations for a dynamic susceptibility contrast MRI protocol for use in high-grade gliomas.** *Neuro Oncol* 2020;22:1262–75 CrossRef Medline

Are Dynamic Arterial Spin-Labeling MRA and Time-Resolved Contrast-Enhanced MRA Suited for Confirmation of Obliteration following Gamma Knife Radiosurgery of Brain Arteriovenous Malformations?

A. Rojas-Villabona, F.B. Pizzini, T. Solbach, M. Sokolska, G. Ricciardi, C. Lemonis, E. DeVita, Y. Suzuki, M.J.P. van Osch, R.I. Foroni, M. Longhi, S. Montemezzi, D. Atkinson, N. Kitchen, A. Nicolato, X. Golay, and H.R. Jäger



ABSTRACT

BACKGROUND AND PURPOSE: Intra-arterial DSA has been traditionally used for confirmation of cure following gamma knife radiosurgery for AVMs. Our aim was to evaluate whether 4D arterial spin-labeling MRA and contrast-enhanced time-resolved MRA in combination can be an alternative to DSA for confirmation of AVM obliteration following gamma knife radiosurgery.

MATERIALS AND METHODS: In this prospective study, 30 patients undergoing DSA for confirmation of obliteration following gamma knife radiosurgery for AVMs (criterion standard) also underwent MRA, including arterial spin-labeling MRA and contrast-enhanced time-resolved MRA. One dataset was technically unsatisfactory, and the case was excluded. The DSA and MRA datasets of 29 patients were independently and blindly evaluated by 2 observers regarding the presence/absence of residual AVMs.

RESULTS: The mean time between gamma knife radiosurgery and follow-up DSA/MRA was 53 months (95% CI, 42–64 months; range, 22–168 months). MRA total scanning time was 9 minutes and 17 seconds. Residual AVMs were detected on DSA in 9 subjects (obliteration rate = 69%). All residual AVMs were detected on at least 1 MRA sequence. Arterial spin-labeling MRA and contrast-enhanced time-resolved MRA showed excellent specificity and positive predictive values individually (100%). However, their sensitivity and negative predictive values were suboptimal due to 1 false-negative with arterial spin-labeling MRA and 2 with contrast-enhanced time-resolved MRA (sensitivity = 88% and 77%, negative predictive values = 95% and 90%, respectively). Both sensitivity and negative predictive values increased to 100% if a composite assessment of both MRA sequences was performed. Diagnostic accuracy (receiver operating characteristic) and agreement (κ) are maximized using arterial spin-labeling MRA and contrast-enhanced time-resolved MRA in combination (area under receiver operating characteristic curve = 1, $P < .001$; $\kappa = 1$, $P < .001$, respectively).

CONCLUSIONS: Combining arterial spin-labeling MRA with contrast-enhanced time-resolved MRA holds promise as an alternative to DSA for confirmation of obliteration following gamma knife radiosurgery for brain AVMs, having provided 100% sensitivity and specificity in the study. Their combined use also enables reliable characterization of residual lesions.

ABBREVIATIONS: ASL = arterial spin-labeling; CE = time-resolved contrast-enhanced; GKR = gamma knife radiosurgery; NPV = negative predictive value; PPV = positive predictive value; ROC = receiver operating characteristic

Brain AVMs are a potential source of neurologic morbidity and mortality due to the life-long risk of intracranial bleeding if left untreated (1.5%–4.0% per year).¹ Gamma knife radiosurgery

(GKR) is a well-established treatment for selected patients with brain AVMs.² It triggers a gradual decrease in blood flow through the AVM nidus a few months after treatment, which progresses so

Received April 10, 2020; accepted after revision October 21, 2021.

From The Gamma Knife Centre at Queen Square (A.R.-V.), The Lysholm Department of Neuroradiology (T.S., H.R.J.), and Department of Neurosurgery (N.K.), National Hospital for Neurology and Neurosurgery, London, UK; Department of Neurosurgery (A.R.-V.), Royal Victoria Infirmary, Newcastle upon Tyne, UK; Department of Radiology (F.B.P., R.I.F.), Department of Diagnostic and Public Health, Verona University, Verona, Italy; Department of Medical Physics and Bioengineering (M.S.), Neuroradiological Academic Unit (M.S., X.G., H.R.J.), Department of Brain Repair and Rehabilitation, Institute of Neurology and Centre for Medical Imaging (D.A.), University College London, London, UK; School of Biomedical Engineering and Imaging Sciences (E.D.V.), King's College London, London, UK; Wellcome Centre for Integrative Neuroimaging (Y.S.), FMRIB, Nuffield Department of Clinical Neurosciences, University of Oxford, Oxford, UK; C.J. Gorter Center for High Field MRI (M.J.P.v.O.), Department of Radiology, Leiden University

Medical Center, Leiden, Netherlands; and Department of Neuroscience (M.L., A.N.) and Radiology Unit (S.M.) and Neuroradiology Unit (G.R., C.L.), Department of Diagnostic and Pathology, University Hospital of Verona, Verona, Italy.

This project was funded by the National Brain Appeal (Small Acorns grant), Elekta (UK) Limited, and the Verona Brain Research Foundation. It was also sponsored by the National Institute for Health Research Biomedical Research Centre and Queen Square Radiosurgery Centre.

Please address correspondence to Alvaro Rojas-Villabona, MBBS, MSc, PhD, MRCS, Department of Neurosurgery, Royal Victoria Infirmary, Queen Victoria Rd, Newcastle upon Tyne, NE1 4LP, United Kingdom; e-mail: a.villabona.11@ucl.ac.uk

Indicates open access to non-subscribers at www.ajnr.org

<http://dx.doi.org/10.3174/ajnr.A6990>

that by 2–3 years posttreatment, approximately 75% of AVMs are completely obliterated.³ The risk of intracranial bleeding is thought to persist until complete obliteration of the nidus is achieved, so it is imperative to confirm AVM cure after treatment.

Intra-arterial DSA has been traditionally used for confirmation of obliteration following GKR.^{4,5} Most GKR centers around the world also use regular MRI and MRA for follow-up, but most patients still undergo DSA to confirm a cure a few years after treatment, usually once obliteration is suggested by MRI/MRA.⁶ Although widely used, DSA conveys some risk, which includes neurologic complications (2.63%), stroke with permanent disability (0.14%), death (0.06%), and access site hematoma (4.2%).⁷ DSA also exposes both patients and medical staff to ionizing radiation, and it carries a risk associated with the injection of iodinated contrast agents. It is an unpleasant experience for patients due to pain, invasiveness, and prolonged bed rest after the procedure.⁸ The cost associated with DSA examinations is also significantly larger than that of diagnostic MRI.

The potential to improve follow-up procedures after GKR using less invasive and radiation-free imaging methods has been described elsewhere, and important attempts have been made using MRA as an alternative to DSA.^{4,5,9,10} Multiple studies have concluded that individually, TOF angiography and time-resolved contrast-enhanced MRA (CE-MRA) have good diagnostic accuracy, which supports their addition to the standard follow-up protocols. However, due to their limited sensitivity and specificity, it is still recommended that DSA be performed to confirm AVM obliteration. MR vascular imaging is being continuously developed, with increasing spatial resolution achieved with contrast-based MR angiography and also subsecond temporal resolution with 4D MRA sequences.^{11,12} The introduction of arterial spin-labeling MRA (ASL-MRA), for instance, has also allowed the acquisition of time-resolved cerebral angiography with temporal resolution comparable with that of DSA (100–200 ms), without the administration of contrast agents.^{13–15} This study aimed to evaluate whether dynamic ASL-MRA and CE-MRA in combination can be an alternative to DSA to confirm obliteration of brain AVMs following GKR and to characterize residual AVMs in cases with an incomplete response.

MATERIALS AND METHODS

Patients

Adult patients undergoing DSA for assessment of obliteration following GKR for AVMs at Verona University Hospital between November 2014 and December 2016 were prospectively recruited. The decision to perform follow-up DSA was made by the clinical team on the basis of their routine follow-up procedures, which are that DSA is performed once obliteration is demonstrated on regular follow-up MR imaging/MRA or after 4 years if no response or only partial response is seen on MR imaging/MRA.

The study was approved by the Verona and Rovigo Research Ethics Committee (European equivalent to an institutional review board), and all participants gave written consent for MRA to be performed on the same day as DSA. Exclusion criteria included contraindications to MR imaging (ie, pacemakers, metallic implants), patients unable to tolerate MR imaging without sedation/anesthesia, abnormal renal function (estimated glomerular

Table 1: Demographic details and AVM characteristics of the study subjects

Characteristics	
Age (mean) (range) (yr)	37 (18–69)
Female (%)	66%
AVM location (No.) (%)	
Temporal	9 (30%)
Frontal	6 (20%)
Parietal	6 (20%)
Occipital	3 (10%)
Basal ganglia/brain stem	4 (13%)
Posterior fossa	2 (7%)
Lateralization (%)	
Right	30%
Left	70%
AVM volume (mean) (range) (mL)	7.01 (0.07–50.54)
GKR (mean) (range)	
Dose (Gy)	17 (11–22)
Percentage isodose	50%
Mean time post-GKR (range) (mo)	53 (22–168)

filtration rate of < 30 mL/min), inability to consent, pregnancy, and history of an allergic reaction to gadolinium.

Thirty consecutive patients were enrolled, and Table 1 shows their demographic details and AVM characteristics. The mean age was 37 years (range, 18–69 years), and 66% of participants were female. Twenty-two patients (73%) presented with a ruptured AVM on diagnosis. The mean AVM volume at the time of GKR was 7.01 [SD, 9.8] mL (range, 0.07–50.54 mL), and the AVMs were well-distributed across the head anatomy. Ten patients (33.3%) had previously undergone glue embolization (*N*-butyl cyanoacrylate), and 3 (10%), microsurgical resection before GKR. One of them had undergone GKR twice for the same AVM.

In 1 case, the contrast agent was not detected by CE-MRA due to mis-timing of the gadolinium injection with respect to the dynamic acquisition. This dataset was considered technically unsatisfactory, and the case was excluded. Final statistical analysis included 29 patients.

MRA

MRA included 4D-ASL-MRA and CE-MRA. These were acquired using an 8-channel head coil on an Achieva 3T MR imaging system (Philips Healthcare) and the scanning parameters shown in Table 2.

ASL-MRA labeling was performed with signal targeting with alternating radiofrequency and a labeling slab of 300 mm positioned 20 mm below the imaging plane.¹⁶ An EPI readout¹⁷ enabled acquisition of 8 dynamic phases with a temporal resolution of 200 ms. CE-MRA included 24 dynamic sagittal acquisitions using a 3D, T1-weighted, fast-field echo sequence. Intravenous injection of 0.1 mL/kg of gadobutrol, 1.0 mmol (Gadovist; Bayer Schering Pharma), was administered with an automated injector at 3.5 mL/s followed by 20-mL normal saline flush at the same rate. A reference scan was acquired before contrast injection for subtraction of stationary tissue, and dynamic sampling was started at the same time as the injection. The dynamic acquisition used contrast-enhanced robust-timing angiography and the keyhole method, with 20% of the *k*-space collected per frame, achieving a temporal resolution of 608 ms/phase. MIPs of the individual MRA sequences were

Table 2: Scanning parameters of ASL-MRA and CE-MRA

Parameter	ASL-MRA	CE-MRA
MRA type	Dynamic (4D)	Dynamic (4D)
Scan duration (min:sec)	5:58	3:19
Contrast		
Acquisition	TI-TFEPI	TI-FFE
TR (ms)	12	3
TE (ms)	5	1
Flip angle	10°	25°
Resolution		
FOV (RL × AP × CC mm)	210 × 210 × 90	150 × 210 × 210
Acquisition	Transversal	Sagittal
Slabs	1	1
Acquisition matrix	172 × 172 × 70	50 × 248 × 248
Acquired voxel size (mm)	1.22 × 1.26 × 1.3	3 × 0.85 × 0.85
Reconstruction matrix	256 × 256	288 × 288
reconstructed voxel size (mm)	0.82 × 0.82 × 0.65	1.5 × 0.73 × 0.73
No. of slices	140	100
SENSE factor	2.5/1	4/2
Dynamic acquisition		
Dynamic imaging mode	TFEPI	CENTRA keyhole
No. of dynamic phases	8	24
Phase interval (temporal resolution) (ms)	200	608
Label delay (ms)	200	–
Contrast	–	Gadovist 0.1 mL/Kg; IV pump injection: 3.5 mL/s

Note:—indicates non-applicable; TFEPI, Turbo-field echo-planar imaging; FFE, fast-field echo; CENTRA, enhanced robust-timing angiography; RL, right-left; AP, anterior-posterior; CC, caudo-cranial; SENSE, sensitivity encoding.

generated in orthogonal planes and transferred to an OsiriX DICOM Viewer 8.4 (<http://www.osirix-viewer.com>) for review.

DSA

DSA was performed using an AlluraXper biplane system (Philips Healthcare) and an iodinated contrast agent (iohexol, Omnipaque, 240 mg/mL; GE Healthcare). DSA acquisitions were performed at a rate of 3–7 frames/s in standard anterior-posterior, lateral, and oblique projections, when necessary.

Data Analysis

The DSA and MRA datasets (MIP reconstruction and source images) were independently evaluated by 2 observers regarding the presence/absence of residual AVMs. The observers were a neuroradiologist with 13 years of experience (F.B.P.) and an interventional neuroradiologist with 15 years of clinical practice (T.S.). They were blinded to the patient's name and demographics, date of the examination, previous clinical reports, and each other's assessments. The observers had not performed or previously interpreted the DSA examinations for clinical purposes. DSA and MRA examinations were anonymized, randomly numbered, and reviewed in different sessions several weeks apart to prevent reporting bias. To simulate the clinical scenario in which radiologic assessment is aided by pre-existing knowledge of the size and location of the treated AVMs, the observers had access to anonymized images of the stereotactic DSA or postcontrast T1WI performed on the day of GKR for comparison with follow-up DSA and MRA, respectively.

AVM obliteration was defined as the complete absence of a nidus and arteriovenous shunt (early-filling draining veins) in both MRA sequences. The Spetzler-Martin grading system (sizes,

<3 cm, 3–6 cm, and >6 cm; venous drainage: deep versus superficial only; adjacent brain: eloquent versus noneloquent) was used to grade residual lesions. Further characterization of residual AVMs included the identification of feeding arteries and draining veins.

DSA was regarded as the criterion standard. The sensitivity, specificity, positive predictive value (PPV), and negative predictive value (NPV) of ASL-MRA, CE-MRA and the combination of both for detection of residual AVMs were calculated. Their diagnostic performance (accuracy) to discriminate between patients with residual AVMs and those with complete obliteration was evaluated using receiver operating characteristic (ROC) curve analysis. An area under the ROC curve of 1 denoted complete agreement, while 0.5 was no agreement other than what would be expected by chance. The

weighed Cohen κ coefficient was calculated to measure agreement between DSA and MRA ($\kappa \leq 0.20$ = poor; ≥ 0.91 = excellent).¹⁸ Statistical significance was defined as $P < .05$, and analyses were performed using the Statistical Package for the Social Sciences (Version 23; IBM).

RESULTS

The mean time between GKR and follow-up DSA/MRA was 53 months (95% CI, 42–64 months; range, 22–168 months). ASL-MRA and CE-MRA scanning time was 5 minutes and 58 seconds and 3 minutes and 19 seconds, respectively. At follow-up imaging, no patients had received further treatment for residual AVMs nor had they experienced any intracranial bleeds post-GKR.

Confirmation of AVM Obliteration

A residual AVM was detected on DSA in 9 subjects, and complete radiographic obliteration was confirmed in 20 patients by both observers using DSA, resulting in an obliteration rate of 69%, which was in complete agreement with the clinical reports produced by the interventional radiologist who had performed the DSA.

The residual AVM was detected by observers on ASL-MRA in 8 subjects and on CE-MRA in 7 of 9 patients who had been shown to have a residual on DSA. Table 3 shows how all residual AVMs were detected on at least 1 MRA sequence. The case in which ASL-MRA failed to show the residual AVM (case 30) is presented in Fig 1. In 2 cases, the residual lesion was not observed on CE-MRA (Fig 2) due to the very small size of the residual lesion (6 mm, case 13) and the diffuse nature of the also very small residual nidus in case 9. No abnormalities were observed on MRA in those patients with complete radiographic obliteration on DSA.

Table 3: Identification of residual AVM with DSA, ASL-MRA, and CE-MRA in cases with a residual lesion

Case	Residual AVM		
	DSA	ASL-MRA	CE-MRA
3	Yes	Yes	Yes
6	Yes	Yes	Yes
9	Yes	Yes	No ^a
10	Yes	Yes	Yes
11	Yes	Yes	Yes
13	Yes	Yes	No ^a
19	Yes	Yes	Yes
23	Yes	Yes	Yes
30	Yes	No ^a	Yes

^a False-negative.

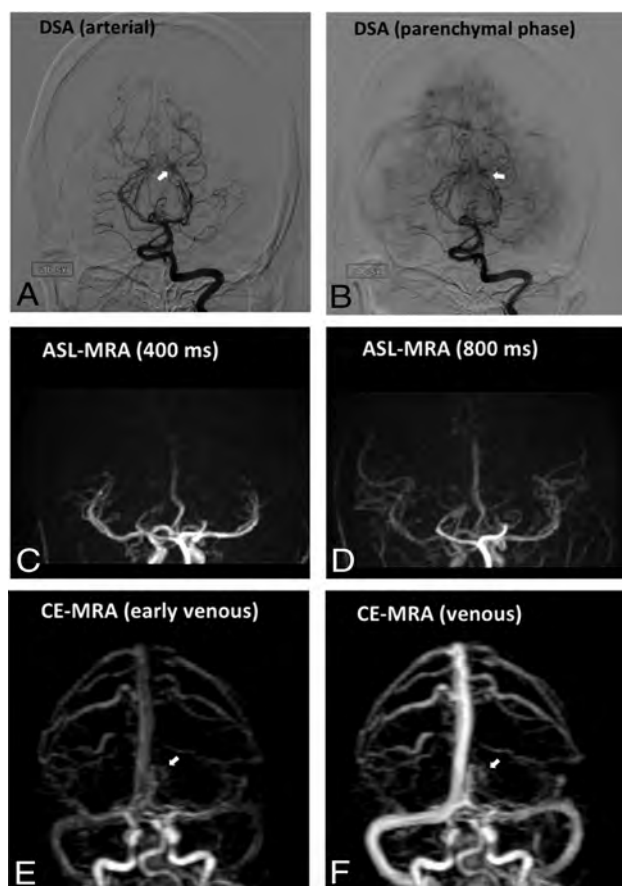


FIG 1. Post-GKR DSA and MRA of a study case in which the residual AVM was not visualized on ASL-MRA (case 30). Post-GKR DSA (A and B) shows a residual AVM nidus (white arrow) fed by the left posterior cerebral artery. CE-MRA (E–F) shows slow filling of the AVM nidus (white arrowhead) lateral to the deep venous system. No residual AVM is noted on ASL-MRA (C and D).

The sensitivity, specificity, PPV, and NPV of ASL-MRA and CE-MRA for detection of residual AVMs are presented in Table 4. ASL-MRA and CE-MRA showed excellent specificity and PPV individually due to the absence of false-positives. Their sensitivity and NPV, however, were suboptimal due to the finding of 1 false-negative with ASL-MRA and 2 with CE-MRA (sensitivity = 88% and 77%; NPV = 95% and 90%, respectively). Both sensitivity and NPV increased to 100% if a composite assessment of both

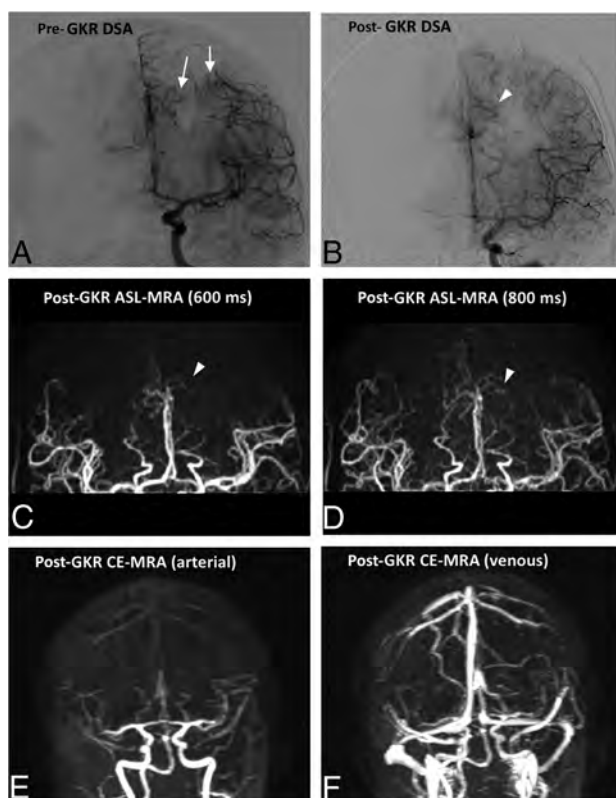


FIG 2. Representative case of a residual AVM not visualized on CE-MRA (case 13). The pre-GKR DSA (A) shows 2 AVM nidi (white arrows) at the time of GKR in a patient with previous partial surgical excision of a ruptured AVM. The most lateral nidus is not identified in post-GKR MRA imaging; however, a residual of the most medial nidus (arrowheads) is identified on post-GKR DSA (B) and ASL-MRA (C and D). The small size of the lesion renders it not identifiable on the CE-MRA (E–F).

MRA sequences was performed. Diagnostic accuracy (ROC) and agreement (κ) are also maximized using ASL-MRA and CE-MRA in combination (area under the ROC curve = 1, $P < .001$; $\kappa = 1$, $P < .001$, respectively).

Characterization of Residual AVMs in Cases of Incomplete Response

Table 5 shows the interpretation of DSA and MRA regarding Spetzler-Martin grading of residual AVMs by both observers. There was complete agreement on size and drainage scores between MRA and DSA for both observers in all 9 residual lesions ($\kappa = 1$; $P < .003$). Different eloquence scores were noted on DSA and MRA in 1 case by the first observer and in 3 cases by the second observer. These were the result of limited anatomic localization on 2D DSA images compared with MRA. Figure 3 shows a representative case of a residual AVM that was fully and accurately characterized in terms of Spetzler-Martin grading using ASL- and CE-MRA compared with DSA.

Observer 1 identified a total of 14 feeding arteries and 13 draining veins on both DSA and MRA. Observer 2 identified 17 feeding arteries and 15 draining veins on DSA and 15 and 12 on MRA, respectively (Table 3). The same blood vessel was identified by both observers as the main feeding artery

Table 4: Sensitivity, specificity, PPV, and NPV of ASL-MRA, CE-MRA, and the combination of the 2 for detection of residual AVMs

	ASL-MRA	CE-MRA	Both
Sensitivity	88%	77%	100%
Specificity	100%	100%	100%
PPV	100%	100%	100%
NPV	95%	90%	100%
Diagnostic accuracy (ROC)	0.94 ($P < .001$) ^a	0.89 ($P = .002$) ^a	1 ($P < .001$) ^a
Agreement (κ)	0.92 ($P < .001$)	0.82 ($P < .001$)	1 ($P < .001$)

^aNull hypothesis: true area = 0.5.

Table 5: Characterization of residual AVMs using ASL-MRA and CE-MRA compared with DSA

	Observer 1		Observer 2	
	DSA	MRA	DSA	MRA
SMS				
Size				
<3 cm	7	7	7	7
3–6 cm	2	2	2	2
>6 cm	–	–	–	–
Drainage				
Superficial only	5	5	5	5
Deep	4	4	4	4
Eloquence				
Noneloquent	5	4	3	4
Eloquent	4	5	6	5
Feeding arteries	14	14	17	15
Draining veins	13	13	15	12

Note:—indicates non-applicable; SMS, Spetzler-Martin Score.

on DSA and MRA for 8 of 9 residual AVMs. In 1 case, observer 1 named the superior cerebellar artery as the only feeder on DSA, and the posterior cerebral artery, on MRA, while observer 2 named the same feeding vessels but in the opposite set of investigations, ie, superior cerebellar artery on MRA and posterior cerebral artery on DSA.

DISCUSSION

This work presents the use of 2 dynamic MRA techniques based on ASL and gadolinium bolus tracking for confirmation of obliteration of brain AVMs following GKR. The ASL-MRA, CE-MRA, and DSA sequences of 29 patients who underwent follow-up imaging to confirm obliteration of brain AVMs following GKR were blindly and independently assessed by 2 observers. ASL-MRA and CE-MRA individually have limited sensitivity and NPV for detection of residual AVMs after radiosurgery. This is of clinical importance because false-negative investigations could result in a persistent risk of hemorrhage from AVMs in patients thought to have been cured. The combined use of ASL-MRA and CE-MRA, which provide both temporal and spatial information, appears to be a reliable method to confirm/rule out the presence of residual AVMs after radiosurgery. The composite use of dynamic ASL-MRA and CE-MRA in our study showed maximal sensitivity and specificity compared with DSA; this outcome makes this the first study demonstrating satisfactory diagnostic accuracy of MRA for confirmation of obliteration following GKR of brain AVMs. The results of this study support the use of ASL-

MRA and CE-MRA as a first-line technique for confirmation of obliteration following GKR, which is of high clinical relevance because this would not only avoid unnecessary DSA examinations for patients with cured AVMs (69% in our study group) but also help rationalize its use in patients with residual AVMs who may need more DSAs for further treatment.

The major accomplishment of using two 4D-MRA sequences is the combination of high temporal and spatial resolution, which is necessary to appreciate the dynamic characteristics of AVMs.¹⁹ AVMs exhibit a high degree of heterogeneity in terms of angioarchitecture and flow dynamics, and even within the same lesion, there may be dramatic and unpredictable differences in terms of vessel configuration and blood flow. This accomplishment is most likely the reason for the disappointing results of previous studies that attempted to detect and fully characterize residual AVMs using either TOF or CE-MRA.^{4,5,9,10} If used independently, those MRA sequences are unable to capture all the complexity and heterogeneity of shapes, sizes, and velocities seen on AVMs. However, in combination, the chance of false-negatives is reduced and their combined ability to detect/rule out residual AVMs after GKR is increased. This feature is demonstrated in our study by the visualization of all residual AVMs in at least 1 MRA sequence and the optimal characterization of residual AVMs using structural and dynamic information obtained from both MRA modalities. Such use of multiple sequences for diagnostic purposes is commonplace in radiology, and it is well-accepted that information from multiple sources (ie, T1WI, T2WI, and contrast imaging) may be required to achieve a full diagnosis.

The main limitation of our study is that a separate review of each MRA sequence, to assess their ability to individually confirm AVM obliteration, was not part of the design. This was because multiple studies had previously concluded that individually, all previously used MRA sequences have suboptimal diagnostic accuracy compared with DSA.^{4,5,9,10} Also, the review of both MRA sequences separately followed by their combined re-assessment would have resulted in increasing and unpredictable reporting bias. Instead, as part of the combined assessment of both MRA sequences, the observers indicated which of the 2 showed the residual AVM, and this information provided some insight into the diagnostic accuracy of each individual sequence. However, we cannot assume that the outcome would have been the same if each MRA technique were assessed independently because the combined assessment of the 2 is highly likely to have resulted in a degree of crossed reinforcement or reassurance of findings between the individual sequences.

In our study, CE-MRA appeared to have lower diagnostic accuracy by failing to show 2 residual AVMs that were clearly visualized on ASL-MRA and DSA (Fig 2). CE-MRA is prone to motion artifacts, and it relies on single-pass bolus tracking, which contributed to a technically unsatisfactory MRA dataset that was excluded from the analysis. Nonetheless, CE-MRA provided

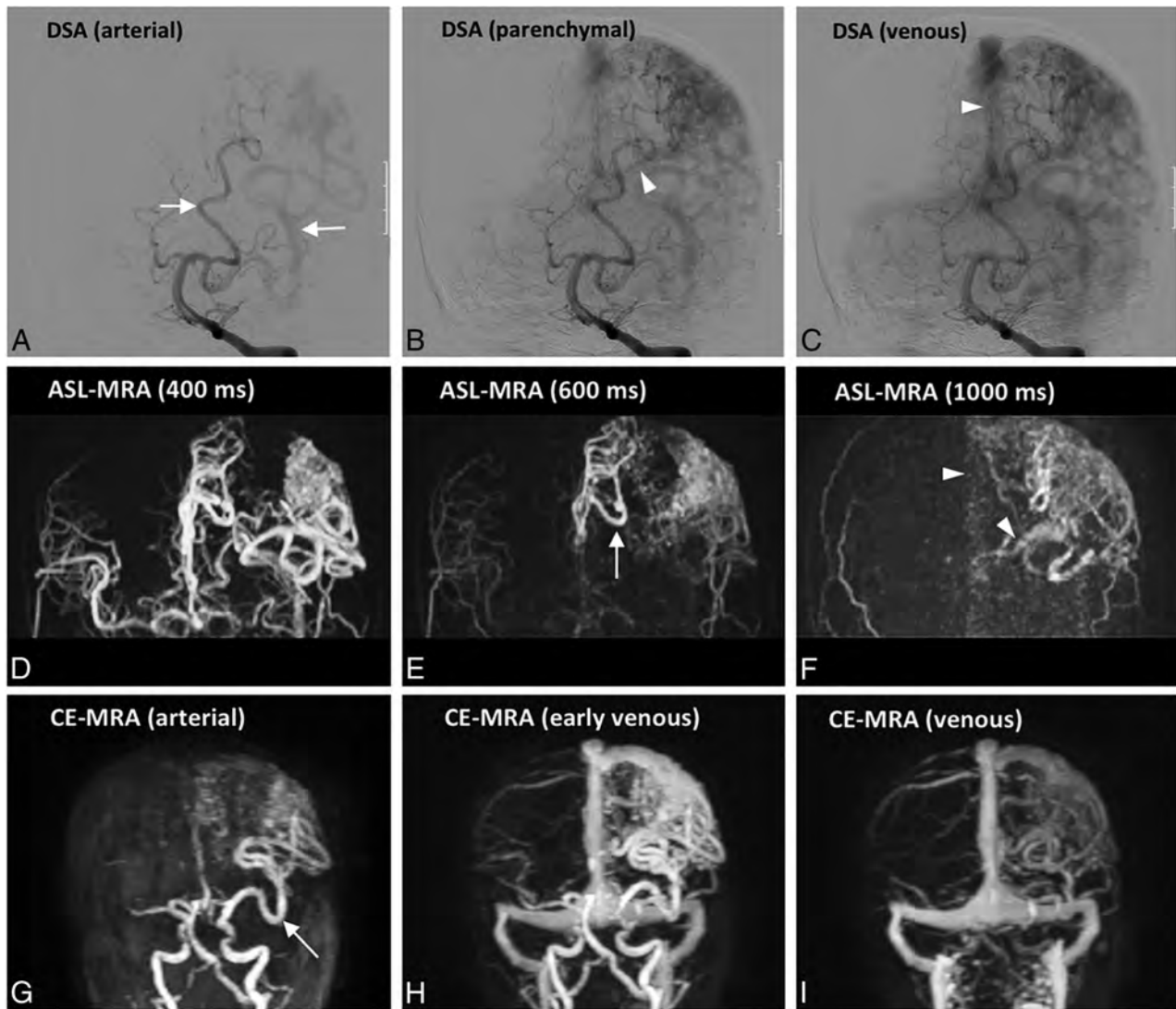


FIG 3. Characterization of a residual AVM (case 19) using ASL (D–F) and CE-MRA (G–I) compared with DSA (A–C). The feeding arteries of this AVM, which are branches of the anterior and middle cerebral arteries (white arrows), are clearly depicted on ASL-MRA and CE-MRA. The draining veins (arrowheads) seen on DSA can also be identified on ASL and CE-MRA, and they involve both the superficial venous system via the superior sagittal sinus and the deep system via the left internal cerebral vein.

valuable dynamic information for the characterization of residual lesions, in terms of feeding arteries and draining veins, and it can also depict arteriovenous shunting, which was essential in the evaluation of AVM obliteration. CE-MRA was very important in a case in which the residual AVM was not visualized on ASL-MRA (Fig 1), and this case demonstrates how the 2 sequences complement each other, increasing the chances of AVM detection and enabling the characterization of residual AVMs.

Regarding ASL-MRA, to date, no previous studies exist on its use for confirmation of AVM obliteration after radiosurgery. A number of studies have used it, together with ASL perfusion, for assessment of AVMs with promising results, but their value compared with DSA is also still to be fully established.^{20–22} ASL is an appealing technique for confirmation of obliteration because venous signal in AVM draining veins can be considered a strong indication of arteriovenous shunting, which is an unequivocal

defining element of an AVM. During an ASL acquisition, the arterial blood water is labeled with a radiofrequency pulse proximal to the brain, and it is used as an endogenous contrast agent.^{17,23} Under normal physiologic conditions, the time it would take for the labeled water to reach the veins (either via intravascular transport through the microvascular bed or via extravasation into the extravascular compartment and subsequently being picked up in the venous system) is longer than the time between the start of labeling and the readout. Thus, there is normally little detectable signal within the intracranial veins on ASL perfusion images²⁴ or on ASL angiography. Furthermore, decay of the tagged spins in ASL angiography is accelerated by the train of readout excitation pulses, resulting in additional signal reduction more distal into the vascular tree. In AVMs, however, the labeled spins are rapidly shunted directly into the venous circulation, giving rise to high signal intensity in AVM draining veins.²⁵ In our study, ASL-MRA proved critical to the assessment of the response to GKR in

2 cases in which CE-MRA failed to demonstrate the residual lesion (Fig 2). It also provided important information on nidus size and the number of feeding arteries. However, as in other individual MRA sequences, ASL-MRA is, by itself, unable to capture all the possible scenarios of size, flow, and velocity to reliably detect residual AVMs, evidenced by the occurrence of a false-positive in which ASL-MRA failed to show the residual nidus (Fig 1).

In our study, the observers were aided by a very high index of suspicion because they were aware of the location of AVMs at treatment and, therefore, knew where to look for residual lesions. It could be argued that results would have been different if the observers had no indication of the potential AVM location; however, the study was pragmatically designed to replicate the clinical scenario in which DSA examinations are reviewed specifically to confirm obliteration. We performed DSA once obliteration was demonstrated on regular follow-up MR imaging/MRA or after 4 years if no response or only partial response was seen on MR imaging/MRA. This procedure could have introduced a degree of selection bias. Also, we had a relatively small sample size, which is a limitation of the study. The assessment of a larger number of patients is needed to strengthen the power of the results.

Optimization of MRA sequences for further implementation should include individualized time resolution of ASL-MRA, which can be used to better characterize the flow dynamics of residual AVMs. There is also a great potential for improvement of MRA by postprocessing the individual datasets and, through their combination, generating a single product that incorporates the information provided by both sequences. This improvement is still to be accomplished and developers should aim for more sophisticated 4D visualization maps, which enhance the visual experience and facilitate interpretation.

CONCLUSIONS

Combining ASL-MRA with CE-MRA holds promise as an alternative to DSA for confirmation of obliteration following GKR for brain AVMs, having provided 100% sensitivity and specificity in the study. In addition, their combined use enables reliable characterization of residual lesions.

ACKNOWLEDGMENTS

We thank Ing Marcello Cadioli, MR Clinical Scientist, for his support on the implementation of CE-MRA at the University Hospital of Verona.

Disclosures: Alvaro Rojas-Villabona—RELATED: Grant: National Brain Appeal, Comments: Small Acorns grant awarded to Alvaro Rojas-Villabona*; Support for Travel to Meetings for the Study or Other Purposes: Queen Square Radiosurgery Center. Matthias J.P. van Osch—UNRELATED: Grants/Grants Pending: Philips Healthcare*; Payment for Lectures Including Service on Speakers Bureaus: Philips Healthcare. Xavier Golay—UNRELATED: Employment: University College London. Hans Rolf Jäger—UNRELATED: Royalties: payment by Springer of £1000, Comments: This is an honorarium for coediting the 3-volume textbook *Clinical Neuroradiology*, published by Springer in 2019. Giuseppe Ricciardi—UNRELATED: Employment: University of Verona; Travel/Accommodations/Meeting Expenses Unrelated to Activities Listed: University of Verona. Christos Lemonis—RELATED: Grant: Verona Brain Research. *Money paid to the institution.

REFERENCES

1. da Costa L, Wallace MC, Ter Brugge KG, et al. **The natural history and predictive features of hemorrhage from brain arteriovenous malformations.** *Stroke* 2009;40:100–05 CrossRef Medline
2. van Beijnum J, van der Worp HB, Buis DR, et al. **Treatment of brain arteriovenous malformations: a systematic review and meta-analysis: Meta-Analysis Research Support, Non-U.S. Gov't Review.** *JAMA* 2011;306:2011–19 CrossRef Medline
3. Koltz MT, Polifka AJ, Saltos A, et al. **Long-term outcome of gamma knife stereotactic radiosurgery for arteriovenous malformations graded by the Spetzler-Martin classification.** *J Neurosurg Sci* 2013;118:74–83 CrossRef Medline
4. Lee CC, Reardon MA, Ball BZ, et al. **The predictive value of magnetic resonance imaging in evaluating intracranial arteriovenous malformation obliteration after stereotactic radiosurgery.** *J Neurosurg* 2015;123:136–44 CrossRef Medline
5. Soize S, Bouquigny F, Kadziolka K, et al. **Value of 4D MR angiography at 3T compared with DSA for the follow-up of treated brain arteriovenous malformation.** *AJNR Am J Neuroradiol* 2014;35:1903–09 CrossRef Medline
6. Starke RM, Kano H, Ding D, et al. **Stereotactic radiosurgery for cerebral arteriovenous malformations: evaluation of long-term outcomes in a multicenter cohort.** *J Neurosurg Sci* 2017;126:36–44 CrossRef Medline
7. Kaufmann TJ, Huston J 3rd, Mandrekar JN, et al. **Complications of diagnostic cerebral angiography: evaluation of 19,826 consecutive patients.** *Radiology* 2007;243:812–19 CrossRef Medline
8. Fifi JT, Meyers PM, Lavine SD, et al. **Complications of modern diagnostic cerebral angiography in an academic medical center.** *J Vasc Interv Radiol* 2009;20:442–47 CrossRef Medline
9. Buis DR, Bot JC, Barkhof F, et al. **The predictive value of 3D time-of-flight MR angiography in assessment of brain arteriovenous malformation obliteration after radiosurgery.** *AJNR Am J Neuroradiol* 2012;33:232–38 CrossRef Medline
10. Lim HK, Choi CG, Kim SM, et al. **Detection of residual brain arteriovenous malformations after radiosurgery: diagnostic accuracy of contrast-enhanced four-dimensional MR angiography at 3.0 T.** *Br J Radiol* 2012;85:1064–69 CrossRef Medline
11. Chang W, Wu Y, Johnson K, et al. **Fast contrast-enhanced 4D MRA and 4D flow MRI using constrained reconstruction (HYPRFlow): potential applications for brain arteriovenous malformations.** *AJNR Am J Neuroradiol* 2015;36:1049–55 CrossRef Medline
12. Hadizadeh DR, Gieseke J, Beck G, et al. **View-sharing in keyhole imaging: Partially compressed central k-space acquisition in time-resolved MRA at 3.0 T.** *Eur J Radiol* 2011;80:400–06 CrossRef Medline
13. Wu H, Block WF, Turski PA, et al. **Noncontrast dynamic 3D intracranial MR angiography using pseudo-continuous arterial spin labeling (PCASL) and accelerated 3D radial acquisition.** *J Magn Reson Imaging* 2014;39:1320–26 CrossRef Medline
14. Lindner T, Jensen-Kondering U, van Osch MJ, et al. **3D time-resolved vessel-selective angiography based on pseudo-continuous arterial spin-labeling.** *Magn Reson Imaging* 2015;33:840–06 CrossRef Medline
15. Suzuki Y, Teeuwisse M, Schmid S. **Improving 4D pCASL angiography by combining Hadamard time-encoding with Look-Locker readout.** In: *Proceedings of the 22th Annual Meeting of the International Society of Magnetic Resonance in Medicine*, Milan, Italy, 2014
16. Nakamura M, Yoneyama M, Tabuchi T, et al. **Non-contrast time-resolved magnetic resonance angiography combining high resolution multiple phase echo planar imaging based signal targeting and alternating radiofrequency contrast inherent inflow enhanced multi phase angiography combining spatial resolution echo planar imaging based signal targeting and alternating radiofrequency in intracranial arteries [in Japanese].** *Nihon Hoshasen Gijutsu Gakkai Zasshi* 2012;68:1525–32 CrossRef Medline
17. Suzuki Y, Fujima N, Ogino T, et al. **Acceleration of ASL-based time-resolved MR angiography by acquisition of control and labeled**

- images in the same shot (ACTRESS). *Magn Reson Med* 2018;79:224–33 CrossRef Medline
18. Machet A, Portefaix C, Kadziolka K, et al. **Brain arteriovenous malformation diagnosis: value of time-resolved contrast-enhanced MR angiography at 3.0T compared to DSA.** *Neuroradiology* 2012;54:1099–108 CrossRef Medline
 19. Khandanpour N, Griffiths P, Warren D, et al. **Prospective comparison of late 3T MRI with conventional angiography in evaluating the patency of cerebral arteriovenous malformations treated with stereotactic radiosurgery: comparative study controlled clinical trial.** *Neuroradiology* 2013;55:683–87 CrossRef Medline
 20. Iryo Y, Hirai T, Nakamura M, et al. **Evaluation of intracranial arteriovenous malformations with four-dimensional arterial-spin labeling-based 3-T magnetic resonance angiography.** *J Comput Assist Tomogr* 2016;40:290–96 CrossRef Medline
 21. Fujima N, Osanai T, Shimizu Y, et al. **Utility of noncontrast-enhanced time-resolved four-dimensional MR angiography with a vessel-selective technique for intracranial arteriovenous malformations.** *J Magn Reson Imaging* 2016;44:834–45 CrossRef Medline
 22. Yu S, Yan L, Yao Y, et al. **Noncontrast dynamic MRA in intracranial arteriovenous malformation (AVM), comparison with time of flight (TOF) and digital subtraction angiography (DSA): Comparative Study Research Support, N.I.H., Extramural Research Support, Non-U.S.** *Magn Reson Imaging* 2012;30:869–77 CrossRef Medline
 23. Petersen ET, Zimine I, Ho Y-CL, et al. **Non-invasive measurement of perfusion: a critical review of arterial spin labelling techniques. other.** *R J Radiol* 2006;79:688–701 CrossRef Medline
 24. Kukuk GM, Hadizadeh DR, Bostrom A, et al. **Cerebral arteriovenous malformations at 3.0 T: intraindividual comparative study of 4D-MRA in combination with selective arterial spin labeling and digital subtraction angiography: comparative study.** *Invest Radiol* 2010;45:126–32 CrossRef Medline
 25. Jang J, Schmitt P, Kim BY, et al. **Non-contrast-enhanced 4D MR angiography with STAR spin labeling and variable flip angle sampling: a feasibility study for the assessment of dural arteriovenous fistula.** *Neuroradiology* 2014;56:305–14 CrossRef Medline

Is Catheter Angiography Still Necessary to Evaluate Obliteration of Brain Arteriovenous Malformations Treated with Stereotactic Radiosurgery?

In this single-center prospective study, the authors investigated the accuracy of 4D arterial spin-labeling MR angiography (ASL-MRA) and contrast-enhanced time-resolved MRA (CE-MRA) sequences for determining obliteration of brain AVMs treated with stereotactic radiosurgery (SRS). Patients with SRS-treated AVMs found to have obliteration on routine follow-up MR imaging/MRA or residual nidus after 4 years of follow-up were enrolled in the study. These patients then underwent MRA with 4D ASL-MRA and CE-MRA sequences in addition to the recommended catheter DSA on the same day. Images were randomly allocated to and independently interpreted by 2 experienced neuroradiologists who were blinded to clinical data. The ability of the 4D ASL-MRA and CE-MRA sequences to distinguish AVM obliteration status was compared with that of DSA, the current the criterion standard.

Thirty consecutive patients were enrolled, but 1 was subsequently excluded because of technical error during imaging acquisition, so the final analysis included 29 patients. The mean follow-up duration was 53 months. Complete obliteration and residual AVMs, based on DSA, were found in 20 (69%) and 9 (31%) patients, respectively. Residual AVMs were accurately identified in 8 and 7 cases based on 4D ASL-MRA (sensitivity = 88%, negative predictive value [NPV] = 95%) and CE-MRA (sensitivity = 77%, NPV = 90%) sequences, respectively. The sensitivity and NPV improved to 100% when these sequences were used together. The authors also reported that 4D ASL-MRA and CE-MRA sequences were able to provide data relevant to the Spetzler-Martin grade in complete agreement with DSA with regard to nidus size and venous drainage pattern (Cohen $k = 1$, $P < .003$). The authors concluded that 4D ASL-MRA and CE-MRA sequences are promising alternatives to DSA for confirming AVM obliteration after SRS, and they may also be able to characterize the angioarchitecture of residual AVMs.

Despite improvements in catheters and its minimally invasive nature, DSA continues to harbor small risks of stroke and access site complications.¹ Advances in image resolution and dynamic imaging with MR imaging have improved contemporary noninvasive radiologic evaluation of AVMs. The role of MR imaging in determining

SRS-induced AVM obliteration has evolved concurrently with technological improvements in its neuroimaging resolution and capabilities.^{2,3} The goal of AVM intervention is obliteration of the nidus because any residual arteriovenous shunting represents persistent hemorrhage risk.⁴ As such, sensitivity and NPV of the imaging technique under investigation for detecting residual AVM nidus are of utmost importance.⁵ These factors are particularly crucial for AVMs treated with SRS because obliteration after this intervention occurs in a delayed fashion over a period of up to 5 years.^{6,7} SRS-treated AVMs often require routine serial imaging follow-up during this latency period, so the accuracy of noninvasive imaging in guiding the necessity and timing of DSA is essential.

4D ASL-MRA and CE-MRA sequences each demonstrated reasonable sensitivities and NPVs for residual AVM detection after SRS, and their combined sensitivity and NPV were both 100%. The authors should be commended for putting forth a well-designed study investigating this topic, though readers should recognize the study's limitations. First, the sample included a highly selected cohort of AVMs with a high likelihood of obliteration (because of obliteration observed on MR imaging) and patent nidi 4 years after SRS. The study did not clearly define whether residual AVMs detected on 4D ASL-MRA and CE-MRA sequences derived from the obliterated or nonobliterated groups based on routine follow-up MR imaging. The utility of DSA for post-SRS follow-up lies in its ability to detect residual AVMs not otherwise identified on MR imaging. Small and poorly defined AVMs usually include residual nidi that are missed on routine follow-up MRI, and detection of these lesions on 4D ASL-MRA and CE-MRA sequences may not have been adequately assessed. Therefore, inclusion of patent AVMs on routine follow-up MR imaging may have falsely inflated the sensitivities and NPVs of these MRA sequences.

Although the overall study cohort included 29 patients, the sample size used to assess the sensitivities of 4D ASL-MRA and CE-MRA included only 9 patients. The small sample size also precluded subgroup analyses. Therefore, future studies of larger cohorts are necessary to confirm the presented findings. The

results of this study demonstrated a promising future for noninvasive imaging in accurately assessing the obliteration status of AVMs treated with SRS, thereby reducing the need for DSA in post-SRS follow-up. Although noninvasive imaging may not entirely supplant the need for DSA in future AVM imaging, a larger proportion of these patients may be spared the procedural risks associated with DSA.

REFERENCES

1. Kaufmann TJ, Huston J, Mandrekar JN, et al. **Complications of diagnostic cerebral angiography: evaluation of 19,826 consecutive patients.** *Radiology* 2007;243:812–19 CrossRef Medline
2. Lee CC, Reardon MA, Ball BZ, et al. **The predictive value of magnetic resonance imaging in evaluating intracranial arteriovenous malformation obliteration after stereotactic radiosurgery.** *J Neurosurg* 2015;123:136–44 CrossRef Medline
3. O'Connor TE, Friedman WA. **Magnetic resonance imaging assessment of cerebral arteriovenous malformation obliteration after stereotactic radiosurgery.** *Neurosurgery* 2013;73:761–66 CrossRef Medline
4. Ding D, Chen CJ, Starke RM, et al. **Risk of brain arteriovenous malformation hemorrhage before and after stereotactic radiosurgery.** *Stroke* 2019;50:1384–91 CrossRef Medline
5. Chen CJ, Ding D, Derdeyn CP, et al. **Brain arteriovenous malformations: a review of natural history, pathobiology, and interventions.** *Neurology* 2020 Oct 1 [Epub ahead of print] CrossRef Medline
6. Chen CJ, Lee CC, Kano H, et al. **Stereotactic radiosurgery for pediatric brain arteriovenous malformations: long-term outcomes.** *J Neurosurg Pediatr* 2020 Feb 7 [Epub ahead of print] CrossRef Medline
7. Starke RM, Kano H, Ding D, et al. **Stereotactic radiosurgery for cerebral arteriovenous malformations: evaluation of long-term outcomes in a multicenter cohort.** *J Neurosurg* 2017;126:36–44 CrossRef Medline

 **Ching-Jen Chen**

Department of Neurological Surgery
University of Virginia
Charlottesville, Virginia

 **Dale Ding**

Department of Neurosurgery
University of Louisville
Louisville, Kentucky

<http://dx.doi.org/10.3174/ajnr.A6954>

Determining the Degree of Dopaminergic Denervation Based on the Loss of Nigral Hyperintensity on SMWI in Parkinsonism

Y.J. Bae, Y.S. Song, J.-M. Kim, B.S. Choi, Y. Nam, J.-H. Choi, W.W. Lee, and J.H. Kim



ABSTRACT

BACKGROUND AND PURPOSE: Nigrostriatal dopaminergic function in patients with Parkinson disease can be assessed using ^{123}I -2 β -carbomethoxy-3 β -(4-iodophenyl)-N-(3-fluoropropyl)-nortropan dopamine transporter (^{123}I -FP-CIT) SPECT, and a good correlation has been demonstrated between nigral status on SWI and dopaminergic denervation on ^{123}I -FP-CIT SPECT. Here, we aim to correlate quantified dopamine transporter attenuation on ^{123}I -FP-CIT SPECT with nigrosome-1 status using susceptibility map-weighted imaging (SMWI).

MATERIALS AND METHODS: Between May 2017 and January 2018, consecutive patients with idiopathic Parkinson disease ($n = 109$) and control participants ($n = 29$) who underwent ^{123}I -FP-CIT SPECT with concurrent 3T SWI were included. SMWI was generated from SWI. Two neuroradiologists evaluated nigral hyperintensity from nigrosome-1 on each side of the substantia nigra. Using consensus reading, we compared the ^{123}I -FP-CIT-specific binding ratio according to nigral hyperintensity status and the ^{123}I -FP-CIT specific binding ratio threshold to confirm the loss of nigral hyperintensity was determined using receiver operating characteristic curve analysis.

RESULTS: The concordance rate between SMWI and ^{123}I -FP-CIT SPECT was 65.9%. The ^{123}I -FP-CIT-specific binding ratios in the striatum, caudate nucleus, and putamen were significantly lower when nigral hyperintensity in the ipsilateral substantia nigra was absent than when present (all, $P < .001$). The ^{123}I -FP-CIT-specific binding ratio threshold values for the determination of nigral hyperintensity loss were 2.56 in the striatum (area under the curve, 0.890), 3.07 in the caudate nucleus (0.830), and 2.36 in the putamen (0.887).

CONCLUSIONS: Nigral hyperintensity on SMWI showed high positive predictive value and low negative predictive value with dopaminergic degeneration on ^{123}I -FP-CIT SPECT. In patients with Parkinson disease, the loss of nigral hyperintensity is prominent in patients with lower striatal specific binding ratios.

ABBREVIATIONS: PD = Parkinson disease; SBR = specific binding ratio; SMWI = susceptibility map-weighted imaging; SN = substantia nigra; ^{123}I -FP-CIT = ^{123}I -2[β]-carbomethoxy-3[β]-[4-iodophenyl]-N-(3-fluoropropyl)-nortropan dopamine transporter; MMSE = Mini-Mental State Examination; MoCA = Montreal Cognitive Asses; UPDRS = Unified Parkinson's Disease Rating Scale; ROC = receiver operating characteristic; AUC = area under the curve

The second most common neurodegenerative disorder,^{1,2} Parkinson disease (PD) is characterized by dopaminergic cell loss within the substantia nigra (SN) of the midbrain that

reportedly progresses from structures called nigrosomes,¹ beginning with the largest subdivision of nigrosome-1.^{3,4} The presence of nigrosome-1 can be assessed using high-resolution MR imaging, and its absence can serve as a powerful diagnostic tool for PD.⁵⁻¹³

The standardized assessment of nigrostriatal dopaminergic function in patients with PD has been performed using SPECT, including ^{123}I -2 β -carbomethoxy-3 β -(4-iodophenyl)-N-(3-fluoropropyl)-nortropane (^{123}I -FP-CIT) SPECT as its more common variation.¹⁴⁻¹⁶ Although research has demonstrated a good correlation between nigral status determined with SWI and the status of dopaminergic denervation revealed with ^{123}I -FP-CIT SPECT,^{5,7} the 2 methods lack absolute agreement. In addition, denervation can reportedly be observed on ^{123}I -FP-CIT SPECT, but nigral hyperintensity is maintained on MR imaging,^{5,7} possibly informing a false-negative diagnosis of PD. To the best of our knowledge, no study has evaluated the relationship between the degree of

Received June 15, 2021; accepted after revision October 21.

From the Departments of Radiology (Y.J.B., B.S.C., J.H.K.), Nuclear Medicine (Y.S.S., W.W.L.), and Neurology (J.-M.K., J.-H.C.), Seoul National University Bundang Hospital, Seoul National University College of Medicine, Seongnam, Korea; Division of Biomedical Engineering (Y.N.), Hankuk University of Foreign Studies, Gyeonggi-do, Korea; and Medical Research Center, Institute of Radiation Medicine (W.W.L.), Seoul National University, Seoul, Korea.

Y.J.B. and Y.S.S. contributed equally to the manuscript.

Source of Funding: This work was supported by a National Research Foundation of Korea (NRF) grant funded by the Korean government (MSIT) (No. 2019R1F1A1063771, 2019M3C7A1032718) and a grant (No. 09-2019-003) from the Seoul National University Bundang Hospital Research Fund.

Please address all correspondence to Jong-Min Kim, MD, PhD, Department of Neurology, Seoul National University Bundang Hospital, 173-82, Gumi-ro, Bundang-gu, Seongnam-si, Gyeonggi-do 463-707, Korea, e-mail: jongminl@snu.ac.kr

Indicates open access to non-subscribers at www.ajnr.org

<http://dx.doi.org/10.3174/ajnr.A6960>

dopaminergic denervation on ^{123}I -FP-CIT SPECT and the status of nigral hyperintensity on SWI.

The present study aims to determine the degree of the dopaminergic denervation on ^{123}I -FP-CIT SPECT according to the presence or loss of nigral hyperintensity on 3T MR imaging in patients with PD. We evaluated the striatal specific binding ratios (SBRs) of the ^{123}I -FP-CIT and used susceptibility map-weighted imaging (SMWI) to enhance the visibility of nigrosome-1.^{17,18} The purpose of this study was to correlate quantified dopamine transporter attenuation on SPECT with the status of nigral hyperintensity on MR imaging.

MATERIALS AND METHODS

This study was approved by the institutional review board of our institution (institutional review board no. B-1610-368-303). Informed consent was obtained from all study participants.

Patients and Clinical Assessment

Consecutive patients who visited our hospital with suspected parkinsonism were enrolled between May 2017 and January 2018. All patients were evaluated by a neurologist (J.-M.K.) with 17 years of experience in diagnosing and treating patients with movement disorders, and the patients who were clinically diagnosed with de novo idiopathic PD were included in this study. Clinical diagnoses of idiopathic PD were made in accordance with UK Parkinson's Disease Society Brain Bank clinical diagnostic criteria, including bradykinesia and at least 1 of muscular rigidity, resting tremor and postural instability, and clinical findings.¹⁹ The exclusion and the supporting criteria were also followed.¹⁹ Cognition was assessed with the Mini-Mental State Examination (MMSE)²⁰ and the Montreal Cognitive Assessment (MoCA),²¹ and motor functioning was assessed with the Unified Parkinson's Disease Rating Scale-III (UPDRS-III) scores²² and Hoehn and Yahr scales.²³ All patients underwent both ^{123}I -FP-CIT SPECT and 3T SWI within a maximum period of 3 months. The clinical diagnosis of PD was consolidated by the results of the ^{123}I -FP-CIT SPECT, 3T MR imaging, and follow-up. Patients were excluded if they were diagnosed with atypical parkinsonism including multiple system atrophy or progressive supranuclear palsy, normal-pressure hydrocephalus, or idiopathic REM sleep behavior disorder or if more than 3 months elapsed between the ^{123}I -FP-CIT SPECT and SWI. Particularly, the patients who were compatible with idiopathic REM sleep behavior disorder according to the corresponding diagnostic criteria²⁴ and polysomnographic examination were excluded. The patients whose SWI was unsuitable for the reconstruction of SMWI because of severe motion artifact were excluded as well. Last, the patients who demonstrated any ischemic lesions on the striatum and occipital cortex on MR imaging were excluded to avoid false-positive result from ^{123}I -FP-CIT SPECT. During the study period, the participants who did undergo neurologic examination, ^{123}I -FP-CIT SPECT, and 3T SWI with suspicion of parkinsonism but who were not diagnosed with idiopathic PD after work-up were enrolled as a control group. The control group was composed of the participants who were diagnosed with frontal gait disorder, essential tremor, and drug-induced parkinsonism. Clinical diagnoses of respective diseases were made according to the established diagnostic criteria²⁵⁻²⁷ and

the results of ^{123}I -FP-CIT SPECT visual inspection. The patients who were suspected to have idiopathic REM sleep behavior disorder²⁴ and the patients who demonstrated striatal or occipital cortical ischemic lesions on MR imaging were excluded from the study.

^{123}I -FP-CIT SPECT

Patients were orally administered 6 mL of Lugol solution before receiving the ^{123}I -FP-CIT injection. Scans were acquired 3 hours after the IV injection of 185 MBq of ^{123}I -FP-CIT (DATrace- ^{123}M , Samyoung Unitech). Scans were performed with a triple-headed rotating gamma camera system (Trionix XLT, Trionix Research Laboratory) with low-energy, ultra-resolution, parallel hole collimators. Scans were in 40 steps spanning 120°, with 40 seconds per step, via the step-and-shoot method. Image reconstruction was performed by filtered back-projection with a Butterworth filter (cutoff frequency 0.4 cycle/cm; order, 13), and attenuation correction with the Chang method (coefficient of 0.12/cm). A nuclear medicine physician (Y.S.S.) with 15 years of experience visually interpreted the ^{123}I -FP-CIT SPECT results. The reader was blinded to the clinical information and the MR imaging finding at the time of the interpretation. The interpretation of SPECT results for the diagnosis was done by visual inspection. For the quantification analysis, images were analyzed with a dedicated software program (DATquant with the software package Xeleris 3.1, GE Healthcare). VOIs were defined automatically with DATquant over the striatum (caudate nucleus and putamen), caudate nucleus, putamen, and occipital cortex. The SBRs of the striatal regions were calculated as follows: (mean counts in striatal regions – mean counts in the occipital cortex)/(mean counts in the occipital cortex).

SWI Protocol and SMWI Processing

SWI was obtained using a 3T MR imaging scanner (Ingenia, Philips) with a 32-channel SENSE head coil (Philips Healthcare). To observe the nigrosome-1 structure, the imaging plane was oriented perpendicular to the midbrain structure. All SWI procedures were conducted using a 3D multiecho fast-field-echo sequence with the following parameters: TR, 88 msec; total 5 echoes; first TE, 10 msec; echo interval, 10 msec; flip angle, 10°; FOV, 192 × 192 mm²; voxel size, 0.5 × 0.5 × 1 mm².

After SWI acquisition, SMWI was generated from the SWI protocol by combining the magnitude images and quantitative susceptibility mapping mask images to enhance the visibility of nigrosome-1.^{17,18} The reconstruction of SMWI was performed following a previously reported protocol.¹⁷

SMWI Analysis

Blinded to the clinical diagnosis and ^{123}I -FP-CIT SPECT findings, 2 neuroradiologists (Y.J.B. and B.S.C., with 10 and 20 years of experience, respectively) independently evaluated the status of the bilateral striatal nigral hyperintensity on the generated SMWI. The normal nigral hyperintensity was defined as a focal oval or linear hyperintense area in the dorsolateral aspect of the SN surrounded by hypointensity.^{5,6,10-12,17,28} The right and left sides were read separately in each participant. After completing 2 independent readings, all discrepancies between the 2 raters were resolved by consensus.

Table 1: Clinical characteristics

	Control Participants (n = 29)	Patients with PD (n = 109)	P Value
Age (years, mean ± SD)	71.8 ± 8.2	67.7 ± 9.2	.075
Sex (n, M:F)	5:24	51:58	.005 ^a
Clinical scores of the PD group			
MMSE (mean ± SD)	26.9 ± 2.4	26.8 ± 6.7	.921
MoCA (mean ± SD)	23.3 ± 2.8	22.9 ± 5.4	.704
UPDRS-III (mean ± SD)	16.7 ± 9.1	17.7 ± 9.2	.597
Hoehn and Yahr scale (mean ± SD)	2.0 ± 0.7	2.1 ± 0.7	.899

^a P values < .05 indicate statistical significance.

Table 2: Nigral hyperintensity on SMWI according to clinical diagnosis

	Control Participants (n = 29)	Patients with PD (n = 109)	P Value
Bilateral presence	26	36	< .001 ^a
Unilateral loss	1	17	
Bilateral loss	2	56	

^a P values < .05 indicate statistical significance.

Statistical Analysis

Demographic data and clinical scores were compared using the Fisher exact test, chi-square test, Student *t* test, and Kruskal-Wallis test. Interobserver agreement concerning the nigral hyperintensity on SMWI was tested using the Cohen κ , with $\kappa > 0.75$, excellent agreement; $\kappa = 0.40$ – 0.75 , fair to good agreement; and $\kappa < 0.40$, poor agreement.²⁹ The diagnostic performance of SMWI was calculated presuming that the loss of unilateral or bilateral nigral hyperintensity on SMWI indicated PD. The ¹²³I-FP-CIT SBRs were compared according to clinical diagnosis using the Student *t* test. The concordance rate between SMWI and ¹²³I-FP-CIT SPECT was then calculated, and the McNemar test was performed. The ¹²³I-FP-CIT SBR was compared according to the status of nigral hyperintensity in a region-based approach using the Student *t* test. Particularly in patients with PD, the clinical scores and the averaged bilateral ¹²³I-FP-CIT SBR were compared between those who showed intact bilateral nigral hyperintensities and those who did not on a per-patient basis as well. Last, the efficacy of using a threshold of the ¹²³I-FP-CIT SBR to determine the loss of nigral hyperintensity was evaluated using a receiver operating characteristic (ROC) curve analysis. P values < .05 were considered to indicate significant differences. All statistical analyses were performed using SPSS v. 25.0 (IBM) and MedCalc 17.9 (MedCalc).

RESULTS

Clinical Characteristics

A total of 138 patients (82 women and 56 men; mean age, 68.4 ± 9.2 years; age range, 42–87 years), including 109 patients with PD and 29 control participants (frontal gait disorder, *n* = 14; essential tremor, *n* = 12; drug-induced parkinsonism, *n* = 3), were included in this study. The demographic findings and clinical characteristics are summarized in Table 1.

Nigral Hyperintensity on SMWI and ¹²³I-FP-CIT SBR on SPECT According to Clinical Diagnosis

Interobserver agreement on the status of nigral hyperintensity between the 2 readers was excellent for both the right ($\kappa = 0.91$; 95% CI, 0.846–0.981; agreement rate, 95.7%) and left sides ($\kappa = 0.97$; 95% CI, 0.931–1.000; agreement rate, 98.6%). According to the results from the consensus reading (Table 2), the use of unilateral or bilateral loss of the nigral hyperintensity on SMWI to diagnose PD achieved a sensitivity of 67.0%, specificity of 89.7%, positive predictive value of 96.1%,

negative predictive value of 41.9%, and accuracy of 71.7%. The results of visual inspection and ¹²³I-FP-CIT SBR analyzed according to the clinical diagnosis are present in Table 3.

Correlation Between Nigral Hyperintensity on SMWI and ¹²³I-FP-CIT SBR on SPECT

The status of nigral hyperintensity on SMWI and the result of visual inspection from ¹²³I-FP-CIT SPECT are presented in Table 4. When we matched the loss of nigral hyperintensity on SMWI with abnormal findings on ¹²³I-FP-CIT SPECT, the concordance rate was 65.2% and 66.7% for the right and left sides of the nigrostriatal tract, respectively. The overall concordance rate was 65.9% (Fig 1).

In a region-based comparison, the ¹²³I-FP-CIT SBRs measured in each right and left striatum, caudate nucleus, and putamen were significantly lower when the nigral hyperintensity in the SN on the same side was lost than when present (Table 5). On a per-patient basis, the averaged ¹²³I-FP-CIT SBRs in bilateral striatum, putamen, and caudate were all significantly lower in patients with PD those who presented unilateral or bilateral loss of nigral hyperintensity than those who presented bilateral intact nigral hyperintensity (Table 5). However, the clinical scores including MMSE (27.5 ± 7.34; 25.3 ± 2.66, *P* = .079), MoCA (23.06 ± 5.13; 22.47 ± 6.04, *P* = .642), UPDRS-III scores (18.37 ± 9.63; 16.20 ± 8.06, *P* = .251), and Hoehn and Yahr scale (2.02 ± 0.64; 2.02 ± 0.63, *P* = .971) did not differ significantly between both groups.

The ROC curve analysis revealed optimal threshold values of the ¹²³I-FP-CIT SBR for the determination of the loss of nigral hyperintensity on SMWI to be 2.56 in the striatum (area under the curve [AUC], 0.890; 95% CI, 0.847–0.924; *P* < .001; sensitivity, 85.1%; specificity, 80.2%), 3.07 in the caudate nucleus (AUC, 0.830; 95% CI, 0.780–0.872; *P* < .001; sensitivity, 69.4%; specificity, 78.8%), and 2.36 in the putamen (AUC, 0.887; 95% CI, 0.843–0.922; *P* < .001; sensitivity, 90.3%; specificity, 73.9%) (Fig 2).

DISCUSSION

The present study performed a correlation analysis between the SBR values of ¹²³I-FP-CIT SPECT and the presence of nigral hyperintensity. We have previously shown that the loss of nigral hyperintensity corresponds to dopaminergic denervation assessed with ¹²³I-FP-CIT SPECT image findings.⁵ In the current study, we have carefully included patients diagnosed with de novo PD and control participants according to the dedicated

Table 3: ¹²³I-FP-CIT SBR according to clinical diagnosis

	Control Participants (n = 29)	Patients with PD (n = 109)	P Value
Right striatum	4.04 ± 1.36	2.48 ± 0.94	< .001 ^a
Left striatum	4.0 ± 1.3	2.45 ± 0.88	< .001 ^a
Right caudate	4.34 ± 1.38	3.14 ± 1.18	< .001 ^a
Left caudate	4.32 ± 1.33	3.12 ± 1.16	< .001 ^a
Right putamen	3.95 ± 1.39	2.21 ± 0.89	< .001 ^a
Left putamen	3.85 ± 1.33	2.12 ± 0.82	< .001 ^a

^a P values < .05 indicate statistical significance.

Table 4: Nigral status on SMWI and visual inspection result on ¹²³I-FP-CIT SPECT

	¹²³ I-FP-CIT SPECT ^a			P Value	Concordance Rate (%)
	Abnormal	Normal	Total		
Right Side SMWI				< .001 ^b	65.2
Loss	64	3	67		
Present	45	26	71		
Total	109	29	138		
Left side SMWI				< .001 ^b	66.7
Loss	65	2	67		
Present	44	27	71		
Total	109	29	138		
Total SMWI				< .001 ^b	65.9
Loss	129	5	134		
Present	89	53	142		
Total	218	58	276		

Note:—Values are numbers of cases.

^a Abnormal finding on SPECT refers to the nigrostriatal dopaminergic denervation determined by a nuclear medicine physician.

^b P values < .05 indicate statistical significance.

clinical criteria with an aid from MR imaging and ¹²³I-FP-CIT SPECT. We also only included patients who did not take any medication that might affect the ¹²³I-FP-CIT SPECT findings, and we excluded patients who demonstrated pathologic findings such as ischemia in the striatum and occipital cortex on MR imaging to prevent possible false-positive SPECT findings. Thereby, we aimed to avoid possible confounders and to provide solid results for the determination of the ¹²³I-FP-CIT uptake level on the basis of the nigral status on MR imaging.

Presynaptic dopaminergic scans are considered more sensitive diagnostic indicators of PD than clinical examination.³⁰⁻³² We observed decreased ¹²³I-FP-CIT uptake in all the striatal regions of patients with PD and the loss of nigral hyperintensity on SMWI in 67% of patients. Moreover, our previous study of patients with idiopathic REM sleep behavior disorder showed that 61% exhibited the loss of nigral hyperintensity, which is a lower prevalence than among patients with PD.²⁸ Considering the fact that a substantial portion of patients with idiopathic REM sleep behavior disorder develop PD and >50% of the whole dopaminergic neurons are already lost during the prodromal stage of PD,³³⁻³⁵ the decrease of striatal FP-CIT binding might precede the loss of nigral hyperintensity in a sequential process, which is an important implication of our

present study because it suggests that the diagnosis of PD based only on the status of nigrosome-1 on MR imaging may result in a false-negative result.

Indeed, our result demonstrated that loss of nigral hyperintensity can strongly support the diagnosis of PD from its high positive predictive value, but intact nigral hyperintensity may not exclude PD because the negative predictive value was low. Therefore, we can suggest that further diagnostic procedures such as ¹²³I-FP-CIT SPECT might not be necessary in patients with the loss of nigral hyperintensity. On the contrary, normal nigral hyperintensity cannot rule out the diagnosis of PD, which may necessitate the further ¹²³I-FP-CIT SPECT evaluation for the concrete diagnosis. Thus, the assessment of nigral hyperintensity on SMWI could assist the diagnostic process of PD on a routine clinical basis.

In this regard, the determination of the quantified ¹²³I-FP-CIT uptake level on the basis of the nigral status on MR imaging can have an important clinical impact. Especially in the present study, we used SMWI to enhance the visibility of nigrosome-1 and to improve the detectability of the nigral hyperintensity. SMWI is a postgenerated image from conventional multiecho SWI. Specifically, a reconstruction algorithm generates a high susceptibility contrast between nigrosome-1 and the neighboring SN structures.^{17,18} Because it incorporates the information related to the iron overload in the SN by quantitative susceptibility mapping, SMWI significantly improves the detectability of nigral hyperintensity relative to the use of SWI alone and may thus increase the diagnostic accuracy for PD.¹⁷

Based on SMWI, we suggest threshold ¹²³I-FP-CIT SBRs of 2.56, 3.07, and 2.36 for determining the loss of nigral hyperintensity in the striatum, caudate nucleus, and putamen, respectively, with high diagnostic performance. The high threshold of the caudate nucleus relative to that of the putamen reflects the anteroposterior gradient of ¹²³I-FP-CIT binding in patients with PD.³⁶ However, the presently observed overlap between SBR values in the intact and the nonintact nigral hyperintensity groups suggests the presence of greater unexplainable causes of nigral hyperintensity loss during the progression of PD. Because the loss of nigral hyperintensity reflects the accumulation of iron in the SN, which is regulated by various genetic predispositions and environmental factors,³⁷ the lack of a direct correlation between iron accumulation and dopaminergic denervation may be 1 such cause.^{6,9}

Among the control participants, 3 of 29 participants, who were diagnosed with frontal gait disorder (*n* = 1) and essential tremor (*n* = 2), showed loss of nigral hyperintensity in 5 regions of the SN (2, bilateral loss; 1, unilateral loss). The mean putamenal SBRs of the 5 corresponding regions with loss of nigral hyperintensity were 1.6 ± 0.24, which were reduced to the level comparable to the patients with PD met in routine clinical practice (data

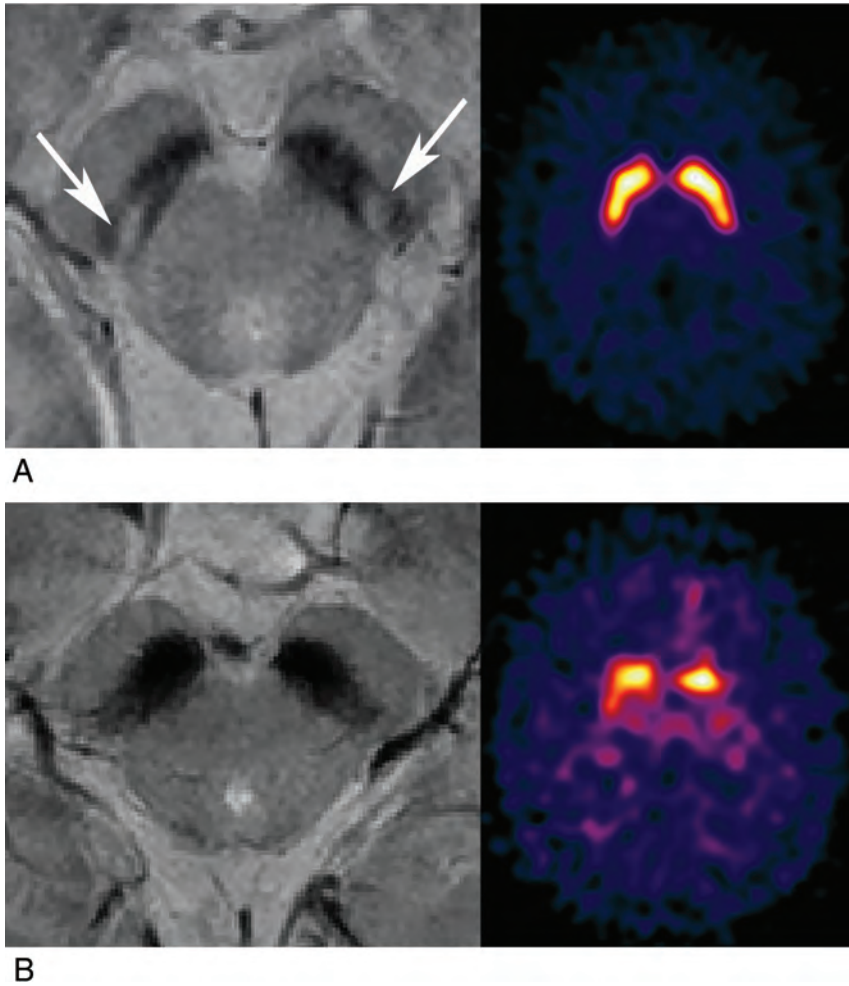


FIG 1. SMWI and accordant ^{123}I -FP-CIT SPECT findings. **A**, SMWI of a 56-year-old female control participant with intact bilateral striatal nigral hyperintensity (*white arrow*). The specific binding ratio values were 4.93 (*right*) and 5.01 (*left*) on ^{123}I -FP-CIT SPECT. **B**, SMWI of a 65-year-old male patient with PD and loss of bilateral striatal nigral hyperintensity. The SBR values were 1.25 (*right*) and 1.10 (*left*) on ^{123}I -FP-CIT SPECT.

not shown). Thus, we can speculate that the striatal SBRs on the same side of the SN that shows loss of nigral hyperintensity may be reduced compared with the normal side. We can also presume that the initial visual assessment of ^{123}I -FP-CIT SPECT of these patients was concluded as normal based on the bilateral symmetric ^{123}I -FP-CIT uptakes without anteroposterior gradients. These 3 participants still do not present parkinsonian features compatible with the clinical diagnostic criteria for PD during follow-up. Therefore, the interpretation of ^{123}I -FP-CIT SPECT should be cautiously performed while taking account of relevant practical issues for both visual assessment and quantitative analysis.³⁸

When defining a false-positive result as the absence of nigral hyperintensity on 3T SMWI on either side but with normal ^{123}I -FP-CIT findings, the false-positive rate was lower than that of diagnoses informed by SWI findings in a previous study.⁵ To date, it remains unclear whether iron accumulation is a primary initiating or secondary event of dopaminergic denervation.³⁹ However, because iron accumulation in the SN is known to increase with age⁴⁰ and most of the control participants showed intact nigral hyperintensity, we surmise that dopaminergic denervation precedes iron accumulation in the SN. Furthermore, the ^{123}I -FP-CIT SBRs in patients with PD who presented loss of nigral hyperintensity on at least 1 side of the SN were significantly lower than those of

Table 5: ^{123}I -FP-CIT SBRs according to the nigral hyperintensity status on SMWI

	Present	Lost	P Value
All patients			
Striatum	3.51 ± 1.15	2.03 ± 0.61	< .001 ^a
Caudate nucleus	4.01 ± 1.20	2.63 ± 0.92	< .001 ^a
Putamen	3.25 ± 1.21	1.76 ± 0.55	< .001 ^a
Patients with PD			
Striatum	3.08 ± 0.89	2.04 ± 0.62	< .001 ^a
Caudate nucleus	3.84 ± 1.09	2.64 ± 0.94	< .001 ^a
Putamen	2.73 ± 0.89	1.77 ± 0.56	< .001 ^a
Control participants			
Striatum	4.22 ± 1.88	1.88 ± 0.16	< .001 ^a
Caudate nucleus	4.50 ± 1.27	2.48 ± 0.35	< .001 ^a
Putamen	4.12 ± 1.20	1.60 ± 0.23	< .001 ^a
Per-patient basis analysis of the averaged SBRs among patients with PD	Bilateral intact nigral hyperintensity (n = 36)	Unilateral or bilateral loss of nigral hyperintensity (n = 73)	P Value
Striatum	3.16 ± 0.90	2.13 ± 0.63	< .001 ^a
Caudate nucleus	3.89 ± 1.10	2.76 ± 0.95	< .001 ^a
Putamen	2.81 ± 0.88	1.84 ± 0.55	< .001 ^a

^a P values < .05 indicate statistical significance.

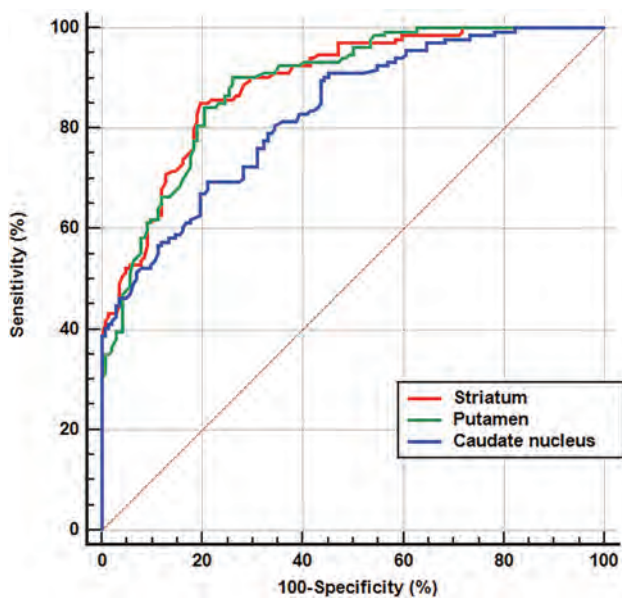


FIG 2. ROC curves for determining the loss of nigral hyperintensity on SMWI using the ^{123}I -FP-CIT SBRs. ROC curves used for determining the loss of nigral hyperintensity with ^{123}I -FP-CIT SBRs measured in the striatum (red), putamen (green), and caudate nucleus (blue) are shown. The detailed data are presented in the Results section.

patients who presented intact bilateral nigral hyperintensity, but the clinical scores between the 2 groups did not differ significantly. Based on this result, we can assume that patients with PD may present normal bilateral nigral hyperintensity when SBRs on ^{123}I -FP-CIT SPECT are slightly decreased, and the nigral hyperintensity becomes lost with further decrease in SBRs. This hypothesis requires investigation by future research.

In our study, we only adopted the qualitative visual assessment for SMWI without quantitative measurement of nigral hyperintensity or susceptibility. A recent study has adopted the quantitative analytic method for nigrosome-1,⁴¹ but the result was preliminary, and the quantitative measurement is not yet widely applied in the clinical practice. Moreover, there has been no study on the precise segmentation of the nigrosome on SMWI, which is the essential prerequisite for correct quantification. Thus, further study for the standardized quantification method for nigrosome-1 is warranted.

Our study has several limitations. First, our PD group lacked the inclusion of participants in either the prodromal or late phases. Because the neurodegenerative process of PD occurs across decades, this omission precluded the elucidation of a more specific relationship between dopaminergic denervation and the loss of nigral hyperintensity. Second, the number of control participants was rather small compared with the number of patients with PD. However, because we included the control participants who underwent both ^{123}I -FP-CIT SPECT and 3T SWI, the number of control participants was unavoidably small. Third, because we focused on visual determination of the nigral hyperintensity, we did not perform quantitative susceptibility analysis of SMWI data. For quantitative analysis, further study on the segmentation of the nigrosome on SMWI is needed. Based on this established method, future studies of the susceptibility quantification in nigrosome-1 on SMWI in correlation with ^{123}I -FP-CIT SBRs are

warranted. Fourth, the diagnostic performances of SMWI for PD in our study were different from those in the previous studies using SWI.^{13,42} This is probably because of the enhanced visibility of nigrosome-1 on SMWI with higher contrast-to-noise ratio than SWI, which may contribute to the higher specificity and positive predictive value of our study. In addition, the differences in the study population and MR imaging protocol between the studies could be another factor resulting in the difference in diagnostic performance. Future multicenter studies with a larger number of patients will be needed to set the optimized imaging protocol for nigrosome-1 assessment.

CONCLUSIONS

Nigral hyperintensity on SMWI showed good concordance with dopaminergic degeneration on ^{123}I -FP-CIT SPECT in patients with PD and control participants. In the PD group, the loss of nigral hyperintensity was dependent on the SBR values of ^{123}I -FP-CIT images. Our results thus suggest that dopaminergic denervation and the loss of nigral hyperintensity might occur in a sequential manner. Future studies on the correlation of clinical characteristics and nigral hyperintensity may help overcome the limitations of ^{123}I -FP-CIT to predict disease severity.⁴³

ACKNOWLEDGMENTS

We thank Editage (www.editage.co.kr) for English language editing. We thank the Medical Research Collaborating Center at Seoul National University Bundang Hospital for consultation on the statistical analyses.

Disclosures: Yun Jung Bae—RELATED: Grant: National Research Foundation of Korea (NRF) grants funded by the Korean government (MSIT) (No. 2019R1F1A1063771, 2019M3C7A1032718) and a grant (No. 09-2019-003) from the Seoul National University Bundang Hospital Research Fund, Comments: These grants provided only financial support. These funding sources have been described in the title page of manuscript.* *Money paid to institution

REFERENCES

1. Davie CA. A review of Parkinson's disease. *Br Med Bull* 2008;86:109–27 CrossRef Medline
2. Poewe W, Seppi K, Tanner CM, et al. Parkinson disease. *Nat Rev Dis Primers* 2017;3:17013 CrossRef Medline
3. Damier P, Hirsch EC, Agid Y, et al. The substantia nigra of the human brain. II. Patterns of loss of dopamine-containing neurons in Parkinson's disease. *Brain* 1999;122:(Pt)1437–48 CrossRef Medline
4. Damier P, Hirsch EC, Agid Y, et al. The substantia nigra of the human brain. I. Nigrosomes and the nigral matrix, a compartmental organization based on calbindin D(28K) immunohistochemistry. *Brain* 1999;122:1421–36 CrossRef Medline
5. Bae YJ, Kim JM, Kim E, et al. Loss of nigral hyperintensity on 3 Tesla MRI of Parkinsonism: comparison with (123) I-FP-CIT SPECT. *Mov Disord* 2016;31:684–92 CrossRef Medline
6. Cosottini M, Frosini D, Pesaresi I, et al. Comparison of 3T and 7T susceptibility-weighted angiography of the substantia nigra in diagnosing Parkinson disease. *AJNR Am J Neuroradiol* 2015;36:461–66 CrossRef Medline
7. Kim JM, Jeong HJ, Bae YJ, et al. Loss of substantia nigra hyperintensity on 7 Tesla MRI of Parkinson's disease, multiple system atrophy, and progressive supranuclear palsy. *Parkinsonism Relat Disord* 2016;26:47–54 CrossRef Medline

8. Kwon DH, Kim JM, Oh SH, et al. **Seven-Tesla magnetic resonance images of the substantia nigra in Parkinson disease.** *Ann Neurol* 2012;71:267–77 CrossRef Medline
9. Lehericy S, Bardinet E, Poupon C, et al. **7 Tesla magnetic resonance imaging: a closer look at substantia nigra anatomy in Parkinson's disease.** *Mov Disord* 2014;29:1574–81 CrossRef Medline
10. Noh Y, Sung YH, Lee J, et al. **Nigrosome 1 detection at 3T MRI for the diagnosis of early-stage idiopathic Parkinson disease: assessment of diagnostic accuracy and agreement on imaging asymmetry and clinical laterality.** *AJNR Am J Neuroradiol* 2015;36:2010–16 CrossRef Medline
11. Reiter E, Mueller C, Pinter B, et al. **Dorsolateral nigral hyperintensity on 3.0T susceptibility-weighted imaging in neurodegenerative Parkinsonism.** *Mov Disord* 2015;30:1068–76 CrossRef Medline
12. Schwarz ST, Afzal M, Morgan PS, et al. **The “swallow tail” appearance of the healthy nigrosome—a new accurate test of Parkinson's disease: a case-control and retrospective cross-sectional MRI study at 3T.** *PLoS One* 2014;9:e93814 CrossRef Medline
13. Mahlknecht P, Krismer F, Poewe W, et al. **Meta-analysis of dorsolateral nigral hyperintensity on magnetic resonance imaging as a marker for Parkinson's disease.** *Mov Disord* 2017;32:619–23 CrossRef Medline
14. Seibyl JP, Kupsch A, Booij J, et al. **Individual-reader diagnostic performance and between-reader agreement in assessment of subjects with Parkinsonian syndrome or dementia using 123I-ioflupane injection (DaTscan) imaging.** *J Nucl Med* 2014;55:1288–96 CrossRef Medline
15. Suwijn SR, van Boheemen CJ, de Haan RJ, et al. **The diagnostic accuracy of dopamine transporter SPECT imaging to detect nigrostriatal cell loss in patients with Parkinson's disease or clinically uncertain parkinsonism: a systematic review.** *EJNMMI Res* 2015;5:12 CrossRef Medline
16. Tatsch K, Poepperl G. **Nigrostriatal dopamine terminal imaging with dopamine transporter SPECT: an update.** *J Nucl Med* 2013;54:1331–8 CrossRef Medline
17. Nam Y, Gho SM, Kim DH, et al. **Imaging of nigrosome 1 in substantia nigra at 3T using multiecho susceptibility map-weighted imaging (SMWI).** *J Magn Reson Imaging* 2017;46:528–36 CrossRef Medline
18. Gho SM, Liu C, Li W, et al. **Susceptibility map-weighted imaging (SMWI) for neuroimaging.** *Magn Reson Med* 2014;72:337–46 CrossRef Medline
19. Hughes AJ, Daniel SE, Kilford L, et al. **Accuracy of clinical diagnosis of idiopathic Parkinson's disease: a clinico-pathological study of 100 cases.** *J Neurol Neurosurg Psychiatry* 1992;55:181–84 CrossRef Medline
20. Shulman KI, Herrmann N, Brodaty H, et al. **IPA survey of brief cognitive screening instruments.** *Int Psychogeriatr* 2006;18:281–94 CrossRef Medline
21. Nasreddine ZS, Phillips NA, Bedirian V, et al. **The Montreal Cognitive Assessment, MoCA: a brief screening tool for mild cognitive impairment.** *J Am Geriatr Soc* 2005;53:695–99 CrossRef Medline
22. Goetz CG, Tilley BC, Shaftman SR, Movement Disorder Society UPDRS Revision Task Force, et al. **Movement Disorder Society-sponsored revision of the Unified Parkinson's Disease Rating Scale (MDS-UPDRS): scale presentation and clinimetric testing results.** *Mov Disord* 2008;23:2129–70 CrossRef Medline
23. Hoehn MM, Yahr MD. **Parkinsonism: onset, progression, and mortality. 1967.** *Neurology* 2001;57:S11–S26 Medline
24. American Academy of Sleep M. **International Classification of Sleep Disorders. Diagnostic and Coding Manual 2005** 51–55
25. Pirker W, Katzenschlager R. **Gait disorders in adults and the elderly: a clinical guide.** *Wien Klin Wochenschr* 2017;129:81–95 CrossRef Medline
26. Elble RJ. **Diagnostic criteria for essential tremor and differential diagnosis.** *Neurology* 2000;54:S2–S6 Medline
27. Shin HW, Chung SJ. **Drug-induced parkinsonism.** *J Clin Neurol* 2012;8:15–21 CrossRef Medline
28. Bae YJ, Kim JM, Kim KJ, et al. **Loss of substantia nigra hyperintensity at 3.0-T MR imaging in idiopathic REM sleep behavior disorder: comparison with (123)I-FP-CIT SPECT.** *Radiology* 2018;287:285–93 CrossRef Medline
29. Senn S. **Review of Fleiss, statistical methods for rates and proportions.** *Res Synth Methods* 2011;2:221–22 CrossRef Medline
30. Sommer U, Hummel T, Cormann K, et al. **Detection of presymptomatic Parkinson's disease: combining smell tests, transcranial sonography, and SPECT.** *Mov Disord* 2004;19:1196–202 CrossRef Medline
31. Jennings D, Siderowf A, Stern M, PARS Investigators, et al. **Imaging prodromal Parkinson disease: the Parkinson associated risk syndrome study.** *Neurology* 2014;83:1739–46 CrossRef Medline
32. Moccia M, Pappata S, Picillo M, et al. **Dopamine transporter availability in motor subtypes of de novo drug-naïve Parkinson's disease.** *J Neurol* 2014;261:2112–8 CrossRef Medline
33. Postuma RB, Gagnon JF, Bertrand JA, et al. **Parkinson risk in idiopathic REM sleep behavior disorder: preparing for neuroprotective trials.** *Neurology* 2015;84:1104–13 CrossRef Medline
34. Haas BR, Stewart TH, Zhang J. **Premotor biomarkers for Parkinson's disease—a promising direction of research.** *Transl Neurodegener* 2012;1:11 CrossRef Medline
35. Fearnley JM, Lees AJ. **Ageing and Parkinson's disease: substantia nigra regional selectivity.** *Brain* 1991;114:2283–301 CrossRef Medline
36. Oh M, Kim JS, Kim JY, et al. **Subregional patterns of preferential striatal dopamine transporter loss differ in Parkinson disease, progressive supranuclear palsy, and multiple-system atrophy.** *J Nucl Med* 2012;53:399–406 CrossRef Medline
37. Berg D, Hochstrasser H. **Iron metabolism in Parkinsonian syndromes.** *Mov Disord* 2006;21:1299–310 CrossRef Medline
38. Marek K, Seibyl J, Eberly S, et al. Parkinson Study Group PRECEPT Investigators. **Longitudinal follow-up of SWEDD subjects in the PRECEPT Study.** *Neurology* 2014;82:1791–97 CrossRef Medline
39. Rhodes SL, Ritz B. **Genetics of iron regulation and the possible role of iron in Parkinson's disease.** *Neurobiol Dis* 2008;32:183–95 CrossRef Medline
40. Zecca L, Stroppolo A, Gatti A, et al. **The role of iron and copper molecules in the neuronal vulnerability of locus coeruleus and substantia nigra during aging.** *Proc Natl Acad Sci U S A* 2004;101:9843–48 CrossRef Medline
41. Cheng Z, Zhang J, He N, et al. **Radiomics features of the nigrosome-1 region of the substantia nigra: Using quantitative susceptibility mapping to assist the diagnosis of idiopathic Parkinson's disease.** *Front Aging Neurosci* 2019;11:167 CrossRef Medline
42. Lee J, Lee AL, Park J-H, et al. **The clinical application of nigrosome 1 detection on high-resolution susceptibility-weighted imaging in the evaluation of suspected Parkinsonism: the real-world performance and pitfalls.** *PLoS One* 2020;15:e0231010 CrossRef Medline
43. Hubbich M, Farmakis G, Schaefer A, et al. **FP-CIT SPECT does not predict the progression of motor symptoms in Parkinson's disease.** *Eur Neurol* 2011;65:187–92 CrossRef Medline

Microstructural Tissue Changes in Alzheimer Disease Brains: Insights from Magnetization Transfer Imaging

I. Colonna, M. Koini, L. Pirpamer, A. Damulina, E. Hofer, P. Schwingenschuh, C. Enzinger, R. Schmidt, and S. Ropele



ABSTRACT

BACKGROUND AND PURPOSE: Reductions in magnetization transfer ratio have been associated with brain microstructural damage. We aim to compare magnetization transfer ratio in global and regional GM and WM between individuals with Alzheimer disease and healthy control participants to analyze the relationship between magnetization transfer ratio and cognitive functioning in Alzheimer disease.

MATERIALS AND METHODS: In this prospective study, participants with Alzheimer disease and a group of age-matched healthy control participants underwent clinical examinations and 3T MR imaging. Magnetization transfer ratios were determined in the cortex, AD-signature regions, normal-appearing WM, and WM hyperintensities.

RESULTS: Seventy-seven study participants (mean age \pm SD, 72 ± 8 years; 47 female) and 77 age-matched healthy control participants (mean age \pm SD, 72 ± 8 years; 44 female) were evaluated. Magnetization transfer ratio values were lower in patients with Alzheimer disease than in healthy control participants in all investigated regions. When adjusting for atrophy and extent of WM hyperintensities, significant differences were seen in the global cortex (OR = 0.47; 95% CI: 0.22, 0.97; $P = .04$), in Alzheimer disease–signature regions (OR = 0.31; 95% CI: 0.14, 0.67; $P = .003$), in normal-appearing WM (OR = 0.59; 95% CI: 0.39, 0.88; $P = .01$), and in WM hyperintensities (OR = 0.18; 95% CI: 0.09, 0.33; $P \leq .001$). The magnetization transfer ratio in these regions was an independent determinant of AD. When correcting for atrophy and WM hyperintensity extent, lower GM magnetization transfer ratios were associated with poorer global cognition, language function, and constructional praxis.

CONCLUSIONS: Alzheimer disease is associated with magnetization transfer ratio reductions in GM and WM regions of the brain. Lower magnetization transfer ratios in the entire cortex and AD-signature regions contribute to cognitive impairment independent of brain atrophy and WM damage.

ABBREVIATIONS: AD = Alzheimer disease; CERAD = Consortium to Establish a Registry for Alzheimer's Disease; MMSE = Mini-Mental State Examination; MTI = magnetization transfer imaging; MTR = magnetization transfer ratio; NAWM = normal-appearing white matter

Alzheimer disease (AD) represents the most common cause of dementia. Only a few neuroimaging biomarkers have been approved for clinical use, and most are still objects of research.¹ Although structural MR imaging contributes to the exclusion of other possible causes of a dementia syndrome, brain atrophy measures have only modest sensitivity and specificity for the differential diagnosis of dementia.² The role of

MR imaging techniques that allow assessment of microstructural brain changes, such as DTI and magnetization transfer imaging (MTI) for detecting AD-related tissue abnormalities, is still widely unknown. Numerous DTI studies have reported loss of WM integrity in AD and related this to tau accumulation in AD-specific regions.³ Only a few studies used MTI to explore microstructural tissue abnormalities in AD.

The magnetization transfer ratio (MTR), which can be derived from MTI, has been shown to be associated with axonal attenuation and myelin content.⁴⁻⁶ In patients with AD, MTR reductions were reported in the whole-brain analyses,⁷⁻⁹ cortical GM,^{8,10}

Received July 1, 2020; accepted after revision October 23.

From the Department of Neurology (I.C., M.K., L.P., A.D., P.S., C.E., R.S., S.R.); Institute for Medical Informatics, Statistics and Documentation (E.H.); and Division of Neuroradiology, Vascular & Interventional Radiology, Department of Radiology (C.E.), Medical University of Graz, Graz, Austria.

The work originated from the Department of Neurology, Medical University of Graz, Auenbruggerplatz 22, 8036 Graz, Austria.

This study was funded by the Austrian Science Fund (FWF grant No. I2889-B31) and the German Research Foundation (DF DU1626/1-1).

Previously presented at: 6th Congress of the European Academy of Neurology, virtual congress, May 23, 2020.

Please address all correspondence to Reinhold Schmidt, Auenbruggerplatz 22, 8036 Graz, Austria; e-mail: reinhold.schmidt@medunigraz.at

Indicates open access to non-subscribers at www.ajnr.org

Indicates article with online supplemental data.

<http://dx.doi.org/10.3174/ajnr.A6975>

global WM,¹⁰ hippocampus,^{7,11,12} and temporal lobes.⁸ In a longitudinal study of our own group, patients with AD had significantly lower global MTR values than control participants. MTR declined significantly over a follow-up period of 12 months and was paralleled by a brain tissue loss of 2.2% per year.¹³ So far, only a few studies have explored the association between regional MTR changes and cognition in patients with AD. Van der Flier et al⁹ reported a strong association between whole-brain MTR and global cognitive deterioration in patients with AD, but there was no significant relationship between regional MTR reductions and domain-specific cognitive impairment. In our previous study, we observed direct associations between MTR and Mini-Mental State Examination (MMSE) scores for the hippocampus, putamen, and thalamus. The relationship was stronger in the left than in the right hemisphere.¹³

Here we extend previous work by assessing the role of MTR reductions in the GM and WM in distinguishing patients with mild to moderate AD from healthy control participants, and we investigate their associations with cognitive decline independent of atrophy and WM damage.

MATERIALS AND METHODS

Study Participants

This prospective study included 77 participants with AD from the longitudinal cohort study Prospective Dementia Registry Austria (PRODEM),¹⁴ a multicenter study. Current study participants originate exclusively from the Graz center because it was the only center where an MTI sequence had been included in the MR imaging protocol. The study was approved by the ethics committee of the Medical University of Graz, and informed consent was signed by all participants or their caregivers. The data that support the findings of this study are available on request from the corresponding author (R.S.). Dementia was diagnosed according to the *Diagnostic and Statistical Manual of Mental Disorders-IV*¹⁵ and National Institute of Neurological and Communicative Disorders and Stroke and the Alzheimer's Disease and Related Disorders Association (NINCDS-ADRDA) criteria.¹⁶ The severity of dementia was determined according to the MMSE score, as previously described.¹⁷ A group of 77 age-matched healthy control participants was selected from the Austrian Stroke Prevention Study, a large prospective single-center longitudinal study of the healthy older adult population of the city of Graz, Austria, including individuals without neuropsychiatric disease randomly selected from the community register.¹⁸ All participants underwent a comprehensive clinical evaluation and 3T MR imaging on the same scanner with identical acquisition parameters. The cognitive function of the participants with AD was assessed with the MMSE¹⁹ and the Consortium to Establish a Registry for Alzheimer Disease (CERAD)²⁰ test battery.

Image Acquisition

MR imaging was performed on a 3T whole-body MR system (Tim Trio, Siemens) with a 12-channel head coil. The MR imaging protocol included a T2 FLAIR sequence (TR/TE/TI = 10,000/69/2500 ms, number of slices = 40, section thickness = 3 mm, in-plane resolution = 0.86 mm × 0.86 mm), a T2-weighted sequence with 2 echoes (TE1/TE2/TR = 10/72/

5260 ms, number of slices = 40, section thickness = 3 mm, in-plane resolution = 0.86 mm × 0.86 mm), and a 3D T1-weighted magnetization-prepared rapid acquisition of gradient echo sequence with whole-brain coverage (TR/TE/TI = 1900/2.19/900 ms, flip angle = 9°, isotropic resolution = 1 mm).

Additionally, MTI was performed with a spoiled 3D gradient-echo sequence (TR/TE = 40/7.38 ms, flip angle = 15°, number of slices = 40, section thickness = 3 mm, in-plane resolution = 0.86 mm × 0.86 mm), which was performed twice, with and without a Gaussian-shaped radiofrequency saturation prepulse.

Image Processing

MTR maps were calculated according to the formula $MTR = (Mo - Mss) / Mo$, in which Mss and Mo are the signal intensities obtained with and without MT saturation, respectively. For regional assessment of MTR values, the cortical structures were segmented fully automated using FreeSurfer (version 5.3; <http://surfer.nmr.mgh.harvard.edu>). The technical details of these procedures are described elsewhere.^{21,22} The volumes of all segmented structures were normalized by the estimated total intracranial volume. A visual quality check was done for each case using an in-house developed bash-script based tool, which provides a graphic summary of the segmentations, overlaid on the T1-weighted image. Of all segmentations provided by FreeSurfer, we analyzed 6 ROIs (AD-signature regions) that were previously identified as sensitive to early effects of AD.²³ These regions included the hippocampus, parahippocampal cortex, cuneus, precuneus, entorhinal cortex, and inferior parietal lobule.

After affine registration with the T1-weighted scan using FSL FLIRT (version 6; <https://fsl.fmrib.ox.ac.uk/fsl/fslwiki/FLIRT>), regional masks were overlaid on the MT-weighted images. To identify and exclude CSF-contaminated voxels in the registered cortical masks, we performed a mask-segmentation optimization using a semiquantitative T2 map,²⁴ which was calculated from the mono-exponential decay of both echoes of the T2-weighted sequence and registered to the T1 sequence. After a histogram analysis of the T2 map for each brain-lobe mask, voxel intensities above the full width at half maximum of the histogram peak were defined as CSF-contaminated voxels and were therefore excluded from further analyses. Finally, median MTR values were extracted from the CSF-corrected brain lobes using FSLSTATS (<https://fsl.fmrib.ox.ac.uk/fsl/fslwiki/Fslutils>). To assess binary masks of WM hyperintensities, we segmented hyperintense T2 lesions on the FLAIR images with an in-house-developed semiautomatic region-growing tool.²⁵ A normal-appearing white matter (NAWM) mask was calculated by subtracting the manually segmented WM hyperintensity masks from the total WM mask obtained by FreeSurfer. The extent of WM hyperintensity was assessed according to the Fazekas scale.²⁶

Statistical Analysis

For data analysis, we used SPSS (version 23; IBM). Assumptions of normal distribution were tested with the Kolmogorov-Smirnov test. For bivariate correlations, we performed the Pearson test and a paired *t* test, and in case of non-normally distributed samples, a Wilcoxon signed-rank test was used to compare the 2 groups. Z-scores were computed for raw scores of

MTR and normalized volumes, and they were used in the regression analyses. Logistic regression analyses were performed to correlate the diagnosis of AD with MTR metrics in the global cortex, AD-signature regions, NAWM, and WM hyperintensities. To assess the associations between MTRs and performance on the MMSE and on CERAD, linear regressions were calculated with cognition as the dependent variable and MTR as the predictor variable. All models were adjusted for age, sex, years of education, normalized regional volumes, and Fazekas score. Brain volume and Fazekas score were considered as covariates to determine if MTRs relate to AD and to cognitive impairment independent of atrophy and extent of WM hyperintensities. For each regression coefficient, the 95% confidence interval and the *P* value were determined. A *P* value <.05 was considered statistically significant.

RESULTS

Participant Characteristics

A total of 156 individuals with dementia were confirmed eligible and recruited in the longitudinal cohort study PRODEM in Graz.

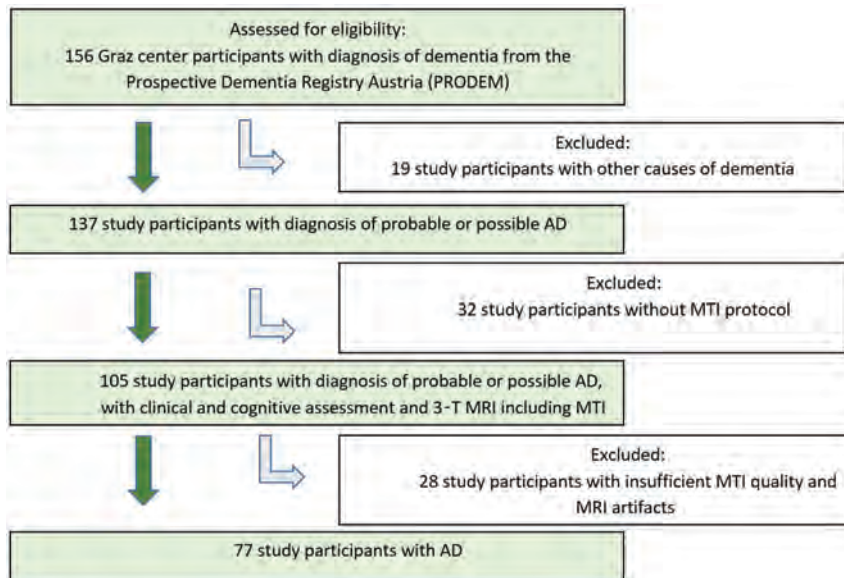


FIG 1. Flowchart shows the recruitment of the study participants with AD.

We excluded 19 participants who were affected by other causes of dementia and 60 individuals who had not undergone a MR imaging examination with sufficient MTI quality (Fig 1). Seventy-seven study participants with AD were included in our study. They were 30 men and 47 women with a mean age of 72 ± 8 years, ranging from 51 to 87 years. Fifty-five patients had mild AD (MMSE score: range 21–28, mean \pm SD: 23.98 ± 2.13), and 22 patients were diagnosed with moderate to severe AD (MMSE score: range 14–20, mean \pm SD: 17.14 ± 1.86). Seventy-seven healthy age-matched individuals (± 1 year) served as control participants. Their mean age was also 72 ± 8 years, ranging from 51 to 87 years. All control participants had MMSE scores ≥ 24 with the exception of 3 individuals who had MMSE scores of 23. None of the control participants had symptoms of dementia or mild cognitive impairment. The comparison of demographics, neuropsychological findings, and MR imaging findings between AD and healthy control participants are displayed in Table 1. Whereas the distribution of sex was similar in both investigational subsets (*P* = .62), the study participants with AD performed significantly worse on the MMSE (*P* < .001), had lower GM (*P* < .001) and NAWM (*P* = .01) volumes, and had higher WM hyperintensity volumes (*P* = .02). A higher grade of chronic small-vessel disease, indicated by Fazekas grade 2 or 3, was present in the 63.7% of the patients with AD and in the 40.3% of the healthy control participants.

Comparison of MTR Between Patients with AD and Healthy Control Participants

The study participants with AD had lower MTR values in the GM (*P* < .001), NAWM (*P* = .003), and WM hyperintensities (*P* < .001) (Table 1). Logistic regression analyses demonstrated that lower MTR values in global cortex (OR = 0.47; 95% CI: 0.22, 0.97; *P* = .04), AD-signature regions (OR = 0.31; 95% CI: 0.14,

Table 1: Demographic, neuropsychological, and MR imaging findings of study participants

Study Participant Characteristic	AD (n = 77)	Healthy Control Participants (n = 77)	<i>P</i> Value ^b
No. female (%)	47 (61)	44 (57)	.62
Age, years, ^a	72 (8)	72 (8)	.98
Age range, years	51–87	51–87	
MMSE ^a	22.03 (3.72)	27.57 (1.75)	<.001
Global cortex volume, cm ^{3a}	329.63 (14.53)	394.04 (41.25)	<.001
AD-signature regions volume, cm ^{3a}	54.81 (10.15)	70.28 (8.86)	<.001
Global NAWM volume, cm ^{3a}	305.77 (63.71)	334.70 (52.52)	.01
WM hyperintensities volume, cm ^{3a}	16.19 (17.69)	11.64 (18.01)	.02
Fazekas grade 2 or 3, no. (%)	49 (63.7)	31 (40.3)	
Global cortex MTRs ^a	0.295 (0.016)	0.309 (0.008)	<.001
AD-signature regions MTRs ^a	0.297 (0.018)	0.309 (0.009)	<.001
Global NAWM MTRs ^a	0.384 (0.009)	0.388 (0.009)	.003
WM hyperintensities MTRs ^a	0.322 (0.028)	0.350 (0.016)	<.001

^a Data are mean \pm SDs.

^b Pearson χ^2 for nominal, Wilcoxon, and paired *t* test for continuous variables were applied.

0.67; $P = .003$), NAWM (OR = 0.59; 95% CI: 0.39, 0.88; $P = .01$), and WM hyperintensities (OR = 0.18; 95% CI: 0.09, 0.33; $P \leq .001$) remained significantly related to AD even after correction for age, sex, and years of education as well as brain atrophy and extent of WM hyperintensities (Table 2). When considering the AD-signature regions individually, we found that decreased MTR values in the parahippocampal cortex (OR = 0.61; 95% CI: 0.37, 0.99; $P = .04$), cuneus (OR = 0.26; 95% CI: 0.09, 0.73; $P = .01$), precuneus (OR = 0.24; 95% CI: 0.12, 0.45; $P \leq .001$), and entorhinal cortex (OR = 0.57; 95% CI: 0.35, 0.95; $P = .03$) were associated with AD diagnosis (Online Supplemental Data). Furthermore, we found that reduced MTRs in NAWM and WM hyperintensities were related to AD independent of dementia severity; by contrast, in only the patients with mild AD, lower MTRs in the AD-signature regions (OR = 0.38, 95% CI: 0.17, 0.82; $P = .02$) were associated with AD.

MTR and Cognition in AD

Table 3 displays the associations between MTRs and cognitive functioning in the AD cohort. Only GM MTRs were significantly related to cognitive measures; no such relationship existed for WM MTRs. When adjusting for age, sex, education, normalized regional volume, and Fazekas score, lower MTRs in the global cortex were related to lower scores on the language subtest of the CERAD test battery ($\beta = 0.31$, $P = .02$). Only a nonsignificant trend was seen for the association between cortical MTR and MMSE and between global MTRs in the AD-signature regions and poorer performance on CERAD subtests for language function and constructional praxis. However, when considering the AD-signature regions individually, lower MTRs in the cuneus ($\beta = 0.30$; 95% CI: 0.26, 1.95; $P = .01$) and hippocampus ($\beta = 0.29$; 95% CI: 0.03, 2.22; $P = .04$) were significantly related to a poorer performance on the MMSE. With regard to the CERAD test, reduced MTRs in the parahippocampal cortex ($\beta = 0.38$; 95% CI: 0.28, 1.41; $P = .006$), cuneus ($\beta = 0.45$; 95% CI: 0.51, 1.56; $P \leq .001$), and entorhinal cortex ($\beta = 0.35$; 95% CI: 0.25,

1.28; $P = .004$) were associated with worse constructional praxis (Online Supplemental Data). There existed no significant associations with other CERAD subtests. No effect of laterality on the MTR correlations with poor language function was found (data not shown).

DISCUSSION

Our study shows lower MTRs in cortical and subcortical structures, including AD-signature regions, in NAWM, and WM hyperintensities in patients with AD. Lower WM MTRs were related to AD diagnosis in patients with both mild and moderately severe AD. However, MTRs in the AD-signature regions were related to AD diagnosis only in study participants with mild disease. One explanation for these discrepant associations between GM MTRs in mild versus moderately severe AD might be that GM microstructural changes are indeed an early disease phenomenon. Yet we cannot exclude that the small sample size of patients with severe disease and resulting low statistical power are responsible for the lack of a significant association between MTR in GM regions and AD diagnosis. With regard to cognition, only GM but none of the WM MTR measures were related to cognitive functioning in patients with AD. The effects of MTR reductions in the cortex and in the AD-signature regions on global cognition, language function, and constructional praxis were modest, but they were independent of brain atrophy and WM damage. Previous work also reported reduced MTRs in the cortex,^{8,10} hippocampus,^{7,27} and WM^{10,28} in AD. So far, only a limited number of studies have examined the relationship between MTR values and cognition in individuals with AD.^{7,9,10,29} In the current work, reduced MTRs in the GM were associated with worse global cognition, language function, and constructional praxis. Van der Flier et al⁹ reported an association between poorer cognitive performance and lower peak heights of the MTR histograms in the whole brain and frontal and temporal lobes. Here we extend this previous study by demonstrating that the association between MTR and cognition in AD exists particularly with cortical MTR and that it is independent of brain atrophy. Like others,^{7,10,29} we failed to observe a relationship between WM MTR and cognition in AD. We realize that we cannot rule out with certainty that reductions in MTR might have been caused by partial volume effects from the CSF as a consequence of atrophy in patients with dementia. CSF has very low MTR values, and sulcal enlargement could cause a reduction of MTR in voxels because of the combination of cortex and CSF.³⁰ However, we do not believe that partial volume effects had a considerable effect in our study because cortical volume was considered as a

Table 2: Logistic regression analysis—lower MTRs relate to AD independent of normalized regional brain volume and white matter damage

MTR Region	OR	95% CI	P Value ^a
Global cortex	0.47	0.22–0.97	.04
AD-signature regions	0.31	0.14–0.67	.003
Global NAWM	0.59	0.39–0.88	.01
WM hyperintensities	0.18	0.09–0.33	<.001

^a Corrected for age, sex, years of education, normalized regional volume, and Fazekas score.

Table 3: Linear regression analysis in AD—cortical MTRs relate to poorer language function in patients with AD

MTR Region	MMSE, $n = 77$			Language Function (CERAD Test: Boston Naming Test), $n = 77$			Constructional Praxis (CERAD Test: Figure Copying), $n = 73$		
	β	95% CI	P Value ^a	β	95% CI	P Value ^a	β	95% CI	P Value ^a
Global cortex	0.23	−0.07–1.96	.06	0.31	0.19–1.95	.02	0.22	−0.09–1.24	.09
AD-signature regions	0.14	−0.50–1.52	.32	0.28	−0.02–1.74	.05	0.29	−0.01–1.32	.05
Global NAWM	0.17	−0.24–1.67	.14	0.11	−0.05–1.23	.40	0.23	−0.05–1.23	.07
WM hyperintensities	0.01	−0.78–0.88	.91	−0.01	−0.81–0.67	.89	0.01	−0.53–0.59	.92

Note:— β indicates standardized regression coefficient.

^a Corrected for age, sex, years of education, normalized regional volume, and Fazekas score.

confounder, and all MTR masks have been corrected by deleting voxels with high intensities in the co-registered pseudo-T2 map to prevent CSF contamination of cortical MTR. However, the histopathologic correlates of MTR reductions in the cortex in AD are widely unknown. Decreased MTRs caused by focal demyelination in the cortex were found in patients with multiple sclerosis,³¹ but it is unlikely that loss of cortical myelin is responsible for lowering of cortical MTRs in those with AD. A more likely explanation comes from a study of Patel and coworkers,³² who found that dendritic branching is likely to be the main driver of MTR values in the cortex because higher surface area of cellular membranes relates to greater magnetization transfer between the free water and bound water pool. The authors indicated that dendrites and their spines contribute 34-fold more exposure to the extracellular water than myelin and concluded that MTRs in the cortex are more sensitive to cellular membranes associated with dendrites than myelin.³² The loss of dendritic spines directly correlates with the loss of synaptic function. Patients with AD show a significant loss of synapses and their cognitive capabilities correlate strongly with synapse attenuation.³³

Another possible explanation for MTR lowering in AD brains is posttranslational modification of axonal proteins. This is suggested by an MTI study on unfixed postmortem brain slices, which assessed blocks containing microscopically nonlesional brain tissue and microdissected adjacent tissue to quantify specific protein levels.³⁴ The authors reported that lowering of MTR was caused by a hyperphosphorylation-related change in proton mobility. In line with this finding, altered cortical MTRs may thus reflect hyperphosphorylation of proteins such as tau and pathologic protein accumulation, a process that is known to precede cell death in AD and other primary neurodegenerative diseases.³⁵ The mentioned mechanisms are in keeping with the main finding of our study that MTR changes in the cortex in patients with AD are at least partly independent of cortical volume and that cortical MTR reductions explain cognitive impairment beyond regional cortical atrophy.

Our study has several strengths. We investigated a considerably large sample of individuals with AD and of healthy community-dwelling older adults. The availability of a structural scan with high resolution allowed segmentation of cortical and WM compartments. One limitation of our study is that we used the 1984 NINCDS-ADRDA criteria for the diagnosis of AD.¹⁶ These criteria were standard at the time of patient recruitment into the study. Recently, the criteria have been revised, yet it was shown that the 1984 criteria provide a diagnostic sensitivity and specificity of 81% and 70%, respectively, in clinicopathologic studies.³⁶ Another limitation was that the spatial resolution of the MT sequence was limited, and therefore partial volume effects caused by CSF in cortical regions cannot be ruled out with certainty. However, these effects should be small, and they have been considered in image postprocessing and in the statistical analyses by correcting for atrophy.

CONCLUSIONS

MTR values were reduced not only in the GM but also in the WM of patients with AD. Only the MTR values in the GM were related to cognitive impairment. At this point, the diagnostic

contribution of MTR in patients with AD is still unknown, but our data indicate that it provides additional information beyond pure assessment of brain atrophy and WM damage. How AD-related pathophysiology can affect the MT mechanism in the GM is not fully determined. Moreover, longitudinal studies in the prodromal stages of AD are needed to evaluate if MTR is able to add to the prediction of conversion to AD.

Disclosures: Reinhold Schmidt—UNRELATED: Consultancy; AXON Neuroscience; Grants/Grants Pending: Austrian Science Fund.* *Money paid to institution.

REFERENCES

1. Bayram E, Caldwell JZK, Banks SJ. **Current understanding of magnetic resonance imaging biomarkers and memory in Alzheimer's disease.** *Alzheimers Dement (N Y)* 2018;4:395–413 CrossRef Medline
2. Mahalingam S, Chen MK. **Neuroimaging in dementias.** *Semin Neurol* 2019;39:188–99 CrossRef Medline
3. Strain JF, Smith RX, Beaumont H, et al. **Loss of white matter integrity reflects tau accumulation in Alzheimer disease defined regions.** *Neurology* 2018;91:E313–18 CrossRef Medline
4. Schmierer K, Scaravilli F, Altmann DR, et al. **Magnetization transfer ratio and myelin in postmortem multiple sclerosis brain.** *Ann Neurol* 2004;56:407–15 CrossRef Medline
5. Mottershead JP, Schmierer K, Clemence M, et al. **High field MRI correlates of myelin content and axonal density in multiple sclerosis: a post-mortem study of the spinal cord.** *J Neurol* 2003;250:1293–1301 CrossRef Medline
6. Schmierer K, Tozer DJ, Scaravilli F, et al. **Quantitative magnetization transfer imaging in postmortem multiple sclerosis brain.** *J Magn Reson Imaging* 2007;26:41–51 CrossRef Medline
7. Ridha BH, Symms MR, Tozer DJ, et al. **Magnetization transfer ratio in Alzheimer disease: comparison with volumetric measurements.** *AJNR Am J Neuroradiol* 2007;28:965–70 Medline
8. Bozzali M, Franceschi M, Falini A, et al. **Quantification of tissue damage in AD using diffusion tensor and magnetization transfer MRI.** *Neurology* 2001;57:1135–37 CrossRef Medline
9. van der Flier WM, van den Heuvel DMJ, Weverling-Rijnsburger AWE, et al. **Cognitive decline in AD and mild cognitive impairment is associated with global brain damage.** *Neurology* 2002;59:874–79 CrossRef Medline
10. Kabani NJ, Sled JG, Chertkow H. **Magnetization transfer ratio in mild cognitive impairment and dementia of Alzheimer's type.** *NeuroImage* 2002;15:604–10 CrossRef Medline
11. Hanyu H, Asano T, Iwamoto T, et al. **Magnetization transfer measurements of the hippocampus in patients with Alzheimer's disease, vascular dementia, and other types of dementia.** *AJNR Am J Neuroradiol* 2000;21:1235–42 Medline
12. Hanyu H, Asano T, Sakurai H, et al. **Magnetisation transfer measurements of the subcortical grey and white matter in Parkinson's disease with and without dementia and in progressive supranuclear palsy.** *Neuroradiology* 2001;43:542–46 CrossRef Medline
13. Ropele S, Schmidt R, Enzinger C, et al. **Longitudinal magnetization transfer imaging in mild to severe Alzheimer disease.** *AJNR Am J Neuroradiol* 2012;33:570–75 CrossRef Medline
14. Seiler S, Schmidt H, Lechner A, et al. **Driving cessation and dementia: results of the Prospective Registry on Dementia in Austria (PRODEM).** *PLoS One* 2012;7:e52710 CrossRef Medline
15. American Psychiatric Association. Section II: Diagnostic Criteria and Codes. *Diagnostic and Statistical Manual of Mental Disorders*. 5th edition. American Psychiatric Association 2013
16. McKhann G, McKhann G, Drachman D, et al. **Clinical diagnosis of Alzheimer's disease: report of the NINCDS-ADRDA Work Group under the auspices of Department of Health and Human Services Task Force on Alzheimer's Disease.** *Neurology* 1984;34:939–44 CrossRef Medline

17. National Institute for Health and Clinical Excellence. *Donepezil, Galantamine, Rivastigmine, and Memantine for the Treatment of Alzheimer's Disease*. National Institute for Health and Clinical Excellence 2011. <https://www.nice.org.uk/guidance/ta217/resources/donepezil-galantamine-rivastigmine-and-memantine-for-the-treatment-of-alzheimers-disease-pdf-82600254699973>. Accessed September 14, 2020
18. Schmidt R, Lechner H, Fazekas F, et al. **Assessment of cerebrovascular risk profiles in healthy persons: definition of research goals and the Austrian Stroke Prevention Study (ASPS)**. *Neuroepidemiology* 1994;13:308–13 CrossRef Medline
19. Folstein MF, Folstein SE, McHugh PR. **“Mini-mental state.” A practical method for grading the cognitive state of patients for the clinician**. *J Psychiatr Res* 1975;12:189–98 CrossRef Medline
20. Morris JC, Heyman A, Mohs RC, et al. **The consortium to establish a registry for Alzheimer's disease (CERAD). Part I. Clinical and neuropsychological assessment of Alzheimer's disease**. *Neurology* 1989;39:1159–65 CrossRef Medline
21. Fischl B, Sereno MI, Dale AM. **Cortical surface-based analysis. I. Segmentation and surface reconstruction**. *NeuroImage* 1999;9:195–207 CrossRef Medline
22. Reuter M, Rosas HD, Fischl B. **Highly accurate inverse consistent registration: a robust approach**. *NeuroImage* 2010;53:1181–96 CrossRef Medline
23. Wu A, Sharrett AR, Gottesman RF, et al. **Association of brain magnetic resonance imaging signs with cognitive outcomes in persons with nonimpaired cognition and mild cognitive impairment**. *JAMA Netw Open* 2019;2:e193359 CrossRef Medline
24. Petrovic A, Scheurer E, Stollberger R. **Closed-form solution for T2 mapping with nonideal refocusing of slice selective CPMG sequences**. *Magn Reson Med* 2015;73:818–27 CrossRef Medline
25. Plummer DL. **DispImage: a display and analysis tool for medical images**. *Rivista di Neuroradiologia* 1992;5:489–95 CrossRef
26. Fazekas F, Chawluk JB, Alavi A. **MR signal abnormalities at 1.5 T in Alzheimer's dementia and normal aging**. *AJNR Am J Neuroradiol* 1987;8:421–26 CrossRef Medline
27. Hanyu H, Asano T, Sakurai H, et al. **Magnetization transfer measurements of the hippocampus in the early diagnosis of Alzheimer's disease**. *J Neurol Sci* 2001;188:79–84 CrossRef Medline
28. van Es ACGM, van der Flier WM, Admiraal-Behloul F, et al. **Lobar distribution of changes in gray matter and white matter in memory clinic patients: detected using magnetization transfer imaging**. *AJNR Am J Neuroradiol* 2007;28:1938–42 CrossRef Medline
29. van Es ACGM, van der Flier WM, Admiraal-Behloul F, et al. **Magnetization transfer imaging of gray and white matter in mild cognitive impairment and Alzheimer's disease**. *Neurobiol Aging* 2006;27:1757–62 CrossRef
30. Seiler S, Pirpamer L, Hofer E, et al. **Magnetization transfer ratio relates to cognitive impairment in normal elderly**. *Front Aging Neurosci* 2014;6:263 CrossRef Medline
31. Chen JTH, Easley K, Schneider C, et al. **Clinically feasible MTR is sensitive to cortical demyelination in MS**. *Neurology* 2013;80:246–52 CrossRef Medline
32. Patel Y, Shin J, Gowland PA, et al. **Maturation of the human cerebral cortex during adolescence: myelin or dendritic arbor?** *Cereb Cortex* 2019;29:3351–62 CrossRef Medline
33. Dorostkar MM, Zou C, Blazquez-Llorca L, et al. **Analyzing dendritic spine pathology in Alzheimer's disease: problems and opportunities**. *Acta Neuropathol* 2015;130:1–19 CrossRef Medline
34. Petzold A, Tozer DJ, Schmierer K. **Axonal damage in the making: neurofilament phosphorylation, proton mobility and magnetisation transfer in multiple sclerosis normal appearing white matter**. *Exp Neurol* 2011;232:234–39 CrossRef Medline
35. Nakamura T, Lipton SA. **Cell death: protein misfolding and neurodegenerative diseases**. *Apoptosis* 2009;14:455–68 CrossRef Medline
36. Knopman DS, DeKosky ST, Cummings JL, et al. **Practice parameter: diagnosis of dementia (an evidence-based review): Report of the quality standards subcommittee of the American Academy of Neurology**. *Neurology* 2001;56:1143–53 CrossRef Medline

Ivy Sign in Moyamoya Disease: A Comparative Study of the FLAIR Vascular Hyperintensity Sign Against Contrast-Enhanced MRI

L.-X. Wang, H. Wang, F.-B. Hao, J.-H. Lv, S.-H. Zhang, D.-S. Han, X.-B. Bian, D.-K. Zhang, Y.-N. Lan, X.-R. Wang, M.-T. Wei, L. Duan, L. Ma, and X. Lou



ABSTRACT

BACKGROUND AND PURPOSE: The ability of the ivy sign on contrast-enhanced T1-weighted MR imaging (CEMR) to reflect cerebral perfusion and postoperative revascularization in Moyamoya disease remains largely unknown. We aimed to compare the capabilities of CEMR and FLAIR.

MATERIALS AND METHODS: CEMR, FLAIR, arterial spin-labeling, and DSA were performed in 44 patients with Moyamoya disease. The ivy sign was scored separately on CEMR and FLAIR using the Alberta Stroke Program Early CT Score. The status of leptomeningeal collaterals was scored on DSA. The postoperative Matsushima grade was evaluated at least 3 months after surgical revascularization.

RESULTS: Scoring of the ivy sign on CEMR showed excellent interrater reliability, and FLAIR vascular hyperintensity showed moderate interrater reliability. Correlation analyses revealed that DSA scores were more consistent with the CEMR-based ivy sign score ($r = 0.25$, $P = .03$) than with FLAIR vascular hyperintensity ($r = 0.05$, $P = .65$). The CEMR-based ivy sign score was significantly correlated with CBF in late-Suzuki stage Moyamoya disease ($t = -2.64$, $P = .02$). The CEMR-based ivy sign score at baseline was significantly correlated with the postoperative Matsushima grade ($r = 0.48$, $P = .03$).

CONCLUSIONS: In this study, CEMR outperformed FLAIR in capturing the ivy sign in Moyamoya disease. In addition, the CEMR-based ivy sign score provided adequate information on hemodynamic status and postoperative neovascularization. The current study suggested that CEMR could be considered as an alternative to FLAIR in future studies investigating leptomeningeal collaterals in Moyamoya disease.

ABBREVIATIONS: CEMR = contrast-enhanced T1-weighted MR imaging; FVH = FLAIR vascular hyperintensity; MMD = Moyamoya disease; PCA = posterior cerebral artery; EDAS = encephaloduroarteriosynangiosis; FOV = field of view

Moyamoya disease (MMD) is an uncommon cerebrovascular disease characterized by chronic progressive occlusion of the terminal portion of the internal carotid artery and its main branches within the circle of Willis.^{1,2} In MMD, the perfusion of brain tissue originates from the narrowed ICA, basal moyamoya vessels, leptomeningeal collaterals derived chiefly from the posterior circulation, and transdural collaterals from the external carotid

arteries. As MMD progresses, leptomeningeal collaterals remain some of the most important sources of blood supply.

Leptomeningeal collateral flow appears as high signal intensity in the subarachnoid space on contrast-enhanced T1-weighted MR imaging (CEMR) and FLAIR images. Because of its characteristic appearance (resembling ivy creeping on stone), this radiologic sign is known as the ivy sign.³ On CEMR, the ivy sign is manifested as leptomeningeal enhancement, which can decrease after bypass surgery, supporting the hypothesis that the enhancement represents the fine vascular network over the pial surface.⁴ Another imaging feature characterizing the ivy sign, namely, FLAIR vascular hyperintensity (FVH), has been extensively studied, especially in acute ischemic cerebrovascular diseases. In recent years, FVH has been introduced into MMD studies and was reported to be related to clinical severity and hemodynamic status in prior literature.^{5,6} However, a previous study reported that the ivy sign was captured better by CEMR than by FLAIR,⁷ raising questions of whether CEMR outperforms FLAIR as a quantitative reflection of leptomeningeal collaterals for estimating cerebral perfusion and predicting the status of postoperative neovascularization in MMD.

Received June 22, 2020; accepted after revision November 3.

From the Medical School of Chinese PLA (L.-X.W., S.-H.Z., D.-S.H.), Beijing, China; Department of Radiology (L.-X.W., J.-H.L., S.-H.Z., D.-S.H., X.-B.B., D.-K.Z., Y.-N.L., X.-R.W., M.-T.W., X.L., L.M.), the First Medical Center, Chinese PLA General Hospital, Beijing, China; and Department of Neurosurgery (H.W., F.-B.H., L.D.), the Fifth Medical Center, Chinese PLA General Hospital, Beijing, China.

L.-X. Wang, H. Wang, and F.-B. Hao contributed equally to this work.

This work was supported by the National Natural Science Foundation of China (No. 81730048, 81825012).

Please address correspondence to Dr. Lin Ma, Department of Radiology, the First Medical Center of Chinese PLA General Hospital, No. 28 Fuxing Rd, Haidian District, Beijing 100853, China; e-mail: cjr.malin@vip.163.com

Indicates open access to non-subscribers at www.ajnr.org

Indicates article with online supplemental data.

<http://dx.doi.org/10.3174/ajnr.A7010>

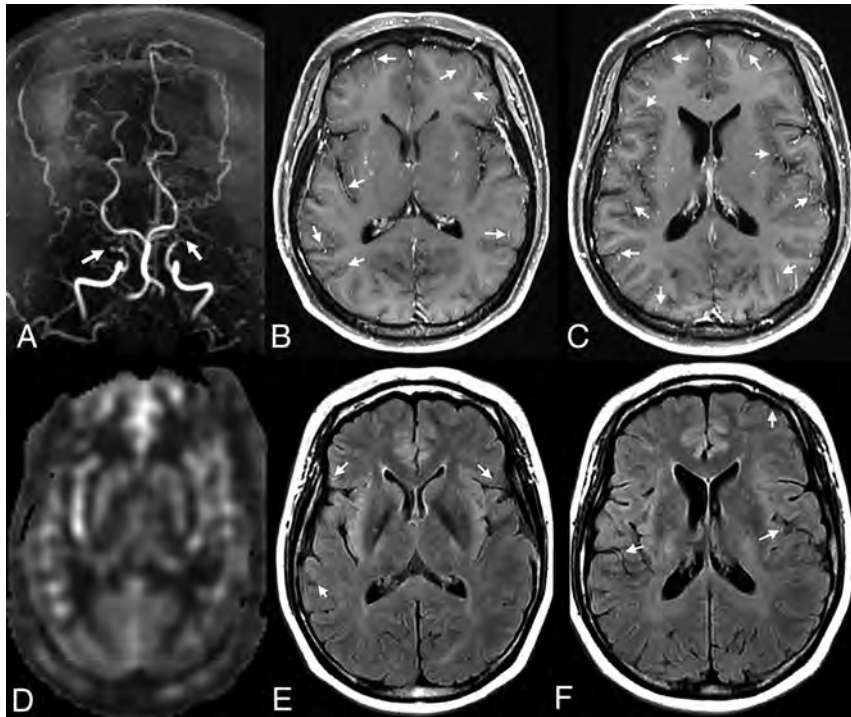


FIG 1. Illustrative case of a 45-year-old woman with bilateral MMD. MRA reveals occlusion of bilateral MCA (white arrow) (A). CEMR shows better delineation of the ivy sign than FWH (white arrows) (B and C, E and F). The CBV of bilateral hemisphere shows no difference (D).

In this study, we compared the ability of CEMR and FLAIR to quantify the leptomeningeal ivy sign using DSA as a reference. We further evaluated the ability of the CEMR-based ivy sign score to reflect deficient perfusion in MMD and predict the post-operative Matsushima grade.

MATERIALS AND METHODS

Patients

This study was approved by the institutional ethics committee and registered as a clinical trial (NCT03785171). Written informed consent was obtained from each patient or his or her legally authorized representative.

From September 2018 to February 2019, this cross-sectional, prospective study enrolled 44 adult patients who were diagnosed with MMD according to the Japanese guidelines published in 2012, with the exclusion of moyamoya syndrome.² All patients received MR imaging and DSA examinations at baseline (DSA was performed within 2 weeks after MR imaging examination). Encephaloduroarteriosynangiosis (EDAS) was performed in 34 patients (57 hemispheres) within 2 weeks after DSA examination. At least 3 months after surgery, 12 patients (21 hemispheres) again underwent DSA examination (the other patients had not met the 3-month requirement before the data were analyzed). The exclusion criteria were as follows: 1) massive cerebral infarction or hemorrhage that could not be evaluated by MR imaging; 2) patients who had previously undergone bypass surgery with direct or indirect revascularization (indirect revascularization consists of encephalomyosynangiosis, EDAS, and encephaloduroarteriomyosynangiosis); and 3) patients with a history of systemic diseases, such as terminal

carcinoma and immune system diseases. Ten patients had suspected family histories of MMD in that their relatives had ischemic or hemorrhagic stroke but had not received a definite diagnosis of MMD.

Imaging Acquisition

All subjects were scanned on a 3T MR scanner with an 8-channel phased-array head coil.

Detailed parameters of CEMR, T2 FLAIR, high-resolution T1-weighted structural imaging, 3D pseudo-continuous arterial spin-labeling, DWI, and MRA were as follows— 1) CEMR: TR = 1850 ms, TE = 24 ms, flip angle = 111°, field of view (FOV) = 240 × 240 mm, matrix = 320 × 256, slice thickness = 6 mm, number of slices = 20, contrast medium administration = 14 ml (2.5 ml/s), acquisition time = 1 minute 49 seconds; 2) T2 FLAIR: TR = 8500 ms, TE = 162 ms, flip angle = 111°, FOV = 240 × 240 mm, matrix = 288 × 224, slice thickness = 6 mm, number of slices = 20, acquisition time = 1 minute 43 seconds; 3) high-resolution T1-weighted structural image: TR = 6 ms, TE = 2.5 ms, flip angle = 15°, FOV = 256 × 256 mm, matrix = 256 × 256, slice thickness = 1 mm, number of slices = 148, acquisition time = 2 minutes 24 seconds; 4) 3D pseudo-continuous arterial spin-labeling: TR = 4844 ms, TE = 10.5 ms, labeling duration = 1500 ms, post-labeling delay = 2000 ms, FOV = 240 × 240 mm, slice thickness = 4.0 mm, number of slices = 36, acquisition time = 3 minutes 33 seconds; 5) DWI: TR = 3000 ms, TE = 67.8 ms, b-value = 1000, FOV = 240 × 240 mm, slice thickness = 6 mm, number of slices = 20, acquisition time = 24 seconds; 6) MRA: TR = 34 ms, TE = 2.1 ms, FOV = 240 × 240 mm, slice thickness = 1.4 mm, acquisition time = 2 minutes 32 seconds.

DSA data were collected after contrast injection in both internal carotid arteries, both external carotid arteries, and 1 or 2 vertebral arteries. Lateral and anteroposterior views of each artery injection were collected.

DSA data were collected after contrast injection in both internal carotid arteries, both external carotid arteries, and 1 or 2 vertebral arteries. Lateral and anteroposterior views of each artery injection were collected.

Imaging Assessment

MRI Assessment at Baseline. The ivy sign was defined on both CEMR and FLAIR images as continuous linear or punctate regions of leptomeningeal high signal intensity along the cortical sulci and subarachnoid space (Fig 1). Two radiologists, each with 2 years of experience, reviewed all CEMR and FLAIR images independently at 2 levels of the cerebral hemisphere (ganglionic and supraganglionic levels). The mean value was used as the final score for statistical analysis. We modified ASPECTS (Alberta Stroke Program Early CT Score, a semiquantitative method for estimating infarct size on CT) by omitting the deeper cerebral structures because they were not relevant to the assessment of

leptomeningeal collaterals (only the M1–M6 cortical regions were included). Thus, each hemisphere was divided into 6 regions (3 regions for each level). The ivy sign score of each region was defined as follows: 0 represents no ivy sign, 1 represents the ivy sign reaching less than half of the region, and 2 represents the ivy sign reaching more than half of the region. The total ivy sign score of each hemisphere was defined as the sum score of 6 regions.^{8,9}

The DWI-positive or DWI-negative (presence of hyperintense lesion on DWI was defined as positive) status of bilateral MCA territory was recorded at baseline and was used to indicate whether cerebral lesions in the acute or subacute phase existed. DWI features were used to investigate whether the ivy sign was related to the time from stroke onset to imaging (which was reflected by the DWI signal).

MCA stenosis was rated on MRA by 1 radiologist and defined as moderate to severe stenosis (50%–99%). MCA occlusion was recorded when no visible blood flow could be seen on MRA images.

DSA Assessment at Baseline. The DSA score was defined as follows: leptomeningeal collateral assessment on DSA was evaluated according to Liu et al¹⁰ by 2 experienced neurosurgeons. This leptomeningeal scoring system ranges from 0 to 6 and includes 3 parts of the collateral networks: pPCA→ACA (the parieto-occipital branch of the posterior cerebral artery (PCA) anastomoses to the ACA), tPCA→tMCA (the anterior temporal branch of the posterior cerebral artery anastomoses to the temporal branch of the MCA), and pPCA→MCA (the pPCA anastomoses to the MCA). Additionally, transdural collaterals were assessed and scored (0 represents the absence of transdural collaterals, and 1 represents the presence of transdural collaterals). The total DSA score was defined as the sum of leptomeningeal collaterals and transdural collaterals and was considered the reference standard in this study.

The Suzuki stage, a well-known cerebral angiographic classification for MMD, was also recorded. In this study, we defined the late-Suzuki stage group as Suzuki stage \geq IV and the early-Suzuki stage group as Suzuki stage \leq III for further subgroup analysis.

DSA Assessment at Follow-up. As stated earlier, postoperative follow-up DSA examinations were valid for 12 patients (21 hemispheres). At least 3 months after EDAS, the 21 hemispheres were graded postoperatively according to the following system proposed by Matsushima et al¹¹: grade I was defined as revascularization of less than one-thirds of the MCA distribution, grade II as revascularization of one-thirds to two-thirds of the MCA distribution, and grade III as revascularization of more than two-thirds of the MCA distribution. The Matsushima score was used to assess the effect of revascularization after EDAS.

Quantitative Estimation of CBF

Quantitative estimation of the CBF of the MCA territory was performed automatically. First, the CBF map of 3D pseudo-continuous arterial spin-labeling was processed and generated using FuncTool (AW 4.5 Workstation, GE Healthcare). Second, high-

resolution T1 structural images were normalized to Montreal Neurological Institute space using FLIRT (FMRIB Linear Image Registration Tool; <https://fsl.fmrib.ox.ac.uk/fsl/fslwiki/FLIRT>) and FNIRT (FMRIB Non-Linear Image Registration Tool; <https://fsl.fmrib.ox.ac.uk/fsl/fslwiki/FNIRT>) within the FMRIB Software Library (FSL, <http://www.fmrib.ox.ac.uk/fsl>). Then CBF maps were affine registered to the normalized T1 structural images using FLIRT.¹² Next, a brain mask of the MCA territory was projected to the normalized CBF maps, as described elsewhere.¹³ Finally, the mean CBF of the MCA territory of each hemisphere was extracted and prepared for further statistical analysis.

Statistical Analysis

The interrater reliability of scoring was evaluated by calculating the intraclass correlation coefficient (ICC). ICC values range from 0 to 1, and a value above 0.75 was considered to indicate excellent reliability.¹⁴ The correlations of the CEMR and FLAIR ivy sign scores with DSA were examined by Pearson correlation analysis. The relationships of these 2 scoring modalities with Suzuki stage were assessed using Spearman correlation analysis. A 2-tailed independent Student *t* test was performed on the CEMR and FLAIR ivy signs to differentiate between MCA stenosis and MCA occlusion. Linear regression was used to evaluate the statistical significance of these 2 scoring modalities in reflecting the CBF of each hemisphere. Because the PCA is a major source of blood supply for leptomeningeal collaterals and the involvement of the PCA may greatly affect cerebral perfusion, PCA involvement was included as a covariant. Other potentially relevant covariates included sex, age, and illness duration. A subgroup analysis was performed in patients with MMD in late versus early Suzuki stages using the same method. Ivy sign scores based on CEMR and FLAIR were compared between DWI-positive and DWI-negative cases using a 2-tailed independent Student *t* test. Partial correlation analysis was used to determine the relationship between imaging parameters and Matsushima grades, with PCA involvement included as a covariate. $P < .05$ was considered to indicate statistical significance. All statistical analyses were performed using SPSS 22.0 (IBM).

RESULTS

Demographic Characteristics

A total of 44 patients with MMD (including 9 patients with unilateral MMD and 35 patients with bilateral MMD, for a total of 79 hemispheres) were recruited in the current study. The demographic and clinical characteristics of the enrolled patients are shown in Table 1.

Consistency of CEMR-Based Ivy Sign Score and FVH with DSA Scores

There was excellent interrater reliability of CEMR-based ivy sign score and DSA scores. FVH showed moderate interrater reliability (Table 2).

Correlation analysis revealed a statistically significant relationship between CEMR-based ivy sign scores and DSA scores ($r = 0.25$, $P = .03$) but not between FVH and DSA scores ($r = 0.05$, $P = .65$). Regarding the correlations between these 2

Table 1: Demographic characteristics and clinical measurements of patients with MMD

	Left Hemisphere (n = 38)	Right Hemisphere (n = 41)
Age (years)	41.63 ± 12.31	
Sex (male/female)	18/26	
Illness duration (months)	45.85 ± 76.76	
Family history (y/n)	3/31	
Initial manifestation on imaging		
Ischemic onset	11	6
Hemorrhagic onset	3	9
DWI (positive/negative)	7/31	3/38
MCA (stenosis/occlusion)	11/27	8/33
PCA (normal/stenosis/occlusion)	25/8/5	29/8/4
Mean Suzuki stage	IV (III–V)	IV (III–V)
CBF of MCA territory (mL/100 g/min)	47.52 ± 11.39	46.50 ± 15.43
Scoring of leptomeningeal collaterals		
FVH	2.91 ± 1.59	2.68 ± 1.52
CEMR-based ivy sign score	7.87 ± 2.18	7.55 ± 2.20
DSA score	2.63 ± 1.84	2.65 ± 1.88

Note:—Continuous data were presented as mean ± SD, and categorical data were presented as median (IQR).

Table 2: Interrater reliability of FVH, CEMR-based ivy sign score, and DSA score

	ICC	95% CI	
		Lower Bound	Upper Bound
FVH	0.71	0.55	0.82
CEMR-based ivy sign score	0.81	0.70	0.88
DSA score	0.83	0.73	0.89

imaging modalities and Suzuki stage, the CEMR-based ivy sign score showed a significant correlation ($\rho = 0.44$, $P < .001$). For FVH, although a significant correlation was found, the correlation coefficient was lower than that of the ivy sign on CEMR ($\rho = 0.24$, $P = .03$) (Fig 2).

Patients with DWI-positive and DWI-negative MMD had significantly different ivy sign scores based on FLAIR ($t = 2.82$, $P = .01$) but not on CEMR ($t = -0.19$, $P = .85$) (Online Supplemental Data).

CEMR-Based Ivy Sign Score and FVH for Differentiating the Severity of MCA Stenosis

The CEMR-based ivy sign score outperformed FVH (FVH, $t = -1.73$, $P = .09$; CEMR-based ivy sign score, $t = -2.32$, $P = .03$; DSA, $t = -3.01$, $P = .005$) in differentiating between MCA stenosis and MCA occlusion.

Relationships between the Ivy Sign and CBF

High-resolution T1-weighted structural images were unavailable in 13 patients with MMD because of severe head motion or patients' reluctance to undergo the scan. A total of 31 patients' CBF (in 54 hemispheres) was quantified and included in the analyses. In stepwise linear regression analysis with the CEMR-based ivy sign score or FVH, involvement of PCA, age, sex, and illness duration specified as independent variables, no variable was included in the final model for either the CEMR-based ivy sign score or FVH.

In the subgroup analyses, the early-Suzuki stage MMD group had a trend of positive correlation between CEMR-based

ivy sign score and CBF, though the correlation was not statistically significant (Online Supplemental Data). In the late-Suzuki stage MMD group, a linear regression model showed that the CEMR-based ivy sign score can serve as an independent indicator for determining CBF (Table 3).

Relationship between Imaging Parameters and Matsushima Grade

Partial correlation analysis demonstrated a statistically significant correlation between the CEMR-based ivy sign score and Matsushima grade ($r = 0.48$, $P = .03$). No significant relationship was found between FVH and Matsushima grade ($r = 0.17$, $P = .46$).

DISCUSSION

In patients with MMD, leptomeningeal collaterals play an important role in maintaining cerebral perfusion. On MR images, these collaterals can be represented by the ivy sign. In this study, we compared 2 MR approaches for assessing the ivy sign (ie, CEMR and FLAIR), with DSA as a reference. We found that the ivy sign on CEMR outperformed the ivy sign on FLAIR in depicting leptomeningeal collaterals, as well as in reflecting the Suzuki stage of MMD. More important, we found that the CEMR-based ivy sign score could serve as an independent biomarker for predicting CBF in late-Suzuki stage MMD. In addition, the CEMR-based ivy sign score can predict the status of postoperative neovascularization in patients with MMD after EDAS.

The current study found that the ivy sign was less obvious on FLAIR than on CEMR. Moreover, FVH failed to reflect the DSA score for leptomeningeal collaterals. FVH has been extensively studied in the field of atherosclerotic diseases, such as ischemic stroke.¹⁵ This radiologic sign is considered to be related to collateralization,¹⁶ stroke severity,¹⁷ and functional outcomes.¹⁶ Physically, FVH is likely to reflect slow retrograde or turbulent flow in the engorged pial collateral arteries through leptomeningeal anastomoses.¹⁸ In recent years, FVH has also been introduced into MMD studies as an indicator of collateral blood flow. With regard to acute ischemic stroke, a previous study reported a 98% prevalence of FVH in the first 6 hours after onset.¹⁹ Another study also suggested that FVH was a temporary phenomenon that commonly disappeared within the first 24–36 hours after stroke onset.¹⁷ The short-term presence of FVH raised the question of whether it is appropriate for use in MMD studies. Although conceptually comparable to MMD, the underlying mechanism of collateral formation in acute stroke and MMD may not be the same. In a chronic state of hypoperfusion, as is found in MMD, FVH was unlikely to appear as a rapid reaction as in acute stroke. In this study, DWI hyperintensity was used to indicate whether lesions in the acute or subacute phase existed, which could indirectly reflect the time from onset to imaging. We found significant differences between patients with DWI-positive and DWI-negative MMD with respect

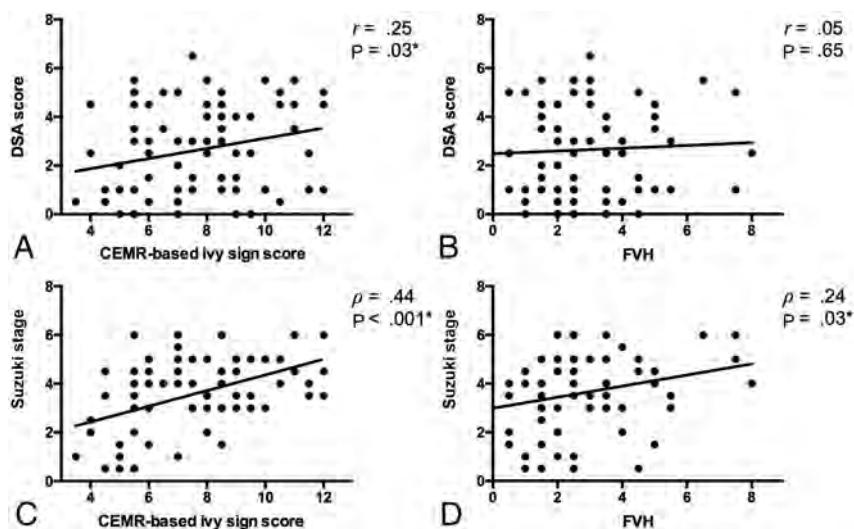


FIG 2. Scatter plots of the correlation between ivy sign score on CEMR (A), FVH (B) and DSA score of leptomeningeal collaterals; correlation between ivy sign score on CEMR (C), FVH (D) and Suzuki stage of Moyamoya disease. The asterisk indicates $P < 0.05$.

Table 3: Multivariable linear regression analysis results for CEMR-based ivy sign score with CBF as the dependent variable in patients with late-Suzuki stage MMD^a

	B	SE	β	t	P Value
Included variable					
Constant	65.91	8.49	—	7.77	<.001 ^b
CEMR-based ivy sign score	-2.49	0.94	-0.49	-2.64	.015 ^b
Excluded variable					
Age	—	—	-0.02	-0.12	.54
Sex	—	—	-0.09	-0.46	.65
Illness duration	—	—	0.12	0.62	.54
PCA	—	—	-0.18	-0.95	.35

^a $F = 6.95$, $P = .015$; $R^2 = 0.24$, adjusted $R^2 = 0.21$.

^b $P < 0.05$.

Note:—CEMR indicated contrast-enhanced T1-weighted MR images; MMD, Moyamoya disease; PCA, posterior cerebral artery; B, partial regression coefficient; β , standardized partial regression coefficient; SE, standard error.

to FVH, which added further evidence in support of this explanation. Physically, the presence of FVH is rooted mainly in slow flow via leptomeningeal collaterals,²⁰ which may not be the case in MMD. A possible hypothesis is that the flow velocity of leptomeningeal collaterals in MMD after a relatively long illness duration was different from that in acute stroke. A previous study demonstrated obviously increased cortical microvascular attenuation and diameter in MMD compared with atherosclerotic disease.²¹ Such differences in the diameters, lengths, and pressures of the collateral routes may induce different flow velocities, which are related to the presence of FVH.

Previous studies have demonstrated that CEMR is superior to FLAIR in capturing the ivy sign.^{7,22} To our knowledge, there has been no quantitative comparison of these 2 modalities with regard to their consistency with DSA. Additionally, previous studies reached different conclusions in terms of the incidence of the ivy sign; that is, Yoon et al⁷ found a higher incidence of the ivy sign on CEMR than FLAIR, but Jung et al²² found the opposite phenomenon. Yoon et al⁷'s finding is readily comprehensible because from a pathophysiological viewpoint, one can predict enhancement of the engorged pial vessels with thickened

arachnoid membranes and edema. Our results agreed with those of Yoon et al⁷; CEMR-based ivy sign score was higher than FVH and was significantly correlated with DSA score, but such a correlation was not found for FVH.

During the course of MMD, MCA stenosis and occlusion can appear at different stages of disease. Some unilateral MMD cases can even show a normal MCA. We included hemispheres with MCA stenosis or occlusion in this study and found that CEMR-based ivy sign scores and DSA scores could differentiate between these levels of stenotic severity, but FVH could not. Such results further supported the hypothesis that FVH might not be appropriate for the evaluation of leptomeningeal collaterals in patients with MMD.

Taking a step further, we studied the relationship of the CEMR-based ivy sign score and FVH with CBF. FVH and CBF were found to be unrelated. A previous study by Noguchi et al²³ found similar results. These investigators found that CBF showed no difference among patients with MMD with 3 levels of FVH, though a different scoring system for the ivy sign was used in their study. Mori et al¹⁸ claimed that the cerebral vasculature in the region with decreased perfusion pressure is already dilated to maintain CBF. In their study, FVH could indi-

cate decreased cerebrovascular reserve, which suggested that the cerebrovascular reserve might be more sensitive than CBF.

We also found a nonsignificant correlation between the CEMR-based ivy sign score and CBF of the MCA territory when all cases were included in the statistical analysis. We then divided the patients with MMD into an early-Suzuki stage group and a late-Suzuki stage group. In patients with early-Suzuki stage MMD, the trend of correlation between CEMR-based ivy sign score and CBF was positive, though no statistical significance was achieved. Interestingly, a negative correlation was found between the CEMR-based ivy sign score and CBF in patients with late-Suzuki stage MMD. A possible explanation for this result was the imbalance between leptomeningeal collaterals and abnormal ICA and moyamoya vessels. We hypothesized that in the late Suzuki stages, the ability of leptomeningeal collaterals to compensate for cerebral perfusion was inadequate. However, in early-Suzuki stage MMD, the trend of a positive correlation between CEMR-based ivy sign scores and CBF suggested that the more collaterals there were, the higher the CBF was. The potentially significant correlation found between CEMR-based ivy sign scores and CBF in all cases might be covered by the inclusion of patients with early-Suzuki stage MMD.

In an article by Liu et al,¹⁰ the grading of leptomeningeal collaterals on DSA was defined as the sum of collaterals from PCA without transdural collateral vessels. However, unlike DSA, MR imaging signs represent all possible leptomeningeal collaterals regardless of the origin of blood flow. In this study, the DSA score for leptomeningeal collaterals was defined as the sum of scores for blood flow originating from the posterior circulation and transdural vessels. The significant correlation between the CEMR-based ivy sign score and DSA score implies that the ivy sign on CEMR may represent all collaterals to brain tissue, including collaterals from the PCA and external carotid artery. The ivy sign on CEMR may have an advantage in that it provides a noninvasive visualization of leptomeningeal collaterals, including transdural collaterals.

Previous literature has reported that leptomeningeal collaterals decrease in abundance after cerebral revascularization in patients with MMD.²⁴ Such findings suggest that leptomeningeal collaterals are associated with cerebral hemodynamics, which would improve after surgery.²⁴ After EDAS, newly formed collaterals from the external carotid artery serve as an important source of cerebral perfusion. Thus, it is possible that leptomeningeal collaterals at baseline could predict the growth of transdural collaterals, an essential indicator of the effectiveness of EDAS. In this study, we found that Matsushima grades correlated significantly with the CEMR-based ivy sign score at baseline. The results indicated that the more leptomeningeal collaterals were present at baseline, the better the outcome of the revascularization operation would be.

Our results should be considered in the context of several limitations. First, among the 79 hemispheres studied, only 10 showed hyperintense lesions on DWI. The statistical power may be jeopardized because of the disparity between DWI-positive and DWI-negative hemispheres. A similar shortage occurred in the linear regression subgroup analysis of CEMR-based ivy sign scores and CBF. The relatively small sample size of early-Suzuki stage MMD may have resulted in failure to find a significant association between these 2 variables. Second, because of the limited number of hemispheres with postoperatively evaluated Matsushima grades (only 21 hemispheres), future studies with additional subjects are needed to estimate the association between leptomeningeal collaterals at baseline and the effectiveness of surgical revascularization. Third, when contrast-enhanced MR imaging is performed, the potential long-term risks associated with gadolinium retention should be carefully considered. Finally, techniques such as deep learning may have the potential to considerably enhance the diagnostic value of the ivy sign on CEMR and FLAIR.

CONCLUSIONS

The current study concerning the application of FVH in the field of MMD suggested that the CEMR-based ivy sign score was superior to FVH in visualizing leptomeningeal collaterals, with DSA as a reference. Furthermore, the CEMR-based ivy sign score could serve as a possible independent predictor of CBF in late-Suzuki stage MMD and reflect the effectiveness of surgical revascularization.

Disclosures: Xin Lou—RELATED: Grant: the National Natural Science Foundation of China, Comments: No. 81730048, 81825012.

REFERENCES

1. Kuroda S, Houkin K. **Moyamoya disease: current concepts and future perspectives.** *Lancet Neurol* 2008;7:1056–66 CrossRef Medline
2. Research Committee on the Pathology and Treatment of Spontaneous Occlusion of the Circle of Willis; Health Labour Sciences Research Grant for Research on Measures for Intractable Diseases. **Guidelines for diagnosis and treatment of moyamoya disease (spontaneous occlusion of the circle of Willis).** *Neurol Med Chir (Tokyo)* 2012;52:245–66 CrossRef Medline
3. Sivrioglu AK, Saglam M, Yildiz B, et al. **Ivy sign in Moyamoya disease.** *Eurasian J Med* 2016;48:58–61 CrossRef Medline
4. Komiyama M, Nakajima H, Nishikawa M, et al. **Leptomeningeal contrast enhancement in moyamoya: its potential role in postoperative assessment of circulation through the bypass.** *Neuroradiology* 2001;43:17–23 CrossRef Medline
5. Kawashima M, Noguchi T, Takase Y, et al. **Unilateral hemispheric proliferation of ivy sign on fluid-attenuated inversion recovery images in moyamoya disease correlates highly with ipsilateral hemispheric decrease of cerebrovascular reserve.** *AJNR Am J Neuroradiol* 2009;30:1709–16 CrossRef Medline
6. Seo K-D, Suh SH, Kim YB, et al. **Ivy sign on fluid-attenuated inversion recovery images in moyamoya disease: correlation with clinical severity and old brain lesions.** *Yonsei Med J* 2015;56:1322–27 CrossRef Medline
7. Yoon H-K, Shin H-J, Chang YW. **“Ivy sign” in childhood moyamoya disease: depiction on FLAIR and contrast-enhanced T1-weighted MR images.** *Radiology* 2002;223:384–89 CrossRef Medline
8. Horie N, Morikawa M, Morofuji Y, et al. **De novo ivy sign indicates postoperative hyperperfusion in moyamoya disease.** *Stroke* 2014;45:1488–91 CrossRef Medline
9. Barber PA, Demchuk AM, Zhang J, et al. **Validity and reliability of a quantitative computed tomography score in predicting outcome of hyperacute stroke before thrombolytic therapy. ASPECTS Study Group.** *Alberta Stroke Programme Early CT Score.* *Lancet* 2000;355:1670–74 CrossRef Medline
10. Liu Z-W, Han C, Zhao F, et al. **Collateral circulation in Moyamoya disease: a new grading system.** *Stroke* 2019;50:2708–15 CrossRef Medline
11. Matsushima Y, Inaba Y. **The specificity of the collaterals to the brain through the study and surgical treatment of moyamoya disease.** *Stroke* 1986;17:117–22 CrossRef Medline
12. Jenkinson M, Bannister P, Brady M, et al. **Improved optimization for the robust and accurate linear registration and motion correction of brain images.** *Neuroimage* 2002;17:825–41 CrossRef Medline
13. Lyu J, Ma N, Liebeskind DS, et al. **Arterial spin labeling magnetic resonance imaging estimation of antegrade and collateral flow in unilateral middle cerebral artery stenosis.** *Stroke* 2016;47:428–33 CrossRef Medline
14. Cho S, Yankanah R, Babyn P, et al. **Inter-rater reliability of the radiographic assessment of simple bone cysts.** *J Child Orthop* 2019;13:226–35 CrossRef Medline
15. Azizyan A, Sanossian N, Mogensen MA, et al. **Fluid-attenuated inversion recovery vascular hyperintensities: an important imaging marker for cerebrovascular disease.** *AJNR Am J Neuroradiol* 2011;32:1771–75 CrossRef Medline
16. Jiang L, Chen Y-C, Zhang H, et al. **FLAIR vascular hyperintensity in acute stroke is associated with collateralization and functional outcome.** *Eur Radiol* 2019;29:4879–88 CrossRef Medline
17. Hohenhaus M, Schmidt WU, Brunecker P, et al. **FLAIR vascular hyperintensities in acute ICA and MCA infarction: a marker for mismatch and stroke severity?** *Cerebrovasc Dis* 2012;34:63–69 CrossRef Medline
18. Mori N, Mugikura S, Higano S, et al. **The leptomeningeal “ivy sign” on fluid-attenuated inversion recovery MR imaging in Moyamoya disease: a sign of decreased cerebral vascular reserve?** *AJNR Am J Neuroradiol* 2009;30:930–05 CrossRef Medline

19. Toyoda K, Ida M, Fukuda K. **Fluid-attenuated inversion recovery intraarterial signal: an early sign of hyperacute cerebral ischemia.** *AJNR Am J Neuroradiol* 2001;22:1021–29 Medline
20. Sanossian N, Saver JL, Alger JR, et al. **Angiography reveals that fluid-attenuated inversion recovery vascular hyperintensities are due to slow flow, not thrombus.** *AJNR Am J Neuroradiol* 2009;30:564–68 CrossRef Medline
21. Czabanka M, Peña-Tapia P, Schubert GA, et al. **Characterization of cortical microvascularization in adult moyamoya disease.** *Stroke* 2008;39:1703–09 CrossRef Medline
22. Jung MY, Kim YO, Yoon W, et al. **Characteristics of brain magnetic resonance images at symptom onset in children with moyamoya disease.** *Brain Dev* 2015;37:299–306 CrossRef Medline
23. Noguchi T, Kawashima M, Nishihara M, et al. **Arterial spin-labeling MR imaging in Moyamoya disease compared with clinical assessments and other MR imaging findings.** *Eur J Radiol* 2013;82:e840–47 CrossRef Medline
24. Kawashima M, Noguchi T, Takase Y, et al. **Decrease in leptomeningeal ivy sign on fluid-attenuated inversion recovery images after cerebral revascularization in patients with Moyamoya disease.** *AJNR Am J Neuroradiol* 2010;31:1713–18 CrossRef Medline

CTA Evaluation of Basilar Septations: An Entity Better Characterized as Aberrant Basilar Fenestrations

J.E. Small, M.B. Macey, A.K. Wakhloo, and S. Sehgal

ABSTRACT

BACKGROUND AND PURPOSE: A basilar artery intraluminal septation is an exceedingly rarely reported, presumed congenital abnormality. In our clinical practice, we have occasionally noticed an intraluminal band within the inferior aspect of the basilar artery on CTA. Furthermore, we have noticed, at times, the presence of a punctate calcification associated with this finding. We hypothesized that what previous studies have called “basilar septations” in fact represent miniature and thus aberrant basilar fenestrations.

MATERIALS AND METHODS: We retrospectively reviewed CTA studies obtained between January 1, 2017, and August 31, 2019. Identified intraluminal basilar abnormalities were classified as either basilar septations or basilar fenestrations. Association with other posterior circulation abnormalities was documented.

RESULTS: A total of 3509 studies were examined. A basilar intraluminal abnormality was evident in 80 patients (2.3%). Of these 80 patients, 59 were classified as having a basilar fenestration (1.7%) and 21 were classified as having basilar septations (0.6%). Associated calcification was evident in 3 of the basilar fenestration cases and 13 of the basilar septation cases.

CONCLUSIONS: Basilar septations most likely represent and should be referred to as aberrant basilar fenestrations. They should be interpreted as benign congenital incidental findings and should not be misinterpreted as focal dissections or arterial webs. Important variations in the morphology of aberrant basilar fenestrations exist, including areas of thinning, varying thickness, and nodularity. Therefore, when associated with calcification or nodularity, aberrant basilar fenestrations should not be confused with focal intraluminal thrombi or calcified or noncalcified emboli.

ABBREVIATIONS: aBF = aberrant basilar fenestration; FMD = fibromuscular dysplasia

The most common congenital finding of the basilar artery is a fenestration (prevalence range, 0.28%–5.26% in postmortem series).^{1–4} Other congenital intraluminal abnormalities of the basilar artery have been rarely reported in the literature. In particular, case reports of intraluminal basilar septations and basilar webs are exceedingly rare.^{5,6} Although infrequently seen, these variations can be detected on routine vascular imaging.

Arterial fenestrations are segmental duplications of the vessel lumen into 2 endothelial cell-lined ducts that share a common origin and reconnect distally.^{7,8,9,10,11} Fenestrations result from an incomplete fusion in the early embryonic stage, yielding a developmental abnormality that can range in length from 1 mm to a near-complete doubling of the artery.¹⁰ A large fenestration

appears like a “window” perforating the vessel, whereas a very small fenestration can look like a dimple in the vessel wall.¹⁰ Prevalence varies greatly between postmortem and imaging reports, with a reported angiographic prevalence of 1.1%.¹³ Additionally, prevalence based on 3D reconstruction of CT and MR angiography has been reported at 13%.^{11,12} Although relationships between fenestration and neurovascular pathology are not well-defined, associations with aneurysms and ischemic stroke have been observed.^{10,12–14}

A basilar intraluminal septation is an exceedingly rarely reported, presumed congenital abnormality. To our knowledge, only 2 published articles describe this entity. These articles describe them as intraluminal bands within the vessel.^{6,15} The most frequent location for this variation is in close proximity to the junction of the vertebral arteries.^{6,15} The initial study describing this finding was published by Davy,¹⁵ in 1839, in which he described 17 cases in 98 postmortem examinations (17.35%). The most recent article is a single cadaveric study that found 1 septation in a sample of 150 cadavers (0.67%).⁶ In this case, the septation measured 3 mm long and 1.5 mm wide.⁶ Tubbs et al⁶ have

Received September 17, 2020; accepted after revision November 5.

From the Departments of Neuroradiology (J.E.S., M.B.M.), Interventional Neuroradiology (A.K.W.), and Neurology (S.S.), Lahey Hospital and Medical Center, Burlington, Massachusetts.

Please address correspondence to Juan E. Small, MD, Lahey Hospital and Medical Center, 41 Mall Rd, Burlington, MA 01805; e-mail: juan.e.small@lahey.org
<http://dx.doi.org/10.3174/ajnr.A7008>

suggested that these septations may represent a form fruste of basilar fenestrations and may be misinterpreted as dissections or thrombus.¹⁶ A similar finding has been described in a few imaging case reports as a presumed basilar web when associated with thrombosis and infarction.⁵ However, only correlational evidence was reported. Of note, these findings were not present at a branching point and did not mirror the ledge-like imaging findings of a carotid web.^{17,18} In fact, the imaging findings appear to be identical in location and morphology to the aforementioned basilar septations.

In our clinical practice, we have occasionally noticed an intraluminal band within the inferior aspect of the basilar artery on routine CTA. Because there is no theoretic inferior limit to the size of a basilar fenestration, we hypothesized that what previous studies have called “basilar septations” or “basilar webs” in fact represent miniature and thus aberrant basilar fenestrations (aBFs).

MATERIALS AND METHODS

In an institutional review board–approved study, we retrospectively reviewed all diagnostic-quality head and neck CTA studies performed between January 1, 2017, and August 31, 2019. Any studies with serious motion at the level of the basilar artery were excluded from the analysis. A total of 3509 diagnostic-quality head and neck CTAs were identified within the time period of analysis. Scanning was performed on 64-, 128-, and 256-section multidetector row CT scanners (VCT 64, GE Healthcare; Definition 64, Siemens; Ingenuity 128, IQon 128, and ICT 256, Philips Healthcare). The standard CTA protocol was intravenous injection of 80 mL of nonionic contrast, with arterial phase imaging performed from the aortic arch to the calvarial apex with an axial CTA source image thickness of 0.625 mm. The arterial vertebrobasilar system was inspected for the presence of any clearly defined, intraluminal abnormality on axial CTA source images. Any other CTA or MRA studies performed previously or subsequently were used to confirm the finding and assess interval changes. Any DSA studies with images of the posterior circulation were also examined.

Identified basilar intraluminal abnormalities were classified as either basilar septations or basilar fenestrations. Basilar fenestrations were defined as areas of incomplete fusion of the basilar artery with a visible extravascular lumen (ie, window) or puckering, indentation, or dimple of the vessel wall. Basilar septations were defined as an intraluminal linear hypodensity without a visible window, puckering, indentation, or dimple. In identified cases, the location within the vessel (inferior, middle, or superior one-third) was documented.

Basilar fenestrations and septations were further classified by appearance. Basilar fenestrations were classified as window-, hourglass-, or funnel-shaped. Basilar septations were classified as either linear if a smooth intraluminal band was evident or nodular if any areas of bulging or protuberance existed along the intraluminal band. Any associated morphologic findings such as calcification were also documented.

Measurements of the intraluminal finding were obtained using axial CTA. In the case of a fenestration, the measurement

was obtained from the point of maximum vessel wall aperture. Alternatively, septations were measured at the point of maximum width. A measurement of ≤ 0.6 mm (CT scanner section thickness) was given for septations whose thickness was at the limit of study resolution.

To ascertain whether any of these findings were associated with any other posterior circulation abnormalities, we also documented the presence of an aneurysm, ischemic infarct, parenchymal hemorrhage, severe atherosclerotic stenosis or occlusion, dissection, and vascular webs. The data obtained from our retrospective review were analyzed using descriptive statistics, and 95% confidence intervals are provided for the estimated proportions of patients with abnormal anatomy. Abnormal anatomy is further divided into basilar fenestrations and basilar septations.

RESULTS

A total of 3509 patients (1727 men [49.2%] and 1782 women [50.8%]; age range, 18–102 years; mean age, 64 years) had a diagnostic-quality head and neck CTA study performed during the designated time period. A normal vertebrobasilar system was seen in 3429 of these patients (3429/3509 [97.7%], 1690 men [49.3%] and 1739 women [50.7%]; age range, 18–102 years; mean age, 64 years). A detectable basilar artery intraluminal abnormality was evident in the remaining 80 patients (80/3509 [2.3%]; 95% CI, 1.79%–2.77%; 43 men and 37 women; age range, 36–94 years; mean age, 67 years). Of these 80 cases, 59 were classified as a basilar fenestration (59/3509 [1.7%]; 95% CI, 1.26%–2.11%; 33 men [55.9%] and 26 women [44.1%]; age range, 38–94 years; mean age, 67 years) and 21 were classified as a basilar septation (21/3509 [0.6%]; 95% CI, 0.34%–0.85%; 10 men [47.6%]; 11 women [52.4%]; age range, 36–92; mean age, 68 years). No cases with >1 fenestration or septation were found.

Of the 59 cases classified as a basilar fenestration, 27 had window-shaped fenestrations, 30 had hourglass-shaped fenestrations, and 2 had funnel-shaped fenestrations (Fig 1). The mean apertures of these 3 variations were 3.9 mm (range, 1.5–15 mm), 1.2 mm (range, 0.8–2.0 mm), and 1.4 mm (range, 0.9–1.9 mm), respectively. All the small basilar fenestrations without a window were associated with visible puckering/indentation of the vessel wall. Of the patients with basilar fenestrations, 53 were located in the inferior third (53/59, 89.8%); 4 in the middle third (4/59, 6.8%); and 2 in the superior third of the vessel (2/59, 3.4%). Of the 59 basilar fenestration cases, 17 had at least 1 other CTA or MRA with the imaging findings evident and unchanged on all studies. Of these 17 cases, 3 also had DSA and VasoCT (Philips Healthcare; conebeam CT with contrast) images of the posterior circulation confirming the basilar fenestration, also well-visualized with this technique.

Of the 21 septations, 9 had at least 1 other CTA or MRA with the imaging findings evident and unchanged on all studies (Fig 2). Of these 9 cases, 3 also had DSA images of the posterior circulation, with the septations not clearly evident on angiographic images. When we compared the saliency of the septations on CTA versus MRA, the septation was more evident on CTA than on MRA in 1 patient, equally evident on CTA and MRA in 2 patients, and better evident on MRA than CTA in 2 patients. Of

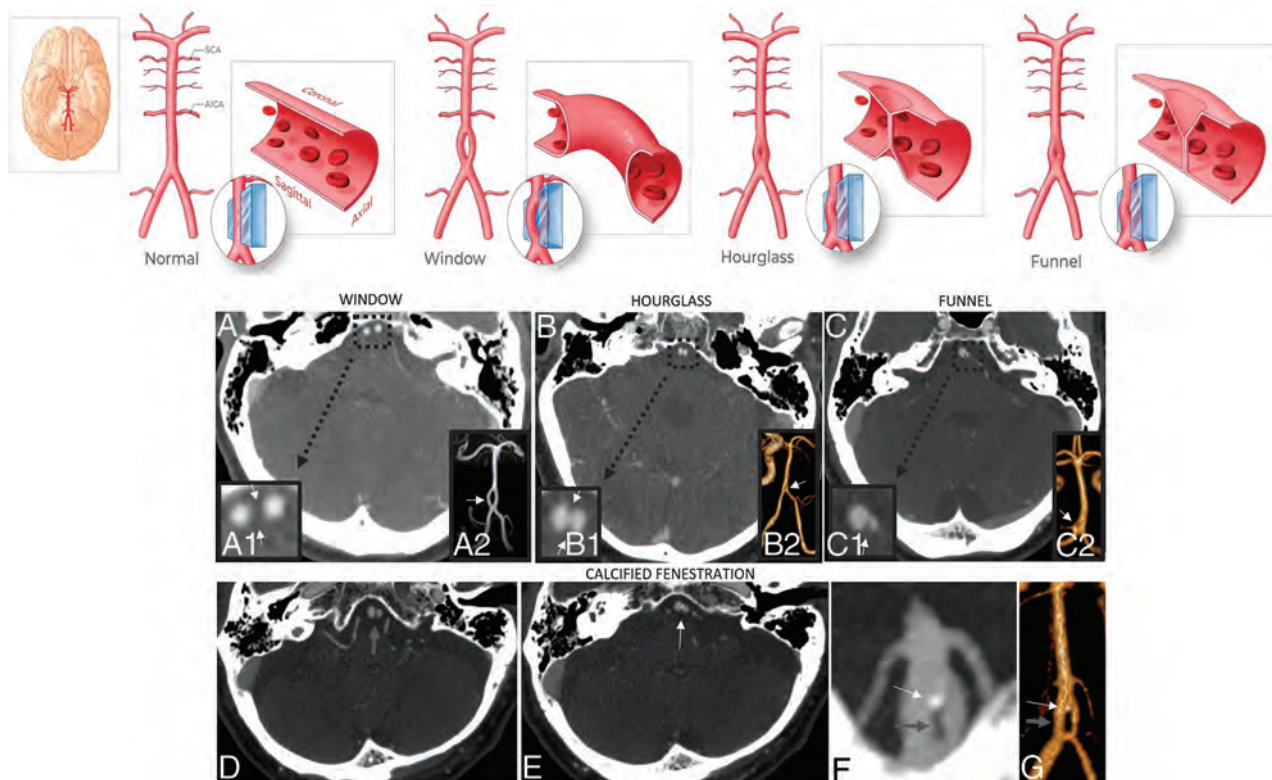


FIG 1. Basilar fenestrations. I) Classification. Basilar fenestrations were classified as either window-, hourglass-, or funnel-shaped (upper row illustrations: printed with permission from Insil Choi, copyright 2020). Axial CTA images (A–C) and magnified axial CTA images focusing on the basilar artery fenestration (A1, B1, C1) and coronal 3D reconstructions of the posterior circulation (A2, B2, C2) in various patients depict different morphologies of basilar fenestration apertures. II) Fenestration with calcification. Associated calcification is evident in 3 of the basilar fenestration cases (3/59; 5.1%). Sequential axial CTA images in one of these patients demonstrate a fenestration (D, wide gray arrow) with a small nodular calcification along its superior aspect (E, thin white arrow), a finding better evident on coronal MIP (F) and 3D reconstruction (G) of the basilar artery (fenestration highlighted by a thick gray arrow, and the nodular calcification, by the thin white arrow).

note, the saliency of the findings appeared primarily related to the quality of the imaging study, including motion, artifacts, and bolus timing rather than superiority of one technique over the other. Of the 21 cases classified as basilar septations, 12 were linear (Fig 2) and 9 were nodular (Fig 3). The mean width of these 2 variations was 0.63 mm (range, ≤ 0.6 –0.7 mm) and 0.98 mm (range, 0.7–1.4 mm), respectively. None of the patients with basilar septations were seen to have puckering/indentation of the vessel wall. Of the patients with basilar septations, 14 septations were located in the inferior third (14/21, 66.7%); 5, in the middle third (5/21, 23.8%); and 2, in the superior third (2/21, 9.5%) of the vessel.

Calcification was associated with intraluminal abnormalities in 16 patients. Associated calcification was evident in 3 of the patients with a basilar fenestration and in 13 of those with the basilar septations (Figs 1 and 3). With respect to calcified basilar septations, 5 of 12 linear septations were associated with calcification, while 8 of 9 nodular septations were associated with calcification.

A total of 16 cases with incidentally detected fenestrations or septations demonstrated coincident evidence of infarction (16/80, 20%). However, 12 patients had infarction involving the anterior circulation only (12/80, 15%), while only 3 patients had evidence of posterior circulation infarction (3/80,

3.8%), and 1 patient had an embolic pattern of infarction involving both the anterior and posterior circulation (1/80, 1.3%). Of the total number of patients with evidence of infarction, only 2 had basilar septations, one involving the anterior circulation (1/21, 4.8%) and the other the posterior circulation (1/21, 4.8%).

A total of 7 cases with either a basilar fenestration or septation demonstrated coincident evidence of parenchymal hemorrhage (7/80, 8.8%). A total of 4 cases had hemorrhage involving the anterior circulation territory only (4/80, 5%), 2 cases had evidence of posterior circulation territory hemorrhage (2/80, 2.5%), and 1 case had a parenchymal hemorrhage involving both the anterior and posterior circulation territories (1/80, 1.3%). Only 2 cases with basilar septations demonstrated coincident evidence of parenchymal hemorrhage, and both involved the anterior circulation territory (2/21, 9.5%).

No cases of intracranial arterial dissection were identified. Basilar fenestrations or septations with coincident dissection of the extracranial neck circulation were seen in 6 cases (6/80, 7.5%). A total of 3 patients had dissection involving the extracranial vertebral arteries (3/80, 3.8%), and the other 3 had dissection involving the extracranial internal carotid arteries (3/80, 3.8%). Extracranial vertebral artery dissection was recognized in 2 of the basilar fenestration cases (2/59, 3.4%) and 1 of the basilar

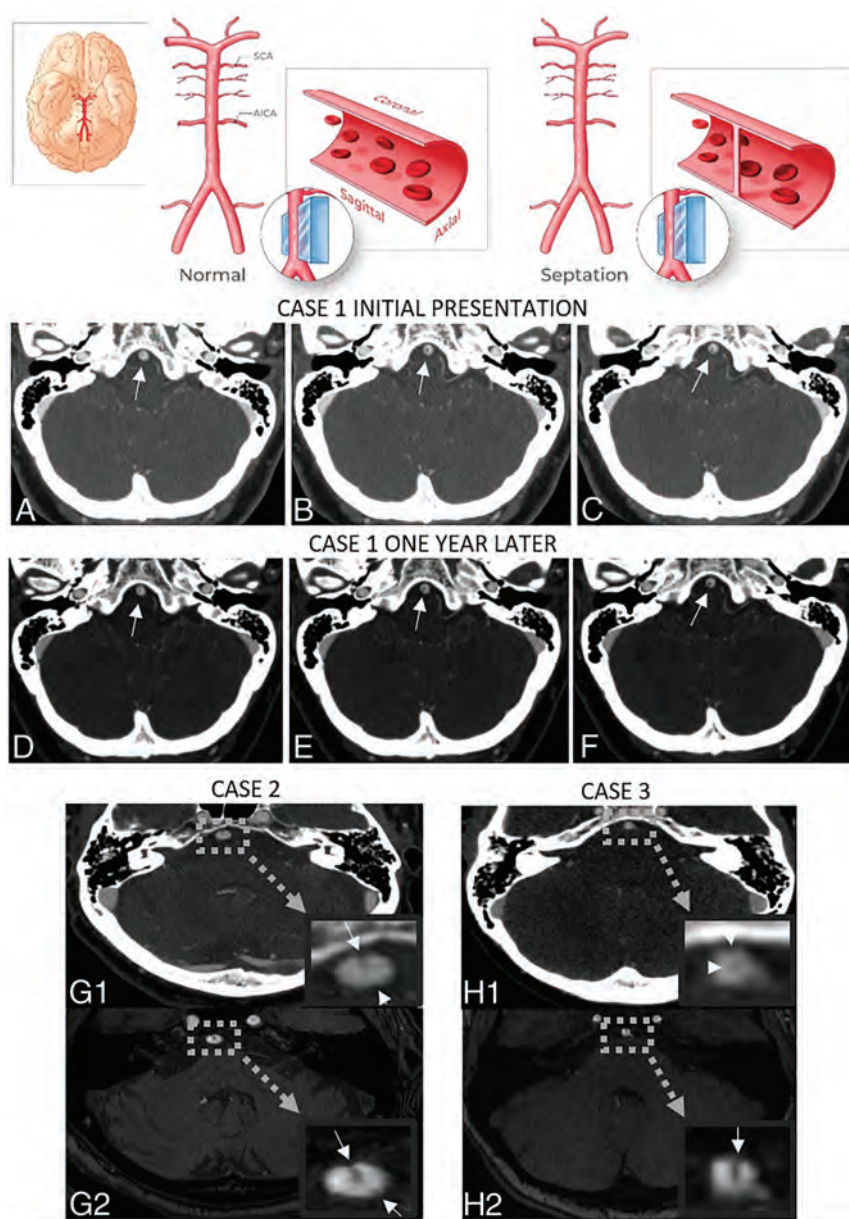


FIG 2. Basilar septations. I) Lack of interval changes: a basilar septation (upper row illustration, printed with permission from Insil Choi, copyright 2020) is identified in 21 patients (0.6%). A typical basilar septation can be seen on sequential axial CTA images at initial presentation in case 1 (A–C). Note the clearly defined linear hypodensity without a visible window or clear evidence of puckering or indentation of the vessel wall (A–C, arrows). Sequential axial CTA images obtained 1 year later (D–F) clearly show the absence of interval changes. Of the small subset of patients with >1 CTA, there is no evidence of interval changes at any time point. II) Evident on CTA and MRA: axial CTA image in case 2 (G1) demonstrates a septation along the ventral aspect of the basilar artery (white arrow). Note that the septation is thick anteriorly but markedly thins posteriorly. This finding is corroborated on axial MRA images with the thin posterior aspect slightly more evident (G2, white arrows). Axial CTA image in a different patient (H1) demonstrates a markedly subtle septation perhaps best visualized along the central lumen of the basilar artery (H1 magnified insert, arrowheads). This finding is again corroborated and much better visualized on a high-quality axial MRA (H2, white arrowhead). Although MRA was available in only a small subset of the patients, the presence of a septation was corroborated on this technique. Of note, depending on the quality of the CTA or MRA acquisition, the septations were, at times, better defined on CTA instead.

septation cases (1/21, 4.8%). Extracranial internal carotid artery dissection was recognized in 2 of the basilar fenestration cases (2/59, 3.4%) and 1 of the basilar septation cases (1/21, 4.8%).

Aneurysms of the cerebral circulation were recognized in 19 cases (19/80, 23.8%). However, almost all aneurysms were present in the anterior circulation, with only a single basilar tip aneurysm noted (1/80, 1.3%) with an associated basilar septation.

No cases fitting the description of an arterial web were found within the basilar artery. An extracranial internal carotid artery carotid web was discovered in 1 patient with an associated basilar fenestration. No arterial webs were evident in cases of basilar septation. Fibromuscular dysplasia (FMD) was recognized in 5 cases (5/80; 6.3%), with an associated basilar fenestration. No cases of FMD associated with basilar septations were noted.

No cases of moderate or severe intracranial posterior circulation atherosclerosis were identified. Severe extracranial atherosclerotic stenosis or occlusion was identified in 22 patients who also were found to have fenestrations or septations (22/80, 27.5%). A total of 15 patients had severe atherosclerosis involving the anterior circulation only (15/80, 18.8%), 4 patients had evidence of severe extracranial posterior circulation atherosclerosis (4/80, 5%), and 3 patients had severe stenosis or occlusion affecting both the anterior and posterior circulation (3/80, 3.8%). Basilar fenestration cases were associated with severe anterior cerebral circulation atherosclerosis 22% of the time (13/59), while severe posterior circulation atherosclerosis was seen in only 6.8% of cases (4/59). Basilar septation was associated with severe anterior cerebral circulation atherosclerosis 8.5% of the time (5/59), while posterior circulation severe atherosclerosis was seen in 5.1% of cases (3/59). Results are summarized in the Table.

DISCUSSION

A basilar intraluminal abnormality was detectable in 2.3% of patients on CTA. Of these, 1.7% had a basilar fenestration. To our knowledge, no previous study has documented morphologic differences in the aperture of basilar fenestrations. Our results reveal there are clear variations in the spectrum of size, morphology, and appearance of basilar fenestrations with less

phologic differences in the aperture of basilar fenestrations. Our results reveal there are clear variations in the spectrum of size, morphology, and appearance of basilar fenestrations with less

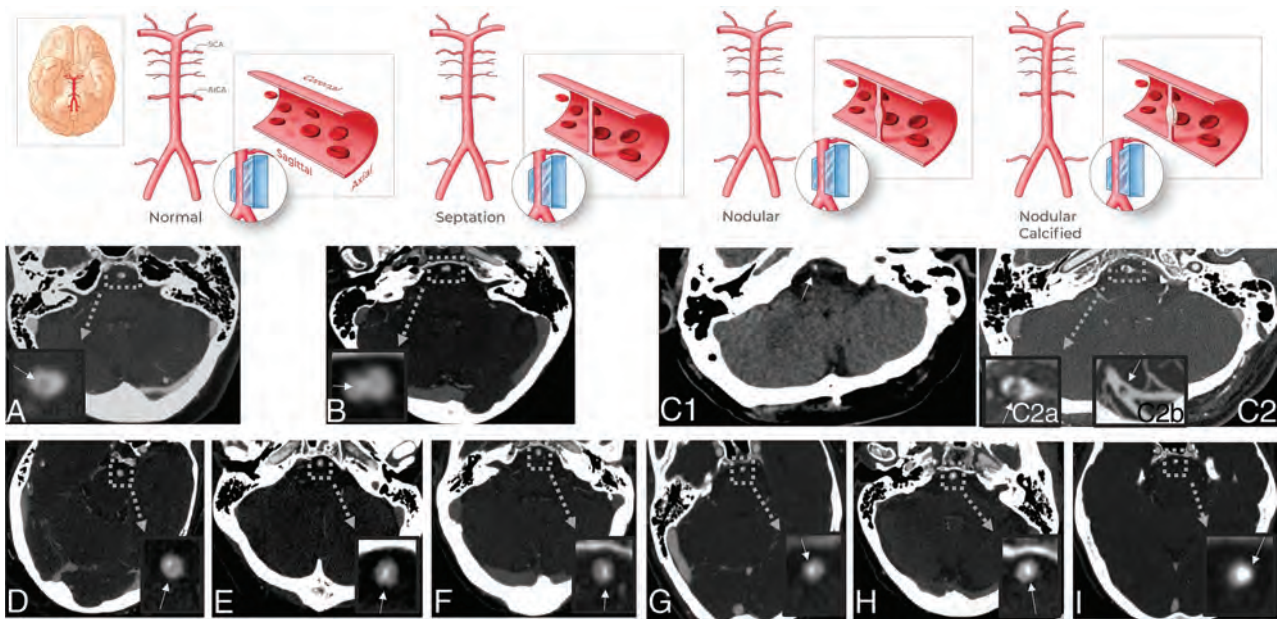


FIG 3. Basilar septations with nodularity without and with calcification (upper row illustrations, printed with permission from Insil Choi, copyright 2020). I) Several basilar septation cases exhibited areas of nodularity. Three representative cases are shown above. Axial CTA in the first case (A) demonstrates subtle nodularity along the midpoint of the basilar septation (A magnified insert, *white arrow*). Axial CTA image in a different patient (B) shows calcification associated with central nodularity (B magnified insert, *white arrow*). Axial CTA in a third patient (C2) demonstrates a prominent but only partially calcified nodular septation. The calcification is clearly evident on an axial noncontrast CT image (C1, *arrow*). The partially calcified prominent nodularity associated with the septation is well-demarcated on axial CTA (C2a magnified insert, *white arrow*) and coronal MIP (C2b, *white arrow*) images. II) Calcified basilar septations: focal calcification associated with basilar septations is seen in 13 cases (13/21, 61.9%). Axial CTA images in 6 different patients (D–I) demonstrate different patterns of calcification with some exhibiting a more linear pattern (D–F, *arrows*) and others exhibiting a more nodular pattern of calcification (G–I, *arrows*). Note the prominent nodular calcification occupying a large portion of the basilar lumen in case I.

Summary of imaging findings^a

Morphology	Fenestration (n = 59)	Septation (n = 21)
Location		
Inferior third (No.) (%)	53 (89.8%)	14 (66.7%)
Middle third (No.) (%)	4 (6.8%)	5 (23.8%)
Superior third (No.) (%)	2 (3.4%)	2 (9.5%)
Associated findings		
Calcification (No.) (%)	3 (5.1%)	13 (61.9%)
Cerebral infarction (No.) (%)	14 (23.7%)	2 (9.5%)
Parenchymal hemorrhage (No.) (%)	5 (8.5%)	2 (9.5%)
Coincident vascular abnormalities		
Vertebral dissection (No.) (%)	2 (3.4%)	1 (4.8%)
Carotid dissection (No.) (%)	2 (3.4%)	1 (4.8%)
Carotid web (No.) (%)	1 (1.7%)	0
Fibromuscular dysplasia (No.) (%)	5 (8.5%)	0

^a A total of 80 cases with basilar artery intraluminal findings were identified. The location and distribution along the course of the basilar artery were similar for fenestrations and septations. Rarely, arterial dissections were found in the extracranial segments of vertebral artery or internal carotid artery. No intracranial dissections were identified in any of the cases.

than half of our cases conforming to a typical window-shaped appearance, a little more than half of the cases exhibiting an hourglass shape, and only a few cases exhibiting funnel morphology depicted in our illustrations. Hourglass and funnel morphologies had smaller-but-measurable apertures in the vessel wall compared with window-type fenestrations. Furthermore, to our knowledge, no previous study has documented a congenital non-atherosclerotic pattern of calcification associated with basilar fenestrations, evident in 3 cases.

No previous imaging study has focused on the prevalence of basilar septations based on CTA. Our results reveal that findings fitting the description of a basilar septation are visible on arterial imaging and exhibit a morphology best described as an intraluminal linear hypodensity without a visible arterial vessel wall aperture, wall puckering, or indentation. Basilar septations comprised 0.6% of our cases. Our results show that septations mirror the location and distribution of basilar fenestrations, with most present in the inferior third of the vessel. Because there is no theoretic inferior limit to the size of a basilar fenestration, we propose that a basilar septation is likely best conceptualized as a miniature fenestration and best referred to as an aberrant basilar fenestration. We will, therefore, refer to basilar septations in the remainder of this discussion as aBFs.

Our findings show that calcification is clearly associated with both basilar fenestrations and aBFs, further supporting the notion that they represent variations in the size of the same entity. As noted above, a nonatherosclerotic pattern of focal calcification was evident in 5.1% of basilar fenestration cases while

calcification was seen in 61.9% of aBF cases. Although calcification is associated with fenestrations of any size, for reasons yet unknown, it is more common in fenestrations of smaller caliber.

Conceptualizing aBFs as tiny fenestrations has important implications. They should be interpreted as benign congenital findings. They should not be confused with dissections or intraluminal webs. Furthermore, we demonstrate important variations in the morphology of aBFs, including areas of thinning, varying thickness, and nodularity. Therefore, when associated with calcification or nodularity, aBFs should not be confused with intraluminal thrombi or emboli with or without calcification. Furthermore, our results demonstrate that there is no notable correlation between aBFs and arterial dissection, thrombosis, or emboli. This benign history contrasts with the poor prognosis of the known ischemic and hemorrhagic complications of isolated basilar dissections,^{18,19,20} as well as the association of arterial webs with ischemic stroke.^{21,22}

None of our aBFs fit the morphologic description of a web or a dissection. None of the basilar septations we found were present at or near an arterial branching point and none displayed the ledge-like imaging findings of a carotid web. In addition, only one of our aBFs was associated with a posterior circulation stroke (4.8%; 1/21), and none were associated with posterior circulation hemorrhage, extracranial arterial web, or FMD. Our single case of an ICA origin web and our 5 cases of FMD were associated with classic appearing basilar fenestrations instead. Therefore, we do not find evidence to support the theory that aBFs represent either webs or a focal dissection. Of note, the presence of extracranial arterial dissection as well as anterior circulation stroke in several of our cases is thought to represent a reflection of the sample because many of our CTAs were performed for acute neurologic symptoms. Only 1 case of a basilar tip aneurysm was identified, with no posterior circulation aneurysms found at the site of basilar fenestrations or aBFs. We, therefore, believe that the concomitant basilar intraluminal findings are purely incidental, without a causal association.

We believe the detection of aBFs has important implications in the era of endovascular procedures, especially in a posterior stroke work-up. Further studies are needed to ascertain their consequences, if any, in cases of basilar catheterization or stent placement or endovascular stroke treatment. Currently, it is unclear whether they are simply displaced against the vessel wall or whether vascular damage is possible. Therefore, we believe that neurointerventionalists should likely be aware of their presence before basilar catheterization.

Our study is limited due to its retrospective nature and the lack of pathologic correlation. Nonetheless, we believe that the 2 previously published pathologic studies relating to basilar septations^{6,15} lend strong support to our findings. Furthermore, our study was conducted in a North American population; therefore, the possibility that racial variations exist cannot be excluded. In addition, because the size of aBFs is near the limit of imaging resolution, certain questions remain that can only be answered by careful microscopic pathologic analysis. These questions include whether areas of vanishing thickness represent thinning or partial absence, whether a microscopic arterial wall aperture remains at the vessel wall or whether it is obliterated, and whether a

collapsed lumen exists within the walls of an aBF or whether the walls are fused and the extraluminal channel has been congenitally obliterated. Last, our study was conducted in an adult population without patients younger than 18 years of age. Further research is necessary to ascertain the presence of the morphologic findings as well as associated calcification in a pediatric population.

CONCLUSIONS

Basilar septations are evident on 0.6% of CTAs and most likely represent and should be referred to as aberrant basilar fenestrations. They should not be misinterpreted as focal dissections, arterial webs, intraluminal thrombi, or emboli with or without calcification. We believe that the detection of aBFs has important theoretic implications in the era of endovascular procedures, and further studies are needed to ascertain their consequences in cases of planned basilar catheterization or stent placement.

Key Results

- Variations in the size and appearance of basilar fenestrations exist with window-, hourglass-, and funnel-shaped morphologies.
- Basilar septations are evident on 0.6% of CTAs and likely represent miniature aBFs. A nonatherosclerotic pattern of focal calcification was evident in 5.1% of basilar fenestrations and 61.9% of aBFs.
- aBFs should be interpreted as benign, congenital findings. They should not be confused with dissections, webs, thrombi, or emboli with or without calcification.

Basilar septations are evident on 0.6% of CTAs, most likely represent aBFs, and should be interpreted as incidental, benign, congenital findings.

ACKNOWLEDGMENTS

We wish to acknowledge and thank Insil Choi for her expert medical illustrations helping to depict our findings.

Disclosures: Ajay K. Wakhloo—*UNRELATED: Consultancy:* Stryker Neurovascular, Cerenovus Johnson & Johnson, Philips Healthcare, NovaSignal, ThrombX, InNeuroCo; *Grants/Grants Pending:* Medtronic, Philips Healthcare, Deinde Medical*; *Patents (Planned, Pending or Issued):* Patents with Medi-Solve and Cordis Neurovascular; *Stock/Stock Options:* Penumbra, BSC Group, InNeuroCo, ThrombX, Nova Digital, Deinde Medical, Analytic 4 Life. *Money paid to the institution.

REFERENCES

1. Wollschlaeger G, Wollschlaeger PB, Lucas FV, et al. **Experience and result with post-mortem cerebral angiography performed as routine procedure of the autopsy.** *Am J Roentgenol Radium Ther Nucl Med* 1967;101:68–87 CrossRef Medline
2. Stopford JS. **The arteries of the pons and medulla oblongata.** *J Anat Physiol* 1916;50:132–64 Medline
3. Busch W. **Contribution to the morphology and pathology of the basilar artery: results of the study of 1000 brains** [in German]. *Arch Psychiatr Nervenkr (1970)* 1966;208:326–44 CrossRef Medline
4. Von Mittelwallner F. **Variationsstatistische Untersuchungen an den basalen Hirngefassen [Statistical studies on variations of the basal cerebral vessels].** *Acta Anat (Basel)* 1955;24:51–87

5. Esenwa C, Labovitz D, Caplan LR. **“Basilar web” causing basilar branch infarction.** *J Stroke Cerebrovasc Dis* 2019;28:104366 CrossRef Medline
6. Tubbs RS, Shaffer WA, Loukas M, et al. **Intraluminal septation of the basilar artery: incidence and potential clinical significance.** *Folia Morphol (Warsz)* 2008;67:193–95 Medline
7. Zhang D, Wang H, Feng Y, et al. **Fenestration deformity of the basilar artery trunk with an aneurysm.** *Medicine (Baltimore)* 2019;98:e16393 CrossRef Medline
8. Cooke DL, Stout CE, Kim WT, et al. **Cerebral arterial fenestrations.** *Interv Neuroradiol* 2014;20:261–74 CrossRef Medline
9. Sogawa K, Kikuchi Y, Ouchi T, et al. **Fenestrations of the basilar artery demonstrated on magnetic resonance angiograms: an analysis of 212 cases.** *Interv Neuroradiol* 2013;19:461–65 CrossRef Medline
10. Finlay HM, Canham PB. **The layered fabric of cerebral artery fenestrations.** *Stroke* 1994;25:1799–806 CrossRef Medline
11. van Rooij S, Bechan RS, Peluso JP, et al. **Fenestrations of intracranial arteries.** *AJNR Am J Neuroradiol* 2015;36:1167–70 CrossRef Medline
12. Tanaka M, Kikuchi Y, Ouchi T. **Neuroradiological analysis of 23 cases of basilar artery fenestration based on 2280 cases of MR angiographies.** *Interv Neuroradiol* 2006;12:39–44 CrossRef Medline
13. Menshawi K, Mohr JP, Gutierrez J. **A functional perspective on the embryology and anatomy of the cerebral blood suppl.** *J Stroke* 2015;17:144–58 CrossRef Medline
14. Liu L, Zhang XB, Lu S, et al. **Plaque distribution of basilar artery fenestration by 3D high-resolution MR vessel wall imaging.** *Cell Transplant* 2019;28:851–55 CrossRef Medline
15. Davy J. **Of a peculiarity of structure occasionally occurring in the basilar artery of man.** *Edinb Med Surg J* 1839;51:70–75 Medline
16. Scherer A, Siebler M, Aulich A. **Virtual arterial endoscopy as a diagnostic aid in a patient with basilar artery fenestration and thromboembolic pontine infarct.** *AJNR Am J Neuroradiol* 2002;23:1237–39 Medline
17. Coutinho JM, Derkatch S, Potvin AR, et al. **Carotid artery web and ischemic stroke: a case-control study.** *Neurology* 2017;88:65–69 CrossRef Medline
18. Hu H, Zhang X, Zhao J, et al. **Transient ischemic attack and carotid web.** *AJNR Am J Neuroradiol* 2019;40:313–18 CrossRef Medline
19. Zhang AJ, Dhruv P, Choi P, et al. **A systematic literature review of patients with carotid web and acute ischemic stroke.** *Stroke* 2018;49:2872–76 CrossRef Medline
20. Li L, Li T, Xue J, et al. **Stent treatment for basilar artery dissection: a single-center experience of 21 patients.** *Interv Neuroradiol* 2016;22:260–65 CrossRef Medline
21. Obusez EC, Jones SE, Hui F, et al. **Vessel wall MRI for suspected isolated basilar artery dissection.** *J Clin Neurosci* 2016;27:177–79 CrossRef Medline
22. Kim BM, Suh SH, Park SI, et al. **Management and clinical outcome of acute basilar artery dissection.** *AJNR Am J Neuroradiol* 2008;29:1937–41 CrossRef Medline

Intra-Arterial Thrombolysis after Unsuccessful Mechanical Thrombectomy in the STRATIS Registry

S.F. Zaidi, A.C. Castonguay, O.O. Zaidat, N. Mueller-Kronast, D.S. Liebeskind, H. Salahuddin, and M.A. Jumaa



ABSTRACT

BACKGROUND AND PURPOSE: Recent data suggest that intra-arterial thrombolytics may be a safe rescue therapy for patients with acute ischemic stroke after unsuccessful mechanical thrombectomy; however, safety and efficacy remain unclear. Here, we evaluate the use of intra-arterial rtPA as a rescue therapy in the Systematic Evaluation of Patients Treated with Neurothrombectomy Devices for Acute Ischemic Stroke (STRATIS) registry.

MATERIALS AND METHODS: STRATIS was a prospective, multicenter, observational study of patients with acute ischemic stroke with large-vessel occlusions treated with the Solitaire stent retriever as the first-line therapy within 8 hours from symptom onset. Clinical and angiographic outcomes were compared in patients having rescue therapy treated with and without intra-arterial rtPA. Unsuccessful mechanical thrombectomy was defined as any use of rescue therapy.

RESULTS: A total of 212/984 (21.5%) patients received rescue therapy, of which 83 (39.2%) and 129 (60.8%) were in the no intra-arterial rtPA and intra-arterial rtPA groups, respectively. Most occlusions were M1, with 43.4% in the no intra-arterial rtPA group and 55.0% in the intra-arterial rtPA group ($P = .12$). The median intra-arterial rtPA dose was 4 mg (interquartile range = 2–12 mg). A trend toward higher rates of substantial reperfusion (modified TIC1 $\geq 2b$) (84.7% versus 73.0%, $P = .08$), good functional outcome (59.2% versus 46.6%, $P = .10$), and lower rates of mortality (13.3% versus 23.3%, $P = .08$) was seen in the intra-arterial rtPA cohort. Rates of symptomatic intracranial hemorrhage did not differ (0% versus 1.6%, $P = .54$).

CONCLUSIONS: Use of intra-arterial rtPA as a rescue therapy after unsuccessful mechanical thrombectomy was not associated with an increased risk of symptomatic intracranial hemorrhage or mortality. Randomized clinical trials are needed to understand the safety and efficacy of intra-arterial thrombolysis as a rescue therapy after mechanical thrombectomy.

ABBREVIATIONS: IA = intra-arterial; MT = mechanical thrombectomy; RT = rescue therapy; sICH = symptomatic intracranial hemorrhage; STRATIS = Systematic Evaluation of Patients Treated with Neurothrombectomy Devices for Acute Ischemic Stroke

Mechanical thrombectomy (MT) is a powerful therapy for patients with acute ischemic stroke with large-vessel occlusions. However, despite its proved success,^{1–5} most patients do not achieve complete reperfusion^{6–9} and only about half of all patients treated with MT achieve a good

clinical outcome at 3 months.⁶ Because patients with complete reperfusion are 2 times more likely to have favorable outcomes than those with near-complete reperfusion,¹⁰ exploration of adjunctive or rescue therapies (RTs) to augment MT complete reperfusion is warranted.

The role of intra-arterial (IA) thrombolysis has evolved from a primary therapy^{11–17} to an adjunctive or RT to MT. Recently, a US survey indicated that 60.6% of neurointerventionalists use IA lytics in their practice, with the most common approach as an RT after MT.¹⁸ Previous studies on the use of IA rtPA in the context of MT either as an RT or adjunctive therapy have yielded promising data, but these studies are limited by their small sample sizes and retrospective design.^{19–21} Here, in this subanalysis, we retrospectively evaluate the use of IA rtPA as an RT after unsuccessful MT in the multicenter, prospective, Systematic Evaluation of Patients Treated with Neurothrombectomy Devices for Acute Ischemic Stroke

Received August 25, 2020; accepted after revision October 21.

From the Department of Neurology (S.F.Z., A.C.C., H.S., M.A.J.), University of Toledo, Toledo, Ohio; St. Vincent Mercy Hospital (O.O.Z.), Toledo, Ohio; Advanced Neuroscience Network (N.M.-K.), Tenet, South Florida, Hialeah, Florida; and Department of Neurology (D.S.L.), University of California Los Angeles, Los Angeles, California.

This study was sponsored by Medtronic.

Syed F. Zaidi and Alcía C. Castonguay contributed equally to this work.

Please address correspondence to Syed F. Zaidi, MD, University of Toledo, 3000 Arlington Ave, Department of Neurology, Toledo, OH, 43614; e-mail: syed.zaidi2@utoledo.edu

Indicates article with online supplemental data.

<http://dx.doi.org/10.3174/ajnr.A6962>

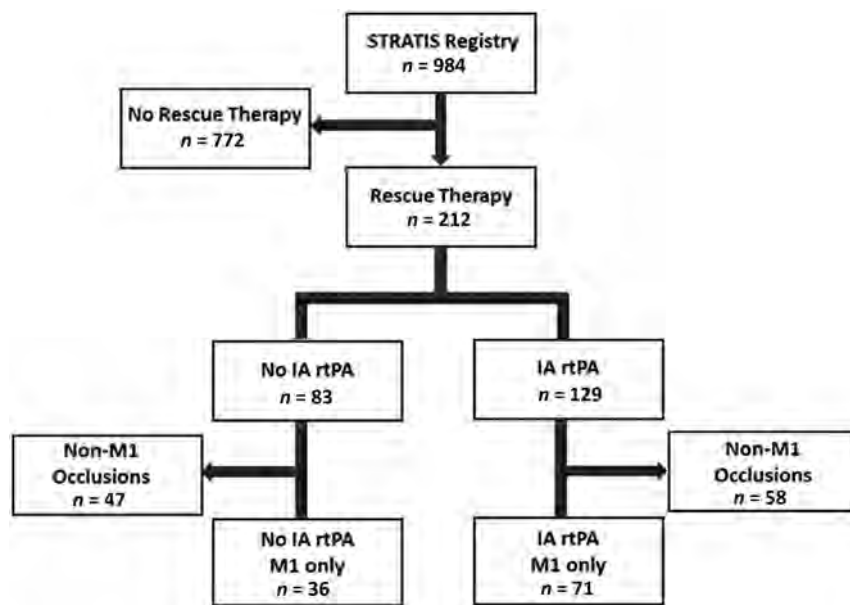


FIG 1. Study flow chart.

(STRATIS) registry (<https://www.clinicaltrials.gov/ct2/show/NCT02239640?term=STRATIS&draw=2&rank=7>).

MATERIALS AND METHODS

Study Population

STRATIS Registry. The STRATIS registry was a prospective, multicenter, nonrandomized, observational study that evaluated the use of the Solitaire revascularization device (Medtronic) and MindFrame Capture low-profile revascularization device (Medtronic) in 1000 patients with anterior circulation large-vessel occlusions between August 2014 and June 2016 at 55 US centers (<https://www.clinicaltrials.gov>; unique identifier: NCT02239640). Ethics approval was obtained by the institutional review board at each center. Before enrollment in the registry, each subject provided written informed consent. The details and results of the STRATIS registry are published elsewhere.⁷ Briefly, key inclusion criteria were the following: 1) confirmed, symptomatic intracranial large-vessel occlusion with associated symptoms; 2) an NIHSS score of 8 to thirty; 3) use of the Medtronic market-released neurothrombectomy device as the initial device; 4) premorbid mRS of ≤ 1 ; and 5) treatment within 8 hours of stroke onset. Procedural information was obtained via core lab analysis of the de-identified complete reports and complete procedural imaging. RT was defined in the STRATIS registry as any mechanical device or thrombolytic used after the primary neurothrombectomy device (Solitaire or MindFrame). MindFrame was recalled on February 26, 2018, due to a risk of the delivery wire breaking or separating during use.

IA Subanalysis

For this subgroup analysis, all patients who underwent RT were included. Within this RT group, patients with and without IA rtPA use were compared. An additional subgroup analysis was

also performed in patients with RT with M1 occlusions only. Baseline and procedural characteristics and outcomes were compared between the 2 subgroups. Clinical outcomes at 90 days included an mRS score and mortality. Safety outcomes included the incidence of symptomatic intracranial hemorrhage (sICH).

Statistical Analysis

Standard descriptive statistics, including mean [SD] and median with interquartile range, were used for continuous variables, and frequency distributions, for categorical variables. For between-group comparisons, χ^2 tests and the Fisher exact test were used for categorical variables, while *t* tests and Wilcoxon rank sum tests were used for continuous variables. All *P* values were 2-sided, and values $\leq .05$ were considered

significant. Multivariable logistic regression models were fit for the following outcomes: substantial reperfusion, good functional outcomes (mRS 0–2), and mortality at 90 days. Clinically relevant variables and variables with *P* < .10 were entered into the models. Statistical analyses were conducted using SAS, Version 9.3 (SAS Institute), and R statistical and computing software, Version 3.2 (<http://www.r-project.org>).

RESULTS

Of the 984 patients in the STRATIS registry, 212 (21.5%) underwent RT and were included in this analysis (Fig 1). From the RT cohort, 129 patients (60.8%) received IA rtPA.

Baseline demographics were balanced between the groups, with the exception of hyperlipidemia, which was more prevalent in the no IA rtPA group (56.6% versus 41.1%, *P* = .03) (Online Supplemental Data). There was no difference in the mean NIHSS scores at presentation (17.6 [SD, 5.7] versus 17.0 [SD, 5.5], *P* = .43). Most patients in both cohorts received IV rtPA (62.7% versus 70.5%, *P* = .24) and had an anterior circulation occlusion (95.2% versus 93.8%, *P* = .09).

The mean time of onset to groin puncture was significantly shorter in the IA rtPA group (227.9 [SD, 91.9] versus 200.2 [SD, 104] minutes, *P* = .05). Only ~11% of patients in each group had an onset-to-groin puncture time of >6 hours. The mean number of passes was lower in the IA rtPA group (3.6 [SD, 1.3] versus 2.2 [SD, 1.4], *P* \leq .001); however, the number of passes in both groups did not differ before RT (Online Supplemental Data). The median dose of IA rtPA administered was 4 mg (interquartile range = 2–12 mg). There was a trend toward faster procedural times in the IA rtPA group (89.1 [SD, 45.1] versus 78.7 [SD, 43.1] minutes, *P* = .10). The rate of substantial reperfusion (modified TICI $\geq 2b$) was numerically higher in the IA rtPA group (73.0% versus 84.7%, *P* = .08) (Online Supplemental Data and Fig 2A).

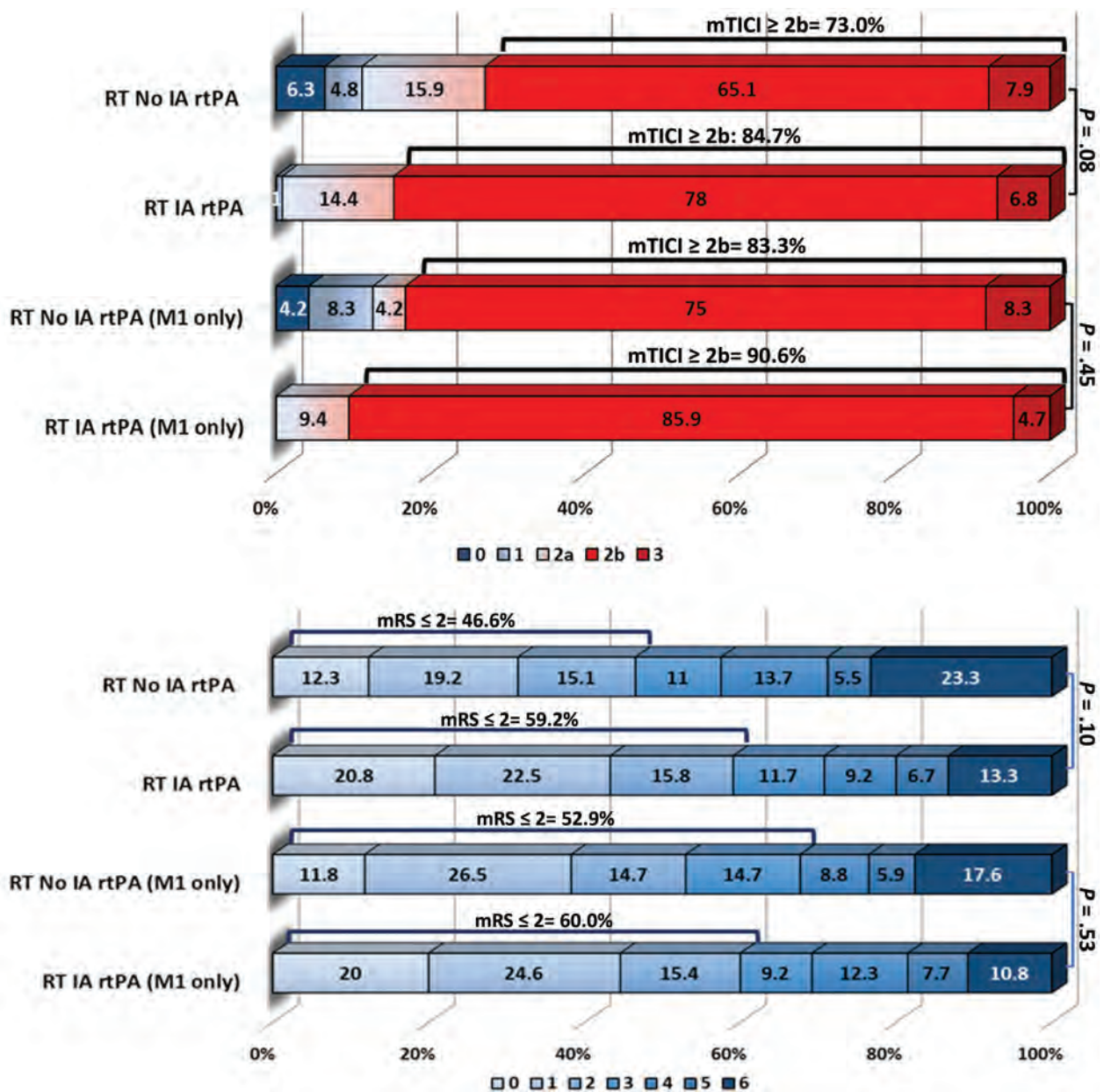


FIG 2. Outcomes in the RT no IA rtPA versus RT IA rtPA groups. A, Revascularization outcomes. B, Ninety-day mRS in the RT no IA rtPA versus RT IA rtPA groups.

There was a trend toward higher rates of good functional outcome (mRS ≤ 2) (46.6% versus 59.2%, $P = .10$) and lower rates of mortality (23.3% versus 13.3%, $P = .08$) at 90 days in the IA rtPA cohort (Online Supplemental Data and Fig 2B). No difference was found in the rate of sICH between the groups (0% versus 1.6%, $P = .54$).

Multivariable logistic regression analysis when adjusting for IA rtPA use, history of hyperlipidemia, number of device passes, time from onset to procedure end, time from onset to arterial puncture, M1 vessel location, and ICA vessel location did not show IA rtPA use as an independent predictor of substantial reperfusion (OR = 1.07; 95% CI, 0.44–2.57; $P = .89$), good functional outcome (OR = 0.92; 95% CI, 0.46–1.83; $P = .80$), or mortality (OR = 0.54; 95% CI, 0.22–1.31; $P = .17$) (Online Supplemental Data).

When further restricting the RT population to M1 occlusions only, there was no difference in the rates of substantial reperfusion (83.3% versus 90.6%, $P = .45$), good functional outcome (52.9% versus 60.0%, $P = .53$), mortality (17.6% versus 10.8%, $P = .36$), and sICH (0% versus 1.4%, $P = 1.0$) in the IA rtPA and no IA rtPA groups, respectively (Online Supplemental Data and Figs 1 and 2).

DISCUSSION

In this subgroup analysis of the STRATIS registry, use of IA rtPA in patients with RT did not result in an increased risk of sICH. Furthermore, there was a trend toward higher rates of successful reperfusion and good clinical outcome and lower rates of mortality in patients with RT receiving IA rtPA.

Our study adds to a small-but-growing body of literature that suggests that IA thrombolytics may be a safe and effective adjunctive or RT during or after MT.¹⁹⁻²³ A recent subanalysis from the multicenter North American Solitaire Acute Stroke (NASA) registry examined the use of IA rtPA after failed MT and reported numerically higher rates of revascularization success (61.2% versus 46.6%, $P = .13$) and faster recanalization times (100 [SD, 85] versus 164 [SD, 235] minutes, $P = .36$) in patients treated with IA rtPA compared with those with no IA rtPA use.¹⁹ Most important, the authors reported no difference in the rates of sICH (13.9% versus 6.8%, $P = .29$) and mortality (42.9% versus 44.7%, $P = .13$) between the groups. Similarly, a single-center retrospective study by Anadani et al²⁰ reported no difference in rates of successful recanalization, hemorrhage, or mortality at 90 days in patients who received IA rtPA as rescue therapy after MT versus MT only. Kaesmacher et al²² examined the use of IA urokinase after failed or incomplete MT in 100 patients with anterior circulation large-vessel occlusion. Use of IA urokinase in this study was not associated with an increased risk of sICH (adjusted OR, 0.81; 95% CI, 0.31–2.13) or mortality (adjusted OR = 0.78; 95% CI, 0.43–1.40) and resulted in improved angiographic reperfusion.

The safety of IA rtPA after IV rtPA administration and MT has not been well-studied. In the present study, most patients receiving IA rtPA RT (62.7%) received IV rtPA. Because the sICH rates were comparable between the cohorts (0% versus 1.6%, $P = .54$), our data suggest that IA rtPA administration in the context of IV rtPA and MT appears to be safe. Anadani et al²⁰ investigated the safety of IA rtPA use after IV rtPA and MT and found no difference in the rate of hemorrhagic complications between the IV rtPA/IA rtPA and IA rtPA-only groups; however, only 13 patients received IV rtPA/IA rtPA in the study. Although the randomized MT trials, Multicenter Randomized CLinical trial of Endovascular treatment for Acute ischemic stroke in the Netherlands [MR CLEAN] and Endovascular Treatment for Small Core and Anterior Circulation Proximal Occlusion with Emphasis on Minimizing CT to Recanalization Times Trial, allowed the use of IA rtPA, no data have been published on the safety of IA thrombolytic use in these studies.^{1,2}

Only a few studies have reported IA rtPA dosing during or after MT.^{20,21,23} The median dose of IA rtPA administered as an RT in our study was 4 mg (interquartile range = 2–12 mg), which was similar to the median dose of 5 mg (interquartile range = 4–6 mg) reported by Anadani et al.²⁰ A recent survey by Castonguay et al¹⁸ showed that 60.6% of respondents used IA thrombolytics in their practice and that most used an IA rtPA dose of 3–10 mg; however, 84.9% do not have a standardized protocol for administration. Because the administration protocols, dosing, and indications varied widely among studies that investigated IA rtPA in the context of MT,^{19-21,23} further study is warranted. Currently, the Chemical Optimization of Cerebral Embolectomy (CHOICE) trial is an ongoing multicenter, randomized, placebo-controlled, double-blinded Phase 2b study to assess the effectiveness of IA thrombolysis (rtPA) after incomplete reperfusion (modified TICI 2b or 2c) with MT.²⁴ Patients will be randomized to receive a 20- to 30-minute intra-arterial infusion of rtPA (up to 22.5 mg) or a placebo. Results from the CHOICE trial will help establish guidance on the potential efficacy and safety of IA rtPA as an RT after MT.

Limitations

This substudy has several limitations. Data reported here were limited to variables captured in the STRATIS registry. Thus, reasons for IA rtPA administration, administration technique, and infusion times were not available, possibly contributing to selection bias and the generalizability of our study results. Reasons for the choice of RT were not recorded in the STRATIS registry; therefore, selection bias needs to be considered when interpreting the results of the study. Onset-to-groin puncture times were significantly faster in the IA rtPA group, possibly impacting the outcomes in this study. The STRATIS registry enrolled patients and treated patients within 8 hours from symptom onset; therefore, the results from this study cannot be extrapolated to later time windows. The number of passes was significantly higher in the RT no IA rtPA group; however, it was adjusted for in multivariate outcome models. Treatment strategies varying in the RT population may limit the generalizability and interpretability of our results. Additionally, the definition of RT was specific to the STRATIS registry and is not reflective of clinical practice.

CONCLUSIONS

To our knowledge, this is the largest multicenter, core lab–adjudicated cohort of patients with RT and IA rtPA after unsuccessful MT with the Solitaire device. Our results demonstrate similar rates of mortality, sICH, and reperfusion and 90-day clinical outcomes compared with patients having RT with no IA rtPA use. Large, prospective, randomized clinical trials are needed to further investigate the safety and efficacy of IA thrombolysis after unsuccessful MT.

Disclosures: Osama O. Zaidat—RELATED: Grant: Medtronic*; Consulting Fee or Honorarium: Medtronic. Nils Mueller-Kronast—RELATED: Support for Travel to Meetings for the Study or Other Purposes: Medtronic, Comments: travel expenses for meeting presentation; Fees for Participation in Review Activities such as Data Monitoring Boards, Statistical Analysis, Endpoint Committees, and the Like: Medtronic, Comments: Steering Committee. David S. Liebeskind—RELATED: Fees for Participation in Review Activities such as Data Monitoring Boards, Statistical Analysis, Endpoint Committees, and the Like: Medtronic, Comments: Imaging Core Lab; UNRELATED: Consultancy: Stryker, Comments: Imaging Core Lab. *Money paid to institution.

REFERENCES

1. Berkhemer OA, Fransen PS, Beumer D, et al; MR CLEAN Investigators. **A randomized trial of intraarterial treatment for acute ischemic stroke.** *N Engl J Med* 2015;372:11–20 CrossRef Medline
2. Goyal M, Demchuk AM, Menon BK, et al; ESCAPE Trial Investigators. **Randomized assessment of rapid endovascular treatment of ischemic stroke.** *N Engl J Med* 2015;372:1019–30 CrossRef Medline
3. Saver JL, Goyal M, Bonafe A, et al; SWIFT PRIME Investigators. **Stent-retriever thrombectomy after intravenous tPA vs. tPA alone in stroke.** *N Engl J Med* 2015;372:2285–95 CrossRef Medline
4. Campbell BC, Mitchell PJ, Kleinig TJ, et al; EXTEND-IA Investigators. **Endovascular therapy for ischemic stroke with perfusion-imaging selection.** *N Engl J Med* 2015;372:1009–18 CrossRef Medline
5. Jovin TG, Chamorro A, Cobo E, et al; REVASCAT Trial Investigators. **Thrombectomy within 8 hours after symptom onset in ischemic stroke.** *N Engl J Med* 2015;372:2296–2306 CrossRef Medline

6. Goyal M, Menon BK, van Zwam WH, et al; HERMES Collaborators. **Endovascular thrombectomy after large-vessel ischaemic stroke: a meta-analysis of individual patient data from five randomised trials.** *Lancet* 2016;387:1723–31 CrossRef Medline
7. Mueller-Kronast NH, Zaidat OO, Froehler MT, et al; STRATIS Investigators. **Systematic evaluation of patients treated with neurothrombectomy devices for acute ischemic stroke: primary results of the STRATIS registry.** *Stroke* 2017;48:2760–68 CrossRef Medline
8. Zaidat OO, Castonguay AC, Gupta R, et al. **North American Solitaire Stent Retriever Acute Stroke registry: post-marketing revascularization and clinical outcome results.** *J Neurointerv Surg* 2014;6:584–88 CrossRef Medline
9. Zaidat OO, Castonguay AC, Nogueira RG, et al. **Trevo stent-retriever mechanical thrombectomy for acute ischemic stroke secondary to large vessel occlusion registry.** *J Neurointerv Surg* 2018;10:516–24 CrossRef Medline
10. Garcia-Tornel A, Requena M, Rubiera M, et al. **When to stop.** *Stroke* 2019;50:1781–88 CrossRef Medline
11. del Zoppo GJ, Higashida RT, Furlan AJ, et al. **PROACT: a phase II randomized trial of recombinant pro-urokinase by direct arterial delivery in acute middle cerebral artery stroke—PROACT investigators. Prolyse in Acute Cerebral Thromboembolism.** *Stroke* 1998;29:4–11 CrossRef Medline
12. Lewandowski CA, Frankel M, Tomsick TA, et al. **Combined intravenous and intra-arterial rtPA versus intra-arterial therapy of acute ischemic stroke: Emergency Management of Stroke (EMS) bridging trial.** *Stroke* 1999;30:2598–2605 CrossRef Medline
13. Furlan A, Higashida R, Wechsler L, et al. **Intra-arterial prourokinase for acute ischemic stroke: the PROACT II study: a randomized controlled trial—Prolyse in Acute Cerebral Thromboembolism.** *JAMA* 1999;282:2003–11 CrossRef Medline
14. Ogawa A, Mori E, Minematsu K, et al; MELT Japan Study Group. **Randomized trial of intraarterial infusion of urokinase within 6 hours of middle cerebral artery stroke: the Middle Cerebral Artery Embolism Local Fibrinolytic Intervention Trial (MELT) Japan.** *Stroke* 2007;38:2633–39 CrossRef Medline
15. IMS Study Investigators. **Combined intravenous and intra-arterial recanalization for acute ischemic stroke: the Interventional Management of Stroke study.** *Stroke* 2004;35:904–11 CrossRef Medline
16. IMS II Trial Investigators. **The Interventional Management of Stroke (IMS) II study.** *Stroke* 2007;38:2127–35 CrossRef Medline
17. Broderick JP, Palesch YY, Demchuk AY, et al; Interventional Management of Stroke (IMS) III Investigators. **Endovascular therapy after intravenous tPA versus tPA alone for stroke.** *N Engl J Med* 2013;368:893–903 CrossRef Medline
18. Castonguay AC, Jumaa MA, Zaidat OO, et al. **Insights into intra-arterial thrombolysis in the modern era of mechanical thrombectomy.** *Front Neurol* 2019;10:1195 CrossRef Medline
19. Zaidi SF, Castonguay AC, Jumaa MA, et al. **Intraarterial thrombolysis as rescue therapy for large vessel occlusions.** *Stroke* 2019;50:1003–06 CrossRef Medline
20. Anadani M, Ajinkya S, Alawieh A, et al. **Intra-arterial tissue plasminogen activator is a safe rescue therapy with mechanical thrombectomy.** *World Neurosurg* 2019;123:e604–08 CrossRef Medline
21. Heiferman DM, Li DD, Pecoraro NC, et al. **Intra-arterial alteplase thrombolysis during mechanical thrombectomy for acute ischemic stroke.** *J Stroke Cerebrovasc Dis* 2017;26:3004–08 CrossRef Medline
22. Kaesmacher J, Bellwald S, Dobrocky T, et al. **Safety and efficacy of intra-arterial urokinase after failed, unsuccessful, or incomplete mechanical thrombectomy in anterior circulation large-vessel occlusion stroke.** *JAMA Neurol* 2020;77:318 CrossRef Medline
23. Yi TY, Chen WH, Wu YM, et al. **Adjuvant intra-arterial rtPA injection at the initially deployed Solitaire stent enhances the efficacy of mechanical thrombectomy in acute ischemic stroke.** *J Neurol Sci* 2018;386:69–73 CrossRef Medline
24. Renu A, Blasco J, Millan M, et al; CHOICE Investigators. **The Chemical Optimization of Cerebral Embolectomy Trial: study protocol.** *Int J Stroke* 2019 Dec 18. [Epub ahead of print] CrossRef Medline

The Prophylactic Use of Tirofiban versus Oral Antiplatelet Medications in Stent-Assisted Coiling of Intracranial Aneurysms: A Meta-analysis

Y. Xiang, H. Zhao, C. Ding, H. Chen, D. Wang, and A. Liu



ABSTRACT

BACKGROUND: The protocol for optimal antiplatelet therapy to prevent thromboembolic and hemorrhagic complications in patients with cerebral aneurysms using an endovascular approach is not clear.

PURPOSE: Our study analyzed the safety and efficacy of prophylactic tirofiban administration compared with oral antiplatelet drug therapy.

DATA SOURCES: We used the PubMed, EMBASE, MEDLINE, and Cochrane library data bases.

STUDY SELECTION: Our study consisted of all case series with >5 patients that reported treatment-related outcomes of patients undergoing endovascular procedures pretreated with tirofiban or oral antiplatelet drug therapy.

DATA ANALYSIS: Random effects or fixed effects meta-analysis was used to pool the cumulative rate of complications, perioperative mortality, and good clinical outcomes.

DATA SYNTHESIS: Fifteen studies with 1981 patients were registered. Thromboembolic complications were significantly lower in the tirofiban group (3.6%; 95% CI, 1.9%–5.8%) compared with the dual-antiplatelet therapy group (8.5%, 95% CI, 4.5%–13%; $P = .04$). Pretreatment with tirofiban did not remarkably increase the rate of hemorrhagic complications (3.5%; 95% CI, 1.8%–5.6%) compared with dual-antiplatelet therapy (5.1%; 95% CI, 2.6%–8.5%; $P = .371$). There was a trend toward lower perioperative mortality with tirofiban (0.8%; 95% CI, 0.2%–1.6%) compared with dual-antiplatelet therapy (1.2%; 95% CI, 0.7%–2.0%; $P = .412$). There was no significant difference in the safety and efficacy between the tirofiban bolus plus drip and drip alone.

LIMITATIONS: The limitations are selection and publication biases.

CONCLUSIONS: Prophylactic therapy with tirofiban resulted in significantly lower rates of thromboembolic complications with no increase in hemorrhagic events or mortality than the prophylactic use of dual-antiplatelet therapy.

ABBREVIATIONS: ASA = acetylsalicylic acid; DAPT = dual-antiplatelet therapy; GP IIb/IIIa = glycoprotein IIb/IIIa; MINORS = methodological index for non-randomized studies; PRISMA = Preferred Reporting Items for Systematic Review and Meta-Analysis

Endovascular treatments such as stent-assisted coiling and flow diversion have recently emerged as an effective option for intracranial aneurysms.^{1,2} In general, thrombosis and subsequent ischemic events are major sources of morbidity and mortality in stent-assisted coiling procedures. Therefore, the adequate prevention of thromboembolic events is of paramount importance during stent-assisted coiling and flow diversion of intracranial

aneurysms. Antiplatelet therapy offers partial prevention of these events.^{3,4} Many clinicians perioperatively use dual oral antiplatelet medications, routinely aspirin and clopidogrel, to prevent associated thromboembolic complications.^{5,6} However, thromboembolic complications still occur in up to 7%–40% of patients treated with dual-antiplatelet therapy (DAPT), even with high on-treatment platelet reactivity.⁷ The reported frequency of symptomatic hemorrhage during aneurysm embolization also varies greatly due to the irreversible inhibition of platelet aggression.^{8,9}

Received July 2, 2020; accepted after revision November 2.

From the Departments of Pharmacy (Y.X., A.L.), Orthopedics (H.Z.), and Neurosurgery (D.W.), Qilu Hospital of Shandong University, Jinan, Shandong, China; Department of Pharmacy (C.D.), Affiliated Hospital of Weifang Medical University, Weifang, Shandong, China; and Department of Pharmacy (H.C.), Special Care Hospital of Jinan City, Jinan, Shandong, China.

This study was supported by the Clinical Practical New Technology Development Foundation of Qilu Hospital (2019-7).

Yanxiao Xiang and Hua Zhao contributed equally to this study.

Please address correspondence to Donghai Wang, MD, Qilu Hospital of Shandong University, Department of Neurosurgery, 44 Wenhua Xi Road, Jinan, Shandong, China; e-mail: drwangdonghai@163.com

Indicates article with online supplemental data.

<http://dx.doi.org/10.3174/ajnr.A6996>

The potent glycoprotein IIb/IIIa (GP IIb/IIIa) inhibitor tirofiban is increasingly used in acute coronary syndromes.¹⁰ Tirofiban provides distinct advantages due to its pharmacodynamic characteristics, such as a short onset of action and a short half-life. Several studies have evaluated its prophylactic use in the endovascular treatment of intracranial aneurysms.^{11,12}

Despite the largest experience of alternative antiplatelet therapy, there are no publicly available guidelines on the use of prophylactic antiplatelet medications, and no systematic reviews evaluated the proper administration of these medications. Our meta-analysis was the first to investigate whether tirofiban is a conceivable alternative to DAPT as a prophylactic therapy for thromboembolism during the endovascular treatment of intracranial aneurysms. We compared clinical outcomes in patients pretreated with tirofiban versus DAPT during intracranial aneurysm treatment. We also performed subgroup analyses to compare outcomes of patients treated with a loading dose plus drip of tirofiban versus drip alone and patients treated with aspirin plus clopidogrel and aspirin plus ticagrelor therapy. This information will guide the selection of safer antiplatelet administration for endovascular treatment of intracranial aneurysms.

MATERIALS AND METHODS

This meta-analysis was performed according to the Preferred Reporting Items for Systematic Review and Meta-Analysis (PRISMA) guidelines.¹³

Literature Search

Two reviewers independently searched the PubMed, EMBASE, MEDLINE, and Cochrane library data bases in March 2020 without restrictions on publication date or language. Search terms included “tirofiban,” “antiplatelet drug prophylactic,” “antiplatelet drip premedication,” “DAPT,” “oral antiplatelet medication,” “pretreatment antiplatelet,” “preventative use of antiplatelet,” “preprocedure antiplatelet,” “preventative clopidogrel,” “intracranial aneurysm,” “cerebral aneurysm,” “brain aneurysm,” “anterior cerebral artery aneurysm,” “anterior communicating artery aneurysm,” “posterior communicating artery aneurysm,” “posterior cerebral artery aneurysm,” “basilar artery aneurysm,” “middle cerebral artery aneurysm,” and “Berry aneurysm.” Search terms were combined using the Boolean operators “AND” or “OR.” References cited in the relevant articles were also reviewed.

Inclusion and Exclusion Criteria

Studies meeting the following criteria were eligible for inclusion: 1) a series of >5 patients, 2) studies with preprocedural antiplatelet medications in stent-assisted coiling of intracranial aneurysms, and (3) available data on periprocedural complications. We excluded studies performed using administrative/insurance data bases, articles that were duplicate reports of an earlier trial, reviews, and case reports.

Data Extraction

Two of the authors independently extracted the following information from the final set of included studies: first author's name, year of publication, original country, sample size, type of agents used for pretreatment, method of administration, duration of

follow-up, perioperative thromboembolic events, perioperative hemorrhage, and perioperative mortality related to antiplatelet therapy. The corresponding author of each study was contacted to obtain any missing information if required. Perioperative complications were events that occurred within 30 days of the procedure. Thromboembolic complications referred to ischemic stroke, territorial infarction, or >6 lesions with positive findings on DWI seen on 24- to 48-hour or long-term follow-up imaging. Hemorrhagic complications included intracerebral hematoma, subdural hematoma, subarachnoid hemorrhage, parenchymal hematoma, and groin puncture complications. Good clinical outcomes were defined as an mRS score of ≤ 2 at long-term (≥ 3 months) follow-up or a Glasgow Outcome Score of ≥ 4 at discharge.

Quality Evaluation (Bias)

Two authors assessed the quality of each study using the methodological index for nonrandomized studies (MINORS).¹⁴ The included studies were scored as 0 if not reported, 1 if reported but inadequate, and 2 if reported and adequate. Discrepancies were resolved via discussion and consensus. Quality was determined on the basis of 12 MINORS items. The items were scored as 0 (not reported), 1 (reported but inadequate), or 2 (reported and adequate). Noncomparative studies with >12 points and comparative studies with >16 points were considered high-quality. Noncomparative studies with 8–12 points and comparative studies with 12–16 points were deemed intermediate-quality, and noncomparative studies with <8 points and comparative studies with <12 points were considered low-quality. The Grading of Recommendations Assessment, Development and Evaluation approach was used to assess the overall quality of the evidence for each outcome.¹⁵

Statistical Analysis

The meta-analysis was performed using STATA, Version 14.0 (StataCorp). Most of the included studies were noncomparative. Therefore, we estimated the cumulative incidence (event rate) from each cohort and the 95% confidence interval for each outcome. Pooled event rates were assessed for heterogeneity using the χ^2 and I^2 tests.¹⁶ A fixed effects model was performed with $I^2 \leq 50\%$. Otherwise, a random effects model was performed. The incidence rates of the different outcomes were compared between tirofiban cohorts and DAPT cohorts using an interaction test as described by Altman and Bland¹⁷ or the χ^2 test. We also performed subgroup analyses to compare outcomes of patients treated with a loading dose plus drip of tirofiban versus drip alone and patients treated with aspirin plus clopidogrel and aspirin plus ticagrelor therapy. $P < .05$ was considered significant in all analyses.

RESULTS

Search Results

Three hundred ninety-one studies were retrieved from the PubMed, EMBASE, MEDLINE, and Cochrane library data bases. A total of 280 studies were excluded because they were duplicate items. Ninety studies were excluded after title and abstract screening. Six studies were removed because of the failure to meet the eligibility criteria; finally, 15 studies^{11,12,18-30} were selected for the meta-analysis. A flow diagram of the selection process for relevant articles is shown in Fig 1.

Characteristics of Studies

The characteristics of the included studies are presented in the Online Supplemental Data. In total, 1981 patients were registered in the 15 included studies. A total of 613 patients were pretreated with tirofiban (30.9%), and 1368 patients (69.1%) received only dual oral antiplatelet medications. Among the patients who received tirofiban as a preventive measure in the stent-assisted coiling of intracranial aneurysms, 65 patients received drip alone and 548 patients received a loading dose plus a drip of tirofiban. Among the patients who received prophylactic dual oral antiplatelet therapy, 1278 patients received acetylsalicylic acid (ASA) plus clopidogrel, and 90 patients received ASA plus ticagrelor.

Quality Evaluation (Bias)

The assessment of the study-specific quality scores from the MINORS items is presented in the Online Supplemental Data. Items such as prospective collection of data, unbiased assessment

of the study end points, and prospective calculation of the study size were not found in all 15 studies, and other items that were involved in most of the 15 studies were scored 2, which indicated good quality. Thirteen of the 15 studies were identified as of relatively intermediate-quality. Two of the 15 studies were considered low-quality.

Tirofiban versus DAPT

The results of the pooled event rates for each study are shown in Table 1. Thromboembolic complications were significantly lower in the tirofiban group (3.6%; 95% CI, 1.9%–5.8%) compared with the DAPT group (8.5%, 95% CI, 4.5%–13%; $P = .04$). Pretreatment with tirofiban did not increase the rate of hemorrhagic complications (3.5%; 95% CI, 1.8%–5.6%) compared with DAPT (5.1%; 95% CI, 2.6%–8.5%; $P = .371$). There was a trend toward lower perioperative mortality with tirofiban (0.8%; 95% CI, 0.2%–1.6%) compared with DAPT (1.2%; 95% CI, 0.7%–2.0%; $P = .412$). A rate analysis of good clinical outcomes indicated that the 2 approaches were associated with similar outcomes (89%; 95% CI, 74.0%–99.0%; and 92.7%; 95% CI, 87.1%–96.8%; $P = .589$) at follow-up or discharge.

Tirofiban Bolus plus Drip versus Drip Alone

The results of the pooled event rates for each study are shown in Table 2. There was no significant difference between the 2 approaches for the rates of thromboembolic complications (3.9%; 95% CI, 1.7%–6.8%; and 2.4%; 95% CI, 0.1%–7.5%; $P = .513$), hemorrhagic complications (3.0%; 95% CI, 1.8%–4.7%; and 2.5%; 95% CI, 0.1%–7.5%; $P = .805$), perioperative mortality (0.8%; 95% CI, 0.2%–1.7%; and 0.7%; 95% CI, 0.1%–4.1%; $P = .927$), or good clinical outcomes (86.3%; 95% CI, 62.8%–99%; and 94.7%; 95% CI, 86.6%–99.2%; $P = .391$). One study reported that after starting a drip protocol that no longer included a loading dose of tirofiban, the overall incidence of hemorrhagic complications fell impressively to 1.9% compared with 18.8% for the protocol that included a bolus dose plus a drip of tirofiban. No major or clinically significant bleeding events were observed using the drip protocol, even in patients with ruptured aneurysms.¹²

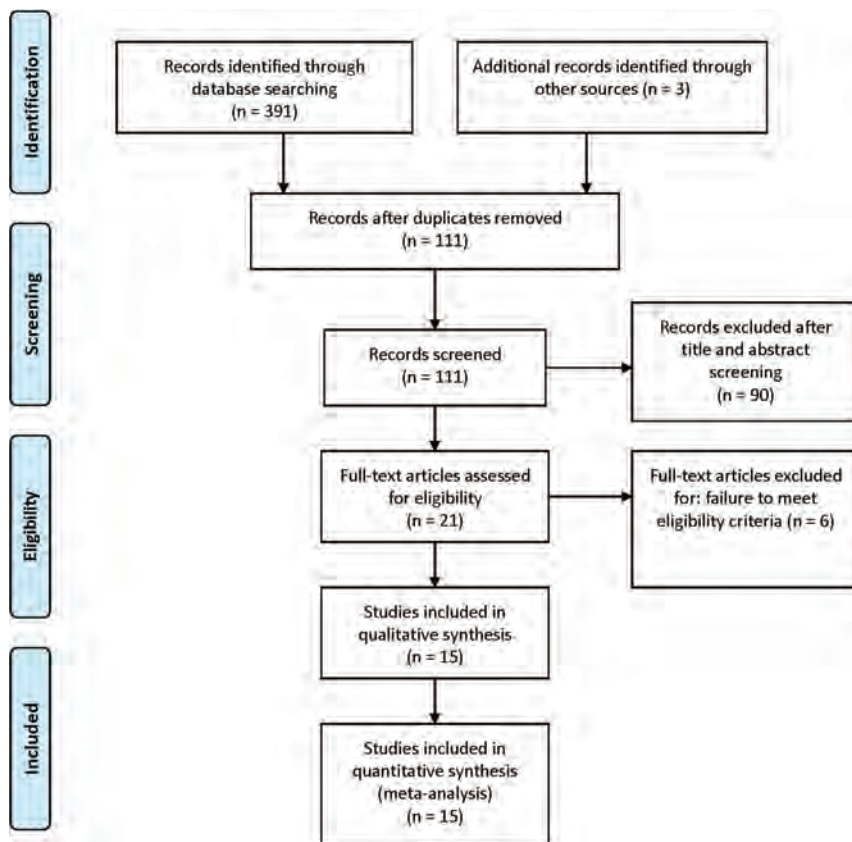


FIG 1. Flow diagram of the selection process for relative articles. A PRISMA-compliant search (www.prisma-statement.org) of MEDLINE, EMBASE, PubMed, the Cochrane library, and the Cochrane Central Register of Controlled Trials (CENTRAL) was performed.

Table 1: Outcomes with tirofiban versus DAPT

Outcome	Tirofiban % (95% CI)	I ²	DAPT % (95% CI)	I ²	P Value
Thromboembolic complications	3.6 (1.9–5.8)	33	8.5 (4.5–13.0)	88	.04
Hemorrhagic complications	3.5 (1.8–5.6)	28	5.1 (2.6–8.5)	80	.371
Perioperative mortality related to antiplatelet medication	0.8 (0.2–1.6)	15	1.2 (0.7–2.0)	0	.412
Good clinical outcomes	89.0 (74.0–99.0)	91	92.7 (87.1–96.8)	87	.589

Table 2: Outcomes with a bolus dose plus drip of tirofiban versus drip alone

Outcome	Bolus + Drip % (95% CI)	I ²	Drip % (95% CI)	I ²	P Value
Thromboembolic complications	3.9 (1.7–6.8)	54	2.4 (0.1–7.5)	0	.513
Hemorrhagic complications	3.0 (1.8–4.7)	30	2.5 (0.1–7.5)	0	.805
Perioperative mortality related to antiplatelet medication	0.8 (0.2–1.7)	42	0.7 (0.1–4.1)	0	.927
Good clinical outcomes	86.3 (62.8–99.0)	94	94.7 (86.6–99.2)	0	.391

Table 3: Outcomes with ASA plus clopidogrel versus ASA plus ticagrelor

Outcome	ASA + Clopidogrel % (95% CI)	I ²	ASA + Ticagrelor (95% CI)	I ²	P Value
Thromboembolic complications	9.2 (4.7–14.8)	88	5.4 (1.7–10.9)	0	.513
Hemorrhagic complications	5.5 (2.8–9.1)	79	2.5 (0–10.5)	65	.321
Perioperative mortality related to antiplatelet medication	1.2 (0.6–1.9)	0	2.4 (0.02–8.5)	47	.583
Good clinical outcomes	93.0 (87.0–97.2)	85	93.1 (84.3–98.5)	47	.982

Table 4: Meta-regression analysis of follow-up time affecting heterogeneity (tirofiban versus DAPT)

Variable	Coefficient (95% CI)	Standard Error	T	P Value
Thromboembolic complications	0.005 (–0.005–0.014)	0.004	1.160	.285
Hemorrhagic complications	0.002 (–0.078–0.116)	0.004	0.460	.656
Perioperative mortality related to antiplatelet medication	0.007 (–0.03–0.017)	1.710	1.710	.131
Good clinical outcomes	–0.006 (–0.017–0.006)	0.005	–1.210	.281

Table 5: Meta-regression analysis of follow-up time affecting heterogeneity (ASA plus clopidogrel versus ASA plus ticagrelor)

Variable	Coefficient (95% CI)	Standard Error	T	P Value
Thromboembolic complications	0.005 (–0.007–0.017)	0.005	1.106	.338
Hemorrhagic complications	0.002 (–0.010–0.014)	0.005	0.42	.69
Perioperative mortality related to antiplatelet medication	0.012 (–0.042–0.066)	0.021	0.59	.581
Good clinical outcomes	–0.006 (–0.020–0.008)	0.005	–1.22	.289

ASA plus Clopidogrel versus ASA plus Ticagrelor

The results of the pooled event rates for each study are shown in Table 3. Patients pretreated with ASA and clopidogrel had a nonstatistically higher rate of thromboembolic complications (9.2%; 95% CI, 4.7%–14.8%) compared with patients pretreated with ASA and ticagrelor (5.4%; 95% CI, 1.7%–10.9%; $P = .513$). There was a trend toward a higher rate of hemorrhagic complications with ASA and clopidogrel (5.5%; 95% CI, 2.8%–9.1%) compared with ASA and ticagrelor (2.5%; 95% CI, 0%–10.5%; $P = .321$). For outcomes at long-term follow-up, perioperative mortality was nonstatistically lower in the clopidogrel group (1.2%; 95% CI, .6%–1.9%) than in the ticagrelor group (2.4%; 95% CI, 0.02%–8.5%; $P = .583$). The rate of good clinical outcomes was not significantly higher in the clopidogrel group (93.0%; 95% CI, 87.0%–97.2%) than in the ticagrelor group (93.1%; 95% CI, 84.3%–98.5%; $P = .982$).

Meta-regression

The meta-regression model quantified the impact of the follow-up time on the P value of cumulative incidences (event rate). The results of the meta-regression analysis indicated that the follow-up period did not influence the effect estimate of tirofiban versus DAPT (Table 4) or ASA plus clopidogrel versus ASA plus ticagrelor (Table 5). The follow-up time of the drip group was not reported in original studies. Therefore, it was not possible to discern whether this factor influenced the heterogeneity in the tirofiban bolus plus drip versus the drip group.

DISCUSSION

The main finding of our meta-analysis was that there was a significantly lower rate of thromboembolic complications ($P < .05$) from the prophylactic use of tirofiban than DAPT in patients with intracranial aneurysms undergoing endovascular treatment. There was no increase in intracranial hemorrhage in the tirofiban group ($P > .05$).

Stent-placement techniques and flow diverters are increasingly used in the management of intracranial aneurysms. Because thromboembolic events associated with stent placement and flow diverters occur often and these events correlate with poor clinical outcomes,^{31,32} antiplatelet agents (eg, prophylactic clopidogrel and aspirin) are used to prevent in-stent thrombosis and ischemic events.³³ However, oral antiplatelet drugs take time to reach therapeutic levels. DAPT is routinely administered 3–5 days before endovascular treatment of intracranial aneurysms, and this therapy may be associated with a heightened risk (18.91%) of intracranial hemorrhage.^{34,35} GP IIb/IIIa inhibitors are considered the most powerful class of antiplatelet therapies, and their adjunctive beneficial effects were shown in several clinical trials.^{36–39}

Tirofiban is a nonpeptide GP IIb/IIIa receptor, which is similar to abciximab because it has a high affinity for the GP IIb/IIIa receptor. However, tirofiban dissociates from the GP IIb/IIIa receptor more rapidly than abciximab. A relatively high level of platelet inhibition is achieved approximately 5–10 minutes after tirofiban administration, and inhibition of platelet function $\geq 95\%$ at 10 minutes after the start of therapy is associated with a

significant decrease in the incidence of major adverse cardiac events.^{40,41} Although the off-label use of tirofiban as a prophylactic and rescue treatment in neuroendovascular procedures is common, no systematic reviews have evaluated the safety and efficacy of tirofiban compared with DAPT as a prophylactic therapy during the endovascular treatment of intracranial aneurysms. The pooled data of our systematic review lend more support to the tirofiban strategy. Most of the studies included in this review indicated that the rates of thromboembolic complications from tirofiban and the DAPT strategy ranged between 0% and 10.0% and 1.7% and 26.5%, respectively. The rates of major hemorrhagic complications from the 2 therapies ranged between 0% and 10.5% and 0.9% and 10.2%, respectively, and higher rates were generally observed in studies with postoperative MR imaging. A study of 281 patients undergoing endovascular treatment of intracranial aneurysms²² revealed that thromboembolic events were observed more often in a DAPT group than a tirofiban group (10.8% versus 3.4%; $P = .01$), with no increase in the rate of intracranial hemorrhage ($P = .16$). Thromboembolic events in the ruptured subgroups were significantly fewer in the tirofiban subgroup than in the DAPT subgroup (3.9% versus 13.2%; $P = .04$), with no increase in the rate of hemorrhage ($P = .36$). Our study found significantly lower rates of thromboembolic complications in patients who received the tirofiban strategy for prophylactic treatment. There was a trend toward lower hemorrhage rates in patients who received the tirofiban strategy.

The short- and long-term clinical outcomes of the prophylactic strategy in the stent-assisted coiling of intracranial aneurysms are variable. The rates of perioperative mortality related to tirofiban and the DAPT strategy ranged between 0% and 3.4% and 0% and 2.0%, respectively. However, more included studies of the tirofiban strategy showed no death compared with the DAPT strategy (4 versus 1). The rates of good clinical outcomes in patients who received tirofiban and the DAPT strategy ranged between 70.0% and 97.7% and 87.8% and 97.8%, respectively. Zi-Liang et al²² reported no difference in good outcome (mRS 0, 1, and 2) at the 3-month follow-up in cases of thromboembolic events between the tirofiban and DAPT groups. The current meta-analysis observed that the prophylactic tirofiban strategy was associated with benefits in mortality (0.8 versus 1.2%), though this difference was not statistically significant because the studies were underpowered to detect a significant reduction in mortality. Our meta-analysis also showed no significant increase in mortality in patients who received tirofiban as a prophylactic therapy compared with DAPT. Overall, the tirofiban protocol provides a reasonable alternative to pretreatment with DAPT for flow-diversion and stent-assisted procedures.

The safety and efficacy of a bolus dose plus drip of tirofiban versus drip alone for prophylactic therapy are not well-established. Chalouhi et al¹² examined a series of 67 patients undergoing stent-assisted coiling and found that a bolus followed by a maintenance dose of tirofiban appeared to have a high risk of cerebral hemorrhage. However, a maintenance infusion without an initial bolus had an exceedingly low risk of hemorrhage and appeared very safe and effective, even in the setting of subarachnoid hemorrhage. Although tirofiban is routinely used in percutaneous coronary interventions, few studies compared the safety and efficacy of different drug-delivery methods of tirofiban.

Kirma et al⁴² performed a study of 47 patients undergoing percutaneous coronary intervention and demonstrated that microvascular perfusion, corrected Thrombolysis in Myocardial Infarction frame counts, myocardial blush grades, and long-term clinical outcomes did not differ significantly between patients with the intravenous bolus plus drip of tirofiban and an intracoronary bolus alone. Our meta-analysis found no significant difference between bolus plus drip and drip alone for the rates of thromboembolic complications, hemorrhagic complications, perioperative mortality, or good clinical outcomes.

The most commonly used first-line oral dual-antiplatelet regimen consists of aspirin and clopidogrel. Ticagrelor is an alternative in patients who are clopidogrel-resistant or clopidogrel-allergic. However, the safety and efficacy of aspirin plus clopidogrel versus aspirin plus ticagrelor for prophylactic therapy in stent-assisted coiling of intracranial aneurysms are also not well-established. The Platelet Inhibition and Patient Outcomes (PLATO) study found that the use of ticagrelor DAPT reduced the collective incidence of death due to myocardial infarction, stroke, and other vascular conditions compared with clopidogrel DAPT (9.8% versus 11.7%; hazard ratio, 0.84; $P < .001$).⁴³ No statistically significant differences in the rate of major hemorrhagic incidents were found between patients administered aspirin plus ticagrelor or aspirin plus clopidogrel.⁴³ However, the results of the POPular AGE (Clopidogrel versus ticagrelor or prasugrel in patients aged 70 years or older with non-ST-elevation acute coronary syndrome)⁴⁴ study showed that clopidogrel was a favorable alternative to ticagrelor in patients 70 years of age or older who presented with non-ST-elevation acute coronary syndrome because it led to fewer bleeding events without an increase in the combined end point of all-cause death, myocardial infarction, stroke, or bleeding. Clopidogrel may be an alternative P2Y₁₂ inhibitor, especially in elderly patients with a higher bleeding risk.

Adeeb et al⁴⁵ investigated 402 patients undergoing Pipeline Embolization Device (Medtronic) placement for the treatment of intracranial aneurysms and found that the risk of a high rate of thromboembolic complications was mitigated in nonresponders who were switched to the alternative ticagrelor. The current meta-analysis found no significant difference in the rate of thromboembolic complications, hemorrhagic complications, perioperative mortality, or good clinical outcomes between patients pretreated with aspirin plus clopidogrel and aspirin plus ticagrelor.

Limitations

The current meta-analysis has a number of limitations, including inevitable clinical heterogeneity among the included studies. There is also a significant publication bias for the variable patient selection and aneurysm features, which may affect the results. The evaluation of good clinical outcomes was inconsistent across studies, and mRS scores or Glasgow Outcome Scores were used in different analyzed studies for outcome assessment. Many included series were cases collected during several years, and it is possible that complication rates and mortality improved as a result of increased operator experience and skill and improved devices and technology. For the method of drug administration, there was variation in the timing of tirofiban and DAPT

administration (just before procedures, before stent placement, before or after the deployment of flow diverter, just before procedure, at least 5 days before the procedures, and at least 7 days before the procedures). The comparisons reported in the current analysis were made across, not within, studies; this feature may greatly weaken the inferences. Most of the series included were noncomparative, and groups were not randomized. Finally, most of the tirofiban studies included in our analysis were limited to short-term mortality of <3 months, but GP IIb/IIIa inhibitor studies often demonstrated an increasing survival benefit with longer follow-up.^{46,47}

CONCLUSIONS

The current meta-analysis revealed that the administration of tirofiban as a premedication had a significant benefit with favorable trends for lower rates of thromboembolic complications with no increase in hemorrhagic events compared with the prophylactic use of DAPT. No difference in outcome was seen on the basis of the method of tirofiban administration. Further evaluations in adequately powered large trials are needed to confirm the clinical benefit of this therapy.

REFERENCES

- Molyneux AJ, Birks J, Clarke A, et al. **The durability of endovascular coiling versus neurosurgical clipping of ruptured cerebral aneurysms: 18-year follow-up of the UK cohort of the International Subarachnoid Aneurysm Trial (ISAT).** *Lancet* 2015;385:691–97 CrossRef Medline
- De Vries J, Boogaarts J, Van Norden A, et al. **New generation of flow diverter (SURPASS) for unruptured intracranial aneurysms: a prospective single-center study in 37 patients.** *Stroke* 2013;44:1567–77 CrossRef Medline
- Awtry EH, Loscalzo J. **Aspirin.** *Circulation* 2000;101:1206–18 CrossRef
- Born G, Patrono C. **Antiplatelet drugs.** *Br J Pharmacol* 2006; 147(Suppl 1):S241–51 CrossRef Medline
- Ries T, Buhk JH, Kucinski T, et al. **Intravenous administration of acetylsalicylic acid in stent-assisted coiling of cerebral aneurysms reduces the rate of thromboembolic events.** *Stroke* 2006;37:1816–21 CrossRef Medline
- Yamada NK, Cross DT, 3rd, Pilgram TK, et al. **Effect of antiplatelet therapy on thromboembolic complications of elective coil embolization of cerebral aneurysms.** *AJNR Am J Neuroradiol* 2007;28:1778–82 CrossRef Medline
- Hwang G, Huh W, Lee JS, et al. **Standard vs modified antiplatelet preparation for preventing thromboembolic events in patients with high on-treatment platelet reactivity undergoing coil embolization for an unruptured intracranial aneurysm: a randomized clinical trial.** *JAMA Neurol* 2015;72:764–72 CrossRef Medline
- Dehdashti AR, Rilliet B, Rufenacht DA, et al. **Shunt-dependent hydrocephalus after rupture of intracranial aneurysms: a prospective study of the influence of treatment modality.** *J Neurosurg* 2004;101:402–07 CrossRef Medline
- Connolly ES Jr, Rabinstein AA, Carhuapoma JR, et al. American Heart Association Stroke Council; Council on Cardiovascular Radiology and Intervention; Council on Cardiovascular Nursing; Council on Cardiovascular Surgery and Anesthesia; Council on Clinical Cardiology. **Guidelines for the management of aneurysmal subarachnoid hemorrhage: a guideline for healthcare professionals from the American Heart Association/American Stroke Association.** *Stroke* 2012;43:1711–37 CrossRef Medline
- Valgimigli M, Biondi-Zoccai G, Tebaldi M, et al. **Tirofiban as adjunctive therapy for acute coronary syndromes and percutaneous coronary intervention: a meta-analysis of randomized trials.** *Eur Heart J* 2010;31:35–49 CrossRef Medline
- Chalouhi N, Jabbour P, Daou B, et al. **A new protocol for anticoagulation with tirofiban during flow diversion.** *Neurosurgery* 2016;78:670–74 CrossRef Medline
- Chalouhi N, Jabbour P, Kung D, et al. **Safety and efficacy of tirofiban in stent-assisted coil embolization of intracranial aneurysms.** *Neurosurgery* 2012;71:710–14; discussion 714 CrossRef Medline
- Moher D, Liberati A, Tetzlaff J, et al. The PRISMA Group. **Preferred reporting items for systematic reviews and meta-analyses: the PRISMA statement.** *BMJ* 2009;339:b2535 CrossRef Medline
- Slim K, Nini E, Forestier D, et al. **Methodological index for non-randomized studies (minors): development and validation of a new instrument.** *ANZ J Surg* 2003;73:712–16 CrossRef Medline
- Guyatt GH, Oxman AD, Vist GE, et al. **GRADE: an emerging consensus on rating quality of evidence and strength of recommendations.** *BMJ* 2008;336:924–26 CrossRef Medline
- DerSimonian R, Laird N. **Meta-analysis in clinical trials.** *Control Clin Trials* 1986;7:177–88 CrossRef Medline
- Altman DG, Bland JM. **Interaction revisited: the difference between two estimates.** *BMJ* 2003;326:219 CrossRef Medline
- Liang XD, Wang ZL, Li TX, et al. **Safety and efficacy of a new prophylactic tirofiban protocol without oral intraoperative antiplatelet therapy for endovascular treatment of ruptured intracranial aneurysms.** *J Neurointerv Surg* 2016;8:1148–53 CrossRef Medline
- Kim S, Choi JH, Kang M, et al. **Safety and efficacy of intravenous tirofiban as antiplatelet premedication for stent-assisted coiling in acutely ruptured intracranial aneurysms.** *AJNR Am J Neuroradiol* 2016;37:508–14 CrossRef Medline
- Limaye K, Zanaty M, Hudson J, et al. **The safety and efficacy of continuous tirofiban as a monoantiplatelet therapy in the management of ruptured aneurysms treated using stent-assisted coiling or flow diversion and requiring ventricular drainage.** *Neurosurgery* 2019;85:E1037–42 CrossRef Medline
- Lee SH, Park IS, Lee JM, et al. **Stent-assisted coil embolization using only a glycoprotein IIb/IIIa inhibitor (tirofiban) for ruptured wide-necked aneurysm repair.** *J Cerebrovasc Endovasc Neurosurg* 2018;20:14–23 CrossRef Medline
- Zi-Liang W, Xiao-Dong L, Tian-Xiao L, et al. **Intravenous administration of tirofiban versus loading dose of oral clopidogrel for preventing thromboembolism in stent-assisted coiling of intracranial aneurysms.** *Int J Stroke* 2017;12:553–59 CrossRef Medline
- Soize S, Foussier C, Manceau PF, et al. **Comparison of two preventive dual antiplatelet regimens for unruptured intracranial aneurysm embolization with flow diverter/disrupter: a matched-cohort study comparing clopidogrel with ticagrelor.** *J Neuroradiol* 2019;46:378–83 CrossRef Medline
- Foreman PM, Enriquez-Marulanda A, Mooney JH, et al. **Whole blood aggregometry prior to Pipeline embolization device treatment of intracranial aneurysms: defining an optimal platelet inhibition cutoff value for clopidogrel.** *J Neurosurg* 2018 Nov 1. [Epub ahead of print] CrossRef Medline
- Park SH, Kim YB, Huh SK. **Effect of premedication method and drug resistance of antiplatelet agent on periprocedural thromboembolic events during coil embolization of an unruptured intracranial aneurysm.** *J Cerebrovasc Endovasc Neurosurg* 2012;14:148–56 CrossRef Medline
- Hudson JS, Nagahama Y, Nakagawa D, et al. **Hemorrhage associated with ventriculoperitoneal shunt placement in aneurysmal subarachnoid hemorrhage patients on a regimen of dual antiplatelet therapy: a retrospective analysis.** *J Neurosurg* 2018;129:916–21 CrossRef Medline
- Hwang G, Jung C, Park SQ, et al. **Thromboembolic complications of elective coil embolization of unruptured aneurysms: the effect of oral antiplatelet preparation on periprocedural thromboembolic**

- complication.** *Neurosurgery* 2010;67:743–48; discussion 748 CrossRef Medline
28. Atallah E, Saad H, Bekelis K, et al. **Safety and efficacy of a 600-mg loading dose of clopidogrel 24 hours before Pipeline Embolization Device treatment.** *World Neurosurg* 2017;106:529–35 CrossRef Medline
 29. Peret A, Mine B, Bonnet T, et al. **Safety and efficacy of a pre-treatment antiplatelet regimen of unruptured intracranial aneurysms: a single-center experience.** *Neuroradiology* 2020;62:1029–41 CrossRef Medline
 30. Moore JM, Adeeb N, Shallwani H, et al. **A multicenter cohort comparison study of the safety, efficacy, and cost of ticagrelor compared to clopidogrel in aneurysm flow diverter procedures.** *Neurosurgery* 2017;81:665–71 CrossRef Medline
 31. Chalouhi N, Jabbour P, Singhal S, et al. **Stent-assisted coiling of intracranial aneurysms: predictors of complications, recanalization, and outcome in 508 cases.** *Stroke* 2013;44:1348–53 CrossRef Medline
 32. Brinjikji W, Murad MH, Lanzino G, et al. **Endovascular treatment of intracranial aneurysms with flow diverters: a meta-analysis.** *Stroke* 2013;44:442–47 CrossRef Medline
 33. Lessne ML, Shah P, Alexander MJ, et al. **Thromboembolic complications after Neuroform stent-assisted treatment of cerebral aneurysms: the Duke Cerebrovascular Center experience in 235 patients with 274 stents.** *Neurosurgery* 2011;69:369–75 CrossRef Medline
 34. Tumialan LM, Zhang YJ, Cawley CM, et al. **Intracranial hemorrhage associated with stent-assisted coil embolization of cerebral aneurysms: a cautionary report.** *J Neurosurg* 2008;108:1122–29 CrossRef Medline
 35. Rahme RJ, Zammar SG, El Ahmadieh TY, et al. **The role of antiplatelet therapy in aneurysm coiling.** *Neurol Res* 2014;36:383–88 CrossRef Medline
 36. Scarborough RM, Kleiman NS, Phillips DR. **Platelet glycoprotein IIb/IIIa antagonists. What are the relevant issues concerning their pharmacology and clinical use?** *Circulation* 1999;100:437–44 CrossRef Medline
 37. Topol EJ, Byzova TV, Plow EF. **Platelet GPIIb-IIIa blockers.** *Lancet* 1999;353:227–31 CrossRef Medline
 38. Yi HJ, Gupta R, Jovin TG, et al. **Initial experience with the use of intravenous eptifibatid bolus in stent-assisted coiling of intracranial aneurysms.** *AJNR Am J Neuroradiol* 2006;27:1856–60 Medline
 39. Jeong HW, Jin SC. **Intra-arterial infusion of a glycoprotein IIb/IIIa antagonist for the treatment of thromboembolism during coil embolization of intracranial aneurysm: a comparison of abciximab and tirofiban.** *AJNR Am J Neuroradiol* 2013;34:1621–25 CrossRef Medline
 40. McClellan KJ, Goa KL. **Tirofiban. A review of its use in acute coronary syndromes.** *Drugs* 1998;56:1067–80 CrossRef Medline
 41. Steinhubl SR, Talley JD, Braden GA, et al. **Point-of-care measured platelet inhibition correlates with a reduced risk of an adverse cardiac event after percutaneous coronary intervention: results of the GOLD (AU-Assessing Ultegra) multicenter study.** *Circulation* 2001;103:2572–78 CrossRef Medline
 42. Kirma C, Erkol A, Pala S, et al. **Intracoronary bolus-only compared with intravenous bolus plus infusion of tirofiban application in patients with ST-elevation myocardial infarction undergoing primary percutaneous coronary intervention.** *Cathet Cardiovasc Intervent* 2012;79:59–67 CrossRef Medline
 43. Wallentin L, Becker RC, Budaj A, et al. **Ticagrelor versus clopidogrel in patients with acute coronary syndromes.** *N Engl J Med* 2009;361:1045–57 CrossRef Medline
 44. Gimbel M, Qaderdan K, Willemsen L, et al. **Clopidogrel versus ticagrelor or prasugrel in patients aged 70 years or older with non-ST-elevation acute coronary syndrome (POPular AGE): the randomised, open-label, non-inferiority trial.** *Lancet* 2020;395:1374–81 CrossRef Medline
 45. Adeeb N, Griessenauer CJ, Foreman PM, et al. **Use of platelet function testing before Pipeline embolization device placement: a multicenter cohort study.** *Stroke* 2017;48:1322–30 CrossRef Medline
 46. Anderson KM, Califf RM, Stone GW, et al. **Long-term mortality benefit with abciximab in patients undergoing percutaneous coronary intervention.** *J Am Coll Cardiol* 2001;37:2059–65 CrossRef Medline
 47. Lincoff AM, Califf RM, Topol EJ. **Platelet glycoprotein IIb/IIIa receptor blockade in coronary artery disease.** *J Am Coll Cardiol* 2000;35:1103–15 CrossRef Medline

Ruptured Intracranial Aneurysms Treated with the Pipeline Embolization Device: A Systematic Review and Pooled Analysis of Individual Patient Data

P.M. Foreman, A. Ilyas, M.C. Cress, J.A. Vachhani, R.A. Hirschl, B. Agee, and C.J. Griessenauer



ABSTRACT

BACKGROUND: The Pipeline Embolization Device (PED) is a flow-diverting stent for the treatment of intracranial aneurysms and is used off-label for a subset of ruptured aneurysms not amenable to traditional treatment.

PURPOSE: Our aim was to evaluate the safety and efficacy of the PED for treatment of ruptured intracranial aneurysms.

DATA SOURCES: A systematic review of the MEDLINE, EMBASE, and Scopus data bases from January 2011 to March 2020 was performed for articles reporting treatment of ruptured intracranial aneurysms with the PED.

STUDY SELECTION: A total of 12 studies comprising 145 patients with 145 treated aneurysms were included for analysis.

DATA ANALYSIS: Individual patient data were collected. Nonparametric tests were used to compare differences among patients. Logistic regression was used to determine an association with outcome variables.

DATA SYNTHESIS: Mean aneurysm size was 5.9 mm, and most were blister (51.0%) or dissecting (26.9%) in morphology. Three (2.1%) aneurysms ruptured following PED placement. Univariate logistic regression identified larger aneurysm size as a significant predictor of aneurysm rerupture ($P = .008$). Of patients with radiographic follow-up, 87.5% had complete aneurysm occlusion. Symptomatic neurologic complications occurred in 16.5%.

LIMITATIONS: Analysis was limited by the quality of the included data, most of which were from small case series representing class III medical evidence. No study assessed outcome in a blinded or independently adjudicated manner.

CONCLUSIONS: Most ruptured aneurysms treated with the PED were blister or dissecting aneurysms. Treatment was associated with a rerupture rate of 2.1% and a complete occlusion rate of 87.5%.

ABBREVIATIONS: DAPT = dual-antiplatelet therapy; PED = Pipeline Embolization Device

The Pipeline Embolization Device (PED; Medtronic) is a braided flow-diverting stent composed of platinum tungsten and cobalt chromium. Its 48 interwoven strands provide between 30% and 35% surface coverage. The stent is placed within the lumen of the parent vessel and leads to progressive aneurysm thrombosis with endoluminal reconstruction of the

parent vessel. In 2011, the Food and Drug Administration approved the PED for the treatment of unruptured large and giant wide-neck aneurysms of the internal carotid artery. Experience with the device has led to an improved understanding of its strengths and limitations and has led to increased use of the PED for off-label indications, including ruptured aneurysms.¹

Flow diversion for the treatment of ruptured aneurysms is complicated by the necessity of dual-antiplatelet therapy (DAPT) and delayed aneurysm occlusion. DAPT can complicate the management of patients with subarachnoid hemorrhage who require external ventricular drain placement, ventriculoperitoneal shunting, or craniotomy. Delayed aneurysm occlusion, especially in the setting of DAPT, theoretically increases the risk of aneurysm rerupture. Despite these limitations, the PED is used for a subset of ruptured aneurysms not amenable to traditional treatment techniques. We sought to evaluate the safety and efficacy of this

Received October 8, 2020; accepted after revision November 2.

From the Neuroscience and Rehabilitation Institute (P.M.F., M.C.C., J.A.V., R.A.H.), Orlando Health, Orlando, Florida; Department of Neurosurgery (A.I., B.A.), University of Alabama at Birmingham, Birmingham, Alabama; Department of Neurosurgery (C.J.G.), Geisinger Health System, Danville, Pennsylvania; and Research Institute of Neurointervention (C.J.G.), Paracelsus Medical University, Salzburg, Austria.

Please address correspondence to Paul M. Foreman, MD, Neuroscience and Rehabilitation Institute, 89 W. Copeland Dr, Orlando, FL 32806; e-mail: paul.foreman@orlandohealth.com

Indicates article with online supplemental data.

<http://dx.doi.org/10.3174/ajnr.A7002>

practice with a systematic review of the literature and pooled analysis of individual patient data.

MATERIALS AND METHODS

Literature Search and Inclusion Criteria

We performed a literature search on October 1, 2020, using MEDLINE, EMBASE, and Scopus, with the following search phrase: “(subarachnoid hemorrhage OR ruptured aneurysm) AND (pipeline OR pipeline embolization device).” The studies were screened by title and abstract to ensure fulfillment of the following inclusion criteria: 1) ≥ 5 patients with ruptured intracranial aneurysms treated with a PED with or without the adjuvant use of coils; 2) individual patient data on clinical outcomes and complications; 3) each patient represented only once among all included studies; and 4) the study written in English. Citations of screened articles were reviewed, and articles meeting the inclusion criteria were included. All included cases used the Pipeline Embolization Device (Pipeline Classic) or Pipeline Flex Embolization Device (Pipeline Flex). No included cases used the Pipeline Flex with Shield Technology (PED Shield).

A traditional meta-analysis consists of statistical comparisons of study outcome data and is limited by heterogeneity across studies and by the outcome data reported by each study. In an attempt to alleviate these limitations and increase the granularity of data, we performed an analysis of pooled individual patient data obtained from each study that met the inclusion criteria.

Data Extraction

Individual patient data regarding patient demographics, Hunt and Hess score, and Fisher grade; aneurysmal angiomorphic features; intervention timing and technique; radiographic and clinical outcomes; and complications were extracted from each study. Demographic data included patient sex and age. Angiomorphic features included aneurysm size, aneurysm type (blister, saccular, dissecting, or fusiform), and aneurysm location. Treatment data included the timing of the intervention (acute, within 3 days of rupture; short delay, within 14 days; or long delay otherwise) and the use of adjuvant coils. Outcome data included the duration of follow-up, rerupture, occlusion at angiographic follow-up, and treatment-related symptomatic neurologic complications. Only aneurysm reruptures following placement of the PED were considered cases of aneurysm rerupture. Symptomatic neurologic complications were chosen due to the increased likelihood of consistent reporting across studies. Complications thought to be inconsistently reported included the use of angioplasty to open the PED, asymptomatic in-stent stenosis, and asymptomatic external ventricular drain hemorrhages. Cases of aneurysm rerupture before PED placement were considered symptomatic neurologic complications due to the possibility that preprocedural antiplatelet therapy contributed to the rerupture.

Statistical Analysis

All statistical analyses were performed using R statistical and computing software (Version 3.3.1; <http://www.r-project.org/>). Descriptive statistics were computed on aggregated individual patient data. The Mann-Whitney-Wilcoxon or Kruskal-Wallis tests were used to compare differences in demographic,

aneurysmal, and treatment characteristics among patients grouped by radiographic outcome and complications. We opted to analyze our data using nonparametric tests, minimizing the number of assumptions regarding the underlying distribution of the data. Logistic regression was used to determine an association of aneurysmal angiomorphic or treatment features with outcome variables. A *P* value of $< .05$ was considered statistically significant.

RESULTS

Study Selection

The literature search yielded a total of 648 studies, 628 of which were excluded after abstract review. Of the 20 remaining studies, 12 studies comprising a total of 145 patients with 145 treated aneurysms met the inclusion criteria and were included in our analysis (Fig 1). After full-text review, 8 articles were excluded for the following reasons: non-PED primary treatment of the aneurysms ($n = 1$), individual outcome data not available ($n = 5$), and overlapping data ($n = 2$).

A sample case of a ruptured intracranial aneurysm treated with a PED is detailed in Fig 2.

Baseline and Treatment Characteristics

The Online Supplemental Data summarize the aggregate baseline characteristics of the included patients. Female patients comprised 72.3% of the cohort. The average age was 51 years. The mean Hunt and Hess score was 2.2 (SD, 1.1) with 84% of cases Hunt and Hess 1–3. The mean Fisher grade was 2.8 (SD, 1.0) with 70% of cases Fisher grades 1–3. The average aneurysm size was 5.9 mm. Small, large, and giant aneurysm comprised 77.9%, 15.9%, and 6.2% of the cohort, respectively. Rates of blister, saccular, dissecting, and fusiform aneurysms were 51.0%, 15.9%, 26.9%, and 6.2%, respectively. Adjuvant use of coil embolization was performed in 24.8% of cases.

Clinical and Radiographic Outcomes

Table 1 summarizes the aggregate outcome data from the included studies. The mean radiographic follow-up ranged from 3 to 18 months. Radiographic occlusion was achieved in 87.5% of patients. Aneurysm size differed among the group of patients who achieved radiographic occlusion versus those who did not ($P = .007$). Rates of radiographic occlusion in small, large, and giant aneurysms were 68.8%, 12.0%, and 3.2%, respectively. The overall rerupture rate following treatment with the PED was 2.1%.

Details of Aneurysm Rerupture following PED Placement

Table 2 details the 3 cases of aneurysm rerupture following treatment with the PED. Of note, 2 of the 3 aneurysm rerupture cases following PED placement were complicated by intraprocedural in-stent thrombosis treated with intra-arterial antithrombotics (tPA and abciximab). The case treated with intra-arterial microcatheter tPA infusion had a rerupture on posttreatment day 1. Given the short half-life and fibrinolytic activity of tPA, it is conceivable but not conclusive that the rerupture was related to the medication. The patient treated with intra-arterial abciximab had rerupture on posttreatment day 8; thus, the one-time medication dose was not thought to influence rerupture. Aneurysm

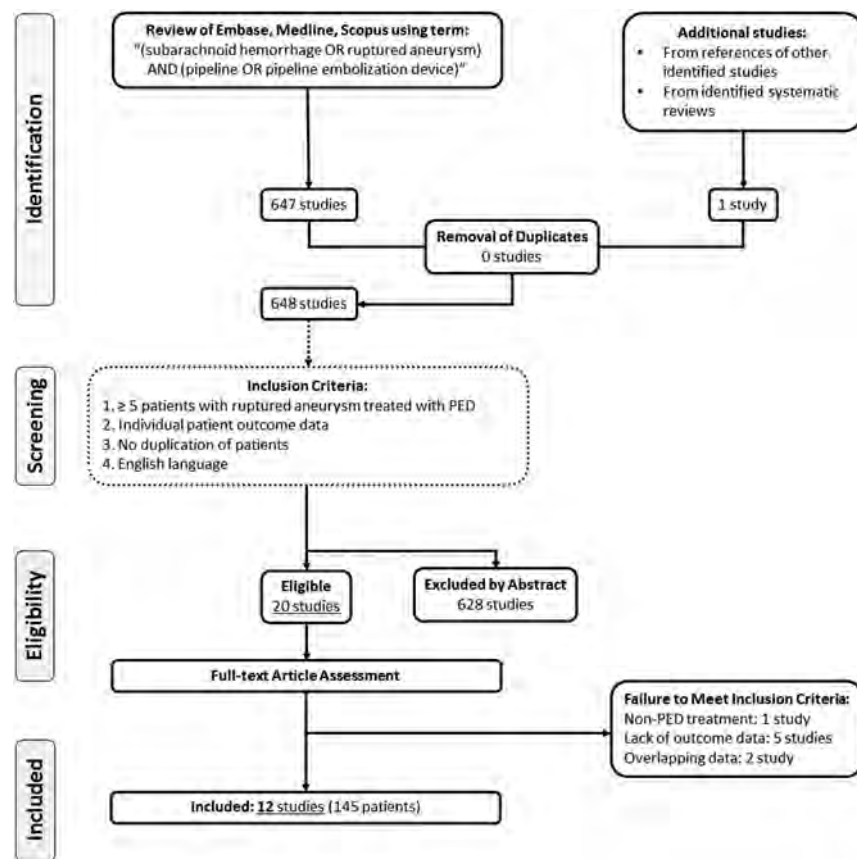


FIG 1. Flow diagram describing the selection process by which studies were included in the analysis of treatment of ruptured intracranial aneurysms with the Pipeline Embolization Device.

morphology differed among the group of patients with rerupture versus those without it ($P = .011$), and the rates of rerupture for blister, saccular, dissecting, and fusiform aneurysms were 0%, 1.4%, 0%, and 0.7%, respectively.

Complications

Symptomatic complications occurred in 23 (16.5%) patients. Of the 23 symptomatic complications, 9 were thromboembolic in origin, resulting in death in a single patient due to brain stem ischemia following treatment of a fusiform basilar artery aneurysm. Other symptomatic thromboembolic complications included ischemic stroke of the brain, spinal cord, and retina. Asymptomatic ischemic stroke occurred in 2 patients, and 5 patients experienced asymptomatic in-stent thrombosis/stenosis. Of note, 3 deaths caused by rerupture before PED placement were included due to the possibility of the rerupture being related to preprocedural antiplatelet use. Two of these reruptures occurred before the procedure, and one occurred intraoperatively. These patients were not included in the rerupture group because the PED had not been placed. None of aneurysm morphologic or treatment-related factors were associated with complications. The Hunt and Hess score was associated with complications ($P = .004$).

The Online Supplemental Data summarize the results of the nonparametric outcome analyses. On the basis of univariate logistic regression, increased aneurysm size was associated with

higher rates of rerupture (log odds = 0.16; 95% CI, 0.05–0.31; $P = .008$). Table 3 summarizes the results of univariate logistic regression.

DISCUSSION

Endovascular treatment of ruptured aneurysms with the PED is off-label and is primarily used to treat ruptured aneurysms not amenable to traditional surgical or endovascular treatment options. Given the relative rarity of the use of the device in this setting, data regarding safety and efficacy are limited to small case series. We sought to systematically review the literature to identify reports of the use of PED for the treatment of ruptured intracranial aneurysms and pool individual patient data in an effort to synthesize the available literature. A total of 145 patients with 145 ruptured aneurysms from 12 independent studies were identified.^{2–13} The aneurysm rerupture rate was 2.1%, with complete aneurysm occlusion in 87.5%.

Flow diversion is not the preferred treatment of ruptured intracranial aneurysms due to the necessity of DAPT and delayed aneurysm occlusion.¹⁴ DAPT increases the risk of hemorrhagic complications with common invasive procedures required in the management of patients with SAH, including external ventricular drain, shunt, central line, and craniotomy. A recently published study of secondary hemorrhagic complications following aneurysmal subarachnoid hemorrhage found that ventriculostomy-

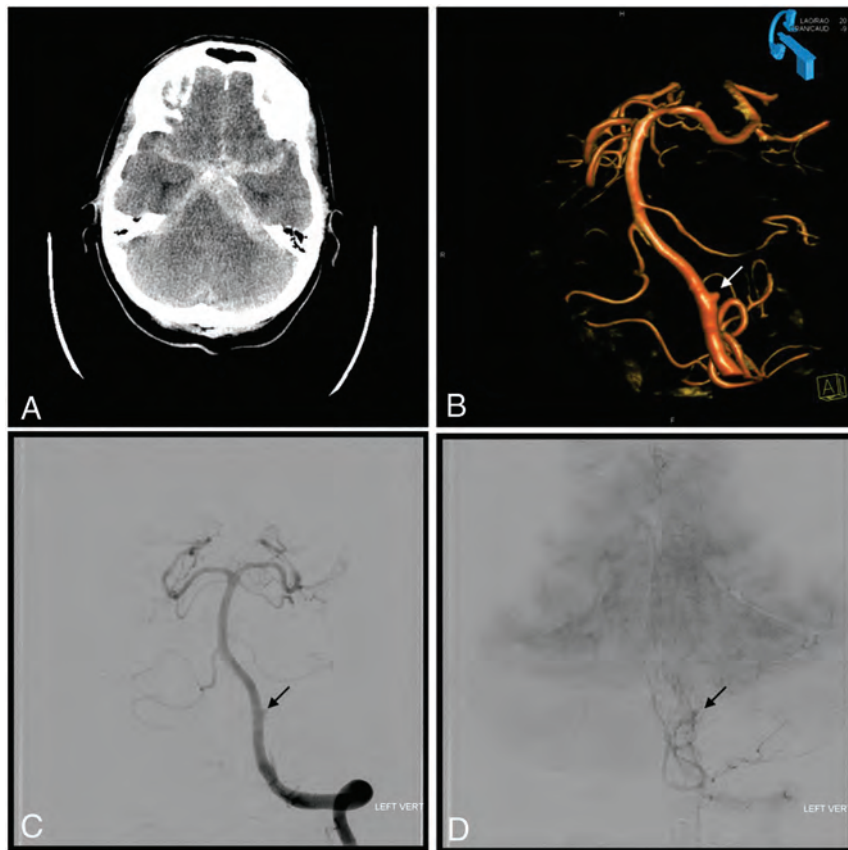


FIG 2. Sample case of a ruptured dissecting aneurysm of the left vertebral artery treated with placement of the PED. A, CT of the head demonstrates subarachnoid hemorrhage consistent with aneurysm rupture. Note the large amount of left-sided posterior fossa SAH. B, 3D rotational angiography of the left vertebral artery shows the dissecting aneurysm (arrow). C, Left vertebral artery angiogram shows the dissecting aneurysm (arrow) following PED placement.

associated bleeding was independently predicted by mono- or dual-antiplatelet therapy but ultimately had no impact on functional outcome. However, use of high-dose thrombolytics such as heparin and abciximab to achieve rapid anticoagulation was associated with a high risk of clinically relevant secondary hemorrhages.¹⁵ Delayed aneurysm occlusion increases the risk of aneurysm rerupture, which is known to be the highest in the days to weeks following the initial bleed.¹⁶ These drawbacks have relegated flow diversion to a secondary option for the treatment of ruptured aneurysms in the acute setting or as definitive therapy following dome protection with coil embolization. The most common indication for flow diversion in the acute setting is aneurysm morphology not amenable to traditional treatment options. Most included aneurysms in our pooled analysis were blister (51.0%) and dissecting (26.9%) aneurysms. Blister aneurysms are broad, shallow, thin-walled sidewall aneurysms most commonly affecting the internal carotid artery and are characterized by a high risk of intraoperative rupture with traditional treatment options.¹⁷ Endoluminal reconstruction with a flow-diverting stent allows a durable cure without the risk of direct aneurysm manipulation. This advantage likely accounts for the over-representation of a rare morphology in our analysis.

The dissecting aneurysm is another uncommon etiology of subarachnoid hemorrhage that is difficult to treat with standard techniques but is amenable with parent artery reconstruction with flow-diverting stents. Flow diversion following initial dome protection with coils represents a hybrid option most commonly used with saccular aneurysms. Unfortunately, data regarding the optimal timing of flow diversion and the use of adjunctive coiling were not consistently reported or sufficiently detailed to allow meaningful analysis.

Guideline recommendations for the treatment of ruptured aneurysms include the surgical clipping or endovascular coiling of the ruptured aneurysm to reduce the rate of rerupture.¹⁸ The risk of aneurysm rerupture is the most important and morbid complication associated with flow-diversion treatment of ruptured aneurysms and is most notable when adjunctive coiling cannot be performed. The relative protection of a flow-diverting stent without aneurysm occlusion in the acute setting is not known. The overall rerupture rate in the pooled analysis was 2.1%, with larger aneurysms being associated with an increased risk of rerupture. Two of the 3 aneurysm reruptures following PED placement

were complicated by in-stent thrombosis requiring treatment with intra-arterial antithrombotics (tPA and abciximab). While a causative relationship is not supported by the available data, this highlights the necessity of adequate preoperative antiplatelet regimens in the setting of aneurysmal SAH to reduce the possibility of thromboembolic complications and a subsequent cascade of management decisions that increase the risk of aneurysm rerupture. Our reported rerupture rate exceeds the rerupture rate of 0.5% reported in the Barrow Ruptured Aneurysm Trial 6-year follow-up, but patient populations are not comparable, given the pronounced difference in aneurysm morphologies. Of note, 1 of the 2 reruptures in the Barrow Ruptured Aneurysm Trial occurred in the in-hospital setting following surgical wrapping of a dissecting aneurysm.¹⁹

Complete aneurysm obliteration is the goal of treatment, and flow diversion has demonstrated the ability to achieve durable occlusion with 6-month complete aneurysm occlusion rates of 73.6% and 93.3% in the Pipeline Embolization Device for Uncoilable or Failed Aneurysms study and the Pipeline Embolization Device for the Treatment of Aneurysms trial, respectively.^{20,21} The current study found a complete occlusion rate of 87.5% in patients with available imaging follow-up.

Table 1: Summary of the patient treatment and outcome data from the 12 included studies

Authors and Year	Treatment		Follow-Up (mo)	Rerupture	Occluded	mRS		Complications	
	PED Only	PED + Coiling				0–2	3–5	Death	All
Capocci et al, ¹³ 2020	6/6	0/6	18.0	0/6	5/5	5/6	1/6	0/6	1/6
Lozupone et al, ² 2018	12/14	2/14	NR	0/14	12/12	10/14	3/14	1/14	2/14
Cerejo et al, ⁷ 2017	8/8	0/8	7.2	0/8	6/8	6/7	1/7	0/8	2/8
Linfante et al, ³ 2017	10/10	0/10	15.2	0/10	9/9	8/10	1/10	1/10	1/10
Ryan et al, ⁴ 2017	13/13	0/13	3.0	0/13	5/10	10/13	1/13	2/13	5/13
Chalouhi et al, ¹¹ 2015	14/20	6/20	5.3	0/20	12/15	19/20	0/20	1/20	1/20
Lin et al, ⁹ 2015	14/26	12/26	10.1	1/26	19/23	20/26	3/26	3/26	3/26
Chan et al, ⁵ 2014	6/8	2/8	5.0	0/8	8/8	NR ^a	NR ^a	0/8	1/8
Yoon et al, ⁸ 2014	9/11	2/11	4.8	0/11	7/8	9/10	0/10	1/11	4/11
Cinar et al, ⁶ 2013	6/6	0/6	7.0	0/6	6/6	4/6	2/6	0/6	0/6
McAuliffe et al, ¹⁰ 2012	6/11	5/11	6.0	2/11	8/9	8/11	1/11	2/11	3/11
de Barrios Faria et al, ¹² 2011	5/12	7/12	6.0	0/12	8/12	NR ^a	NR ^a	0/12	0/12
Total	109/145	36/145		3/139	105/120	99/123	13/123	11/139	23/139
Range			3–18						

Note:—NR indicates not reported.

^a Reported Glasgow Outcome Scale scores: grades 1–3: 3/8 (Chan et al), 6/12 (de Barrios Faria et al); grades 4–5: 5/8 (Chan et al), 6/12 (de Barrios Faria et al).

Table 2: Details regarding all 3 patients with Pipeline Embolization Device–related intracranial hemorrhage

Authors and Year	Sex	Age (yr)	Clinical Score	Treatment Time	Aneurysm Size (mm)	Aneurysm Location	Aneurysm Morphology	Treatment Method	Procedure and Complication Details
Lin et al, ⁹ 2015	NR	Mid-30s	HH 2	Acute	3	Paraclinoid ICA	Saccular	PED only	Treatment complicated by in-stent thrombosis treated with intra-arterial tPA; patient died of re-hemorrhage on posttreatment day 1
McAuliffe et al, ¹⁰ 2012	F	56	WFNS II	Acute	21	Superior hypophyseal	Saccular	PED only	Two PEDs deployed with plans for adjuvant coiling; however, in-stent thrombosis was seen and treated with intra-arterial abciximab; patient experienced rerupture on day 8 with vasospasm of ipsilateral M1 segment, treated with balloon angioplasty and 3rd PED; patient died 3 days later
McAuliffe et al, ¹⁰ 2012	F	37	WFNS V	Acute	34	Dorsal paraclinoid ICA	Fusiform	PED only	Two PEDs telescoped across the aneurysms, which re-ruptured immediately after deployment of the second device; active treatment was withdrawn

Note:—HH indicates Hunt and Hess grade; WFNS, World Federation of Neurosurgical Societies grade.

Table 3: Univariate logistic regression analysis of outcome and function of aneurysm and treatment features

Outcome	Aneurysm Size (Log Odds)	Aneurysm Morphology	Treatment Time	Treatment Method
Rerupture	0.16 (0.05–0.31) P value = .008 ^a	0.995	0.998	0.995
Radiographic occlusion	0.141	0.234	0.261	0.078
Symptomatic complication	0.134	0.332	0.140	0.449

^a P value of < .05.

Smaller aneurysms were more commonly associated with complete occlusion.

Symptomatic neurologic complications, including all aneurysm reruptures, occurred in 16.5% of cases. Eleven of the 23 symptomatic neurologic complications were hemorrhagic in

nature, highlighting the potential danger of DAPT. Given the challenge of treating these complex aneurysm morphologies in the acute setting, the neurologic complication rate was thought to be acceptable but represents an opportunity for improvement with technologic advancement. A recently developed surface-modified

PED, the PED Shield, has a coating of phosphorylcholine covalently bound to the braid wires and has demonstrated reduced surface thrombus formation compared with the PED without shield technology.²² The 2019 case series by Manning et al²³ evaluated patients who underwent acute treatment of a ruptured aneurysm with the PED Shield. Of the 9 patients treated with mono-antiplatelet therapy alone, no symptomatic hemorrhagic or ischemic complications occurred. However, the addition of postoperative heparin was associated with a significantly increased risk of all complications and symptomatic complications. The authors concluded that their preliminary data suggested that the PED Shield may be safe to use in the acute treatment of ruptured aneurysms with mono-antiplatelet therapy.²³

Limitations

A systematic review is limited by the quality of the included data. The included data came from small case series and represent class III medical evidence. Delineation between PED-related complications and SAH-related morbidity and mortality across all studies was not possible due to differing methods of reporting. We have reported our pooled results in a granular manner to allow critical review of the included data. Criteria for PED treatment of ruptured aneurysms are also likely to differ among centers, allowing heterogeneity among included cases. Additionally, observer bias within the included studies should be considered due to a lack of blinded or independently adjudicated assessment of outcomes and complications. These shortcomings have the potential to overestimate treatment success and minimize treatment-related complications.

CONCLUSIONS

Treatment of ruptured aneurysms with the PED is primarily performed for blister and dissecting aneurysm morphologies. Complete aneurysm occlusion was achieved in 87.5% of cases, and symptomatic neurologic complications occurred in 16.5%. Symptomatic neurologic complications were most often hemorrhagic in etiology. Treatment of ruptured aneurysms not thought to be good candidates for standard surgical or endovascular treatment options can be successfully treated with the PED with an acceptable complication risk.

Disclosures: Marshall C. Cress—UNRELATED: Consultancy: Cerenovus. Jay A. Vachhani—UNRELATED: Consultancy: MicroVention, Comments: proctor for physicians using the Woven EndoBridge. Christoph J. Griessenauer—UNRELATED: Consultancy: Stryker, MicroVention; Employment: Geisinger Health System.

REFERENCES

- Patel PD, Chalouhi N, Atallah E, et al. **Off-label uses of the Pipeline Embolization Device: a review of the literature.** *Neurosurg Focus* 2017;42:E4 CrossRef Medline
- Lozupone E, Piano M, Valvassori L, et al. **Flow diverter devices in ruptured intracranial aneurysms: a single-center experience.** *J Neurosurg* 2018;128:1037–43 CrossRef Medline
- Linfante I, Mayich M, Sonig A, et al. **Flow diversion with Pipeline Embolic Device as treatment of subarachnoid hemorrhage secondary to blister aneurysms: dual-center experience and review of the literature.** *J Neurointerv Surg* 2017;9:29–33 CrossRef Medline
- Ryan RW, Khan AS, Barco R, et al. **Pipeline flow diversion of ruptured blister aneurysms of the supraclinoid carotid artery using a single-device strategy.** *Neurosurg Focus* 2017;42:E11 CrossRef Medline
- Chan RS, Mak CH, Wong AK, et al. **Use of the Pipeline Embolization Device to treat recently ruptured dissecting cerebral aneurysms.** *Interv Neuroradiol* 2014;20:436–41 CrossRef Medline
- Cinar C, Oran I, Bozkaya H, et al. **Endovascular treatment of ruptured blister-like aneurysms with special reference to the flow-diverting strategy.** *Neuroradiology* 2013;55:441–47 CrossRef Medline
- Cerejo R, Bain M, John S, et al. **Flow diverter treatment of cerebral blister aneurysms.** *Neuroradiology* 2017;59:1285–90 CrossRef Medline
- Yoon JW, Siddiqui AH, Dumont TM, et al. Endovascular Neurosurgery Research Group. **Feasibility and safety of Pipeline embolization device in patients with ruptured carotid blister aneurysms.** *Neurosurgery* 2014;75:419–29; discussion 429 CrossRef Medline
- Lin N, Brouillard AM, Keigher KM, et al. **Utilization of Pipeline Embolization Device for treatment of ruptured intracranial aneurysms: US multicenter experience.** *J Neurointerv Surg* 2015;7:808–15 CrossRef Medline
- McAuliffe W, Wenderoth JD. **Immediate and midterm results following treatment of recently ruptured intracranial aneurysms with the Pipeline Embolization Device.** *AJNR Am J Neuroradiol* 2012;33:487–93 CrossRef Medline
- Chalouhi N, Zanaty M, Whiting A, et al. **Treatment of ruptured intracranial aneurysms with the Pipeline embolization device.** *Neurosurgery* 2015;76:165–172; discussion 172 CrossRef Medline
- de Barros Faria M, Castro RN, Lundquist J, et al. **The role of the Pipeline embolization device for the treatment of dissecting intracranial aneurysms.** *AJNR Am J Neuroradiol* 2011;32:2192–95 CrossRef Medline
- Capocci R, Shotar E, Di Maria F, et al. **Delayed treatment (≥5 days) by flow diversion of ruptured blister-like cerebral aneurysms: case series of 8 consecutive patients.** *Clin Neuroradiol* 2020;30:287–96 CrossRef Medline
- Natarajan SK, Shallwani H, Fennell VS, et al. **Flow diversion after aneurysmal subarachnoid hemorrhage.** *Neurosurg Clin N Am* 2017;28:375–88 CrossRef Medline
- Darkwah Oppong M, Buffen K, Pierscianek D, et al. **Secondary hemorrhagic complications in aneurysmal subarachnoid hemorrhage: when the impact hits hard.** *J Neurosurg* 2019 Jan 25. [Epub ahead of print] CrossRef Medline
- Kassel NF, Torner JC. **Aneurysmal rebleeding: a preliminary report from the Cooperative Aneurysm Study.** *Neurosurgery* 1983;13:479–81 CrossRef Medline
- Peschillo S, Miscusi M, Caporlingua A, et al. **Blister-like aneurysms in atypical locations: a single-center experience and comprehensive literature review.** *World Neurosurg* 2015;84:1070–79 CrossRef Medline
- Connolly ES Jr, Rabinstein AA, Carhuapoma JR, et al; Council on Clinical Cardiology. **Guidelines for the management of aneurysmal subarachnoid hemorrhage: a guideline for healthcare professionals from the American Heart Association/American Stroke Association.** *Stroke* 2012;43:1711–37 CrossRef Medline
- Spetzler RF, McDougall CG, Zabramski JM, et al. **The Barrow Ruptured Aneurysm Trial: 6-year results.** *J Neurosurg* 2015;123:609–17 CrossRef Medline
- Becske T, Kallmes DF, Saatci I, et al. **Pipeline for uncoilable or failed aneurysms: results from a multicenter clinical trial.** *Radiology* 2013;267:858–68 CrossRef Medline
- Nelson PK, Lylyk P, Szikora I, et al. **The Pipeline Embolization Device for the Intracranial Treatment of Aneurysms trial.** *AJNR Am J Neuroradiol* 2011;32:34–40 CrossRef Medline
- Marosfoi M, Clarencon F, Langan ET, et al. **Acute thrombus formation on phosphorylcholine surface modified flow diverters.** *J Neurointerv Surg* 2018;10:406–11 CrossRef Medline
- Manning NW, Cheung A, Phillips TJ, et al. **Pipeline Shield with single antiplatelet therapy in aneurysmal subarachnoid haemorrhage: multicenter experience.** *J Neurointerv Surg* 2019;11:694–98 CrossRef Medline

Fast Stent Retrieval during Mechanical Thrombectomy Improves Recanalization in Patients with the Negative Susceptibility Vessel Sign

S. Soize, J.-B. Eymard, S. Cheikh-Rouhou, P.-F. Manceau, C. Gelmini, M. Sahnoun, M. Gawlitza, M. Zuber, L. Pierot, and E. Touzé



ABSTRACT

BACKGROUND AND PURPOSE: In acute ischemic stroke, the negative susceptibility vessel sign on T2*-weighted images traditionally highlights fibrin-rich clots, which are particularly challenging to remove. In vitro, fast stent retrieval improves fibrin-rich clot extraction. We aimed to evaluate whether the speed of stent retrieval influences the recanalization and clinical outcome of patients presenting with the negative susceptibility vessel sign.

MATERIALS AND METHODS: Patients were identified from a registry of patients with ischemic stroke receiving mechanical thrombectomy between January 2016 and January 2020. Inclusion criteria were the following: 1) acute ischemic stroke caused by an isolated occlusion of the anterior circulation involving the MCA (Internal Carotid Artery-L, M1, M2) within 8 hours of symptom onset; 2) a negative susceptibility vessel sign on prethrombectomy T2*-weighted images; and 3) treatment with a combined technique (stent retriever + contact aspiration). Patients were dichotomized according to retrieval speed (fast versus slow). The primary outcome was the first-pass recanalization rate.

RESULTS: Of 68 patients who met inclusion criteria, 31 (45.6%) were treated with fast retrieval. Patients receiving a fast retrieval had greater odds of first-pass complete (relative risk and 95% confidence interval [RR 95% CI], 4.30 [1.80–10.24]), near-complete (RR 95% CI, 3.24 [1.57–6.68]), and successful (RR 95% CI, 2.60 [1.53–4.43]) recanalization as well as greater odds of final complete (RR 95% CI, 4.18 [1.93–9.04]), near-complete (RR 95% CI, 2.75 [1.55–4.85]), and successful (RR 95% CI, 1.52 [1.14–2.03]) recanalization. No significant statistical differences in procedure-related serious adverse events, distal embolization, or symptomatic intracranial hemorrhage were reported. No differences were noted in terms of functional independence (RR 95% CI, 1.01 [0.53–1.93]) and all-cause mortality (RR 95% CI, 0.90 [0.35–2.30]) at 90 days.

CONCLUSIONS: A fast stent retrieval during mechanical thrombectomy is safe and improves the retrieval of clots with the negative susceptibility vessel sign.

ABBREVIATIONS: eTICI = extended TICI; ICA-L occlusion = internal carotid artery distal L-type occlusion; RR = relative risk; SVS = susceptibility vessel sign

In acute ischemic stroke, the susceptibility vessel sign (SVS) on T2*-weighted sequences is thought to highlight the red blood cells in the clot.¹⁻³ Histopathologic correlations of retrieved

thrombi with MR imaging features showed that clots not visible on T2*-weighted images (negative SVS) contained a high proportion of fibrin,^{1,2} which makes them particularly firm and sticky,^{4,5} and thus very challenging to remove mechanically.⁵⁻⁷ Approximately 20% of patients receiving bridging therapy cannot achieve recanalization,^{7,8} possibly due, in part, to how difficult it is to tailor the retrieval technique to clot properties.⁹ Recent in vitro experiments have shown that fast retrieval of the clot using a combined technique (contact aspiration + stent retriever) can improve recanalization, especially with fibrin-rich clots.¹⁰ Currently, device manufacturers' instructions advise operators to withdraw stent retrievers slowly to avoid potential artery dissection or rupture. Yet, the effect of retrieval speed on mechanical thrombectomy success in vivo has yet to be explored. A fast retrieval may mobilize the clot suddenly, enhance clot wedging, and minimize loss of apposition during retrieval.¹⁰ The present

Received September 23, 2020; accepted after revision November 2.

From the Unité Mixte de recherche-S UI237 (S.S., M.Z., E.T.), Institut National de la Santé et de la Recherche Médicale, Normandie University, Université Caen-Normandie, Cyceron, Caen, France; Department of Neuroradiology (S.S., J.-B.E., S.C.-R., P.-F.M., C.G., M.S., M.G., L.P.), Hôpital Maison Blanche, Centre Hospitalier Universitaire de Reims, Université de Champagne-Ardenne, Reims, France; Department of Neurology (M.Z.), Université de Paris, Hôpital Saint-Joseph, Paris, France; and Department of Neurology (E.T.), Centre Hospitalier Universitaire Caen Normandie, Caen, France.

Please address correspondence to Sebastien Soize, MD, Department of Neuroradiology, CHU Reims, Hôpital Maison Blanche, 45 Rue Cognacq-Jay, Reims 51092, France; e-mail: ssoize@chu-reims.fr



Indicates article with online supplemental data.



Indicates article with supplemental on-line videos.

<http://dx.doi.org/10.3174/ajnr.A6989>

study aimed to evaluate whether stent-retrieval speed influences recanalization rates and clinical outcome in patients presenting with negative SVS clots.

MATERIALS AND METHODS

Study Setting

Patients were identified from a registry of patients with ischemic stroke treated by mechanical thrombectomy between January 2016 and January 2020. Inclusion criteria for this retrospective review included the following:

1. A patient with an acute ischemic stroke caused by an isolated occlusion of the anterior circulation involving the MCA (Internal Carotid Artery-L, M1, M2) confirmed by MRA within 8 hours of symptom onset
2. A negative SVS on prethrombectomy MRI T2*-weighted images
3. Treatment with an aspiration + stent retriever technique (see “Thrombectomy Techniques”).¹¹⁻¹³

During the study period, mechanical thrombectomy was provided regardless of age, baseline NIHSS severity, or infarct size. Patients experienced either fast or slow stent retrieval (and a distal aspiration catheter), depending on the operator’s discretion. Catheters and stent retrievers were standardized to reduce bias risk. The present report follows the Strengthening the Reporting of Observational Studies in Epidemiology (STROBE) statement guidelines.¹⁴

Collected Data

We collected demographic data, vascular risk factors, the NIHSS score at several time points (admission, 24 hours, discharge), admission blood glucose levels, stroke side, symptom onset to imaging and to groin puncture times, intravenous thrombolysis administration (bridging therapy), baseline imaging and angiographic variables, 24-hour imaging assessment, and 90-day mRS score. Functional independence was defined as mRS \leq 2. Hemorrhagic transformation was graded in line with the European Cooperative Acute Stroke Study (ECASS III).¹⁵ Symptomatic intracranial hemorrhage corresponded to any hemorrhagic transformation or subarachnoid hemorrhage responsible for an increase of \geq 4 points on the NIHSS. Stroke etiology was determined in line with the Trial of Org 10172 in Acute Stroke Treatment (TOAST) classification.¹⁶

Imaging Protocol and Analysis

All prethrombectomy examinations were performed on a 3T unit (Magnetom Skyra; Siemens), with a protocol including at least DWI, FLAIR, T2*, and TOF-MRA sequences. The T2* sequence parameters were the following: TR = 658 ms, TE = 10 ms, flip angle = 20°, FOV = 220 \times 220 mm, matrix size (reconstructed) = 282 \times 352, and section thickness = 3 mm without a gap.

Images were anonymized and reviewed by 2 neuroradiologists (with 5 and 8 years of experience) blinded to clinical data in a consensus fashion. The SVS was defined as a hypointense signal on T2*-weighted images within a vascular cistern exceeding the size of the homologous contralateral arterial diameter.^{1-3,17-20} The SVS was classified as present or absent.

Thrombectomy Techniques

All patients were treated with a combined technique,¹¹⁻¹³ aiming to wedge the thrombus between a stent retriever (Solitaire 2/Platinum; Medtronic) and an aspiration distal catheter (ACE 64/68, Penumbra; Sofia Plus, MicroVention) connected to a pump or a syringe. The use of a balloon-guide catheter was optional. Depending on the operator’s discretion, retrieval speed of the stent retriever + the distal aspiration catheter unit was fast or slow. Fast retrieval involved a strong and very quick movement to remove the stent retriever + the distal aspiration catheter unit in $<$ 5 seconds (Supplemental Online Video 1); in contrast, slow retrieval was a smoother, uniform movement, lasting approximately 15 seconds (Supplemental Online Video 2). Stent retriever sizes were standardized at 4 \times 20 mm or 4 \times 40 mm for M1 or M2 occlusions and 6 \times 20 mm for ICA-L occlusions. When possible, procedures were performed with the patient under conscious sedation rather than general anesthesia. The procedures were performed by 4 operators with 15 and 8 years’ experience (slow retrieval) and 8 and 5 years’ experience (fast retrieval).

Angiographic Evaluation

Two researchers reviewed blinded, anonymized angiographic records: no patient/procedural data, imaging data, or stent retrieval speed was included. Researchers assessed occlusion site and anterior cerebral artery collaterals using the American Society of Interventional and Therapeutic Neuroradiology/Society of Interventional Radiology classification. Researchers then rated the first-pass and final angiographic result using the extended TICI (eTICI) score.²¹ Complete recanalization was defined as eTICI 3; near-complete recanalization, as eTICI \geq 2c; and successful recanalization, as eTICI \geq 2b. Procedure-related serious adverse events were also collected (artery perforation or dissection).

Outcome Measures

The primary outcome was the proportion of patients with first-pass complete, near-complete, and successful recanalization. Secondary outcomes included the occurrence of distal emboli, emboli in a new territory, procedure-related serious adverse events, the number of device passes, time from puncture to the end of thrombectomy, the degree of disability at 90 days (mRS), and all-cause mortality at 90 days.

We also evaluated the rate of hemorrhagic transformation, subarachnoid hemorrhage, symptomatic intracranial hemorrhage (defined by any hemorrhage responsible for an increase of \geq 4 points on the NIHSS), and perforating artery lesions (defined as a subarachnoid hemorrhage restricted to the vicinity of the M1 segment) on 24-hour CT follow-up.

Statistical Analyses

Interreader agreement for eTICI grading was assessed using the Cohen κ coefficient. Discrepancies were resolved by consensus.

Distribution normality was assessed using the Shapiro-Wilk test. Continuous variables were described as mean [SD] or median and interquartile range and were compared using the Student *t* test or Mann-Whitney *U* test. Categorical variables were presented as counts and compared using the χ^2 or Fisher exact

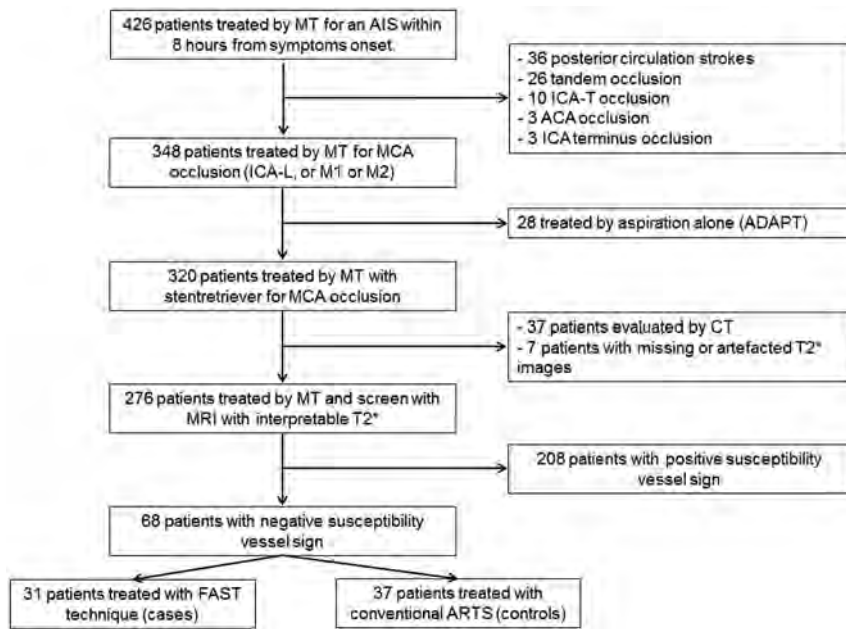


FIG 1. Study flow chart. AIS indicates acute ischemic stroke; MT, mechanical thrombectomy; ACA, anterior cerebral artery; ADAPT, a direct aspiration first pass technique.

test. The relative risk and 95% confidence intervals (RR 95% CIs) were calculated. A *P* value < .05 was considered statistically

Table 1: Baseline patient characteristics^a

Variables	Fast Retrieval (n = 31)	Slow Retrieval (n = 37)	<i>P</i> Value
Demographics			
Age (yr)	77 (57.5–83.7)	65 (49–75.7)	.10
Women	20 (64.5%)	19 (51.4%)	.28
Medical history			
Smoking	7 (22.6%)	13 (35.1%)	.26
Hypertension	19 (61.3%)	22 (59.5%)	.88
Diabetes mellitus	7 (22.6%)	8 (21.6%)	.92
Dyslipidemia	12 (38.7%)	12 (32.4%)	.59
Cardiovascular events	9 (29.0%)	11 (29.7%)	.95
Clinical data at presentation			
NIHSS	17 (13.25–19.75)	17 (14–20)	.94
Serum glucose level (mmol/L) ^b	7.5 (5.9–8.7)	6.8 (5.7–9.5)	.92
Intravenous thrombolysis	16 (51.6%)	26 (70.3%)	.12
Imaging data			
DWI-ASPECTS	6 (6–8)	7 (5–8.25)	.47
Left cerebral territory	10 (32.3%)	19 (51.4%)	.12
Occlusion site			
ICA-L	4 (12.9%)	5 (13.5%)	.50
M1	24 (77.4%)	25 (67.6%)	
M2	3 (9.7%)	7 (18.9%)	
Stroke etiology			
Large-artery atherosclerosis	4 (12.9%)	7 (18.9%)	.76
Cardioembolism	10 (32.3%)	11 (29.7%)	
Other known etiology	3 (9.7%)	2 (5.4%)	
Unknown	14 (45.2%)	17 (45.9%)	
Angiographic data			
Symptom onset to thrombectomy (min)	254.5 (184–295)	230.5 (189.5–310.5)	.90
Good collaterals (ASITN/SIR 3–4)	10 (32.3%)	18 (48.6%)	.37
Balloon-guided catheter	2 (6.5%)	3 (8.1%)	1

Note:—ASITN/SIR indicates American Society of Interventional and Therapeutic Neuroradiology/Society of Interventional Radiology.

^a Continuous variables are described as median and interquartile range, and categoric variables, as number and percentage.

^b Missing data for 13 and 10 patients, respectively.

significant. Analyses were performed using MedCalc (Version 18.2, MedCalc Software).

RESULTS

Patients

Of 426 patients receiving mechanical thrombectomy during the study period, 68 patients met the inclusion criteria. Of the 68 patients, 31 (45.6%) were treated with fast retrieval, and 37 (54.4%), with slow retrieval (Fig 1). No significant differences in baseline demographic, clinical, and imaging data between the 2 groups were reported (Table 1). Interreader agreements ranged from moderate to excellent for first-pass and final angiographic assessments (Online Supplemental Data).

Primary Outcome

Patients receiving fast retrieval had greater odds of first-pass complete (RR 95% CI, 4.30 [1.80–10.24]), near-complete (RR 95% CI, 3.24 [1.57–6.68]), and successful (RR 95% CI, 2.60 [1.53–4.43]) recanalization than those receiving slow retrieval (Fig 2A). Patients receiving fast retrieval also had greater odds of final complete (RR 95% CI, 4.18 [1.93–9.04]), near-complete (RR 95% CI, 2.75 [1.55–4.85]), and successful (RR 95% CI, 1.52 [1.14–2.03]) recanalization than those receiving slow retrieval (Fig 2B).

Secondary Outcomes

No significant differences were found between fast and slow retrieval with regard to distal embolization, embolization in a new territory, procedure-related serious adverse events, thrombectomy duration, and the number of device passes (Table 2).

At 24 hours, follow-up CT was available for 31 (100%) patients receiving fast retrieval and 35 patients (94.6%) receiving slow retrieval. There were no differences in terms of hemorrhagic transformation, subarachnoid hemorrhage, and symptomatic intracranial hemorrhage between the 2 groups (Table 2).

At 90 days, there were no differences in terms of functional independence (RR 95% CI, 1.01 [0.53–1.93])

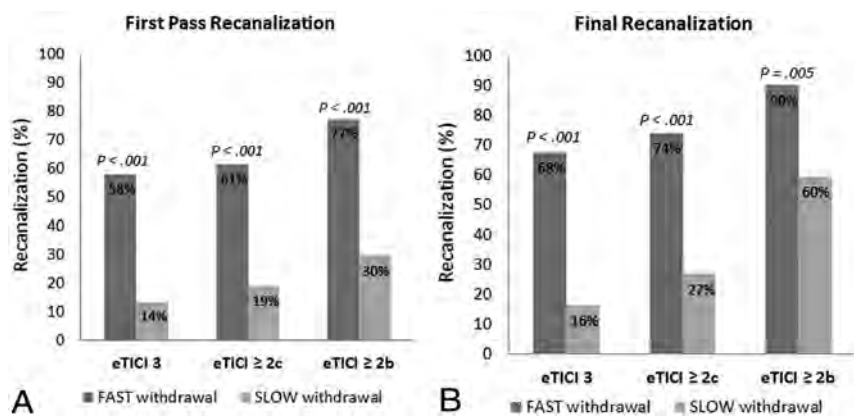


FIG 2. A, First-pass recanalization rates according to fast and slow retrieval. B, Recanalization rates according to fast and slow retrieval.

Table 2: Secondary outcomes^a

	Fast Retrieval (n = 31)	Slow Retrieval (n = 37)	P Value
Angiographic outcomes			
Distal embolization	4 (12.9%)	9 (24.3%)	.35
Embolization in a new territory	0 (0%)	3 (8.1%)	.24
Procedure-related SAE	2 (6.5%)	1 (2.7%)	.59
Thrombectomy duration (min)	29 (19–75.5)	44 (26.5–71.25)	.16
No. of passes	1 (1–2)	1 (1–3)	.16
One-pass thrombectomy	21 (67.7%)	19 (51.4%)	.22
Imaging outcomes at 24 h^b			
Hemorrhagic transformation			
None	18 (58.1%)	24 (68.6%)	.48
HI 1	3 (9.7%)	4 (11.4%)	
HI 2	6 (19.4%)	3 (8.6%)	
PH 1	2 (6.4%)	1 (2.8%)	
PH 2	2 (6.4%)	3 (8.6%)	
Subarachnoid hemorrhage	2 (6.4%)	3 (8.6%)	1
Symptomatic ICH	2 (6.4%)	2 (5.7%)	1
Perforating artery lesions	1 (3.2%)	1 (2.8%)	.60
Clinical outcome at 90 days			
Functional independence	11 (35.5%)	13 (35.1%)	.98
All-cause mortality	6 (19.4%)	8 (21.6%)	.82

Note:—SAE indicates serious adverse event; HI, hemorrhage infarction; PH, parenchymal hematoma; ICH, intracranial hemorrhage.

^aContinuous variables are described as median and interquartile range, and categoric variables, as counts. Functional independence is defined by an mRS ≤ 2.

^bMissing data for 2 patients in the slow retrieval group.

and all-cause mortality (RR 95% CI, 0.90 [0.35–2.30]) (Table 2). Even after adjusting for common confounding variables (age, baseline NIHSS, DWI-ASPECTS, occlusion site, collateral status, left-sided infarction, and bridging therapy), a fast retrieval did not lead to better functional outcomes (OR 95% CI, 2.08 [0.47–9.15]; $P = .33$).

DISCUSSION

In patients with an acute occlusion involving the MCA and a negative SVS, a fast stent retrieval during thrombectomy led to a higher chance of first and final recanalization. The safety of a fast retrieval did not differ from that of conventional slow retrieval. However, this result did not translate into better functional

outcome in this small series of patients, a result likely due to the small sample of patients with wide selection criteria for mechanical thrombectomy.

The primary challenge for neuro-interventionists is the 20%–30% of thrombi resistant to current retrieval approaches.^{7,8} Among causes for recanalization failure, 1 reason may be the discrepancy between the thrombus mechanical properties and the device/technique used to remove it.^{7,9} Thrombus composition determines friction forces and adhesion to the vessel wall.⁷ A negative SVS corresponds to the presence of a fibrin-rich clot, which is particularly difficult to remove with mechanical approaches.^{6,17,18} Indeed, in vitro experiments demonstrated that such clots were firm and sticky, with higher friction coefficients and more difficulty in fitting into stent-retriever mesh.^{4,5} Moreover, the negative SVS is more frequently observed in patients with underlying intracranial atherosclerotic stenosis¹⁹ or atypical thrombi (such as infective endocarditis).²⁰

After clot is wedged, fast retrieval may mobilize the clot more suddenly and minimize apposition loss during retrieval by reducing time for device compression during its passage in tight curves. Indeed, other in vitro experiments demonstrated that removal efficacy was related to the ability of a device to maintain constant expansion and apposition in the retrieval path, especially in sharp vessel angles.⁵ Moreover, in an in vitro model, when one used a fast retrieval, the extraction of fibrin-rich clots was 4 times greater.¹⁰

This result was confirmed by our in vivo study in which reaching a complete first-pass recanalization (first-pass effect) was 4 times greater with a fast retrieval. Although a first-pass effect is infrequently obtained (20%–35% of patients), it is associated with improved clinical outcome, reduced adverse effects, and decreased mortality.²² Even so, achieving complete first-pass recanalization did not translate into better functional outcome in our study. This result may be due to a significant number of futile recanalizations that resulted from the wide range of patients selected to receive mechanical thrombectomy. Indeed, during the study period, mechanical thrombectomy was provided without regard for age, baseline NIHSS severity, or infarct size. Additionally, more than one-quarter of our population was older than 80 years of age, had baseline a NIHSS score of >20, and DWI-ASPECTS of <5.

On the other hand, a negative SVS is only seen in approximately 25% of patients (in our study as well as in the literature),¹⁷⁻²⁰ resulting in fewer patients in each group and, therefore, reducing the likelihood that we could detect any potential differences. Larger studies in carefully selected patients are necessary to confirm whether fast retrieval translates into better patient outcomes.

The major concern when removing a device from the intracranial arteries is the risk of vessel damage.²³ In a negative SVS, this is all the more important because a significant number of patients have underlying atherosclerosis.¹⁹ When one performs a fast retrieval, the effect of stretching forces on perforating arteries and intracranial plaques is unknown. However, in this study, we did not observe differences in terms of artery perforation or dissection and symptomatic intracranial hemorrhage. We observed 1 case in each group of subtle subarachnoid hemorrhage on the perforating artery side of the M1 segment, likely due to perforator rupture after being sheared off. Although reassuring, these results need to be confirmed in a larger patient sample.

Our study has potential limitations. First, a primary limitation is its retrospective character and monocentric design, which may have contributed to selection bias. The mechanical thrombectomy technique and devices were standardized to limit bias among operators. Also, the small sample size limits the interpretability of the results. Second, the clot burden, which can impact recanalization rates, was not evaluable in this study. This evaluation would have necessitated systematic contrast-enhanced MRA or a double-injection technique during DSA. Third, only 1 thrombectomy setup was evaluated (the combined technique);¹¹⁻¹³ thus, our results cannot translate to other techniques such as direct aspiration. Also, balloon-guided catheter use was left to the operator's discretion and was rarely used in this study (7.4% of the patients). Although proximal aspiration was always provided, the use of a balloon-guided catheter may reduce distal embolization and enhance recanalization.^{24,25}

Another limitation comes from the lack of a precise measure of the retrieval speed; however, we think an overlap in withdrawal times between the two groups was very unlikely to occur. Indeed, the differences between retrieval speeds were obviously conspicuous, and the operators of the slow group were concerned about the uncertainty of the risk of vascular damage with fast retrieval. Finally, during the study period, patient selection criteria were broad, leading to potential futile recanalization. This feature means that our study cannot draw clear conclusions with regard to functional outcome. Ideally, our results need confirmation with a larger sample of selected patients. In addition, having additional information about the per-pass histologic composition of the retrieved thrombus would improve our understanding of negative SVS clot behavior during mechanical thrombectomy.^{26,27}

CONCLUSIONS

A fast stent retrieval during mechanical thrombectomy is safe and enhances the retrieval of negative SVS clots. Larger studies are needed to confirm this result and evaluate the potential impact on functional independence.

Disclosures: Laurent Pierot—UNRELATED: Consultancy: Balt, MicroVention, Perflow Medical, phenox, Vesalio.

REFERENCES

1. Liebeskind DS, Sanossian N, Yong WH, et al. **CT and MRI early vessel signs reflect clot composition in acute stroke.** *Stroke* 2011;42:1237-43 CrossRef Medline
2. Kim SK, Yoon W, Kim TS, et al. **Histologic analysis of retrieved clots in acute ischemic stroke: correlation with stroke etiology and gradient-echo MRI.** *AJNR Am J Neuroradiol* 2015;36:1756-62 CrossRef Medline
3. Molina CA. **Imaging the clot: does clot appearance predict the efficacy of thrombolysis?** *Stroke* 2005;36:2333-34 CrossRef Medline
4. Gunning GM, McArdle K, Mirza M, et al. **Clot friction variation with fibrin content; implications for resistance to thrombectomy.** *J Neurointerv Surg* 2018;10:34-38 CrossRef Medline
5. Machi P, Jourdan F, Ambard D, et al. **Experimental evaluation of stent retrievers' mechanical properties and effectiveness.** *J Neurointerv Surg* 2017;9:257-63 CrossRef Medline
6. Yuki I, Kan I, Vinters HV, et al. **The impact of thromboemboli histology on the performance of a mechanical thrombectomy device.** *AJNR Am J Neuroradiol* 2012;33:643-48 CrossRef Medline
7. Yoo AJ, Andersson T. **Thrombectomy in acute ischemic stroke: challenges to procedural success.** *J Stroke* 2017;19:121-30 CrossRef Medline
8. Goyal M, Menon BK, van Zwam WH, et al; HERMES Collaborators. **Endovascular thrombectomy after large-vessel ischaemic stroke: a meta-analysis of individual patient data from five randomised trials.** *Lancet* 2016;387:1723-31 CrossRef Medline
9. Kaesmacher J, Gralla J, Mosimann PJ, et al. **Reasons for reperfusion failures in stent-retriever-based thrombectomy: registry analysis and proposal of a classification system.** *AJNR Am J Neuroradiol* 2018;39:1848-53 CrossRef Medline
10. Soize S, Pierot L, Mirza M, et al. **Fast stent retrieval improves recanalization rates of thrombectomy: experimental study on different thrombi.** *AJNR Am J Neuroradiol* 2020;41:1049-53 CrossRef Medline
11. Massari F, Henninger N, Lozano JD, et al. **ARTS (Aspiration-Retriever Technique for Stroke): initial clinical experience.** *Interv Neuroradiol* 2016;22:325-32 CrossRef Medline
12. Mizokami T, Uwatoko T, Matsumoto K, et al. **Aspiration Catheter Reach to Thrombus (ART) sign in combined technique for mechanical thrombectomy: impact for first-pass complete reperfusion.** *J Stroke Cerebrovasc Dis* 2019;28:104301 CrossRef Medline
13. Liu ZS, Zhou LJ, Sun Y, et al. **Thrombectomy using "clamping embolus with semi-retrieval" technique in acute ischemic stroke.** *J Stroke Cerebrovasc Dis* 2018;27:733-39 CrossRef Medline
14. Vandembroucke JP, von Elm E, Altman DG, et al; STROBE Initiative. **Strengthening the Reporting of Observational Studies in Epidemiology (STROBE): explanation and elaboration.** *Ann Intern Med* 2007;147:W163-94 CrossRef Medline
15. Hacke W, Kaste M, Fieschi C, et al. **Intravenous thrombolysis with recombinant tissue plasminogen activator for acute hemispheric stroke: the European Cooperative Acute Stroke Study (ECASS).** *JAMA* 1995;274:1017-25 CrossRef Medline
16. Adams HP Jr, Bendixen BH, Kappelle LJ, et al. **Classification of subtype of acute ischemic stroke: Definitions for use in a multicenter clinical trial—TOAST. Trial of Org 10172 in Acute Stroke Treatment.** *Stroke* 1993;24:35-41 CrossRef Medline
17. Liebeskind DS, Bracard S, Guillemin S, HERMES Collaborators, et al. **eTICI reperfusion: defining success in endovascular stroke therapy.** *J Neurointerv Surg* 2019;11:433-38 CrossRef Medline
18. Bourcier R, Ben Hassen W, Soize S, et al; ASTER and the THRACE Investigators. **Susceptibility vessel sign on MRI predicts better clinical outcome in patients with anterior circulation acute stroke treated with stent retriever as first-line strategy.** *J Neurointerv Surg* 2019;11:328-33 CrossRef Medline
19. Darcourt J, Withayasuk P, Vukasinovic I, et al. **Predictive value of susceptibility vessel sign for arterial recanalization and clinical improvement in ischemic stroke.** *Stroke* 2019;50:512-15 CrossRef Medline

20. Kim SK, Yoon W, Heo TW, et al. **Negative susceptibility vessel sign and underlying intracranial atherosclerotic stenosis in acute middle cerebral artery occlusion.** *AJNR Am J Neuroradiol* 2015;36:1266–71 CrossRef Medline
21. Bourcier R, Duchmann Z, Sgreccia A, et al. **Diagnostic performances of the susceptibility vessel sign on MRI for the prediction of macroscopic thrombi features in acute ischemic stroke.** *J Stroke Cerebrovasc Di* 2020;29:105245 CrossRef Medline
22. Zaidat OO, Castonguay AC, Linfante I, et al. **First pass effect: a new measure for stroke thrombectomy devices.** *Stroke* 2018;49:660–66 CrossRef Medline
23. Balami JS, White PM, McMeekin PJ, et al. **Complications of endovascular treatment for acute ischemic stroke: prevention and management.** *Int J Stroke* 2018;13:348–61 CrossRef Medline
24. Ospel JM, Volny O, Jayaraman M, et al. **Optimizing fast first pass complete reperfusion in acute ischemic stroke: the BADDASS approach (BALloon guiDe with large bore Distal Access catheter with dual aspiration with Stent-retriever as Standard approach).** *Expert Rev Med Devices* 2019;16:955–63 CrossRef Medline
25. Brinjikji W, Starke RM, Murad MH, et al. **Impact of balloon guide catheter on technical and clinical outcomes: a systematic review and meta-analysis.** *J Neurointerv Surg* 2018;10:335–39 CrossRef Medline
26. Duffy S, McCarthy R, Farrell M. T, al. **Per-pass analysis of thrombus composition in patients with acute ischemic stroke undergoing mechanical thrombectomy.** *Stroke* 2019;50:1156–63 CrossRef Medline
27. Bourcier R, Desilles JP, Consoli A. **Letter by Bourcier et al regarding article, “Per-Pass Analysis of Thrombus Composition in Patients with Acute Ischemic Stroke Undergoing Mechanical Thrombectomy.”** *Stroke* 2019;50:e295 CrossRef Medline

Clot Meniscus Sign: An Angiographic Clue for Choosing between Stent Retriever and Contact Aspiration in Acute Basilar Artery Occlusion

S.H. Baik, C. Jung, B.M. Kim, K. Han, and D.J. Kim



ABSTRACT

BACKGROUND AND PURPOSE: The efficacy of mechanical thrombectomy methods may differ depending on the characteristics of the occlusion. The purpose of this study was to compare the recanalization efficacy and treatment outcome of a stent retriever versus contact aspiration in patients with acute basilar artery occlusion according to the angiographic characteristics of the occlusion.

MATERIALS AND METHODS: One hundred sixty-one patients with acute basilar artery occlusion who underwent mechanical thrombectomy were retrospectively analyzed. A stent retriever was compared with contact aspiration thrombectomy according to the clot meniscus sign, defined as a meniscoid/tram-track-like sidewall contrast opacification of the thrombus. A propensity score matching analysis was performed. Clinical/angiographic characteristics and treatment and clinical outcomes were compared.

RESULTS: Overall, a stent retriever ($n = 118$) and contact aspiration ($n = 43$) did not show significant differences in the successful recanalization (82.2% versus 86.0%) and good clinical outcome rates (32.2% versus 39.5%). In patients with the positive meniscus sign, contact aspiration was associated with shorter procedural time (44 versus 26 minutes, $P = .018$), a lower number of passes (2 versus 1, $P = .041$), a higher complete recanalization rate (58.8% versus 85.7%, $P = .021$), and a higher rate of first-pass effect (27.9% versus 53.6%, $P = .031$) compared with a stent retriever. After propensity score matching, contact aspiration was associated with higher complete recanalization rates (59.3% versus 85.7%, $P = .033$). No significant differences in the outcomes were noted between a stent retriever and contact aspiration in patients negative for the meniscus sign.

CONCLUSIONS: The efficacy of the mechanical thrombectomy techniques may differ according to the angiographic characteristics of occlusion in patients with basilar artery occlusion. Contact aspiration may be more effective in terms of recanalization compared with a stent retriever in patients with the clot meniscus sign.

ABBREVIATIONS: BAO = basilar artery occlusion; CA = contact aspiration; MT = mechanical thrombectomy; PSM = propensity score matching; SR = stent retriever

Randomized controlled trials have shown the safety and efficacy of mechanical thrombectomy (MT) in patients with acute ischemic stroke due to intracranial large-vessel occlusion.¹

The 2 most widely used concepts of MT are a stent retriever (SR) and contact aspiration (CA). Recent randomized trials have demonstrated comparable efficacy between the SR and CA

techniques as first-line thrombectomy approaches in the anterior circulation.^{2,3} However, little is known about the differences in the efficacy of the MT methods in terms of the angiographic characteristics of the occlusion. The differences in the anatomy of the occlusion between the anterior and posterior circulation may also cause different efficacies of MT techniques.

Angiographic morphology of the occlusive lesion may be an imaging biomarker reflecting the characteristics of the occlusion. Some previous studies have shown that the efficacy of MT methods may be influenced by the nature of the occlusion suggested by its angiographic morphologic features.⁴⁻⁷ A clot meniscus sign is a descriptive angiographic finding of meniscoid or sidewall opacification at the occlusion site, suggesting an embolic mechanism rather than an intracranial atherosclerosis-related occlusion.^{4,8}

We hypothesized that the clot meniscus sign could be associated with a differential response according to the MT technique

Received September 1, 2020; accepted after revision November 3.

From the Department of Radiology (S.H.B., C.J.), Seoul National University Bundang Hospital, Seongnam, Korea; and Department of Radiology (B.M.K., K.H., D.J.K.), Yonsei University College of Medicine, Seoul, Korea.

This study was supported by a grant from the Research Institute of Radiological Science, Yonsei University College of Medicine (grant No. 4-2017-0877).

Please address correspondence to Dong Joon Kim, MD, PhD, Department of Radiology, Yonsei University College of Medicine, 50-1 Yonsei-ro, Seodaemun-gu, Seoul 03722, Korea; e-mail: djkimmd@yuhs.ac

Indicates article with online supplemental data.

<http://dx.doi.org/10.3174/ajnr.A6988>

in patients with posterior circulation stroke. Therefore, we aimed to compare the recanalization efficacy and treatment outcomes of an SR versus CA according to the presence of the clot meniscus sign in patients with basilar artery occlusion (BAO).

MATERIALS AND METHODS

Patients

Data were collected from prospective registries of 2 tertiary university hospitals. From the registries, all consecutive acute patients with BAO referred for MT between March 2013 and December 2019 were enrolled. This study was conducted with the approval of the institutional review boards, which waived the need for written informed consent because of the retrospective nature of the study.

Both centers used the following inclusion criteria: 1) acute symptomatic patients with BAO identified on CT or MR angiography, 2) time from onset of symptoms to groin puncture of ≤ 12 hours, 3) a baseline NIHSS score of equal or more than four, 4) no intracranial hemorrhage detected on initial CT, and 5) patients having undergone MT using SR or CA thrombectomy as the primary treatment. Exclusion criteria were the following: 1) BAO due to other causes such as arterial dissection, vasculitis, or Moyamoya disease; 2) thrombolysis as first-line endovascular therapy or navigation failure; and 3) poor quality of the angiographic image for review. Part of the patient cohort was included in a prior study examining the overall significance of the clot meniscus sign.⁴

Image Analysis

The imaging findings were investigated by 2 interventional neuroradiologists in consensus (D.J.K. and S.H.B. with 18 and 4 years of experience, respectively). The reviewers were blinded to the clinical outcome during image analysis. The clot meniscus sign was defined as a meniscoid/edge-like appearance at the proximal occlusion site or a tram-track-like appearance and antegrade sidewall contrast opacification distal to thrombus on the arterial phase image of the presenting initial angiography. All other findings such as fading/tapering and abrupt cutoff were considered as absence of the clot meniscus sign.⁴ The angiographic assessment of the clot meniscus sign was based on cerebral angiographic images, which were selected from the arterial phase with best vessel contrast filling. Both centers used the same standard DSA machine (Allura Xper FD 20/20; Philips Healthcare).

The location of the BAO was divided into proximal (from the vertebrobasilar junction to the origin of the anterior inferior cerebellar artery), middle (from the origin of the anterior inferior cerebellar artery to the origin of the superior cerebellar artery), and distal occlusion (distal to the origin of the superior cerebellar artery) according to the cerebral angiography findings.⁹

Endovascular Treatment

All included patients were treated with MT using either the SR or CA technique. The patients were divided into SR and CA groups on the basis of the first-line MT technique used. All endovascular procedures were performed by 3 interventional neuroradiologists (D.J.K., B.M.K., and C.J., with 18, 17, and 12 years of experience, respectively). Before the procedure, the CTA images were

reviewed for evaluation of the site of the occlusion and the access route. In general, the procedure was performed via the femoral approach using a 6F shuttle sheath and/or a 5F or 6F guiding/intermediate catheter for access to the vertebral artery.

The first-line MT approach was chosen at the operator's discretion. SR thrombectomy was performed using a stent retriever device (Solitaire FR, Covidien; Trevo, Stryker) with or without the use of an intermediate catheter ($n = 29$, Sofia or Sofia Plus, MicroVention; AXS Catalyst, Stryker Neurovascular; Navien, Medtronic). When an SR was used as the first-line device, the case was classified as the SR group irrespective of concomitant intermediate catheter use. The intermediate catheter in these cases was mostly placed in the distal vertebral artery and used for support during microcatheter navigation. CA thrombectomy was performed using a large-bore aspiration catheter (Penumbra System Reperfusion Catheter; Penumbra) or an intermediate catheter. If successful reperfusion was not achieved with the initially selected first-line approach despite multiple attempts, rescue therapy was performed by switching to another strategy. A balloon-guiding catheter for proximal flow control was not used in any cases. The details of the techniques used for an SR or CA for BAO have been described previously.¹⁰

Outcome Measures

Clinical and radiologic data regarding patient demographics, angiographic findings, and time intervals (ie, onset, puncture, recanalization time) were prospectively collected. The procedural time was defined as the interval from puncture to final recanalization in successful recanalization and from the time of the last angiographic series in patients with unsuccessful recanalization. Recanalization status was assessed on the final angiogram and was classified according to the modified TICI scale: Successful recanalization was defined as modified TICI grades 2b or 3, and complete recanalization was defined as modified TICI grade 3. First-pass effect was defined as achieving complete recanalization with a single thrombectomy device pass. Good clinical outcome was defined as a 90-day mRS score of 0–2. All neurologic examinations were performed by board-certified neurologists. The patients were routinely evaluated for determination of the stroke etiology, which included echocardiography, continuous electrocardiography monitoring in a stroke unit or Holter monitoring, and cardiac CT.

The adverse events of interest included procedural complications (vessel perforation and dissection), hemorrhagic complications, and any cause of mortality at 90 days. A nonenhanced brain CT or MR imaging was routinely performed in the first 24 hours after the procedure. An intracerebral hemorrhage was classified according to the Second European-Australasian Acute Stroke Study classification, and symptomatic intracerebral hemorrhage was defined as any hemorrhage associated with an NIHSS score increase of ≥ 4 within 24 hours.¹¹

Statistical Analysis

The baseline characteristics and clinical outcomes between patients treated with SR and CA first-line thrombectomy were compared (SR versus CA groups). The treatment and clinical outcomes between the SR and CA groups were also compared

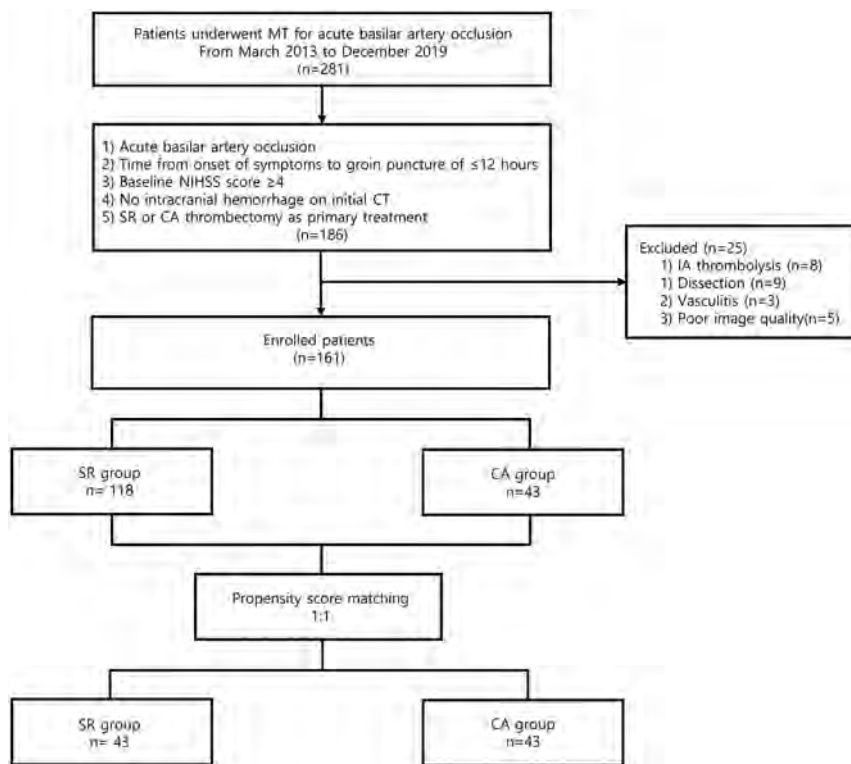


FIG 1. Flow chart of patient selection. NIHSS indicates National Institutes of Health Stroke Scale; IA, intra-arterial; SR, stent retriever; CA, contact aspiration.

according to the presence of the clot meniscus sign. To reduce data bias and confounding variables, we performed the propensity score matching (PSM) analysis by matching patients in the 2 groups at a 1:1 ratio according to nearest neighbor matching algorithm. The covariates used to generate these propensity scores included age, sex, hypertension, diabetes, dyslipidemia, smoking, coronary artery disease, baseline NIHSS score, intravenous tPA, the clot meniscus sign, and onset-to-puncture time.

In the overall sample, the Pearson χ^2 test or Fisher exact test was used for categorical variables, and the Mann-Whitney *U* test, for comparison of continuous variables. In the PSM sample, the McNemar test was used for categorical variables, and the Wilcoxon signed-rank test, for comparison of continuous variables. Multivariable logistic regression was performed to evaluate the independent variables for complete recanalization in patients with the clot meniscus sign. A *P* value < .05 was considered statistically significant. Statistical analyses were performed using SPSS for Windows (Version 20.0; IBM) and R statistical and computing software (Version 3.6.2; <http://www.r-project.org/>).

RESULTS

During the study period, 281 patients who underwent MT for acute BAO were initially enrolled. Among them, 186 patients who met the inclusion criteria were included. Of these, 25 patients were excluded due to the following: intra-arterial thrombolysis as a first-line method (*n* = 8), occlusion due to dissection (*n* = 9) or vasculitis (*n* = 3), and poor quality of the angiography

for review (*n* = 5). The remaining 161 (median age 73 years; interquartile range, 66–80 years; 94 men [58.4%]) patients were finally enrolled in the present study. A total of 118 (73.3%) of the 161 patients were treated with an SR as the first-line thrombectomy (SR group), and 43 (26.7%) patients were treated with CA as the first-line thrombectomy (CA group). After PSM, 43 patients in each group were matched (Fig 1).

The baseline characteristics and treatment outcomes of the overall and PSM samples between the 2 groups are shown in the Online Supplemental Data. Overall, the median baseline NIHSS score was 16 (interquartile range, 8–25) in the SR group and 21 (interquartile range, 11–25) in the CA group (*P* = .438). There were no statistically significant differences in the successful recanalization (82.2% versus 86.0%) and good clinical outcome rates (32.2% versus 39.5%), but CA was associated with a shorter procedural time (56 versus 33 minutes, *P* = .009), fewer passes (3 versus 1, *P* = .001), higher complete recanalization rates (47.5% versus 69.8%, *P* = .012), higher first-pass effect (19.5% versus 39.5%, *P* = .009), and a lower symptomatic intracerebral hemorrhage rate (11.0% versus 0%, *P* = .021). Three cases of vessel perforation were identified in the patients treated with an SR. The vessel perforations occurred at the basilar artery perforator (*n* = 2) and the P1–2 segments (*n* = 1). In the latter case, coil embolization was performed at the proximal parent artery due to continued contrast leakage. All patients with vessel perforation showed poor clinical outcome. There were 3 cases (7.0%) of iatrogenic vertebral artery dissection at the V2 segment in the CA group. Two patients underwent stent placement for management of the dissection and had poor clinical outcomes. One patient was treated with 0.5 mg of intra-arterial tirofiban and did not show flow impairment or thrombus formation on the delayed angiogram. This patient had a good clinical outcome. After PSM, the CA group was associated with a lower number of passes (median, 3 versus 1; *P* = .045). Other baseline factors did not show any significant differences between the 2 groups.

The treatment and clinical outcomes according to the presence of the clot meniscus sign are summarized in the Online Supplemental Data. The clot meniscus sign was seen in 59.6% (96/161) of patients. In the patients positive for the meniscus sign, the CA group showed a shorter procedural time (44 versus 26 minutes; *P* = .018), a lower total number of passes (median, 2 versus 1; *P* = .041), a higher rate of complete recanalization (58.8% versus 85.7%; *P* = .021), and a higher rate of first-pass effect (27.9% versus 53.6%; *P* = .031) compared with the SR group (Fig 2). After PSM, the CA group was associated with a

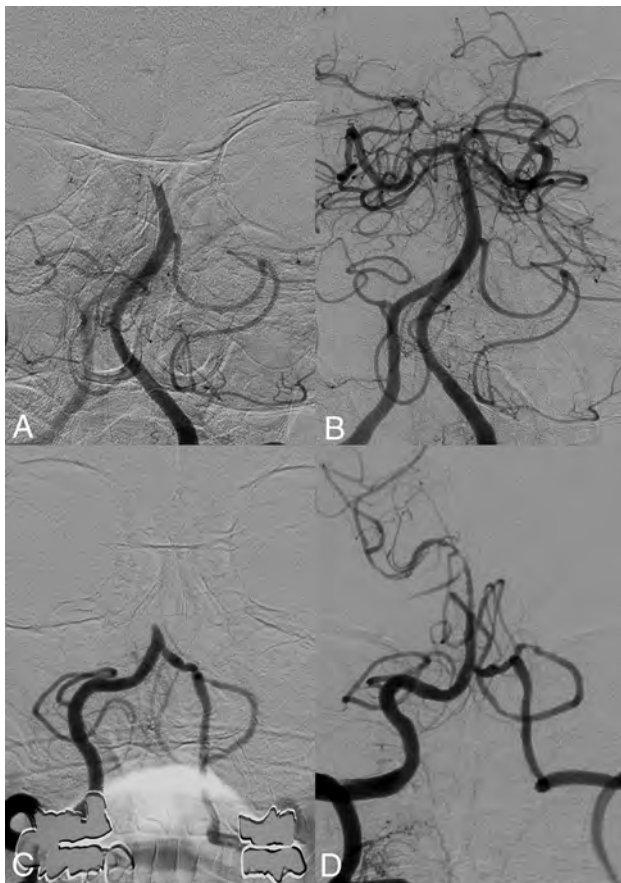


FIG 2. Pre- (A) and post- (B) thrombectomy images of a basilar artery occlusion in a patient with the positive clot meniscus sign. Complete recanalization was achieved using a single attempt of contact aspiration. Pre- (C) and post- (D) thrombectomy images of a patient with a basilar artery occlusion with the negative clot meniscus sign. Following an unsuccessful first-line approach with contact aspiration, multiple attempts of rescue thrombectomy were performed with the stent retriever, revealing an underlying atherosclerotic stenosis (not shown). Recanalization was achieved by permanent stent placement.

higher complete recanalization rate (59.3% versus 85.7%, $P = .033$) and a tendency toward a higher first-pass effect (29.6% versus 53.6%, $P = .084$). No significant differences in the outcomes were noted between the SR and CA groups in the patients negative for the meniscus sign except for the shorter procedural time in patients with PSM and CA (90 versus 56 minutes, $P = .02$).

Multivariate logistic regression analysis showed that procedural time (OR, 0.96; 95% CI, 0.94–0.98; $P = .001$) and CA thrombectomy (OR, 7.09; 95% CI, 1.33–37.85; $P = .022$) were independent predictors of complete recanalization in patients with the positive clot meniscus sign when adjusting for age, hypertension, diabetes, baseline NIHSS score, intravenous tPA, distal BAO, onset-to-puncture time, number of passes, and the hospital (Table).

DISCUSSION

The results of the present study showed that the clot meniscus sign in patients with posterior circulation stroke could be a discriminative imaging biomarker for predicting the recanalization

Multivariable analysis for complete recanalization in patients with a positive clot meniscus sign

	Complete Recanalization (mTICI 3)	
	Adjusted OR (95% CI)	P Value
Age	0.98 (0.93–1.04)	.624
Hypertension	1.31 (0.29–5.97)	.720
Diabetes	1.88 (0.53–6.62)	.290
Baseline NIHSS	0.98 (0.92–1.04)	.540
Distal occlusion	1.86 (0.53–6.53)	.328
Onset-to-puncture time	0.99 (0.99–1.00)	.175
Procedural time	0.96 (0.94–0.98)	.001
No. of passes	0.74 (0.45–1.23)	.248
Contact aspiration	7.09 (1.33–37.85)	.022
Hospital	0.49 (0.12–1.93)	.314

efficacy of MT techniques. Patients with BAO with the clot meniscus sign treated with CA as the first-line approach exhibited a higher rate of complete recanalization, a shorter procedural time, and a higher rate of first-pass effect compared with those treated with SR thrombectomy. CA was an independent predictor of complete recanalization in patients with BAO with the clot meniscus sign.

Currently, CA is considered as noninferior to an SR as a primary MT modality for anterior circulation stroke.^{2,3,12} However, little is known about the association between the morphologic features of the occlusion and the preferred MT technique. Also, the posterior circulation differs from the anterior circulation in terms of anatomy, such as the caliber, tortuosity of the vessels, and the pattern of collaterals. These differences may alter the MT strategy such as forgoing the use of balloon-guide catheters. In the posterior circulation, stroke is also more frequently associated with in situ intracranial atherosclerotic stenosis than in the anterior circulation; this characteristic may also influence the efficacy of MT.^{10,13}

There are mixed retrospective results and insufficient evidence supporting a specific technique for MT of acute BAO. Similar to the anterior circulation stroke, a few retrospective studies have reported that successful recanalization rates and clinical outcome did not differ significantly between the CA and SR devices for acute BAO,^{14–16} whereas there have also been some reports demonstrating the superiority of CA over an SR in acute BAO. Selection of CA as the first-line MT achieved higher rates of complete recanalization with shorter procedural times compared with an SR in these studies.^{14,16,17}

In terms of the morphologic features of the occlusion and the efficacy of MT methods, only a limited number of studies are available. Baik et al⁴ showed that the clot meniscus sign was a reliable imaging biomarker and predictor of successful recanalization in acute patients with BAO with excellent inter-/intra-reader agreement. Yamamoto et al¹⁸ reported that the angiographic claw sign, thrombus that protruded proximally by more than half the diameter of the parent artery, is associated with successful recanalization after MT. Consoli et al^{5,6} and Kaiser et al⁷ showed that the regular thrombus morphology, a smooth and straight profile of the occlusion with a linear interruption of flow, was associated with better procedural and clinical outcomes when treated with CA compared with thrombus with irregular morphology, any kind of evident modification of the linearity of the occlusion, which seemed to show better results with an SR.

Our results showed that the recanalization efficacy is better with CA than an SR in patients with BAO with the positive clot meniscus sign. There may be several explanations for the superiority of CA over an SR. One reason could be the absence of proximal flow control in MT of posterior circulation strokes coupled with the embolic etiology of the occlusion in patients with the meniscus sign. In the anterior circulation MT studies, the use of a balloon-guide catheter is consistently associated with improved recanalization and clinical outcome.¹⁹⁻²² A balloon-guide catheter will reduce the impact force on the thrombus, allowing more effective retrieval, as well as minimizing the tendency for thrombus fragmentation and distal migration, but as in our study, it is rarely used in posterior circulation stroke due to collateral flow through the contralateral vertebral artery and the cervical arteries.^{23,24} Thus, a large-bore aspiration/intermediate catheter in the basilar artery during CA occupying a large percentage of the cross-sectional area of the vessel lumen can effectively decrease the impact force on the embolic clot, improving the recanalization efficacy.²⁴ A recent study also showed the superiority of CA compared with an SR in achieving successful reperfusion for the treatment of terminal ICA occlusions in the absence of proximal flow arrest with balloon-guide catheters.²⁵

In terms of the etiology of BAO, a previous study has shown that the positive clot meniscus sign was highly associated with distal BAO and an embolic etiology, whereas the negative clot meniscus sign was associated with proximal occlusion and arterial wall calcifications, suggestive of an underlying intracranial atherosclerotic stenosis.⁴ Imaging features similar to the meniscus sign such as the claw sign were also associated with the embolic etiology of the occlusion.¹⁸ Under these conditions, the action mechanism of CA may be more favorable than that of an SR. “Contact” between the tip of the aspiration catheter and proximal surface of the thrombus is the key technical element for achieving successful recanalization during CA thrombectomy.²⁶ The meniscoid appearance of the occlusion may allow more area for contact with the aspiration catheter and also decrease the surface area interaction with the vessel wall, reducing friction/adhesion. With respect to SR thrombectomy, the key mechanism for effective thrombus removal is the integration of the SR device with the thrombus, which may be mostly determined by the histologic composition and consistency of the clot.²⁷⁻²⁹ However, this relationship between the imaging morphology and the histologic clot composition/consistency has not been fully elucidated.

Last, in contrast to the SR technique in which a microcatheter is necessarily navigated across the clot, crossing the clot may be avoided, decreasing the risk of clot fragmentation, using the so-called “thrombus no-touch technique” in many cases of CA, especially with the relatively straight course of the basilar artery.³⁰

In the meniscus sign–negative occlusions, the etiology of the BAO in many patients may have been due to an underlying intracranial atherosclerotic stenosis.⁴ Intracranial atherosclerotic stenosis is known to be associated with lower rates of successful recanalization and poorer clinical outcomes with conventional MT techniques.^{10,31} Thus, these patients negative for the meniscus sign did not show a significant difference in treatment efficacy between an SR and CA in our series. Further research on specific imaging/clinical features for predicting optimal recanalization methods for these specific groups of patients is warranted.

There are several limitations to this study. First, due to the retrospective design, selection of the first-line MT device was at the discretion of the operator, resulting in potential bias. PSM was performed to reduce this potential bias between the 2 groups, and the superiority of CA was maintained in the patients positive for the meniscus sign. Another limitation in our study could be the lack of histologic examination of the retrieved clots. The relationship between the thrombus composition and the angiographic morphology could be a topic for future research.

CONCLUSIONS

The efficacy of the MT techniques may differ according to the angiographic morphology of the occlusion in patients with BAO. CA as the first-line MT approach may be more effective in terms of complete recanalization compared with an SR in patients with BAO with the clot meniscus sign. The clot meniscus sign may be used as an imaging biomarker for planning therapeutic strategies and maximizing procedural outcome.

Disclosures: Dong Joon Kim—UNRELATED: Payment for Lectures Including Service on Speakers Bureaus: Stryker Pacific Limited.

REFERENCES

1. Goyal M, Menon BK, van Zwam WH, et al; HERMES Collaborators. **Endovascular thrombectomy after large-vessel ischaemic stroke: a meta-analysis of individual patient data from five randomised trials.** *Lancet* 2016;387:1723–31 CrossRef Medline
2. Lapergue B, Blanc R, Gory B, et al; ASTER Trial Investigators. **Effect of endovascular contact aspiration vs stent retriever on revascularization in patients with acute ischemic stroke and large vessel occlusion: the ASTER Randomized Clinical Trial.** *JAMA* 2017;318:443–52 CrossRef Medline
3. Turk AS 3rd, Siddiqui A, Fifi JT, et al. **Aspiration thrombectomy versus stent retriever thrombectomy as first-line approach for large vessel occlusion (COMPASS): a multicentre, randomised, open label, blinded outcome, non-inferiority trial.** *Lancet* 2019;393:998–1008 CrossRef Medline
4. Baik SH, Kim JW, Kim BM, et al. **Significance of angiographic clot meniscus sign in mechanical thrombectomy of basilar artery stroke.** *J Neurointerv Surg* 2020;12:477–82 CrossRef Medline
5. Consoli A, Rosi A, Coskun O, et al. **Thrombectomy for m1-middle cerebral artery occlusion: angiographic aspect of the arterial occlusion and recanalization: a preliminary observation.** *Stroke* 2018;49:1286–89 CrossRef Medline
6. Consoli A, Zhu F, Bourcier R, et al; ASTER Trial Investigators. **Effect of the phenotype of the M1-middle cerebral artery occlusion on the recanalization rates in the ASTER trial.** *J Neurointerv Surg* 2020;12:7–12 CrossRef Medline
7. Kaiser D, Laske K, Winzer R, et al. **Impact of thrombus surface on first pass reperfusion in contact aspiration and stent retriever thrombectomy.** *J Neurointerv Surg* 2020 June 11. [Epub ahead of print] CrossRef Medline
8. Pillai JJ, Lanzieri CF, Trinidad SB, et al. **Initial angiographic appearance of intracranial vascular occlusions in acute stroke as a predictor of outcome of thrombolysis: initial experience.** *Radiology* 2001;218:733–38 CrossRef Medline
9. Caplan L, Chung CS, Wityk R, et al. **New England medical center posterior circulation stroke registry, I: methods, data base, distribution of brain lesions, stroke mechanisms, and outcomes.** *J Clin Neurol* 2005;1:14–30 CrossRef Medline
10. Baik SH, Park HJ, Kim JH, et al. **Mechanical thrombectomy in subtypes of basilar artery occlusion: relationship to recanalization rate and clinical outcome.** *Radiology* 2019;291:730–37 CrossRef Medline

11. Hacke W, Kaste M, Fieschi C, et al. **Randomised double-blind placebo-controlled trial of thrombolytic therapy with intravenous alteplase in acute ischaemic stroke (ECASS II): Second European-Australasian Acute Stroke Study Investigators.** *Lancet* 1998;352:1245–51 CrossRef Medline
12. Phan K, Maingard J, Kok HK, et al. **Contact aspiration versus stent-retriever thrombectomy for distal middle cerebral artery occlusions in acute ischemic stroke: meta-analysis.** *Neurointervention* 2018;13:100–09 CrossRef Medline
13. Lee JS, Hong JM, Lee KS, et al. **Endovascular therapy of cerebral arterial occlusions: intracranial atherosclerosis versus embolism.** *J Stroke Cerebrovasc Dis* 2015;24:2074–80 CrossRef Medline
14. Gory B, Mazighi M, Blanc R, et al. **Mechanical thrombectomy in basilar artery occlusion: influence of reperfusion on clinical outcome and impact of the first-line strategy (ADAPT vs stent retriever).** *J Neurosurg* 2018;129:1482–91 CrossRef Medline
15. Mokin M, Sonig A, Sivakanthan S, et al. **Clinical and procedural predictors of outcomes from the endovascular treatment of posterior circulation strokes.** *Stroke* 2016;47:782–88 CrossRef Medline
16. Son S, Choi DS, Oh MK, et al. **Comparison of Solitaire thrombectomy and Penumbra suction thrombectomy in patients with acute ischemic stroke caused by basilar artery occlusion.** *J Neurointerv Surg* 2016;8:13–18 CrossRef Medline
17. Gerber JC, Daubner D, Kaiser D, et al. **Efficacy and safety of direct aspiration first pass technique versus stent-retriever thrombectomy in acute basilar artery occlusion—a retrospective single center experience.** *Neuroradiology* 2017;59:297–304 CrossRef Medline
18. Yamamoto Y, Yamamoto N, Kanematsu Y, et al. **The claw sign: an angiographic predictor of recanalization after mechanical thrombectomy for cerebral large-vessel occlusion.** *J Stroke Cerebrovasc Dis* 2019;28:1555–60 CrossRef
19. Baek JH, Kim BM, Kang DH, et al. **Balloon guide catheter is beneficial in endovascular treatment regardless of mechanical recanalization modality.** *Stroke* 2019;50:1490–96 CrossRef Medline
20. Nguyen TN, Malisch T, Castonguay AC, et al. **Balloon guide catheter improves revascularization and clinical outcomes with the Solitaire device: analysis of the North American Solitaire Acute Stroke Registry.** *Stroke* 2014;45:141–45 CrossRef Medline
21. Zaidat OO, Mueller-Kronast NH, Hassan AE, et al; STRATIS Investigators. **Impact of balloon guide catheter use on clinical and angiographic outcomes in the STRATIS Stroke Thrombectomy Registry.** *Stroke* 2019;50:697–704 CrossRef Medline
22. Jeong DE, Kim JW, Kim BM, et al. **Impact of balloon-guiding catheter location on recanalization in patients with acute stroke treated by mechanical thrombectomy.** *AJNR Am J Neuroradiol* 2019;40:840–44 CrossRef Medline
23. Chueh JY, Puri AS, Wakhloo AK, et al. **Risk of distal embolization with stent retriever thrombectomy and ADAPT.** *J Neurointerv Surg* 2016;8:197–202 CrossRef Medline
24. Yoo AJ, Andersson T. **Thrombectomy in acute ischemic stroke: challenges to procedural success.** *J Stroke* 2017;19:121–30 CrossRef Medline
25. Xing PF, Yang PF, Li ZF, et al. **Comparison of aspiration versus stent retriever thrombectomy as the preferred strategy for patients with acute terminal internal carotid artery occlusion: a propensity score matching analysis.** *AJNR Am J Neuroradiol* 2020;41:469–76 CrossRef Medline
26. Kang DH, Hwang YH. **Frontline contact aspiration treatment for emergent large vessel occlusion: a review focused on practical techniques.** *J Stroke* 2019;21:10–22 CrossRef Medline
27. Imahori T, Okamura Y, Sakata J, et al. **Stent expansion and in-stent thrombus sign in the Trevo stent retriever predict recanalization and possible etiology during mechanical thrombectomy: a case series of 50 patients with acute middle cerebral artery occlusion.** *World Neurosurg* 2018 Dec 8. [Epub ahead of print] CrossRef Medline
28. Maekawa K, Shibata M, Nakajima H, et al. **Erythrocyte-rich thrombus is associated with reduced number of maneuvers and procedure time in patients with acute ischemic stroke undergoing mechanical thrombectomy.** *Cerebrovasc Dis Extra* 2018;8:39–49 CrossRef Medline
29. Hashimoto T, Hayakawa M, Funatsu N, et al. **Histopathologic analysis of retrieved thrombi associated with successful reperfusion after acute stroke thrombectomy.** *Stroke* 2016;47:3035–37 CrossRef Medline
30. Mohlenbruch MA, Kabbasch C, Kowoll A, et al. **Multicenter experience with the new SOFIA Plus catheter as a primary local aspiration catheter for acute stroke thrombectomy.** *J Neurointerv Surg* 2017;9:1223–27 CrossRef Medline
31. Kim YW, Hong JM, Park DG, et al. **Effect of intracranial atherosclerotic disease on endovascular treatment for patients with acute vertebrobasilar occlusion.** *AJNR Am J Neuroradiol* 2016;37:2072–78 CrossRef Medline

Low-Dose Eptifibatide for Tandem Occlusion in Stroke: Safety and Carotid Artery Patency

A. Jost, C. Roels, M. Brown, R. Janjua, and D. Heck

ABSTRACT

BACKGROUND AND PURPOSE: Maintaining carotid patency and avoiding symptomatic intracranial hemorrhage are competing concerns in tandem occlusions. This study provides data regarding the safety and efficacy of eptifibatide in stroke from tandem occlusion of the extracranial carotid artery and the intracranial carotid or middle cerebral artery.

MATERIALS AND METHODS: This is a retrospective analysis of 58 consecutive patients who received low-dose eptifibatide (135-mcg/kg bolus, 1-mcg/kg/min infusion) during treatment of tandem occlusions. Brain imaging and carotid sonography were performed at 24–36 hours. mRS was documented at 90 days, and carotid sonography, at 30–60 days.

RESULTS: The median age and NIHSS score were 64 years and 15, respectively. Twenty-five patients (43%) received tPA. ASPECTSs were 8–10 in 47 (81%) and 5–7 in 11 (19%) patients. Thirty-eight patients had angioplasty/stent placement acutely; 20 had angioplasty alone. Symptomatic intracranial hemorrhage occurred in 1 patient (2%). TIC1 2b or higher was achieved in 56 patients (96%). Fifty-seven of 58 patients had clinical follow-up at 90 days (1 lost to follow up). The 90-day mRS was 0–2 in 42 patients (72%). There were 4/58 (7%) re-occlusions within 24–36 hours, all originally treated with stent placement. Forty-nine of 53 surviving patients had carotid sonography at 30–60 days, with 3 delayed re-occlusions, 2 with stents and 1 with angioplasty alone. The overall carotid patency at 30–60 days was 42/49 (86%). Carotid re-occlusion was not associated with clinical decline.

CONCLUSIONS: Low-dose eptifibatide seemed to be safe in tandem occlusions (symptomatic intracranial hemorrhage, 2%), although asymptomatic cervical carotid artery re-occlusions still occurred in 14% of patients.

ABBREVIATIONS: mTICI = modified TIC1; SICH = symptomatic intracranial hemorrhage

Tandem occlusion presents the simultaneous problem of an intracranial embolic large-vessel occlusion and an acute plaque rupture/thrombotic event in the cervical carotid artery. Tandem occlusion is common, representing between 13% and 32% of patients with large-vessel occlusion.^{1–3} Outcomes in the Endovascular Treatment for Small Core and Anterior Circulation Proximal Occlusion with Emphasis on Minimizing CT to Recanalization Times (ESCAPE) trial were similar between patients with and without tandem occlusions.⁴ The goal of tandem occlusion treatment is to remove the intracranial embolus and re-establish normal flow in the cervical carotid artery without

causing hemorrhage. Optimal conditions for elective carotid stent placement include therapeutic dual-antiplatelet therapy, statin loading, and intraprocedural anticoagulation. Unfortunately, such a strategy, and particularly the use of heparin, increases the risk of intracranial hemorrhage in the setting of acute stroke and particularly tandem occlusion.⁵ In general, following a successful intracranial embolectomy, extracranial carotid re-occlusion is not always associated with neurologic deterioration and poor neurologic outcome, whereas symptomatic intracranial hemorrhage (SICH) almost always is.^{5–7} Avoiding SICH must be the primary consideration. However, re-occlusion of the internal carotid artery may be associated with repeat embolization. Also, direct carotid inflow to support pial collaterals may be beneficial when less-than-perfect results were achieved with intracranial thrombectomy (eg, modified TIC1 [mTICI] <3). At least 1 retrospective study suggested that re-occlusion is associated with worse clinical outcomes in the tandem occlusion population.⁸ Judicious medical therapy to preserve the patency of the internal carotid artery following angioplasty or stent placement is therefore reasonable, providing this can be accomplished without increasing the risk of

Received September 4, 2020; accepted after revision October 21.

From the Wake Forest School of Medicine (A.J.), Winston Salem, North Carolina; Departments of Pharmacy (C.R.) and Neurosurgery (R.J.) Novant Health, Forsyth Medical Center, Winston Salem, North Carolina; and Triad Radiology Associates (M.B., D.H.), Forsyth Medical Center, Winston Salem, North Carolina.

Paper previously presented presented, in part, at: Annual Meeting of the American Society of Neuroradiology, May 23 to June 4, 2020; Virtual.

Please address correspondence to Don Heck, MD, Triad Radiology Associates, 3015 Maplewood Avenue, Winston Salem, NC, 27103; e-mail: dheck@triadradiology.com
<http://dx.doi.org/10.3174/ajnr.A6985>

SICH. This report aims to provide evidence regarding the safety of a specific low-dose eptifibatide antiplatelet strategy in the tandem occlusion population applied uniformly to both patients who were treated with stents and those treated with angioplasty alone and also to provide data regarding carotid artery patency in both the acute phase and the postoperative period.

MATERIALS AND METHODS

The research protocol involving retrospective review of 58 patients was approved by the Novant Health institutional review board. Individual patient consent was not required by the institutional review board due to minimal patient risk and no individual patient identifiers.

Fifty-eight patients with consecutive tandem occlusions treated between February 2016 and January 2020 at Novant Health Forsyth Medical comprehensive stroke center were administered low-dose perioperative eptifibatide (135-mcg/kg bolus, 1-mcg/kg/min infusion) during intracranial thrombectomy and extracranial carotid angioplasty with or without stent placement. All patients had occlusive or near-occlusive atherosclerotic stenosis of the internal carotid artery and an embolus in the internal carotid terminus or middle cerebral artery. A prospective data base was reviewed retrospectively for patient characteristics and clinical and imaging outcomes. SICH was defined as a parenchymal hematoma with mass effect or any hemorrhage associated with a decline in the NIHSS of ≥ 4 points. Management of the intracranial occlusion by contact aspiration (ADAPT, A Direct Aspiration first Pass Technique) or combination therapy with an aspiration catheter and stent retriever (CAPTIVE, Continuous Aspiration Prior To Intracranial Vascular Embolectomy) was according to the physician's choice, as was management of the extracranial lesion with angioplasty and stent placement or angioplasty alone.^{9,10} In general, a distal-to-proximal approach, with angioplasty of the carotid artery and placement of a base catheter just below the skull base to facilitate the thrombectomy, was used first.¹¹ Stents were then placed after the thrombectomy due to the frequent suboptimal results in the cervical carotid occlusion after angioplasty. The eptifibatide infusion was continued until patients were converted to dual oral antiplatelet therapy if the 24-hour sonography and CT demonstrated carotid patency and no concerning hemorrhage. Dual oral antiplatelet therapy consisted of 81–325 mg of aspirin and clopidogrel (load of 300–600 mg) or ticagrelor (180-mg load). No patients received heparin during the procedure.

Preoperative imaging consisted of noncontrast CT and CTA or multiphase CTA. DWI was used in a minority of patients when collaterals were judged to be poor and a large infarct was suspected, and in some patients with unknown time of onset. Patients were selected for intervention on the basis of clinical-imaging mismatch (eg, when the treatment team determined that the clinical deficit was not explained by the size of the estimated core infarct after imaging). The ASPECTS on the preprocedural CT and angiographic mTICI scores were determined by visual inspection by a neuroradiologist. All interventions were performed with the patient under general anesthesia. Patients were admitted to the neuroscience critical care unit postprocedure, with blood pressure goals commensurate with the angiographic

Summary of population and results

Summary	
Age (median) (IQR) (yr)	64 (57–76)
Male (No.) (%)	38 (68%)
Hypertension (No.) (%)	41 (71%)
Diabetes (No.) (%)	17 (29%)
Dyslipidemia (No.) (%)	41 (71%)
Current aspirin use (No.) (%)	22 (38%)
Current clopidogrel use (No.) (%)	6 (10%)
Current/former smoker (No.) (%)	22 (38%)/14 (24%)
Baseline NIHSS (median) (IQR)	15 (11–20)
Baseline ASPECTS 8–10/5–7 (No.) (%)	47 (81%)/11 (19%)
Carotid Terminus occlusion (No.) (%)	25 (43%)
M1 occlusion (No.) (%)	22 (38%)
M2 occlusion, (No.) (%)	11 (19%)
tPA administration (No.) (%)	25 (43%)
Acute angioplasty alone (No.) (%)	20 (34%)
Acute angioplasty and stent placement (No.) (%)	38 (66%)
Delayed stent or endarterectomy within a week (No.) (%)	6 (10%)
mTICI score > 2a (No.) (%)	56 (96%)
Acute carotid artery re-occlusion (No.) (%)	4 (7%)
Any ICH (No.) (%)	18 (31%)
Symptomatic ICH (No.) (%)	1 (2%)
30- to 60-Day carotid patency (No.) (%)	42/49 (86%)
90-Day mRS 0–2 (No.) (%)	42 (72%)

Note:—IQR indicates interquartile range; ICH, intracranial hemorrhage.

outcome (eg, target systolic blood pressure of <140 for mTICI 3 or mTICI 2c; <180 for mTICI 2b or worse). All patients underwent carotid sonography the following day to assess carotid artery patency and residual stenosis and repeat brain imaging with CT, MR imaging, or both. A follow-up clinical visit and carotid sonography were routinely scheduled 30–60 days postprocedure for all surviving patients. mRS scores were determined by a nurse, certified in the test and independent of the care team, in person or by telephone.

RESULTS

Patient population characteristics and results are summarized in the Table.

The median NIHSS score and age were 15 and 64 years, respectively, with tPA use in 25 (43%) patients. Current aspirin use was documented in 22 (38%) patients; clopidogrel as a single therapy in 5 (9%); and clopidogrel with 81 mg of aspirin in just 1 patient. The ASPECTSs were 8–10 in 47 (81%) and 5–7 in 11 (19%) patients. Thirty-eight patients had stent placement acutely, while 20 had angioplasty alone. Six patients who originally had angioplasty alone subsequently had elective endarterectomy or stent placement within the first week; these patients were recovering well, had a low stroke burden on imaging, and had persistent, severe stenosis. All patients had brain imaging within 24–36 hours. Any evidence of intracranial hemorrhage was present in 18 (31%) patients, mostly petechial or small subarachnoid hemorrhage, with only 1 case of SICH (2%). Technical success (TICI 2b, 2c, or 3) was achieved in 56 (96%) patients. The mRS at 90 days was documented in 57/58 patients (1 patient was lost to follow-up). Functional independence (mRS 0–2) was achieved in 42 (72%) patients. Five patients (9%) died by 90 days (mRS of 6).

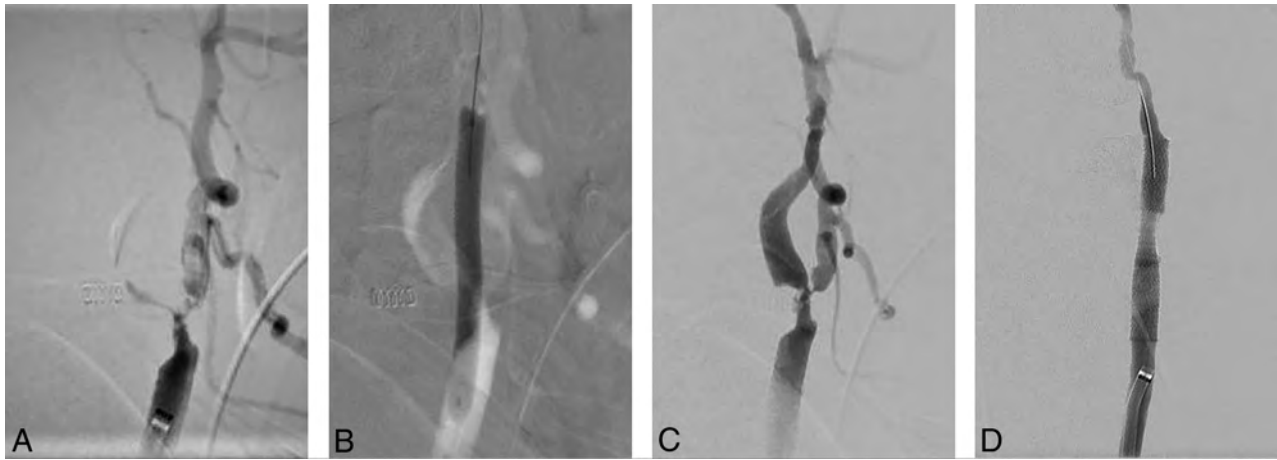


FIGURE. A, Occlusive internal carotid stenosis at the bifurcation; severe external carotid artery stenosis. B, Angioplasty with a 4-mm balloon. C, After successful intracranial thrombectomy, note severe residual stenosis. D, An 8 × 6 × 30 mm stent was placed. Note occlusion of the external carotid artery (the stent was occluded on sonography the next morning).

All patients had carotid sonography within 36 hours. There were 4 (7%) re-occlusions within the first 24 hours, all in patients originally treated with stent placement and all with normal flow at the end of the procedure (Figure). Forty-nine patients had carotid imaging at 30–60 days (5 died, 3 were not scheduled, 1 was lost to follow-up), with an additional 3 re-occlusions (6%): Two had stents and 1 had angioplasty alone. Carotid artery patency for surviving patients imaged at 30–60 days was 86% (42/49). No acute or delayed carotid re-occlusion was associated with neurologic decline, and 5/7 (71%) patients with carotid re-occlusion had a 90-day mRS of 0–2, similar to that in the group as a whole (72%).

DISCUSSION

Full-dose intravenous abciximab may have an unacceptably high rate of SICH, up to 22%, especially in older patients.⁶ Another glycoprotein IIb/IIIa inhibitor, eptifibatid, has the advantage of quicker platelet function return after discontinuation if bleeding complications occur (4–8 hours versus 1–7 days). While abciximab is theoretically reversible with platelet transfusion, in practice this is difficult to accomplish soon enough in the setting of acute intracranial hemorrhage. The choice of the dose of eptifibatid was based on limited available evidence.^{12,13} Our own initial unpublished experience with eptifibatid at a lower dose (135-mcg/kg bolus, but a 0.5-mcg/kg/min infusion) indicated that the drug may be safe but perhaps not efficacious at that dose because a 25% re-occlusion rate within 24 hours was experienced. For the 58 patients in the current study, the same bolus was used, but the infusion rate was increased to 1 mcg/kg/min to achieve greater inhibition of platelet aggregation. The infusion was administered to patients who were treated with stent placement or angioplasty alone because the stroke mechanism of plaque rupture and thromboembolism was considered the same in both groups. The advantages and disadvantages of various antiplatelet medications in tandem occlusion have been recently reviewed.¹¹

No randomized trials comparing techniques or medical therapies for treatment of tandem occlusions exist. The literature consists of retrospective case series in which the techniques and

medical therapies, even within those case series, are often heterogeneous. One might reasonably ask whether any type of intervention in the carotid artery or any addition of antithrombotic therapy is needed in addition to intracranial thrombectomy for patients with tandem occlusion. Papanagiotou et al¹⁴ reported a retrospective review of 482 patients from 18 stroke centers treated for tandem occlusion and found that carotid stent placement plus at least 1 antithrombotic medication resulted in both improved intracranial recanalization and improved clinical outcomes compared with mechanical thrombectomy alone. They also found a non-statistically significant trend toward better recanalization and clinical outcomes when comparing stent placement and antithrombotic medication with stent placement or angioplasty without antithrombotic medication. As one might expect, the medical regimens used varied widely. The overall SICH rate was 5%. Behme et al⁷ reported a retrospective review of 170 patients with tandem occlusions treated between 2007 and 2014 at 4 German centers and noted a 9% incidence of SICH, which had a 73% mortality in the acute phase. The study used 4 different antithrombotic medical strategies at the 4 different centers, one of which used a full-dose (180-mcg/kg) eptifibatid bolus and one of which used another glycoprotein IIb/IIIa inhibitor, tirofiban. They did not note any difference in SICH among the various medical regimens. Stent patency was not reported. A 2017 review and meta-analysis of 11 case series with a total of 237 patients reported 81% successful revascularizations (TICI 2b or TICI 3), a 7% risk of SICH, and good clinical outcomes in 44% (mRS 0–2).¹⁵ A 2018 meta-analysis of 33 studies noted no difference in clinical outcomes of patients treated with thrombectomy and angioplasty alone or stent placement of the cervical carotid lesion; 49% of the time both groups achieved an mRS of ≥ 2 .¹⁶ In their analysis of 395 patients from 17 comprehensive stroke centers, Gory et al¹⁷ noted good clinical outcomes in 52.2%. Stent placement was associated with successful reperfusion, but most interesting, it was not an independent predictor of good clinical outcome.

From a safety perspective, the incidence of SICH in this series was low, just 2%. This result may be for a variety of reasons.

ASPECTSs were high (81% were 8–10, and none were <5), indicating small core infarcts, and revascularization was good (mTICI 2b or better in 96%). Also an indication of small core infarcts and perhaps, more important, of healthy patients at the stroke ictus, the patients did very well clinically (mRS 0–2 in 72%, with just 9% with an mRS of 6). While it may be tempting to discount the safety evidence presented here due to the high ASPECTS, it has been previously noted by Behme et al⁷ that neither procedural timing nor ASPECTS predicted SICH in a tandem occlusion population. In addition to the low incidence of SICH, the favorable clinical outcomes presented here compared with previously published tandem occlusion experience may also be due to an improved technology for thrombectomy (stent retrievers and larger, more easily deliverable aspiration catheters), making the procedures shorter and more effective. Wallocha et al¹⁸ reported similarly good clinical outcomes, 73.6% mRS 0–2 at 90 days in their series.

Reporting of acute in-stent thrombosis or longer-term carotid artery patency has not been routine among case series; therefore, the incidence of acute or subacute stent thrombosis is often not reported. While carotid artery re-occlusions within the first 30 days are rare in elective carotid stent procedures, they are not rare in the tandem occlusion population. In their retrospective review of 163 patients treated for tandem occlusions between 2009 and 2016, Wallocha et al¹⁸ noted 4.9% stent re-occlusion at 24 hours among patients with stents and 42% re-occlusion in patients treated with angioplasty alone. Notably, they administered intravenous aspirin during the procedure to the patients with stents, but not to those with angioplasty alone, who received no additional antithrombotic therapy. Longer-term patency was not reported. In another single-center series of 81 patients with tandem occlusion, Pop et al⁸ reported a 19.1% incidence of delayed stent thrombosis. They used a heterogeneous antithrombotic regimen, with most patients receiving IV aspirin with or without a loading dose of clopidogrel, with none receiving glycoprotein IIb/IIIa inhibitors.

Compared with most published series of patients with tandem occlusion, this report is unique due to the rigorous follow-up for cervical carotid artery patency within the acute phase and the perioperative period. In the present series, acute re-occlusion occurred within the first 24 hours in 4 (7%) patients despite the use of our adjusted eptifibatide protocol, and 3 additional patients re-occluded before the first month, despite being on dual oral antiplatelet therapy. Overall, 7/49 (14%) patients who had follow-up imaging had re-occluded by the 30- to 60-day visit. This finding highlights the different nature of angioplasty and stent placement in a carotid artery in patients undergoing an acute thrombotic event, compared with an elective procedure. Carotid artery patency cannot be assumed in the absence of clinical deterioration. Indeed, none of the re-occlusions were associated with a clinical deterioration.

Placing a stent did not seem to protect against re-occlusion in this series. Of the 4 re-occlusions within the first 24 hours, all patients had stents, and 2 of 3 patients with delayed re-occlusions also had stents. Unlike the experience of Pop et al,⁸ none of the 20 patients initially treated with angioplasty alone re-occluded in the first 24 hours. Within the present series, all of the patients

who underwent angioplasty received the same antiplatelet therapy as the patients who had stents. The data presented here do not inform regarding the superiority of angioplasty alone versus stent placement because there was no attempt to randomize patients to angioplasty alone or stent placement. These decisions were left to the judgment of the interventionalist. It is also not known whether using eptifibatide at this dose results in fewer carotid re-occlusions compared with aspirin alone or any other regimen because no comparisons were made.

Limitations

The study is limited by the small sample size, retrospective nature, and lack of core lab adjudication of outcomes.

CONCLUSIONS

Low-dose eptifibatide (135-mcg/kg bolus, 1-mcg/kg/min infusion) in the population with tandem occlusions seemed safe with a low incidence of SICH. Cervical carotid artery re-occlusions did occur, with an overall 30- to 60-day patency of 86%. Re-occlusion was not associated with clinical decline in any patient. In the absence of a control arm, it is unknown whether cervical carotid patency is improved with low-dose eptifibatide compared with any other regimen. Given the frequently benign course of extracranial carotid re-occlusion compared with the known poor outcomes with SICH, medical therapy to maintain extracranial carotid artery patency should be judicious.

ACKNOWLEDGMENTS

The authors acknowledge Crystal Myers for her tireless help with maintenance of the database and chart review.

Disclosures: Donald Heck—UNRELATED: Consultancy: Stryker.

REFERENCES

1. Berkhemer OA, Fransen PS, Beumer D, et al; MR CLEAN Investigators. **A randomized trial of intraarterial treatment of acute ischemic stroke.** *N Engl J Med* 2015;372:11–20 CrossRef Medline
2. Goyal M, Demchuk AM, Menon BK, et al; ESCAPE Trial Investigators. **Randomized assessment of rapid endovascular treatment of ischemic stroke.** *N Engl J Med* 2015;372:1019–30 CrossRef Medline
3. Jovin TG, Chamorro A, Cobo E, et al; REVASCAT Trial Investigators. **Thrombectomy within 8 hours after symptom onset in ischemic stroke.** *N Engl J Med* 2015;372:2296–2306 CrossRef Medline
4. Assis Z, Menon BK, Goyal M, et al; ESCAPE trialists. **Acute ischemic stroke with tandem lesions: technical endovascular management and clinical outcomes from the ESCAPE trial.** *J Neurointerv Surg* 2018;10:429–33 CrossRef Medline
5. Neuberger U, Moteva K, Vollherbst DF, et al. **Tandem occlusions in acute ischemic stroke: impact of antithrombotic medication and complementary heparin on clinical outcome and stent patency.** *J Neurointerv Surg* 2020;12:1088–93 CrossRef Medline
6. Heck D, Brown M. **Carotid stenting and intracranial thrombectomy for treatment of acute stroke due to tandem occlusions with aggressive antiplatelet therapy may be associated with a high incidence of intracranial hemorrhage.** *J Neurointerv Surg* 2015;7:170–75 CrossRef Medline
7. Behme D, Mpotsaris A, Zeyen P, et al. **Emergency stenting of the extracranial internal carotid artery in combination with anterior circulation thrombectomy in acute ischemic stroke: a**

- retrospective multicenter study.** *AJNR Am J Neuroradiol* 2015;36:2340–45 CrossRef Medline
8. Pop R, Zinchenko I, Quenardelle V, et al. **Predictors and clinical impact of delayed stent thrombosis after thrombectomy for acute stroke with tandem lesions.** *AJNR Am J Neuroradiol* 2019;40:533–39 CrossRef Medline
 9. Turk AS, Spiotta A, Frei D, et al. **Initial clinical experience with the ADAPT technique: a direct aspiration first pass technique for stroke thrombectomy.** *J Neurointerv Surg* 2014;6:231–37 CrossRef Medline
 10. McTaggart RA, Tung EL, Yaghi S, et al. **Continuous aspiration prior to intracranial vascular embolectomy (CAPTIVE): a technique which improves outcomes.** *J NeuroInterv Surg* 2017;9:1154–59 CrossRef Medline
 11. Heck D, Roels C. Tandem occlusions. In: Spiotta A, Turner R, Chaudry M, et al, eds. *Management of Cerebrovascular Disorders*. Springer-Verlag; 2019:511–22
 12. **Randomised placebo-controlled trial of effect of eptifibatid on complications of percutaneous coronary intervention: IMPACT-II—Integrilin to Minimise Platelet Aggregation and Coronary Thrombosis-II.** *Lancet* 1997;349:1422–28 Medline
 13. Kirmani J, Korya D, Choi G, et al. **Abstract T P3: safety of eptifibatid after full dose IV tPA and endovascular treatment for ischemic stroke.** In: *Proceedings of the International Stroke Conference*, Nashville, Tennessee; February 11–13, 2015
 14. Papanagiotou P, Haussen DC, Turjman F, et al; TITAN Investigators. **Carotid stenting with antithrombotic agents and intracranial thrombectomy leads to the highest recanalization rate in patients with acute stroke with tandem lesions.** *JACC Cardiovasc Interv* 2018;11:1290–99 CrossRef Medline
 15. Sivan-Hoffman R, Gory B, Armoiry X, et al. **Stent-retriever thrombectomy for acute anterior ischemic stroke with tandem occlusion: a systematic review and meta-analysis.** *Eur Radiol* 2017;27:247–54 CrossRef Medline
 16. Wilson MP, Murad MH, Krings T, et al. **Management of tandem occlusions in acute ischemic stroke - intracranial versus extracranial first and extracranial stenting versus angioplasty alone: a systematic review and meta-analysis.** *J Neurointerv Surg* 2018;10:721–28 CrossRef Medline
 17. Gory B, Haussen DC, Piotin M, et al; Thrombectomy in TANdem lesions (TITAN) investigators. **Impact of intravenous thrombolysis and emergent carotid stenting on reperfusion and clinical outcomes in patients with acute stroke with tandem lesion treated with thrombectomy: a collaborative pooled analysis.** *Eur J Neurol* 2018;25:1115–20 CrossRef Medline
 18. Wallocha M, Chapot R, Nordmeyer H, et al. **Treatment methods and early neurologic improvement after endovascular treatment of tandem occlusions in acute ischemic stroke.** *Front Neurol* 2019; 10:127 CrossRef Medline

Value of Emergent Neurovascular Imaging for “Seat Belt Injury”: A Multi-institutional Study

 F.G. Sherbaf,  B. Chen,  T. Pomeranz,  M. Shahriari,  M.E. Adin,  S. Mirbagheri,  E. Beheshtian,  R. Jalilianhasanpour,  J. Pakpoor,  J.W. Lazor,  A. Kamali, and  D.M. Yousem



ABSTRACT

BACKGROUND AND PURPOSE: Screening for blunt cerebrovascular injury in patients after motor vehicle collision (MVC) solely based on the presence of cervical seat belt sign has been debated in the literature without consensus. Our aim was to assess the value of emergent neurovascular imaging in patients after an MVC who present with a seat belt sign through a large-scale multi-institutional study.

MATERIALS AND METHODS: The electronic medical records of patients admitted to the emergency department with CTA/MRAs performed with an indication of seat belt injury of the neck were retrospectively reviewed at 5 participating institutions. Logistic regression analysis was used to determine the association among age, sex, and additional trauma-related findings with blunt cerebrovascular injury.

RESULTS: Five hundred thirty-five adult and 32 pediatric patients from June 2003 until March 2020 were identified. CTA findings were positive in 12/567 (2.1%) patients for the presence of blunt cerebrovascular injury of the vertebral ($n = 8$) or internal carotid artery ($n = 4$) in the setting of acute trauma with the seat belt sign. Nine of 12 patients had symptoms, signs, or risk factors for cervical blunt cerebrovascular injury other than the seat belt sign. The remaining 3 patients (3/567, 0.5%) had Biffi grades I–II vascular injury with no neurologic sequelae. The presence of at least 1 additional traumatic finding or the development of a new neurologic deficit was significantly associated with the presence of blunt cerebrovascular injury among adult patients, with a risk ratio of 11.7 ($P = .001$). No children had blunt cerebrovascular injury.

CONCLUSIONS: The risk of vascular injury in the presence of the cervical seat belt sign is small, and most patients diagnosed with blunt cerebrovascular injury have other associated findings. Therefore, CTA based solely on this sign has limited value (3/567 = a 0.5% positivity rate). We suggest that in the absence of other clinical findings, the seat belt sign does not independently justify neck CTA in patients after trauma.

ABBREVIATIONS: BCVI = blunt cerebrovascular injury; FND = focal neurologic deficit; GCS = Glasgow Coma Scale; LOC = loss of consciousness; MVC = motor vehicle collision

Motor vehicle collision (MVC) is a major cause of blunt cerebrovascular injury (BCVI).¹ Historically, the incidence of BCVI was reported to be as low as 0.1%–0.67% among patients with blunt trauma.^{2,3} However, implementation of more rigorous screening protocols in trauma centers has revealed a 10-fold

higher rate of BCVI, as high as 2.7%, among severely injured patients.^{4–6} Although uncommon, the neurologic sequelae of BCVI are potentially serious. Many patients do not manifest stroke symptoms until hours to days after the injury,⁷ and when not treated in a timely fashion, up to 80% develop permanent neurologic sequelae with an estimated 40% mortality rate.^{3,8,9} Thus, screening CTA or MRA for BCVI has become commonplace in

Received August 18, 2020; accepted after revision November 9.

From the Division of Neuroradiology (F.G.S., E.B., R.J., D.M.Y.), Russell H. Morgan Department of Radiology and Radiological Science, Johns Hopkins Medical Institutions, Baltimore, Maryland; Department of Diagnostic and Interventional Imaging (B.C., A.K.), Division of Neuroradiology, University of Texas Health Science Center at Houston, Houston, Texas; Department of Radiology (T.P., J.P., J.W.L.), University of Pennsylvania, Philadelphia, Pennsylvania; Department of Radiology (M.S.), Christiana Care Health System, Newark, Delaware; Department of Radiology and Biomedical Imaging (M.E.A.), Yale University School of Medicine, New Haven, Connecticut; and Department of Diagnostic Radiology (S.M.), Mount Sinai Beth Israel, New York, New York.

Paper previously presented, in part, at: Annual Meeting of the American Society of Neuroradiology, May 30 to June 4, 2020; Virtual.

The authors declare that they had full access to all the data in this study and they take complete responsibility for the integrity of the data and the accuracy of the data analysis.

Please address correspondence to Farzaneh Ghazi Sherbaf, MD, Department of Radiology and Radiological Science, Division of Neuroradiology, Johns Hopkins Medical Institutions, 600 N Wolfe St, Phipps B100, Baltimore, MD 21287; e-mail: dyousem1@jhu.edu; @dyousem1

 Indicates article with online supplemental data.
<http://dx.doi.org/10.3174/ajnr.A6992>

the management of patients after an MVC.^{10,11} However, the selection of which patients to screen has been a controversial topic during the past 4 decades.⁶

Various screening algorithms, including the modified Memphis and Denver criteria or the Western Trauma Association algorithm, may be used as guidelines (Online Supplemental Data). These guidelines, developed on the basis of observational studies and expert opinion, have adopted a liberal approach to imaging patients with possible BCVI.^{7,12,13} Although this approach helps avoid missing occult injuries, it may lead to unnecessary imaging, discovery of incidental findings, increased radiation exposure, and low-value health care expenditures.¹⁴⁻¹⁷ Many believe that advanced imaging studies are being overused in many medical centers, in part, due to a “defensive medicine” mentality. It is estimated that up to 50% of ordered studies lead to no improvement in patient welfare.^{15,18}

One of the controversial indications for BCVI is the physical sign of neck abrasion or contusion caused by a seat belt, the so-called cervical seat belt sign. Screening for BCVI solely based on the presence of this sign has been debated in the literature without consensus.¹⁹⁻²² The existing guidelines also recommend contradictory approaches regarding the use of the seat belt sign as a sole indicator to stratify patients for screening (Online Supplemental Data). Despite some single-center studies suggesting that discoloration of the skin from the seat belt is not a reliable indicator of risk to the cervical vessels,²³⁻²⁵ many trauma centers persist in ordering emergent CTAs to exclude BCVI in patients with this finding because of continued debate as to the validity of the seat belt sign as an indicator of vascular injury. To address this controversy, we aimed to assess the value of emergent neurovascular imaging in patients with a seat belt sign after an MVC through a large-scale multi-institutional study that would identify the situations in which the seat belt sign may be predictive of cervical vascular injury. We hypothesized that cervical CTA performed solely on the basis of a seat belt sign has limited value.

MATERIALS AND METHODS

The acquisition of patient data for this study was Health Insurance Portability and Accountability Act-compliant. This retrospective study protocol was approved by the institutional review board at each institution separately, and informed consent was not required.

Study Population

Local radiology information systems or electronic medical records were searched in all institutions for patients who underwent CTA and/or MRA of the neck after an MVC, in which “seat,” “belt,” “seat belt,” “seat-belt,” “seatbelt,” “lap,” “lap belt,” “lap-belt,” or “lapbelt” injury of the neck was stated in the indication, body, or impression of the radiology report. The start and end points of the study were not strictly predefined but were decided separately for each institution on the basis of access to the electronic records of the patients, the period during which each institution had adopted the guidelines to screen for BCVI using a cervical seat belt sign, and the number of cases available in that time period. We were interested in separately investigating the association between the cervical seat belt sign and BCVI in

adults and pediatric (younger than 18 years of age) patients. Therefore, no age limit was set for the inclusion criteria.

Data Collection

Clinical data and imaging reports for all patients were gathered from the participating centers. Scans with positive findings were identified on the basis of the imaging reports and then confirmed by subspecialty trained neuroradiologists at each center. The neurology notes were reviewed for patients with negative findings to confidently rule out the diagnosis of a BCVI in those patients. Clinical variables included age, sex, a subjective report of on-scene loss of consciousness (LOC), the initial Glasgow Coma Scale (GCS) score, physical examination, neurologic findings as per the neurology report, and associated trauma-related injuries to the head, neck, and chest. Treatment, hospital course, outcome, and other proposed indications for screening of the BCVI as outlined in the Online Supplemental Data were further retrieved for patients with confirmed BCVI. The side of the seat belt sign was gathered from their medical records for patients with positive findings on a scan and was compared with the evident soft-tissue injury, if present, on imaging. The vascular injury scale proposed by Biffel et al²⁶ was adopted to grade the severity of BCVI: intimal irregularity or dissection with <25% narrowing (grade I), dissection or intramural hematoma with >25% narrowing (grade II), pseudoaneurysm (grade III), vessel occlusion (grade IV), and transection with extravasation (grade V).

Statistical Analysis

Data from independent participating institutions were pooled. Descriptive statistics were used to summarize the baseline data. Non-normality of the distribution of age and the GCS score was determined by the Shapiro-Wilk test. Demographic and clinical features were compared between patients with and without BCVI using the Fisher exact test for categorical and the Mann-Whitney *U* test for continuous variables. Univariate analysis was performed with exact logistic regression to determine the association among age, sex, and the presence of at least 1 additional trauma-related finding with BCVI. Because the sample size of patients with BCVI was small, we could not perform multivariate analysis to determine the association between each single traumatic finding with BCVI. STATA 16.0 software (StataCorp) was used for statistical analysis. The level of significance was set to <.05.

RESULTS

Study Group Description

Data were collected from 5 independent medical/trauma centers. In total, 567 consecutive patients underwent screening angiography for BCVI in the setting of an MVC with the seat belt sign. In this population, there were 535 adult (67.6% women; mean age, 42.2 [SD, 18.4] years) and 32 pediatric (younger than 18 years of age) (56.2% female; mean age, 13.0 [SD, 4.0] years) patients. The demographic and clinical profiles of included patients are summarized in Table 1 (details from each center are given in the Online Supplemental Data). The imaging studies were performed between June 2003 and March 2020. CTA (*n* = 526) or MRA (*n* = 41) was performed within 24 hours of admission, following detection of a cervical seat belt abrasion.

Table 1: Clinical and imaging characteristics of patients with cervical seat belt sign

Characteristics	
No. (% female)	
Adult	535 (67.6)
Pediatric	32 (56.2)
Total	567 (67.0)
Age (mean) [SD] (range) (yr)	
Adult	42.2 [SD, 18.4], (18–91)
Pediatric	13.0 [SD, 4.0], (6–17)
Mean GCS [SD] (No.)	14.9 [SD, 0.8], (519)
On-scene LOC (No.) (%)	
No	400 (70.5)
Yes	65 (11.5)
Unclear or amnesic to the event	51 (9.0)
Clinical data not available	51 (9.0)
Neurologic deficit (No.) (%)	
New FND	6 (1.1)
New FND inconsistent with head CT/MR imaging	3 (0.5)
Clinical data not available	41 (7.2)
Associated traumatic findings (No.)	
Fractures	
Skull	2
Midface (maxilla, mandible)	5
Cervical vertebrae (only C1–3)	20 (6)
First rib or clavicle	20
Upper ribs (2–4)	35
Lower ribs (5–12)	10
Sternum	30
Upper thoracic vertebra	10
Cervical ligamentous injury	3
Scalp/neck hematoma	7/7
Thoracic vascular injuries	1
Intracranial hemorrhage	13
No additional finding per patient (%)	450 (79.4)
At least 1 additional finding ^a (%)	117 (20.6)
No. of patients with BCV (%)	12 (2.1)

^a Including a new FND, a GCS score of <8, or any of the above-listed associated traumatic findings to the head, neck, or chest.

Patient Symptoms

All patients had GCS scores of 15 or 14, except 7 patients with a GCS score between 7 and 13 and 1 patient with a GCS score of 3 at initial evaluation. Sixty-five patients (11.5%) reported an episode of LOC at the time of the MVC; a history of LOC was unclear for 51 patients (9.0%). Six patients were reported to have a focal neurologic deficit (FND) on physical examination. This was associated with closed head injury and intracranial hemorrhage in 3 patients and episodes of temporary unresponsiveness due to low blood pressure in 1 patient. Another patient presented with temporary facial nerve palsy. FNDs were manifest at the first emergency department encounter, except for 1 patient who presented after 2 days with subjective deterioration of pre-existing visual symptoms due to amblyopia.

Non-BCVI Injuries

Head, neck, and chest traumatic injuries, other than the seat belt sign, included cervical spinal fracture or ligamentous injury ($n=23$), thoracic skeletal injuries ($n=105$), thoracic vascular injury ($n=1$), fracture of the skull or midface ($n=7$), and intracranial hemorrhage ($n=13$). No patients had a stroke. The

overall mortality rate was zero during the hospital admission and at follow-up of at least 1 month (Online Supplemental Data). In total, 117 patients had at least 1 injury other than the seat belt sign to the head, neck, or chest, were reported to have a GCS score of <8, or developed new FNDs. The remaining 450 patients had only a cervical seat belt sign, with a GCS score of >8 without any other traumatic findings, signs, or symptoms of BCVI.

Patients Diagnosed with BCVI: Characteristics

Figure 1 shows the flow chart of a subgroup of patients based on the diagnosis of BCVI and the presence of additional traumatic findings other than the cervical seat belt sign. There were 12/567 patients (2.1%) with a seat belt sign who had BCVI discovered on initial cervical CTA and confirmed on review by an expert neuro-radiologist (Fig 2). The Online Supplemental Data show clinical profiles and imaging findings for each patient with positive BCVI findings on CTA of the neck. The side of the seat belt sign was contralateral to the site of the BCVI in 5/12 patients. BCVI was detected in the internal carotid ($n=4$) or vertebral artery ($n=8$) with a Biffl grade I ($n=6$), II ($n=4$), or IV ($n=2$).

One patient had initially negative cervical CTA findings confirmed on review by an expert neuroradiologist. The patient presented 2 days later with subjective exacerbation of pre-existing visual symptoms due to a history of amblyopia. The neurologic examination was limited due to the amblyopia. Repeat CTA and ultrasonography of the neck were compatible with grade I traumatic dissection of the proximal left internal carotid artery. The patient was discharged on anticoagulation, and the symptoms were resolved on 1-month follow-up.

Another patient had multiple neurologic deficits that were attributed to the coexisting brain injury. No other patient diagnosed with BCVI showed any neurologic sequelae during the hospital course or available follow-ups. No patients showed clinically overt signs of vascular trauma, including pulsatile bleeding, expanding hematoma, palpable thrill, cervical bruit, or stroke.

Patients with BCVI: Treatment and Follow-up

No vascular intervention was performed for any patients. Those with BCVI were all discharged on antiplatelet or anticoagulation therapy after neurologic consultation, except 1 patient who was merely observed for a cervical vascular injury. In 4 patients, the grade I BCVI resolved on follow-up vascular imaging (up to 2 months). Other vascular injuries were stable at 1- to 3-month follow-up in 4 patients with grade I, II, or IV vascular injury. Four patients with grade I or II BCVI did not have any follow-up imaging (Online Supplemental Data). Patients with BCVI were more likely to present with a new FND ($P=.007$), intracranial hemorrhage ($P=.03$), cervical vertebral fracture ($P<.001$), or sternal fracture ($P=.02$) (Table 2).

Patients with BCVI: Comparison of an Isolated Seat Belt Sign with a Seat Belt Sign with Additional Traumatic Injuries

Of a total of 12 patients diagnosed with BCVI, 9 had additional clinical or imaging evidence of cervicothoracic trauma. In

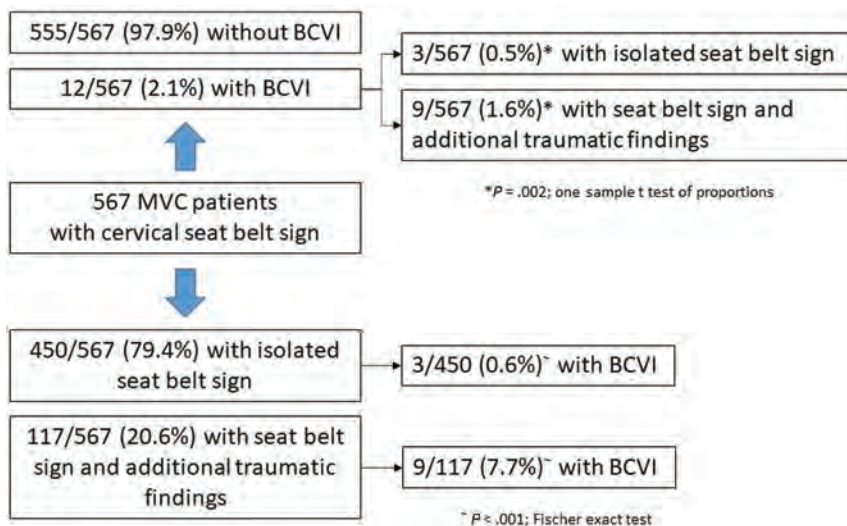


FIG 1. Flow chart of patients showing the incidence rate of BCVI among 2 subgroups of patients after an MVC based on the presence of additional traumatic findings other than the cervical seat belt sign.

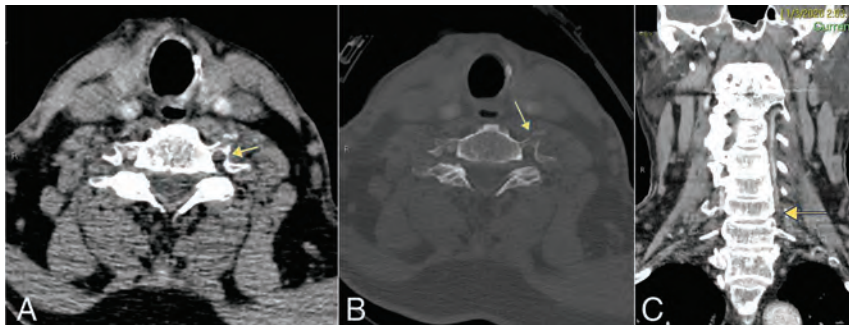


FIG 2. CTA of a 71-year-old male patient shows absent vascular opacification (arrow) in an occlusive dissection of the left vertebral artery (A). There is a mildly displaced fracture of the left transverse process/foramen of C5 (arrow) evident on the corresponding bone window (B). The coronal reconstructed image demonstrates occlusion of the V1 and proximal V2 segments and the absence of flow below the C6 vertebral level (grade IV) (arrow) (C), with a reconstituted left vertebral artery above from collaterals.

another 3 patients with BCVI, there were no traumatic findings or BCVI risk factors other than the seat belt sign during the initial presentation, hospital course, or additional follow-ups. These 3 patients had grade I or II BCVI. The incidence of BCVI among patients without traumatic findings other than a seat belt injury (0.6%, $n = 3/450$) was significantly lower than in patients with BCVI and at least 1 additional traumatic finding (7.7%, $9/117$) ($P < .001$) (Fig 1). The presence of at least 1 additional traumatic finding (including fractures in the skull, midface, cervical or upper thoracic vertebrae, ribs, or sternum; cervical spinal ligamentous injury; intracranial hemorrhage; or closed head injury) or development of a new FND was significantly associated with the presence of BCVI among adult patients, with a risk ratio of 11.7 ($P = .001$). Age and sex were not associated with the presence of BCVI in adult patients on univariate logistic regression analysis ($P = .77$ and $.68$, respectively).

DISCUSSION

In this multi-institutional study, we found that the incidence of BCVI in the setting of an isolated cervical seat belt sign after MVC was 0.5% (3/567), which is less than in previous reports of the incidence of BCVI among severely injured patients.⁴⁻⁶ Additionally, the presence of at least 1 additional traumatic finding to the head, neck, or upper chest, including skeletal injury, closed head injury, or a new FND, was significantly associated with BCVI in our study population, with a relative risk of 11.7. Currently, CTA or MRA is being ordered in many emergency departments or trauma centers for patients with a cervical seat belt sign. However, our results indicate that the seat belt sign alone has a low predictive value for BCVI and should not be considered as an independent indicator for radiologic screening. Exceptions to this rule may be applied to patients with known vascular fragility risk factors including fibromuscular dysplasia or connective tissue disorders such as Marfan or Loeys-Dietz syndrome.²⁷

Existing literature on the use of this sign in isolation is scant and contradictory. Following several early reports of catastrophic BCVI in patients with a seat belt sign, this finding has appeared in some guidelines as a reliable marker to screen for BCVI (Online Supplemental Data). A review of a national trauma databank from 2008 to 2014 with 2,174,244 adult patients with blunt trauma revealed 5970 (0.27%) patients with BCVI and 859/5970 (14.4%) patients with a seat belt sign. Multivariate analysis confirmed the association of the seat belt sign with BCVI in adult patients,²⁸ leading to an impression that neurovascular imaging is warranted. However, this report did not address the predictive value of this sign by itself or the impact of other signs of cervicothoracic trauma; therefore, it only obfuscated the assessment of the seat belt sign as an indication for screening.

More recent studies have argued against the cervical seat belt sign as an independent factor warranting BCVI screening for adult and pediatric patients. DiPerna et al²¹ retrospectively reviewed 131 consecutive patients with a cervical seat belt sign. Only 1 patient with neurologic deficits and multiple associated injuries was diagnosed with BCVI. Similarly, in a prospective study of another 131 patients with a cervicothoracic seat belt sign, the authors found 4 positive reports of BCVI. Rozycki et al²² demonstrated that the seat belt sign in combination with other abnormal findings such as a GCS score of <14 , first rib or clavicle

Table 2: Comparison of adult patients without BCVI versus patients with BCVI (18 years of age or older)

	Without BCVI (n = 523)	With BCVI (n = 12)	P Value
Female/male	355:168	7:5	.53
Age (mean) [SD] (yr)	42.1 [SD, 18.4]	43.6 [SD, 20.7]	.86 ^a
GCS (mean) [SD]	14.9 [SD, 0.8] (GCS: 3 = 1 patient GCS: 7 = 1 patient Others: >8)	14.8 [SD, 0.6] (GCS: 13 = 1 patient Others = 15)	.55 ^a
On-scene LOC (No/yes/unclear)	370/56/48	8/4/0	.06
Neurologic deficit			
New FND	4 (0.7%)	2 (16.7%)	.007
New FND inconsistent with head CT/MR imaging	2 (0.4%)	1 (8.3%)	.07
At least 1 additional traumatic head/neck/chest injury			
All	103 (19.7%)	9 (75%)	<.001
All except scalp/neck hematoma	82 (15.7%)	7 (58.3%)	.001
Head injury			
Intracranial hemorrhage	11 (2.1%)	2 (16.7%)	.031
Skull fracture/hematoma	2 (0.4)/7 (1.3%)	0	
Midface fracture	5 (0.9%)	0	
Cervical injury			
Cervical spine fracture	15 (2.9%)	4 (33.3%)	<.001
C1–3 fracture	5 (1.0%)	1 (8.3%)	.12
Spinal ligamentous injury	2 (0.4%)	0	
Neck hematoma	7 (1.3%)	0	
Thoracic injury			
First rib/clavicle fracture	19 (3.6%)	1 (8.3%)	.37
Upper rib fracture	43 (8.2%)	2 (16.7%)	.26
Any rib fracture	53 (10.1%)	3 (25%)	.12
Sternal fracture	27 (5.2%)	3 (25%)	.02
Vertebral fracture	8 (1.5%)	0	
Vascular injury	1 (0.2%)	0	

^a The Mann-Whitney test was used for those marked with a, and Fischer exact test, for the rest.

fracture, or an injury severity score of >16 was associated with a higher risk of BCVI. Therefore, a larger multi-institutional study was warranted for resolution of this controversy. Our study shows that the incidence of BCVI in the presence of an isolated seat belt sign is negligible (3/567; 0.5%). The 3 patients with an isolated seat belt sign were diagnosed with mild BCVI (grades I–II). A higher grade IV BCVI was detected in 2 patients who also had associated cervical vertebral fractures. In addition, the presence of vascular injury on the side opposite the seat belt sign (4/12 in our cohort) serves as an indicator of the severity of the MVC and/or the presence of a to-and-fro acceleration-deceleration injury, placing all vessels, ipsilateral or contralateral, at risk.²⁹ On the basis of these lines of evidence, we suggest that this sign should initiate a careful evaluation for other factors related to BCVI via a thorough physical examination and standard trauma imaging rather than a reflexive order of neck CTA. By doing so, a CTA could have been safely avoided in at least 450/567 (79.4%) patients without any associated trauma-related cervicothoracic finding, new neurologic deficits, or a reported GCS score of <8 among our cohort.

Although the number of pediatric patients identified through searching imaging data bases of participating sites was small (n = 32), there were no BCVIs detected in the included children. Three retrospective studies on pediatric patients have also recommended against the use of the seat belt sign as a sole indicator of BCVI screening in this population.^{23,25,28}

Limitations

There are several limitations to this study that stem from its retrospective design. The clinical information of 40 patients was not retrievable because of missing data in the transition from paper to electronic medical records. Because the details of the kinematics and the severity of the MVC injury as well as the type of seat belt were not available for almost all of the patients, such information could not be assessed in our study. However, our reported incidence of BCVI (12/567; 2.1%) was nearly as high as in previous reports of its incidence among severely injured patients.^{4–6} Patients were identified on the basis of the language of imaging reports/orders, which may have led to the exclusion of some patients after an MVC with a seat belt injury who underwent neurovascular imaging. The CTA/MRA protocols were not standardized across the institutions and may have varied within the same institution, given the wide date range. Because we intended to assess the predictive value of seat belt injury for BCVI, we did not include all patients after an MVC and thus could not study all risk factors for BCVI. Finally, all except 1 patient with BCVI received treatment. Although the number of patients with an isolated seat belt sign and BCVI was small and they experienced only mild vascular injury, neurovascular imaging resulted in a change in their management.

Therefore, we cannot exclude the possibility that a very small number of patients could have experienced an adverse outcome (ie, an embolic stroke) in follow-up as a result of not performing CTA/MRA of the neck (because they would not have received antiplatelet therapy in that case). Future studies with a case-control design are warranted to investigate this possibility.

CONCLUSIONS

In a multi-institutional study, we found that the incidence of BCVI in patients with an isolated seat belt sign was negligible (0.5%). Thus, we recommend elimination of this indication for CTA in the absence of other clinical findings. While the seat belt sign should not trigger reflexive imaging, it should prompt a careful neurologic examination and evaluation for associated injuries that could increase the risk for BCVI.

Disclosures: David M. Yousem—UNRELATED: Expert Testimony: medicolegal expert witness; Payment for Lectures Including Service on Speakers Bureaus: MRI Online; Royalties: Elsevier 5 books; Payment for Development of Educational Presentations: MRI Online lecture material.

REFERENCES

1. Biffi WL, Moore EE, Offner PJ, et al. **Blunt carotid and vertebral arterial injuries.** *World J Surg* 2001;25:1036–43 CrossRef Medline
2. Berne JD, Norwood SH, McAuley CE, et al. **The high morbidity of blunt cerebrovascular injury in an unscreened population: more evidence of the need for mandatory screening protocols.** *J Am Coll Surg* 2001;192:314–21 CrossRef Medline
3. Davis JW, Holbrook TL, Hoyt DB, et al. **Blunt carotid artery dissection: incidence, associated injuries, screening, and treatment.** *J Trauma* 1990;30:1514–17 CrossRef Medline
4. Biffi WL, Moore EE, Ryu RK, et al. **The unrecognized epidemic of blunt carotid arterial injuries: early diagnosis improves neurologic outcome.** *Ann. Surg* 1998;228:462–70 CrossRef Medline
5. Esnault P, Cardinale M, Boret H, et al. **Blunt cerebrovascular injuries in severe traumatic brain injury: incidence, risk factors, and evolution.** *J Neurosurg* 2017;127:16–22 CrossRef Medline
6. Franz RW, Willette PA, Wood MJ, et al. **A systematic review and meta-analysis of diagnostic screening criteria for blunt cerebrovascular injuries.** *J Am Coll Surg* 2012;214:313–27 CrossRef Medline
7. Burlew CC, Biffi WL. **Blunt cerebrovascular trauma.** *Curr Opin Crit Care* 2010;16:587–95. CrossRef Medline
8. Cogbill TH, Moore EE, Meissner M, et al. **The spectrum of blunt injury to the carotid artery: a multicenter perspective.** *J Trauma* 1994;37:473–79 CrossRef Medline
9. Parikh AA, Luchette FA, Valente JF, et al. **Blunt carotid artery injuries.** *J Am Coll Surg* 1997;185:80–86 CrossRef Medline
10. Cothren CC, Moore EE, Ray CE Jr, et al. **Screening for blunt cerebrovascular injuries is cost-effective.** *Am J Surg* 2005;190:845–49 CrossRef Medline
11. Kerwin AJ, Bynoe RP, Murray J, et al. **Liberalized screening for blunt carotid and vertebral artery injuries is justified.** *J Trauma Acute Care Surg* 2001;51:308–14 CrossRef Medline
12. Biffi WL, Cothren CC, Moore EE, et al. **Western Trauma Association critical decisions in trauma: screening for and treatment of blunt cerebrovascular injuries.** *J Trauma* 2009;67:1150–53 CrossRef Medline
13. Ciapetti M, Circelli A, Zagli G, et al. **Diagnosis of carotid arterial injury in major trauma using a modification of Memphis criteria.** *Scand J Trauma Resusc Emerg Med* 2010;18:61 CrossRef Medline
14. Beheshtian E, Sahraian S, Yousem DM, et al. **Incidental findings on cervical spine computed tomography scans: overlooked and unimportant?** *Neuroradiology* 2018;60:1175–80 CrossRef Medline
15. Hendee WR, Becker GJ, Borgstede JP, et al. **Addressing overutilization in medical imaging.** *Radiology* 2010;257:240–45 CrossRef Medline
16. Levin DC, Rao VM, Parker L, et al. **Continued growth in emergency department imaging is bucking the overall trends.** *J Am Coll Radiol* 2014;11:1044–47 CrossRef Medline
17. Schauer DA, Linton OW. **National Council on Radiation Protection and Measurements report shows substantial medical exposure increase.** In: *Proceedings of the Annual Meeting of the Radiological Society of North America*, Chicago, Illinois; November 20 to December 4, 2009
18. Callan AK, Bauer JM, Mir HR. **Over-utilization of computed tomography angiography in extremity trauma.** In: *Proceedings of the Orthopaedic Trauma Association International*, Denver, Colorado; September 25–28, 2019
19. Biffi WL, Moore EE, Offner PJ, et al. **Optimizing screening for blunt cerebrovascular injuries.** *Am J Surg* 1999;178:517–22 CrossRef Medline
20. Bromberg WJ, Collier BC, Diebel LN, et al. **Blunt cerebrovascular injury practice management guidelines: the Eastern Association for the Surgery of Trauma.** *J Trauma* 2010;68:471–77 CrossRef Medline
21. DiPerna CA, Rowe VL, Terramani TT, et al. **Clinical importance of the “seat belt sign” in blunt trauma to the neck.** *Am Surgeon* 2002;68:441–45 Medline
22. Rozycki GS, Tremblay L, Feliciano DV, et al. **A prospective study for the detection of vascular injury in adult and pediatric patients with cervicothoracic seat belt signs.** *J Trauma* 2002;52:618–23 CrossRef Medline
23. Desai NK, Kang J, Chokshi FH. **Screening CT angiography for pediatric blunt cerebrovascular injury with emphasis on the cervical “seatbelt sign”.** *AJNR Am J Neuroradiol* 2014;35:1836–40 CrossRef Medline
24. Dhillon RS, Barrios C, Lau C, et al. **Seatbelt sign as an indication for four-vessel computed tomography angiogram of the neck to diagnose blunt carotid artery and other cervical vascular injuries.** *Am Surgeon* 2013;79:1001–04 CrossRef Medline
25. Ugalde IT, Claiborne MK, Cardenas-Turanza M, et al. **Risk factors in pediatric blunt cervical vascular injury and significance of seatbelt sign.** *West J Emerg Med.* 2018;19:961–69 CrossRef Medline
26. Biffi WL, Moore EE, Offner PJ, et al. **Blunt carotid arterial injuries: implications of a new grading scale.** *J Trauma* 1999;47:845–53 CrossRef Medline
27. Rodrigues V, Elsayed S, Loeys B, et al. **Neuroradiologic manifestations of Loeys-Dietz syndrome type 1.** *AJNR Am J Neuroradiol* 2009;30:1614–19 CrossRef Medline
28. Leraas HJ, Kuchibhatla M, Nag UP, et al. **Cervical seatbelt sign is not associated with blunt cerebrovascular injury in children: a review of the national trauma databank.** *Am J Surg* 2019;218:100–05 CrossRef Medline
29. Danelson KA, Gayzik FS, Mao MY, et al. **Bilateral carotid artery injury response in side impact using a vessel model integrated with a human body model.** *Ann Adv Automot Med* 2009;53: 271–279 Medline

Variations in the Course of the Carotid Arteries in Patients with Retropharyngeal Parathyroid Adenomas

G.K. Steinl, R. Yeh, C.M. McManus, J.A. Lee, and J.H. Kuo

ABSTRACT

SUMMARY: The carotid arteries, classically described as taking a relatively straight course through the neck, deviate medially in a minority of patients. At the extreme, the internal carotid arteries may “kiss” in the midline, coming extremely close to the pharyngeal wall. In this clinical report, we describe 5 patients with primary hyperparathyroidism, all with ectopic retropharyngeal parathyroid adenomas but all with varying carotid artery anatomy. We describe these variations using a previously developed clinical grading system that highlights 1) the relationship between carotid artery location and risk of injury during pharyngeal procedures and 2) the importance of universal, objective criteria to classify carotid anatomy. Radiologists should be familiar with variations in carotid anatomy and communicate them to the operative team.

ABBREVIATIONS: PHPT = primary hyperparathyroidism; MIBI = technetium Tc99m sestamibi; PTH = parathyroid hormone

Although the carotid arteries classically run straight to the base of the skull, abnormalities in their anatomy may include tortuosity, kinking, or coiling of 1 or both of the arteries.¹ The vessels may deviate medially so much that they come together at the midline, colloquially referred to as “kissing carotids.” Previously, there was no official classification system for carotid anatomy, making it difficult to estimate how common these anomalies are. Anatomic and radiologic studies have reported incidences ranging from 0.2% to 30% depending on the criteria used to define “abnormal.”^{1–5} Pfeiffer et al⁵ recognized the need for a universal classification system and developed a convenient grading scale of I through IV based on the minimal distance from the internal carotid artery to the pharyngeal wall and the level of the pharynx (nasopharynx, oropharynx, or hypopharynx) where this occurs.

It is critical that radiologists be aware of these variations in carotid anatomy and, when discovered incidentally on preoperative imaging, accurately report these findings to the surgeon. Aberrant carotid arteries can have serious implications if unknown or unreported before procedures involving the pharyngeal area, such as tracheal intubation, tonsillectomy, retropharyngeal abscess drainage, removal of neoplasms, or removal of an ectopic parathyroid adenoma.^{6–8} They can also cause symptomatic

widening of the retropharyngeal space.^{9,10} In the Pfeiffer et al⁵ classification system, class I indicates a normal distance between the ICA and the pharynx, representing a presumably low risk for injury during pharyngeal procedures, and grade IV indicates a severely medialized ICA that poses a very high risk.

The retropharyngeal (paraesophageal) space is a common location for ectopic parathyroid glands.¹¹ The incidence of ectopic glands is as high as 11%–16% among patients undergoing parathyroid surgery, and missed ectopic adenomas are a leading cause of persistent hyperparathyroidism requiring reoperation.^{11–13} Because of advances in imaging techniques such as technetium Tc99m sestamibi (MIBI), often performed with SPECT/CT, and more recently the multiphase parathyroid 4D CT, radiologists are now frequently able to localize these adenomas before surgery.^{14,15}

Anomalies of both the parathyroid glands and the ICAs have been well described independently, but there is no literature that draws an association between the two. We present preoperative imaging and intraoperative findings of 5 patients with primary hyperparathyroidism (PHPT) who presented for surgical consultation and were found to have ectopic parathyroid adenomas in the retropharyngeal space. The patients had varying carotid anatomy, ranging from a unilateral, slightly medialized ICA to “kissing” ICAs. Here we report on their presentation, work-up, and surgical procedures.

Case Series

Patient characteristics are described in the Table. All 5 patients were diagnosed with PHPT after routine screening laboratory studies revealed hypercalcemia, and all met the International Workshop

Received June 6, 2020; accepted after revision November 24.

From the Department of Surgery, Division of GI/Endocrine Surgery (G.K.S., C.M.M., J.A.L., J.H.K.), Vagelos College of Physicians and Surgeons, Columbia University Irving Medical Center, New York, New York, and Department of Radiology (R.Y.), Memorial Sloan Kettering Cancer Center, New York, New York.

Please address correspondence to Jennifer H. Kuo, MD, Herbert Irving Pavilion, 161 Fort Washington Ave, 8th Floor, Suite 829, New York, NY 10032; e-mail: jhk2029@cumc.columbia.edu
<http://dx.doi.org/10.3174/ajnr.A6995>

Patient characteristics

	Patient 1	Patient 2	Patient 3	Patient 4	Patient 5
Age, years	64	58	80	72	76
Sex	Female	Female	Female	Female	Female
Nephrolithiasis	No	No	Yes	No	No
Osteoporosis	No	Yes	Yes	No	Yes
Biochemical					
Preoperative serum calcium, mg/dL	10.8 (8.6–10.4)	10.4 (8.6–10.2)	14.0 (8.4–10.2)	10.8 (8.6–10.3)	10.6 (8.5–10.5)
Preoperative PTH, pg/mL	38 (14–64)	65 (15–65)	356 (12–88)	87 (15–65)	200 (12–88)
Preoperative 25 OH-vitamin D, ng/mL	41.0 (30–100)	46.2 (30–100)	Not available	27.7 (30–100)	16.0 (30–100)
Surgical approach	Normal anterior	Normal anterior	Focused lateral	Normal anterior	Not available
Minimal distance from ICA to pharyngeal wall					
Right ICA	4.6 mm (hypopharynx)	7.1 mm (oropharynx)	9.5 mm (oropharynx)	7.3 mm (oropharynx)	3.5 mm (oropharynx)
Left ICA	2.0 mm (oropharynx)	4.8 mm (oropharynx)	8.8 mm (oropharynx)	12.8 mm (oropharynx)	7.5 mm (nasopharynx)
ICA classification per Pfeiffer et al ^a					
Right ICA, grade	III	II	II	II	III
Left ICA, grade	IV	III	II	I	II

^aThis classification of ICA anatomy on a scale of I–IV (“I” being effectively normal and “IV” being extremely close to the pharynx) takes into account 1) the minimal distance to the pharyngeal wall and 2) the level at which this distance occurs.⁵

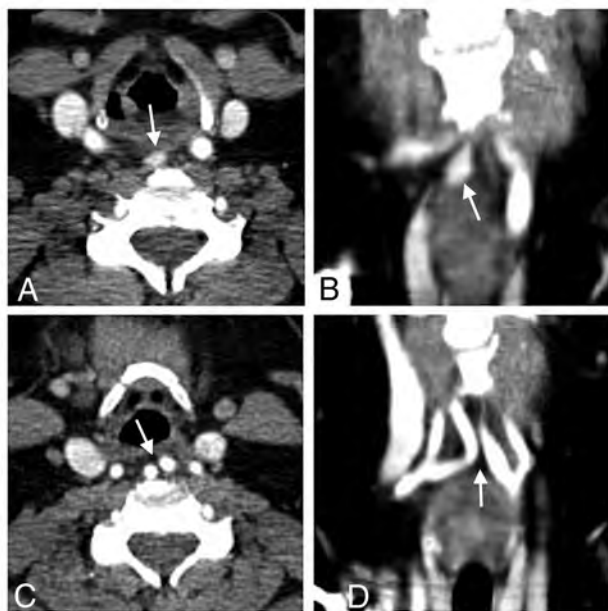


FIG 1. Case 1. Contrast-enhanced CT scan shows axial (A) and coronal (B) images of the retropharyngeal parathyroid adenoma (arrow) and axial (C) and coronal (D) images of the nearly “kissing” carotid arteries (arrow).

on Asymptomatic Primary Hyperparathyroidism criteria for parathyroidectomy.¹⁶ For surgical planning, per institutional protocol for PHPT, all patients underwent 4D CT, and all but 1 also had MIBI SPECT/CT performed at the same time using a combined acquisition method.¹⁷ We classified the ICAs of each patient using the grading system developed by Pfeiffer et al⁵ (Table). In the 4 patients who underwent parathyroidectomy, intraoperative parathyroid hormone (PTH) levels fell appropriately by greater than 50% from pre-

excision to 10 minutes postexcision, and final pathology was consistent with parathyroid adenoma. There were no complications, and all patients had normalized serum calcium levels at 6 months after surgery. One patient’s operation was delayed because of the coronavirus 2019 pandemic.

In case 1, 4D CT revealed an ectopically located right superior parathyroid adenoma in the retropharyngeal space (14 mm × 9 mm × 5 mm), posterior to the larynx at the level of the piriform sinuses, slightly right of midline (Fig 1A, -B). The adenoma was MIBI avid on SPECT/CT. The bilateral carotid arteries appeared medialized such that they nearly “kissed” immediately posterior to the oropharynx and larynx (Fig 1C, -D). The patient underwent a focused parathyroidectomy. After the right thyroid lobe and thyroid cartilage were mobilized and retracted, the bilateral internal carotid arteries were noted to be very medialized as expected. Posterior to the larynx in the retropharyngeal space, just anterior to the spine, a well-defined parathyroid adenoma was identified and resected.

In case 2, 4D CT revealed a 6 mm × 9 mm × 20 mm enhancing paraesophageal nodule, consistent with a left upper parathyroid adenoma (Fig 2). The adenoma was MIBI avid on SPECT/CT. The adenoma was approximately 9 mm posterior to the lower pole of the left thyroid lobe and immediately anteromedial to the left carotid artery. The patient underwent a focused parathyroidectomy. The left thyroid lobe and thyroid cartilage were mobilized and retracted anteromedially. In the retropharyngeal space, posterior to the left lower pole, a well-defined parathyroid adenoma was identified, dissected, and excised.

In case 3, the patient had undergone 2 neck explorations with resection of right upper and left lower adenomas 7 years and 2 years, respectively, before presenting to our institution for work-up of persistent hyperparathyroidism. An ectopic parathyroid adenoma (21 mm × 14 mm × 6 mm) was identified on 4D CT in the left retropharyngeal space immediately posterior to the

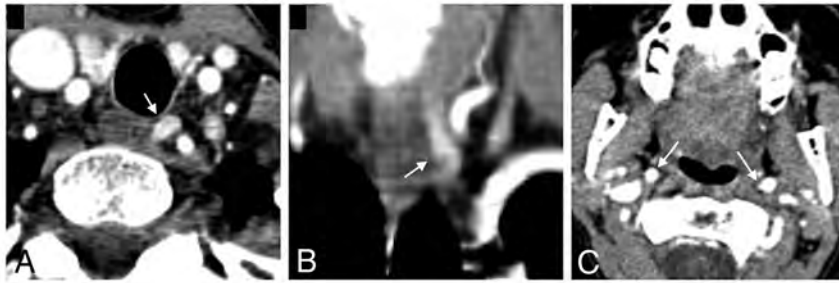


FIG 2. Case 2. Contrast-enhanced CT scan shows axial (A) and coronal (B) images of the retropharyngeal adenoma (arrow) and an axial (C) image of the bilateral internal carotid arteries (arrow) at the level of the oropharynx.

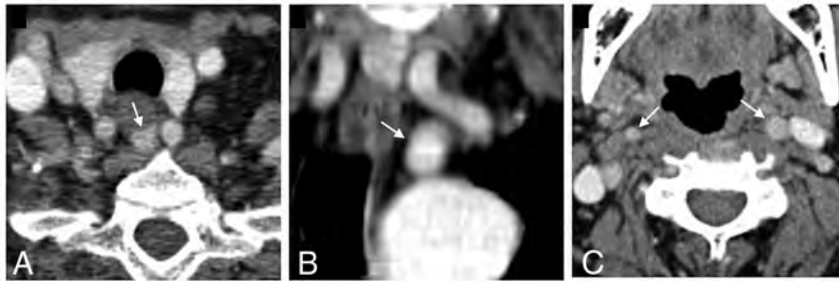


FIG 3. Case 3. Contrast-enhanced CT scan shows axial (A) and coronal (B) images of the retropharyngeal parathyroid adenoma (arrow) between the common carotid arteries and an axial (C) image of the bilateral internal carotid arteries (arrow) at the level of the oropharynx.

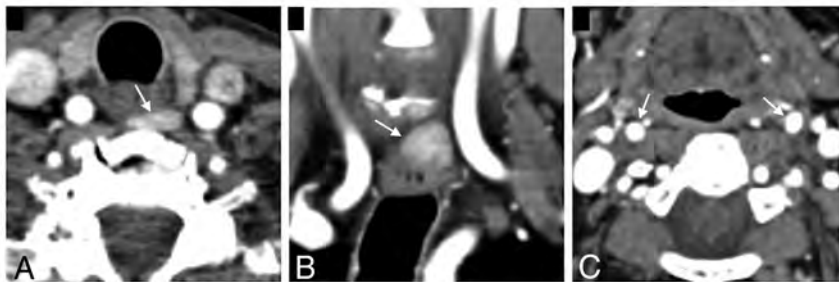


FIG 4. Case 4. Contrast-enhanced CT scan shows axial (A) and coronal (B) images of the retropharyngeal parathyroid adenoma (arrow) and an axial (C) image of the bilateral carotid arteries (arrow) at the level of the oropharynx.



FIG 5. Case 5. Contrast-enhanced CT scan shows axial (A) and coronal (B) images of the double retropharyngeal parathyroid adenomas (arrow) and an axial (C) image of the bilateral carotid arteries (arrow) at the level of the oropharynx.

esophagus and medial to the left common carotid artery (Fig 3), with corresponding increased MIBI uptake on SPECT/CT. The bilateral common carotid arteries appeared to be retropharyngeal and medialized with the adenoma in between the 2 arteries. The patient underwent a third parathyroidectomy. The left thyroid lobe was mobilized and retracted anteriorly, at which point the left common carotid artery was noted to be significantly medial, preventing easy identification of the parathyroid adenoma. After switching to a “backdoor” lateral approach (retraction of the sternohyoid and sternothyroid muscles anteriorly and more posterior dissection anterior to the sternocleidomastoid muscle), a classic parathyroid adenoma was accessed and identified in the retropharyngeal space posterior to the esophagus and medial to the left common carotid artery. The adenoma was dissected and excised.

In case 4, 4D CT revealed a left superior retroesophageal adenoma (12 × 12 × 5 mm), located immediately posterior to the left upper thyroid gland, 2 mm medial to the left common carotid artery (Fig 4). There was also an additional smaller hyperenhancing nodule adjacent to the right thyroid suggestive of a potential additional adenoma. The bilateral carotid arteries appeared to be in a relatively typical position. Because imaging suggested 2 potential adenomas, the patient underwent a bilateral neck exploration. Although imaging had suggested a left upper parathyroid adenoma, the left upper, left lower, and right lower glands all appeared to be of normal size and color in their usual positions. The retropharyngeal adenoma appeared to be an adenomatous right upper parathyroid gland, which was dissected and excised.

In case 5, 4D CT revealed bilateral superior parathyroid adenomas (double adenomas) in the retropharyngeal space: right (8 × 7 × 14 mm) and left (5 × 4 × 8 mm) (Fig 5). Both adenomas were located immediately medial to medialized bilateral carotid arteries and posterior to the esophagus. The right superior adenoma was approximately 5 mm posterior to the right mid-thyroid gland, and the left superior adenoma was

12 mm posteromedial to the left mid-thyroid gland. On SPECT/CT, the larger right adenoma was MIBI avid, but the smaller left adenoma was not. The patient is currently taking cinacalcet (Sensipar) for medical management of PHPT and was scheduled for parathyroidectomy, but this was delayed because of the coronavirus 2019 pandemic. Of note, 6 months before her 4D CT, she underwent a left adrenalectomy for a left pheochromocytoma with elevated plasma metanephrines and normetanephrines. Given the patient's age, both diseases were likely unrelated, sporadic, and not attributable to a genetic predisposition.

DISCUSSION

We have presented 5 patients with retropharyngeal parathyroid adenomas with varying anatomy of the carotid arteries. After applying the previously discussed grading system, all of these patients had at least 1 ICA that was grade II or higher, suggesting at least a moderate risk during pharyngeal procedures.⁵ Fortunately, all 4 patients who underwent surgery experienced no complications from intubation or the operation itself. To our knowledge, we are the first to report on a possible association between ectopic adenomas and medial deviations of the carotid arteries.

Theoretically, it is possible that these variants are related secondary to anomalous embryonic development in the neck. The parathyroid glands originate from the third (inferior glands) and fourth (superior glands) pharyngeal pouches, and the common carotid arteries and proximal ICAs derive from the third pharyngeal arch.⁷ Unsurprisingly, ectopic parathyroid glands are often found within structures that derive from neighboring embryologic tissues and descend into the neck, such as the thyroid, thymus, and carotid sheath.¹⁸ Other common locations for ectopic glands include the aforementioned retropharyngeal space, the tracheoesophageal groove, the thyrothymic ligament, and elsewhere in the mediastinum.¹¹

Clinically, this series highlights the importance of imaging for operative planning in parathyroid surgery. Advances in preoperative imaging have made it possible to localize disease and perform a focused parathyroidectomy in many patients, whereas the previous standard was a bilateral neck exploration.¹⁵ However, the utility of imaging in PHPT is dependent on the experience of the radiologist, who must be trained and experienced in parathyroid imaging to accurately interpret preoperative scans. Furthermore, when the radiologist suspects a retropharyngeal adenoma, it is especially critical to communicate to the surgeon any aberrant carotid anatomy that is at increased risk of injury when dissecting into the retropharyngeal space.

In summary, our experience with 5 patients raises the question of whether some association exists between retropharyngeal ectopic parathyroid adenomas and abnormal carotid artery anatomy, which could have implications for the radiologist and the parathyroid surgeon. Radiologists and surgeons alike should be aware of variations in carotid anatomy, and we agree with Pfeiffer et al⁵ on the importance of using a

universal grading system to describe these variations objectively and relate them to operative risk.

Disclosures: James Lee—UNRELATED: Board Membership: Medscape, Summus; Expert Testimony: Various firms on individual basis.

REFERENCES

1. Ozgur Z, Celik S, Govsa F, et al. **A study of the course of the internal carotid artery in the parapharyngeal space and its clinical importance.** *Eur Arch Otorhinolaryngol* 2007;264:1483–89 CrossRef Medline
2. Togay-Isikay C, Kim J, Betterman K, et al. **Carotid artery tortuosity, kinking, coiling: stroke risk factor, marker, or curiosity?** *Acta Neurol Belg* 2005;105:68–72 Medline
3. Munoz A, De Vergas J, Crespo J. **Imaging and clinical findings in patients with aberrant course of the cervical internal carotid arteries.** *Open Neuroimag J* 2010;4:174–81 CrossRef Medline
4. Paulsen F, Tillmann B, Christofides C, et al. **Curving and looping of the internal carotid artery in relation to the pharynx: frequency, embryology and clinical implications.** *J Anat* 2000;197(Pt 3):373–81 CrossRef Medline
5. Pfeiffer J, Becker C, Ridder GJ. **Aberrant extracranial internal carotid arteries: new insights, implications, and demand for a clinical grading system.** *Head Neck* 2016;38:E687–93 CrossRef Medline
6. Sai Kiran NA, Kiran Kumar VA, Sivaraju L, et al. **Management issues in a case of congenital craniovertebral junction anomaly with aberrant retropharyngeal midline course of bilateral cervical internal carotid arteries at C1-C2.** *World Neurosurg* 2018;114:94–98 CrossRef Medline
7. Mnatsakanian A, Minutello K, Anatomy BB. *Head and Neck, Retropharyngeal Space.* StatPearls Publishing; Updated 2020 Apr 3: <https://www.ncbi.nlm.nih.gov/books/NBK537044>. Accessed 2020 May 5
8. Wasserman JM, Sclafani SJ, Goldstein NA. **Intraoperative evaluation of a pulsatile oropharyngeal mass during adenotonsillectomy.** *Int J Pediatr Otorhinolaryngol* 2006;70:371–75 CrossRef Medline
9. Windfuhr JP, Stow NW, Landis BN. **Beware of kissing carotids.** *ANZ J Surg* 2010;80:668–69 CrossRef Medline
10. Basekim C, Gungor A, Kizilkay E. **Unilateral aberrant retropharyngeal internal carotid artery.** *Eurorad* 2005;Case 4282. <https://www.eurorad.org/case/4282>
11. Tatera D, Wong LM, Vikse J, et al. **The prevalence and anatomy of parathyroid glands: a meta-analysis with implications for parathyroid surgery.** *Langenbecks Arch Surg* 2019;404:63–70 CrossRef Medline
12. Phitayakorn R, McHenry CR. **Incidence and location of ectopic abnormal parathyroid glands.** *Am J Surg* 2006;191:418–23 CrossRef Medline
13. McIntyre CJ, Allen JL, Constantinides VA, et al. **Patterns of disease in patients at a tertiary referral centre requiring reoperative parathyroidectomy.** *Ann R Coll Surg Engl* 2015;97:598–602 CrossRef Medline
14. Wilhelm SM, Wang TS, Ruan DT, et al. **The American Association of Endocrine Surgeons Guidelines for Definitive Management of Primary Hyperparathyroidism.** *JAMA Surg* 2016;151:959–68 CrossRef Medline
15. Bunch PM, Kelly HR. **Preoperative imaging techniques in primary hyperparathyroidism: a review.** *JAMA Otolaryngol Head Neck Surg* 2018;144:929–37 CrossRef Medline
16. Bilezikian JP, Brandi ML, Eastell R, et al. **Guidelines for the management of asymptomatic primary hyperparathyroidism: summary statement from the Fourth International Workshop.** *J Clin Endocrinol Metab* 2014;99:3561–69 CrossRef Medline
17. Yeh R, Tay YD, Tabacco G, et al. **Diagnostic performance of 4D CT and sestamibi SPECT/CT in localizing parathyroid adenomas in primary hyperparathyroidism.** *Radiology* 2019;291:469–76 CrossRef Medline
18. Okuda I, Nakajima Y, Miura D, et al. **Diagnostic localization of ectopic parathyroid lesions: developmental consideration.** *Jpn J Radiol* 2010;28:707–13 CrossRef Medline

Postoperative Imaging Appearance of Iliac Crest Free Flaps Used for Palatomaxillary Reconstructions

M.L. Sandler, M. Griffin, M.H. Xing, E. Ansari, A.S. Khorsandi, and M.L. Urken



ABSTRACT

SUMMARY: The osteomyocutaneous iliac crest free flap is a reconstructive option for segmental mandibular or complex palatomaxillary defects. Familiarity with the radiographic appearance of free flaps such as the iliac crest is necessary for the postoperative evaluation of patients after mandibular, maxillary, or palatal reconstructions because it allows radiologists to properly monitor and interpret the appearance of the flap over time. This study presents a retrospective review of 5 patients who underwent palatomaxillary reconstruction with an iliac crest free flap at our institution. The imaging appearances of the 5 patients were analyzed to determine the key radiographic characteristics of a healthy and successful iliac crest free flap. Radiographic fluency with the imaging appearance of the iliac crest free flap, as well as the new anatomy of the region in the postoperative period, will allow for better interpretation of the flap appearance on imaging and will prevent false identification of tumor recurrence.

ABBREVIATIONS: ICFE = iliac crest free flap; DCIA = deep circumflex iliac artery; DCIV = deep circumflex iliac vein

Microvascular free tissue transfer is used for the reconstruction of complex defects, particularly after surgical treatment of malignant head and neck disease.¹ The ability to reliably transport free tissue into a defect has resulted in the innovation and refinement of a multitude of surgical approaches.² As a result, free flaps have been commonly used after ablative surgery for head and neck cancer. However, large defects of the midface area still represent a major reconstructive challenge to achieve a favorable cosmetic and functional outcome.

Free flaps can be broken down into 4 subtypes: muscular, fasciocutaneous, visceral, and osseous. Furthermore, free flaps can also be performed as composite tissue allografts consisting of heterogeneous tissues such as skin, fat, muscle, nerves, and in some instances, lymphatic tissue. Vascularized bone containing free flaps may be harvested as bone only or in combination with additional tissue types such as skin, subcutaneous tissue, fascia, and muscle.² This article focuses on the imaging appearance of the iliac crest free flap (ICFF) in the setting of

head and neck reconstruction. The ICFE has been described for the reconstruction of segmental mandibular and complex palatomaxillary defects.^{2,3} Because of the length, width, and contour of the iliac bone, the ICFE is considered to be an excellent source of vascularized bone for use in mandibular reconstruction.³⁻⁵ In the setting of primary maxillary reconstruction, this free flap can be used as a single-staged composite tissue transfer of vascularized soft tissue and bone to rehabilitate extensive palatomaxillary defects.⁶ The addition of the internal oblique muscle to this flap provides increased flexibility of the soft tissue component, above and beyond what the skin flap yields.^{4,5}

Fluency in the radiographic appearance of free flaps, like the iliac crest, is crucial in the evaluation of patients after palatomaxillary resections.¹ Reconstructive surgery disrupts the appearance of the normal anatomy, so it is important for radiologists and surgeons to be in close communication regarding details of the surgical procedure, flap type, and imaging findings.^{7,8} Not only will a basic understanding of the reconstructive techniques for patients with head and neck cancer allow radiologists to provide accurate and useful imaging reports,¹ such understanding will also prevent the potential misdiagnosis of subtle tumor recurrence or focal infection.⁹

In this study, we discuss the imaging appearance of the iliac crest–internal oblique osteomyocutaneous free flap and retrospectively review the postoperative imaging of 5 cases of palatomaxillary reconstruction with an ICFE. The goal of this study is to determine the key radiographic characteristics of an ICFE

Received August 31, 2020; accepted after revision November 24.

From the Thyroid, Head & Neck Cancer (THANC) Foundation, (M.L.S., M.G., M.H.X., M.L.U.), New York, New York; Department of Otolaryngology–Head and Neck Surgery (E.A., M.L.U.), Icahn School of Medicine at Mount Sinai Hospital, Mount Sinai Beth Israel, New York, New York; and Department of Radiology, (A.S.K.), NY Eye & Ear Infirmary of Mount Sinai, New York, New York.

Please address correspondence to Monica Xing, Research Associate, Thyroid, Head & Neck Cancer (THANC) Foundation, 10 Union Square East, Suite 5B, New York, NY 10003; e-mail: mxing@thancfoundation.org

<http://dx.doi.org/10.3174/ajnr.A7005>

Demographic information of 5 patients included in this study

Patient	Age at Surgery (years)	Sex	Tumor Type
1	55	Male	Squamous cell carcinoma with inverting papilloma
2	57	Female	Adenoid cystic carcinoma
3	59	Male	Adenocarcinoma
4	63	Female	Squamous cell carcinoma
5	13	Female	Ossifying fibroma

facilitate the analysis of postoperative imaging in patients with head and neck cancer.

MATERIALS AND METHODS

A retrospective review was performed of 5 patients who underwent palatomaxillary reconstruction with an ICFF at our institution between 1998 and 2016. We included only cases that had available postoperative imaging. Institutional review board approval was not required to report 5 retrospective cases. Relevant patient demographics, clinical information, and available imaging were reviewed and recorded. Postoperative imaging was reviewed by our senior head and neck radiologist and analyzed for key findings regarding flap appearance. Radiographic assessment points with respect to the appearance of the bone component of the flap included cortical thickness, attenuation, and continuity. Radiographic assessment points with respect to the appearance of muscle components included striations, enhancement, and atrophy. Imaging was reviewed from the immediate postoperative setting to 1 year postoperatively.

RESULTS

We selected 5 cases of iliac crest–internal oblique free flap reconstruction for review. Demographic information can be found in the Table. This cohort included 2 men and 3 women, with an average age of 49.4 years (range, 13–63 years). Primary tumor types included squamous cell carcinoma, adenoid cystic carcinoma, adenocarcinoma, and ossifying fibroma. Two cases involved an additional radial forearm free flap, and 1 case involved an additional lateral arm free flap.

In each of the 5 cases, the ICFF appeared as a thick sheet of bone with 2 cortical layers encasing the medullary bone. When used for palatomaxillary reconstruction, the cortical surfaces appear as U-shaped configurations with medullary bone encased within. There are 3 cortical surfaces, inferior, lingual, and buccal. The maxillary antrum was noted to be obliterated by the internal oblique muscle. The bone was seen to have an attenuated to hyperattenuated cortex and intermediate attenuation of the trabecular layer in 3 cases (cases 1–3). The osteotomy initially appeared as a bony fragment. On follow-up imaging, there were progressive callous formation and bony fusion at the osteotomy site. On CT imaging, the osseointegrated implants are seen as tubular metallic densities at the expected site of the dental implantation and created an extensive amount of streak artifact. Osseointegrated dental implants were present in 1 case (case 2). The muscle component of the flap appeared as areas of striation

similar to the appearance of skeletal muscle. The fat within the adjacent subcutaneous soft tissue appeared as low attenuation with a negative Hounsfield unit. On initial and follow-up postcontrast imaging, the muscular portion of the flap showed uniform enhancement. Progressive atrophy of the muscular component of the flap was shown in a 12-month follow-up period.

DISCUSSION

The ICFF, often harvested in conjunction with the internal oblique muscle, is highly versatile and well-suited for large head and neck defects because of the width, length, and natural curvature of the iliac bone, as well as its rich blood supply (Fig 1).^{2,3} The deep circumflex iliac artery and vein (DCIA and DCIV) are used as the flap pedicle.^{4,5,10} In most instances, the internal oblique muscle is supplied in an axial pattern by the ascending branch of the DCIA and DCIV, which run on its deep surface. The iliac bone can withstand the forces of mastication and can accommodate osseointegrated implants, thereby adding to its versatility.¹¹ The incorporation of the internal oblique muscle in conjunction with the mobility of the skin paddle relative to the bone flap enables the flap to be used in the restoration of complex 3D composite surgical defects of the palatomaxillary complex.¹² The flap may also be used to restore defects involving the inferior orbital rim, the zygoma, and the skin of the cheek.¹²

The iliac crest flap is commonly oriented vertically during flap inset to restore the vertical height of the maxilla, along with the alveolus, providing a fixed segment of bone ideal for osseointegrated dental implants.^{10,13} When oriented in this fashion, the thick cortical surface of the iliac crest is turned upside down and becomes the new alveolar ridge. Furthermore, this inset configuration permits reconstruction of the orbital rim and the pyriform aperture.¹² The orbital floor can also be reconstructed with a mesh alloplast, which is screwed into the anterior face of the iliac bone and the lateral orbital rim (Fig 1).¹² An onlay free bone graft can also be screwed into the bone of the iliac flap to replicate the anterior projection of the zygomatic body.¹² The internal oblique muscle, when harvested with the iliac crest bone, is transposed through the defect in the palatal shelf and medial to the neoalveolar ridge formed by the iliac bone. The muscle can then be used to fill the maxillectomy cavity, thereby obliterating the dead space and relining the lateral wall of the nose (Figs 1–3).¹² This muscle also provides a source of oral and nasal lining and serves as a neopalate and lateral nasal wall. In this way, the internal oblique muscle separates the oral and nasal cavities and creates a permanent soft tissue seal. As the muscle atrophies and undergoes epithelization, it effectively replicates the native palatal architecture.¹² Additionally, the flexibility of the soft tissue components of the iliac crest flap allow for large amounts of skin to be used to resurface the midface.¹² When imaged over time, the thickness and attenuation of the internal oblique muscle decrease as atrophic changes occur because of denervation.

The ICFF therefore offers improved functional and aesthetic rehabilitation over traditional methods (eg local or regional flaps, soft tissue only–free flaps, and obturation) given its ability to restore both osseous and soft tissue defects and to accommodate implants for dental rehabilitation.^{3,14} Although palatomaxillary reconstruction can be achieved with the fibular and scapular

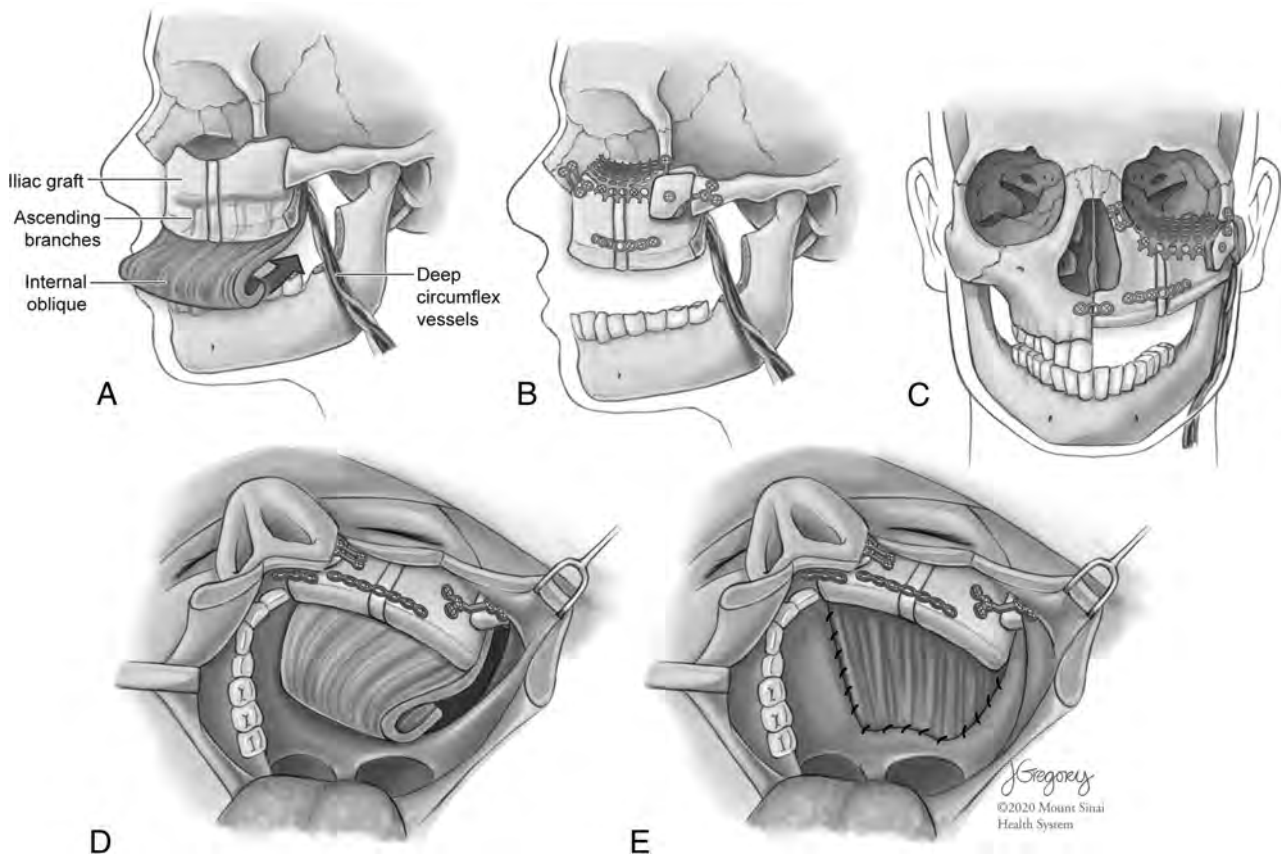


FIG 1. Use of ICFF with internal oblique muscle (A) and orbital floor plate. The iliac bone is used to restore the inferior orbital rim as well as to reconstruct the pyriform aperture. An onlay bone graft is lag screwed into the iliac bone to restore the anterior projection of the midface (B and C). The curvature of the neomaxilla has been created by performing a unicortical osteotomy and filling it with corticocancellous bone followed by a fixation plate to hold it in position. The internal oblique muscle is used to reline the lateral wall of the nose and obliterate the maxillectomy cavity (D and E). The muscle is transposed through the palatal defect to achieve a permanent separation of the mouth from the sinonasal cavity. Illustration by Jill Gregory. Used with permission from ©Mount Sinai Health System.

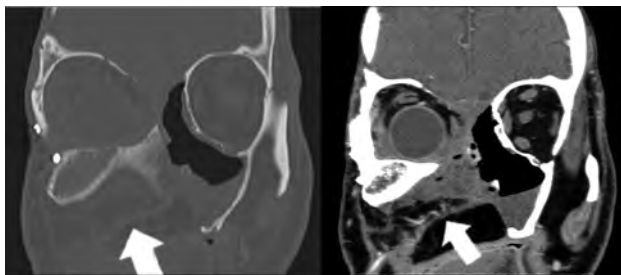


FIG 2. The internal oblique muscle from the flap eliminates the maxillectomy cavity, thereby preventing the presence of dead space (arrows).

donor sites, the iliac crest provides a large amount of good-quality bone for harvest, which can then be contoured to reconstruct both the horizontal and vertical components of even extensive defects.¹⁰

Traditionally, the ICFF was thought to cause high rates of donor site morbidity, including abdominal wall weakness, risk of hernia, abnormal hip contour, and difficulty with ambulation in the early postoperative period.¹⁵ However, improvements in surgical technique have mitigated this risk, thereby increasing the value of the flap.^{4,5,13-16}

Conventional Imaging Appearance

On postoperative CT imaging, the osseous component of the ICFF appears as a thick sheet of bone with 2 cortical layers and a sclerotic trabecular surface. The bone has a hyperattenuated cortex and intermediate attenuation of the trabecular layer (Fig 4). The osseous component of the flap may be used to restore the normal osseous boundaries of the maxilla, alveolus, orbital rim, and pyriform aperture. The ilium is thickest at the spine and narrows posteriorly but appears on 2D imaging as a uniformly thick sheet of bone.¹⁷

When the internal oblique muscle is used to obliterate the maxillary cavity, it is seen on imaging as opacification of the maxillary antrum.¹² Transposition of the internal oblique muscle through the defect creates a neopalate medial to the neopalveolar ridge formed by iliac bone. The muscular components of the flap will appear striated and thin.¹ McCarty et al¹ have reported that in the initial postoperative period, the muscular components of the flap may appear hypointense on T1-weighted images and hyperintense on T2-weighted images and enhance with gadolinium contrast. However, as the muscle atrophies and becomes more fatty, it will appear heterogeneous on both T1-weighted and T2-weighted images and more hypoattenuated on CT.¹⁸ Muscle denervation

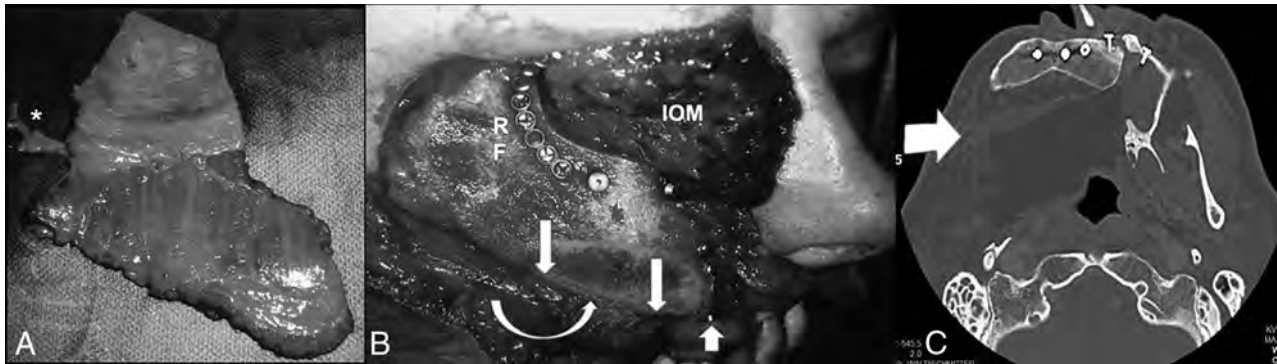


FIG 3. A, An iliac crest–internal oblique flap has been harvested based on the DCIA and DCIV (*asterisk*). B, The iliac crest is shown inset into a palatomaxillectomy defect with the crest oriented toward the bottom (*arrow*). The internal oblique muscle based on the ascending branch of the DCIA has been brought through the palatal defect, medial to the iliac bone (*curved arrow*). This patient underwent an orbital exenteration, and the internal oblique muscle (IOM) is shown filling the orbital defect as well as obliterating the maxillectomy cavity. Rigid fixation (RF) is achieved to the lateral and superior orbital rim. The *upgoing arrow* shows a dental implant placed into the neoalveolar ridge. C, The internal oblique muscle, which is not optimally visualized on bone window, is used to fill the maxillectomy defect (*arrow*).



FIG 4. Axial imaging of a normal ICF demonstrating a thick sheet of bone with a hyperattenuated cortex and intermediate attenuation of the trabecular surface. An osteotomy site is demonstrated and filled with corticocancellous bone (*arrow*). Images were obtained in the immediate postoperative period. Left cheek prominence is an expected immediate postoperative finding in the flap setting. Normal cheek cosmesis will be obtained over time.

after flap harvest is believed to contribute to the increased enhancement of the muscular components of the flap over time.¹⁹ The muscular enhancement with gadolinium should not be mistaken for tumor recurrence.¹⁹ Sharp boundaries between the muscular components of the flap and nearby native structures generally indicate a benign process.⁷ Familiarity with flap maturation is important, specifically the tendency of the muscular portion of the flap to progress toward fatty atrophic changes, to avoid false identification of recurrent disease. The

fatty components of the flap should contain no areas of nodularity or focal enhancement.¹

Contouring of the iliac bone can be accomplished by performing a unicortical osteotomy in the lateral surface and the iliac crest, which permits the bone to be “green stick fractured,” if a bend in the bone is required to accommodate to the normal architecture of the palatomaxillary complex. By creating this cut in this orientation, the DCIA and DCIV are preserved along the medial surface. The resulting “open osteotomy” is usually filled with corticocancellous bone chips that are harvested from the remaining iliac bone. Over time, this osteotomy will form solid bone. It should be noted that the goal of reconstruction is to place the neoalveolar maxillary ridge in direct apposition to the mandibular alveolus to facilitate dental restoration and normal occlusal relationships.

Osseointegrated dental implants are often inset into the ICF (Figs 3 and 5).¹² Postoperative imaging evaluation is crucial for accurate monitoring of the angular position of the implants, their relationship with the adjacent bone, and the condition of the implants over time.²⁰ Periapical radiographs, panoramic radiographs, and CT imaging can all be used to evaluate dental implants.²¹ In particular, CT imaging can be used to evaluate bone-to-metal contact and identify any implant complications, such as hardware loosening.²²

The ICF also accommodates a mesh alloplast, which can be screwed to the anterior face of the iliac bone and lateral orbital rim to restore the orbital floor and reestablish a normal orbital volume (Figure 1B, -C). Imaging can be used to evaluate the position of these reconstructive techniques in the postoperative period and can also assess the orbital volume if there is any evidence of dystopia after disruption and reconstruction of the orbital floor. Any plates used in the procedure should appear level with both the new and native bone, and no lucency should be seen surrounding any screws (Fig 5).¹

Although the DCIA and ascending branches are important components of the flap, they are generally too small to be visible on standard diagnostic imaging but can be readily seen on CTA or MRA. The normal course of the DCIA and DCIV extends



FIG 5. Normal appearance of reconstructive plates and osseointegrated dental implants (arrow).

from the lingual surface of the iliac bone and passes either medial or lateral to the mandible to reach recipient vessels in the neck to revascularize the free flap.

Optimal Timing of Postoperative Imaging

The following postoperative imaging recommendations are based on author experience and may be approached more flexibly depending on individual institutional guidelines. Initial posttreatment imaging should be used to evaluate the appearance of the flap itself. Radiologists can ensure that no osteolysis nor bony erosion are present.¹ Initial posttreatment images can serve as a baseline to document any changes caused by treatment (both surgical and nonsurgical). These images can also provide a comparison for future examinations to better detect possible complications.²³ The CT portion of the examination should be used to evaluate the osseous borders of the flap for union, ensure that all fixation plates are still flush with the bone, and monitor for hardware lucency surrounding any inset screws.¹ Bridging new bone may be observed at the interface between the iliac bone and the native bone of the midface. Additionally, radiologists should re-examine preoperative scans in the postoperative setting to establish the extent and location of resection.¹ An understanding of both the preoperative and initial postoperative scans will assist in avoiding incorrect identification of recurrence on future imaging. For example, lymph nodes are sometimes transposed as part of the flap. This finding should be noted on baseline imaging to avoid falsely identifying such lymph nodes as recurrent disease on future imaging.

Approximately 12 weeks after treatment (either postsurgery or postradiation treatment), a PET/CT examination with contrast is recommended. This examination can be used to detect any persistent or recurrent tumor or metastases and to distinguish between treatment-related changes and new neoplastic changes.¹ The CT with contrast and the PET scan should be used in combination to evaluate the muscular portion and borders of the flap as a baseline.

These scans will also improve the future detection of any recurrent, residual, or persistent disease.¹ MR imaging can be useful in detecting perineural invasion, intracranial extension, and cartilaginous involvement, among others.¹ As such, this imaging technique should be used in patients in whom there is a concern for risk for perineural invasion.⁷ Depending on a patient's tumor type and surgical margin status, clinician familiarity with perineural extension of disease at the time of preoperative imaging interpretation is also recommended. Subsequently, surveillance imaging is recommended every 4 months for 2 years after surgery.⁷ The authors concede that the imaging intervals specified may not conform to the practice of all institutions.

CONCLUSIONS

Radiographic imaging is crucial to the postoperative management of microvascular free flaps. The ICF is highly versatile in reconstructing large head and neck defects because of the bone's natural curvature, its rich blood supply, and its ability to accommodate osseointegrated implants. Harvest of the ICF in conjunction with the internal oblique muscle allows for the restoration of complex 3D defects of the palatamaxillary complex. Each component of the flap is associated with an expected radiographic appearance, which should be assessed throughout the postoperative period. Familiarity with the radiographic appearance of the ICF is necessary for the evaluation of patients after maxillary or palatal resections because it allows clinicians to provide accurate imaging reports and to properly monitor the appearance of the flap over time.

REFERENCES

1. McCarty JL, Corey AS, El-Deiry MW, et al. **Imaging of surgical free flaps in head and neck reconstruction.** *AJNR Am J Neuroradiol* 2019;40:5-13 CrossRef Medline
2. Urken ML, Cheney M, Blackwell K, et al. *Atlas of Regional and Free Flaps for Head and Neck Reconstruction.* Philadelphia: Wolters Kluwer Health/Lippincott Williams & Wilkins; 2012
3. Cariati P, Arroyo Rodriguez S, Pampin Ozan D, et al. **Iliac crest free flap: indications, tips and pitfalls.** *Front Oral Maxillofac Med* 2020; 2:15 CrossRef
4. Urken ML, Vickery C, Weinberg H, et al. **The internal oblique-iliac crest osseomyocutaneous free flap in oromandibular reconstruction. Report of 20 cases.** *Arch Otolaryngol Head Neck Surg* 1989; 115:339-49 CrossRef Medline
5. Urken ML, Vickery C, Weinberg H, et al. **The internal oblique-iliac crest osseomyocutaneous microvascular free flap in head and neck reconstruction.** *J Reconstr Microsurg* 1989;5:203-14; discussion 215-16 CrossRef Medline
6. Genden EM, Wallace D, Buchbinder D, et al. **Iliac crest internal oblique osteomusculocutaneous free flap reconstruction of the postablative palatamaxillary defect.** *Arch Otolaryngol Head Neck Surg* 2001;127:854-61 Medline
7. Saito N, Nadgir RN, Nakahira M, et al. **Posttreatment CT and MR imaging in head and neck cancer: what the radiologist needs to know.** *Radiographics* 2012;32:1261-82; discussion 1282-84 CrossRef Medline
8. Hudgins PA. **Flap reconstruction in the head and neck: expected appearance, complications, and recurrent disease.** *Eur J Radiol* 2002;44:130-38 CrossRef Medline
9. Kumar VA, Hofstede TM, Ginsberg LE. **CT imaging features of obturator prostheses in patients following palatotomy or maxillectomy.** *AJNR Am J Neuroradiol* 2011;32:1926-29 CrossRef Medline

10. Brown JS. **Deep circumflex iliac artery free flap with internal oblique muscle as a new method of immediate reconstruction of maxillectomy defect.** *Head Neck* 1996;18:412–21 CrossRef Medline
11. Blackwell KE, Urken ML. **Iliac crest free flap.** *Facial Plast Surg* 1996; 12:35–43 CrossRef Medline
12. Urken ML, Roche AM, Kiplagat KJ, et al. **Comprehensive approach to functional palatomaxillary reconstruction using regional and free tissue transfer: report of reconstructive and prosthodontic outcomes of 140 patients.** *Head Neck* 2018;40:1639–66 CrossRef Medline
13. Leporati M, Ferrari S, Ferri A, et al. **Iliac crest free flap for maxillary reconstruction.** *J Oral Maxillofac Surg* 2011;40:1040 CrossRef Medline
14. Bianchi B, Ferri A, Ferrari S, et al. **Iliac crest free flap for maxillary reconstruction.** *J Oral Maxillofac Surg* 2010;68:2706–13 CrossRef Medline
15. Shenao SM, Klebuc MJA, Shenaq J, et al. **Mandibular reconstruction with the iliac crest, composite, microsurgical free flap.** *Oper Tech Plast Reconstruct Surg* 1996;3:289–94 CrossRef
16. Safak T, Klebuc MJ, Mavili E, et al. **A new design of the iliac crest microsurgical free flap without including the “obligatory” muscle cuff.** *Plast Reconstr Surg* 1997;100:1703–09 CrossRef Medline
17. Hernigou J, Alves A, Homma Y, et al. **Anatomy of the ilium for bone marrow aspiration: map of sectors and implication for safe trocar placement.** *Int Orthop* 2014;38:2585–90 CrossRef Medline
18. Offiah C, Hall E. **Post-treatment imaging appearances in head and neck cancer patients.** *Clin Radiol* 2011;66:13–24 CrossRef Medline
19. Chong J, Chan LL, Langstein HN, et al. **MR imaging of the muscular component of myocutaneous flaps in the head and neck.** *AJNR Am J Neuroradiol* 2001;22:170–74 Medline
20. Al-Ekrish AA. **Radiology of implant dentistry.** *Radiol Clin North Am* 2018;56:141–56 CrossRef Medline
21. Zohrabian VM, Sonick M, Hwang D, et al. **Dental implants.** *Semin Ultrasound CT MR* 2015;36:415–26 CrossRef Medline
22. DelBalso AM, Greiner FG, Licata M. **Role of diagnostic imaging in evaluation of the dental implant patient.** *Radiographics* 1994;14: 699–719 CrossRef Medline
23. Hermans R. **Post-treatment imaging of head and neck cancer.** *Cancer Imaging* 2004;4(Spec No A):S6–S15 CrossRef Medline

Radiomics of Pediatric Low-Grade Gliomas: Toward a Pretherapeutic Differentiation of *BRAF*-Mutated and *BRAF*-Fused Tumors

M.W. Wagner, N. Hainc, F. Khalvati, K. Namdar, L. Figueiredo, M. Sheng, S. Laughlin, M.M. Shroff, E. Bouffet, U. Tabori, C. Hawkins, K.W. Yeom, and B.B. Ertl-Wagner



ABSTRACT

BACKGROUND AND PURPOSE: *B-Raf proto-oncogene, serine/threonine kinase (BRAF)* status has important implications for prognosis and therapy of pediatric low-grade gliomas. Currently, *BRAF* status classification relies on biopsy. Our aim was to train and validate a radiomics approach to predict *BRAF* fusion and *BRAF* V600E mutation.

MATERIALS AND METHODS: In this bi-institutional retrospective study, FLAIR MR imaging datasets of 115 pediatric patients with low-grade gliomas from 2 children's hospitals acquired between January 2009 and January 2016 were included and analyzed. Radiomics features were extracted from tumor segmentations, and the predictive model was tested using independent training and testing datasets, with all available tumor types. The model was selected on the basis of a grid search on the number of trees, opting for the best split for a random forest. We used the area under the receiver operating characteristic curve to evaluate model performance.

RESULTS: The training cohort consisted of 94 pediatric patients with low-grade gliomas (mean age, 9.4 years; 45 boys), and the external validation cohort comprised 21 pediatric patients with low-grade gliomas (mean age, 8.37 years; 12 boys). A 4-fold cross-validation scheme predicted *BRAF* status with an area under the curve of 0.75 (SD, 0.12) (95% confidence interval, 0.62–0.89) on the internal validation cohort. By means of the optimal hyperparameters determined by 4-fold cross-validation, the area under the curve for the external validation was 0.85. Age and tumor location were significant predictors of *BRAF* status (P values = .04 and <.001, respectively). Sex was not a significant predictor (P value = .96).

CONCLUSIONS: Radiomics-based prediction of *BRAF* status in pediatric low-grade gliomas appears feasible in this bi-institutional exploratory study.

ABBREVIATIONS: AUC = area under the curve; JPA = juvenile pilocytic astrocytoma; NPV = negative predictive value; pLGG = pediatric low-grade glioma; PPV = positive predictive value; ROC = receiver operating characteristic

Pediatric low-grade gliomas (pLGGs) are the most common brain tumors in children, accounting for approximately 40% of central nervous system tumors in childhood.¹ pLGGs comprise a heterogeneous variety of tumors classified by the World Health Organization as grades I or II and include juvenile pilocytic astrocytoma (JPA), ganglioglioma, dysembryoplastic neuroepithelial tumor, pleomorphic xanthoastrocytoma, and diffuse low-grade

glioma.² A mainstay of pLGG therapy is surgical excision when possible, which may be curative in case of total resection.² When total resection is not possible, pLGGs become a chronic disease with protracted reduction in the quality of life.^{2,3} While death from these tumors is rare with standard chemotherapy and radiation, 10-year progression-free survival is <50%.^{4,5} Thus, many patients will have multiple recurrences requiring multimodal therapy, leading to considerable morbidity.

In addition to patients with neurofibromatosis type 1 who develop pLGG, molecular characterization of sporadic pLGG has

Received May 20, 2020; accepted after revision October 23.

From the Departments of Diagnostic Imaging (M.W.W., N.H., F.K., K.N., M.S., S.L., M.M.S., B.B.E.-W.), Division of Neuroradiology, Neurooncology (L.F., E.B., U.T.), and Paediatric Laboratory Medicine (C.H.), Division of Pathology, The Hospital for Sick Children and Department of Medical Imaging, University of Toronto, Toronto, Ontario, Canada; Department of Neuroradiology (N.H.), Zurich University Hospital, University of Zurich, Zurich, Switzerland; and Department of Radiology (K.W.Y.), Stanford University School of Medicine, Lucile Packard Children's Hospital, Palo Alto, California.

M.W. Wagner and N. Hainc are shared first authors.

C. Hawkins was supported by the Canadian Cancer Society (grant No. 702296) and the Canadian Institute of Health Research (grant No. 159805).

Please address correspondence to Matthias W. Wagner, MD, The Hospital for Sick Children, Department of Diagnostic Imaging, 555 University Ave, Toronto, ON M5G 1X8, Canada; e-mail: m.w.wagner@me.com

Indicates open access to non-subscribers at www.ajnr.org

Indicates article with online supplemental data.

<http://dx.doi.org/10.3174/ajnr.A6998>

also identified frequent alterations in the mitogen-activated protein kinase pathway, most commonly fusions or mutations in the *B-Raf proto-oncogene, serine/threonine kinase (BRAF)* gene. The 2 major *BRAF* gene alterations are *BRAF* fusion and *BRAF* V600E point mutation (p.V600E). The chromosomal alteration in *BRAF* fusion involves the duplication of the *BRAF* oncogene, followed by its insertion into one of several fusion targets, most often the *KIAA1549* gene.⁶ The transcript of this duplication/fusion contains the kinase terminus of the *BRAF* protein but lacks the autoregulatory domain, resulting in constant up-regulation of several downstream pathway elements. *BRAF* V600E point mutations constitutively activate *BRAF*, causing a deregulation in the mitogen-activated p.V600E protein kinase pathway.⁷

Lassaletta et al⁸ recently demonstrated that patient prognosis differed in pLGGs on the basis of the underlying molecular alteration. Patients with *BRAF* fusion and neurofibromatosis type 1 have a favorable outcome, while those with the *BRAF* V600E mutation, particularly in association with *cyclin dependent kinase inhibitor 2A (CDKN2A)* deletion, are at increased risk of progression and transformation.^{8,9} This finding has led to clinical trials using mitogen-activated protein kinase pathway-targeted agents such as mitogen-activated protein kinase enzyme inhibitors and *BRAF* V600E inhibitors for patients with molecular evidence of *BRAF* alterations. These new therapies seem promising, and many pLGGs that were refractory to traditional chemotherapy have had meaningful responses to these targeted agents.^{10,11}

In the past decade, radiomics has emerged as an imaging-based method to link quantitative features extracted from medical images to outcomes, such as cancer genotype or survival.^{12,13} Radiomic signatures have been extensively investigated for different cancer sites including liver cancer,¹⁴ bone tumors,¹⁵ and adult brain tumors including glioblastoma,¹⁶ medulloblastoma,¹⁷ and midline high-grade glioma.^{18,19} To our knowledge, no prior study has investigated radiomic approaches to subtype pLGGs.

Using a bi-institutional cohort, we aimed to develop and validate a radiomic signature that is predictive of the *BRAF* status of pLGGs.

MATERIALS AND METHODS

Patients

This retrospective study was approved by the institutional review board or research ethics board of the 2 participating academic institutions: The Hospital for Sick Children (Toronto, Ontario, Canada) and the Lucile Packard Children's Hospital (Stanford University, Palo Alto, California). Because of the retrospective nature of the study, informed consent was waived by the local research ethics boards. An interinstitutional data-transfer agreement was obtained for data-sharing. All patients were identified from the electronic health record data base at Toronto and Stanford from January 2009 to January 2016. Patient inclusion criteria were the following: 1) 0–18 years of age, 2) availability of molecular information on *BRAF* status in histopathologically confirmed pLGG, and 3) availability of preoperative brain MR imaging with a non-motion-degraded FLAIR sequence. Patients with histone H3 K27M mutation were excluded. Spinal cord tumors were also not considered for this study.

Molecular Analysis

BRAF fusion status was determined using an nCounter Metabolic Pathways Panel (NanoString Technologies) or fluorescence in situ hybridization, while the *BRAF* p.V600E mutation was determined using immunohistochemistry or droplet digital polymerase chain reaction as previously described.²⁰ For most patients, molecular analysis was performed with formalin-fixed paraffin-embedded tissue that was obtained at the time of the operation. Nineteen patients had molecular subtyping based on frozen tissue.

MR Imaging Acquisition, Data Retrieval, and Image Segmentation

All patients from The Hospital for Sick Children, Toronto, underwent brain MR imaging at 1.5T or 3T across various vendors (Signa, GE Healthcare; Achieva, Philips Healthcare; Magnetom Skyra, Siemens). Sequences acquired included 2D axial and coronal T2 FLAIR (TR/TE, 7000–10,000/140–170 ms; 3- to 6-mm section thickness; 3- to 7.5-mm gap), 2D axial T2-weighted fast spin-echo, 3D axial or sagittal precontrast, and 3D axial gadolinium-based contrast agent-enhanced T1-weighted turbo or fast-field echo. Patients from the Lucile Packard Children's Hospital, Stanford, underwent brain MR imaging at 1.5T or 3T from a single vendor (Signa or Discovery 750; GE Healthcare). MRIs were performed using the brain tumor protocol of the institution, which included 2D axial T2-weighted fast spin-echo, 2D axial or sagittal precontrast T1-weighted spin-echo, 2D axial T2 FLAIR (TR/TE, 7000–10,000/140–170 ms; 4- to 5-mm section thickness; 1- to 1.5-mm gap), and 2D axial gadolinium-based contrast agent-enhanced T1-weighted spin-echo sequences. All MR imaging data were extracted from the respective PACS and were de-identified for further analyses.

Tumor segmentation was performed by a fellowship-trained pediatric neuroradiologist with 6 years of neuroradiology research experience (M.W.W.) using 3D Slicer (Version 4.10.2,²¹ <http://www.slicer.org>). The scripted loadable module SlicerRadiomics extension was used to obtain access to the radiomics feature-calculation classes implemented in the pyradiomics library (<http://pyradiomics.readthedocs.io/>). This extension selects all available feature classes and ensures isotropic resampling under “resampled voxel size” when extracting 3D features. The bin width was set to 25 (ie, default), and symmetric gray level co-occurrence matrix was enforced. Semiautomated tumor segmentation on FLAIR images was performed with the level tracing-effect tool. This semiautomatic approach had been found superior to multiuser manual delineation with regard to the reproducibility and robustness of results.¹⁷ Final and proper placement of ROIs was confirmed by a board-certified neuroradiologist (B.B.E.-W., with 15 years of postfellowship experience).

Radiomic Feature-Extraction Methodology

A total of 851 MR imaging-based radiomic features were extracted from the ROIs on FLAIR images. Radiomic features included histogram, shape, and texture features with and without wavelet-based filters. Features of Laplacian of Gaussian filters were not extracted. All features are summarized in the Online Supplemental Data. Bias field correction before *z* score normalization was used to standardize the range of all image

features.^{22,23} Once the features were extracted, we applied *z* score normalization again followed by L2 normalization to the features of cohort 1 and used the distribution of the features in cohort 1 (training data) to normalize cohort 2 (test data). Details of pre-processing and radiomic feature extraction in 3D Slicer and other software have been described elsewhere.^{12,16,24}

Statistical Analysis

Feature Selection, Radiomics, and Machine Learning Approach. We used random forest as the classification model²⁵ and performed both internal cross-validations using cohort 1 data (*n* = 94) as well as external validation using cohort 2 (*n* = 21) with the molecular subtype as the end point.

Internal Cross-Validation. First, we used cohort 1 in *k*-fold cross-validation to find the best hyperparameter for the random forest model, namely the number of trees in the random forest. Once the optimal number of trees was found, it was used to perform 4-fold internal cross-validations using cohort 1.

External Validation. Next, using the optimal number of trees found in the previous step, the entire dataset in cohort 1 was used to train a random forest model, which was then tested on cohort 2. Cohort 2 was never used in any stage of the training of the random forest model and was only used for external validation.

Next, the area under the receiver operating characteristic (ROC) curve (AUC) was calculated for both internal and external validations. In addition, the top 10 features that contributed the most to the random forest model were extracted.

Clinical Factors. For clinical factors (age, sex, anatomic location of tumor), logistic regression was performed to determine the predictive power of each factor in determining the molecular subtypes.

RESULTS

Patients

A total of 115 patients were included (The Hospital for Sick Children, *n* = 94, Lucile Packard Children's Hospital, *n* = 21) comprising 57 boys; mean age, 9.21 (SD, 10.81) years (Table 1). Patient demographic and pathologic information consisted of age at diagnosis, sex, histologic diagnosis, molecular diagnosis regarding the *BRAF* status, and anatomic location of the tumor (supra-versus infratentorial). We used the patient data from The Hospital for Sick Children (cohort 1, *n* = 94) for internal validation using cross-validation. We then used cohort 1 to train an optimized model and tested it (external validation) on the patient data from the Lucile Packard Children's Hospital (cohort 2, *n* = 21).

Radiomics Model Evaluation

Internal Validation. The number of trees, best-performing features, AUC, and other classification metrics for the 4-fold cross-validation are shown in Tables 2 and 3. For the internal validation, only data from cohort 1 were used. The ROC curve with a 4-fold cross-validation scheme to predict *BRAF* status is shown in Fig 1. The internal validation yielded an AUC of 0.75 (SD, 0.1) (95% CI, 0.62–0.89) for the 4-fold cross-validation. The mean sensitivity, specificity, positive predictive value (PPV), and

Table 1: Patient demographics

	Institutional Cohort	
	Toronto	Stanford
No. of patients	94	21
Age (mean) (yr)	9.4	8.37
Male sex (No.) (%)	45 (48)	12 (57)
Histologic diagnosis (No.)		
JPA	54	12
GG	14	7
LGA	11	
PMA	4	2
PXA	5	
DNET	2	
DA	2	
GC	1	
ODG	1	
Molecular subgroup (No.) (%)		
<i>BRAF</i> fusion	62 (66)	14 (66)
<i>BRAF</i> mutation	32 (34)	7 (34)
FLAIR availability (No.)	94	21
Supratentorial (No.) (%)	43 (46)	6 (28)
Transtentorial (No.) (%)	0	1 (5)
Infratentorial (No.) (%)	51 (54)	14 (67)

Note:—GG indicates ganglioglioma; LGA, low-grade astrocytoma; PMA, pilomyxoid astrocytoma; PXA, pleomorphic xanthoastrocytoma; DNET, dysembryoplastic neuroepithelial tumor; DA, diffuse astrocytoma; GC, gangliocytoma; ODG, oligodendroglioma.

negative predictive value (NPV) were 0.72, 95% CI, 0.60–0.84; 0.86, 95% CI, 0.76–0.95; 0.73, 95% CI, 0.60–0.87; and 0.85, 95% CI, 0.80–0.91, respectively.

External Validation. By means of the optimal hyperparameters obtained from 4-fold internal validation, the AUC for external validation was 0.85 (Fig 2). The Youden J statistic²⁶ was used to determine the optimal threshold on the external ROC curve to calculate sensitivity, specificity, PPV, and NPV, which are listed in the Online Supplemental Data.

Identification of Discriminative Clinical Factors

Clinical Factors. The distribution of infratentorial and supratentorial tumors is shown in Table 1. Predictive clinical factors for *BRAF* status were analyzed on cohort 1 (Table 4). Older age was a predictor of *BRAF* V600E mutation (*P* value = .04; OR, 1.14; 95% CI, 1.008–1.30) and as expected, supratentorial tumor location was a very strong predictor of *BRAF* V600E (*P* value < .001; OR, 18.80; 95% CI, 4.96–94.6). Sex was not a predictor (*P* value = .96).

Combined Clinical and Radiomics Model Evaluation

Internal Validation. We appended the 2 predictive clinical factors for *BRAF* status (age and tumor location) to the radiomics model outlined above. For the internal validation, only data from cohort 1 were used. The internal validation yielded an AUC of 0.77 (SD, 0.10) (95% CI, 0.65–0.88) for 4-fold cross-validation. The mean sensitivity, specificity, PPV, and NPV were 0.72, 95% CI, 0.60–0.84; 0.86, 95% CI, 0.78–0.93; 0.73, 95% CI, 0.63–0.83; and 0.86, 95% CI, 0.80–0.91, respectively. The improvement of our internal cross-validation compared with the radiomics-only model was not statistically significant (*P* value > .05).

Table 2: Performance of radiomic features

No. of Folds	No. of Trees	AUC (SD) (95% CI)	Mean Sensitivity (95% CI)	Mean Specificity (95% CI)	Mean PPV (95% CI)	Mean NPV (95% CI)	Top 10 Predictive Features on the External Dataset
4	25	0.75 (SD, 0.12) (0.62–0.89)	0.72 (0.60–0.84)	0.86 (0.76–0.95)	0.73 (0.60–0.87)	0.85 (0.80–0.91)	(585, 374, 761, 22, 17, 560, 344, 258, 148, 108)

Note:—SD indicates Standard Deviation; PPV, Positive Predictive Value; NPV; Negative Predictive Value.

Table 3: Predictive radiomic features^a

No.	Source	Feature Category	Feature
585	3D wavelet transform	Gray-level difference matrix	Small dependence low gray-level emphasis
374	3D wavelet transform	Gray-level size zone matrix	Zone percentage
761	3D wavelet transform	Gray-level difference matrix	Dependence entropy
22	Original	Gray-level difference matrix	Dependence nonuniformity normalized
17	Original	Gray-level difference matrix	Dependence entropy
560	3D wavelet transform	Gray-level size zone matrix	Zone percentage
344	3D wavelet transform	Histogram	Entropy
258	3D wavelet transform	Gray-level run-length	Gray-level variance
148	3D wavelet transform	Histogram	Uniformity
108	3D wavelet transform	Gray-level difference matrix	Gray-level variance

^aRadiomic features are ranked from top to bottom according to their importance.

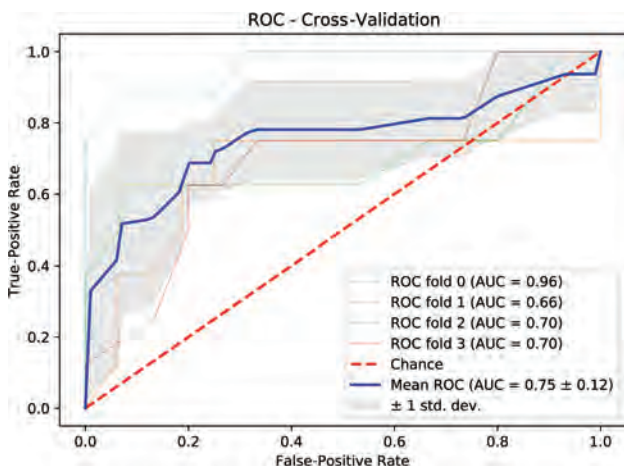


FIG 1. Receiver operating characteristic curve with a 4-fold cross-validation scheme to predict *BRAF* status using radiomics of FLAIR MR images. Std. dev. indicates standard deviation.

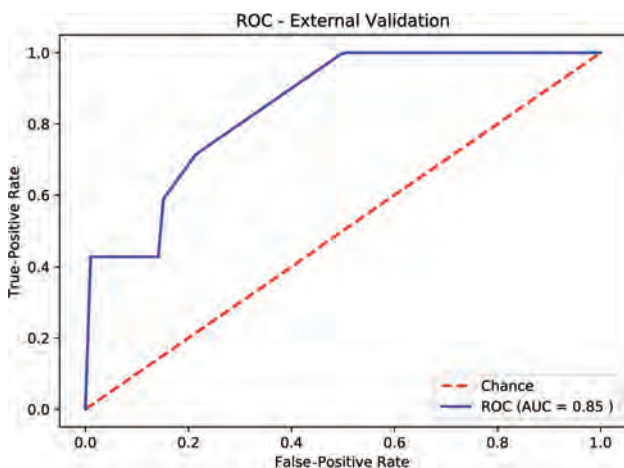


FIG 2. Receiver operating characteristic curve of the external validation using the optimal hyperparameters obtained by 4-fold cross-validation.

External Validation. After we appended the 2 predictive clinical factors to the radiomics model, the AUC for external validation decreased to 0.67. The Youden J statistic²⁶ was used to determine the optimal threshold on the external ROC curve to calculate sensitivity, specificity, PPV, and NPV, which are listed in the Online Supplemental Data.

DISCUSSION

In this bi-institutional study, we generated and validated a radiomic signature predictive of the *BRAF* status of pLGGs. The optimal random forest model achieved an AUC of 0.85 on the external validation dataset.

Currently, the molecular signature of pLGG is assessed through analysis of the tumor tissue. To that end, patients with nonresectable tumors are submitted to surgical procedures. Prognostication and targeted therapy depend on the mutational status. In this context, imaging could play a pivotal role if it allows identification of pLGG molecular subgroups. However, to date, we lack accurate imaging biomarkers that may facilitate this task.

Although genetic alterations of pLGGs are well-analyzed,^{8,20,27} little is known about the correlation between molecular markers and imaging characteristics. While many studies investigated the use of qualitative and quantitative features derived from conventional and advanced sequences to differentiate high- and low-grade pediatric brain tumors,^{28–38} only a few studies tried to link imaging characteristics to molecular markers.^{18,19,39–44} Ho et al³⁹ described different MR imaging patterns based on 15 cases of *BRAF* V600-mutated diencephalic pLGGs and 25 cases of *BRAF* V600 wild-type JPA/pilomyxoid astrocytomas. Among their findings, which were based on analysis of T2WI and contrast-enhanced T1 sequences, they reported that *BRAF* V600 wild-type JPA/pilomyxoid astrocytoma presented predominantly as a solitary solid mass with homogeneous or heterogeneous contrast enhancement, whereas the mutated pLGG appeared multiloculated or multinodular following contrast administration.³⁹ Quantitative imaging features differentiating pLGG molecular subgroups were studied in only 1 small case

Table 4: Discriminative clinical factors^a

Variable	P Value	Odds Ratio (95% CI)
Age	.04	1.14 (1.008–1.30)
Location	<.001	18.80 (4.96–94.6)
Sex	.96	

^aOlder age and supratentorial location of tumor are significant predictors of *BRAF* V600E mutation. Sex is not a predictor.

series of 7 patients.⁴⁴ Ishi et al⁴⁴ found a lower T2WI signal and a larger T2WI/contrast-enhanced FLAIR mismatch to be indicative of *BRAF* V600E mutation in optic pathway gliomas. In their study, T2WI/contrast-enhanced FLAIR mismatch was defined as a mismatch of a tumor region with high signal intensity on T2WI or FLAIR sequences with enhancement on contrast-enhanced T1WI sequences.

In our study, we trained and validated radiomic features of FLAIR MR images to predict *BRAF* fusion or mutation status in pLGG. As expected, the location of the tumor and age at presentation significantly predicted the mutational status. Histologically and radiomorphologically, pLGGs are largely heterogeneous.⁶ On the FLAIR sequence alone, tumors display a variety of qualitative differences, including the volume of their cystic and solid components, sharp and indistinct borders, presence or absence of hemorrhage, location, and volume at initial presentation. Our training cohort reflected the large spectrum of pLGGs with regard to the prevalence of tumor types and imaging characteristics on the FLAIR sequence (Fig 3). However, the independent external validation cohort comprised JPA, ganglioma, and pilomyxoid astrocytoma only. This feature may explain the difference between the internal and external prediction of our model (best model; internal AUC = 0.75, external AUC = 0.85) and warrants further investigation. A less comprehensive approach with prediction of *BRAF* status either restricted to 1 or a few pLGG subtypes or anatomic location such as the optic pathway or cervicomedullary junction may further improve prediction accuracy. Future studies could adopt a more restrictive approach and analyze molecular markers within a given pLGG type or anatomic location. Due to the need for a large sample size and the low prevalence of these tumors, radiomic studies may be limited to large multinational and multi-institutional collaborations.

Another factor that may further improve our model prediction is the incorporation of patient demographic information such as age at presentation and qualitative radiographic features such as tumor location. This may be particularly helpful for the *BRAF* V600E mutation, which is known to be strongly associated with supratentorial location as seen in our study.⁴⁵

Our study has limitations. Due to the retrospective and bi-institutional nature of the study, there was heterogeneity in the FLAIR sequence acquisition, including the use of different scanner vendors, field strengths, and imaging parameters. However, because the heterogeneity in image acquisition reflects clinical practice, a robust and predictive model needs to incorporate these technical variations. In addition, our exploratory study used only FLAIR images for feature discrimination and model development. Incorporating additional MR imaging sequences such as

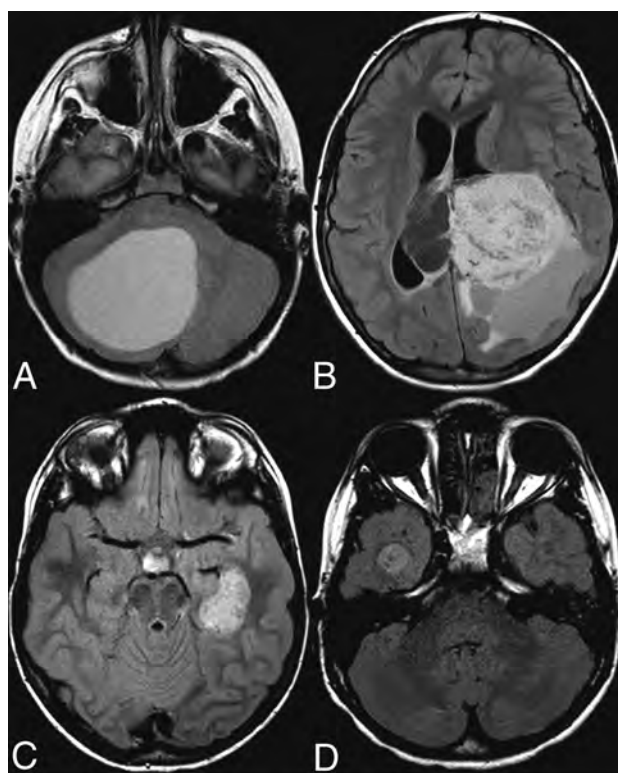


FIG 3. Axial FLAIR images of pLGG. A, A 7-year-old boy. Infratentorial, *BRAF* V600E-mutated JPA. B, A 12-year-old boy. Supratentorial intraventricular, *BRAF*-fused ganglioma. C, A 7-year-old boy. Left temporal *BRAF* V600E-mutated dysembryoplastic neuroepithelial tumor. D, An 8-year-old boy. Right temporal *BRAF* V600E-mutated pleomorphic xanthoastrocytoma.

T2WI, DWI, and contrast-enhanced T1WI sequences could further increase random forest model performance.

CONCLUSIONS

We present the exploratory results for the application of radiomics and machine learning for the prediction of *BRAF* status in pLGGs using independent bi-institutional training and validation sets based on FLAIR images. The optimal random forest model achieved an AUC of 0.85 in the validation cohort. Future investigations with a larger sample size for all histologic tumor types are warranted to further improve *BRAF* classifier training and validation. The use of other imaging sequences, including DWI, T2WI, and contrast-enhanced T1WI, and patient age and tumor location, may also help improve prediction accuracy.

Disclosures: Liana Figueiredo—RELATED: Grant: Meagan's Walk Fellowship.* Manohar M. Shroff—UNRELATED: Payment for Lectures Including Service on Speakers Bureaus: speaker for BioMarin Pharmaceutical on CLN 2 disease, Comments: invited once with a stipend paid in November 2019, money paid to author. Eric Bouffet—UNRELATED: Grants/Grants Pending: Bristol Myers Squibb and Roche, Comments: funding for investigator-initiated trials.* Uri Tabori—RELATED: Grant: Canadian Cancer Society Grant No. 702296*; A Kid's Brain Tumor Cure/PLGA Foundation*; The LivWise Foundation*; The Brain Child Foundation*; Canadian Institutes for Health Research, Grant No. 159805*; The Elmaglachli Family Foundation*; The Garron Family Cancer Centre with funds from the SickKids Foundation*; The Garron Family Chair in Childhood Cancer Research at the Hospital for Sick Children.* Cynthia Hawkins—RELATED: Grant: Canadian Institute of Health Research, Comments: operating grant from the federal funding agency*.

RELATED: Grant: Canadian Cancer Society Research Institute.* UNRELATED: Employment: The Hospital for Sick Children. *Money paid to the institution.

REFERENCES

- Ostrom QT, Gittleman H, Liao P, et al. **CBTRUS statistical report: primary brain and other central nervous system tumors diagnosed in the United States in 2010–14.** *Neuro Oncol* 2017;19:v1–88 CrossRef Medline
- Sturm D, Pfister SM, Jones DT. **Pediatric gliomas: current concepts on diagnosis, biology, and clinical management.** *J Clin Oncol* 2017; 35:2370–77 CrossRef Medline
- Armstrong GT, Conklin HM, Huang S, et al. **Survival and long-term health and cognitive outcomes after low-grade glioma.** *Neuro Oncol* 2011;13:223–34 CrossRef Medline
- Lassaletta A, Scheinemann K, Zelcer SM, et al. **Phase II weekly vinblastine for chemotherapy-naïve children with progressive low-grade glioma: a Canadian Pediatric Brain Tumor Consortium Study.** *J Clin Oncol* 2016;34:3537–43 CrossRef Medline
- Krishnatreya R, Zhukova N, Guerreiro Stucklin AS, et al. **Clinical and treatment factors determining long-term outcomes for adult survivors of childhood low-grade glioma: a population-based study.** *Cancer* 2016;122:1261–69 CrossRef Medline
- AlRayahi J, Zapotocky M, Ramaswamy V, et al. **Pediatric brain tumor genetics: what radiologists need to know.** *Radiographics* 2018; 38:2102–22 CrossRef Medline
- Chalil A, Ramaswamy V. **Low-grade gliomas in children.** *J Child Neurol* 2016;31:517–22 CrossRef Medline
- Lassaletta A, Zapotocky M, Mistry M, et al. **Therapeutic and prognostic implications of BRAF V600E in pediatric low-grade gliomas.** *J Clin Oncol* 2017;35:2934–41 CrossRef Medline
- Mistry M, Zhukova N, Merico D, et al. **BRAF mutation and CDKN2A deletion define a clinically distinct subgroup of childhood secondary high-grade glioma.** *J Clin Oncol* 2015;33:1015–22 CrossRef Medline
- Fangusaro J, Onar-Thomas A, Poussaint TY, et al. **LGG-08: a PHASE II prospective study of selumetinib in children with recurrent or refractory low-grade glioma (LGG)—a Pediatric Brain Tumor Consortium (PBTC) study.** *Neuro-Oncology* 2017;19:iv34–35 CrossRef
- Hargrave DR, Bouffett E, Tabori U, et al. **Efficacy and Safety of DaBRAfenib in pediatric patients with BRAFV600 mutation-positive relapsed or refractory low-grade glioma: results from a Phase I/IIa study.** *Clin Cancer Res* 2019;25:7303–11 CrossRef Medline
- Aerts HJ, Velazquez ER, Leijenaar RT, et al. **Decoding tumour phenotype by noninvasive imaging using a quantitative radiomics approach.** *Nat Commun* 2014;5:4006 CrossRef Medline
- Khalvati F, Zhang Y, Wong A, et al. **Radiomics-based prognosis analysis for non-small cell lung cancer.** *Sci Rep* 2017;7:46349 CrossRef Medline
- Stocker D, Marquez HP, Wagner MW, et al. **MRI texture analysis for differentiation of malignant and benign hepatocellular tumors in the non-cirrhotic liver.** *Heliyon* 2018;4:e00987 CrossRef Medline
- Fritz B, Müller DA, Sutter R, et al. **Magnetic resonance imaging-based grading of cartilaginous bone tumors: added value of quantitative texture analysis.** *Invest Radiol* 2018;53:663–72 CrossRef Medline
- Chaddad A, Kucharczyk MJ, Daniel P, et al. **Radiomics in glioblastoma: current status and challenges facing clinical implementation.** *Front Oncol* 2019;9:374 CrossRef Medline
- Iv M, Zhou M, Shpanskaya K, et al. **MR imaging-based radiomic signatures of distinct molecular subgroups of medulloblastoma.** *AJNR Am J Neuroradiol* 2019;40:154–61 CrossRef Medline
- Goya-Outi J, Calmon R, Orhac F, et al, eds. **Can structural MRI radiomics predict DIPG histone H3 mutation and patient overall survival at diagnosis time?** In: *Proceedings of the 2019 IEEE IEEE Engineering in Medicine and Biology Society on Biomedical & Health Informatics*, Chicago, Illinois; May 19–22, 2019 CrossRef
- Ryall S, Zapotocky M, Fukuoka K, et al. **Integrated molecular and clinical analysis of 1,000 pediatric low-grade gliomas.** *Cancer Cell* 2020;37:569–83 CrossRef Medline
- Pieper S, Halle M, Kikinis R, eds. **3D Slicer.** In: *Proceedings of the 2004 2nd IEEE International Symposium on Biomedical Imaging: Nano to Macro (IEEE Cat No 04EX821)*, Arlington, Virginia; April 15–18, 2004
- Parmar C, Velazquez ER, Leijenaar R, et al. **Robust radiomics feature quantification using semiautomatic volumetric segmentation.** *PLoS One* 2014;9:e102107 CrossRef Medline
- Tustison NJ, Avants BB, Cook PA, et al. **N4ITK: improved N3 bias correction.** *IEEE Trans Med Imaging* 2010;29:1310–20 CrossRef Medline
- Li J, Liu S, Qin Y, et al. **High-order radiomics features based on T2 FLAIR MRI predict multiple glioma immunohistochemical features: a more precise and personalized gliomas management.** *PLoS One* 2020;15:e0227703 CrossRef Medline
- Park JE, Kim HS. **Radiomics as a quantitative imaging biomarker: practical considerations and the current standpoint in neuro-oncologic studies.** *Nucl Med Mol Imaging* 2018;52:99–108 CrossRef Medline
- Breiman L. **Bagging predictors.** *Mach Learn* 1996;24:123–40 CrossRef
- Youden WJ. **Index for rating diagnostic tests.** *Cancer* 1950;3:32–35 CrossRef Medline
- Fukuoka K, Mamatjan Y, Tatevossian R, et al. **Clinical impact of combined epigenetic and molecular analysis of pediatric low-grade gliomas.** *Neuro Oncol* 2020;22:1474–83 CrossRef Medline
- de Blank P, Badve C, Gold DR, et al. **Magnetic resonance fingerprinting to characterize childhood and young adult brain tumors.** *Pediatr Neurosurg* 2019;54:310–18 CrossRef Medline
- Wagner MW, Narayan AK, Bosemani T, et al. **Histogram analysis of diffusion tensor imaging parameters in pediatric cerebellar tumors.** *J Neuroimaging* 2016;26:360–65 CrossRef Medline
- Kikuchi K, Hiwatashi A, Togao O, et al. **Correlation between arterial spin-labeling perfusion and histopathological vascular density of pediatric intracranial tumors.** *J Neurooncol* 2017;135:561–69 CrossRef Medline
- Morana G, Piccardo A, Tortora D, et al. **Grading and outcome prediction of pediatric diffuse astrocytic tumors with diffusion and arterial spin labeling perfusion MRI in comparison with 18F-DOPA PET.** *Eur J Nucl Med Mol Imaging* 2017;44:2084–93 CrossRef Medline
- Morana G, Tortora D, Stagliano S, et al. **Pediatric astrocytic tumor grading: comparison between arterial spin labeling and dynamic susceptibility contrast MRI perfusion.** *Neuroradiology* 2018;60:437–46 CrossRef Medline
- Kikuchi K, Hiwatashi A, Togao O, et al. **Intravoxel incoherent motion MR imaging of pediatric intracranial tumors: correlation with histology and diagnostic utility.** *AJNR Am J Neuroradiol* 2019;40:878–84 CrossRef Medline
- Raja R, Sinha N, Saini J, et al. **Assessment of tissue heterogeneity using diffusion tensor and diffusion kurtosis imaging for grading gliomas.** *Neuroradiology* 2016;58:1217–31 CrossRef Medline
- Ditmer A, Zhang B, Shujaat T, et al. **Diagnostic accuracy of MRI texture analysis for grading gliomas.** *J Neurooncol* 2018;140:583–89 CrossRef Medline
- Sui Y, Wang H, Liu G, et al. **Differentiation of low-and high-grade pediatric brain tumors with high b-value diffusion-weighted MR imaging and a fractional order calculus model.** *Radiology* 2015; 277:489–96 CrossRef Medline
- Koral K, Mathis D, Gimi B, et al. **Common pediatric cerebellar tumors: correlation between cell densities and apparent diffusion coefficient metrics.** *Radiology* 2013;268:532–37 CrossRef Medline
- Karaman MM, Sui Y, Wang H, et al. **Differentiating low-and high-grade pediatric brain tumors using a continuous-time random-walk diffusion model at high b-values.** *Magn Reson Med* 2016; 76:1149–57 CrossRef Medline

39. Ho CY, Mobley BC, Gordish-Dressman H, et al. **A clinicopathologic study of diencephalic pediatric low-grade gliomas with *BRAF* V600 mutation.** *Acta Neuropathol* 2015;130:575–85 CrossRef Medline
40. Perreault S, Ramaswamy V, Achrol AS, et al. **MRI surrogates for molecular subgroups of medulloblastoma.** *AJNR Am J Neuroradiol* 2014;35:1263–69 CrossRef Medline
41. Chen H, Hu W, He H, et al. **Noninvasive assessment of H3 K27M mutational status in diffuse midline gliomas by using apparent diffusion coefficient measurements.** *Eur J Radiol* 2019;114:152–59 CrossRef Medline
42. Aboian MS, Solomon DA, Felton E, et al. **Imaging characteristics of pediatric diffuse midline gliomas with histone H3 K27M mutation.** *AJNR Am J Neuroradiol* 2017;38:795–800 CrossRef Medline
43. Pan CC, Liu J, Tang J, et al. **A machine learning-based prediction model of H3K27M mutations in brainstem gliomas using conventional MRI and clinical features.** *Radiother Oncol* 2019;130:172–79 CrossRef Medline
44. Ishi Y, Yamaguchi S, Yoshida M, et al. **Correlation between magnetic resonance imaging characteristics and *BRAF* alteration status in individuals with optic pathway/hypothalamic pilocytic astrocytomas.** *J Neuroradiol* 2019 Jun 20. [Epub ahead of print] CrossRef Medline
45. Behling F, Schittenhelm J. **Oncogenic *BRAF* alterations and their role in brain tumors.** *Cancers (Basel)* 2019;11:794 CrossRef Medline

Longitudinal Assessment of Enhancing Foci of Abnormal Signal Intensity in Neurofibromatosis Type 1

 N. Hainc,  M.W. Wagner,  S. Laughlin,  J. Rutka,  C. Hawkins,  S. Blaser, and  B.B. Ertl-Wagner

ABSTRACT

BACKGROUND AND PURPOSE: Patients with neurofibromatosis 1 are at increased risk of developing brain tumors, and differentiation from contrast-enhancing foci of abnormal signal intensity can be challenging. We aimed to longitudinally characterize rare, enhancing foci of abnormal signal intensity based on location and demographics.

MATERIALS AND METHODS: A total of 109 MR imaging datasets from 19 consecutive patients (7 male; mean age, 8.6 years; range, 2.3–16.8 years) with neurofibromatosis 1 and a total of 23 contrast-enhancing parenchymal lesions initially classified as foci of abnormal signal intensity were included. The mean follow-up period was 6.5 years (range, 1–13.8 years). Enhancing foci of abnormal signal intensity were followed up with respect to presence, location, and volume. Linear regression analysis was performed.

RESULTS: Location, mean peak volume, and decrease in enhancing volume over time of the 23 lesions were as follows: 10 splenium of the corpus callosum (295 mm³, 5 decreasing, 3 completely resolving, 2 surgical intervention for change in imaging appearance later confirmed to be gangliocytoma and astrocytoma WHO II), 1 body of the corpus callosum (44 mm³, decreasing), 2 frontal lobe white matter (32 mm³, 1 completely resolving), 3 globus pallidus (50 mm³, all completely resolving), 6 cerebellum (206 mm³, 3 decreasing, 1 completely resolving), and 1 midbrain (34 mm³). On average, splenium lesions began to decrease in size at 12.2 years, posterior fossa lesions at 17.1 years, and other locations at 9.4 years of age.

CONCLUSIONS: Albeit very rare, contrast-enhancing lesions in patients with neurofibromatosis 1 may regress over time. Follow-up MR imaging aids in ascertaining regression. The development of atypical features should prompt further evaluation for underlying tumors.

ABBREVIATIONS: FASI = focus of abnormal signal intensity; NF-1 = neurofibromatosis type 1; CE = contrast-enhanced

Neurofibromatosis type 1 (NF-1) is an autosomal dominant tumor predisposition syndrome characterized by optic pathway gliomas, neurofibromas, skin manifestations, iris hamartomas, and bone lesions, affecting approximately 1 in 3000 individuals.^{1,2} Foci of abnormal signal intensity, previously known as unidentified bright objects or neurofibromatosis bright objects of the brain, are not among the diagnostic criteria but can be found in 43%–95% of pediatric patients with NF-1.^{3–7} On MR imaging,

FASI appear as T2/FLAIR hyperintense lesions of the brain with a predilection for the basal ganglia, cerebellum, and brain stem. Although FASI are not completely understood, myelin vacuolization is commonly considered as an underlying feature of these lesions.^{1,4,5,7–9}

Patients with NF-1 are at an increased risk of developing low- and high-grade brain tumors, including cerebral and cerebellar astrocytomas, ependymomas, and brain stem gliomas, many of which can mimic FASI on MR imaging.^{3,10–14} On the other hand, FASI are known for their dynamic properties and may increase or decrease in size or resolve over time.⁸ Although the reference standard for differentiating brain lesions is transcranial biopsy with its own inherent risks, brain signal abnormalities in patients with NF-1 are primarily followed up by MR imaging to screen for possible tumors.^{15–18} Contrast enhancement after administration of a gadolinium-based contrast agent is usually considered atypical for FASI and likely to indicate the presence of a brain tumor. Reports considering contrast enhancement in FASI are

Received June 8, 2020; accepted after revision October 23.

From the Department of Diagnostic Imaging (N.H., M.W.W., S.L., S.B., B.B.E.-W.), Division of Neuroradiology; Department of Surgery, Division of Neurosurgery (J.R.); and Department of Paediatric Laboratory Medicine (C.H.), The Hospital for Sick Children, and University of Toronto, Toronto, Ontario, Canada; and Department of Neuroradiology (N.H.), Clinical Neuroscience Center, University Hospital Zurich, University of Zurich, Zurich, Switzerland.

N.H. and M.W.W. contributed equally to the manuscript.

Please address all correspondence to Birgit Ertl-Wagner, The Hospital for Sick Children, 555 University Ave, Toronto, ON, Canada, M5G 1X8; e-mail: Birgitbetina.ertl-wagner@sickkids.ca
<http://dx.doi.org/10.3174/ajnr.A6974>

sparse, limited to case reports and small numbers in cohort studies.^{3,6,19–29} We therefore aimed to characterize lesions considered to represent enhancing FASI based on location, volume of enhancement, and demographics to advance the understanding of these rare lesions.

MATERIALS AND METHODS

Patients

This retrospective study was approved by the institutional review board (REB 1000065561). Informed consent was waived because of the retrospective nature of the study. Electronic MR imaging reports stored in the PACS at our institution (The Hospital for Sick Children, Toronto, Canada) were searched for patients with NF-1 with the term “enhancing FASI” between 1993 and 2019. Inclusion criteria were 1) patients with NF-1 with a contrast-enhancing lesion within the brain parenchyma considered to be an enhancing focus of abnormal signal intensity in the report and 2) MR imaging studies with axial FLAIR sequences and postcontrast axial and coronal T1-weighted images available. Studies containing images not of diagnostic quality were excluded. A maximum of 1 MR imaging study per year per patient was taken if multiple yearly acquisitions were present.

MR Imaging

Brain MR imaging was acquired on 1.5 and 3T Achieva systems (Philips Healthcare), a 3T Magnetom Skyra (Siemens), and a 1.5T Signa (GE Healthcare) using a standardized departmental protocol including axial FLAIR and contrast-enhanced (CE) axial and coronal T1-weighted sequences. Sequence parameters were as follows:

FLAIR sequence: range of in-plane resolutions, 0.43 mm × 0.43 mm to 0.75 mm × 0.75 mm; section thickness, 3–5 mm; TE, 85–148.5 ms; TR, 7000–9825 ms

3D CE-T1 sequence: in-plane resolution, 0.42 mm × 0.42 mm to 0.52 mm × 0.52 mm; section thickness, 0.42–0.52 mm; TE, 2.7–3.2 ms; TR, 6.8–1970 ms

2D CE-T1 sequence: axial and coronal in-plane resolution, 0.82 mm × 0.82 mm; section thickness, 6 mm (axial) and 5 mm (coronal); TE/TR, 20/666.7 (axial) and 650 (coronal) ms

As per our institutional protocol, the time delay for acquisition of the CE brain sequences was constant. Acquisition of the axial T1-weighted sequence was started 3 minutes after the IV administration of a gadolinium-based contrast agent. The coronal T1-weighted sequence was acquired thereafter. If spine sequences were performed, the CE spine sequences were generally acquired after the brain sequences. All nonenhancing and enhancing FASI were documented for each patient in consensus by a board-certified neuroradiologist with 5 years of neuroradiology experience and a fellowship-trained pediatric neuroradiologist with 6 years of neuroradiology research experience (N.H. and M.W.W.). Disputes were resolved by a senior pediatric neuroradiologist (S.B.) with more than 30 years of experience in pediatric neuroradiology. Enhancing FASI were defined as T2/FLAIR hyperintense, contrast-enhancing lesions on T1-weighted images without cystic, necrotic, or hypercellular features. Lesions that demonstrated

diffusion restriction or residual lesions on FLAIR sequences after cessation of contrast enhancement were not considered enhancing FASI. Regression of enhancement was seen as confirmatory of enhancing FASI. Nonregressing lesions lost to follow-up but otherwise fulfilling these criteria were considered enhancing FASI. The outermost edge of enhancement was used to define the diameter. Diameters of the contrast-enhancing aspect of FASI were measured on axial and coronal planes of CE T1-weighted sequences using 2D sequences only when 3D sequences were not available. The volume was estimated for each time point using the ellipsoid formula below in which a, b, and c represent radius in the right-left, anteroposterior, and craniocaudal orientations, as was done in a previous publication focusing on volumetric assessment of nonenhancing FASI.⁶

$$V = \frac{4\pi abc}{3}$$

Data Analysis

For the purpose of cross-sectional analysis of nonenhancing and enhancing FASI, the cohort was divided into 8 groups of 2-year intervals based on patient age, from 2 to 3.9 years to 16 to 17.9 years. These groups were further subdivided based on lesion location, either in the posterior fossa (brain stem and cerebellum) or supratentorial. Differences between nonenhancing and enhancing FASI in terms of temporal evolution, including first appearance and peak number of lesions, were assessed using the cross-sectional analysis described earlier.

For analysis of enhancing FASI, timelines of all individual enhancing FASI were created based on patient age at beginning and end of the observation period (ie, from first to last MR imaging in our PACS). Volume increase and decrease were documented for every MR imaging study. Nonenhanced T1-weighted images and diffusion-weighted images were reviewed when available. Linear regression analysis of relative volume change with respect to maximum lesion volume, correlated to patient age, was performed for 3 groups of lesion locations (splenium, posterior fossa, and other locations).

RESULTS

Patients

A total of 146 MR imaging examinations from 19 patients diagnosed with NF-1 with a total of 23 contrast-enhancing lesions were included. The mean age was 8.6 years (range, 2.3–16.8 years). Seven patients were male, with a mean age of 7.8 years (range, 2.3–13.5 years); the 12 female patients had a mean age of 9.1 years (range, 2.6–16.8 years) (Fig 1). The mean follow-up period was 6.5 years (range, 1–13.8 years). All MR imaging studies were performed upon referral of a provider directly involved in the patient's care; indications for initial MR imaging included suspected optic glioma, plexiform neurofibromas of the neck or face with additional brain imaging, headaches, new-onset hemifacial and extremity weakness, and developmental difficulties. Two patients developed tumors of the splenium, which were ascertained by biopsy (gangliocytoma and astrocytoma WHO II). Both lesions had been initially thought to represent enhancing FASI based on imaging. Images from 1 patient were unavailable

for review; thus, information regarding enhancing FASI (1 cerebellar and 1 globus pallidus) for the timeline was obtained from the radiologic reports. Contrast enhancement completely resolved over time for both of this patient's lesions. This patient was only included in the longitudinal evaluation of location of enhancement because neither measurement of lesions nor correlation with other imaging sequences was possible. A further 16 studies missing axial FLAIR images, 6 studies missing CE T1-weighted sequences, and 2 studies not retrievable from long-term PACS storage were excluded. In summary, a total of 109 MR imaging studies of 23 lesions were included, 2 of which were later proved to be tumors, and 2 lesions from 1 patient were not available for viewing in PACS.

FASI

Patient age group data for nonenhancing and enhancing FASI are listed in Table 1 as total, mean, and range. Notably, age at peak number of nonenhancing FASI within the basal ganglia and thalamus group was 8 to 9.9 years (mean, 5.3 lesions) and in the brain stem and cerebellum group was 2 to 3.9 years (mean, 6.5 lesions) (Fig 2). These lesions demonstrated high ADC (ie, facilitated diffusion) and variable signal intensities on nonenhanced T1-weighted images, ranging from hypo- to hyperintense. Of note, hyperintense lesions on T1-weighted images were found predominantly in the basal ganglia and cerebellum.

Of the 21 contrast-enhancing FASI, 8 (38%) were found in the splenium of the corpus callosum, 1 (5%) in the body of the corpus callosum, 2 (10%) in the white matter of the frontal lobe, 3 (14%) in the globus pallidus, 6 in the cerebellum (28%), and 1 (5%) in the midbrain. For the 19 contrast-enhancing FASI accessible in PACS, lesions were round to

ovoid in shape and demonstrated enhancement patterns ranging from homogeneous and well-defined to inhomogeneous or irregular with predominantly peripheral enhancement. Fourteen lesions had DWI sequences available for correlation. All of these lesions demonstrated increased ADC. Of the 5 lesions for which no DWI sequence was available, 1 lesion demonstrated a continuous increase in size until final follow-up (cerebellum). Of the remaining 4 lesions without DWI sequences, 1 completely resolved

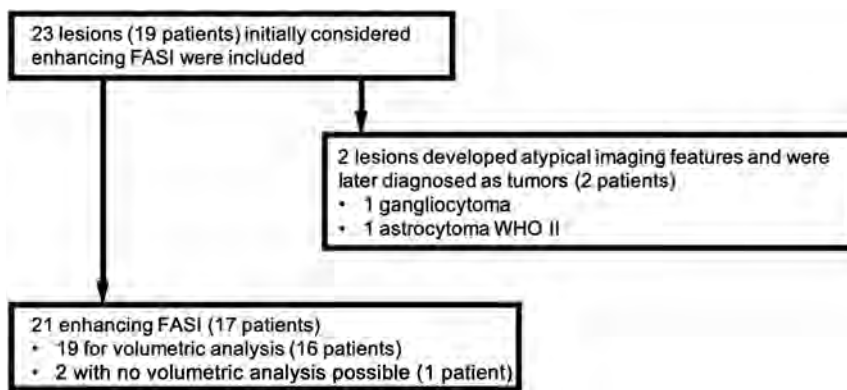


FIG 1. Diagram showing the number of patients with NF-1 included in the study.

Table 1: Patient age group data for enhancing FASI (total) and nonenhancing FASI according to subgroup

Age Group (years)	2–3.9	4–5.9	6–7.9	8–9.9	10–11.9	12–13.9	14–15.9	16–17.9
Participants	5	7	8	15	17	16	13	14
Enhancing FASI								
Total	0	1	1	7	11	9	9	7
Splenium of CC				2	5	4	4	2
Body of CC				1	1			
Frontal lobe				1	1			1
Globus pallidus		1	1	1		1 ^a	1 ^a	
Cerebellum				2	4	4	2 + 1 ^a	3
Midbrain						0	1	1
Nonenhancing FASI BG and T								
Total	18	29	39	83	86	54	27	26
Mean	3.6	4.1	4.9	5.3	5.1	3.4	2.1	1.9
Range	0–7	1–8	1–10	0–11	1–11	1–10	0–4	0–3
Nonenhancing FASI BS and CB								
Total	65	85	89	121	141	81	51	62
Mean	6.5	6.1	5.6	4	4.1	2.3	2	2.2
Range	0–13	2–12	0–14	0–11	0–9	0–7	1–3	0–8
Nonenhancing FASI splenium CC								
Total	6	7	5	11	27	35	23	33
Mean	1.2	1	0.6	0.7	1.6	2.2	1.8	2.4
Range	0–3	0–3	0–3	0–2	0–5	0–7	1–3	1–6
Nonenhancing FASI remainder CC								
Total	2	2	1	1	3	3	0	2
Mean	0.8	0.3	0.1	0.1	0.2	0.2	0	0.1
Range	0–2	0–1	0–1	0–1	0–1	0–1	0	0–1

Note:—BG indicates basal ganglia; BS, brain stem; CB, cerebellum; CC, corpus callosum; T, thalamus.

^aLesions with images not available for volumetric analysis.

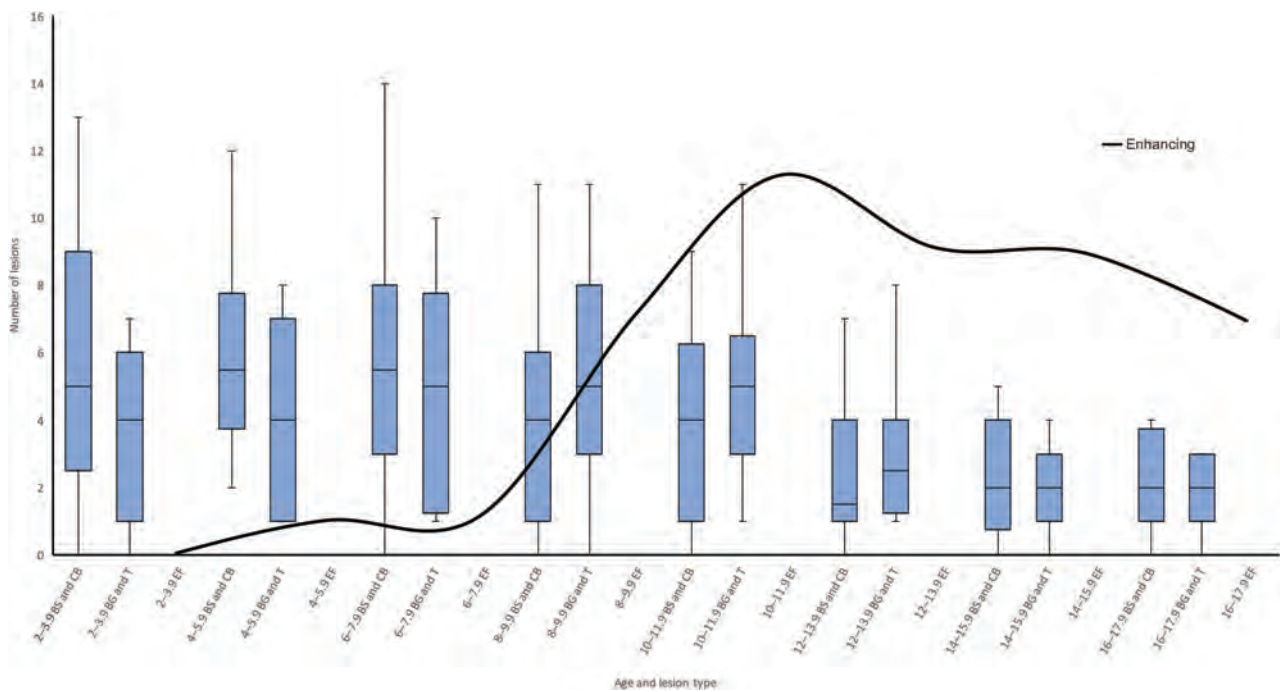


FIG 2. Combined box-and-whisker plot of the temporal evolution of FASI in the brain stem and cerebellum (BS and CB) group (left box-and-whisker plot in the doublet), basal ganglia and thalamus (BG and T) group (right box-and-whisker plot in the doublet), and enhancing FASI (EF, total of all patients, continuous curved black line), grouped in 2-year patient-age intervals, beginning at 2–3.9 years. Contrast-enhancing FASI appear later and peak later (11 lesions, 10- to 11.9-year-old age group) compared with nonenhancing FASI (BS/CB peak in 6- to 7.9-year-old age group and BG/T peak in 8- to 9.9-year-old age group).

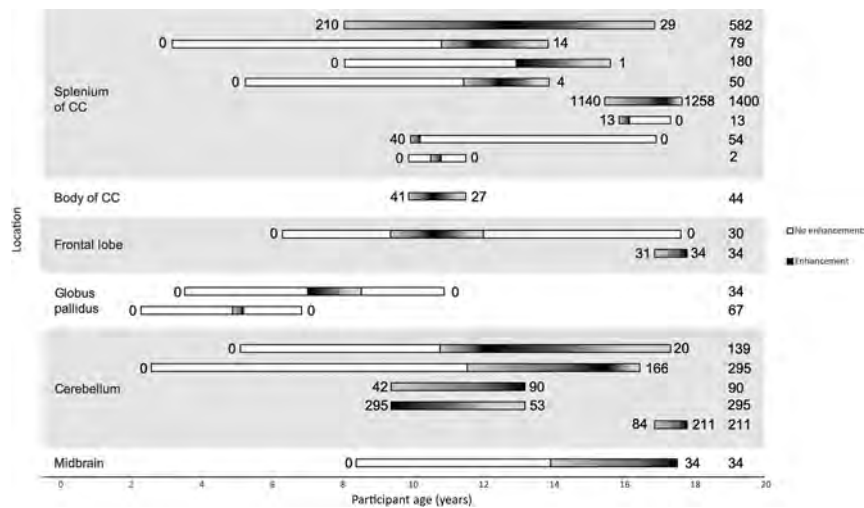


FIG 3. Horizontal plot of all volumetrically assessed contrast-enhancing FASI. White bars represent imaging studies where no contrast enhancement was noted. The white-to-black (left to right) gradient represents increasing enhancing volume; the black-to-white (left-to-right) gradient represents decreasing enhancing volume. The numbers to the left and right of the bars indicate the enhancing FASI volume on first and last MR imaging. The numbers on the far right indicate the largest measured enhancing volume for the respective lesion; all values are in cubic millimeters. All 8 lesions within the splenium are seen to either decrease in size or completely resolve before age 18 years (not including the 2 lesions later proved to be tumors). Both globus pallidus lesions completely resolved before age 11 years. Only 3 of 6 posterior fossa (cerebellum and midbrain) lesions were seen to decrease in size on final MR imaging. Body of corpus callosum (1 lesion) and frontal lobe lesions (2 lesions) did not show any conceivable trends. The 2 contrast-enhancing FASI not available for viewing in the PACS are not included in this figure.

(globus pallidus), and 3 decreased in size (2 splenium, 1 cerebellum), paralleling the natural evolution of their nonenhancing FASI counterparts. Nonenhanced T1-weighted images were available for 16 of 19 lesions and demonstrated a spectrum of findings. One globus pallidus lesion was hyperintense, 2 cerebellar lesions contained areas of hyperintensity, and 2 splenium lesions contained areas of isointensity relative to white matter. Mass effect, a finding previously described in enhancing FASI,^{23,27,29} was seen in 1 cerebellar lesion and 4 splenium lesions, which persisted on final MR imaging.

Patients with splenium lesions had an average of 5.5 MR imaging studies per patient (range, 2–9). Apart from the 2 biopsy-proven tumors, all 8 lesions demonstrated a decrease in enhancing lesion volume over the course of follow-up (Fig 3), with 3 lesions (38%) completely resolving. Mean age at first depiction of an enhancing splenium lesion was 11.5 years (range, 8.0–15.8), and mean age at maximum lesion volume was 12.9 years (range, 10.2–17.1). Median

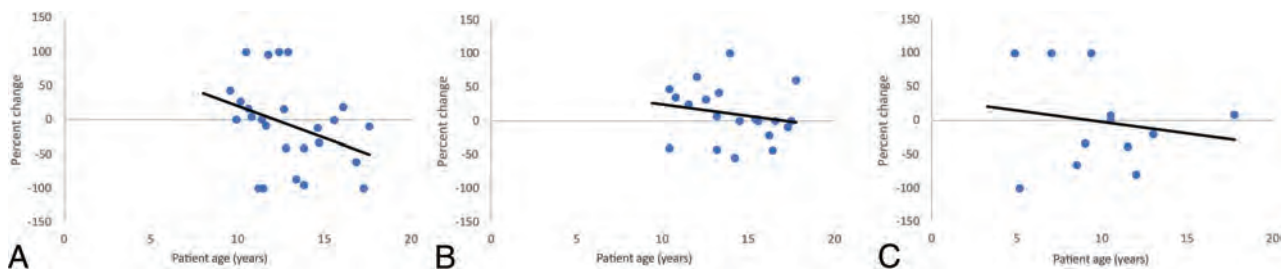


FIG 4. Linear regression analysis of splenium lesions (A); posterior fossa lesions, including the cerebellum and midbrain (B); and other lesions, including the globus pallidus, body of the corpus callosum, and frontal lesions (C). Enhancing FASI lesion volumes are expressed as ratios of interval change divided by maximum lesion volume. The x-intercept represents the transition point at which lesions begin to decrease in size. Splenium lesions began decreasing in size at 12.2 years, posterior fossa at 17.1 years, and other lesions at 9.4 years of age.

enhancing lesion volume at first depiction was 26 mm^3 (range, 1–1140 mm^3), and median peak lesion volume was 66 mm^3 (range, 2–1400 mm^3). The 3 enhancing FASI demonstrating complete resolution of contrast enhancement were among the 4 smallest peak enhancing lesion volumes (54, 13, and 2 mm^3). Further data on enhancing volumes are shown in Fig 3.

Of the remaining (nonsplenium) 13 enhancing FASI, 11 could be assessed volumetrically. Patients had an average of 6.2 studies (range, 2–10). Six lesions decreased in enhancing volume: 1 in the body of the corpus callosum, 1 in the frontal lobe white matter (completely resolved), 1 in the globus pallidus (completely resolved), and 3 in the cerebellum. Three of 6 posterior fossa lesions decreased in volume. Four lesions (1 frontal lobe lesion, 2 cerebellar lesions, and the midbrain lesion) increased in enhancing volume before being lost to follow-up. In 3 of these 4 patients, the last MR imaging was performed just before the age of 18 years (mean, 17.5 years; range, 17.5–17.7 years), after which the patients were followed up at adult hospitals. Mean age at first depiction of the enhancing lesion was as follows: cerebellum, 10.7 years (range, 9.4–16.8); globus pallidus, 6 years (range, 4.9–7); and other locations (1 body of corpus callosum, 1 midbrain, 2 frontal lobe), 12 years (range, 9.3–16.8). Median lesion volume at first depiction of all 11 enhancing FASI was 44 mm^3 (range, 30–295 mm^3), and median maximum depicted lesion volume was 67 mm^3 (range, 30–295 mm^3).

Regression analysis revealed the age at which lesions transitioned from an overall increase in size to a decrease in size (Fig 4). Splenium lesions began decreasing in size at 12.2 years (R^2 coefficient, 0.12); posterior fossa at 17.1 years (R^2 coefficient, 0.04); and globus pallidus, frontal, and body of corpus callosum lesions were grouped together as “other” at 9.4 years of age (R^2 coefficient, 0.03).

Biopsy-Proven Tumors

Two biopsy-proven tumors were included in our study, both located in the splenium and initially indistinguishable from enhancing FASI. One of these lesions developed cystic components after a follow-up period of 2 years 1 month and was thus resected (at patient age of 12 years); histology confirmed gangliocytoma. This lesion was hypointense on nonenhanced T1-weighted imaging; DWI was not performed before resection. The second lesion, also located in the splenium, initially demonstrated

an imaging appearance and time course indistinguishable from FASI; it increased in size and enhancement, peaking at the age of 15 years before beginning to regress (Fig 5). After 2 further follow-up studies, however, an enhancing focus within the lesion again began to increase in size at age 17 years. At this point, the lesion was resected; histology confirmed a WHO II astrocytoma. This lesion was hypointense on T1-weighted imaging and demonstrated high ADC (increased diffusivity). Mass effect was seen in both lesions.

DISCUSSION

In this study, we characterized the natural evolution of 23 rare, contrast-enhancing lesions initially thought to represent enhancing FASI in patients with NF-1. Two lesions developed atypical features on follow-up and were demonstrated to be tumors by biopsy. The temporal evolution of contrast-enhancing FASI appeared to begin later compared with nonenhancing FASI: no contrast-enhancing FASI were observed before the age of 4 years, but nonenhancing FASI were already found at the age of 2 years with a mean number of 6.5 lesions in the brain stem or cerebellum and 3.6 lesions in the basal ganglia or thalamus. The peak number of enhancing FASI in our cohort was also seen at a later age compared with nonenhancing FASI.

Enhancing FASI

In our study, regional differences in the evolution of enhancing FASI are noted. Apart from the 2 lesions later proved to be tumors, all 8 (100%) contrast-enhancing FASI in the splenium decreased in enhancing volume before the age of 18 years. By contrast, 3 of 6 (50%) contrast-enhancing FASI located in the posterior fossa increased in size up to the final MR imaging, with 2 of these patients imaged just before the age of 18 years. This difference was also reflected in regression analysis because lesions in the splenium demonstrated a transition to overall decrease in size at the age of 12.2 years, but this transition was observed much later at the age of 17.1 years in lesions located in the posterior fossa.

In the largest previous study involving contrast-enhancing FASI, Salman et al²³ describe 14 enhancing FASI in 8 patients. Of 5 cerebellar lesions, 3 demonstrated resolution of enhancement (at ages 13.5, 11.2, and 5.5 years, respectively), and 2 demonstrated persistent enhancement on their last MR imaging scan (at

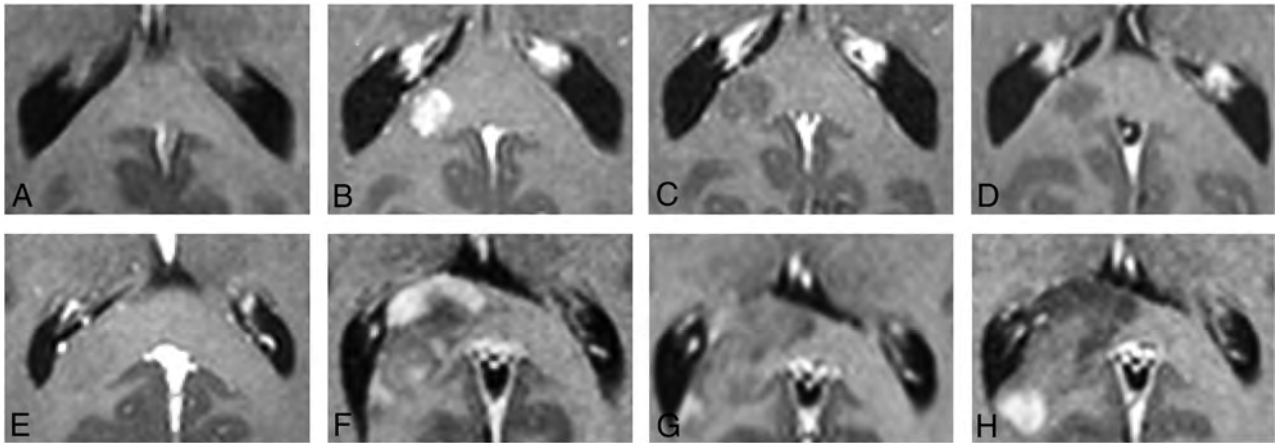


FIG 5. Typical (A–D) and atypical (E–H) evolutions of enhancing FASI. A–D demonstrate, a lesion in the splenium or right forceps major increasing in size to age 13 years (B) and decreasing thereafter with near complete resolution of contrast enhancement on final imaging (D). E–H represent an atypical contrast enhancement pattern in a histologically proved WHO II astrocytoma. This lesion initially demonstrated evolution identical to FASI, increasing in size up to age 15 years (F) before beginning to regress (G). At this point, however, the small right periventricular enhancing aspect again began increasing in size at age 17 years (H). At this point, the lesion was resected because this was considered to be atypical for an enhancing FASI. Mass effect was noted in both lesions.

ages 19 and 19.9 years), which is similar to our findings. Other publications on contrast-enhancing FASI have been limited to case reports and very small numbers in cohort studies, and only a few of these provide details on follow-up and age.^{3,6,19–29}

Considerations Regarding MR Imaging Follow-up

In a study focusing on the splenium of the corpus callosum, Mimouni-Bloch et al³⁰ argue that baseline MR imaging should be considered in all patients with NF-1. Although lesions in the splenium are typically asymptomatic, current recommendations state MR imaging to be mandatory only in symptomatic patients.³¹ Brain lesions may spontaneously regress in patients with NF-1. Our study demonstrated that both enhancing and nonenhancing FASI can regress and disappear over time. Studies focusing on optic pathway and hypothalamic gliomas have documented spontaneous regression of these lesions, and a single case report describes the rare, spontaneous involution of a histologically proved pilocytic astrocytoma of the internal capsule.^{32–36} The subclinical manifestation and spontaneous regression of brain lesions in NF-1 make follow-up decisions including reimaging and possible intervention a challenge.

Two lesions in our study first thought to be enhancing FASI of the splenium began demonstrating atypical features on follow-up, prompting resection; both turned out to be histologically proven tumors. One lesion, ultimately demonstrated to be a gangliocytoma, developed a cystic component, a finding considered atypical for FASI and likely indicative of a tumor.^{3,23} The second lesion, ultimately shown to be a WHO grade II astrocytoma, demonstrated a second wave of increasing volume and contrast enhancement after near complete resolution. Although small areas of this lesion did not fully stop enhancing, it is conceivable that lesions in patients with NF-1 exist that completely resolve before recommending enhancement.

DWI and nonenhanced T1-weighted sequences were not able to differentiate biopsy-proven tumors from enhancing FASI or

differentiate among the enhancing FASI found at different locations in our study. Signal hyperintensity on T1-weighted imaging has been previously described in FASI³⁷ and could help to differentiate FASI from generally T1-hypointense low-grade tumors. In our study, many FASI (both enhancing and nonenhancing) were found to be hypointense on T1-weighted imaging as well, though. Moreover, both FASI and low-grade tumors demonstrated facilitated diffusivity on ADC in our study. These findings reiterate the uncertain nature of FASI. Contrast-enhancing FASI and low-grade glioma may be impossible to distinguish even on follow-up imaging because they may share similar imaging features and may regress over time.^{32–36} Our study demonstrated that enhancing FASI tend to regress, paralleling the evolution of the more prevalent nonenhancing FASI. The underlying pathophysiology, however, remains uncertain, and low-grade gliomas and contrast-enhancing FASI cannot be differentiated with final certainty.

Although rare, radiologists should be aware of contrast-enhancing FASI, their possible initial increase in size, and their potential to regress with location dependent timelines because this may help prevent unnecessary biopsy or resection. Awareness regarding atypical follow-up behavior (ie, a second wave of contrast enhancement or development of atypical features) is warranted, and follow-up examinations after cessation of contrast enhancement are recommended.

Limitations

Some limitations of our study need to be taken into account. Our relatively small cohort precluded statistical analysis of contrast-enhancing FASI with respect to differences between age groups and locations. Variable durations of follow-up also limited the longitudinal characterization of contrast-enhancing lesions, especially of those that demonstrated continued enhancing volumes on their final studies and were lost to follow-up. As a further limitation of this retrospective

study, MR acquisition protocols varied, and nonenhanced T1-weighted sequences and DWI were not acquired in all patients. Variable section thicknesses may have influenced the measurements of small lesions and minor variations in volume are possible. Apart from the biopsy-proven tumors, no histologic correlation for the enhancing FASI was obtained, and the term “enhancing FASI” was used for lack of better terminology. Finally, referral bias may play a role because our institution is a tertiary care center and may experience a different spectrum of patients compared with what is seen elsewhere.

CONCLUSIONS

In this study, we characterize the natural evolution of 23 rare, contrast-enhancing lesions initially thought to represent enhancing FASI in patients with NF-1, with 2 of these lesions developing atypical features on follow-up and later proved to be tumors. The largest subgroup of these lesions occurred in the splenium of the corpus callosum and followed a benign course. MR imaging follow-up of size-increasing, contrast-enhancing lesions in patients with NF-1 differentiates between a benign course (decrease or resolution of enhancement) and new findings (cysts, recurrent increase of enhancement), prompting further evaluation for underlying tumors.

REFERENCES

- Aoki S, Barkovich AJ, Nishimura K, et al. **Neurofibromatosis types 1 and 2: cranial MR findings.** *Radiology* 1989;172:527–34 CrossRef Medline
- Williams VC, Lucas J, Babcock MA, et al. **Neurofibromatosis type 1 revisited.** *Pediatrics* 2009;123:124–33 CrossRef Medline
- Mentzel H-J, Seidel J, Fitzek C, et al. **Pediatric brain MRI in neurofibromatosis type 1.** *Eur Radiol* 2005;15:814–22 CrossRef Medline
- DiMario FJ, Ramsby G, Greenstein R, et al. **Neurofibromatosis type 1: magnetic resonance imaging findings.** *J Child Neurol* 1993;8:32–39 CrossRef Medline
- Itoh T, Magnaldi S, White RM, et al. **Neurofibromatosis type 1: the evolution of deep gray and white matter MR abnormalities.** *AJNR Am J Neuroradiol* 1994;15:1513–19 Medline
- Griffiths PD, Blaser S, Mukonoweshuro W, et al. **Neurofibromatosis bright objects in children with neurofibromatosis type 1: a proliferative potential?** *Pediatrics* 1999;104:e49 CrossRef Medline
- Duffner PK, Cohen ME, Seidel FG, et al. **The significance of MRI abnormalities in children with neurofibromatosis.** *Neurology* 1989;39:373–78 CrossRef Medline
- DiMario FJ, Ramsby G. **Magnetic resonance imaging lesion analysis in neurofibromatosis type 1.** *Arch Neurol* 1998;55:500–05 CrossRef Medline
- DiPaolo DP, Zimmerman RA, Rorke LB, et al. **Neurofibromatosis type 1: pathologic substrate of high-signal-intensity foci in the brain.** *Radiology* 1995;195:721–24 CrossRef Medline
- Cecen E, Ince D, Uysal KM, et al. **Soft tissue sarcomas and central nervous system tumors in children with neurofibromatosis type 1.** *Childs Nerv Syst* 2011;27:1885–93 CrossRef Medline
- Vinchon M, Soto-Ares G, Ruchoux MM, et al. **Cerebellar gliomas in children with NF1: pathology and surgery.** *Childs Nerv Syst* 2000;16:417–20 CrossRef Medline
- Guillamo J-S, Créange A, Kalifa C, et al. **Prognostic factors of CNS tumours in neurofibromatosis 1 (NF1): a retrospective study of 104 patients.** *Brain J Neurol* 2003;126:152–60 CrossRef Medline
- Molloy PT, Bilaniuk LT, Vaughan SN, et al. **Brainstem tumors in patients with neurofibromatosis type 1: a distinct clinical entity.** *Neurology* 1995;45:1897–902 CrossRef Medline
- Ratner N, Miller SJ. **A RASopathy gene commonly mutated in cancer: the neurofibromatosis type 1 tumour suppressor.** *Nat Rev Cancer* 2015;15:290–301 CrossRef Medline
- Chen C-C, Hsu P-W, Wu T-WE, et al. **Stereotactic brain biopsy: single center retrospective analysis of complications.** *Clin Neurol Neurosurg* 2009;111:835–39 CrossRef Medline
- Dammers R, Haitsma IK, Schouten JW, et al. **Safety and efficacy of frameless and frame-based intracranial biopsy techniques.** *Acta Neurochir (Wien)* 2008;150:23–29 CrossRef Medline
- Hall WA. **The safety and efficacy of stereotactic biopsy for intracranial lesions.** *Cancer* 1998;82:1749–55 CrossRef Medline
- Kongkham PN, Knifed E, Tamber MS, et al. **Complications in 622 cases of frame-based stereotactic biopsy, a decreasing procedure.** *Can J Neurol Sci* 2008;35:79–84 CrossRef Medline
- Gill DS, Hyman SL, Steinberg A, et al. **Age-related findings on MRI in neurofibromatosis type 1.** *Pediatr Radiol* 2006;36:1048–56 CrossRef Medline
- Sevick RJ, Barkovich AJ, Edwards MS, et al. **Evolution of white matter lesions in neurofibromatosis type 1: MR findings.** *AJR Am J Roentgenol* 1992;159:171–75 CrossRef Medline
- Lucchetta M, Manara R, Perilongo G, et al. **Regression of gadolinium-enhanced lesions in patients affected by neurofibromatosis type 1.** *Radiol Med* 2016;121:214–17 CrossRef Medline
- Hyman SL, Gill DS, Shores EA, et al. **Natural history of cognitive deficits and their relationship to MRI T2-hyperintensities in NF1.** *Neurology* 2003;60:1139–45 CrossRef Medline
- Salman MS, Hossain S, Alqublan L, et al. **Cerebellar radiological abnormalities in children with neurofibromatosis type 1: part 1—clinical and neuroimaging findings.** *Cerebellum Ataxias* 2018;5:14 CrossRef Medline
- Van Es S, North KN, McHugh K, et al. **MRI findings in children with neurofibromatosis type 1: a prospective study.** *Pediatr Radiol* 1996;26:478–87 CrossRef Medline
- Morris PW, Glasier CM, Smirniotopoulos JG, et al. **Disappearing enhancing brain lesion in a child with neurofibromatosis type 1.** *Pediatr Radiol* 1997;27:260–61 CrossRef Medline
- Ullrich NJ, Raja AI, Irons MB, et al. **Brainstem lesions in neurofibromatosis type 1.** *Neurosurgery* 2007;61:762–66; discussion 766–67 CrossRef Medline
- Margari L, Presicci A, Ventura P, et al. **Clinical and instrumental (magnetic resonance imaging [MRI] and multimodal evoked potentials) follow-up of brain lesions in three young patients with neurofibromatosis 1.** *J Child Neurol* 2006;21:1085–90 CrossRef Medline
- Vinhais S, Nunes S, Salgado D. **Focal brain enhancing lesions of evanescent type in patients with neurofibromatosis-1.** *ECR 2013 PosterNG* 2013
- Raininko R, Thelin L, Eeg-Olofsson O. **Non-neoplastic brain abnormalities on MRI in children and adolescents with neurofibromatosis type 1.** *Neuropediatrics* 2001;32:225–30 CrossRef Medline
- Mimouni-Bloch A, Kornreich L, Kaadan W, et al. **Lesions of the corpus callosum in children with neurofibromatosis 1.** *Pediatr Neurol* 2008;38:406–10 CrossRef Medline
- Miller DT, Freedenberg D, Schorry E, et al. **Health supervision for children with neurofibromatosis type 1.** *Pediatrics* 2019;143:e20190660 CrossRef Medline
- Gottschalk S, Tavakolian R, Buske A, et al. **Spontaneous remission of chiasmatic/hypothalamic masses in neurofibromatosis type 1: report of two cases.** *Neuroradiology* 1999;41:199–201 CrossRef Medline
- Menor F, Marti-Bonmati L, Arana E, et al. **Neurofibromatosis type 1 in children: MR imaging and follow-up studies of central nervous system findings.** *Eur J Radiol* 1998;26:121–31 CrossRef Medline

34. Parsa CF, Hoyt CS, Lesser RL, et al. **Spontaneous regression of optic gliomas: thirteen cases documented by serial neuroimaging.** *Arch Ophthalmol* 2001;119:516–29 CrossRef Medline
35. Leisti EL, Pyhtinen J, Poyhonen M. **Spontaneous decrease of a pilocytic astrocytoma in neurofibromatosis type 1.** *AJNR Am J Neuroradiol* 1996;17:1691–94 Medline
36. Cakirer S, Karaarslan E. **Spontaneous involution of a non-optic astrocytoma in neurofibromatosis type I: serial magnetic resonance imaging evaluation.** *Acta Radiol* 2004;45:669–73 CrossRef Medline
37. Hegde AN, Mohan S, Lath N, et al. **Differential diagnosis for bilateral abnormalities of the basal ganglia and thalamus.** *RadioGraphics* 2011;31:5–30 CrossRef Medline

Evaluation of DISORDER: Retrospective Image Motion Correction for Volumetric Brain MRI in a Pediatric Setting

 K. Vecchiato,  A. Egloff,  O. Carney,  A. Siddiqui,  E. Hughes,  L. Dillon,  K. Colford,  E. Green,  R.P.A.G. Teixeira,  A.N. Price,  G. Ferrazzi,  J.V. Hajnal,  D.W. Carmichael,  L. Cordero-Grande, and  J. O'Muircheartaigh



ABSTRACT

BACKGROUND AND PURPOSE: Head motion causes image degradation in brain MR imaging examinations, negatively impacting image quality, especially in pediatric populations. Here, we used a retrospective motion correction technique in children and assessed image quality improvement for 3D MR imaging acquisitions.

MATERIALS AND METHODS: We prospectively acquired brain MR imaging at 3T using 3D sequences, T1-weighted MPRAGE, T2-weighted TSE, and FLAIR in 32 unsedated children, including 7 with epilepsy (age range, 2–18 years). We implemented a novel motion correction technique through a modification of *k*-space data acquisition: Distributed and Incoherent Sample Orders for Reconstruction Deblurring by using Encoding Redundancy (DISORDER). For each participant and technique, we obtained 3 reconstructions as acquired (Aq), after DISORDER motion correction (Di), and Di with additional outlier rejection (DiOut). We analyzed 288 images quantitatively, measuring 2 objective no-reference image quality metrics: gradient entropy (GE) and MPRAGE white matter (WM) homogeneity. As a qualitative metric, we presented blinded and randomized images to 2 expert neuroradiologists who scored them for clinical readability.

RESULTS: Both image quality metrics improved after motion correction for all modalities, and improvement correlated with the amount of intrascan motion. Neuroradiologists also considered the motion corrected images as of higher quality (Wilcoxon $z = -3.164$ for MPRAGE; $z = -2.066$ for TSE; $z = -2.645$ for FLAIR; all $P < .05$).

CONCLUSIONS: Retrospective image motion correction with DISORDER increased image quality both from an objective and qualitative perspective. In 75% of sessions, at least 1 sequence was improved by this approach, indicating the benefit of this technique in unsedated children for both clinical and research environments.

ABBREVIATIONS: DISORDER = Distributed and Incoherent Sample Orders for Reconstruction Deblurring by using Encoding Redundancy; Aq = acquired; Di = after DISORDER motion correction; DiOut = Di with additional outlier rejection; GE = gradient entropy

Head motion is a common cause of image degradation in brain MR imaging. Motion artifacts negatively impact MR image quality and therefore radiologists' capacity to read the images, ultimately affecting patient clinical care.¹ Motion artifacts

are more common in noncompliant patients,² but even in compliant adults, intrascan movement is reported in at least 10% of cases.³ For children who require high-resolution MR images, obtaining optimal image quality can be challenging, owing to the

Received September 14, 2020; accepted after revision November 2.

From the Department for Forensic and Neurodevelopmental Sciences (K.V., J.O.), Institute of Psychiatry, Psychology and Neuroscience; Centre for the Developing Brain (K.V., A.E., O.C., E.H., L.D., K.C., E.G., R.P.A.G.T., A.N.P., J.V.H., L.C.-G., J.O.), School of Biomedical Engineering and Imaging Sciences; EPSRC/Wellcome Centre for Medical Engineering, Biomedical Engineering (D.W.C.); and MRC Centre for Neurodevelopmental Disorders (J.O.), King's College London, London, United Kingdom; Department of Radiology (O.C.), Great Ormond Street Hospital for Children, NHS Foundation Trust London, United Kingdom; Department of Radiology (A.S.), Guy's and Saint Thomas' Hospitals NHS Trust, London, United Kingdom; IRCCS San Camillo Hospital (G.F.), Venice, Italy; and Biomedical Image Technologies, ETSI Telecomunicación (L.C.-G.), Universidad Politécnica de Madrid e CIBER-BBN, Madrid, Spain.

L.C.-G. and J.O. contributed equally to the manuscript.

This research received funding from a Sir Henry Dale Fellowship jointly funded by the Wellcome Trust and the Royal Society (Grant Number 206675/Z/17/Z). The study was also supported in part by the Wellcome Engineering and Physical Sciences Research Council Center for Medical Engineering at King's College London (grant WT 203148/Z/16/Z), the Medical Research Council (UK) (grants MR/

K006355/1 and MR/LO11530/1), and Medical Research Council Center for Neurodevelopmental Disorders, King's College London (MR/N026063/1). Infrastructure support was provided by the National Institute for Health Research Mental Health Biomedical Research Center at South London, Maudsley NHS Foundation Trust, King's College London, the National Institute for Health Research Mental Health Biomedical Research Center at Guys, and St Thomas' Hospitals NHS Foundation Trust.

Paper previously presented as a poster at: European Congress of Magnetic Resonance in Neuropediatrics, February 26–29, 2020; in Marseille, France.

Please address correspondence to Dr. Katy Vecchiato, MD, Centre for the Developing Brain, School Biomedical Engineering and Imaging Sciences, Department of Perinatal Imaging and Health, King's College London, First Floor, South Wing, St Thomas' Hospital, SE17EH, London, United Kingdom; e-mail: katy.vecchiato@kcl.ac.uk

 Indicates open access to non-subscribers at www.ajnr.org

<http://dx.doi.org/10.3174/ajnr.A7001>

requirement to stay still over long durations needed for acquisition.⁴ Sedation can be an option, but it carries higher risks, costs, and preparation and recovery time.⁵

In conditions such as intractable focal epilepsy, identification of an epileptogenic lesion is clinically important to guide surgical treatment. However, these lesions can be visually subtle, particularly in children in whom subtle cortical dysplasias are more common.⁶ Dedicated epilepsy MR imaging protocols use high-resolution 3D sequences to allow better cortical definition and free reformatting of orientation but involve acquisition times in the order of minutes, so data collection becomes more sensitive to motion.⁷

For children in particular, multiple strategies are available for minimizing motion during MR examinations. Collaboration with play specialists using mock scanners and training or projecting a cartoon are good approaches to reduce anxiety.^{8,9} These tools are not always available in clinical radiology and, even with these strategies, motion can still be an issue.¹⁰ Different scanning approaches to correct for intrascan motion have been proposed. Broadly, prospective methods track head motion in real time and modify the acquisition directions accordingly.¹¹ These approaches are applicable to a wide range of sequences but require optical systems with external tracking markers, sometimes uncomfortable or impractical, and extra setup can ultimately result in longer examinations. Furthermore, these approaches may also not be robust to continuous motion.¹¹⁻¹³ Retrospective techniques have also been proposed, in some cases relying on imaging navigators that are not compatible with all standard sequences or contrasts.¹²

Descriptive demographics of the study population

Characteristics	Healthy Control Participants	Patients with Epilepsy	Total
Number	25	7	32
Age at scan (years)			
Mean + SD	11.32 ± 4.8	11.6 ± 3.7	11.4 ± 4.5
1-5	3	0	3
6-10	9	3	12
11-15	7	3	10
16-18	6	1	7
Sex			
Male	13	3	16
Female	12	4	16

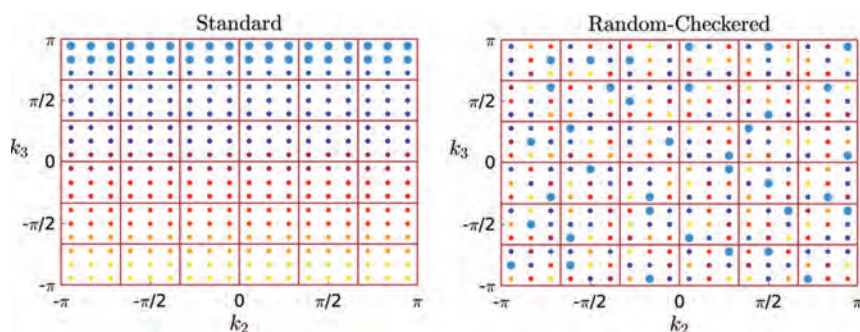


FIG 1. The different k -space data acquisitions. On the *left side*, the standard acquisition that sequentially acquires adjacent lines in the grid, with an example shot given as bigger dots in blue. The image on the *right* represents DISORDER's "random-checkedred" acquisition, in which every shot acquires distributed information in k -space with a certain degree of randomness.

Here, we use a more general retrospective motion correction technique: Distributed and Incoherent Sample Orders for Reconstruction Deblurring by using Encoding Redundancy (DISORDER). In this method, k -space samples are reordered to enable retrospective motion correction during image reconstruction.¹⁴ Our hypothesis is that DISORDER improves clinical MR imaging quality and readability. To assess its use for clinical sequences, we acquired a dedicated epilepsy MR imaging protocol in 32 children across a wide age range. We used both objective image quality metrics and expert neuroradiologist ratings to evaluate the outcome after motion correction.

MATERIALS AND METHODS

Study Population

We recruited families for a prospective study of pediatric epilepsy (ethics ref 18/LO/1766). Informed consent was obtained from all participants or their parents, as appropriate. From June to November 2019, we recruited 32 participants: 25 healthy control participants and 7 children with focal epilepsy, ages 2-18 years (median 11), including 16 females (50%) (Table). Exclusion criteria were age younger than 6 months or older than 18 years, major neurologic conditions unrelated to epilepsy, and contraindications for 3T MR imaging.

Image Acquisition

Children were scanned without sedation on a 3T Achieva-TX (Philips Healthcare) using a 32-channel head coil. They were asked to stay still during scanning while watching a movie. The protocol was T1-weighted MPRAGE: TR = 7.7 ms, TE = 3.6 ms, flip angle = 8°, TI = 900 ms, echo-train length = 154 and acquisition time = 286 s; T2-weighted: TSE: TR = 2500 ms, TE = 344 ms, echo-train length = 133, acquisition time = 342 s; T2-weighted FLAIR: TR = 5000 ms, TE = 422 ms, TI = 1800 ms, echo-train length = 182, acquisition time = 510 s. Parallel imaging acceleration (SENSE) of 1.4 was used along both phase-encoding directions. Field of view was 240 × 188 × 240 mm, and images were 1 mm isotropic. The combined acquisition time was approximately 22 minutes.

All scans were acquired using the DISORDER scheme (Fig 1). A shot of k -space is defined as a portion of k -space phase-encoding data in the k_2k_3 plane, acquired within a single acquisition block. In Fig 1, each shot is represented by a different color. As demonstrated by Cordero-Grande et al,¹⁴ DISORDER aims to improve motion tolerance by guaranteeing that the acquisition of every shot contains a series of samples distributed incoherently throughout k -space. This is achieved with a modified phase-encoding sampling order. We adopted the "random-checkedred" approach illustrated in Fig 1. Data are acquired in the inferior-superior k_1 , anteroposterior k_2 , and left-right k_3 orientations; this way rotations on the sagittal plane (k_1k_2) are sampled faster within each shot, improving robustness to intrashot

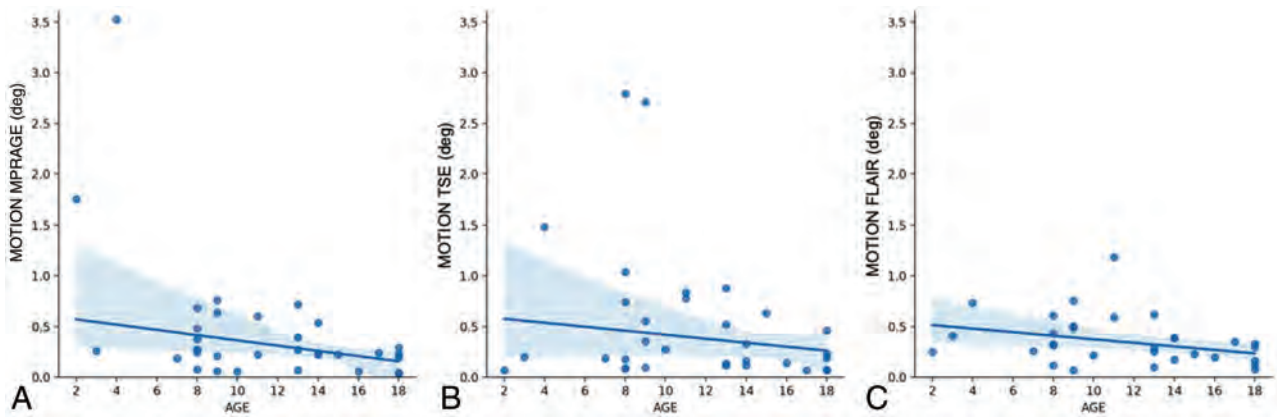


FIG 2. Estimated motion in relation to age. Older children tended to move less than younger ones. This was statistically significant for MPRAGE (A) and FLAIR (C) but not for TSE (B).

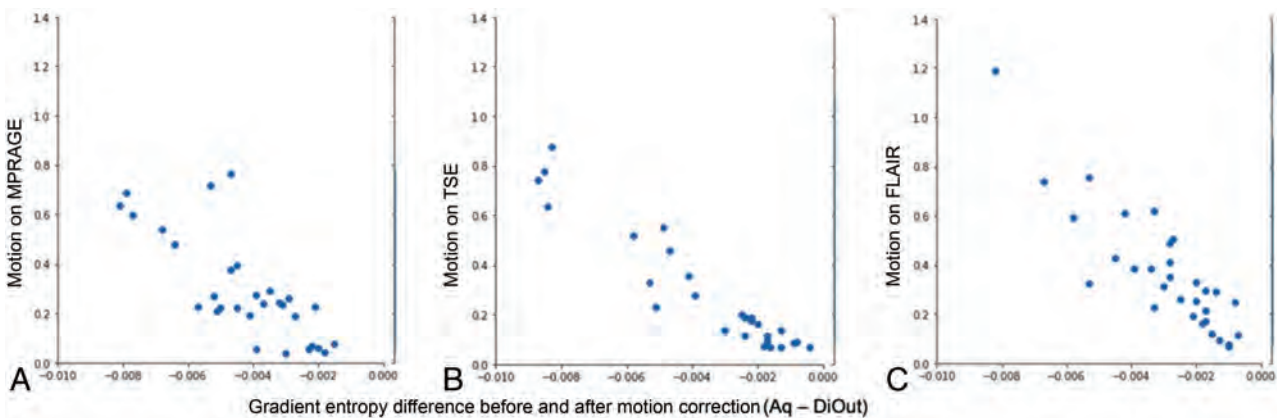


FIG 3. The reduction in gradient entropy by motion correction (DiOut compared with Aq) relative to the estimated amount of motion for every participant in all 3 modalities: MPRAGE (A), TSE (B), and FLAIR (C).

motion. In our protocol, the numbers of shots are 120 (duration, 1200 ms each) for MPRAGE, 135 (658 ms) for TSE, and 100 (859 ms) for FLAIR.

There was not a substantial difference in image quality between data acquired via standard acquisition and DISORDER acquisition. This was tested in the pilot phase of the study for all structural images (MPRAGE, TSE, and FLAIR).

Motion Correction

Motion and reconstruction were estimated jointly using a parallel k -space model in the presence of rigid motion.¹⁴ Starting from a standard reconstruction assuming no motion, a first approximation of the motion parameters for each shot is obtained by maximizing the likelihood of the k -space measures for current reconstructed volume. Then a new volume is reconstructed with current motion parameters, and the method alternates between motion estimation and reconstruction until convergence. Motion correction is performed as part of the reconstruction stage; an in-depth description of the reconstruction algorithm has been described previously.^{14,15}

The time for reconstruction varied from 5 to 40 minutes, depending on degree of intrascan motion. In the case of high intrascan motion, the DISORDER framework can further

improve the image quality by dismissing outlier shots. Therefore, each subject had their images reconstructed in 3 different ways: as acquired without motion correction (Aq), with DISORDER reconstruction (Di), and with DISORDER reconstruction including outlier shot rejection (DiOut).

Motion estimates from DISORDER correction can also provide a measure of intrascan motion. To summarize and quantify this intrascan motion, we averaged the temporal standard deviations of the 3 rotation parameters (in degrees) for every scan.

Image Quality Assessment

For all quality assessments, there were 288 images available (32 participants, 3 imaging modalities, and 3 reconstructions). To objectively compare image quality, we used 2 metrics that do not rely on reference datasets: gradient entropy (GE) and white matter (WM) signal homogeneity (MPRAGE only).

The entropy of an image is a measure of sharpness that characterizes its texture based on intensity.¹⁶ GE has been previously used to characterize image definition, smaller when areas of uniform signal intensity are separated by sharp edges.¹⁷ We calculated the normalized GE for Aq, Di, and DiOut. Decreased GE indicates that image information is concentrated at the edges, a measure of

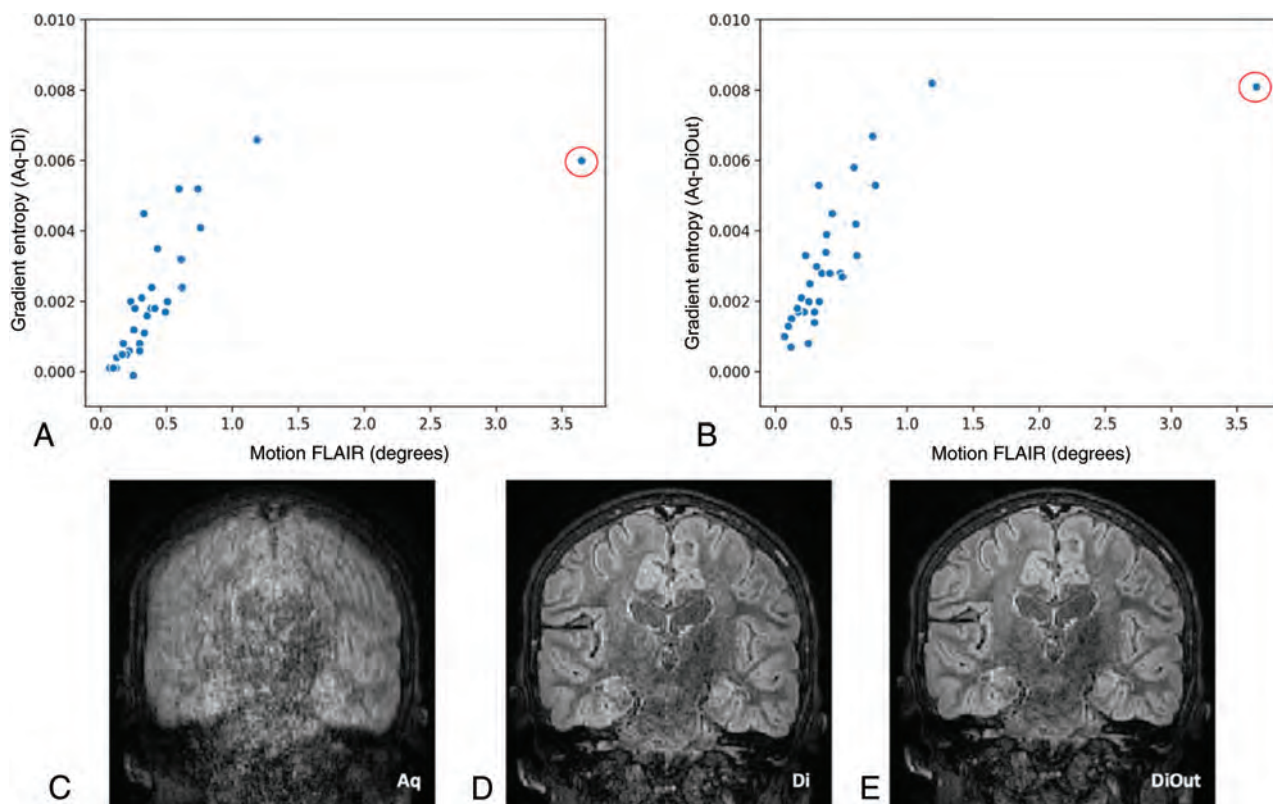


FIG 4. Differences in gradient entropy before and after motion correction (Di in A and DiOut in B) in relation to intrascan motion for the FLAIR images. The highlighted outlier datapoint (red circle) is shown on the bottom row. The example images show the reconstruction outcome in the participant with the highest intrascan motion. In this case, GE decreased after motion correction (more in the DiOut image), which visually relates to observers' score that improved from unreadable (1) in the Aq image (C) to good and excellent (3/4) in Di (D) and DiOut (E), respectively.

sharpness. This metric has a high correspondence with visual assessment of clinical MR imaging.¹⁸

WM signal homogeneities of the T1-weighted images were obtained using an automatic segmentation in FreeSurfer¹⁹ (version 6; <http://surfer.nmr.mgh.harvard.edu>). After calculating a WM mask, the mean and SD of the signal intensity were computed within the mask. The WM signal homogeneity was then measured as the mean scaled by SD, with higher WM signal homogeneity associated with higher image quality.

Image quality was further visually inspected by 2 pediatric neuroradiologists with more than 9 years' experience each (A.E. and O.C.). Radiology scoring was explicitly for assessment of focal epilepsy, which needs very high contrast between gray matter (GM) and WM. They scored the images with a 4-point Likert scale: 1, unreadable (not suited for clinical use); 2, poor quality (main structures identifiable but heavily blurred or artifacts covering >50% of the image); 3, good quality (good GM-WM differentiation, little blurring, or minor artifacts); and 4, excellent quality (no motion artifacts, good contrast, and perfectly defined GM-WM boundaries). Sagittal, coronal, and axial views of all images were presented to the 2 radiologists on the same screen and room environment in a randomized and blinded fashion. Each rater looked at all 288 cases in several sessions. The image viewer was rview (<https://biomedica.doc.ic.ac.uk/software/irtk>). In all reported comparisons (quantitative metrics and quality ranks), Wilcoxon signed-rank tests were used.

RESULTS

Quantitative Metrics

As expected, older children tended to move less than younger ones. This was a consistent relationship, statistically significant for MPRAGE and FLAIR (Spearman rho: -0.416 , -0.363 , both $P < .05$) but not for TSE scans (Spearman rho: -0.229 , $P = .21$) (Fig 2).

GE was reduced after motion correction across all modalities: the Wilcoxon rank test performed on mean scores before and after motion correction showed a statistically significant difference (for Di, $z = -4.861$ MPRAGE, $z = -4.769$ TSE, $z = -4.884$ FLAIR; for DiOut, $z = -4.937$ MPRAGE, $z = -4.937$ TSE, $z = -4.938$ FLAIR; all $P < .05$) (Fig 3).

There was a linear association between GE decrease after motion correction and degree of intrascan motion. We calculated the difference in GE before and after motion corrected data and estimated a linear regression against motion for each technique. The coefficients of determination (R^2) for MPRAGE images against motion were $R^2 = 0.24$ in Aq-Di and $R^2 = 0.48$ in Aq-DiOut; for T2-weighted images, they were $R^2 = 0.63$ in Aq-Di and $R^2 = 0.69$ Aq-DiOut; for FLAIR images, they were $R^2 = 0.44$ in Aq-Di and $R^2 = 0.51$ in Aq-DiOut; all $P < .05$. The reduction of GE was larger after outlier rejection (Fig 4).

There was an increase of WM signal homogeneity after motion correction on the MPRAGE images ($R^2 = 0.16$ for Aq-Di and $R^2 = 0.15$ for Aq-DiOut; both $P < .05$). One case was

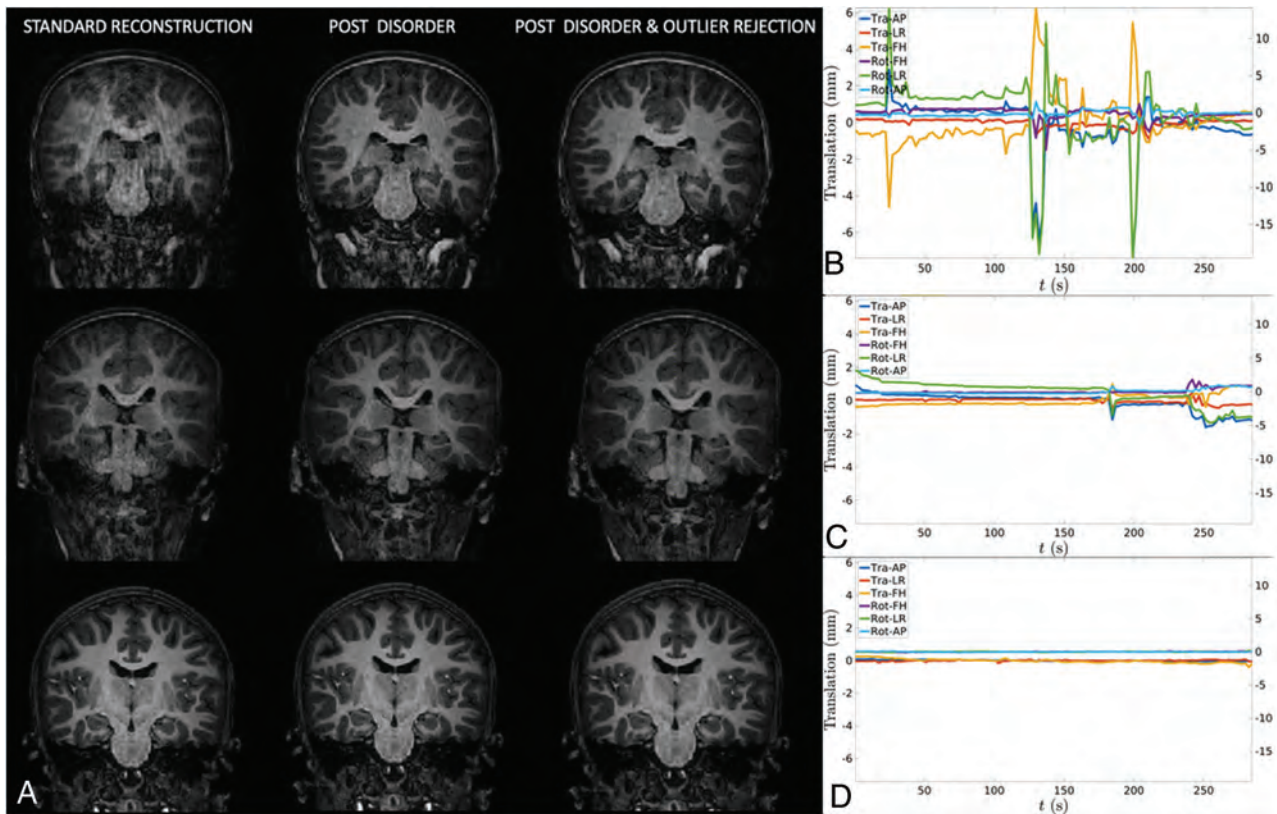


FIG 5. A, Three individual cases of MPRAGE images before and after motion correction and the corresponding motion trace displaying translations (Tra) and rotations (Rot) in 3 directions: anteroposterior (AP), left–right (LR), and foot–head (FH). B, High motion. C, Moderate motion. D, Little to no motion.

excluded from this analysis because of large motion during the MPRAGE acquisition and the resulting failure of the FreeSurfer pipeline for the uncorrected reconstruction. Full-brain segmentation was possible on the motion-corrected version of the images, and WM signal homogeneity was measured (Fig 5).

Qualitative Metrics

Expert visual inspection showed that image quality generally improved after motion correction (Fig 6). There was agreement between observers in raw image scores according to Cohen kappa coefficient for interrater reliability: $\kappa > 0.3$ for FLAIR and MPRAGE images, $\kappa > 0.6$ for TSE images, all $P < .05$. The intraclass correlation of the score change was used as another measure of interrater consistency on rating improvement. The intraclass correlation coefficient for absolute agreement in the change in scores after motion correction of the images was > 0.8 for TSE (Di and DiOut); for FLAIR, it was 0.64 for Di and 0.56 for DiOut images; all $P < .05$. The rating increase was less consistent between observers for MPRAGE images: 0.52 ($P < .05$) for Di and 0.37 ($P = .09$) for DiOut.

Wilcoxon signed-rank tests were conducted to compare the expert scores before and after image correction: the improvement of scores was statistically significant both for Di and DiOut and for both radiologists (for observer 1, $z = -3.164$ MPRAGE, $z = -2.066$ TSE, $z = -2.645$ FLAIR; for observer 2, $z = -3.162$ MPRAGE, $z = -2.714$ TSE, $z = -3.419$ FLAIR; all $P < .05$).

The Wilcoxon signed-rank test performed on mean scores between the 2 types of motion correction (Di and DiOut) did not show any statistically significant difference except for higher scores for FLAIR DiOut compared with Di ($z = -1.97$, $P = .049$) for 1 observer only.

For observer 2, the motion-corrected images (Di and DiOut) were all scored equally or higher than the Aq ones. Observer 1 gave lower ratings for motion-corrected reconstructions (Di) compared with acquired in 6/32 cases for FLAIR, 7/32 cases for MPRAGE, and 4/32 cases for TSE (by a maximum of 1 point). However, for most scans, the scores increased: 23/32 for FLAIR, 22/32 cases for MPRAGE, and 12/32 cases for TSE. For both raters, the score tended to remain good and equal in scans with little or no motion.

As expected, the Spearman rho showed a negative correlation between the amount of motion and the resulting score of acquired images in all modalities and for both observers (observer 1: $\rho = -0.558$ for MPRAGE, $\rho = -0.496$ for T2, both $P < .05$, $\rho = -0.216$ for FLAIR, $P = .24$; observer 2: $\rho = -0.619$ for MPRAGE, $\rho = -0.641$ for T2, $\rho = -0.544$ for FLAIR, all $P < .05$).

DISCUSSION

Successful neuroimaging in children is important for both clinical evaluation and research in brain development and disease. However, obtaining high-quality data in children is challenging in the highly motion-sensitive MR imaging context.²⁰ In this work, we demonstrated the benefits of retrospective motion

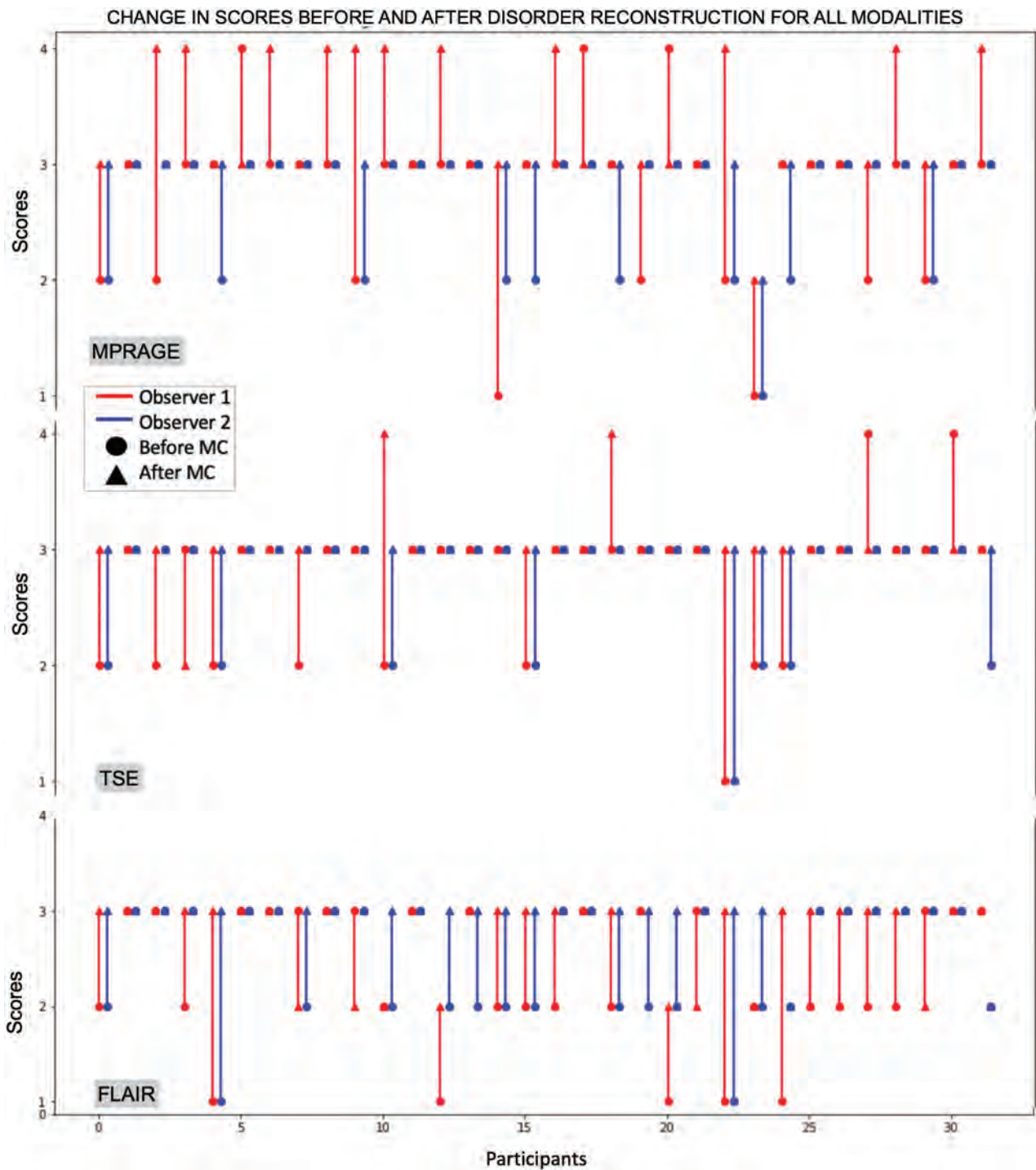


FIG 6. Scores before and after motion correction (DiOut) for all modalities. *Red* and *blue* correspond to observer 1 and 2's scores, respectively. The *dot* indicates the score before motion correction, and the *triangle* indicates the score after correction. Motion correction generally improved the image quality from a radiologic perspective.

correction on a nonsedated pediatric cohort undertaking brain MR imaging on a 3T scanner using the DISORDER framework. We applied this method to a dedicated high-resolution epilepsy protocol across a wide age range and showed that DISORDER motion correction increases image quality both quantitatively and qualitatively.

The 2 neuroradiologist raters broadly agreed on the improved diagnostic value of motion-corrected images; on average, ratings

were higher after DISORDER. In 24/32 (75%) participants, at least 1 technique was improved by DISORDER in a clinically significant way—from being considered unreadable or of poor quality to good or excellent quality. Images acquired in the presence of no or little motion maintained their high quality after motion correction.

In a small number of cases, DISORDER reconstructions were rated lower, though all in the context of very low motion.

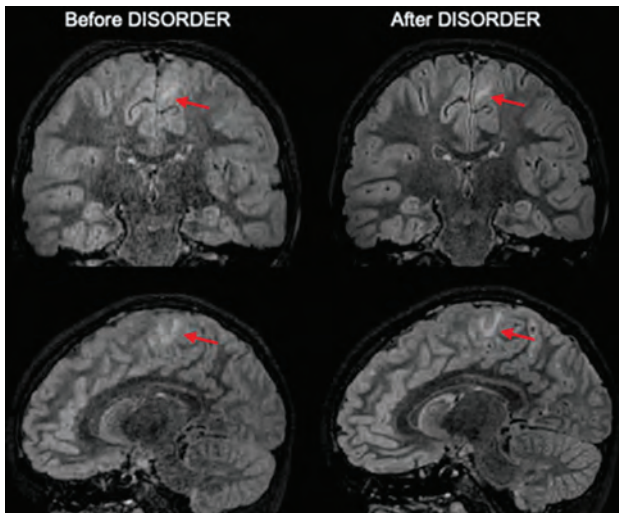


FIG 7. FLAIR images with and without motion correction. The *red arrows* highlight an area of focal cortical dysplasia in the left mesial frontoparietal region. These abnormalities are clearly better appreciated after applying DISORDER.

However, an advantage of this retrospective method is that images both before and after motion correction are always available for radiologic evaluation. Observed differences between raters are in line with previous studies²¹ in which differences in subjective radiologic judgment are reported.

As expected from practical experience and previous studies,^{22,23} younger children tended to move more than older ones, which was observed statistically significant for MPRAGE and FLAIR, though not for TSE. None of the participants exhibited very high motion during this acquisition. This was the third sequence acquired in our protocol; it may be that participants at that time point were simply more settled or comfortable (engaging with the movie they were watching or spontaneously falling asleep).

The proposed motion compensation method is particularly flexible for use, and it is applicable to any volumetrically encoded sequence. It does require modification of the scanner software to meet the requirements of data acquisition ordering, but it does not involve any additional hardware, relevant manipulation of imaging parameters, or additional operator training. The image reconstruction is operated with a vendor-independent off-line open-source code (<https://github.com/mriphysics/DISORDER/tree/1.1.0>), so the technique is not restricted to a specific vendor and has been tested on scanners from several manufacturers.

To comply with the requirements of enough SNR for high image resolution (1 mm) and strong motion tolerance, data are acquired with moderate acceleration factors (SENSE factor 1.4×1.4). However, the DISORDER encoding does not increase the sequence acquisition time per se. In practice, it may reduce the need for repeat scans and the time overhead would compare favorably with times required for sedation. The method can also provide motion correction for additional 3D sequences in which motion correction can be crucial (eg, relaxometry²⁴).

The approach provides clinically useful improvements. In this study, it is applied to a dedicated epilepsy protocol in which

clinicians aim to identify sometime subtle abnormalities such as focal changes in cortical thickness, subcortical signal abnormalities, or blurring of the GM–WM junction. In the presence of motion, DISORDER can be a helpful tool because these image features can be enhanced as shown in Fig 7.

More broadly, DISORDER could be helpful in a clinical setting to improve identification of other types of lesions not necessarily related to epilepsy including smaller injuries such as punctate bleeds (in which small motion may blur out the injury) or more obvious such as a brain mass (in which the extent and edge of pathologic tissue can be difficult to discern on blurry images). This method would be beneficial not only for children but also for patients with high anesthesiologic risk, situations in which time constrains the possibility to repeat scans, and for adult patients with intellectual disabilities.

Some limitations are noted. First, the method may require longer scan times to perform well in cases of very quick, large range, or continuous motion, and this is not assessed here. Second, DISORDER sampling increases motion sensitivity, facilitating its subsequent correction, so some enhancement of artifact levels compared with standard acquisition schemes is likely on the uncorrected images. Two further clinical considerations are also not yet addressed, the impact of reconstruction delay (up to 1 hour) and a quantification of maximum tolerable degradation before an acquisition needs to be repeated (how bad an image can be before it needs to be repeated). However, given the almost global improvement in data quality for motion-corrupted data, the reconstruction delay is probably not a large concern and will be addressable with future software implementations. Certainly, in this case, no DISORDER-reconstructed sequences were considered radiologically unreadable.

This framework for motion-tolerant structural 3D brain images improves clinical MR imaging quality both quantitatively and qualitatively. This might have substantial safety and economic implications for health care, reducing the clinical indication for sedation and repeat scans in children and adults.

ACKNOWLEDGMENTS

We are grateful to the families who generously supported this study. We also thank the Pediatric Neurology team from the Evelina London Children Hospital, including Dr. Ruth Williams, Dr. Elaine Hughes, Dr. Shan Tang, and Dr. Karine Lascelles.

Disclosures: Emer Hughes—UNRELATED: Employment: Kings College London. Kathleen Colford—UNRELATED: Employment: Kings College London. Anthony Price—RELATED: Grant: ERC grant agreement no. 319456 (dHCP project), Comments: Covers salary*. Joseph Hajnal—RELATED: Grant: ERC, Comments: Research grant that supported development of the underlying methodology*. David Carmichael—UNRELATED: Consultancy: Ives EEG Solutions, Comments: Consultancy for electrode safety testing performed in November 2017; Grants/Grants Pending: I have grants awarded from GOSHCC a UK children's medical charity*. Lucilio Cordero-Grande—RELATED: Grant: European Research Council/Ministry of Science and Innovation, Spain, Comments: Funds to pay salary respectively at King's College London/Technical University of Madrid*. Jonathan O'Muircheartaigh—RELATED: Grant: Wellcome Trust*; UNRELATED: Employment: King's College London. *Money paid to institution.

REFERENCES

1. Andre JB, Bresnahan BW, Mossa-Basha M, et al. **Toward quantifying the prevalence, severity, and cost associated with patient**

- motion during clinical MR examinations. *J Am Coll Radiol* 2015;12:689–95 CrossRef Medline
2. Cox AD, Virues-Ortega J, Julio F, et al. **Establishing motion control in children with autism and intellectual disability: applications for anatomical and functional MRI.** *J Appl Behav Anal* 2017;50:8–26 CrossRef Medline
 3. Gedamu EL, Gedamu A. **Subject movement during multislice interleaved MR acquisitions: prevalence and potential effect on MRI-derived brain pathology measurements and multicenter clinical trials of therapeutics for multiple sclerosis.** *J Magn Reson Imaging* 2012;36:332–43 CrossRef Medline
 4. Byars AW, Holland SK, Strawsburg RH, et al. **Practical aspects of conducting large-scale fMRI studies in children.** *J Child Neurol* 2002;17:885–90 CrossRef Medline
 5. Ho ML, Campeau NG, Ngo TD, et al. **Pediatric brain MRI part 1: basic techniques.** *Pediatr Radiol* 2017;47:534–43 CrossRef Medline
 6. Blumcke I, Spreafico R, Haaker G, et al. **Histopathological findings in brain tissue obtained during epilepsy surgery.** *N Engl J Med* 2017;377:1648–56 CrossRef Medline
 7. Wellmer J, Quesada CM, Rothe L, et al. **Proposal for a magnetic resonance imaging protocol for the detection of epileptogenic lesions at early outpatient stages.** *Epilepsia* 2013;54:1977–87 CrossRef Medline
 8. Thieba C, Frayne A, Walton M, et al. **Factors associated with successful MRI scanning in unsedated young children.** *Front Pediatr* 2018;6:6–8 CrossRef Medline
 9. Dean DC, Dirks H, O’Muircheartaigh J, et al. **Pediatric neuroimaging using magnetic resonance imaging during non-sedated sleep.** *Pediatr Radiol* 2014;44:64–72 CrossRef Medline
 10. Centeno M, Tierney TM, Perani S, et al. **Optimising EEG-fMRI for localisation of focal epilepsy in children.** *PLoS One* 2016;11:e0149048 CrossRef Medline
 11. Maclaren J, Herbst M, Speck O, et al. **Prospective motion correction in brain imaging: a review.** *Magn Reson Med* 2013;69:621–36 CrossRef Medline
 12. Kecskemeti S, Samsonov A, Velikina J, et al. **Robust motion correction strategy for structural MRI in unsedated children demonstrated with three-dimensional radial MPnRAGE.** *Radiology* 2018;289:509–16 CrossRef Medline
 13. Stucht D, Danishad KA, Schulze P, et al. **Highest resolution in vivo human brain MRI using prospective motion correction.** *PLoS One* 2015;10:e0133921–17 CrossRef Medline
 14. Cordero-Grande L, Ferrazzi G, Teixeira RPAG, et al. **Motion-corrected MRI with DISORDER: distributed and incoherent sample orders for reconstruction deblurring using encoding redundancy.** *Magn Reson Med* 2020;84:713–26 CrossRef Medline
 15. Cordero-Grande L, Teixeira RPAG, Hughes EJ, et al. **Sensitivity encoding for aligned multishot magnetic resonance reconstruction.** *IEEE Trans Comput Imaging* 2016;2:266–80 CrossRef
 16. Atkinson D, Hill DLG, Stoye PNR, et al. **Automatic correction of motion artifacts in magnetic resonance images using an entropy focus criterion.** *IEEE Trans Med Imaging* 1997;16:903–10 CrossRef Medline
 17. Thum CH. **Measurement of the entropy of an image with application to image focusing.** *Opt Acta (Lond)* 1984;31:203–11 CrossRef
 18. McGee KP, Manduca A, Felmlee JP, et al. **Image metric-based correction (autocorrection) of motion effects: analysis of image metrics.** *J Magn Reson Imaging* 2000;11:174–81 CrossRef Medline
 19. Fischl B, Van Der Kouwe A, Destrieux C, et al. **Automatically parcellating the human cerebral cortex.** *Cereb Cortex* 2004;14:11–22 CrossRef Medline
 20. Edwards AD, Arthurs OJ. **Paediatric MRI under sedation: is it necessary? What is the evidence for the alternatives?** *Pediatr Radiol* 2011;41:1353–64 CrossRef Medline
 21. Tschampa HJ, Kallenberg K, Urbach H, et al. **MRI in the diagnosis of sporadic Creutzfeldt-Jakob disease: a study on inter-observer agreement.** *Brain* 2005;128:2026–33 CrossRef Medline
 22. Greene DJ, Koller JM, Hampton JM, et al. **Behavioral interventions for reducing head motion.** *Neuroimage* 2018;171:234–45 CrossRef
 23. Dosenbach NUF, Koller JM, Earl EA, et al. **Real-time motion analytics during brain MRI improve data quality and reduce costs.** *Neuroimage* 2017;161:80–93 CrossRef Medline
 24. Kecskemeti S, Alexander AL. **Three-dimensional motion-corrected T1 relaxometry with MPnRAGE.** *Magn Reson Med* 2020;84:2400–12 CrossRef Medline

Beyond Isolated and Associated: A Novel Fetal MR Imaging–Based Scoring System Helps in the Prenatal Prognostication of Callosal Agenesis

S. Glatter, G. Kasprian, D. Bettelheim, B. Ulm, M. Weber, R. Seidl, D. Prayer, and M.C. Diogo



ABSTRACT

BACKGROUND AND PURPOSE: Although “corpus callosum agenesis” is an umbrella term for multiple entities, prenatal counseling is based reductively on the presence (associated) or absence (isolated) of additional abnormalities. Our aim was to test the applicability of a fetal MR neuroimaging score in a cohort of fetuses with prenatally diagnosed isolated corpus callosum agenesis and associated corpus callosum agenesis and correlate it with neurodevelopmental outcomes.

MATERIALS AND METHODS: We performed a single-center retrospective analysis of a cohort of cases of consecutive corpus callosum agenesis collected between January 2011 and July 2019. Cases were scored by 2 raters, and interrater agreement was calculated. Outcome was assessed by standardized testing (Bayley Scales of Infant and Toddler Development, Kaufman Assessment Battery for Children) or a structured telephone interview and correlated with scores using 2-way ANOVA.

RESULTS: We included 137 cases (74 cases of isolated corpus callosum agenesis), imaged at a mean of 27 gestational weeks. Interrater agreement was excellent (0.98). Scores were higher in associated corpus callosum agenesis ($P < .0001$) without a significant score difference between complete and partial corpus callosum agenesis ($P = .38$). Outcome was assessed in 42 children with isolated corpus callosum agenesis and 9 with associated corpus callosum agenesis (mean age, 3.1 years). MR imaging scores correctly predicted developmental outcome in 90.7% of patients with isolated corpus callosum agenesis, improving neurodevelopmental risk stratification in corpus callosum agenesis.

CONCLUSIONS: The scoring system is very reproducible and can differentiate isolated corpus callosum agenesis and associated isolated corpus callosum agenesis (significantly higher scores) but not between partial and complete corpus callosum agenesis. Scores correlated with outcome in isolated corpus callosum agenesis, but there were too few associated postnatal cases of isolated corpus callosum agenesis to draw conclusions in this group.

ABBREVIATIONS: aCCA = associated corpus callosum agenesis; CC = corpus callosum; CCA = corpus callosum agenesis; DCC = deleted in colorectal cancer; iCCA = isolated corpus callosum agenesis; MCD = malformations of cortical development; TOP = termination of pregnancy

Corpus callosum (CC) agenesis (CCA) is one of the most common malformations of the CNS.¹ Rather than a single entity, CCA is an umbrella term defined by anatomy, independent of etiology or outcome. To further complicate matters, CCA includes several subtypes, including complete (when the entire

CC is missing) and partial (when part but not all of the CC is absent), but CCA often also includes several degrees of hypoplasia (CC present but of reduced dimensions) and dysgenesis (CC present yet malformed). Each option may be seen in isolation (no other fetal brain or body malformations) or in the context of a polymalformative or genetic condition.¹⁻³

In terms of outcome risk stratification, patients with associated CCA (aCCA) are at a high risk of neurodevelopmental delay,⁴ while isolated CCA (iCCA) is associated with development within the normal range in up to 88% of children.⁵⁻⁹ Other features, such as the

Received August 5, 2020; accepted after revision November 10.

From the Department of Radiology (S.G., G.K., M.W., D.P., M.C.D.), Division of Neuro- and Musculoskeletal Radiology, Department of Pediatrics and Adolescent Medicine (S.G., R.S.), Division of Pediatric Neurology, and Department of Gynecology and Obstetrics (D.B.), Medical University of Vienna, Vienna, Austria; Department of Gynecology and Obstetrics (B.U., D.B.), Medical University of Vienna, Vienna, Austria; and Neuroradiology Department (M.C.D.), Hospital Garcia de Orta, Portugal.

Mariana C. Diogo and Sarah Glatter were partially funded by the Austrian Science Fund, grant I 3925-B27.

Preliminary results of this paper were previously presented at: Annual Meeting of the European Congress of Magnetic Resonance in Neuropediatrics, February 26–29, 2020; Marseille, France.

Please address correspondence to Gregor Kasprian, MD, Department of Radiology, Division of Neuro- and Musculoskeletal Radiology, Medical University of Vienna, Währinger Gürtel 18–20, 1090 Vienna, Austria; e-mail: gregor.kasprian@meduniwien.ac.at

Indicates open access to non-subscribers at www.ajnr.org

Indicates article with online supplemental data.

<http://dx.doi.org/10.3174/ajnr.A7064>

Summarized outcome by subgroup of corpus callosum agenesis

CCA Group	Neurodevelopment				Therapy				School		
	Normal	Delay			Phy	Occ	Spc	Other	Regular	Assisted	Not Age
		Mild	Moderate	Severe							
I											
C	15	5	1	1	9	2	1		12		9
P	16	2	1	1	11				11		7
A											
C	2			2	2		1	2	1	2	1
P	2	2		1	3	1	2	1	1	3	1

Note:—I indicates isolated; A, associated; C, complete; P, partial; Phy, physiotherapy; Occ, occupational therapy; Spc, speech therapy; Not Age, children not attending school, who were still under the local mandatory school age (5 years-old).

presence of Probst bundles or sigmoid bundles, have been used inconsistently in an attempt to predict outcome.^{10,11} In an attempt to improve risk stratification in iCCA, we developed and tested a score based on anatomic features evaluated on fetal brain MR imaging in patients with detailed postnatal neuropsychological outcomes.¹²

This study aimed to test the validity of an MR imaging score initially developed for isolated congenital CCA in a heterogeneous group of complete and partial CCA and to correlate it with neurodevelopmental outcomes.

MATERIALS AND METHODS

Patients and Setting

A retrospective cohort of consecutive cases of prenatally diagnosed CCA with fetal MR imaging between January 2011 and September 2019 was collected in a single tertiary care center (Medical University of Vienna).

Fetuses were subdivided into 4 groups based on imaging characteristics (determined on MR imaging by consensus of 2 experts): complete isolated, complete associated, partial isolated, and partial associated CCA. CCA was considered isolated when no other brain, spine, or extra-CNS anomalies were detected on ultrasound or MR imaging antenatally and no chromosomal anomalies were identified, in accordance with previous publications.^{4,6,13-16} In non-isolated CCA, associated anomalies were recorded. Severe global brain structural malformations that course without a CC (eg, holoprosencephaly, anencephaly) and the absence of the CC secondary to destructive lesions (eg, porencephaly) were excluded.^{17,18}

Imaging Analysis

Images were independently scored by 1 neuroradiologist with 7 years' experience in fetal MR imaging and a pediatrics resident with 1 year's basic experience in fetal MR imaging, using a previously published anatomic fetal MR imaging score,¹² consisting of 7 categories: gyration, opercularization, temporal lobe symmetry or asymmetry, lamination, hippocampal abnormalities, basal ganglia, and ventricular enlargement in a 0- to 2-point score (Table 1 and Online Supplemental Data), with a maximum attainable score of 11 points. Interrater agreement was calculated.

MR imaging examinations included a detailed evaluation of the fetal CNS and body, following published guidelines.¹⁹ For the fetal brain assessment, we obtained T2-weighted single-shot FSE imaging in 3 orthogonal planes (section thickness = 2–4 mm, section gap = 0–0.4 mm, FOV = 230–260 mm, matrix = 256). Body MR imaging evaluation comprised T2-weighted steady-state free

precession sequences in 3 orthogonal planes, and T2-weighted spin-echo FSE, T1WI, EPI, and DWI in at least 1 plane. Further sequences were acquired depending on examination findings and fetal and maternal cooperation. No maternal or fetal sedation was administered before the examination.

Neurodevelopmental Assessment

Patients who are followed in our center were evaluated by a neuropediatrician (R.S.) and a psychologist (S.G.) as previously described in detail in a previous publication.¹² The Bayley Scales of Infant and Toddler Development, Third Edition, was used for neurodevelopmental assessment of motor control, cognitive functioning, and language skills (1–42.5 months of age). Normal development was defined as a development quotient score of ≥ 85 , and moderate-to-severe developmental delay was defined as a development quotient score of < 70 . Children older than 42.5 months were tested for cognitive and language skills using the Kaufman Assessment Battery for Children, Second Edition, complemented by the *Peabody Developmental Motor Scales, Second Edition* or the Bruininks-Oseretsky Test of Motor Proficiency, Second Edition to evaluate motor skills. Normal development was defined as a Global Scale Index of ≥ 85 .

For children not followed up in our center, a structured telephone interview with 1 or both parents or legal guardians was conducted by a trained psychologist (S.G.). Besides assessment of developmental milestones, the need for further support, type of therapy, and type of kindergarten/schooling were also collected.

Statistical Analysis

Metric data are described using mean [SD] and range if normally distributed or median and maximum and minimum values for skewed metric or ordinal data. Additionally, 95% confidence intervals were calculated. Categorical data are presented as absolute frequencies and percentages. One-way ANOVAs and Bonferroni-corrected post hoc tests were used for differences in age among the 4 groups. Two-way ANOVAs were post hoc tests used to compare the groups regarding MR imaging and neurodevelopmental outcome scores to be able to model a moderation effect additionally. The Spearman rank correlation coefficient (ρ) was calculated to describe the correlation between MR imaging and neurodevelopmental variables. Image ratings were summed, and the resulting score was correlated with the neurodevelopmental outcome scores. Crosstabs and χ^2 tests were used to compare groups regarding nominal data.

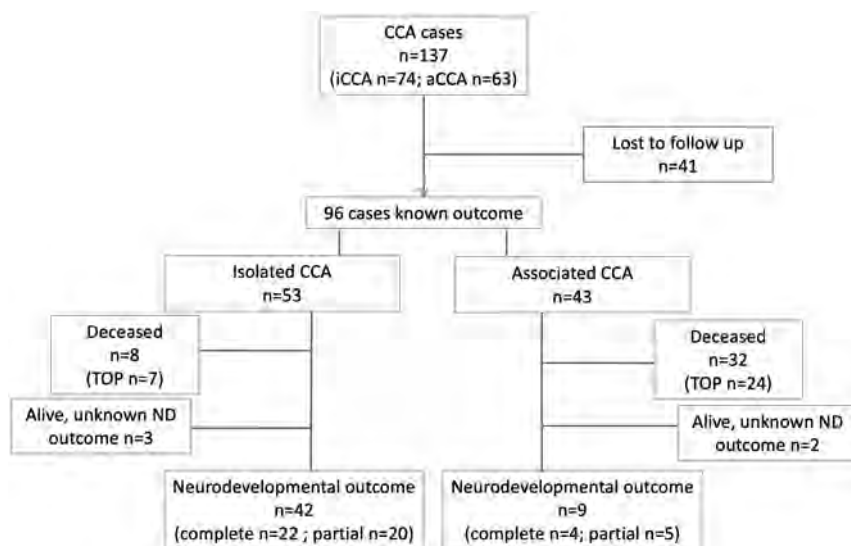


FIG 1. Flowchart detailing patient inclusion and exclusion criteria. ND indicates neurodevelopmental.

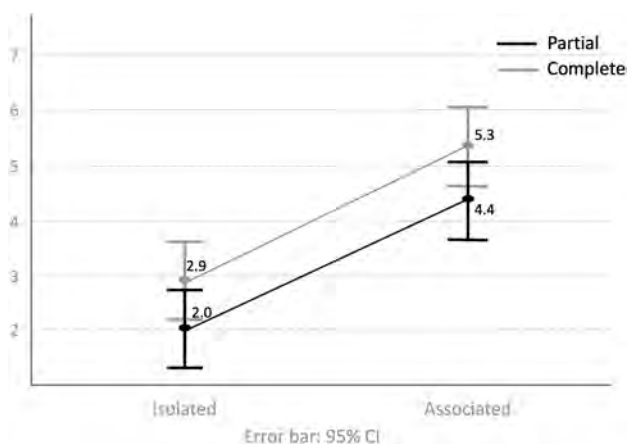


FIG 2. Comparison of mean MR imaging scores and 95% confidence intervals among the 4 CCA groups: isolated (complete and partial) and associated (complete and partial).

A P value $\leq 5\%$ ($P = .05$) indicated significant results. To avoid an increasing error of the second type, we did not perform multiplicity corrections. All analyses were performed using SPSS Statistics for Window, Version 26.0 (IBM).

RESULTS

A total of 137 cases of CCA were imaged in our center during the study period (Fig 1), with a mean gestational age of 27 gestational weeks (range, 19 + 4 to 37 + 1 gestational weeks). Of these, 74 fetuses (complete: $n = 45$; partial $n = 29$) presented with iCCA, while 63 fetuses (complete: $n = 32$; partial $n = 31$) had associated conditions. The most common associated anomalies involved the CNS ($n = 58/64$), mostly involving the supratentorial brain and specifically malformations of cortical development (MCD) (MCD: $n = 34/64$; only MCD: $n = 16$; MCD with other associated anomalies: $n = 18$), followed by posterior fossa anomalies ($n = 23/64$).

There were extra-CNS anomalies in 31 fetuses, and these were the only findings besides CCA in 6 cases (congenital diaphragmatic hernia, $n = 1$; heart malformation, $n = 2$; limb anomalies alone, $n = 1$; and in association with head and neck malformations, $n = 2$).

Interrater agreement was excellent (0.98).

By means of the MR imaging score, there was a statistically significant difference between associated and complete CCA ($P < .0001$), but not between partial and complete CCA within each group (mean iCCA: partial = 2.69 [SD, 0.31], 95% CI, 2.07–3.31; complete = 2.04 [SD, 0.38], 95% CI, 1.28–2.80; aCCA: partial = 4.92 [SD, 0.37], 95% CI, 4.19–5.65; complete = 4.96 [SD, 0.37], 95% CI, 4.23–5.69; $P = .38$) (Fig 2).

Forty-one cases were lost to follow-up, leaving 96 pregnancies with known outcomes (Fig 1). Parents opted for termination of pregnancy (TOP) more often in the aCCA subgroup (aCCA, $n = 24/43$, [55.8%]; iCCA, $n = 7/53$, [13.2%]; $P < .001$). There were also more cases of natural deaths in this group (aCCA $n = 8$), 4 cases in each complete and partial aCCA group; 3 children were stillborn (gestational age unknown); and 5 died after birth. In iCCA, all TOPs were in the complete iCCA group.

In 3 cases of iCCA and 2 of aCCA, children were alive, but no detailed follow-up was available. In the 51 remaining cases, the mean age at the time of evaluation or interview was 3.1 [SD, 2.08] years, and there was no significant difference in the mean age of the 4 subgroups (iCCA: complete = 3.07 [SD, 2.36] years; partial = 2.76 [SD, 1.36] years; aCCA: complete = 4.38 [SD, 2.69] years; partial = 3.96 [SD, 2.46] years; $P = .42$).

Outcome was assessed in the remaining 42 cases of iCCA and 9 of aCCA. The neurodevelopmental outcome overall and divided into domains (speech, cognition, and motor) and the need for special schooling and therapy are summarized in the Table and Online Supplemental Data. In the iCCA group, 31/42 patients (73.8%) had normal development, with all school-age children attending regular school in the appropriate year, without need for special education. By means of the established cutoff of ≤ 3 for good neurodevelopmental outcome and ≥ 4 for a high risk of neurodevelopmental delay, MR imaging was correct in 90.7% of cases. In the normally developing group, there was 1 fetus with a high MR imaging score of 4. In the remaining 96.8% (30/31) of cases, the score predicted the favorable outcome correctly. In the developmental delay group, the MR imaging score was incorrect in 4/43 cases (9.3%). There were too few cases in the associated group to evaluate the correlation of scoring and outcome (Fig 3). Due to the small sample size for iCCA, it was not possible to adequately compare the outcomes in the associated and isolated groups further.

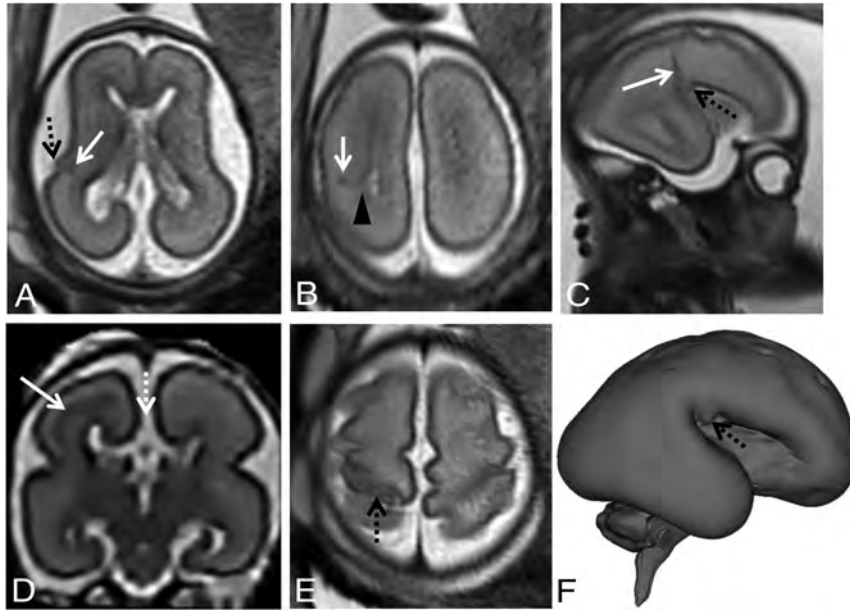


FIG 3. Example of associated partial CCA (white dashed arrow, D) in fetuses at 24 gestational weeks (A and B), 26 gestational weeks (C, D, F), and 31 gestational weeks (E). T2-weighted single-shot FSE images in the axial (A, B, E) and sagittal planes (C) and super-resolution 3D reconstruction of T2-weighted spin-echo FSE images through the coronal plane (D) and cortical surface (F). There is a malformation of cortical development with an abnormal “bump” in the insular region (dashed black arrow, A, C, F) and abnormal gyration in the posterior frontal cortex (dashed black arrow, E). There is a concurrent signal abnormality with low T2 signal intensity that follows the intermediate zone/subplate limit on the left (white arrow, A–D), also reaching the ventricular lining (black arrowhead, B), with slight ectasia of the homolateral posterior aspect of the lateral ventricle.

DISCUSSION

This recently developed fetal MR neuroimaging score outperforms the current oversimplified categorization of isolated CCA in terms of prognostication. When one exclusively uses the current criterion standard of excluding associated disorders, 26.2% of children had some degree of developmental delay in the iCCA group, in accordance with most literature available on the subject.^{5,6,8,9,20} By applying this systematic evaluation of specific brain regions, we improved the diagnostic power of MR imaging by correctly stratifying high- and low-risk cases in 90.7%. The score accuracy was higher in the normally developing group, in which 96.8% (30/31) of prognostications were correct, with the incorrect case with a borderline score of 4. In patients with some degree of neurodevelopmental delay, there were 3 incorrect classifications, all of which presented with a mild delay and MR imaging scores of 3, close to the threshold.

The MR imaging scoring system has been derived from a variety of previous structural neuroimaging findings known to be associated with CCA. Given the complexity of human brain development, the score is based on the principle that morphologic assessment of interhemispheric connectivity alone is not sufficient to offer an appropriate prognostic counseling in cases of CCA.

Despite the difference in experience in fetal MR imaging interpretation, interrater agreement was 0.98. This is similar to our previously published findings when comparing the ratings of 2 experienced raters.¹²

There was a significant difference in the MR imaging scores between isolated and associated CCA ($P < .001$), detecting a higher degree of deviation from normal brain development in aCCA despite being primarily designed for the specific assessment of cases classified as iCCA.¹² Application of the MR imaging score did not, however, help stratify the risk in aCCA. It does not account for severe or even life-threatening extra-CNS malformations. There was also a low number of surviving children in this group with known outcomes, of which 4 patients (4/9) are developing within normal ranges, though we have a limited maximum follow-up period of 7.5 years. It can be argued that these results are skewed because minor associated anomalies are more likely to be positively counseled and not terminated, but the 4 children mentioned presented with associated CNS anomalies (MCD in 3 cases and germinolytic cyst in 1). In our opinion, this highlights the need to better understand this entity. The simplified categorization into isolated and associated does not do justice to the complex neurobiology behind this malformation.^{21,22}

As would be expected, parents opted for TOP more often when fetuses presented with multiple malformations (aCCA: TOP, $n = 24/43$ [55.8%]; iCCA: TOP, $n = 7/63$ [9.6%]), because neurodevelopmental outcome is expected to be poor in most of these children, particularly taking into consideration that most of our associated findings were related to other CNS anomalies (90.6%). An interesting finding in our cohort was that parents opted for TOP more often when presented with a fetus with complete iCCA ($n = 7/32$ [21.9%]) than in cases of partial iCCA ($n = 0/21$), despite extensive literature proving the lack of difference in outcomes between these groups.^{20,23} We could not determine whether this choice related to the personal beliefs of the parents alone or to the prenatal counseling received by a variety of medical professionals (within and outside our center). In our cohort, we found no statistical difference in the neurodevelopmental outcome ($P = .20$), area of deficits ($P = .89$), need for therapy (physiotherapy, $P = .40$; occupational, $P = .55$; speech, $P = 1.0$), or schooling ($P = .87$) between partial and complete iCCA. This finding is in accordance with previous literature,^{8,23,24} as is the percentage of children with iCCA and some degree of developmental delay (26.2%).^{20,25} Furthermore, these data support the notion that counseling in cases of CCA requires further refinement and updates concerning recent genetic, morphologic, and functional neurobiologic insights into this condition. Also, in the future, more complex imaging techniques

such as diffusion tensor imaging may further optimize the assessment of fetuses with CCA.

The retrospective nature of the data collection has inherent limitations. Furthermore, a large group of patients was lost to follow-up due to the tertiary referral nature of our center, with most patients coming from outside clinics or hospitals and often from foreign countries, making it challenging to obtain outcome data. Furthermore, particularly in the associated group, more than half of the pregnancies were terminated, leaving a small surviving aCCA group and limiting the intergroup comparisons. However, this information is still relevant in relation to the outcome of these pregnancies. There was also a relatively inhomogeneous assessment of outcome. Twenty-one of the iCCAs had detailed in-person neurodevelopmental assessments, while the remaining children were assessed via structured telephone interview, which can be less precise. To further validate our data and indirectly evaluate the neurodevelopmental status of the children, we also collected data on schooling (level for age and need for special schooling) as well as any specific therapy attended.

CONCLUSIONS

Despite increasing the ability to stratify the risk of neurodevelopmental delay of these patients, the MR imaging score does not substitute in any way for other investigations, namely genetic studies, which were not uniformly available in our cohort and hence were not discussed in detail. It is established that some genetic mutations are associated with a poorer prognosis, while others, such as deleted in colorectal cancer (DCC) gene, usually have a mild course.²⁶ However, we should aim to improve our diagnostic accuracy on fetal MR imaging, independent of other studies that may or may not be available. It is the last imaging resource in prenatal diagnosis, and it should add useful information for parents and counseling whenever possible.

Disclosures: Gregor Kasprian—RELATED: Grant: Austrian Science Fund, Comments: Joint Project Grant, role of Micro-Ribonucleic acid (mRNA) in Fetal alcohol spectrum disorders (FASD);* Mariana C. Diogo—RELATED: Grant: Austrian Science Fund*; UNRELATED: Employment: Instituto de Telemedicina, Comments: neuroradiologist. Sarah Glatter—RELATED: Grant: Austrian Science Fund 3925-B27*; Support for Travel to Meetings for the Study or Other Purposes: Medical University of Vienna. *Money paid to the institution.

REFERENCES

1. Edwards TJ, Sherr EH, Barkovich AJ, et al. **Clinical, genetic and imaging findings identify new causes for corpus callosum development syndromes.** *Brain* 2014;137:1579–613 CrossRef Medline
2. Bedeschi MF, Bonaglia MC, Grasso R, et al. **Agenesis of the corpus callosum: clinical and genetic study in 63 young patients.** *Pediatr Neurol* 2006;34:186–93 CrossRef Medline
3. Schell-Apacik CC, Wagner K, Bihler M, et al. **Agenesis and dysgenesis of the corpus callosum: clinical, genetic and neuroimaging findings in a series of 41 patients.** *Am J Med Genet A* 2008;146A:2501–11 CrossRef Medline
4. Yeh HR, Park HK, Kim HJ, et al. **Neurodevelopmental outcomes in children with prenatally diagnosed corpus callosal abnormalities.** *Brain Dev* 2018;40:634–41 CrossRef Medline
5. Pisani F, Bianchi ME, Piantelli G, et al. **Prenatal diagnosis of agenesis of corpus callosum: what is the neurodevelopmental outcome?** *Pediatr Int* 2006;48:298–304 CrossRef Medline
6. Vergani P, Ghidini A, Strobelt N, et al. **Prognostic indicators in the prenatal diagnosis of agenesis of corpus callosum.** *Am J Obstet Gynecol* 1994;170:753–58 CrossRef Medline
7. Brown WS, Paul LK. **The neuropsychological syndrome of agenesis of the corpus callosum.** *J Int Neuropsychol Soc* 2019;25:324–30 CrossRef Medline
8. Folliot-Le Doussal L, Chadie A, Bresseur-Daudruy M, et al. Perinatal Network of Haute-Normandie. **Neurodevelopmental outcome in prenatally diagnosed isolated agenesis of the corpus callosum.** *Early Hum Dev* 2018;116:9–16 CrossRef Medline
9. Mangione R, Fries N, Godard P, et al. **Neurodevelopmental outcome following prenatal diagnosis of an isolated anomaly of the corpus callosum.** *Ultrasound Obstet Gynecol* 2011;37:290–95 CrossRef Medline
10. Tovar-Moll F, Moll J, de Oliveira-Souza R, et al. **Neuroplasticity in human callosal dysgenesis: a diffusion tensor imaging study.** *Cereb Cortex* 2007;17:531–41 CrossRef Medline
11. Benezit A, Hertz-Pannier L, Dehaene-Lambertz G, et al. **Organising white matter in a brain without corpus callosum fibres.** *Cortex* 2015;63:155–71 CrossRef Medline
12. Diogo MC, Glatter S, Prayer D, et al. **Improved prognostication in isolated callosal agenesis: a fetal magnetic resonance imaging-based scoring system.** *Ultrasound Obstet Gynecol* 2020 Jun 2. [Epub ahead of print] CrossRef Medline
13. Ballardini E, Marino P, Maietti E, et al. **Prevalence and associated factors for agenesis of corpus callosum in Emilia Romagna (1981–2015).** *Eur J Med Genet* 2018;61:524–30 CrossRef Medline
14. Kim SE, Jang HI, Chang KH, et al. **Clinical outcomes and neurodevelopmental outcome of prenatally diagnosed agenesis of corpus callosum in single center of Korea.** *Obstet Gynecol Sci* 2017;60:8–17 CrossRef Medline
15. Manfredi R, Tognolini A, Bruno C, et al. **Agenesis of the corpus callosum in fetuses with mild ventriculomegaly: role of MR imaging.** *Radiol Med* 2010;115:301–12 CrossRef Medline
16. des Portes V, Rolland A, Velazquez-Dominguez J, et al. **Outcome of isolated agenesis of the corpus callosum: a population-based prospective study.** *Eur J Paediatr Neurol* 2018;22:82–92 CrossRef Medline
17. Glass HC, Shaw GM, Ma C, et al. **Agenesis of the corpus callosum in California 1983–2003: a population-based study.** *Am J Med Genet A* 2008;146A:2495–2500 CrossRef Medline
18. Knezovic V, Kasprian G, Stajduhar A, et al. **Underdevelopment of the human hippocampus in callosal agenesis: an in vivo fetal MRI study.** *AJNR Am J Neuroradiol* 2019;40:576–81 CrossRef Medline
19. Prayer D, Malinge G, Brugger PC, et al. **ISUOG Practice Guidelines: performance of fetal magnetic resonance imaging.** *Ultrasound Obstet Gynecol* 2017;49:671–80 CrossRef Medline
20. Sotiriadis A, Makrydimas G. **Neurodevelopment after prenatal diagnosis of isolated agenesis of the corpus callosum: an integrative review.** *Am J Obstet Gynecol* 2012;206:e331–35 CrossRef Medline
21. Richards L, Plachez C, Ren T. **Mechanisms regulating the development of the corpus callosum and its agenesis in mouse and human.** *Clin Genet* 2004;66:276–89 CrossRef Medline
22. Paul LK, Brown WS, Adolphs R, et al. **Agenesis of the corpus callosum: genetic, developmental and functional aspects of connectivity.** *Nat Rev Neurosci* 2007;8:287–99 CrossRef Medline
23. Al-Hashim AH, Blaser S, Raybaud C, et al. **Corpus callosum abnormalities: neuroradiological and clinical correlations.** *Dev Med Child Neurol* 2016;58:475–84 CrossRef Medline
24. Palmer EE, Mowat D. **Agenesis of the corpus callosum: a clinical approach to diagnosis.** *Am J Med Genet C Semin Med Genet* 2014;166C:184–97 CrossRef Medline
25. Santo S, D'Antonio F, Homfray T, et al. **Counseling in fetal medicine: agenesis of the corpus callosum.** *Ultrasound Obstet Gynecol* 2012;40:513–21 CrossRef Medline
26. Marsh APL, Edwards TJ, Galea C, et al. IRC5 Consortium. **DCC mutation update: congenital mirror movements, isolated agenesis of the corpus callosum, and developmental split brain syndrome.** *Hum Mutat* 2018;39:23–39 CrossRef Medline

Validation of the National Institute of Neurological Disorders and Stroke Spinal Cord Injury MRI Common Data Elements Instrument

J. Fisher, L. Krisa, D.M. Middleton, B.E. Leiby, J.S. Harrop, L.M. Shah, E.D. Schwartz, A. Doshi, S.H. Faro, F.B. Mohamed, and A.E. Flanders



ABSTRACT

BACKGROUND AND PURPOSE: The National Institute of Neurological Disorders and Stroke common data elements initiative was created to provide a consistent method for recording and reporting observations related to neurologic diseases in clinical trials. The purpose of this study is to validate the subset of common data elements related to MR imaging evaluation of acute spinal cord injury.

MATERIALS AND METHODS: Thirty-five cervical and thoracic MR imaging studies of patients with acute spinal cord injury were evaluated independently in 2 rounds by 5 expert reviewers. Intra- and interrater agreement were calculated for 17 distinct MR imaging observations related to spinal cord injury. These included ordinal, categorical, and continuous measures related to the length and location of spinal cord hemorrhage and edema as well as spinal canal and cord measurements. Level of agreement was calculated using the interclass correlation coefficient and kappa.

RESULTS: The ordinal common data elements spinal cord injury elements for lesion center and rostral or caudal extent of edema or hemorrhage demonstrated agreement ranging from interclass correlation coefficient 0.68 to 0.99. Reproducibility ranged from 0.95 to 1.00. Moderate agreement was observed for absolute length of hemorrhage and edema (0.54 to 0.60) with good reproducibility (0.78 to 0.83). Agreement for the Brain and Spinal Injury Center score showed the lowest interrater agreement with an overall kappa of 0.27 (0.20, 0.34). For 7 of the 8 variables related to spinal cord injury, agreement improved between the first and second evaluation. Continuous diameter measures of the spinal cord and spinal canal using interclass correlation coefficient varied substantially (0.23 to 0.83).

CONCLUSIONS: Agreement was more consistent for the ordinal measures of spinal cord injury than continuous measures. Good to excellent agreement on length and location of spinal cord hemorrhage and edema can be achieved with ordinal measures alone.

ABBREVIATIONS: BASIC = Brain and Spinal Injury Center; CDE = common data element; CRF = case report form; NINDS = National Institute of Neurological Disorders and Stroke; SCI = spinal cord injury; ICC = interclass correlation coefficient

In 2006, the National Institute of Neurological Disorders and Stroke (NINDS) began a process to develop common data elements (CDEs) to provide a standardized method for the

collection of clinical data related to neurologic diseases.¹⁻³ Recognizing that there is a lack of clear and consistent terminology for spine disorders, particularly spinal cord injury (SCI), in 2014, the NINDS convened a workgroup comprising expert stakeholders for the development of SCI CDE instruments that included clinical care assessments and imaging.³⁻⁸ This new set of SCI CDE instruments aimed to increase the efficiency and value of clinical research studies and treatment, increase data quality, facilitate data sharing, and help educate new clinical investigators.³ Investigators are expected to incorporate the CDE modules in grant applications and National Institutes of Health-funded research.

The MR imaging SCI CDE subset was created to be a comprehensive and standardized terminology for describing MR imaging findings in patients with SCI. This collection consists of a case report form (CRF) containing 35 discrete measures and responses divided into 4 main categories: general imaging characteristics,

Received August 7, 2020; accepted after revision October 26.

From the Departments of Radiology (J.F., D.M.M., S.H.F., F.B.M., A.E.F.), Physical Therapy/Occupational Therapy (L.K.), Biostatistics (B.E.L.), and Neurosurgery (J.S.H.), Thomas Jefferson University Hospital, Philadelphia, Pennsylvania; Department of Radiology (L.M.S.), University of Utah, Salt Lake City, Utah; Department of Radiology (E.D.S.), Saint Elizabeth's Medical Center, Brighton, Massachusetts; and Department of Radiology (A.D.), Mount Sinai Medical Center, New York, New York.

Originating institution: Department of Radiology, Thomas Jefferson University Hospital, Suite 1080B Main Building, 132 S. Tenth St, Philadelphia, PA, 19107.

Funding: Craig H. Nielson Foundation (16G.565).

Please address correspondence to Adam E. Flanders, MD, Department of Radiology, Thomas Jefferson University Hospital, Suite 1080B Main Building, 132 S. Tenth St, Philadelphia, PA, 19107; e-mail: adam.flanders@jefferson.edu; @BFlinksteak

Indicates article with online supplemental data.

<http://dx.doi.org/10.3174/ajnr.A7000>

spinal injury features, canal and cord measurements, and chronic SCI features. The responses are of 3 types: Boolean, categoric, and an ordinal range representing specific anatomic locations. These measures were chosen to represent both objective and subjective assessment derived from routine clinical MR images. The workgroup codified these features using existing CDEs that have proved value in the published literature, and when ones did not exist, the workgroup developed the feature and the response parameters.

As with the development of any CRF used for a clinical trial or research, the goal is to provide an instrument that provides useful data representations that are reproducible across trained observers and institutions, require minimal cognitive effort, minimize ambiguity, and are both accurate and precise. Reproducibility of the observations through rigorous testing by multiple observers is a needed step to validate the instrument before clinical or research use. However, the evaluation process may not entirely reproduce the clinical environment in which it is meant to be used such that datasets and observers are overly prepared or optimized. Therefore, the goal of this study is to determine the inter- and intrarater reliability of the NINDS MR imaging CDEs when assessed by MR imaging experts with familiarity with SCI. We hypothesize that there will be good to excellent agreement ($\kappa > 0.4$) among the expert raters after limited training.

MATERIALS AND METHODS

Collection of the MR Imaging Dataset

This study was given exemption status from the institutional review board. An MR imaging evaluation dataset was assembled to represent a range of subjective visual MR SCI features that would be used to validate the NINDS SCI MR imaging CRF feature set. Examinations were preselected from a research MR imaging archive of adult patients with spinal injuries (without SCI) and patients with SCIs assembled from 12 different institutions. All examinations were previously de-identified and anonymized. Thirty-five suitable patients were selected by the principal investigator (A.E.F.) to represent the range of features and responses that constitute the NINDS adult SCI CDE collection. This number of cases was determined based on estimates provided by a statistical power analysis assuming an interclass correlation coefficient (ICC) of 0.8 and a desired 95% confidence interval of ± 0.1 (ie, 0.7–0.9).

The selected representative examinations consisted of 31 acute cervical and 4 thoracic SCIs of varying levels and degrees of severity. Each preoperative MR imaging examination consisted of a localizer, sagittal T1, sagittal T2, T2 axial gradient-echo, and axial T2 sequence. The emphasis on cervical injuries reflected the prevalence of cervical injuries in the general population at large.

Import of Dataset into the Web-Based DICOM Viewer

Case selection, training, and scoring of the evaluation set were performed using a cloud-based zero-footprint DICOM web viewer on a suitable monitor. All 35 cases were uploaded to this platform for each rater to review and report on from any location. Five pilot or test examinations were also included for the purpose

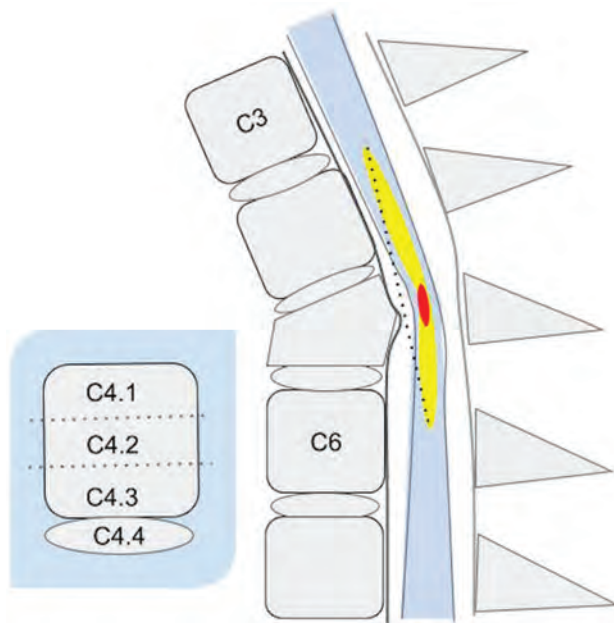


FIG 1. Graphic of a SCI on a sagittal T2-weighted image showing the anatomic location designations of the impact zone (*center*), rostral and caudal limits of spinal cord edema (*yellow*), and hemorrhage (*red*). By convention, each vertebral body is arbitrarily subdivided into 3 equal parts (designated as level.1, level.2, and level.3) with the intervertebral disc below the body as the fourth subpart (level.4). On this diagram, the rostral limit of edema is at C3.4, and the caudal extent is at C6.2. Hemorrhage (*red*) is demarcated by C5.1 and C5.2. Lesion center is at C5.2. The *dotted line* represents actual continuous measurement of length of edema demarcated by the upper and lower boundaries on a T2-weighted image that a reviewer would create with electronic calipers.

of training and familiarizing the examiners with the platform. These cases were not used in the statistical analysis.

Development of the CRF

The complete NINDS MR imaging CDE case report form contains 35 elements that encompass all facets of spinal trauma, including bony injury, surgical instrumentation, soft tissue injury, and SCI. Because the goal of this investigation was to evaluate features specific to SCI, a subset was selected for use. A limited-scope CRF was created using an extract of the most relevant NINDS SCI CDEs that could be used to describe SCI on clinical MR imaging. This included 8 specific imaging features focused on length and location of hemorrhage and edema in the spinal cord referenced by anatomic location. Each cervical segment is visually subdivided into 4 relatively equal subparts: upper, middle, and lower third of each vertebral body with the adjacent caudal intervertebral disc as the fourth part.⁹ This anatomic reference is used to designate the location of the rostral or caudal extent of hemorrhage and edema as well as the injury center (Fig 1). The CRF also included an additional CDE that is not included in version 1 of the NINDS MR imaging CRF, called the Brain and Spinal Injury Center (BASIC) score,¹⁰ which is a 5-part categoric assessment of spinal cord damage on axial T2-weighted images (Fig 2). The BASIC score is an ordinal scale that reflects the extent of hyperintensity on a select axial T2-weighted image.

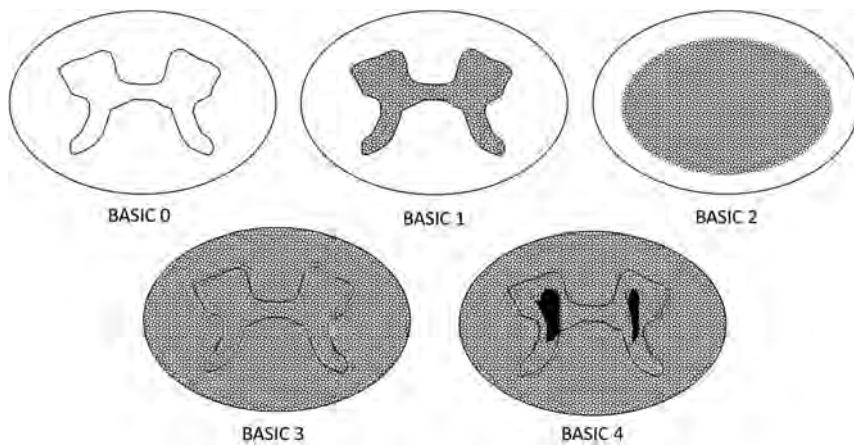


FIG 2. Graphic representation of the BASIC score CDE. The score is based on the extent of the cross-sectional T2-weighted abnormality. A score of 0 is normal. A score of 1 represents signal change in the central GM. A score of 2 represents signal change that extends beyond the central GM but does not involve the entire cross-sectional area. A score of 3 involves the entire cross-section of the spinal cord. A score of 4 features a grade III injury as well as hypointense foci in the central GM indicative of hemorrhage.

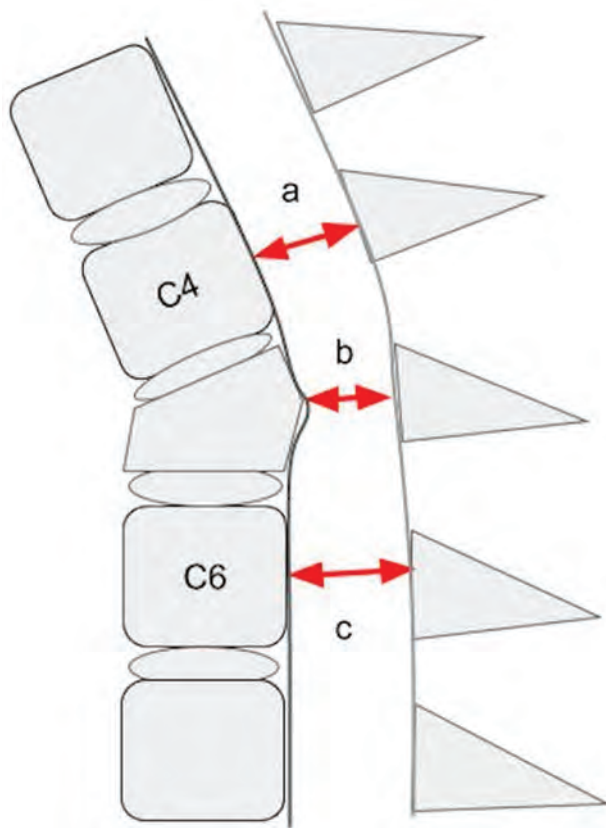


FIG 3. Graphic representation of a T2-weighted sagittal MR imaging illustrating an example of 3 key absolute measurements of the sagittal diameter of the spinal canal at the level of injury (b), above the level of injury (a), and below the level of injury (c). Reviewers were instructed to obtain the measurements from the dural boundaries instead of the cortical margins. Measurements obtained rostral and caudal to the injury level are made at the midbody level of the first normal-appearing body above and below the injury level, respectively.

The second set of CDEs used in this study includes 9 continuous measures specified by the NINDS SCI CDE set that focus on discrete dimensions of the spinal canal and spinal cord that have been shown to be relevant to posttraumatic spinal cord dysfunction. These include measurements obtained directly at the level of injury compared with relatively normal canal or cord dimensions rostral and caudal to the injury (Figs 3–5).

The entire subset used for the study CRF consisted of 17 discrete elements derived from the original NINDS MR imaging SCI CDEs. Technical items related to scanner or software type, pre-existing hardware, injury subtype, and associated bony and soft tissue injury were not included in this assessment. The final CRF was published on a cloud-

based form system with instructional material and visual references (Figs 1–5). Each rater was given access to the webform, and the data entries were automatically transferred to a spreadsheet (Google Forms and Google Sheets, Google Alphabet LLC) for analysis.

Training of Expert Raters

Five distinct MR imaging examinations were selected to be used as a training set. A training guide was written and distributed based on the general and specific instructions given via the CRF module instructions (NINDS SCI CDEs version 1.0). This training guide outlined how to open the image viewer, view each case, make annotations, and record responses. This included visual examples of the controlled responses to each CDE (when applicable). Graphic references (Figs 1–5) were incorporated into the reviewer entry form to provide visual guidance for specific measurements.

Four Certificate of Added Qualification-certified neuroradiologists with expertise in spine imaging and 1 spine neurosurgeon with expertise in SCI were recruited and trained for correct use of the CRF using a combination of independent and virtual training. The incorporation of a clinician in the rater pool was intended to confirm that the CDEs could generalize to a nonradiology specialty. All raters were from 5 separate institutions, and all had greater than 10 years' experience in their specialty. The goal was to review the training manual, the terminology, the CDEs, and the response types. Examples were shown of each feature, criteria for assessment, and response. Training was kept to a single session with the expectation that the raters would apply their expertise to the criteria stipulated on the CRF using minimal supplemental instruction.

The 25 reviews on the 5 training cases were collected, outliers were identified based on consensus, and remediation was planned accordingly when necessary. This remediation included retraining of an individual reader(s) or modification

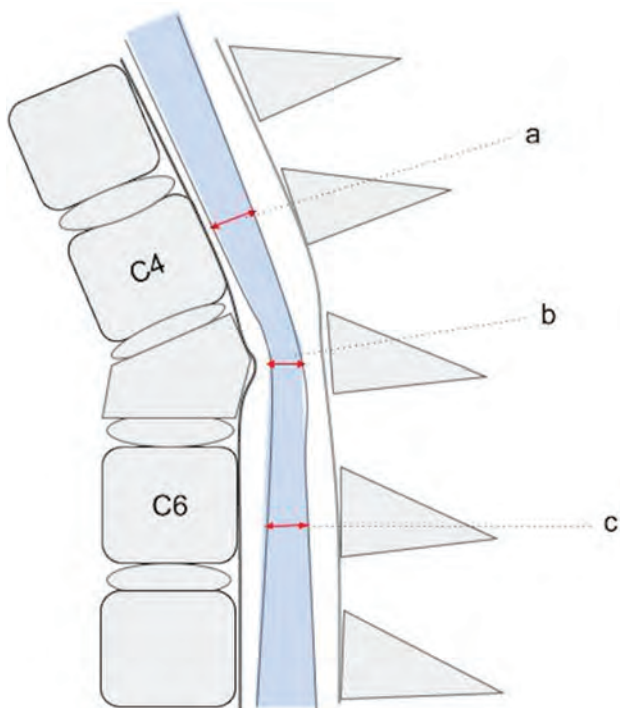


FIG 4. Graphic representation of a T2-weighted sagittal MR imaging illustrating an example of 3 key absolute measurements of the sagittal diameter of the spinal cord at the level of injury (*b*), above the level of injury (*a*), and below the level of injury (*c*). Measurements obtained rostral and caudal to the injury level are made at the midbody level of the first normal-appearing vertebral body above and below the injury level, respectively.

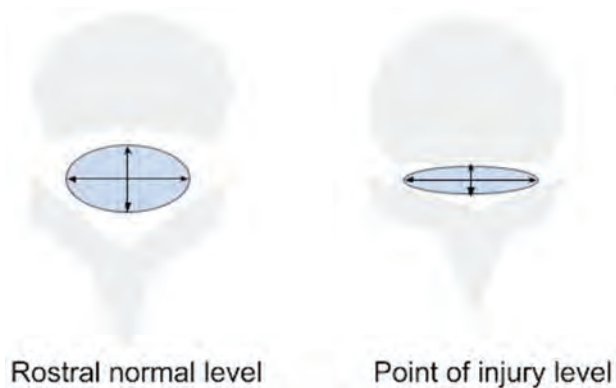


FIG 5. Graphic representation of an axial MR image of the spine illustrating the methodology for generating absolute measurements of the transverse and anteroposterior dimensions of the dural envelope (*arrows*). These were measured at 2 locations, the point of maximal compression on the axial dataset and at the first normal rostral midvertebral body level. Reviewers were instructed to estimate the margins from the dural envelope and not the bony cortical boundaries.

of a CDE description to mitigate ambiguity and revision of the training manual and the CRF. The NINDS CDEs and the BASIC scoring system were not modified in any way from their original form.

Data Collection

De-identified examinations were uploaded to the web viewer in batches of 5 numbered sequentially. The 5 expert raters reviewed each case independently and entered their responses into the web form accordingly. The readers were given the latitude to use the entire clinical imaging dataset to perform their evaluations. Data entries were checked in real time for missing entries, and evaluators were requested to complete entries as needed. No modifications to the values were allowed after the entries were recorded. One month after the completion of the first-round evaluation MR imaging dataset, the cases were randomized in order and reassessed by each of the readers to test both inter- and intrarater reliability. The second round of measurements and responses were performed de novo because the results from the first round of evaluation were not available to the readers.

Statistical Analysis

The CRF contained variables of 2 different data types: ordinal and continuous. Because the injury level convention for the entire spine (Fig 1) consists of more than 5 choices, the ordinal responses, which can range from C2.1 to C8.4, were treated as continuous variables. The BASIC score, with 5 ordinal choices, was assessed for agreement using the kappa statistic and a measure of percent agreement. For the continuous measures that included absolute measures of hemorrhage and edema length, as well as sagittal and transverse diameters of the spinal cord and spinal canal at multiple levels, each continuous element was rounded to the nearest integer (in millimeters). Assessing agreement of ratings among raters (ie, interrater reliability) and assessing the agreement of rating of a rater to the same patient's images over time (ie, test-retest reliability) was done with the ICC with confidence intervals.¹¹ Interrater ICCs were repeated, leaving out a single reviewer to assess for inconsistencies among the readers themselves.

RESULTS

Agreement results for the 7 SCI features are listed in Table 1. Reader agreement related to injury level, edema, and hemorrhage ranged from good to excellent (kappa > 0.4). The ordinal CDEs that referenced the spinal cord feature of center and rostral or caudal extent of edema or hemorrhage to anatomic location (eg, Cx.1–Cx.4; Fig 1) demonstrated agreement among the 5 reviewers and showed an ICC ranging from 0.68 to 0.99. Moreover, reproducibility of these measures was excellent, ranging from 0.95 to 1.00. Agreement for absolute length of hemorrhage and edema was moderate, ranging from 0.54 to 0.60, with good reproducibility at 0.78 to 0.83. Agreement for the BASIC score was poor, showing the lowest interrater agreement, with an overall kappa of 0.27 (0.20, 0.34) with a percent agreement of 54.86 in round 1 and 0.42 (0.35, 0.50) and a percent agreement of 66% in round 2 with moderate intrarater agreement at 0.62 (0.53, 0.72). For 7 of the 8 variables related to SCI, agreement improved between the first and second evaluation with a modest reduction in agreement for absolute hemorrhage length (0.59 to 0.54).

Table 2 lists the agreement for morphologic continuous measurements of spinal canal and spinal cord diameter measured at, rostral to, and below the center of injury. Agreement on measures

Table 1: Inter- and intrarater agreement (ICC) and confidence intervals for CDE features related to SCI using 5 raters, 35 cases, and 2 rounds of evaluations^a

	Interrater ICC: Round 1	Interrater ICC: Round 2	Intrarater ICC
Center of injury level	0.99 (0.99, 1.00)	0.99 (0.99, 1.00)	1.00 (1.00, 1.00)
Rostral extent of spinal cord edema	0.99 (0.98, 0.99)	0.98 (0.98, 0.99)	1.00 (1.00, 1.00)
Caudal extent of spinal cord edema	0.97 (0.95, 0.98)	0.97 (0.95, 0.98)	0.98 (0.98, 0.99)
Rostral extent of spinal cord hemorrhage	0.68 (0.56, 0.81)	0.70 (0.58, 0.82)	0.96 (0.95, 0.98)
Caudal extent of spinal cord hemorrhage	0.69 (0.56, 0.81)	0.69 (0.57, 0.82)	0.95 (0.93, 0.97)
Hemorrhage length (mm) ^b	0.59 (0.44, 0.74)	0.54 (0.39, 0.70)	0.78 (0.72, 0.84)
Edema length (mm) ^b	0.57 (0.42, 0.72)	0.60 (0.46, 0.75)	0.83 (0.78, 0.88)

^a Quantitative and categoric features are specified per the methodology illustrated in Fig 1.

^b Continuous data.

Table 2: Inter- and intrarater agreement (ICC) and confidence intervals for direct measures of spinal canal and spinal cord diameters derived from sagittal and axial MR images using the methodology featured in Figs 3–5 using 5 raters, 35 patients, and 2 rounds of evaluations

	Interrater ICC: Round 1	Interrater ICC: Round 2	Intrarater ICC
Sagittal cord diameter at level of injury (mm) ^a	0.83 (0.75, 0.91)	0.82 (0.74, 0.90)	0.84 (0.80, 0.89)
Sagittal cord diameter at first rostral segment above injury (mm) ^a	0.37 (0.20, 0.53)	0.27 (0.11, 0.43)	0.79 (0.73, 0.85)
Sagittal cord diameter at first caudal segment below injury (mm) ^a	0.43 (0.27, 0.60)	0.51 (0.36, 0.67)	0.69 (0.61, 0.77)
Sagittal canal measurement at level of injury (mm) ^a	0.80 (0.71, 0.89)	0.72 (0.60, 0.83)	0.85 (0.81, 0.90)
Sagittal canal measurement rostral to injury (mm) ^a	0.23 (0.07, 0.38)	0.31 (0.15, 0.48)	0.86 (0.82, 0.91)
Sagittal canal measurement caudal to injury (mm) ^a	0.56 (0.41, 0.71)	0.38 (0.21, 0.54)	0.90 (0.86, 0.93)
Anteroposterior diameter (mm) of the spinal cord at the point of maximal compression or epicenter of injury from axial image ^a	0.76 (0.65, 0.86)	0.69 (0.57, 0.82)	0.86 (0.82, 0.90)
Transverse diameter (mm) of the spinal cord at the point of maximal compression or epicenter of injury from axial image ^a	0.41 (0.25, 0.58)	0.33 (0.17, 0.50)	0.78 (0.72, 0.85)
Anteroposterior diameter (mm) of the spinal cord on axial image at the nearest adjacent rostral normal level ^a	0.37 (0.20, 0.53)	0.27 (0.11, 0.43)	0.82 (0.77, 0.87)

^a Continuous data.

of the spinal cord and spinal canal using ICC varied substantially, ranging from poor to good categories (0.23 to 0.83). The most consistent and reproducible measure was sagittal cord and canal diameter at the level of injury in which interrater agreement ranged from 0.72 to 0.83. Intrarater agreement was more consistent at 0.84 and 0.85 for cord and canal, respectively. There was more of a disparity in agreement for measures that theoretically are less cognitively challenging, above and below the lesion center. Sagittal canal measurements obtained at the closest rostral segment showed consistently poor agreement at 0.23 and 0.31 with consistent performance with repeat measures at 0.86. Similarly, sagittal cord measurements at the closest normal rostral level also demonstrated poor overall agreement at 0.37 and diminished performance in the second review at 0.27. Intrarater performance was good at 0.79. Sagittal canal and cord diameter agreements obtained caudal to the level of injury also showed poor to moderate overall agreement (ICC, 0.38–0.56). Anteroposterior and transverse dimensions of the spinal cord measured in the axial plane also varied widely among the reviewers (ICC range, 0.27–0.76) with lowest agreement paradoxically at the levels that were traditionally cognitively easier to measure compared with the level of maximum compression or injury epicenter, where agreement was moderate to good. Intrarater performance for all 9 of these continuous measures fell in the moderate to excellent range (ICC, 0.69–0.90).

The Online Supplemental Data show the change of the aggregate ICC when a single observer is removed from the calculations for each of the continuous measures. This provides a general understanding of outlier observers as the source of variability of agreement. A substantial increase in ICC value for any 1 feature compared with the aggregate mean suggests outlier behavior. Although there was some source of variation attributed to 1 reader, in no case did the change in ICC value shift the degree of agreement into the next category. ICC for the BASIC score was also included for comparison, which remains in a similar performance category to the kappa. There was no consistent pattern for change from overall in inter- or intrarater agreement when ICCs were recalculated with a single observer removed.

DISCUSSION

The NINDS MR imaging CDE instrument for SCI was devised by a consensus expert panel based on existing literature and experience. The published instrument is endorsed by the NINDS as a recommended means for conducting clinical research and for evaluating specific features of MR imaging as they relate to SCI. No validation or reproducibility study was conducted after the publication by the NINDS. Therefore, the goal of this study was to validate the NINDS imaging CDE feature set for potential use in SCI clinical trials. To adhere to this objective, the experimental

design included several key elements: 1) the evaluation panel included a clinical (nonradiologic) domain expert, 2) we provided only a minimal amount of training to reduce training bias, and 3) we provided a complete clinical imaging dataset such that each reviewer expert was given the latitude to select the optimal image (s) to address each of the 17 CDE features without being directed to a specific image or series to make each assessment.

Several interesting patterns arise in examining the agreement among the groups of features. Absolute or continuous measures were less reliable or reproducible than ordinal or categoric features. That is, absolute measures requiring use of an electronic caliper were less reliable than semiquantitative ordinal methodologies overall, and this was reproducible on repeated measures. Selection of section and window or level also introduces measurement error caused by varying partial volume effects, resolution differences, and changes in cord angle between slices. Alternatively, the ordinal methodology for assessing edema or hemorrhage length and location based upon anatomic reference to the nearest adjacent vertebral segment⁹ demonstrated consistent agreement in moderate, good, and excellent categories by ICC. This methodology has been successfully adapted for use in a series of SCI and MR imaging studies and was adopted by the NINDS as the preferred methodology for assessing extent and location of SCI on sagittal T2-weighted MR imaging because of the limited cognitive effort required. These results suggest that the method is sound and reproducible for characterizing lesion size and location on clinical MR imaging studies and more robust to real-world confounds than continuous distance metrics.

The BASIC score was developed as an axial adjunct to the sagittal method. It is an analogous visual measure of SCI by assessing the relative cross-sectional involvement of the spinal cord parenchyma in a single axial image. Using 7 evaluators with varied clinical backgrounds, Talbott et al¹⁰ demonstrated mean and median kappa scores of 0.83 and 0.81 for BASIC assessment on preselected MR images of 20 patients with SCI. Kappa assessment for the BASIC CDE in our cohort performed substantially lower than reported by Talbott et al's original work (ICC 0.27 and 0.42) with only moderate intrarater agreement. The reason for this large disparity is not entirely clear, but the results do point to variations in how the studies were conducted. This includes more heterogeneity in our dataset with respect to scanner type and imaging protocol compared with Talbott et al's work. Image selection bias could have played a role in our lower performance. Moreover, in our analysis, there was no significant difference in agreement when removing the results of any single observer. One additional factor relates to reader inattention: the BASIC score was inserted as the last and final CDE in the CRF, and it is possible that this produced an inadvertent attention bias. Fortunately, this CDE is supplemental to the other SCI features.

Two related reliability studies were conducted by Fehlings et al¹² and Furlan et al.¹³ These studies aimed to validate quantitative measures related to SCI. Fehlings et al¹² focused on determining reliability of 2 specific quantitative measures: maximum canal compromise and spinal cord compression in acute cervical SCI. Using 10 acute SCI MR imaging and CT cases rated by 28 spine surgeons, Fehlings et al¹² were able to detect an interobserver reliability range of 0.35–0.58 and intrarater reliability of

0.95–0.97 using the MR imaging.¹² These ranges of ICC for continuous responses are comparable to our own. Similarly, Furlan et al¹³ conducted a study that measured cord compression and canal stenosis on 5 cases rated by 13 raters on 10 occasions. They reported an interrater reliability range of 0.55–0.61 and intrarater reliability range of 0.68–0.70 for their continuous variables.¹³

A number of spine-based reliability studies have been conducted to validate specific grading scales or systems for specific features or findings in spine imaging. These CDEs were created as a means to standardize reporting grading system for the evaluation of disc herniation and lumbar spinal stenosis.^{14–16} A panel of 3 or 4 readers was trained to read a dataset of MR images on 2 separate occasions. The Spine Patient Outcomes Research Trial (SPORT) trained 4 clinical experts in spine MR imaging to use a grading system for determining nerve root compression after a lumbar intervertebral disc herniation.¹⁴ They found overall intrarater kappa coefficients of 0.90, 0.84, and 0.63, respectively. Interrater reliability was found to be 0.81, 0.54, and 0.47.

Two other studies by Pfirrmann et al¹⁵ and Schizas et al¹⁶ used similar methods. Pfirrmann et al's¹⁵ grading system determined an intraobserver kappa range of 0.72–0.77 and an interobserver kappa range 0.62–0.67. Schizas et al¹⁶ found an intraobserver stenosis morphologic grading of 0.65 and interobserver kappa of 0.44.¹⁶ These studies demonstrate that there is a broad range of agreement and reproducibility of spine MR imaging features and that agreements in the moderate or good range may still be adequate both to drive clinical decision making and to categorize patients for research and clinical trials. The magnitude of our agreement figures falls in line with other MR spine imaging reliability assessments and shows greatest value in characterizing SCI on sagittal T2-weighted images.

Limitations of this study included uncontrolled technical variations such as the browser type, screen resolution, and luminance of the monitors and environment used for the evaluations at the 5 different locations, which may have had an effect on perceptual abilities. Because the order of the responses on the CRF may have played a role in diminishing agreement for the items that appeared near the end of the CRF such as the BASIC score, one mitigation strategy might have been to reorder the 17 items for the second round of responses. Availability of the PACS presentation state of the annotated images from each observer might have provided direct comparison of the image selection and annotations, which may have provided some insight into the individual variation of absolute linear measures, choice of images, optimal window or width, and level of the spine and spinal cord dimensions on sagittal and axial images. Because the presentation state was not readily accessible as discrete data, this additional analysis was not pursued.

In summary, this investigation has demonstrated that the NINDS SCI MR imaging CDE set provides a valid and reproducible instrument for documenting the MR imaging features of SCI for clinical trials research, radiology reporting, and ultimately clinical decision making. The levels of agreement for the spinal cord features exhibited good to excellent agreement with multiple independent observers. Absolute measures of injury and dimensions of the residual spinal canal and spinal cord showed lower

reliability with repeat measures than ordinal semiquantitative measures overall. However, the magnitude of agreement was shown to be equivalent to prior multireader assessments of similar features. The recommended NINDS CDE system can be relied on for obtaining consistent results from domain experts with the minimum requisite amount of training.

Disclosures: Joshua Fisher—*RELATED: Grant: **; *UNRELATED: Employment: .* Scott Faro—*RELATED: Grant:* See information from first author, Dr. Adam Flanders*; *Consulting Fee or Honorarium:* See information from first author, Dr. Adam Flanders, *Comments:* Reimbursed to provided quantitative analysis of the imaging data. Adam Flanders—*RELATED: Grant:* Nielson Foundation, *Comments:* Grant support for the research*. Laura Krisa—*RELATED: Grant:* Craig H. Nielson Foundation*; *UNRELATED: Grants/Grants Pending:* NIH. James Harrop—*UNRELATED: Consultancy:* Depuy, Globus, Stryker Spine, *Comments:* Consulting and education honorariums not related to paper. Eric Schwartz—*RELATED: Consulting Fee or Honorarium:* Craig H. Nielson Foundation; *UNRELATED: Royalties:* LWW, *Comments:* Book royalties. Feroze Mohamed—*UNRELATED: Board Membership:* NIH. *Money paid to institution.

REFERENCES

1. Grinnon ST, Miller K, Marler JR, et al. **National Institute of Neurological Disorders and Stroke Common Data Element Project—approach and methods.** *Clin Trials* 2012;9:322–29 CrossRef Medline
2. Sheehan J, Hirschfeld S, Foster E, et al. **Improving the value of clinical research through the use of Common Data Elements.** *Clin Trials* 2016;13:671–76 CrossRef Medline
3. National Institute of Neurological Disorders and Stroke. **NINDS Common Data Elements Database 2006**, n.d. <https://commondataelements.ninds.nih.gov>
4. Mulcahey MJ, Vogel LC, Sheikh M, et al. **Recommendations for the National Institute for Neurologic Disorders and Stroke spinal cord injury common data elements for children and youth with SCI.** *Spinal Cord* 2017;55:331–40 CrossRef Medline
5. Bauman WA, Wecht JM, Biering-Sørensen F. **International spinal cord injury endocrine and metabolic extended data set.** *Spinal Cord* 2017;55:466–77 CrossRef Medline
6. Biering-Sorensen F, Charlifue S, Devivo MJ, et al. **Incorporation of the International Spinal Cord Injury Data Set elements into the National Institute of Neurological Disorders and Stroke Common Data Elements.** *Spinal Cord* 2011;49:60–64 CrossRef Medline
7. Biering-Sorensen F, Alai S, Anderson K, et al. **Common data elements for spinal cord injury clinical research: a National Institute for Neurological Disorders and Stroke project.** *Spinal Cord* 2015; 53:265–77 CrossRef Medline
8. Biering-Sorensen F, Charlifue S, Devivo MJ, et al. **Using the spinal cord injury common data elements.** *Top Spinal Cord Inj Rehabil* 2012;18:23–27 CrossRef Medline
9. Flanders AE, Spettell CM, Tartaglino LM, et al. **Forecasting motor recovery following cervical spinal cord injury: value of MR imaging.** *Radiology* 1996;201:649–55 CrossRef Medline
10. Talbot JF, Whetstone WD, Readdy WJ, et al. **The Brain and Spinal Injury Center score: a novel, simple, and reproducible method for assessing the severity of acute cervical spinal cord injury with axial T2-weighted MRI findings.** *J Neurosurg Spine* 2015;23:495–504 CrossRef Medline
11. Koo TK, Li MY. **A guideline of selecting and reporting intraclass correlation coefficients for reliability research.** *J Chiropr Med* 2016;15:155–63 CrossRef Medline
12. Fehlings MG, Furlan JC, Massicotte EM, et al. **Interobserver and intraobserver reliability of maximum canal compromise and spinal cord compression for evaluation of acute traumatic cervical spinal cord injury.** *Spine (Phila Pa 1976)* 2006;31:1719–25 CrossRef Medline
13. Furlan JC, Fehlings MG, Massicotte EM, et al. **A quantitative and reproducible method to assess cord compression and canal stenosis after cervical spine trauma: a study of interrater and intrarater reliability.** *Spine (Phila Pa 1976)* 2007;32:2083–91 CrossRef Medline
14. Lurie JD, Tosteson ANA, Tosteson TD, et al. **Reliability of magnetic resonance imaging readings for lumbar disc herniation in the Spine Patient Outcomes Research Trial (SPORT).** *Spine (Phila. Pa. 1976)* 2008;33:991–98 CrossRef Medline
15. Pfirrmann CWA, Dora C, Schmid MR, et al. **MR image-based grading of lumbar nerve root compromise due to disk herniation: reliability study with surgical correlation.** *Radiology* 2004;230:583–88 CrossRef Medline
16. Schizas C, Theumann N, Burn A, et al. **Qualitative grading of severity of lumbar spinal stenosis based on the morphology of the dural sac on magnetic resonance images.** *Spine (Phila Pa 1976)* 2010; 35:1919–24 CrossRef Medline

Cervical Cordotomy for Intractable Pain: Do Postoperative Imaging Features Correlate with Pain Outcomes and Mirror Pain?

A. Berger, M. Artzi, O. Aizenstein, T. Gonen, R. Tellem, U. Hochberg, D. Ben-Bashat, and I. Strauss

ABSTRACT

BACKGROUND AND PURPOSE: Percutaneous cervical cordotomy offers relief of unilateral intractable oncologic pain. We aimed to find anatomic and postoperative imaging features that may correlate with clinical outcomes, including pain relief and postoperative contralateral pain.

MATERIALS AND METHODS: We prospectively followed 15 patients with cancer who underwent cervical cordotomy for intractable pain during 2018 and 2019 and underwent preoperative and up to 1-month postoperative cervical MR imaging. Lesion volume and diameter were measured on T2-weighted imaging and diffusion tensor imaging (DTI). Lesion mean diffusivity and fractional anisotropy values were extracted. Pain improvement up to 1 month after surgery was assessed by the Numeric Rating Scale and Brief Pain Inventory.

RESULTS: All patients reported pain relief from 8 (7–10) to 0 (0–4) immediately after surgery ($P = .001$), and 5 patients (33%) developed contralateral pain. The minimal percentages of the cord lesion volume required for pain relief were 10.0% on T2-weighted imaging and 6.2% on DTI. Smaller lesions on DWI correlated with pain improvement on the Brief Pain Inventory scale ($r = 0.705$, $P = .023$). Mean diffusivity and fractional anisotropy were significantly lower in the ablated tissue than contralateral nonlesioned tissue ($P = .003$ and $P = .001$, respectively), compatible with acute-phase tissue changes after injury. Minimal postoperative mean diffusivity values correlated with an improvement of Brief Pain Inventory severity scores ($r = -0.821$, $P = .004$). The average lesion mean diffusivity was lower among patients with postoperative contralateral pain ($P = .037$).

CONCLUSIONS: Although a minimal ablation size is required during cordotomy, larger lesions do not indicate better outcomes. DWI metrics changes represent tissue damage after ablation and may correlate with pain outcomes.

ABBREVIATIONS BPI = Brief Pain Inventory; FA = fractional anisotropy; MD = mean diffusivity; RF = radiofrequency; NRS = Numeric Rating Scale; STT = spinothalamic tract; POD = postoperative day

Percutaneous cervical cordotomy is used to selectively disconnect the nociceptive spinothalamic fibers traveling in the anterolateral quadrant of the spinal cord.¹ It offers relief for patients with unilateral intractable oncologic pain below the C4 dermatome level who have failed conservative treatment.² Success rates in contemporary series reach nearly 80% with advancing technology, including combined intraoperative CT guidance and radiofrequency (RF)

tools.^{3–5} The 2 main reasons for patient dissatisfaction from the procedure include failure in achieving complete and long-standing pain relief (up to 20%) and the development of postoperative pain in the contralateral side (at least 17%).^{6–8}

Previous studies showed that a lesion of at least 20% of the entire cord and localized in the anterolateral quadrant is necessary to achieve effective pain relief, yet no clear correlation was found between the size of the lesion and the degree of improvement.^{9–11} More recent MR imaging- and DWI-based studies found direct correlations between the degree of the lesion's mean diffusivity (MD) as a measurement of local neural damage and improvement on pain assessment scores after surgery.¹² However, data on the mechanisms behind the postoperative contralateral pain phenomenon and its predicting factors are still lacking.

We performed this prospective study to analyze potential correlations between clinical responses to surgery, including pain relief and contralateral pain with several postoperative MR imaging-based parameters, such as the size of the lesions and their

Received August 6, 2020; accepted after revision October 28.

From the Department of Neurosurgery (A.B., I.S.); Sagol Brain Institute (M.A., T.G., D.B.-B.); Department of Radiology (O.A.), The Palliative Care Service (R.T.); Institute of Pain Medicine (U.H.); Division of Anesthesiology, Tel Aviv Medical Center (U.H.), Tel Aviv, Israel; and Sackler School of Medicine (A.B., M.A., O.A., T.G., R.T., U.H., D.B.-B., I.S.), Tel Aviv University, Tel Aviv, Israel.

A. Berger and M. Artzi contributed equally to the manuscript.

Please address correspondence to Assaf Berger, MD, Department of Neurosurgery, Tel Aviv Medical Center, 6 Weizmann St, Tel Aviv, Israel 6423906; e-mail: assaf.berger@gmail.com

Indicates article with online supplemental data.

<http://dx.doi.org/10.3174/ajnr.A6999>

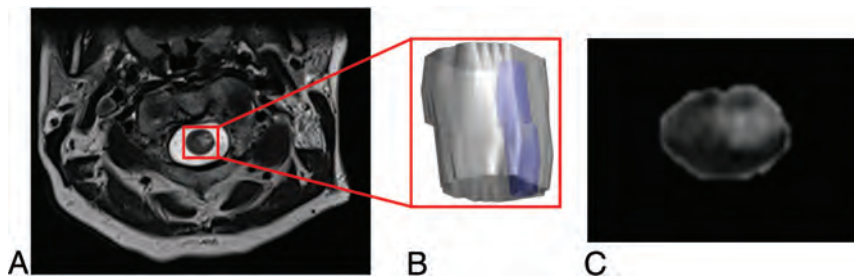


FIG 1. Manual-based segmentation of the hyperintense lesion area (blue) and the spinal cord that delineates it (gray) based on T2-weighted imaging.

DWI metrics, including trace, MD, and fractional anisotropy (FA) measurements.

METHODS

Demographic and Clinical Parameters

We prospectively collected data of patients with intractable oncologic pain who underwent cordotomy in our center during 2018 and 2019, focusing on the following parameters: age, sex, cancer type, original pain side, location, and duration before surgery. All patients who signed informed consent and underwent pre- and postoperative MR imaging were included in the study. Their data were recorded throughout their course of treatment and follow-up period, and they are reported in this article. We also reviewed oncologic imaging work-ups to seek lesions that were considered nonpainful before surgery and that were located along the midline (spine or pelvis) or contralateral to the original painful side.

Patients were asked to fill in pain assessment questionnaires before and after surgery, including the Numeric Rating Scale (NRS) and Brief Pain Inventory (BPI) scores. NRS is used to evaluate the average degree of pain as it is currently being experienced. The BPI score has been validated for patients with cancer, and it estimates several aspects of the magnitude of pain outcomes over a longer time period.¹³ We measured the relative decrease in BPI severity score after surgery and present the results as the percentage of decrease from the preoperative BPI severity score.

Surgical Technique

Our surgical technique has been previously described.³ In short, the procedure requires cooperation of the patient for electrophysiologic verification of the spinothalamic tract (STT), usually with mild sedation (remifentanyl and propofol) during the initial needle insertion until dural puncture. Patients are first injected with 8 mL of intrathecal iohexol contrast dye (Omnipaque 300 mg/mL) by means of either lumbar puncture or direct cervical injection. We then use O-arm lateral fluoroscopy to insert the needle into the lateral C1–C2 interspace. Needle location and trajectory are verified with CT. After the correct angle is achieved, an RF electrode is introduced through the cannula and slowly advanced while the impedance is monitored. When the cord has been penetrated as indicated by an increase in impedance, we perform another CT scan to verify the anatomic position of the electrode. Then electrophysiologic monitoring testing with both motor and

sensory stimulation is used to confirm proper electrode location inside the spinothalamic tract. After this has been accomplished, a test lesion is created at 60° for 30 seconds while simultaneously monitoring motor strength. A permanent lesion is then created at 80° for 60 seconds. If the painful area is not completely covered, additional lesions are often created in the same manner after gentle repositioning of the electrode until satisfactory pain relief is achieved. The procedure usually involves more than 1 pial penetration (median, 4; range, 2–10) to find the optimal target and usually more than 1 ablation to achieve satisfactory pain relief (median, 3; range, 2–5). The electrode is repositioned either anteroposteriorly or mediolaterally, according to the findings of intraoperative stimulation. The STT is organized in the cervical spinal cord with the fibers from the leg located posterolaterally and fibers from the hand and shoulder located more anteromedially.

Imaging

Patients underwent MR imaging of the cervical spine before and again 1–2 days after the procedure ($n=15$). They were also scheduled to undergo an MR imaging 1 month after surgery, but only 5 of them were able to do so because of the complexity of their condition. Scans were performed on a 3T MR imaging scanner (Magnetom Prisma; Siemens) and included axial turbo spin-echo T2-weighted imaging with TR of 5080 ms, echo time TE of 90 ms, and voxel dimensions of $0.56 \times 0.56 \times 3.3 \text{ mm}^3$. Also included was diffusion tensor imaging (DTI) acquired with TR of 10,000 ms, TE of 69 ms, with 24 gradient directions, b-values of 0.1000 s/mm^2 , and voxel dimensions of $0.65 \times 0.65 \times 3 \text{ mm}^3$. Transverse slices were set to cover the C1–C7 vertebral levels. To minimize possible deviations between pre- and postoperative MR imaging that might result from differences in angulation of the axial slices or orientation of the neck, examinations were performed by the same technician and in the same clinical setting.

Image Analysis

Imaging analysis was performed using FMRIB Software Library (<http://www.fmrib.ox.ac.uk/fsl>) and Analyze (version 11.0; AnalyzeDirect) software. It included manual-based segmentation of the hyperintense lesion area and the spinal cord that delineates it by means of AnalyzeDirect separately for the T2-weighted imaging (Fig 1) and diffusion trace images. Segmentation was performed on axial images using a semiautomatic threshold-based algorithm (region of interest module). Segmentation was initiated by manually setting a seed point at the hyperintense lesion area or at the lesioned cord on the trace image and manually adapting the threshold range. Semiautomatic segmentation of the region of interest by means of a threshold-based algorithm instead of manual segmentation is expected to minimize the effects of partial volume averaging. The following numeric parameters were extracted based on the extracted lesion area: lesion volume (in cc), lesion-to-cord ratio (in percentages) at the level

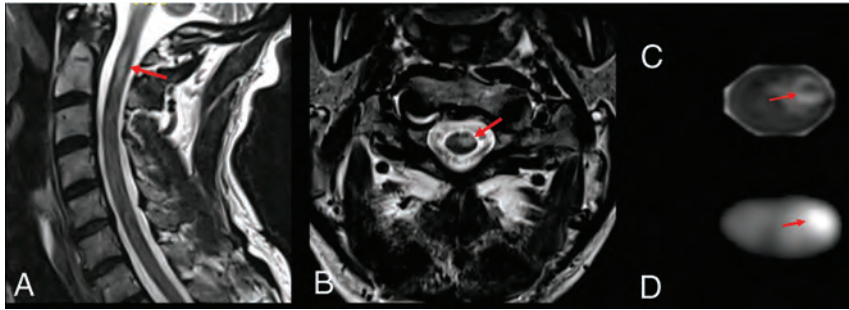


FIG 2. Postoperative MR imaging findings 1 day after cervical cordotomy. Red arrows indicate the cordotomy ablation. A, Sagittal T2-weighted imaging. B, Axial T2-weighted imaging. C and D, Axial diffusion trace images.

of ablation, and largest in-plane axial (minor axis) and sagittal (major axis) lengths (in millimeters).

Last, we measured the minimal, maximal, and average MD and FA values of the lesions' DWI areas (Fig 2) and of the nonlesioned cord as measured contralateral to the side of the lesion on postoperative DTI. In addition, we measured preoperative MD and FA on DTI of the future lesion's area on the same anatomic cervical segment.

Statistical Analysis

Statistical procedures were performed with SPSS 21.0 software (IBM).

Categoric characteristics of patients with and without postoperative contralateral pain were compared using the Fisher exact test. Comparison of continuous variables between unrelated samples was performed using the Mann-Whitney U test, and the Wilcoxon test was used for related samples. Correlations between continuous study parameters were performed with the Spearman correlation. Analyses were performed by nonparametric tests because of the small sample size and the fact that several parameters did not show normal distribution on normality tests. A P value $<.05$ (2-sided) was considered statistically significant.

This study was approved by the institutional review board.

RESULTS

Clinical and Demographic Data

Twenty patients with cancer underwent percutaneous cervical cordotomy as part of a prospective trial in our center between February 2018 and July 2019. Five patients were excluded from this study because they could not undergo preoperative MR imaging because of pain or general fatigue. The mean age of our study population was 65 ± 9 years. The Online Supplemental Data describe individual demographic, clinical, and imaging parameters of the study group. All 15 patients had localized unilateral intractable pain. The average duration of pain before surgery was 10 ± 7 months. Four patients (27%) had pain in the upper extremities and 11 in the lower part of the body (73%). Most patients mainly had tumor-associated nociceptive pain, but 1 patient with sciatic malignant peripheral nerve sheath tumor also had painful plexopathy. One patient died from a general deterioration associated with his primary disease within 1 month after

surgery; therefore, only relatively short-term postoperative data are available for that patient.

Imaging Data

All lesions were hyperintense on T2-weighted imaging sequences with an average volume of 0.28 ± 0.13 cc and $19\% \pm 8\%$ of the total cord volume at the level of ablation. Lesions on diffusion trace images were smaller and measured 0.08 ± 0.05 cc and $15\% \pm 9\%$ of the total cord volume at the same level. The average percentages of the lesioned cross-sectional area of the cord on T2-weighted imaging and diffusion trace images were $24\% \pm 8\%$ and $26\% \pm 8\%$, respectively. The mean major axis (sagittal) length on T2-weighted imaging and trace images was 15 ± 1.8 mm and 7.6 ± 1.8 mm, respectively.

The average MD and FA of the measured lesions were $0.905 \pm 0.216 \times 10^{-3}$ mm²/s and 0.406 ± 0.07 a.u. (arbitrary unit), respectively (Online Supplemental Data).

Clinical Outcomes and Imaging Correlations

All 20 patients reported a substantial improvement in the original pain intensity immediately after surgery: the median preoperative NRS was 8 (range 7–10) compared with the postoperative NRS of 0 (0–4) ($P = .001$). One month after surgery, 1/14 surviving patients had pain in the original distribution of a similar intensity as the preoperative levels. The other 13 patients reported a complete or near-complete resolution of the original pain.

The average percentages of the ablated cord's cross-sectional area were $22.1\% \pm 7.6\%$ and $26.4\% \pm 8.0\%$ on the T2-weighted imaging and diffusion trace images, respectively, for the group of patients who survived 1 month after surgery. The minimal lesion volumes that achieved adequate pain response were 13.4% and 9.6% for T2-weighted imaging and the diffusion trace images, respectively. The average volumes of the lesioned cord on the T2-weighted imaging and diffusion images were 0.3 ± 0.1 cc and 0.1 ± 0.05 cc, which respectively included $17.8\% \pm 6.9\%$ and $14.4\% \pm 8.3\%$ of the cord's volume at the ablated segments. The minimal volumes were 0.15 cc and 0.03 cc, including 10.0% and 6.2% of the cord's volume on T2-weighted imaging and diffusion images, respectively. No significant differences were noted in the degree of 1-month postoperative decrease in NRS when comparing patients with ablation below or above 20% of the cord's T2-weighted imaging cross-sectional area (8 ± 1 , $n = 5$ and 8 ± 3 , $n = 9$, respectively; $P = .518$). Similarly, no significant differences between the groups were noted when diffusion was used ($P = .635$).

Ten patients completed BPI questionnaires and reported a significant improvement in pain severity scores, from 28 ± 6 before surgery to 18 ± 13 at 1 month after surgery ($P = .022$). We measured the relative decrease in the BPI severity score after surgery as the percentage of decrease from the preoperative BPI severity score. There was a correlation between the minor axis (in-plane, axial) length of the lesion on diffusion trace images and the change in BPI severity score ($r = 0.827$, $P = .003$): the

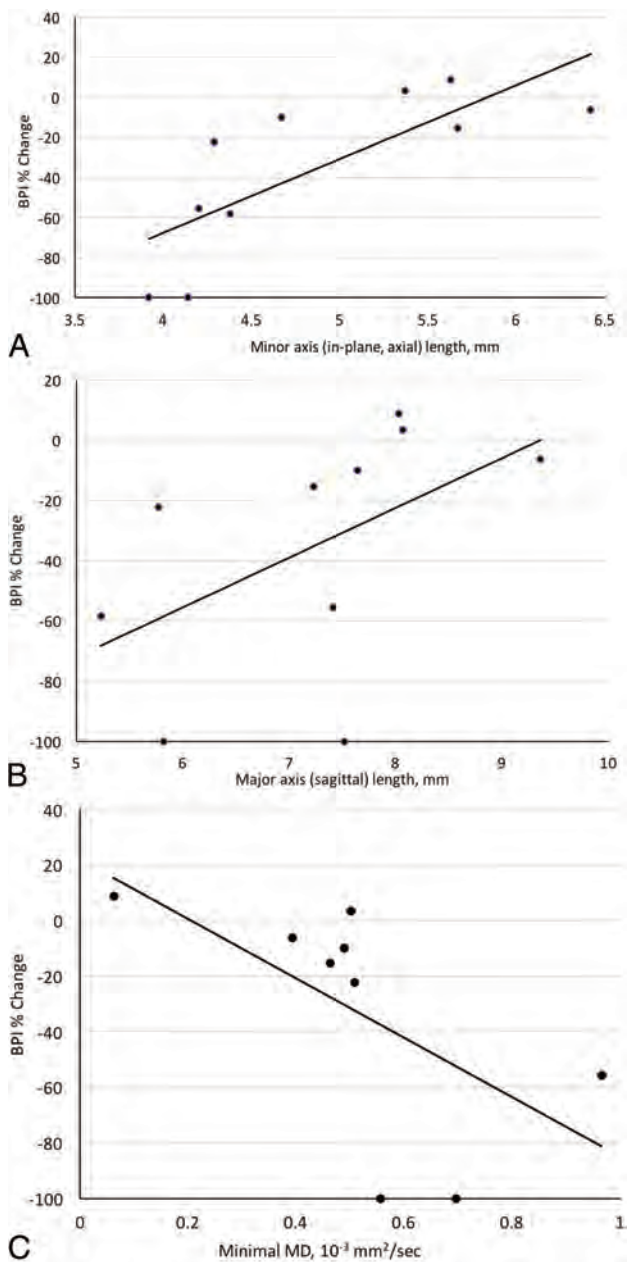


FIG 3. Spearman correlation between percentage of change in BPI 1 month after cordotomy and the following values: A, Ablation size of minor axis (in-plane, axial) on diffusion trace images ($r = 0.827$, $P = .003$). B, Major axis (sagittal) length on diffusion trace images ($r = 0.705$, $P = .023$). C, Lesion minimal MD, $10^{-3} \text{ mm}^2/\text{s}$ ($r = -0.821$, $P = .004$).

shorter the lesion, the greater was the relative (percent) decrease in BPI severity score after surgery. Similarly, a possible correlation was demonstrated between the change in BPI severity and the major axis (sagittal) length of the lesion on diffusion trace images ($r = 0.705$, $P = .023$) (Fig 3).

In addition, we evaluated the correlation between the size of the lesion on the postoperative MR imaging and the number of pial penetrations and the number of ablations during surgery. The results showed a significant correlation between the major axis (sagittal) length of the lesion on T2-weighted imaging and

Table 1: Change in BPI after cordotomy and its correlation with different postoperative imaging characteristics

% BPI Change Correlation (n = 10/15)	Spearman Rho	Significance (2-Tailed)
T2-weighted imaging total cord, %	-0.091	.802
Diffusion, total cord, %	0.590	.073
Major axis (sagittal), T2-weighted imaging, mm	-0.529	.116
Minor axis (in-plane, axial), T2-weighted imaging, mm	-0.091	.802
Major axis (sagittal), DWI, mm	0.705	.023
Minor axis (in-plane, axial), DWI, mm	0.827	.003
Minimal MD	-0.821	.004
Maximal MD	-0.091	.802
Average MD	-0.450	.192
Minimal FA	-0.148	.688
Maximal FA	0.255	.476
Average FA	0.292	.413

the number of penetrations ($r = 0.566$, $P = .028$). There were no additional significant correlations between any of the other imaging parameters and the number of pial penetrations or ablations.

Furthermore, we measured each lesion's minimal, maximal, and average MD and FA on the pre- and postoperative DTI studies. The postoperative MD was significantly lower at the site of the lesion compared with the preoperative MD values of the same area ($0.947 \pm 0.213 \times 10^{-3} \text{ mm}^2/\text{s}$ and $1.125 \pm 0.304 \times 10^{-3} \text{ mm}^2/\text{s}$, respectively; $P = .023$). Postoperatively, the lesion's MD was also significantly lower than the nonlesioned cord on the contralateral side ($1.121 \pm 0.259 \times 10^{-3} \text{ mm}^2/\text{s}$; $P = .003$). The lesion's FA values ($0.406 \pm .69$) were significantly lower than the preoperative values of the normal cervical cord at the same segment (0.603 ± 0.145 ; $P = .001$) as well as the contralateral nonlesioned cord values on the postoperative scan (0.565 ± 0.130 ; $P = .001$).

Interestingly, patients with higher minimal MD values had improved postoperative BPI severity scores. The minimal MD correlated significantly with a greater relative decrease in the BPI severity score ($r = -0.821$, $P = .004$). A higher average MD showed a tendency toward similar trends, but results were not statistically significant ($r = -0.450$, $P = .192$). No significant association was demonstrated between either minimal, maximal, or average FA and changes in postoperative BPI severity ($r = -0.148$, $P = .688$; $r = 0.255$, $P = .476$; and $r = 0.292$, $P = .413$, respectively) (Table 1).

Lesion Parameters Over Time

Five patients were able to undergo a repeat MR imaging 1 month after surgery. The lesion volume on T2-weighted imaging significantly decreased from $0.25 \text{ cc} \pm 0.06 \text{ cc}$ on postoperative day 1 (POD 1) to $0.05 \text{ cc} \pm 0.02 \text{ cc}$ 1 month later ($P = .043$). The lesion volume on diffusion images decreased nonsignificantly, from $0.08 \text{ cc} \pm 0.04 \text{ cc}$ to $0.05 \text{ cc} \pm 0.03 \text{ cc}$ over 1 month ($P = .066$). However, the lesion's percentage of the cord's cross-sectional area on T2-weighted imaging and diffusion decreased significantly, from 21.5 ± 5.4 to 14.2 ± 3.2 ($P = .043$) and from 24.11 ± 12.77 to 13.19 ± 7.71 ($P = .043$), respectively.

The sagittal length (major axis) on T2-weighted imaging decreased significantly, from $12.8 \text{ mm} \pm 2.4 \text{ mm}$ on POD 1 to

Table 2: Imaging characteristics of patients with and without immediate postoperative contralateral pain

POD 1 Contralateral Pain	Yes 5/15	No 10/15	Sig.
Pain side, right, <i>n</i> (%)	2 (40%)	6 (60%)	.608
T2-weighted imaging total cord, %	17.46 ± 10.27	20.10 ± 7.91	.270
Diffusion, total cord, %	14.60 ± 7.60	15.67 ± 9.65	.999
MD	0.804 ± 0.98	1.019 ± 0.222	.037
FA	0.402 ± 0.07	0.408 ± 0.073	.903

Note:—Sig indicates significance.

8.8 mm ± 0.8 mm 1 month later ($P = .043$). The lesion's in-plane axial length (minor axis) on diffusion decreased significantly, from 5.2 ± 0.98 mm to 4.6 ± 1.0 mm ($P = .043$). We did not find any significant differences when we compared the lesion's sagittal length on diffusion or axial length on T2-weighted imaging between the POD 1 and the 1-month postoperative MRIs ($P = .08$ and $P = .08$, respectively). The MD showed a nonsignificant increase from 0.926 ± 0.251 to $1.070 \pm 0.285 \times 10^{-3}$ mm²/s; $P = .08$). We found no significant changes in FA from POD 1 to 1 month after surgery (0.409 ± 0.083 and 0.361 ± 0.063 , respectively; $P = .225$).

Contralateral Pain

Pain contralateral to the original one appeared immediately after surgery in 5 of the 15 patients (33%), which, with 1 exception, was considered less severe than the original one. We did not detect any significant differences between patients with and those without immediate postoperative contralateral pain in terms of lesion volume or percentage of the involved cord ($P = .270$ and $P = .999$ for T2-weighted imaging and DWI, respectively). The MD was significantly lower among patients with contralateral pain ($P = .037$), but the FA showed no significant association ($P = .903$) (Table 2).

Three patients in our cohort had clear preoperative documentation of metastatic lesions contralateral to the side of the originally painful lesion. All 3 had relief of their original pain, but 2 of them developed postoperative contralateral pain. Eight patients had lesions that were assumed to at least partially involve midline structures. However, because of their frailty, we were unable to obtain more recent adequate oncologic imaging data from all 15 patients.

One month after surgery, 9/14 (64%) reported developing contralateral pain, which was as severe as the original pain in 1 patient. Six of these 9 patients (66%) required medical treatment for relief of the contralateral pain. Of note, 8 of them had tumors along the midline or on the contralateral side that could be the cause of the new contralateral pain.

DISCUSSION

In this prospective study, we characterized the postoperative changes on MR imaging studies after percutaneous RF cordotomy. We further examined the correlations between postcordotomy diffusivity and T2 MR imaging changes and 2 clinical outcomes, pain improvement and the development of contralateral pain. In addition, we observed the evolution of the imaging characteristics of the ablated area up to 1 month from surgery. We hypothesize that postoperative parenchymal

imaging changes could reflect intraoperative events, and after correlating such changes to clinical results, we might therefore be able to search for ways to improve surgical technique and outcomes.

It has been previously shown that ablation of at least 20% of the cord is required to achieve optimal pain improvement after cordotomy.⁹ However, these

numbers derive from a histology-based cohort from the 1990s, and they were based on older surgical techniques that were associated with relatively lower success and safety profiles. That report was later challenged by a more contemporary series by Vedantam et al,¹⁰ who showed similar degrees of pain relief when comparing patients with ablations above and below 20% of the cord-cross sectional area, as represented by postoperative T2-weighted MR imaging. Similarly, our current study did not detect any significant differences in the decrease in NRS between patients with lesions below or above 20% of the cord's cross-sectional area based on both T2-weighted imaging and DWI. Lesions encompassing as low as 13% of the cord's cross-sectional area achieved excellent and long-term pain control. Therefore, our findings agree with the conclusions of Vedantam et al,¹⁰ who stated that larger lesions do not necessarily represent adequate ablation of the STT. In fact, we showed that smaller lesions on diffusion imaging correlated with greater improvement on the BPI severity score, probably signifying better intraoperative localization of the STT while sparing the need for repeated repositioning of the electrodes (Table 1, Fig 3). This is also explained by the fact that, as was previously shown and in accordance with our results, the size of the lesions on postcordotomy T2-weighted imaging directly correlates with the number of pial penetrations.¹⁰ We believe that more accurate localization of the STT, based on improved imaging and neurophysiologic techniques, may decrease the need for unnecessary repeated positioning of the electrodes and result in smaller surgical lesions and better pain control outcomes.

To our knowledge, this is the first study to describe the evolution of the imaging characteristics of cordotomy ablated areas up to 1 month after surgery. Our results showed that the lesions' percentage of the cord's cross-sectional areas on both T2-weighted imaging and diffusion imaging decreased significantly from POD1 to 1 month after surgery. Because only 5 patients were able to arrive for the scheduled 1-month postoperative MR imaging, we were not able to search for potential correlations between the lesions' dynamics and clinical outcomes at this point. We are currently gathering more data on this topic.

Furthermore, we analyzed the MD and FA values of the lesion on DTI. Whereas MD quantifies the diffusion of water molecules within tissues, FA estimates the degree of tissue organization. Overall, these parameters may indicate the degree of tissue injury, as was previously shown in patients after cordotomy and patients with spinal injuries.^{12,14-16}

Similar to previous reports, FA was significantly lower in the lesioned side of the cord compared with the nonlesioned side.¹² Our study also demonstrated a significant decrease in tissue FA of the targeted cervical cord area from pre- to postoperative DTI. FA values did not change at 1 month after surgery ($P = .225$).

Tissue FA decreased after neuronal tissue ablation because of disruption of axons that are aligned longitudinally, as was previously shown in studies of spinal cord injuries.^{17,18} Decreased FA has been associated with impaired white matter microstructure, including myelin damage, increased axonal diameter, low axonal attenuation, and impaired cellular membrane.^{19,20} In addition, we found significantly lower MD values in the lesioned area compared with the nonlesioned cord on the contralateral side. The lesion's MD was also significantly lower compared with the same area's MD on preoperative imaging. We then observed a non-significant increase in the lesion's MD at 1 month after surgery ($P = .08$). These results represent acute changes that typically follow sudden neural tissue insults, such as trauma or ischemic stroke.^{17,18,21} MD is initially decreased within the first few hours because of restriction of the movement of water molecules in the intracellular compartment. MD is later increased after the disruption of tissue barriers and the formation of necrotic tissue, but FA often stays decreased because of permanent axonal disruption.²¹

Interestingly, we found a significant correlation between the lesions' minimal MD values on postoperative scans and improved BPI severity scores after cordotomy. Average MD values showed a similar trend in relation to BPI severity, but the correlation was nonsignificant. No significant correlations were seen between FA values and changes in BPI after surgery. Our results are therefore in line with a previous study that found a correlation between the lesions' MD (but not FA) and the degree of improvement in the 1-week postoperative BPI severity score.¹² A higher MD is believed to be associated with cellular edema, demyelination, and disruption of membranes, which follow RF ablation.¹² Therefore, although MD values on immediate postoperative MR imaging are generally lower in the ablated area compared with nonlesioned tissue, higher MD values may, in fact, indicate better ablation of the neural tissue during cordotomy.

The development of contralateral pain after unilateral cordotomy has been reported in 17%–73% of patients.^{3,6-8} This type of pain is commonly reported as less severe when compared with the original one and is usually well controlled with pain medications. The mechanisms behind this phenomenon are still controversial because it is often difficult to differentiate between pure new-onset mirror pain and pain that is related to an underlying midline or contralateral disease. It is believed that pure mirror-image pain is a type of referred pain resulting from chronic changes in the spinal cord circuitry, coupled with disinhibition following ablation of descending pain inhibitory pathways.⁷ In our study, pain in the contralateral side appeared immediately after surgery in 33% of the cases and increased to 64% within 1 month after surgery. In most cases, this new pain was significantly less severe than the original one. We did not find any significant impact of the size of the lesion on the occurrence of immediate postoperative contralateral pain. However, patients who developed postoperative contralateral pain had lower MD on their immediate postoperative MR imaging.

Even though our patients were not asked to undergo preoperative total-body imaging, we assume that at least some of them harbored nonpainful metastatic lesions involving midline axial or contralateral structures. Previous reports emphasized the role of the dorsal columns in transmitting visceral and potentially also

midline axial pain. They mentioned the higher effectiveness of midline myelotomy (either thoracic or cervical) in eliminating midline pain compared with anterolateral cordotomy.²²⁻²⁴ It is therefore plausible that pain transmitted from silent midline spinal or pelvic tumors could potentially reach the surface after eliminating the more dominant original pain by unilateral cordotomy and contribute to the contralateral pain phenomenon. We plan to gather more preoperative total-body imaging data to investigate the correlation between the distribution of nonpainful metastatic spread, the ablation's anatomic characteristics, and the contralateral pain phenomenon.

Limitations

The main limitation of this study is its small cohort size. Additional correlations between different factors, including subgroup analyses, would have been possible with a larger patient population. Furthermore, pre- and 1-month postoperative BPI questionnaires were available for only 10/15 of the patients, mainly because of the medical and psychosocial complexity of our patients, as well as clinical deterioration and even death. Having more data derived from this well-validated tool would allow a better quantification of the studied associations.¹³ In addition, our imaging studies were performed within 24 hours after surgery. The patients' complex conditions made it too difficult to bring them back for a 1-month follow-up MR imaging study in parallel to the clinical evaluation. Therefore, we are currently working on increasing our data to analyze whether changes in diffusion MD values and the size of the lesions over time correlate with clinical outcomes.

CONCLUSIONS

The results of this study suggest that postoperative MR imaging has a role in predicting clinical outcomes after cordotomy. Even though a minimal size of ablation is required, larger lesions do not necessarily indicate better outcomes. Smaller lesions may signify better intraoperative localization of the spinothalamic tract and are correlated with better outcomes. Changes in MD and FA values represent neural tissue damage after ablation, and increased lesion MD values may be linked to better clinical response.

Disclosure: Ido Strauss—RELATED: Grant: European Society for Stereotactic and Functional Neurosurgery.* *Money paid to institution.

REFERENCES

1. Harsh V, Viswanathan A. **Surgical/radiological interventions for cancer pain.** *Curr Pain Headache Rep* 2013;17:331 CrossRef Medline
2. Raslan AM, Cetas JS, McCartney S, et al. **Destructive procedures for control of cancer pain: the case for cordotomy.** *J Neurosurg* 2011;114:155–70 CrossRef Medline
3. Strauss I, Berger A, Arad M, et al. **O-arm-guided percutaneous radiofrequency cordotomy.** *Stereotact Funct Neurosurg* 2017;95:409–16 CrossRef Medline
4. Raslan AM. **Percutaneous computed tomography-guided radiofrequency ablation of upper spinal cord pain pathways for cancer-related pain.** *Neurosurgery* 2008;62:226–33; discussion 233–34 CrossRef Medline
5. Kanpolat Y, Ugur HC, Ayten M, et al. **Computed tomography-guided percutaneous cordotomy for intractable pain in malignancy.** *Neurosurgery* 2009;64:ons187–93; discussion ons193–94 CrossRef Medline

6. Berger A, Hochberg U, Zegerman A, et al. **Neurosurgical ablative procedures for intractable cancer pain.** *J Neurosurg* 2019;1–8 CrossRef
7. Nagaro T, Adachi N, Tabo E, et al. **New pain following cordotomy: clinical features, mechanisms, and clinical importance.** *J Neurosurg* 2001;95:425–31 CrossRef Medline
8. Bain E, Hugel H, Sharma M. **Percutaneous cervical cordotomy for the management of pain from cancer: a prospective review of 45 cases.** *J Palliat Med* 2013;16:901–07 CrossRef Medline
9. Lahuerta J, Bowsher D, Lipton S, et al. **Percutaneous cervical cordotomy: a review of 181 operations on 146 patients with a study on the location of “pain fibers” in the C-2 spinal cord segment of 29 cases.** *J Neurosurg* 1994;80:975–85 CrossRef Medline
10. Vedantam A, Hou P, Chi TL, et al. **Postoperative MRI evaluation of a radiofrequency cordotomy lesion for intractable cancer pain.** *AJNR Am J Neuroradiol* 2017;38:835–39 CrossRef Medline
11. Vedantam A, Bruera E, Hess KR, et al. **Somatotopy and organization of spinothalamic tracts in the human cervical spinal cord.** *Neurosurgery* 2019;84:E311–17 CrossRef Medline
12. Vedantam A, Hou P, Chi TL, et al. **Use of spinal cord diffusion tensor imaging to quantify neural ablation and evaluate outcome after percutaneous cordotomy for intractable cancer pain.** *Stereotact Funct Neurosurg* 2017;95:34–39 CrossRef Medline
13. Bendinger T, Plunkett N. **Measurement in pain medicine.** *BJA Education* 2016;16:310–15 CrossRef
14. Vedantam A, Jirjis MB, Schmit BD, et al. **Diffusion tensor imaging of the spinal cord: insights from animal and human studies.** *Neurosurgery* 2014;74:1–8; discussion 8; quiz 8 CrossRef Medline
15. Martin AR, Aleksanderek I, Cohen-Adad J, et al. **Translating state-of-the-art spinal cord MRI techniques to clinical use: a systematic review of clinical studies utilizing DTI, MT, MWF, MRS, and fMRI.** *NeuroImage Clin* 2016;10:192–238 CrossRef Medline
16. Vedantam A, Eckardt G, Wang MC, et al. **Clinical correlates of high cervical fractional anisotropy in acute cervical spinal cord injury.** *World Neurosurg* 2015;83:824–28 CrossRef Medline
17. Shanmuganathan K, Gullapalli RP, Zhuo J, et al. **Diffusion tensor MR imaging in cervical spine trauma.** *AJNR Am J Neuroradiol* 2008;29:655–59 CrossRef Medline
18. Li XH, Li JB, He XJ, et al. **Timing of diffusion tensor imaging in the acute spinal cord injury of rats.** *Sci Rep* 2015;5:12639 CrossRef Medline
19. Sampaio-Baptista C, Johansen-Berg H. **White matter plasticity in the adult brain.** *Neuron* 2017;96:1239–51 CrossRef Medline
20. Takahashi M, Hackney DB, Zhang G, et al. **Magnetic resonance microimaging of intraaxonal water diffusion in live excised lam-prey spinal cord.** *Proc Natl Acad Sci U S A* 2002;99:16192–96 CrossRef Medline
21. Alegiani AC, MacLean S, Braass H, et al. **Dynamics of water diffusion changes in different tissue compartments from acute to chronic stroke—a serial diffusion tensor imaging study.** *Front Neurol* 2019;10:158 CrossRef Medline
22. Willis WD, Al-Chaer ED, Quast MJ, et al. **A visceral pain pathway in the dorsal column of the spinal cord.** *Proc Natl Acad Sci U S A* 1999;96:7675–79 CrossRef Medline
23. Nauta HJ, McIlwrath SL, Westlund KN. **Punctate midline myelotomy reduces pain responses in a rat model of lumbar spine pain: evidence that the postsynaptic dorsal column pathway conveys pain from the axial spine.** *Cureus* 2018;10:e2371 CrossRef Medline
24. Nauta HJ, Hewitt E, Westlund KN, et al. **Surgical interruption of a midline dorsal column visceral pain pathway. Case report and review of the literature.** *J Neurosurg* 1997;86:538–42 CrossRef Medline

MRI T2-Hyperintense Signal Structures in the Cervical Spinal Cord: Anterior Median Fissure versus Central Canal in Chiari and Control—An Exploratory Pilot Analysis

T.A. Tomsick, L.L. Wang, M. Zuccarello, and A.J. Ringer



ABSTRACT

BACKGROUND AND PURPOSE: Cervical spine axial MRI T2-hyperintense fluid signal of the anterior median fissure and round hyperintense foci resembling either the central canal or base of the anterior median fissure are associated with a craniocaudal sagittal line, also simulating the central canal. On the basis of empiric observation, we hypothesized that hyperintense foci, the anterior median fissure, and the sagittal line are seen more frequently in patients with Chiari malformation type I, and the sagittal line may be the base of the anterior median fissure in some patients.

MATERIALS AND METHODS: Sagittal line incidence and the incidence/frequency of hyperintense foci and anterior median fissure in 25 patients with Chiari I malformation and 25 contemporaneous age-matched controls were recorded in this prospective exploratory study as either combined (hyperintense foci+anterior median fissure in the same patient), connected (anterior median fissure extending to and appearing to be connected with hyperintense foci), or alone as hyperintense foci or an anterior median fissure. Hyperintense foci and anterior median fissure/patient, hyperintense foci/anterior median fissure ratios, and anterior median fissure extending to and appearing to be connected with hyperintense foci were compared in all, in hyperintense foci+anterior median fissure in the same patient, and in anterior median fissure extending to and appearing to be connected with hyperintense foci in patients with Chiari I malformation and controls.

RESULTS: Increased sagittal line incidence (56%), hyperintense foci (8.5/patient), and anterior median fissure (4.0/patient) frequency were identified in patients with Chiari I malformation versus controls (28%, 3.9/patient, and 2.7/patient, respectively). Increased anterior median fissure/patient, decreasing hyperintense foci/anterior median fissure ratio, and increasing anterior median fissure extending to and appearing to be connected with hyperintense foci/patient were identified in Chiari subgroups. A 21%–58% increase in observed anterior median fissure extending to and appearing connected to hyperintense foci in the entire cohort and multiple sagittal line subgroups compared with predicted occurred.

CONCLUSIONS: In addition to the anticipated increased incidence/frequency of sagittal line and hyperintense foci in patients with Chiari I malformation, an increased incidence and frequency of anterior median fissure and anterior median fissure extending to and appearing to be connected with hyperintense foci/patient were identified. We believe an anterior median fissure may contribute to a sagittal line appearance in some patients with Chiari I malformation. While thin sagittal line channels are usually ascribed to the central canal, we believe some may be due to the base of the anterior median fissure, created by pulsatile CSF hydrodynamics.

ABBREVIATIONS: AMF = anterior median fissure; AMF>HIF = anterior median fissure extending to and appearing to be connected with hyperintense foci; CTM = CT myelography; HIF = hyperintense foci; HIF+AMF = hyperintense foci and anterior median fissure in the same patient; pt. = patient; SL = sagittal line

Axial MR imaging of the cervical spine frequently demonstrates hyperintense, linear, anatomically, sagittally-oriented

T2 fluid signal of the anterior median fissure (AMF) and hyperintense foci (HIF) resembling the central canal or the base of the AMF.¹⁻³ These axial T2 findings may be associated with a

Received June 26, 2021; accepted after revision November 6.

From the Department of Radiology (T.A.T., L.L.W.), Neuroradiology Section and Department of Neurosurgery (M.Z.), University of Cincinnati Medical Center, Cincinnati, Ohio; and Mayfield Clinic (A.J.R.), Cincinnati, Ohio.

Paper previously presented, in part, at: Annual Meeting of the American Society of Neuroradiology and Foundation of the ASNR Symposium, April 22–27, 2017; Long Beach, California.

Please address correspondence to T.A. Tomsick, MD, University of Cincinnati Medical Center, Department of Radiology, Neuroradiology Section, 231 Albert Sabin Way, Cincinnati, OH 45267-0762; e-mail: tomsicta@ucmail.uc.edu

Indicates article with online supplemental data.
<http://dx.doi.org/10.3174/ajnr.A7046>



FIG 1. A patient with Chiari I with 19 HIF up to 3 mm in diameter, 1 AMF, no AMF>HIF, and an SL of various hyperintensity and diameter from C4 through T1, consistent with hydromyelia.

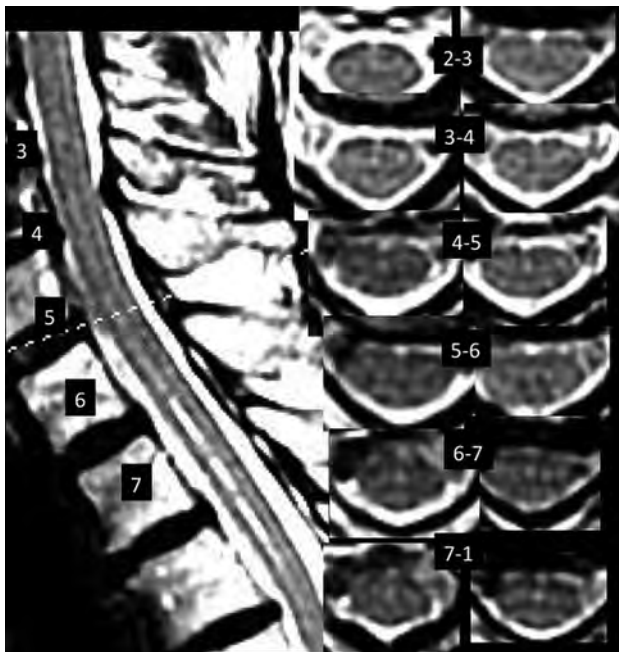


FIG 2. Postdecompressive craniectomy patient with Chiari I with 9 HIF, 4 AMFs, 1 AMF>HIF, and sharp and hyperintense SLs at C6–C7 and less hyperintense, sharp, and defined SLs at C2–C6.

channel-like T2-hyperintense craniocaudal line on images parallel to the sagittal plane (a sagittal line [SL]), simulating the central canal (Fig 1).^{4,5} A previous analysis of HIF, AMF, and a thin SL in a population without Chiari I malformation provided not only a baseline for their identification but also a confirmation of a relationship between not only the AMF and HIF but also their relationship to the SL.¹ It found the following:

1. HIF were greater in number than AMFs, but AMFs increase in the presence of increasing HIF, suggesting an anatomic relationship.
2. SLs were associated with greater numbers of both HIF and AMF/patient (pt.) versus no SL, 6.7 versus 2.7/pt. and 3.3 versus 2.0/pt., respectively. SL presence correlated more closely to HIF than to AMF presence within the entire 358-patient group.
3. When HIF and AMF were classified as combined (concurrent HIF and AMF, with ≥ 1 of each both present in the same patient [HIF+AMF]) or continuous (AMF appearing to extend to and join an HIF [AMF>HIF]), HIF and AMF/pt. each differed numerically and patients with an SL had more combined HIF+AMF and continuous AMF>HIF than patients without an SL.
4. In patients with both SL and combined HIF+AMF (a circumstance allowing the possibility of a relationship of all 3 structures), HIF become proportionally fewer compared with AMFs. In patients with an SL actually exhibiting continuous AMF>HIF, the HIF/AMF ratio decreased further.

While it is expected that manifestations of the central canal as an SL and HIF are more frequent in patients with Chiari syndrome type I,⁶ past experience leads us to hypothesize that AMFs are also seen more frequently in patients with Chiari I malformation and that the SL or channel may represent the base of a wide AMF, rather than the central canal, in some patients (Figs 1 and 2). Therefore, we performed an exploratory prospective analysis of HIF, AMF, and SL in patients with Chiari I malformation to examine their relationships.

MATERIALS AND METHODS

The presence of HIF, AMF, and SL on cervical MR imaging in 25 patients with Chiari I malformation and 25 age-matched controls performed on a single scanner was recorded by a single reader. Reader blinding by hiding the tonsil position and postoperative changes was not performed. SL presence was assessed and recorded before HIF and AMF assessment.

The scanning facility is associated with the Mayfield Clinic Chiari Center, a multidisciplinary outpatient center for evaluation and treatment of Chiari I malformation. Patients with Chiari I were symptomatic with headache, dizziness, and/or nystagmus and were confirmed to have a cerebellar tonsil position below the foramen magnum with reduced CSF signal ventral to the cervicomedullary junction at the tectorial membrane and dorsal to the tonsils at the opisthion. The population with Chiari I included 10 postoperative patients. Preoperative images were not available for review. Approval was obtained by Mayfield Clinic and University of Cincinnati institution's review board.

Technical imaging scanning parameters included the following: a Signa Excite high-definition 1.5T scanner (GE Healthcare); 7.9T/m, 120 T/m/s gradients, standard fast spin-echo T2 sequences; sagittal: 256 × 256 pixel matrix, 3.0-mm thickness, with 1-mm spacing, 24 × 24 cm FOV; axial: 256 × 224 pixel, 3.0-mm thickness, 0.5-mm spacing, 22 × 22 cm FOV. Images were reviewed at ×2.5 magnification on a diagnostic eFilm Workstation (IBM). Patients with an SL diameter of >3 mm, indicative of syringohydromyelia, were excluded from analysis.

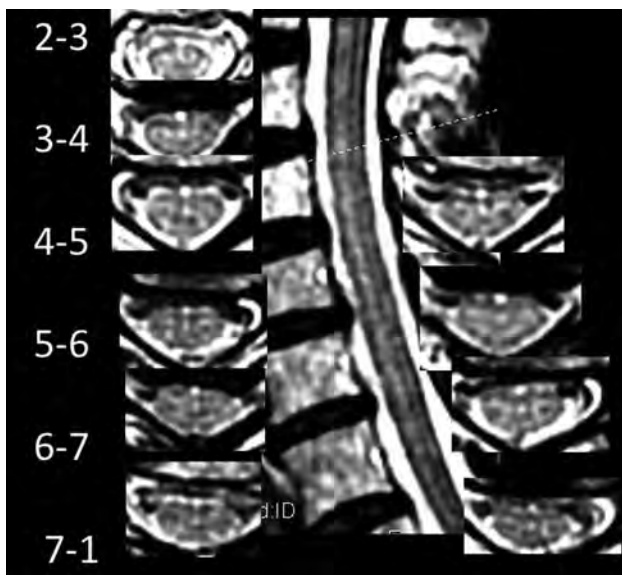


FIG 3. Control patient with 15 HIF, 3 AMFs, 3 AMF>HIF, and SL with variably hyperintense and variably sharp dots and dashes from C3–4 to C7. Note hyperintense pixels immediately anterior to the AMF on axial images, despite crescentic flow-related signal loss immediately anterior to the cord on most images.

AMFs were recorded as anterior, midline, linear hyperintensities continuing from a dimple-shaped indentation between the ventral hemicords. AMFs may be oriented minimally to the perpendicular.¹ HIF were recorded as focal, round, midline fluid-signal hyperintensities of the anterior 25%–50% of the cord. SLs were recorded as sharply-margined hyperintense craniocaudal lines on sagittal images located in the anterior 25%–50% of the sagittal dimension of the cord (Figs 1 and 2) or as discontinuous craniocaudal alignments of dots and dashes of varying lengths and hyperintensity (Fig 3). They may be associated with wider less hyperintense and less sharp bands and may be seen with partial volume structures (Fig 4).

HIF and AMF numbers per patient (frequency) in the control and Chiari I groups were determined. Differences in the incidence of HIF, AMF, SL, and HIF and AMF/pt. between patients with Chiari I and controls were analyzed in Excel (Microsoft) with χ^2 and Student *t* tests. Comparison of the incidence and numbers of AMF+HIF and AMF>HIF/pt. in patients with and without an SL in the Chiari I versus non-Chiari I groups was also performed. Incidence and frequency of HIF and AMF in the 25-patient control group were compared with those of the original, published 356-patient control group.¹

RESULTS

Age, sex, and incidence and frequency of HIF, AMF, and SL are listed in Table 1 for the 25 Chiari I, 25 current control, and 356 prior non-Chiari I groups. A female predominance was present in both current groups, with no age difference. No difference was identified in HIF and AMF incidence in the Chiari I and current control groups, present in 88%–100% of both. Both HIF/pt. and AMF/pt. were significantly greater in the Chiari I group compared with current controls (8.5 versus 3.9 HIF/pt. and 4.1 versus

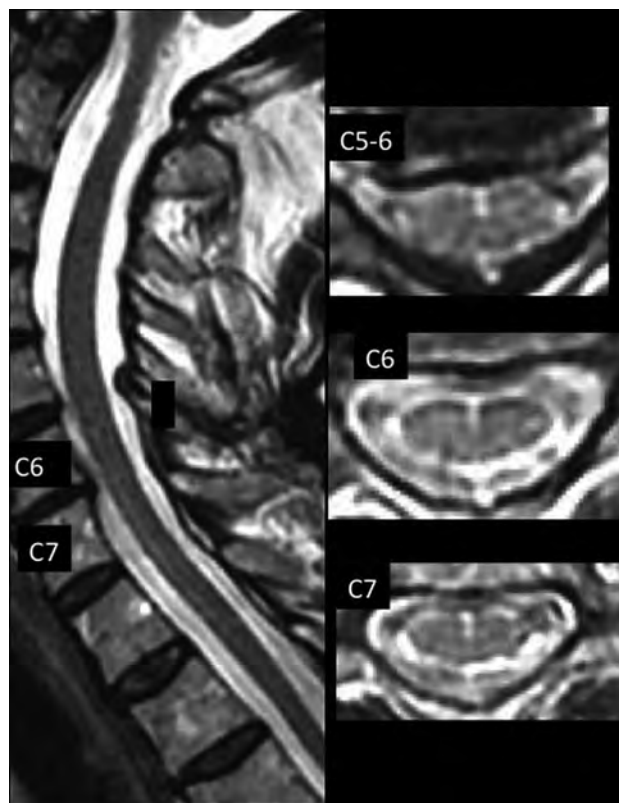


FIG 4. Postoperative patient with Chiari I with 19 HIF, 3 AMFs, and 2 AMF>HIF, with a faintly hyperintense ventral line at C6–T1.

2.7 AMF/pt., respectively). HIF/pt. and AMF/pt. were similar for the current control and the original earlier multis Scanner non-Chiari I analysis group¹ (3.9 versus 3.7 and 2.7 versus 2.3, respectively), as was the SL incidence (28% versus 25%).

No differences in HIF or AMF were identified in 15 patients without an operation versus 10 postoperative patients with Chiari I (Table 2). Twenty HIF measured < 1 mm in width (8 postoperative), 4 measured 1–2 mm (2 postoperative), and 1 patient without an operation had HIF that measured 2–3 mm. (Fig 1). The postoperative group exhibited a higher incidence of SLs (8/10, 80% versus 5/15 [33.3%]), with numerically greater AMF>HIF (2.8 versus 1.9).

Table 3 outlines HIF and AMF/pt., HIF/AMF ratios, and AMF>HIF/pt. in Chiari I versus controls, with and without SLs. Fourteen patients with Chiari I and an SL demonstrated increased HIF/pt. (10.1 versus 6.6, $P < .04$) and numerically greater AMF (4.6 versus 3.5, $P = .18$) versus 11 patients with Chiari I and no SL. Seven control patients with an SL demonstrated increased HIF/pt. (7.0 versus 2.7/pt., $P < .04$) and greater AMF/pt. (3.4 versus 2.4, $P = .02$) versus 18 controls without an SL. One patient with Chiari I and HIF-only with 7 HIF and no SL and 1 control with HIF-only with 12 HIF with an SL were identified. One control had no HIF or AMF.

The observed AMF>HIF/pt. was greater for all patients with Chiari I versus all controls (Online Supplemental Data; 2.2 versus 1.0/pt., $P < .001$), for 14 patients with Chiari I and an SL versus 7 controls with an SL (2.9 versus 1.3/pt., $P < .02$), and for 11 patients with Chiari I versus 18 controls without an SL (1.9 versus 0.8, $P = .01$). The incidence of observed AMF>HIF was also greater than predicted for 12 patients with Chiari I and an SL

Table 1: Age, sex, incidence (%), and frequency (No./Pt), for HIF, AMF, SL, and AMF>HIF in the Chiari I and non-Chiari I control groups

	Age (Median)	Sex (F) (%)	HIF (%)	HIF/Pt.	AMF (%)	AMF/Pt.	SL (No.) (%)	AMF>HIF (Mean)
Chiari I (n = 25)	40	23 (92%)	25 (100%)	8.5 ^a	24 (96%)	4.0 ^b	14 ^c (56%)	2.2
Control (n = 25)	40	17 (68%)	24 (96%)	3.9 ^a	22 (88%)	2.7 ^b	7 ^c (28%)	1.0

^a P = .0004.

^b P = .025.

^c P < .02 (χ^2).

Table 2: Incidence HIF and AMF/pt., SL incidence, and number of AMFs extending to HIF (AMF>HIF) in Chiari I without an operation versus patients having undergone postdecompressive craniectomy

	HIF		AMF		SL	AMF>HIF
	%	HIF/Pt.	%	AMF/Pt.	No. (%)	No.
Chiari I no surgery (n = 15)	100	8.9	100	4.0	5 (33%) ^a	1.9 ^b
Chiari I post-op (n = 10)	100	8.1	90	4.3	8 (80%) ^a	2.8 ^b

Note:—Post-op indicates postoperative.

^a P = .009.

^b P = .07.

Table 3: Number patients, HIF/pt., AMF/pt., HIF to AMF ratio, and AMF>HIF/pt. in HIF or AMF-only, HIF+AMF, and AMF>HIF subgroups for all Chiari I and control groups, with and without SL

	No.	HIF/Pt.	AMF/Pt.	Ratio	AMF>HIF
All Chiari I	25	8.6	4.1	2.1	2.2
All control	25	3.9	2.7	1.4	1
All Chiari I and controls					
HIF only					
Chiari I	1	7	NA	NA	2.3
Control	1	12	NA	NA	1.0
AMF only	0	NA	NA	NA	NA
HIF+AMF					
Chiari I	24	8.6	4.3	2.0	2.1
Control	23	3.9	3	1.3	1.1
AMF-HIF					
Chiari I	22	7.9	4.7	1.7	2.5
Control	16	4.4	3.3	1.3	1.5
No AMF→HIF					
Chiari I	3	13.7	1.7	8.2	0
Control	9	3	1.7	1.8	0
SL					
Chiari I	14	10.1	4.6	2.2	2.9
Control	7	7	3.4	2.1	1.3
HIF+AMF					
Chiari I	14	10.1	4.6	2.2	2.2
Control	6	6.2	4	1.6	1.5
AMF-HIF					
Chiari I	12	8.6	5	1.7	2.9
Control	5	7.2	4	1.8	1.8
No SL					
Chiari I	11	6.6	3.5	1.9	1.9
Control	18	2.7	2.4	1.1	0.8
HIF+AMF					
Chiari I	11	6.8	3.9	1.7	2.1
Control	17	2.9	3	0.9	0.9
AMF-HIF					
Chiari I	9	7	4.2	1.7	2.2
Control	11	3.1	3	1.1	1.2

Note:—NA indicates not applicable.

compared with 5 controls (3 versus 1.8/pt., $P < .02$) (Online Supplemental Data)

DISCUSSION

Patients with Chiari I are known to have a high incidence of hydrosyringomyelia. Therefore, identification of round foci on

axial images (HIF) and thin craniocaudad channels on sagittal images (SL), both usually considered manifestations of the central canal, is anticipated. However, the higher incidence of identification and frequency of an AMF in patients with Chiari I compared with controls has not been previously reported. AMF/pt. increased progressively from all (2.7/pt.), to HIF+AMF (4.3/pt.), to

AMF>HIF (4.7/pt.), and to SL AMF>HIF in patients with Chiari I (5.1/pt.). The ratio of HIF/AMF decreased among patients with SL, while AMF/pt. and AMF>HIF/pt. were increasing. AMF>HIF/pt. was highest among patients with an SL (2.9/pt.). Increasing AMF/pt., a decreasing HIF/AMF ratio, and increased AMF>HIF/pt. in patients with SL represent a stronger association of AMF-to-SL identification than suggested in the original non-Chiari I study,¹ in which the AMF>HIF/pt. were not counted.

It may be argued that with increases in AMF, identification of an AMF>HIF becomes more likely. However, the observed AMF>HIF/pt. was 47% greater in number than expected on the basis of HIF and AMF numbers for all patients with Chiari I and 58% greater for patients with an SL with AMF>HIF. The correlation of increasing AMF to AMF>HIF/pt. numbers in the setting of a decreasing HIF/AMF ratio supports an etiologic relationship between the visible cleft of an AMF and the round HIF of a potential channel or SL and indicates a potential anatomic connection of the 3 structures. This raises the question of whether some thin craniocaudad channels simulating the central canal on midline sagittal imaging are actually due to widened bases of AMFs. While numbers of AMF>HIF/pt. were not counted in the original non-Chiari I study,¹ other measures of HIF, AMF, and SL occurrence in that study are generally consonant with current control findings.

Despite an inability to resolve and separate without question the base of the AMF and HIF or the central canal individually on the same axial image in routine clinical scanning,⁷ the relationships in our previously published analysis of HIF, AMF, and thin SL in a non-Chiari I MR image population provided not only a baseline control for their incidence of identification but also a confirmation of a relationship among AMF, HIF, and SL.¹ This confirmation led us to believe that depictions of HIF and AMF are not totally independent occurrences of 2 different structures (the AMF and the central canal) but rather identification of different manifestations of the same structure: the sagittal cleft of the AMF as well as its wider base, in some instances.

In our prior review of 35 patients without Chiari I with both cervical MR imaging and cervical CT myelography (CTM), iodinated contrast media-filled AMFs were more common than HIF on CTM.¹ When present, HIF on CTM appeared almost exclusively as a focal dilation of the base of an AMF on CTM. A number of AMFs on CTM were seen at the same spinal level where MR imaging HIF were identified when an MR imaging AMF had not been identified. In several instances, the AMF on CTM was wide, possibly freely communicating on multiple, contiguous, consecutive axial images, while seen as an atypical broad, indistinct channel on a sagittal image due to partial volume effects on MR imaging. These CTM data are also consistent with HIF representing a wide base of the AMF.^{8,9}

Our findings raise the question of the physiologic origin and basis for imaging findings of the increased HIF, AMF-related channel, or SL simulating hydromyelia on MR imaging. CSF flow dynamics are known to be altered in patients with Chiari I, resulting in imaging of complex, pulsatile CSF motion that is subject to greater or lesser bright-T2 conspicuity with certain pulse sequences, even varying between systole and diastole.¹⁰⁻¹² Pulsatile CSF flow effects directed in a Craniocaudal or transverse radial

fashion that have been suggested to cause syringomyelia¹³ may be transmitted to the AMF, whose entire cervicomedullary course may not be subject to equal directions and magnitude of force. This possibility may be suggested by variable signal changes of flow and flow-related signal loss on axial images (Figs 3 and 4). Pial/arachnoidal coverings and vessels within the AMF¹⁴ may limit communication with the subarachnoid space and secondarily alter local transverse pressure transmission, but they may not limit and may even amplify craniocaudad effects (Figs 1-4). The effects may vary among subjects, and their depiction may vary among field strengths and imaging parameters applied. A formula for the production and/or loss of T2-signal in the AMF has yet to be elucidated.

The main limitation of this study lies in subjective observations of a single, potentially biased reader. That the current explorative study identified control SL incidence similar to prior non-Chiari study (28% versus 25%) as well as similar AMFs and HIF/pt. (3.9 versus 3.7 HIF, and 2.7 versus 2.3 AMF/pt.) suggests that scanners and reader performed similarly in this regard. However, the higher incidence of both HIF and AMF in 25 controls was seen compared with the original 6-scanner retrospective control study with 2 readers (96% versus 66% HIF, 88% versus 60% AMF). Scanner and reader performance may explain this discrepancy. Wide ranges of contributions to the identified HIF and AMF totals were found in the original 2-reader, 6-scanner analysis of controls without Chiari I: 5.9%–15.4% for HIF and 5.9%–16.7% for AMF among the 6 individual scanners (Online Supplemental Data).¹ At these rates of identification, a hypothetical similar top-performing scanner might record nearly 100% HIF and/or AMF (16% × 6 scanners = 96%) in a Chiari I population, and 6 similar lowest-performing scanners, just 36% (6% × 6 = 36%). The single scanner of the current study did perform at a similar level for HIF and AMF incidence compared with the highest-performing scanner in the prior 6-scanner non-Chiari I study. However, no single scanner performed best for identification of HIF, AMF, and SL, and no single scanner performed worst for individual structures in the prior study.

That the percentage of SLs was similar for both control subgroups without Chiari I is also consistent with the anticipated range of scanner performance (identified as 12.7%–34.2% in the 6-scanner study) and with the κ analysis in the original study, in which both readers agreed that <70% of patients did not have an SL. The small numeric increase of SLs in patients with Chiari I without operations versus controls is consistent with the original study, in which scanners that identified high numbers of HIF and AMFs did not identify high numbers of SLs. The discrepancy may reflect case selection, in which many patients with Chiari I with larger channels were already excluded from analysis. That a higher percentage of SLs was identified in postoperative patients with Chiari I may indicate a bias in favor of an operation for patients with hydrosyringomyelia preoperatively. The numeric increase of AMF and AMF>HIF in patients with Chiari with and without an operation remains of interest. A more comprehensive review of a larger population of pre- and postoperative scans in patients with Chiari I is required to answer these questions.

The observations reported here may appear to be of little immediate and direct clinical importance, because thin channels of

<3 mm in patients with Chiari I are thought to be of little clinical consequence.^{5,15} However, MR imaging reports attributing an SL or thin channel in a patient with Chiari I to hydro- or syringomyelia may increase patient concern, causing him or her to consider any neurologic symptom as potentially related, leading to unnecessary restudy. To solidify a relationship between conspicuous AMFs and such SLs or channels would serve to diminish concerns based on historical hydrosyringomyelic relationships.

CONCLUSIONS

We identified an increase of not only HIF and SLs in patients with Chiari I compared with controls as anticipated, but also of AMFs, not previously reported. The presence of increased frequency of HIF, AMFs, and thin SLs in the Chiari I population is consistent with a hydrodynamic effect likely created by CSF pressure/pulsation/flow phenomena. We believe that HIF and AMF are also manifestations of the same structure in some instances and may be responsible for some thin SL channels seen in some healthy patients and those with Chiari I as well, not due to the central canal or hydromyelia but rather to the widened base of the AMF.

Disclosures: Mario Zuccarello—UNRELATED: Employment: University of Cincinnati.

REFERENCES

1. Tomsick T, Peak E, Wang L. **Fluid-signal structures in the cervical spinal cord on MRI: anterior median fissure versus central canal.** *AJNR Am J Neuroradiol* 2017;38:840–45 CrossRef Medline
2. Cavlin MJ, Asato R, Hackney DB, et al. **High-resolution MR of the spinal cord in humans and rats.** *AJNR Am J Neuroradiol* 1989;10:13–17 Medline
3. Solsberg MD, Lemaire C, Resch L, et al. **High-resolution MR imaging of the cadaveric human spinal cord: normal anatomy.** *AJNR Am J Neuroradiol* 1990;11:3–7 Medline
4. Petit-Lacour MC, Lasjaunias P, Iffenecker C, et al. **Visibility of the central canal on MRI.** *Neuroradiology* 2000;42:756–61 CrossRef Medline
5. Holly LT, Batzdorf U. **Slitlike syrinx cavities: a persistent central canal.** *J Neurosurg* 2002;97:161–65 CrossRef Medline
6. Roser F, Ebner FH, Sixt C, et al. **Defining the line between hydromyelia and syringomyelia. A differentiation is possible based on electrophysiological and magnetic resonance imaging studies.** *Acta Neurochir* 2010;152:213–19 CrossRef
7. Zhao W, Cohen-Adad J, Polimeni JR, et al. **Nineteen-channel receive array and four-channel transmit array coil for cervical spinal cord imaging at 7T.** *Magn Reson Med* 2014;72:291–300 CrossRef Medline
8. Perez V, Peak E, Wang L, et al. **MR vs CT myelography in demonstrating normal CSF structures of the cervical spinal cord.** In: *Proceedings of the Annual Meeting of the American Society of Neuroradiology and the Foundation of the ASNR Symposium*, Washington, DC. May 21–26, 2016
9. Oichi Y, Hanakita J, Takahashi T, et al. **Morphologic patterns of the anterior median fissure in the cervical spinal cord evaluated by computed tomography after myelography.** *Neurospine* 2018;15:388–93 CrossRef
10. Brugières P, Idy-Peretti I, Iffenecker C, et al. **CSF flow measurement in syringomyelia.** *AJNR Am J Neuroradiol* 2000;21:1785–92 Medline
11. Haughton V, Mardal KA. **Spinal fluid biomechanics and imaging: an update for neurobiologists.** *AJNR Am J Neuroradiol* 2014;35:1864–69 CrossRef
12. Stoverud KH, Mardal KA, Haughton V, et al. **CSF flow in Chiari I and syringomyelia from the perspective of computational flow dynamics.** *Neuroradiol J* 2011;24:20–23 CrossRef Medline
13. Støverud KH, Alnæs M, Langtangen HP, et al. **Poroelastic modeling of syringomyelia: a systematic study of the effects of pia mater, median fissure, white and grey matter on pressure wave propagation and fluid movement within the cervical spinal cord.** *Comput Methods Biomech Biomed Engin* 2016;19:686–98 CrossRef Medline
14. Jacquesson T, Streichenberger N, Sindou M, et al. **What is the dorsal median sulcus of the spinal cord? Interest for surgical approach of intramedullary tumors.** *Surg Radiology Anat* 2014;36:345–51 CrossRef Medline
15. Strahle J, Muraszko KM, Garton HJL, et al. **Syrinx location and size according to etiology: identification of Chiari I-associated syrinx.** *PED* 2015;16:21–29 CrossRef Medline

Douglas Gordon Potts, MD

We are saddened to inform you that Dr Douglas “Gordon” Potts passed away on March 6, 2021, at the age of 94.

Gordon Potts was born on January 27, 1927, in Otahuhu, a suburb of Auckland, New Zealand. He went to a university in Christchurch and obtained a bachelor of science degree, majoring in atomics, nuclear physics, and mathematics. His initial intent was to become a physicist but he changed that later to radiotherapist, which subsequently led to a career in radiology. In 1953, he started training in radiology at the Auckland Hospital, where he was very much influenced by Stephen Moor, who had recently returned from neuroradiology training with James Bull at the National Hospital for Nervous Diseases in London, England, and Eric Lysholm at the Serafimer Hospital in Stockholm, Sweden. Intrigued by the new techniques in neuroimaging developed in Europe, Gordon decided to further pursue training in neuroradiology.

In 1955, he embarked on a 7-week journey as a cargo ship’s doctor from Auckland to London, where he completed his radiology training at University College Hospital. He then started his neuroradiology training at the Atkinson Morley Hospital. This institution was known to be the most active neurosurgical unit in Britain with Wylie McKissock as Head of Neurosurgery and James Bull as the Consultant Neuroradiologist. After 1 year, Gordon moved to Queens Square as a senior registrar working with James Bull, who was the neuroradiologist in charge at that time.

In 1960, Gordon was recruited by Juan Taveras to join the staff at the Neurological Institute at the Columbia Presbyterian Center in New York, which included Norman Chase and Ernest Wood. It was one of the first institutions in the United States to receive National Institutes of Health funding for neuroimaging research. This focus on research was further strengthened by the recruitment of Sadek Hilal, who was interested in cerebral vascular flow conditions.

In 1967, Dr. John Evans, Chairman of Radiology, recruited Gordon to the New York Hospital-Cornell Medical Center to become Head of the Division of Neuroradiology. The National Institutes of Health approved the neuroradiology training program at Cornell and provided funding for research in CSF production and absorption. Michael Deck was recruited from Queens Square to further complete the neuroradiology research team at Cornell.

It was at this time that Gordon and Hans Newton decided to embark on creating a textbook on neuroradiology, entitled *Radiology of the Skull and Brain*, which consisted of 2 volumes and a series of 6 books. Theirs was a joint work that took more than a decade to complete and resulted in one of the most admired and respected textbooks in our field, often referred to as the “Red Bible.”

Gordon was also an inventor and designed the “Pottometer,” a device that demonstrated on the radiographs at the time of myelography the degree of angulation from the horizontal, as well as the “Potts” needle for direct puncture of the carotid and brachial arteries. He also designed the “Potts Chair,” which made it possible to obtain biplane radiographs during a somersault procedure at the time of pneumoencephalography.

From 1968 to 1978, Gordon Potts was very much involved in the National Institutes of Health and served on multiple committees including the Radiation Sciences study section, and he was the Chairman of its Diagnostic Committee.

By 1985, Gordon had acquired an interest in health care organization and planning. Having had previous experience with public health care systems in New Zealand and Great Britain, he decided to accept the position of Chairman of Radiology at the University of Toronto, Canada. Gordon was instrumental in restructuring the previously independent radiology training programs at the 5 University of Toronto–affiliated hospitals and merging them into a single program. In doing so, Gordon enhanced the experience of the trainees and created the largest such program in Canada. The University of Toronto’s annual Best Resident Award in Radiology was named in Gordon’s honor. During his tenure from 1985 to 1992, Gordon was also the Radiologist in Chief at the Toronto Western Hospital, and his presence, guidance, and active participation greatly contributed to the successful formation of a dedicated Neuroscience Center at that institution.

During his professional career, Gordon remained strongly focused on research and teaching in neuroradiology, while always striving for innovation, scientific excellence, and education. He was one of the 14 founders of the American Society of Neuroradiology in 1962, was its President from 1970–1971, and received its Gold Medal in 1998.

In retirement, Gordon remained active at his country home on Shelter Island, NY, where he was known to make a delicious “Potts” jam and participated in growing oysters as part of a program at Cornell University to replenish the shellfish stocks of the Peconic Bay system on the East End of Long Island. Gordon’s annual oyster-fest party was a highlight for many of his friends and neighbors.

At the same time, he remained committed to his New Zealand roots. In the 1980s, he acquired a large plot of bush land on the Northern Island of New Zealand called Doubtless Bay. For almost 30 years, he slowly developed the land and constructed a simple, country home near its waterfront. One of his greatest achievements and pleasures there was to be part of the Whakaangi Landcare Trust, which aimed to protect and promote the native bush and the Kiwi population.

As part of his ongoing commitment toward neuroscience education in New Zealand, he founded the Moor Trust Annual Educational Meeting in 2014 in honor of his mentor Stephen Moor, to facilitate a Visiting Professorship in Neuroradiology at the University of Auckland, providing exposure to and discussion between radiology residents and staff in Auckland with innovative leaders in neuroradiology from around the world.

We will remember Gordon as a genuine, warm human being, who was down-to-earth even as an innovative world leader in neuroradiology. He had a skill for making friends all around the globe and was a role model for many. Gordon is survived by his 3 children, their partners, and his 6 grandchildren.

K. ter Brugge

<http://dx.doi.org/10.3174/ajnr.A7127>

Evolution of Radial Access in Neurointerventional Surgery

Incorporating innovative technologies and techniques often precipitates paradigm shifts in patient care. Despite the rapid evolution of endovascular devices and techniques, the idiom “primum non nocere” or “first, do no harm” must remain at the forefront of the interventionalist’s use of new therapies. While change at times may be driven by innovations that increase the speed or ease of a procedure, new techniques that facilitate improved efficacy, an enhanced safety profile, or the ability to treat an otherwise untreatable pathology should be the primary driving force behind technologic advances. One such therapy, the move to transradial access (TRA) for neurointerventional procedures, has marked a sizeable paradigm shift in the literature and care of neurovascular patients during the past several years.

Following compelling data from the cardiovascular literature,^{1,2} a boom in the use of transradial access in diagnostic and interventional endovascular neurosurgery procedures has been observed.³⁻⁶ In addition to an improved patient safety profile, TRA tends to enhance patient comfort and allows earlier mobilization and shorter observation for outpatient procedures. As neurointerventionalists have gained further experience, TRA has been used with increasing frequency for interventions as well.^{7,8}

The learning curve may be steep at the onset of converting to a radial-first approach, with increased procedural and fluoroscopic times a legitimate concern.⁹ Nonetheless, while fluoroscopy times may be marginally increased (approximately 4 minutes), a significant reduction in overall complications has been observed with TRA, generating a near 4-fold decrease in the rate of complications.⁹ Additionally, while the learning curve may be daunting at the onset, high success and low rates of crossover are experienced after as little as 30 TRA cases, with many skills from transfemoral access (TFA) being readily transferrable to TRA.¹⁰

In the setting of mechanical thrombectomy for acute ischemic stroke, access site complications are not infrequent with TFA, with major and overall access site complication rates of 1.67% and 4.59%, respectively, leaving room for improvement in the treatment of this patient population.¹¹ While robust head-to-head comparisons of TFA and TRA do not yet exist in the neurointerventional literature, the use of TRA in interventional procedures has been shown to have lower major (0.15%) and overall

(2.75%) access site complication rates.⁷ As TRA experience has grown, so has its use in the setting of acute thrombectomy, where time and efficiency remain paramount. In fact, equivalent procedural times have been observed in this time-sensitive interventional procedure.^{12,13} A comparison of mean procedural times between TRA (60 minutes) to TFA (66 minutes) in the setting of thrombectomy for large-vessel occlusion found no difference in time metrics between the 2 approaches.¹²

Despite its advantages, certain anatomic features may not prove favorable for transradial access. Previous studies have shown that the presence of a proximal radial loop, severe subclavian and innominate artery tortuosity, and proximal common carotid tortuosity yield a higher degree of difficulty for TRA with a higher conversion rate to TFA.¹⁴ Particularly in time-sensitive procedures, patients having these anatomic configurations may be best served with TFA, because the benefits afforded by TRA must be weighed against the potential time lost. Nonetheless, TRA has demonstrably lower rates of access site complications and resultant patient morbidity; thus, partiality ought to be shown to TRA in the absence of certain anatomic constraints.

While transradial access for middle meningeal artery embolization is being used with greater frequency,¹⁵ Shotar et al¹⁶ presented their experience using a patient-tailored approach to the access site based on preprocedural CT angiograms and interventionalist’s discretion, with a strong radial recommendation for right carotid catheterization in patients with a type III aortic arch with proximal common carotid artery tortuosity and for left carotid navigation in case of a bovine arch configuration. Using this approach, they found a greater rate of procedural success with less catheterization failures.

Given the safety benefit afforded by transradial access, in addition to the secondary gains of improved patient comfort and early mobilization, a radial-first approach for both diagnostic and interventional procedures has continued to evolve within neurointerventional surgery. A tailored approach using frontline TRA for both diagnostic and interventional procedures, augmented with TFA for certain hostile anatomic configurations, maintains a patient-centered focus, aimed at improving care through enhanced safety. As more familiarity with the technique and new devices develop, rates of crossover and potential time differences will decrease while maintaining the improved safety profile

afforded by TRA, thus enhancing the neurointerventional care provided to our patients.

REFERENCES

1. Valgimigli M, Frigoli E, Leonardi S, et al. MATRIX Investigators. **Radial versus femoral access and bivalirudin versus unfractionated heparin in invasively managed patients with acute coronary syndrome (MATRIX): final 1-year results of a multicentre, randomised controlled trial.** *Lancet* 2018;392:835–48 CrossRef Medline
2. Jolly SS, Yusuf S, Cairns J, et al. **Radial versus femoral access for coronary angiography and intervention in patients with acute coronary syndromes (RIVAL): a randomised, parallel group, multicentre trial.** *Lancet* 2011;377:1409–20 CrossRef Medline
3. Almallouhi E, Leary J, Wessell J, et al. **Fast-track incorporation of the transradial approach in endovascular neurointervention.** *J Neurointerv Surg* 2020;12:176–80 CrossRef Medline
4. Snelling BM, Sur S, Shah SS, et al. RIVAL trial group. **Transradial cerebral angiography: techniques and outcomes.** *J Neurointerv Surg* 2018;10:874–81 CrossRef Medline
5. Chivot C, Bouzerar R, Yzet T. **Transitioning to transradial access for cerebral aneurysm embolization.** *AJNR Am J Neuroradiol* 2019;40:1947–53 CrossRef Medline
6. Layton KF, Kallmes DF, Cloft HJ. **The radial artery access site for interventional neuroradiology procedures.** *AJNR Am J Neuroradiol* 2006;27:1151–54 Medline
7. Joshi KC, Beer-Furlan A, Crowley RW, et al. **Transradial approach for neurointerventions: a systematic review of the literature.** *J Neurointerv Surg* 2020;12:886–92 CrossRef Medline
8. Li Y, Chen SH, Spiotta AM, et al. **Lower complication rates associated with transradial versus transfemoral flow diverting stent placement.** *J Neurointerv Surg* 2021;13:91–95 CrossRef Medline
9. Catapano JS, Fredrickson VL, Fujii T, et al. **Complications of femoral versus radial access in neuroendovascular procedures with propensity adjustment.** *J Neurointerv Surg* 2020;12:611–15 CrossRef Medline
10. Zussman BM, Tonetti DA, Stone J, et al. **Maturing institutional experience with the transradial approach for diagnostic cerebral arteriography: overcoming the learning curve.** *J Neurointerv Surg* 2019;11:1235–38 CrossRef Medline
11. Shapiro SZ, Sabacinski KA, Mantripragada K, et al. **Access-site complications in mechanical thrombectomy for acute ischemic stroke: a review of prospective trials.** *AJNR Am J Neuroradiol* 2020;41:477–81 CrossRef Medline
12. Khanna O, Velagapudi L, Das S, et al. **A comparison of radial versus femoral artery access for acute stroke interventions.** *J Neurosurg* 2020 Nov 13. [Epub ahead of print] CrossRef Medline
13. Chen SH, Snelling BM, Sur S, et al. **Transradial versus transfemoral access for anterior circulation mechanical thrombectomy: comparison of technical and clinical outcomes.** *J Neurointerv Surg* 2019;11:874–78 CrossRef Medline
14. Khan NR, Peterson J, Dornbos D III, et al. **Predicting the degree of difficulty of the trans-radial approach in cerebral angiography.** *J Neurointerv Surg* 2020 Aug 13. [Epub ahead of print] CrossRef Medline
15. Rajah GB, Tso MK, Dossani R, et al. **Transradial embolization of the left middle meningeal artery and accessory middle meningeal artery for treatment of subacute-chronic subdural hematoma.** *J Neurointerv Surg* 2020;12:436 CrossRef Medline
16. Shotar E, Pouliquen G, Premat K, et al. **CTA-based patient-tailored femoral or radial frontline access reduces the rate of catheterization failure in chronic subdural hematoma embolization.** *AJNR Am J Neuroradiol* 2021;42:495–500 CrossRef

© D. Dornbos III

Department of Neurosurgery
Semmes-Murphey Clinic
University of Tennessee Health Science Center
Memphis, Tennessee

COVID-19-Associated Acute Disseminated Encephalomyelitis–Like Disease



We read with great interest the article by Toledano-Massiah et al¹ entitled, “Unusual Brain MRI Pattern in 2 Patients with COVID-19 Acute Respiratory Distress Syndrome.” The authors reported 2 patients hospitalized in their intensive care unit with confirmed coronavirus disease 2019 (COVID-19) in whom brain MR imaging had shown an unusual DWI pattern with nodular and ring-shaped lesions involving the periventricular and deep white matter. Based on the recent literature, the authors discussed the probable mechanism of action for Severe Acute Respiratory Syndrome coronavirus disease 2 (SARS-CoV-2) neurologic invasion.

We treated 2 hospitalized patients who share some similarities with the reported unusual brain MR imaging pattern. Patient 1 was a previously healthy 49-year-old man whose CT revealed interstitial pneumonia and with real-time polymerase chain reaction (RT-PCR) was positive for SARS-CoV-2. Endotracheal intubation and mechanical ventilation with prolonged sedation were required because of severe respiratory failure. He presented with delayed recovery of consciousness after protracted sedation. Patient 2 was a previously healthy 9-year-old child with a family history of COVID-19 who had difficulty walking and speaking, right hemiparesis, and impaired ocular motor function. There were no respiratory symptoms. The serologic test for COVID-19 was positive.

Brain MR imaging was performed on day 30 from hospitalization for patient 1 (day 5 after the sedation) (Fig 1) and on day 7 for patient 2 (day 37 after the first symptoms) (Fig 2). At that time, patient 1 showed progressive clinical and laboratory improvement of COVID-19, and patient 2 remained without respiratory symptoms with blood RT-PCR negative for SARS-CoV-2. The CSF RT-PCR for SARS-CoV-2 was negative for patient 1 and not available for patient 2.

Even though the authors have concluded that the etiology and physiopathology of these unusual brain lesions are still not clarified, these 2 additional patients reinforce the inflammatory mechanism hypothesis. Acute disseminated encephalomyelitis (ADEM) is a rare immune-mediated demyelinating disease that has been associated with vaccine and viral infections, including SARS-CoV-2 infection.²

The causative neuropathogenic mechanism of SARS-CoV-2 infection should be carefully analyzed. In particular, patient 2 was asymptomatic for about 30 days, and the RT-PCR test was not performed. Nevertheless, we presumed that the infection had acted as a trigger for developing an autoimmune response that manifested in the central nervous system as ADEM in these 2 additional patients. The perception that the appearance of neurologic symptoms had happened simultaneously with both progressive clinical and laboratory improvement or after the SARS-CoV-2 infection reinforces this hypothesis. Furthermore, the imaging findings also suggested an “ADEM-like” pattern.

In conclusion, we thank the authors for sharing their experiences. Together, we provide valuable information about unusual brain MR imaging patterns in patients with COVID-19. We believe that given the cumulative evidence of the probable neuroinvasive nature of SARS-CoV-2, the association of COVID-19 with neurologic manifestations cannot be ignored, either by direct cytopathic effect or, mainly, by an immune-mediated inflammatory response. Thus, it is vital to be aware of the multitude of neurologic manifestations in patients with COVID-19 and be open-minded about possible new clinical-radiologic presentations and courses.

REFERENCES

1. Toledano-Massiah S, Badat N, Leberre A, et al. **Unusual brain MRI pattern in 2 patients with COVID-19 acute respiratory distress syndrome.** *AJNR Am J Neuroradiol* 2020 Sept 3. [Epub ahead of print] CrossRef Medline
2. Novi G, Rossi T, Pedemonte E, et al. **Acute disseminated encephalomyelitis after SARS-CoV-2 infection.** *Neurol Neuroimmunol Neuroinflamm* 2020;7:e797 CrossRef Medline

F.B. Assunção
Division of Neuroradiology
Santa Casa de Misericórdia de São Paulo
São Paulo-SP, Brazil
Division of Neuroradiology
Rede de Hospitais São Camilo de São Paulo
São Paulo-SP, Brazil

D.C. Fragoso
Division of Neuroradiology
Santa Casa de Misericórdia de São Paulo
São Paulo-SP, Brazil

T.L.P. Donoso Scoppetta
Division of Neuroradiology
Santa Casa de Misericórdia de São Paulo
São Paulo-SP, Brazil
Division of Neuroradiology
Rede de Hospitais São Camilo de São Paulo
São Paulo-SP, Brazil

A.C. Martins Maia
Division of Neuroradiology
Santa Casa de Misericórdia de São Paulo
São Paulo-SP, Brazil

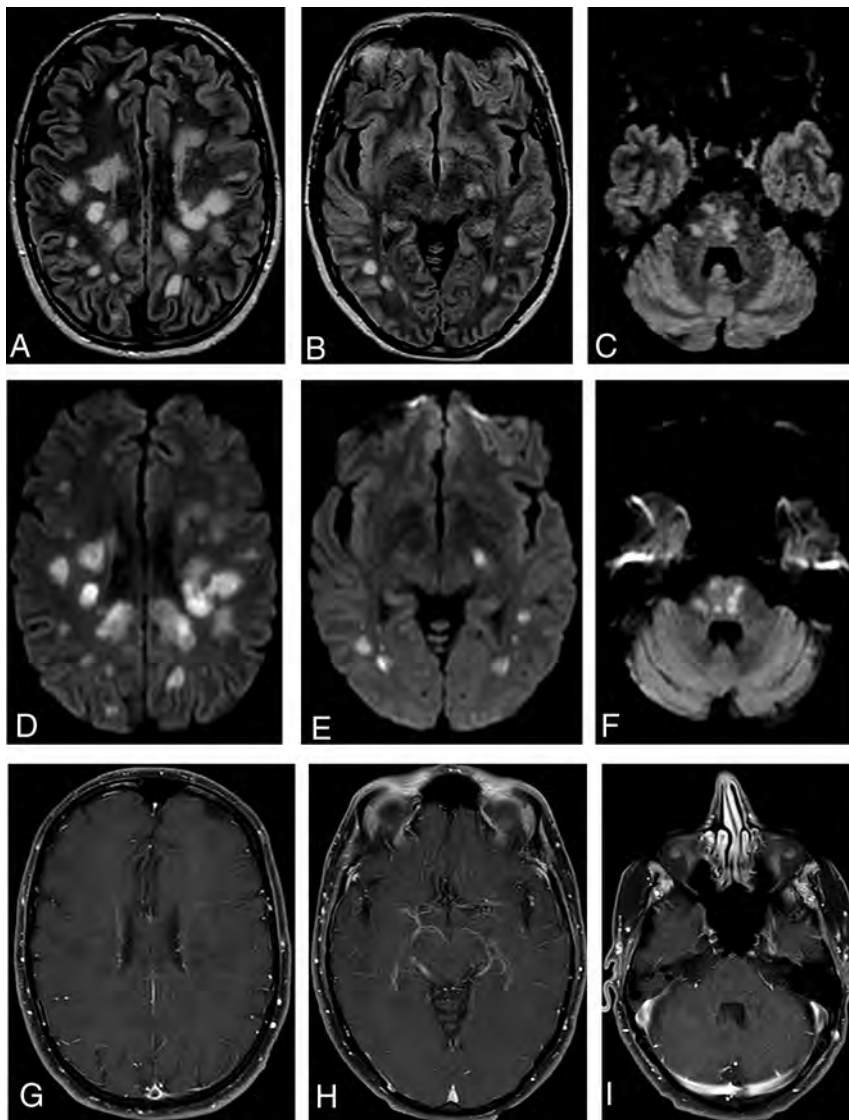


FIG 1. FLAIR images (A–C) depict multiple nodular/oval hyperintensities that involve the deep and periventricular cerebral white matter, splenium of the corpus callosum, and pons. All lesions show restricted diffusion on DWI sequences (D–F). Neither gadolinium enhancement (G–I) nor hemorrhages (not shown) were demonstrated.

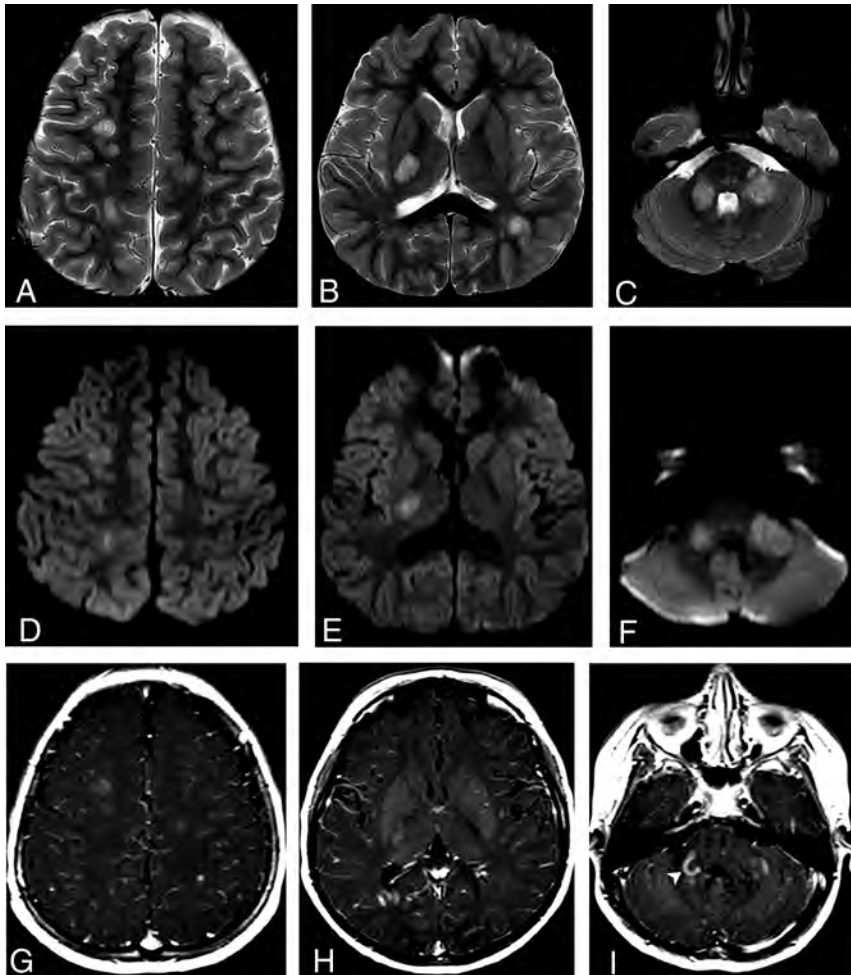


FIG 2. Axial T2WI (A–C) demonstrates multiple large hyperintense oval lesions predominantly affecting the subcortical WM of the cerebral hemispheres, the posterior arm of the right internal capsule, and the infratentorial fossa structures, particularly in the middle cerebellar peduncles. All lesions concurrently demonstrate diffusion restriction observed in the diffusion sequence (D–F) and gadolinium enhancement in the postcontrast T1 sequence (G–I). Most lesions have an open-ring enhancement pattern, best characterized in the right middle cerebellar peduncle (arrowhead in I).

Primary Angiitis of the CNS with Unremarkable Vessel Wall MR Imaging: How the “T1 Shinethrough” Effect on SWI Adds to the Detection of Gadolinium Enhancement of Small Intraparenchymal Brain Vessels

The article published by Suthiphosuwat et al¹ in the September 2020 edition of *AJNR* made a strong impression on us. The authors elaborate on the clinical, histopathologic, and imaging findings of biopsy-proved cases of primary central nervous system vasculitis (PCNSV).

One of the major difficulties in the diagnosis of tumefactive primary CNS vasculitis (t-PCNSV) is the differentiation of this condition from malignant neoplasms.^{1,2} The absence of abnormalities in large- and medium-sized vessels on CTA, MRA, and high-resolution vessel wall imaging makes it even more unlikely for this entity to be included in the list of differential diagnoses for expansive-appearing lesions of the brain.¹ The main reason for the unremarkable angiographic studies might be the preferential involvement of small-sized vessels with relative sparing of medium and large arteries in this PCNSV subtype.^{1,2}

An imaging pattern that has been associated with cerebral small-vessel inflammatory disease is that of linear or punctuate enhancement in the brain parenchyma identified in postgadolinium T1-weighted imaging.^{1,2} That pattern of enhancement mimics the location of perivascular spaces, suggesting a distribution along the axis of small vessels in the brain, and has therefore been termed perivascular enhancement.² However, on most conventional gadolinium-enhanced T1-weighted imaging sequences, this perivascular distribution can only be presumed because most clinically available MR imaging equipment does not offer enough spatial resolution to visually identify the gadolinium enhancement actually surrounding the vessels. Even vessel wall imaging, which can clearly demonstrate gadolinium enhancement in large- and medium-sized artery walls, fails to visually depict the perivascular nature of linear and punctuate enhancement in the brain (Fig 1).

SWI is a relatively recent technique of MR imaging that combines both phase and magnitude signal to produce

high-resolution images that provide higher sensitivity than T2*-weighted imaging to detect brain hemorrhage and calcification.³ It is also useful to acquire intracranial venography (venous bold imaging).³ Although in that sequence the T2* and phase effects are dominant, the signal intensity is also a function of molecular transverse relaxation time for gradient-echo imaging; therefore, T1 effects are still present.⁴ This phenomenon is termed the “T1 shinethrough” effect and can be exploited for the detection of pathologic gadolinium enhancement in the brain tissue with several applications, ranging from neuro-oncology to demyelinating diseases.⁴ The strong contrast resolution provided by gadolinium-enhanced SWI caused by the combination of its T2* intracranial venographic effect and T1 shinethrough effect might prove itself helpful in the characterization of perivascular gadolinium enhancement in small-sized vessel vasculitis (Fig 2). The strong T2* effect in SWI sequences allows the identification of the very low-intensity signal of small vessels within the brain parenchyma, surrounded by a hyperintense background determined by a T1 shinethrough effect caused by the highly paramagnetic gadolinium in the vessel walls and adjacent tissues. In some studies, it is possible to identify a perivascular annular area of enhancement surrounding the vessels, which we coined the “silver ring sign” (Fig 2D). This high-contrast resolution obtained between small vessels and the surrounding tissue gadolinium enhancement is the same principle that allows the visualization of a small-sized central medullary vein in demyelinating lesions in MS.⁴

The applications of the gadolinium-enhanced SWI sequence have been growing recently. Therefore, we believe this sequence might also have the potential to add information on the currently difficult issue of diagnosing t-PCNSV. Further research is necessary to determine whether it can add to the sensitivity and specificity of such diagnosis. Also, we encourage the study of postgadolinium SWI for

<http://dx.doi.org/10.3174/ajnr.A6973>

other potential applications in this scenario, such as biopsy guidance and treatment follow-up.

ACKNOWLEDGMENTS

The authors would like to thank GE Healthcare LATAM for the scientific support.

REFERENCES

1. Suthiphosuwat S, Bharatha A, Hsu CC, et al. **Tumefactive primary central nervous system vasculitis: imaging findings of a rare and underrecognized neuroinflammatory disease.** *AJNR Am J Neuroradiol* 2020;41:2075–81 CrossRef Medline
2. Abdel Razek AAK, Alvarez H, Bagg S, et al. **Imaging spectrum of CNS vasculitis.** *Radiographics* 2014;34:873–94 CrossRef Medline
3. Haacke EM, Mittal S, Wu Z, et al. **Susceptibility-weighted imaging: technical aspects and clinical applications, part 1.** *AJNR Am J Neuroradiol* 2009;30:19–30 CrossRef Medline
4. Hsu CCT, Haacke EM, Heyn CC, et al. **The T1 shine through effect on susceptibility weighted imaging: an under recognized phenomenon.** *Neuroradiology* 2018;60:235–37 CrossRef Medline

© A.P.A. Fonseca

© R.L. do Carmo

© F.T. Pacheco

© R.H. Nunes

© A.J. da Rocha

Division of Neuroradiology
Diagnosticos da America SA
Sao Paulo, Brazil

Division of Neuroradiology
Santa Casa de Sao Paulo School of Medical Sciences
Sao Paulo, Brazil

Division of Neuroradiology
United Health Group
Sao Paulo, Brazil

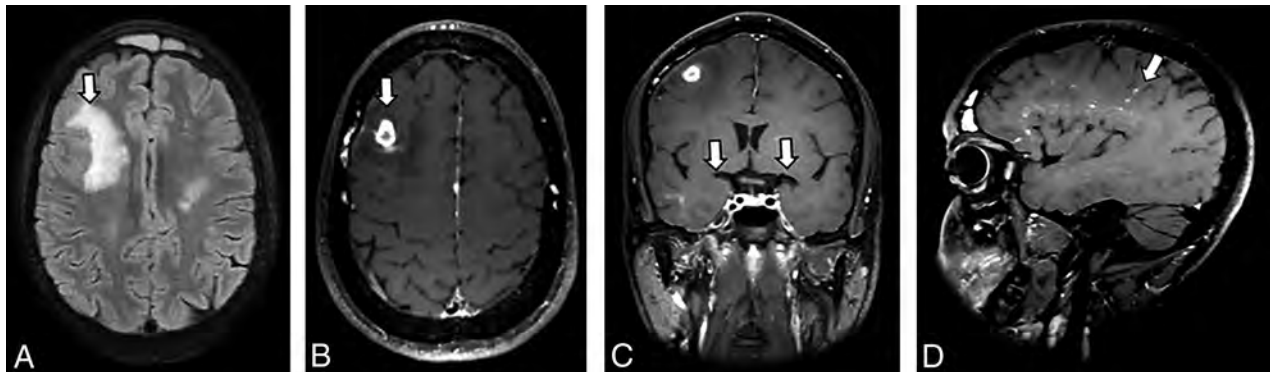


FIG 1. MR imaging findings in a 42-year-old man with biopsy-confirmed t-PCNSV. Axial fluid-attenuated inversion recovery (A) and postgadolinium T1-weighted imaging (B) demonstrate an expansive-appearing lesion (arrows) with ring enhancement in the right frontal lobe surrounded by an area of vasogenic edema. Coronal reformat 3D CUBE T1-weighted vessel wall image (C) at the internal carotid bifurcation shows no large- or medium-sized artery wall enhancement (arrows). Sagittal reformat of the 3D CUBE T1-weighted vessel wall image (D) depicts multiple linear or nodular foci of enhancement (arrow) within the right hemisphere white matter, with a striking radial distribution attributable to a perivascular location.

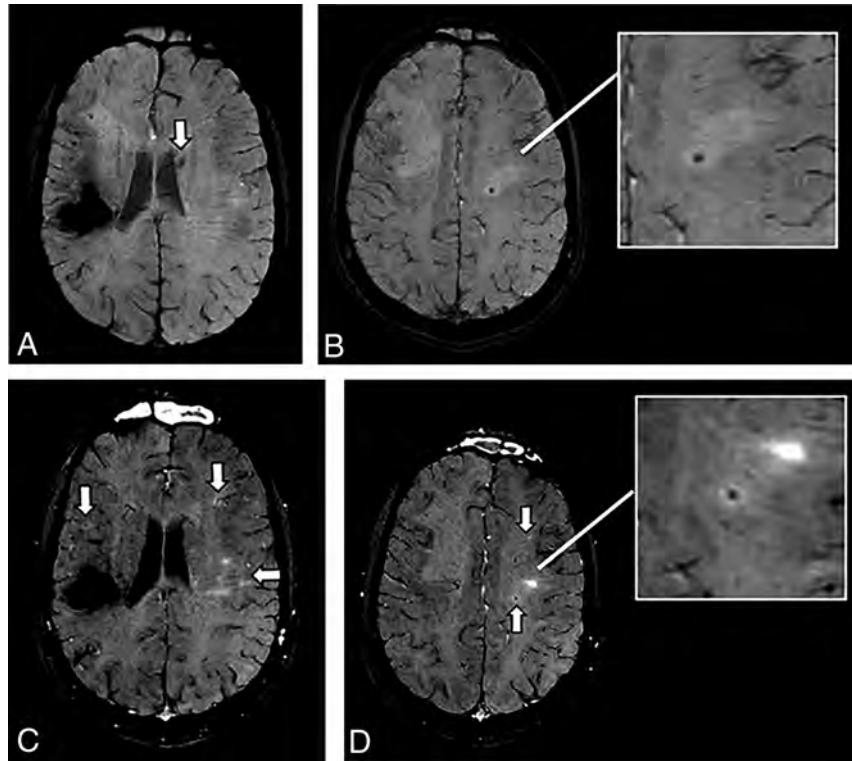


FIG 2. SWI findings of the same patient. Axial pregadolinium SWI (A and B) shows a large hemorrhage in the right brain hemisphere and a smaller hematic focus in the body of left caudate nucleus (*arrow*). Postgadolinium SWI (C and D) shows selective perivascular gadolinium enhancement along the parenchymal small-sized vessel walls (*arrows*). The “silver ring sign” is depicted in the amplified image in D.

Inconsistencies between Radiologic and Cadaveric Studies of the Occipital Sinus

The fetal and postnatal development patterns of dural venous sinuses are not fully understood. In their article, published in the *American Journal of Neuroradiology* in October 2020, Larson et al¹ examined the development of dural venous sinuses using MR venography in more than 400 patients. They found that all dural venous sinuses reached their maximum diameters around 5–10 years of age, and the occipital sinus was found in only 2.8% of individuals 16–20 years of age. These findings led the authors to conclude that the occipital sinus disappears gradually from birth to 20 years of age; therefore, it is rarely observed in postnatal life. However, these findings ignore the technical limitations of MR imaging. In another study using MR venography, the occipital sinus was observed in 10% of cases, and it was suggested that artifacts encountered due to flow gaps and the complexity of intravascular blood flow may have caused this low percentage.² In contrast, human cadaver studies have shown that 90% of individuals have an obvious occipital sinus.³ During the opening of the dura of the posterior cranial fossa, various surgical maneuvers are performed to specifically avoid damage to the occipital sinus and unnecessary bleeding.⁴ Consequently, the infrequent observation of the occipital sinus in MR venograms is likely related to

technical factors, because it is not supported by either anatomic or clinical observations.

Disclosures: Naci Balak—UNRELATED: Employment: Istanbul Medeniyet University, Göztepe Hospital, Istanbul, Turkey.

REFERENCES

1. Larson AS, Lanzino G, Brinjikji W. Variations of intracranial dural venous sinus diameters from birth to 20 years of age: an MRV-based study. *AJNR Am J Neuroradiol* 2020;41:2351–57 CrossRef Medline
2. Ayanzen RH, Bird CR, Keller PJ, et al. Cerebral MR venography: normal anatomy and potential diagnostic pitfalls. *AJNR Am J Neuroradiol* 2000;21:74–78 Medline
3. Balak N, Ersoy G, Uslu Ü, et al. Microsurgical and histomorphometric study of the occipital sinus: quantitative measurements using a novel approach of stereology. *Clin Anat* 2010;23:386–93 CrossRef Medline
4. Yaşargil MG, Curcic M, Abernathy CD. *Microneurosurgery of CNS Tumors*. Vol 4B. Thieme Medical Publishers; 1996:62–64

 Naci Balak

Department of Neurosurgery
Istanbul Medeniyet University
Göztepe Hospital
Istanbul, Turkey

<http://dx.doi.org/10.3174/ajnr.A6977>

REPLY:

We read with interest the letter by Balak regarding our study. We appreciate the interest in our study. We agree that perhaps the right terminology is not to say that the occipital sinus regresses, because it is likely always persistent, but that it no longer plays a dominant role in the dural venous sinus drainage pathway. There have been numerous examples in the literature of embryonic sinuses (of which we consider the occipital sinus to be one) recanalizing or playing a dominant role in cerebral venous drainage due to the presence of arteriovenous shunting lesions or venous sinus thrombosis.¹⁻³ In this regard, the author is correct; in all likelihood, the occipital sinus is present but just does not have enough flow to be opacified on the MRV study.

<http://dx.doi.org/10.3174/ajnr.A6986>

REFERENCES

1. Varma D, Reddy B, Rao R. **Recanalization and obliteration of falcine sinus in cerebral venous sinus thrombosis.** *Neurology* 2008;70:79–80 CrossRef Medline
2. Kawauchi T, Ikeda H, Miyakoshi A, et al. **Occipital sinus dural arteriovenous fistula presenting with cerebellar hemorrhage.** *World Neurosurg* 2019;131:116–19 CrossRef Medline
3. Tanaka J, Fujita A, Maeyama M, et al. **Cognard type V dural arteriovenous fistula involving the occipital sinus.** *J Stroke Cerebrovasc Dis* 2017;26:e62–63 CrossRef Medline

 **A.S. Larson**

Department of Radiology

 **W. Brinjikji**

Department of Radiology

Department of Neurosurgery

Mayo Clinic

Rochester, Minnesota

The So-Called Cranial Dural Channels and Their Relationship with the Bridging Veins

With great interest, we read the paper “Dural Venous Channels: Hidden in Plain Sight—Reassessment of an Under-Recognized Entity” by M. Shapiro et al.¹ The authors should be commended for drawing the attention of readers to what is a common experience among neurointerventionalists performing cerebral angiographies on a daily basis: the extreme variation of the cerebral venous—including the dural—system. In the literature and in everyday practice, we used to call these channels “convexial sinuses,” “accessory sinuses,” “tributary sinuses,” or even “no-name sinuses” when located in the convexial dura. Therefore, it is a common finding, but certainly their recognition requires a minimum angiographic experience and attention. We definitely concur that their frequency is at least 26% as the authors found, if not higher. These flattened channels may be very short or very long.² In the latter, the bridging veins emptying into them appear away from the typical sinuses, and this is the reason why a bridging vein fistula³ is sometimes found in a convexial location.

However, we should not forget that we are talking about images and radiologic impressions. Therefore, we have to clarify the following point: do they really represent a part of the dural sinus network, as the name “dural channel” implies, or is it simply the intradural course of the bridging vein, which may be short or longer? In the first case, the channel should be indistinguishable from the rest of the dural venous sinuses and histologically equivalent to a sinus, whereas in the second, we are dealing with a vein covered by or embedded in the dura but still a vein. Although we cannot answer this question in an absolute way for all observed cases, we can certainly state that often we are dealing with the intradural course of the bridging vein and not with a “dural,” properly speaking, channel. In our dural anatomy project, we have seen several bridging veins with such an intradural course (Figure). The same configuration can be seen, though extremely rarely, also in the spinal cord (anecdotal data), where no sinuses exist. In our study, we have not found yet a dural channel as meant by the authors;¹ however, it may well be related to the small number of the cases studied until now. Therefore, we are not sure if the proposed unifying name “dural venous channels” is a good idea.

Regarding the statement “They may play a role in the angioarchitecture of dural arteriovenous fistulas that appear to

drain directly into the cortical vein,” it is unclear if the authors mean that these dural channels may represent the actual location of the shunt. In our experience, the shunt is not located in that channel. Until now, we have not seen a fistula located in such a channel, in a tentorial one (tentorial sinus), or in a falcine or a convexial one, despite years of observation trying to distinguish features implying such a location. On the contrary, detailed analyses of the angiographic images, sometimes also correlated with surgical views, convince us that the exact location of the shunt is the junction of the bridging vein with the dura.³ This is why bridging vein fistulas occur even without such a “dural venous channel.”

Disclosures: Gerasimos Baltasvias—UNRELATED: Employment: International Neuroscience Institute (INI); RELATED: Grant: Gesellschaft für die Förderung der Wissenschaft in der Neurochirurgie e.V, Hannover, Germany.*; RELATED: Employment: Neuroradiology, Hannover Medical School, Germany. Heinrich Lanfermann—UNRELATED: Employment: Director of the Institute of Diagnostic and Interventional Neuroradiology, Hannover Medical School, Germany.

REFERENCES

- Shapiro M, Srivatanakul K, Raz E, et al. **Dural venous channels: hidden in plain sight—reassessment of an under-recognized entity.** *AJNR Am J Neuroradiol* 2020;41:1434–40 CrossRef Medline
- Baltasvias G, Bhatti A, Valavanis A. **Lateral convexial tributary sinus of superior sagittal sinus. A rare anatomic variation and the importance of its recognition.** *Clin Neurol Neurosurg* 2013;115:2268–69 CrossRef Medline
- Baltasvias G, Parthasarathi V, Aydin E, et al. **Cranial dural arteriovenous shunts. Part 1. Anatomy and embryology of the bridging and emissary veins.** *Neurosurg Rev* 2015;38:253–63 CrossRef Medline

 **Gerasimos Baltasvias**
International Neuroscience Institute
Hannover, Germany
Neuroradiology Department
Medical School Hannover
Hannover, Germany

 **Vincenzo Paterno**
International Neuroscience Institute
Hannover, Germany

 **Heinrich Lanfermann**
Neuroradiology Department
Medical School Hannover
Hannover, Germany

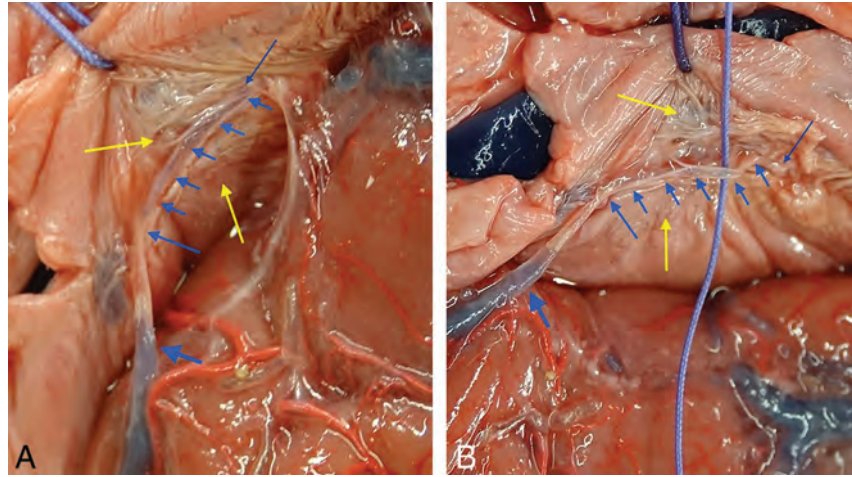


FIGURE. A, Cadaveric preparation showing a bridging vein (*thick blue arrow*) reaching the dura (*blue arrow*) at the lateral wall of the superior sagittal sinus and falx (*yellow arrows*), continuing (*incomplete silicon penetration*), embedded into the dura (*multiple short blue arrows*) to its piercing point (*thin blue arrow*), where it enters the sinus. Even macroscopically, one may see the bridging vein buried, not just adherent to and still easily distinguishable from the dura. The vein can be microsurgically prepared and separated from the dura, as it is shown in B (photo slightly tilted to the right compared with A).

REPLY:

We are extremely thankful to the Hannover group for forwarding to the Editor their deep insights and critique. We see the resulting exchange as an excellent opportunity for a substantive anatomic discussion and debate in the Journal.

It appears that we agree on most points. We agree that study of vascular dural anatomy requires gross pathology and histology material, as acknowledged in the Limitations section of our publication. We agree that the channels we both reported go by varied names, hindering a comprehensive literature search. We also agree that the distinction between dural venous channels and bridging veins traversing the dura is not semantic, and furthermore, we agree that from the perspective of surgical safety this distinction is immaterial. We have also observed, in a less structured setting than your group (during surgery), the appearance of bridging veins traversing the dura to join with the recipient dural sinus.

The question as to whether a venous structure, once inside the dura, retains anatomic characteristics of a vein or assumes those of a venous sinus is a histologic question and, in our opinion, cannot be answered for all structures in question by either imaging or gross examination. Where we disagree is that we believe, based on existing evidence, that the structures we illustrated are sinuses:

1. They are lens-shaped, not round. This morphology closely resembles undisputed venous sinuses that traverse the dural sheets such as duplicated superior sagittal, falcine, and occipital sinuses (Fig 1A–F, Fig 2A, -B).
2. We have observed what appear to be arachnoid granulations inside several of the channels we called “dural venous sinuses,” which are certainly not a structure expected in a bridging vein (Fig 2C,-D and Fig 6 in our original publication).
3. Existence of tentorial venous sinuses is generally accepted, which is no proof of truth, but a strong supporting argument for the presence of similar channels in the supratentorial compartment (Fig 1G).

We view the dura as a sort of arterial and venous “tabula rasa”—meaning any part of the dura can form a sinus when sufficient flow or other factors encourage it—both in utero and under pathologic circumstances such as a falcotentorial fistula. Indeed, we feel this

view is entirely consistent with Padgett’s investigations,¹ repeatedly emphasizing the plexiform nature of dural venous structures.

Regarding the relationship between dural venous channels and dural fistulas, we feel that the varied opinions held by multiple groups as to their etiology and vascular pathoanatomy, given the relative paucity of data, are such that a productive discussion on the matter at this stage may be premature.

In conclusion, we believe that both bridging veins traversing the dura and supratentorial dural venous channels exist, and both are common. We continue to prefer the term “dural venous channel,” unless new data disprove this view. Perhaps “intradural venous channel” would be more of a semantic compromise. Regardless of whether any name at all will “catch,” we feel confident that both our efforts in this arena will continue.

ACKNOWLEDGMENTS

We thank Dr. Matthew G. Young (Department of Radiology, NYU Grossman School of Medicine, New York, New York) for generating the cinematic rendering images in Figure 1.

REFERENCE

1. Padgett DH. **The cranial venous system in man in reference to development, adult configuration, and relation to the arteries.** *Am J Anat* 1956;98:307–55 CrossRef Medline

M. Shapiro

Department of Radiology and Neurology
NYU Grossman School of Medicine
New York, New York

K. Srivatanakul

Department of Neurosurgery
Tokai University
Kanagawa, Japan

E. Raz

Department of Radiology
NYU Grossman School of Medicine
New York, New York

M. Litao

Department of Radiology
NYU Grossman School of Medicine
New York, New York

E. Nossek

Department of Neurosurgery
NYU Grossman School of Medicine
New York, New York

P.K. Nelson

Department of Neurosurgery
NYU Grossman School of Medicine
New York, New York

<http://dx.doi.org/10.3174/ajnr.A7098>

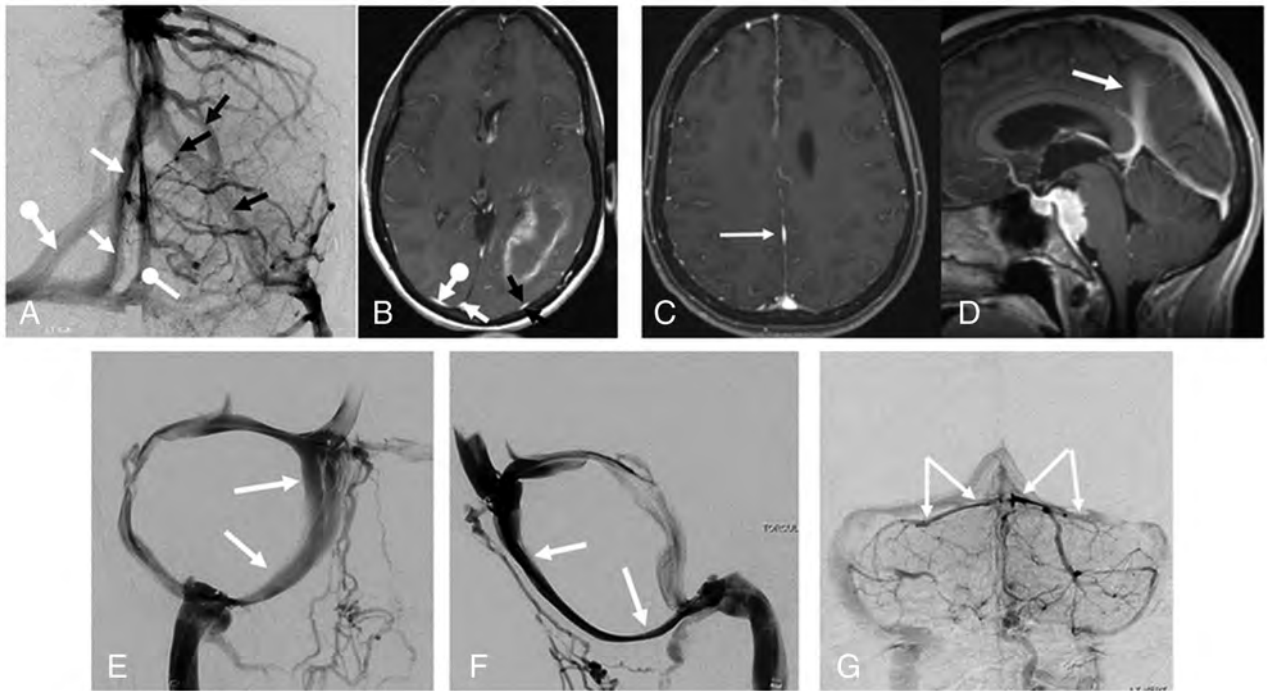


FIG 1. Examples of dural venous sinuses/channels similar to those described in our index article. Angiography (A) and MR imaging (B) of same patient, with multiple dural channels in addition to the usual superior sagittal sinus. The additional channels, marked by similar *arrows* on both angiogram and MR image, are flattened, lens-shaped structures, just like the dural venous channels we describe. C and D, Axial and sagittal MR images of patient with a falcine sinus variant—the same flattened morphology as in A and B. E and F, Morphology of the occipital sinus on a venous digital subtraction injection. G, Typical flattened appearance of tentorial venous sinuses.

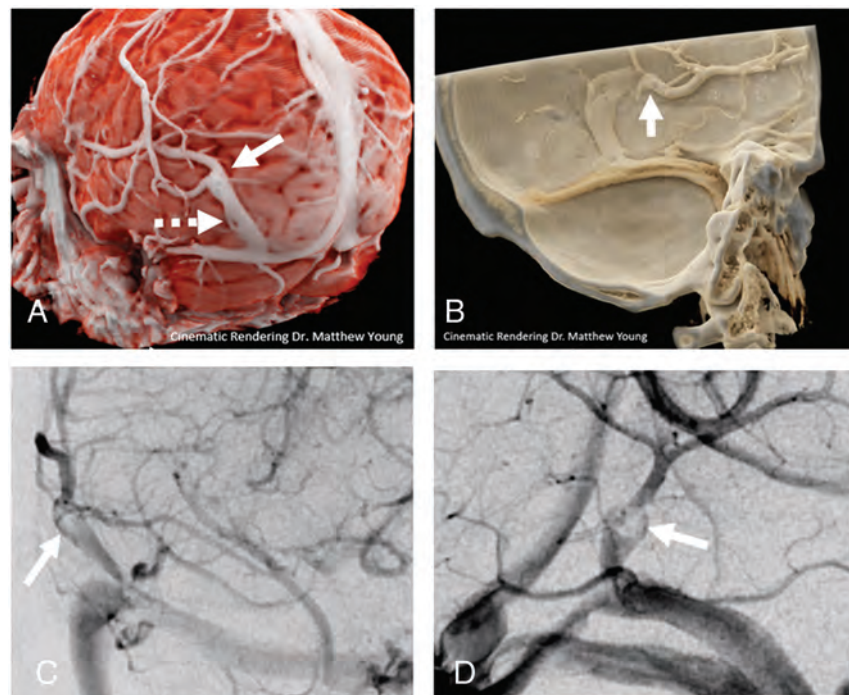


FIG 2. A and B, Cinematic renderings, highlighting transition points (*arrows*) between round bridging vein and flattened dural venous channel in 2 different cases. A small fenestration versus arachnoid granulation is present in A (*dashed arrow*); neither structure would be expected in a bridging vein. Frontal (C) and lateral (D) views of another arachnoid granulation inside a dural venous channel.